Conference Proceedings of the Society for Experimental Mechanics Series

Juan Caicedo · Shamim Pakzad *Editors*

# Dynamics of Civil Structures, Volume 2

## Proceedings of the 35th IMAC, A Conference and Exposition on Structural Dynamics 2017


Springer

# Conference Proceedings of the Society for Experimental Mechanics Series

*Series Editor*

Kristin B. Zimmerman, Ph.D.
Society for Experimental Mechanics, Inc.,
Bethel, CT, USA

More information about this series at http://www.springer.com/series/8922

Juan Caicedo • Shamim Pakzad
Editors

# Dynamics of Civil Structures, Volume 2

## Proceedings of the 35th IMAC, A Conference and Exposition on Structural Dynamics 2017

Springer

*Editors*
Juan Caicedo
Department of Civil
and Environmental Engineering
University of South Carolina
Columbia, SC, USA

Shamim Pakzad
Department of Civil
and Environmental Engineering
Lehigh University
Bethlehem, PA, USA

ISSN 2191-5644 ISSN 2191-5652 (electronic)
Conference Proceedings of the Society for Experimental Mechanics Series
ISBN 978-3-319-54776-3 ISBN 978-3-319-54777-0 (eBook)
DOI 10.1007/978-3-319-54777-0

Library of Congress Control Number: 2017938029



Printed on acid-free paper

This Springer imprint is published by Springer Nature
The registered company is Springer International Publishing AG
The registered company address is: Gewerbestrasse 11, 6330 Cham, Switzerland

# Preface

*Dynamics of Civil Structures* represents one of ten volumes of technical papers presented at the 35th IMAC, A Conference and Exposition on Structural Dynamics, organized by the Society for Experimental Mechanics, and held in Garden Grove, California, January 30–February 2, 2017. The full proceedings also include volumes on *Nonlinear Dynamics*; *Model Validation and Uncertainty Quantification*; *Dynamics of Coupled Structures*; *Sensors and Instrumentation*; *Special Topics in Structural Dynamics*; *Structural Health Monitoring and Damage Detection*; *Rotating Machinery, Hybrid Test Methods, Vibro-Acoustics & Laser Vibrometry*; *Shock & Vibration, Aircraft/Aerospace and Energy Harvesting*; and *Topics in Modal Analysis & Testing*.

Each collection presents early findings from analytical, experimental, and computational investigations on an important area within structural dynamics. *Dynamics of Civil Structures* is one of these areas which cover topics of interest of several disciplines in engineering and science.

The Dynamics of Civil Structures Technical Division serves as a primary focal point within the SEM umbrella for technical activities devoted to civil structure analysis, testing, monitoring, and assessment. This volume covers a variety of topics including damage identification, human-structure interaction, hybrid testing, vibration control, model updating, modal analysis of in-service structures, sensing and measurements of structural systems, and bridge dynamics. Papers cover testing and analysis of all kinds of civil engineering structures such as buildings, bridges, stadiums, dams, and others.

The organizers would like to thank the authors, presenters, session organizers, and session chairs for their participation in this track.

Columbia, SC, USA — Juan Caicedo
Bethlehem, PA, USA — Shamim Pakzad

# Contents

# Chapter 1
# Semi-Active Base Isolation of Civil Engineering Structures Based on Optimal Viscous Damping and Zero Dynamic Stiffness

**Felix Weber, Hans Distl, and Christian Braun**

**Abstract** Spherical friction pendulums (FP) represent the common approach to isolate civil engineering structures against earthquake excitation. As these devices are passive and friction damping is nonlinear the optimal friction coefficient for minimum absolute acceleration of the building depends on the peak ground acceleration (PGA). Therefore, the common procedure is to optimize the friction coefficient for the PGA of the design basis earthquake (DBE) and to verify by simulations that the absolute structural acceleration for the maximum considered earthquake (MCE) is within a tolerable limit which is far from optimal. In order to overcome this drawback of passive FPs, a semi-active FP based on real-time controlled oil damper with the use of the collocated bearing displacement only is described in this paper. Four different semi-active control laws are presented that target to produce controlled dynamic stiffness depending on the actual bearing displacement amplitude in order to control the isolation period in real-time. The desired damping is formulated based on optimal viscous damping taking into account the passive lubricated friction of the spherical surface. The four control laws are compared in terms of absolute structural acceleration, bearing force, bearing displacement and residual bearing displacement. The results point out that the approach of zero dynamic stiffness at center position of the slider and nominal stiffness at design displacement of the FP improves the isolation of the structure within the entire PGA range significantly and at the same time minimize maximum bearing force, maximum bearing displacement and maximum residual bearing displacement.

**Keywords** Control • Damping • Seismic • Semi-active • Negative stiffness

## 1.1 Introduction

Spherical friction pendulums (FP) are widely used to significantly reduce the absolute structural acceleration due to ground excitation by their effective radius that shifts the fundamental time period of the isolated structure into the region of attenuation and their friction damping that augments the damping of the structure [1]. The inherent drawback of FPs is that friction damping is nonlinear whereby the optimal friction coefficient depends on the displacement amplitude of the FP and consequently peak ground acceleration (PGA) [2]. The common approach is therefore to optimize the friction coefficient for the PGA of the design basis earthquake (DBE) and, subsequently, to check if the absolute structural acceleration due to the maximum credible earthquake (MCE) is acceptable. In addition, it must be checked if the isolation of the structure at very small PGAs is acceptable from the comfort point of view since the constant friction coefficient being optimal for the PGA of the DBE may lead to clamping effects in the FP whereby the relative motion stops in the FP and consequently the structural absolute acceleration is equal to the ground acceleration. In order to overcome these drawbacks of FPs several types of adaptive FPs have been developed: FPs with several sliding surfaces with different friction coefficients and effective radii [3] and pendulums that are extended by an external active or semi-active actuator such as hydraulic cylinders and controllable dampers on the basis of oil dampers with controlled bypass valve or magnetorheological fluids [4–7]. Controllable dampers

F. Weber (✉)
Maurer Switzerland GmbH, Neptunstrasse 25, 8032 Zurich, Switzerland
e-mail: F.Weber@maurer.eu

H. Distl
Maurer Söhne Engineering GmbH & Co. KG, Frankfurter Ring 193, 80807 Munich, Germany
e-mail: Distl@maurer.eu

C. Braun
MAURER SE, Frankfurter Ring 193, 80807 Munich, Germany
e-mail: Braun@maurer.eu



J. Caicedo, S. Pakzad (eds.), *Dynamics of Civil Structures, Volume 2*, Conference Proceedings of the Society for Experimental Mechanics Series, DOI 10.1007/978-3-319-54777-0_1

are seen to provide a promising solution as the resulting closed-loop is unconditionally stable and their power consumption is very low compared to hydraulic actuators. This paper describes a novel approach of a semi-active isolator with the following main features:

- controlled dynamic stiffness depending on the actual displacement amplitude of the pendulum,
- optimum viscous damping, and
- collocated control based on one displacement sensor.

## 1.2 Systems Under Consideration

### *1.2.1 Friction Pendulum*

The common way to decouple the building/structure from the shaking ground is to support the building by FPs. The effective radius $R_{eff} = R - h$ of the FP is selected to shift the time period $T$ of the non-isolated structure from the region of amplification, i.e. $T$ is typically in the region 0.5–2.0 s, to the region of attenuation with associated isolation time period $T_{iso}$ of typically 3–4 s. Subsequent to the design of the effective radius the friction coefficient $\mu$ of the sliding surface is optimized for minimum absolute structural acceleration for given $T_{iso}$. As **friction damping is nonlinear**, the optimal value of $\mu$ depends on the **bearing displacement amplitude and consequently on PGA**. As a result, $\mu$ is commonly optimized for the PGA of the DBE. Finally, the structure with the designed FP is computed for the PGA due to the MCE to check if the absolute structural acceleration resulting from the MCE is acceptable and to know the displacement capacity of the FP that is required for the MCE.

### *1.2.2 Viscous Pendulum*

In addition to the passive FP an "ideal" pendulum without friction but with linear viscous damping is considered as benchmark for passive isolators. Its effective radius is equal to that of the FP to ensure the same isolation time period $T_{iso}$. Its viscous damping coefficient $c$ is optimized for minimum absolute structural acceleration. Thanks to the **linear behavior of viscous damping** the optimization of $c$ in **independent of the bearing displacement amplitude and therefore independent of PGA**.

### *1.2.3 Semi-Active Isolator*

The semi-active isolator consists of a passive FP and a semi-active damper that is installed between ground and top bearing plate of the pendulum (Fig. 1.1). The design of the effective radius will be explained in the section "CONTROL LAW" as it is related to the formulation of the control law. The **sliding surface** of the passive FP is **lubricated to minimize the passive and therefore uncontrollable friction damping** of the semi-active isolator and thereby to maximize the controllability of the total isolator force. The dissipative force of the semi-active damper is controlled by the electromagnetic bypass valve. The desired control force is computed by the real-time controller based on the measured bearing displacement which is identical to the relative motion between damper cylinder and damper piston. Based on the desired control force a force tracking module computes the valve command signal such that the actual force of the semi-active damper tracks closely its desired counterpart in real-time.

## 1.3 Modelling

Due to the large isolation time period $T_{iso} = 3.5$ s of the building with isolator the building may be modelled as a single degree-of-freedom system [1]. The according equation of motion becomes

$$m_s\,\ddot{u}_s + c_s\,\left(\dot{u}_s - \dot{u}\right) + k_s\,\left(u_s - u\right) = -m_s\,\ddot{u}_g \tag{1.1}$$

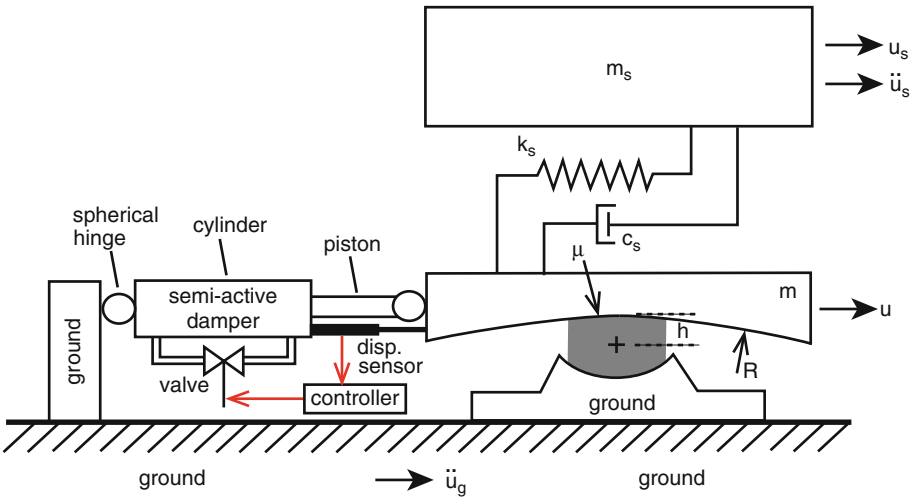


**Fig. 1.1** Schematic of structure with semi-active isolator

where $m_s$, $c_s$, $k_s$ denote the modal mass, the viscous damping coefficient and the stiffness of the building, $\ddot{u}_s$, $\dot{u}_s$ and $u_s$ denote the acceleration, velocity and displacement of the structure relative to the ground, $\dot{u}$ and $u$ are the velocity and displacement of the top bearing plate relative to the ground and $\ddot{u}_g$ is the ground acceleration given by the accelerogram of the El Centro North-South earthquake. The mass $m_s$ is determined by the typical vertical load of $W = 6$ MN on the isolator, $c_s = 2\ \zeta_s\ \sqrt{k_s\ m_s}$ is computed based on the damping ratio $\zeta_s = 1\%$ and $k_s = 24.15$ MN/m is selected such that the natural frequency of the building without isolator is 1 Hz representing a typical value for structures that require base isolation. The equation of motion of the top plate of the isolator with mass $m$ and with actual force $f^{actual}_{semi-active}$ of the semi-active oil damper is

$$m\ \ddot{u} + f_h + \frac{W}{R_{eff}}\ u = c_s\ \ (\dot{u}_s - \dot{u}) + k_s\ \ (u_s - u) - f^{actual}_{semi-active} - m_s\ \ddot{u}_g \tag{1.2}$$

where $f_h$ is the friction force of the curved sliding surface and $W/R_{eff}$ is the restoring stiffness due to the effective radius $R_{eff} = R - h$ of the pendulum. The force $f_h$ is modelled by the hysteretic damper modelling approach [8]

$$f_h = \begin{cases} k_h\ u & : pre - sliding \\ \mu\ W\ sign\ (\dot{u}) & : \quad sliding \end{cases} \tag{1.3}$$

where $k_h$ is the pre-sliding stiffness that is selected two orders of magnitude greater than $W/R_{eff}$. In case of the passive pendulum without any friction but linear viscous damping $f_h$ in (1.2) is replaced by the term $c^{opt}\ \dot{u}$ where $c^{opt}$ denotes the optimal viscous damping coefficient of the isolator.

## 1.4 Control Law

### *1.4.1 General Formulation*

The desired active control force is formulated as follows

$$f^{desired}_{active} = \begin{cases} k_{control}\ u + \left(c^{opt} - c_\mu\right)\ \dot{u} : c - c_\mu \geq 0 \\ k_{control}\ u \qquad\qquad\quad : c - c_\mu < 0 \end{cases} \tag{1.4}$$

in order to produce:

1. the controlled stiffness $k_{control}$ that **is controlled as function of the bearing displacement amplitude** $U$ to compensate for the passive stiffness of the curved surface given by $W/R_{eff}$ and thereby produce **zero dynamic stiffness by** $k_{control} < 0$ **for maximum decoupling of the structure from the ground**, and
2. the controlled damping force $\left(c^{opt} - c_{\mu}\right)\ \dot{u}$ that **dissipates the same amount of damping as resulting from optimal linear viscous damping**.

The desired optimal viscous damping coefficient $c^{opt}$ is reduced by the viscous damping coefficient $c_{\mu}$ that is energy equivalent to the friction damping of the lubricated curved surface [2]

$$c_{\mu} \approx \frac{4}{\pi} \frac{\mu\ W}{\omega_{iso}\ U} \tag{1.5}$$

in order to dissipate the cycle energy of optimal viscous damping. Since $c_{\mu}$ is inversely proportional to the displacement amplitude $U$ of the isolator, i.e. $c_{\mu} \sim U^{-1}$, $c_{\mu}$ may become greater than $c^{opt}$ at small $U$ which necessitates the distinction of cases in (1.4). Notice that (1.5) represents an approximation because $c_{\mu}$ according to Eq. (1.5) is derived based on the constant isolation radial frequency

$$\omega_{iso} = \sqrt{\frac{g}{R_{eff}}} \tag{1.6}$$

but the actual frequency of the bearing displacement due to earthquake excitation is time-variant and therefore not detectable in real-time. However, the **approximation** (1.5) represents a **good engineer's solution** as the actual frequency is in the vicinity of $\omega_{iso}$. The actual force of the semi-active oil damper can only produce the dissipative forces of the desired active control force $f_{active}^{desired}$, that is

$$f_{semi-active}^{actual} = \begin{cases} f_{active}^{desired} & : \dot{u}\, f_{active}^{desired} \geq 0 \\ 0 & : \dot{u}\, f_{active}^{desired} < 0 \end{cases} \tag{1.7}$$

The formulation (1.7) assumes that control force constraints such as minimum and maximum forces of the semi-active oil damper and control force tracking errors do not exist. Hence, the formulation (1.7) of the semi-active force represents the ideal behavior of a controllable damper.

### *1.4.2 Adaptive Controlled Stiffness*

The maximum decoupling of the structure from the shaking ground and therefore minimum absolute structural acceleration $\ddot{u}_s + \ddot{u}_g$ is obtained from **zero dynamic stiffness** of the isolator [9]. Since the passive (and positive) stiffness of the isolator is given by $W/R_{eff}$, the controlled stiffness $k_{control}$ must be **negative** to reduce the total stiffness $k_{total}$ of the isolator to zero under dynamic operation. However, $k_{total} = 0$ for the entire bearing displacement range could not **re-center** the structure sufficiently. Hence, four adaptive stiffness control laws are suggested that produce zero dynamic stiffness either at $U = 0$ or at $U \geq U_{\max}$ due to the MCE:

- Control law #1 (CL #1, Fig. 1.2a): The effective radius $R_{eff}$ of the curved surface is 50% of the nominal effective radius $R_{eff-no\min al}$ generating the targeted isolation time period $T_{iso} = 3.5$ s. The controlled stiffness is formulated to produce $k_{total} = k_{control} + W/R_{eff} = k_{R-eff-no\min al} = W/R_{eff-no\min al}$ at $U = 0$ and zero dynamic stiffness, i.e. $k_{total} = 0$, at $U \geq U_{\max} = 0.25$ m. Between $U = 0$ and $U = U_{\max}$ the controlled stiffness is a linear function of $U$.
- Control law #2 (CL #2, Fig. 1.2b): The effective radius $R_{eff}$ of the curved surface is 50% of $R_{eff-no\min al}$. The controlled stiffness is formulated to produce zero total stiffness at $U = 0$ and $k_{total} = W/R_{eff-no\min al}$ at $U \geq U_{\max} = 0.25$ m. Between $U = 0$ and $U = U_{\max}$ the controlled stiffness is a linear function of $U$.
- Control law #3 (CL #3, Fig. 1.3a): The effective radius $R_{eff}$ of the curved surface is equal to $R_{eff-no\min al}$. The controlled stiffness is formulated to produce $k_{total} = W/R_{eff-no\min al}$ at $U = 0$ and zero dynamic stiffness at $U \geq U_{\max} = 0.25$ m. Between $U = 0$ and $U = U_{\max}$ the controlled stiffness is a linear function of $U$.

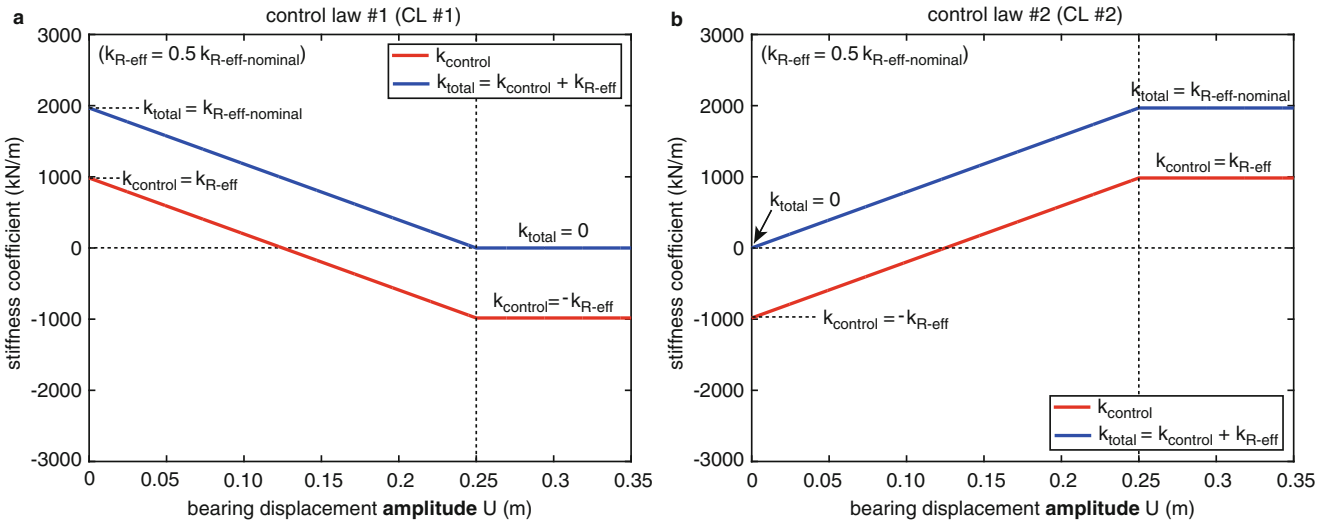


**Fig. 1.2** Controlled stiffness and total bearing stiffness due to (**a**) control law #1 and (**b**) control law #2

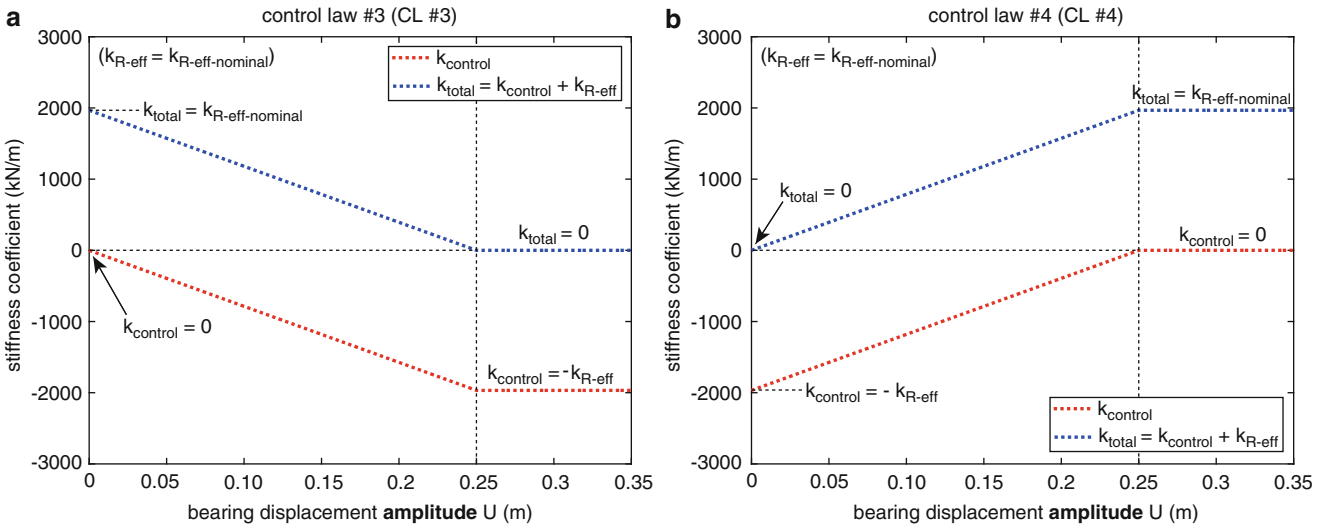


**Fig. 1.3** Controlled stiffness and total bearing stiffness due to (**a**) control law #3 and (**b**) control law #4

- Control law #4 (CL #4, Fig. 1.3b): The effective radius $R_{eff}$ of the curved surface is equal to $R_{eff-no\,min\,al}$. The controlled stiffness is formulated to produce zero dynamic stiffness at $U = 0$ and $k_{total} = W/R_{eff-nom}$ at $U \geq U_{\max} = 0.25$ m. Between $U = 0$ and $U = U_{\max}$ the controlled stiffness is a linear function of $U$.

The main difference between CL #1 and CL #3 (and between CL #2 and CL #4) is that the maximum (positive) and minimum (negative) controlled stiffness coefficients due to CL #1 (and CL #2) are only 50% of the maximum negative controlled stiffness of CL #3 (and CL #4) due to the different designs of $R_{eff}$ for CL #1 (and CL #2) and CL #3 (and CL #4). The control law leading to smaller controlled stiffness is more suitable for controllable dampers since the emulation of large stiffness with semi-active dampers is inherently combined with the generation of damping that is larger than the desired viscous damping given in (1.4) whereby the actual stiffness and damping of the actual semi-active force are far from their desired counterparts. Detailed information on the emulation errors of desired stiffness and damping with controllable dampers is beyond the scope of this paper but can found in [10]. The main difference between CL #1 (and CL #3) and CL #2 (and CL #4) is that CL #1 (and CL #3) results in zero dynamic stiffness at $U = U_{\max}$ which improves the isolation of the structure at large PGAs due to earthquakes between DBE and MCE while CL #2 (and CL #4) generate zero dynamic stiffness at $U = 0$ which improves the isolation of the structure due to earthquakes up to DBE.

## 1.5 Results

### *1.5.1 Optimized Friction Pendulums*

The effective radius of the passive FP is designed to produce the targeted isolation time period $T_{iso} = 3.5$ s. Given this effective radius the friction coefficient $\mu$ is optimized for minimum max $\left(|\ddot{u}_s + \ddot{u}_g|\right)$ for the PGA of the DBE that is assumed to be 5 m/s$^2$ (Fig. 1.4b). The optimization of $\mu$ is also performed for PGA $= 3.5$ m/s$^2$ and PGA $= 6.5$ m/s$^2$ (Fig. 1.4a, c) to demonstrate that the best performance of the optimized FP is only obtained at the PGA value used for optimization highlighted by the green circles Fig. 1.4e.

### *1.5.2 Pendulum with Optimized Linear Viscous Damping*

The effective radius of the pendulum is the same as for the FP in order to guarantee equal time periods. The viscous damping coefficient is optimized for minimum max $\left(|\ddot{u}_s + \ddot{u}_g|\right)$ (Fig. 1.4d) which does not depend on the PGA of the ground acceleration as can be seen from the linear behavior of max $\left(|\ddot{u}_s + \ddot{u}_g|\right)$ as function of PGA depicted in Fig. 1.4e.

### *1.5.3 Semi-Active Pendulum*

The isolation performance in terms of absolute structural acceleration of the semi-active pendulum with passive friction of 1.5% (lubricated) resulting from the four suggested control laws is depicted in Fig. 1.5a. The main observations are:

- CL #1 and CL #2 perform better than CL #3 and CL #4 because the maximum controlled stiffness of CL #1 and CL #2 are only 50% of the maximum value due to CL #3 and CL #4 whereby the actual stiffness and actual damping produced by the semi-active damper are closer to their desired counterparts for CL #1 and CL #2 than for CL #3 and CL #4; further information on stiffness and damping emulations with semi-active dampers are available in [10].
- CL #1 performs better than CL #2 at large PGAs because CL #1 is formulated to produce zero dynamic stiffness at $U \geq U_{\max} = 0.25$ m whereas CL #2 outperforms CL #1 at smaller PGAs because CL #2 produces zero dynamic stiffness at $U = 0$.

In order to select the "best performing control law" not only the maximum reduction of the absolute structural acceleration should be considered but also the maximum force of the isolator (costs!, Fig. 1.5b), the maximum bearing displacement

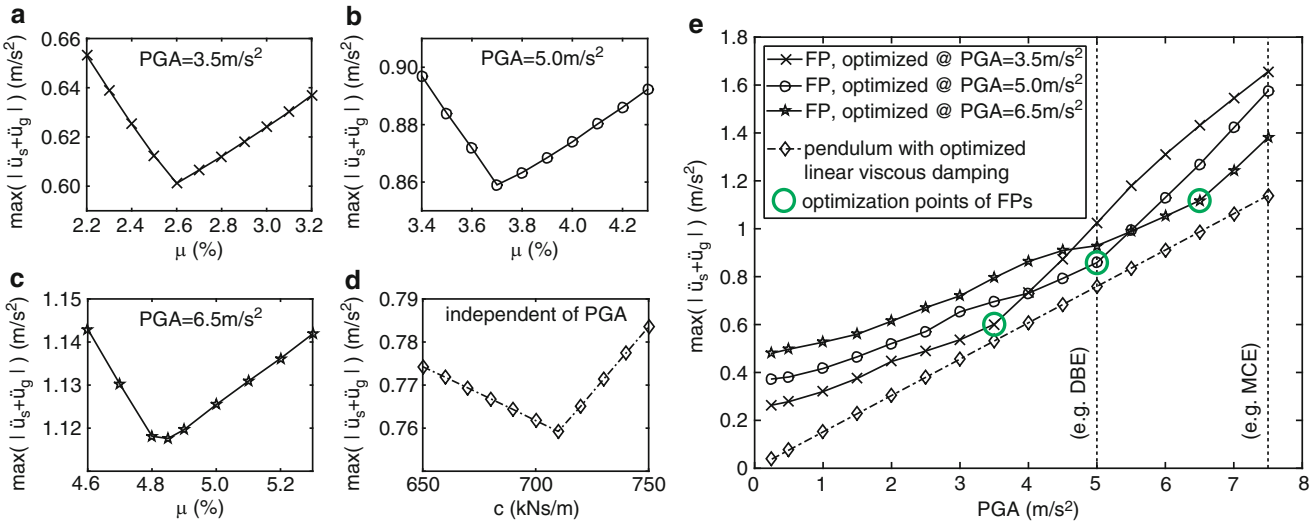


**Fig. 1.4** Optimal friction coefficients (**a**–**c**) of passive FPs and optimal viscous coefficient (**d**) of passive pendulum with viscous damping; absolute structural acceleration (**e**) due to optimized passive FPs and pendulum with optimized viscous damping

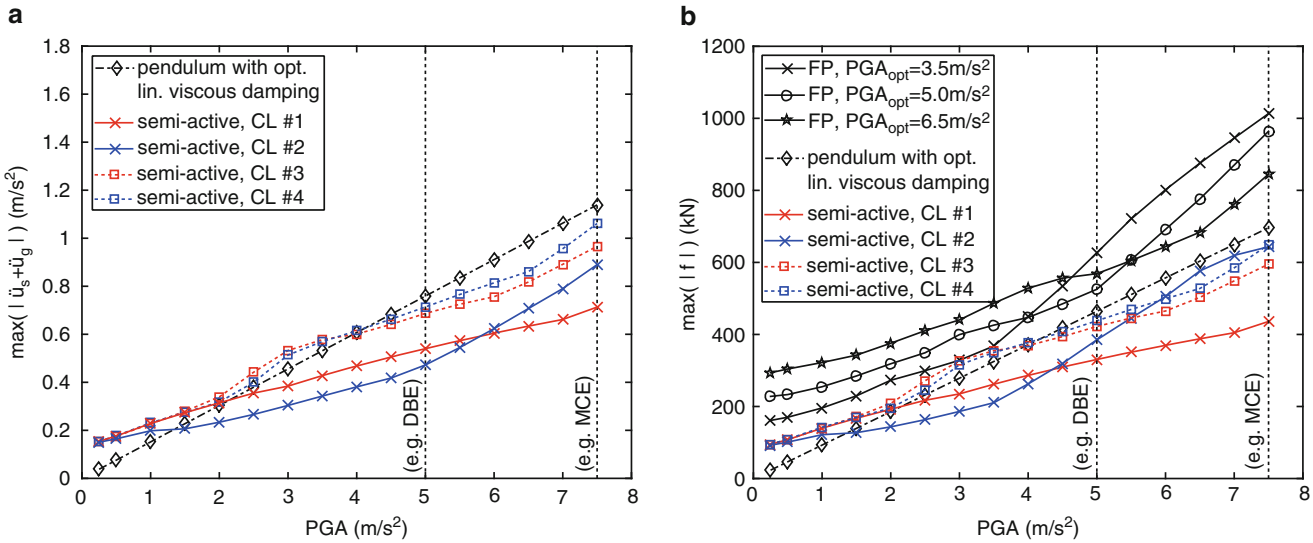


**Fig. 1.5** Absolute structural acceleration (**a**) due to semi-active pendulums and (**b**) maximum total forces of all considered isolators

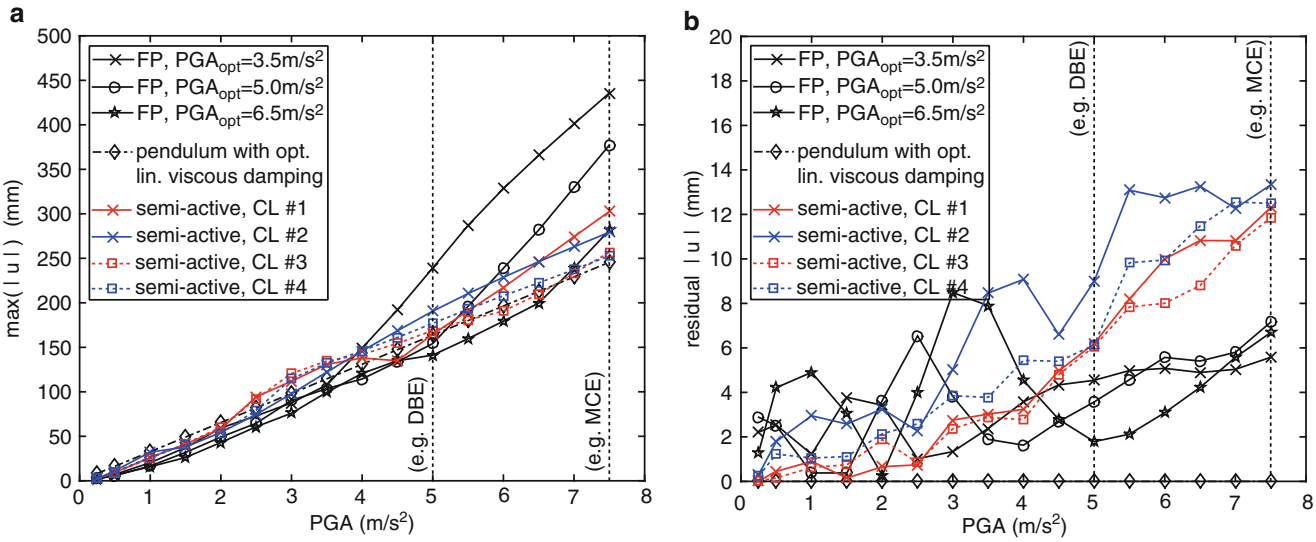


**Fig. 1.6** Maximum displacements (**a**) and residual displacements (**b**) of all considered isolators

(costs!, Fig. 1.6a), the re-centering capability (Fig. 1.6b, re-centering error must not be larger than 50% of the bearing displacement capacity, i.e. 50% of 250 mm) and the maximum force of the semi-active damper (costs!, Figs. 1.7 and 1.8). The review of all these results reveals that CL #1 and CL #2 represent promising solutions. None of these two control laws can be denoted as superior as the project specifications alone determine if CL #1 or CL #2 is more appropriate for the isolation task, i.e. if the absolute structural acceleration should be minimized for PGAs corresponding to DBE and earthquakes beyond of DBE (CL #1) or for PGAs corresponding to DBE and earthquakes below DBE (CL #2).

## 1.6 Summary

This paper presents a novel semi-active base isolator based on a pendulum with uncontrollable lubricated friction of 1.5% and a semi-active oil damper in parallel. Four different control laws are formulated that target to control the total stiffness of the semi-active isolator in real-time as function of the actual bearing displacement amplitude and to produce optimal viscous damping. The numerical results demonstrate that the semi-active isolator significantly improves the isolation of the structure

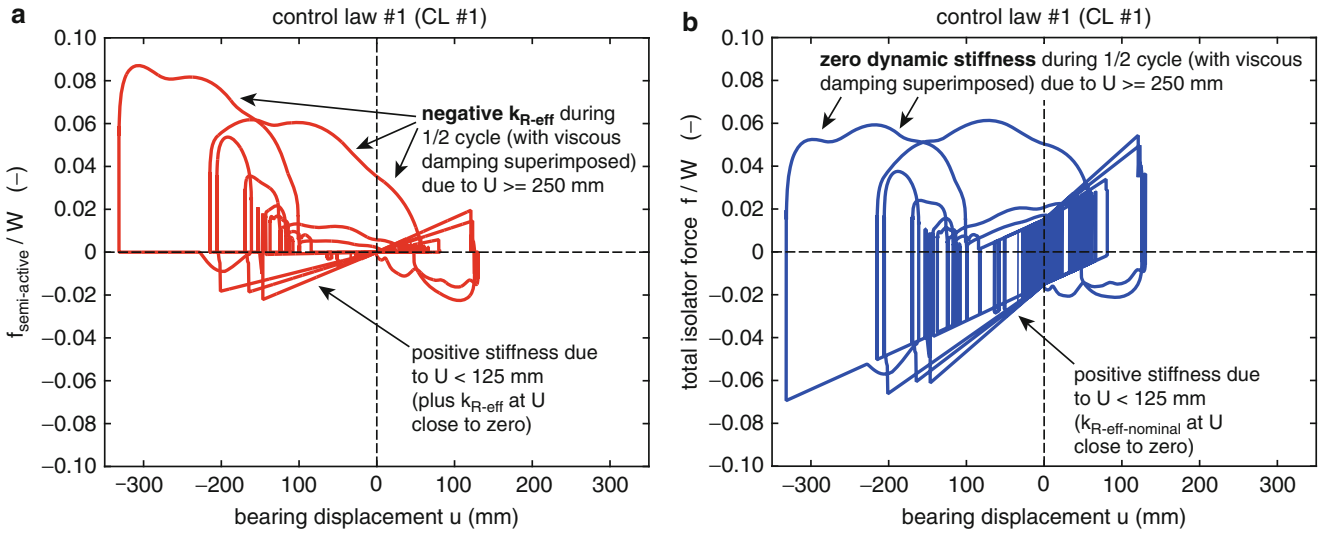


**Fig. 1.7** Force displacement trajectories of (**a**) semi-active control force and (**b**) total force of semi-active isolator due to control law #1

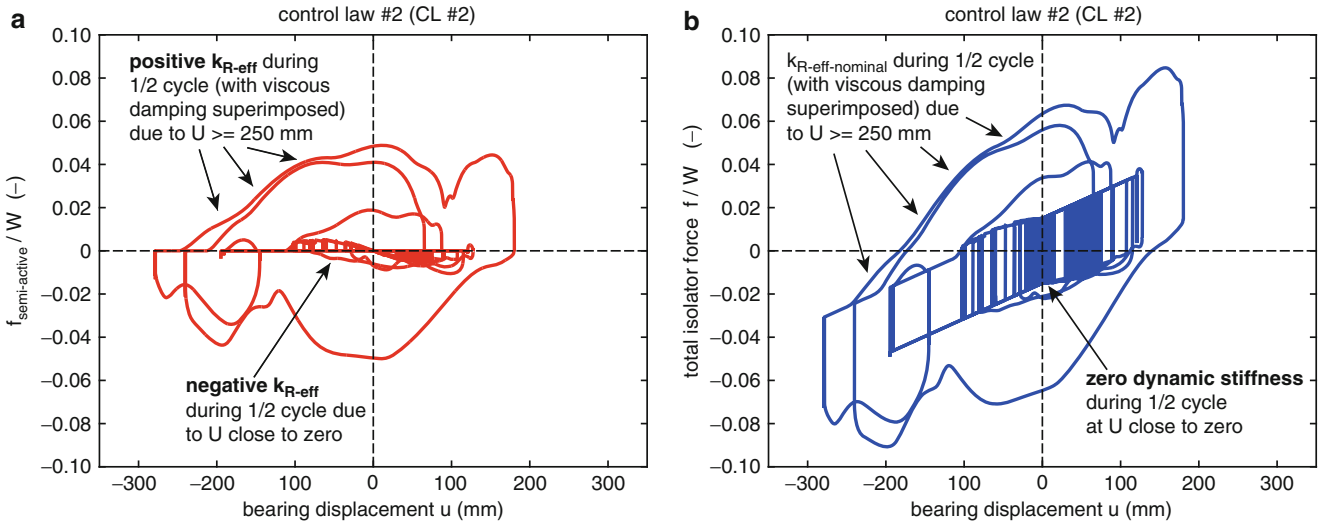


**Fig. 1.8** Force displacement trajectories of (**a**) semi-active control force and (**b**) total force of semi-active isolator due to control law #2

compared to optimized friction pendulums and a hypothetical pendulum without friction but optimal viscous damping. This result is achieved without getting larger bearing displacements and forces and the re-centering requirement is also fulfilled semi-active base isolator.

**Acknowledgements** The authors gratefully acknowledge the financial support of MAURER SE.

## References

1. Tsai, C.S., Chiang, T.-C., Chen, B.-J.: Experimental evaluation of piecewise exact solution for predicting seismic responses of spherical sliding type isolated structures. Earthq. Eng. Struct. Dyn. **34**, 1027–1046 (2005)
2. Weber, F., Boston, C.: Energy based optimization of viscous-friction dampers on cables. Smart Mater. Struct. **19**, 045025 (11pp) (2010)
3. Fenz, D.M., Constantinou, M.C.: Spherical sliding isolation bearings with adaptive behavior: theory. Earthq. Eng. Struct. Dyn. **37**, 163–183 (2008)
4. Feng, M.Q., Shinozuka, M., Fujii, S.: Friction-controllable sliding isolation system. J. Eng. Mech. (ASCE). **119**(9), 1845–1864 (1993)

5. Kobori, T., Takahashi, M., Nasu, T., Niwa, N.: Seismic response controlled structure with active variable stiffness system. Earthq. Eng. Struct. Dyn. **22**, 925–941 (1993)
6. Ramallo, J.C., Johnson, E.A., Spencer Jr., B.F.: 'Smart' base isolation systems. J. Eng. Mech. (ASCE). **128**(10), 1088–1100 (2002)
7. Nagarajaiah, S., Sahasrabudhe, S.: Seismic response control of smart sliding isolated buildings using variable stiffness systems: an experimental and numerical study. Earthq. Eng. Struct. Dyn. **35**(2), 177–197 (2006)
8. Ruderman, M.: Presliding hysteresis damping of LuGre and Maxwell-slip friction models. Mechatronics. **30**, 225–230 (2015)
9. Preumont, A.: Vibration Control of Active Structures, Chapter 6. Kluwer Academic Publishers, Dordrecht (2002)
10. Weber, F., Maślanka, M.: Precise stiffness and damping emulation with MR dampers and its application to semi-active tuned mass dampers of Wolgograd Bridge. Smart Mater. Struct. **23**, 015019 (2014)

# Chapter 2
# Long-Term Performance of Specialized Fluid Dampers Under Continuous Vibration on a Pedestrian Bridge

**Alan R. Klembczyk**

**Abstract** In 2001, Taylor Devices Inc. developed special Viscous Dampers for use on the Millennium Bridge in London, England. These dampers were specified and designed to be used for mitigating the dynamic response of the bridge due to pedestrian traffic. Prior to the integration of the dampers, the bridge had experienced unacceptable movements, especially during periods when larger crowds of people were on the bridge. The result was that the bridge had to be closed until a solution was found. Much research was done and several papers were published about the nature of that problem and the ensuing solution. After successful component level testing and the installation of 37 Taylor Viscous Dampers, the bridge was re-opened to the public in February, 2002. Tests with approximately 2000 people demonstrated a much improved dynamic response. Since that time, the dampers have been subjected to almost constant dynamic input, some more than others. Due to the location of the bridge in central London, there has been nearly constant pedestrian traffic on the bridge each day and even throughout the night. However, because of the specialized nature of the damper design, no degradation in damper performance or in the dynamic response of the bridge itself has been experienced. This paper will outline the specifics in quantifying the continued damper performance through an intermediate inspection after 7 years, followed by a successful comprehensive inspection after 11 years. This included the removal, dynamic testing, and re-installation of three selected dampers.

**Keywords** Millennium Bridge • Bridge damper test results • Fluid viscous dampers • Continuous vibration • Vibration damper

## 2.1 Introduction

The unique design and the resulting unacceptable response of the Millennium Bridge in central London (see Fig. 2.1) have been well publicized and documented. The specifics of this dynamic response and the resulting solution will not be reiterated within the context of this paper. However, in order to provide a necessary background, a short summary is presented here.

In June 2000, the bridge was first opened to the public. Shortly thereafter, with substantial pedestrian traffic present, the bridge began to sway in a lateral motion to the discomfort of many of the pedestrians. The bridge was subsequently shut down and significant studies were performed to provide solutions to stop the excessive swaying. Since the response frequency was near the frequency of human footfalls during walking, it was determined that stiffening of the structure was not a practical solution. The unique design and its aesthetic appearance would have been sacrificed if structural modifications were made to keep the various modal frequencies away from walking frequencies. A more acceptable solution was determined to substantially increase the damping level of the bridge over all input conditions in order to prevent pedestrian traffic from exciting the bridge. The required amount of added damping was determined to be nearly 20% critical, a value that is effectively unachievable with typical solutions, such as tuned mass dampers, frictional elements, or structural modifications.

Many challenges became immediately apparent when proposing a damping solution for this unique structure. One of the most significant was the fact that the owner of the bridge required a permanent and maintenance-free solution that would last throughout the life of the bridge; this being in excess of 50 years. Since the expected pedestrian traffic was such that the dampers would cycle nearly continuously at 1.3 Hz, it was necessary to specify a cycle life of $2 \times 10^9$ cycles minimum. Due to this stringent requirement, Taylor Devices proposed the use of specialized Fluid Dampers that employed the use of flexing metal bellows seals, rather than traditional sliding seals that are elastomeric in nature and therefore subject to wear and degradation over long-term environmental and cyclic conditions.

A.R. Klembczyk (✉)
Taylor Devices, Inc., 90 Taylor Drive, North Tonawanda, NY, 14120-0748, USA
e-mail: alanklembczyk@taylordevices.com



J. Caicedo, S. Pakzad (eds.), *Dynamics of Civil Structures, Volume 2*, Conference Proceedings
of the Society for Experimental Mechanics Series, DOI 10.1007/978-3-319-54777-0_2

**Fig. 2.1** The Millennium Bridge

## 2.2 Specialized Damper Design [1]

Taylor Devices' Fluid Dampers with metal bellows seals had been previously used exclusively by NASA and other U.S. Government agencies for space based optical systems. These previous applications had similar requirements for long life and high resolution at low amplitudes, but required relatively low damper forces from small, lightweight design envelopes. Figure 2.2 is a photograph of a pair of typical dampers of this design, used in space on more than 70 satellites to protect delicate solar array panels. This figure also shows the metal bellows seals; one in the compressed position and one in the extended position. This type of seal does not slide, but rather flexes without hysteresis as the damper moves. This patented design is known as a Frictionless Hermetic Damper.

A cutaway of a typical damper of this type is shown in Fig. 2.3. Two metal bellows seals are used to seal fluid in each damper, one at each end of the damping chamber. As the damper moves, the two metal bellows alternately extend and retract, by flexure of the individual bellows segments. Since the seal element elastically flexes rather than slides, seal hysteresis is nearly zero. The volume displaced by the compressing bellows passes through the crossover ports to the extending bellows at the opposite end of the damper. While this is occurring, damping forces are being produced by orifices in the damping head, and the pressures generated are kept isolated from the metal bellows by high restriction hydrodynamic labyrinth bushings. Because hydrodynamic bushings are used, no sliding contact with the piston rod occurs, assuring near-frictionless performance.

Adapting this basic design for use on the Millennium Bridge largely involved simply scaling the small satellite Dampers to the required size range. All parts, including the metal bellows seals, were designed with low stress levels to provide an endurance life in excess of $2 \times 10^9$ cycles. The metal bellows and other moving parts were constructed from stainless steel for corrosion resistance. To assure a high resolution output, it was required that all damper attachment clevises be fabricated with fitted spherical bearings and fitted mounting pins, such that zero net end play existed in the attachment brackets.

A total of 37 dampers of this design were manufactured, component-level tested, and installed on the bridge in late 2001. There are three basic types of dampers. These are referred to as the Pier Dampers, the Deck Dampers, and the Vertical Dampers and are described below:

Damper Nomenclature: Pier Damper
Quantity on the Bridge: 16
Description: Two Pier Dampers are located on each side of each of two piers on both the east and west side of the bridge, for a total of eight dampers per pier. Damping coefficient values for the eight dampers connected directly to the center span of the bridge are significantly higher than the other Pier Dampers. Dampers have varying over-all lengths due to the

**Fig. 2.2** Space satellite dampers

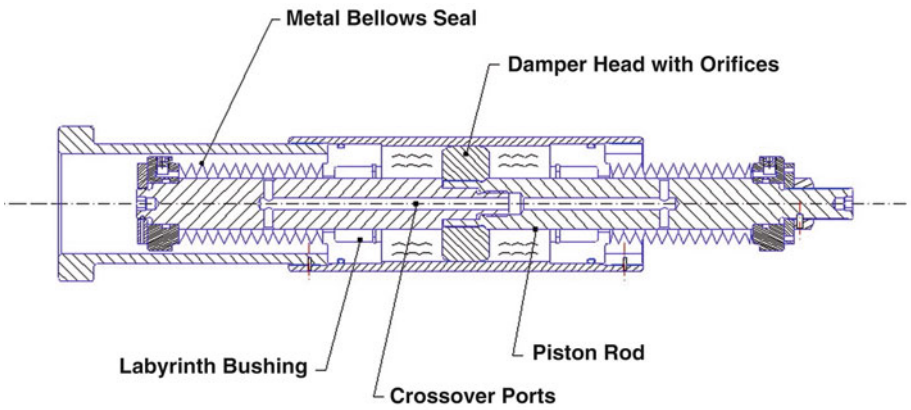


**Fig. 2.3** Cutaway of frictionless hermetic damper

location of the attachment points, the longest being 8.3 m long. These dampers are quite apparent to pedestrians when crossing the bridge as illustrated in Figs. 2.4 and 2.5 below.

Damper Nomenclature: Deck Damper
Quantity on the Bridge: 17
Description: The Deck Dampers are located under various deck sections. A very limited number can be seen from under the north end of the bridge. Most deck dampers are not visible since they are situated directly under the deck panels. Lateral motions of the bridge are transmitted to the dampers through pairs of relatively long V-shaped chevron braces as shown in Figs. 2.6 and 2.7 below.

Damper Nomenclature: Vertical Damper
Quantity on the Bridge: 4
Description: Vertical Dampers are located in two pairs under the south end of the bridge with damper ends connected between a structural arm and the ground. As illustrated below in Figs. 2.8 and 2.9, the dampers are directly accessible to pedestrian traffic. Nearly continuous damped motion is felt and observed with even low to moderate pedestrian traffic on the bridge overhead.

**Fig. 2.4** 4 of 16 pier dampers

**Fig. 2.5** Moving end of pier damper over the River Thames

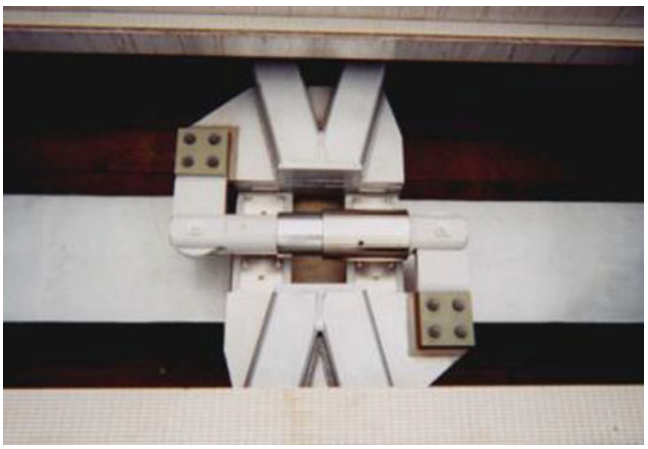

**Fig. 2.6** Deck damper shown with chevron connection

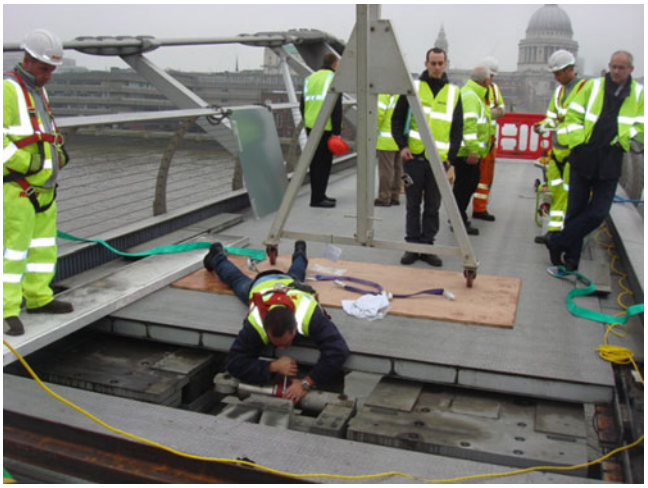

**Fig. 2.7** Deck panels removed deck damper showing

**Fig. 2.8** Inspection of vertical damper pair

**Fig. 2.9** Vertical damper pair with pedestrian access

## 2.3 Intermediate Inspection After 7 Years in Service

A visual inspection of each damper was performed looking for corrosion, damage to the unit from use or the surrounding environment, and for fluid leakage. The units were all found to be in 100% working condition with minimal signs of physical damage or deterioration, as well as no signs of fluid leakage. There were only minor signs of corrosion and some external contamination noted. The units had been subjected to nearly constant cycling for a period of use of over 7 years at the time of this inspection. The total estimated cycles after 7 years was as many as $2.0 \times 10^8$. The owner required no formal testing of installed dampers at this time.

## 2.4 Principal Inspection and Testing After 11 Years in Service

The Principal Inspection after 11 years of service included two phases. The first was a visual inspection of all Pier Dampers and all four Vertical Dampers. All dampers appeared to be in 100% working order. A sample of five of the seventeen deck dampers were inspected per the owner's request to minimize deck panel removal costs. Similar to the case for the Intermediate Inspection 4 years earlier, there were only minor signs of corrosion and some external contamination noted. This minor corrosion and contamination appears to have been caused by caustic chemicals from the exhaust plumes from boats and ships navigating under the bridge. Dampers located under the deck of the bridge near the shore or over land exhibited nearly new appearance. Two of the five Deck Dampers and one of the four Vertical Dampers were temporarily removed for testing purposes as outlined below.

The second phase of the Principal Inspection consisted of performing dynamic tests on the three dampers that were removed. These three dampers were shipped to the Taylor Devices facility in North Tonawanda, New York so that they could be tested to the original Acceptance Test Procedure and compared to the original acceptance tests from 2001. This was done to determine if any of the performance outputs had deteriorated in any way. This Acceptance Test Procedure consisted of two types of tests. The first type consisted of subjecting the dampers to a series of sinusoidal input tests throughout the specified velocity range. These tests are referred to as the "Force vs. Velocity" tests. The second type of test was performed at approximately 0.50 mm amplitude. These tests are referred to as the "Low Amplitude" tests. The Low Amplitude test demonstrates the ability of each Damper to produce substantial damping force for very small vibrations, and demonstrate that there has been no loss of fluid. If any loss of fluid had occurred, the damper would demonstrate an inability to produce any substantial force for these small displacements.

Figures 2.10, 2.11, and 2.12 show the results of the Force versus Velocity tests for each Damper, measuring the output force at several velocity inputs. These plots also show the data points recorded through the same testing methods 11 years prior. The graphical data illustrates the fact that there is virtually no difference in output characteristics when comparing the results from 2001 to the results from 2012.

Figures 2.13, 2.14 and 2.15 demonstrate the results of the Low Amplitude Tests for each of the three dampers that were tested. Note that in each case, the hysteresis loops (force vs. displacement) show no signs of free-play, loss of fluid, excessive friction, wear or degradation of any sort. It should be noted that the dampers were tested with their spherical bearings in place and their end attachment brackets still connected. Therefore, no degradation to these components has occurred and the bearings have maintained their tight fit requirement that is necessary to produce damping for very low displacements.

Subsequent to the successful testing of these three dampers, they were sent back to London and reinstalled on the bridge in January 2013.

## 2.5 Conclusions

The results of the 7-year Intermediate Inspection, the 11-year Principal Inspection, and dynamic testing show that the Millennium Bridge dampers have experienced no physical or functional deterioration. The dampers displayed no measurable change in output, as well as no signs of leakage after 11 years of continuous service and nearly constant cycling.

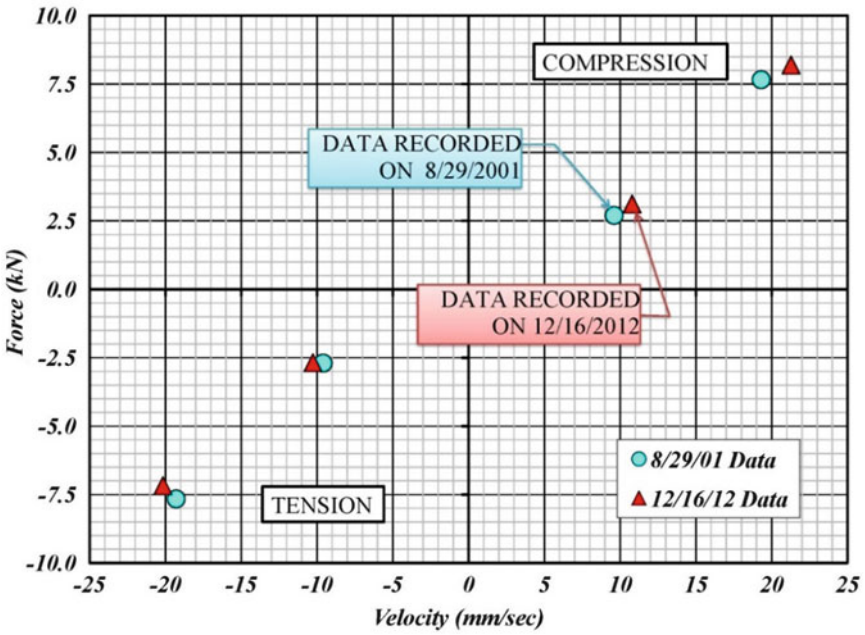


**Fig. 2.10** Force vs. Velocity test results of deck damper 2001 & 2012

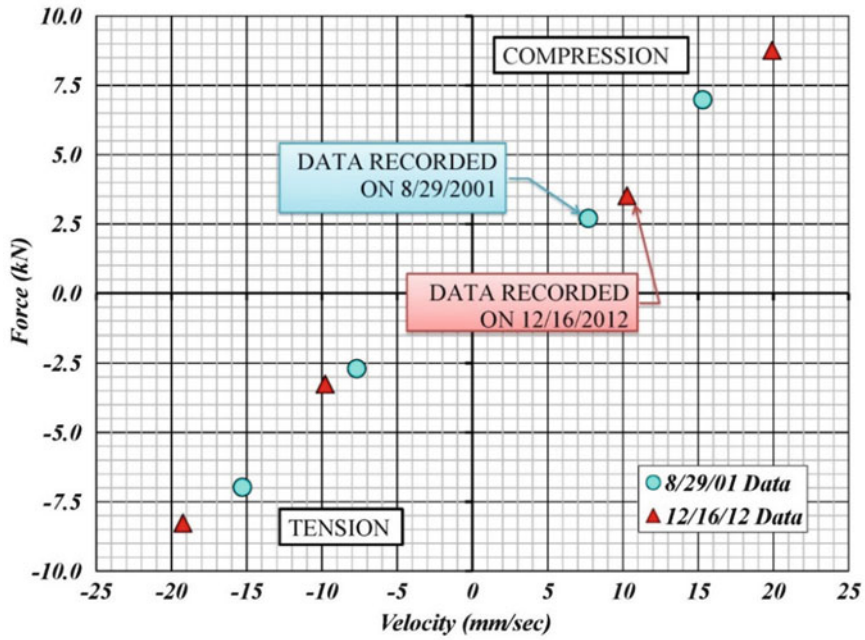


**Fig. 2.11** Force vs. Velocity test results of deck damper 2001 & 2012

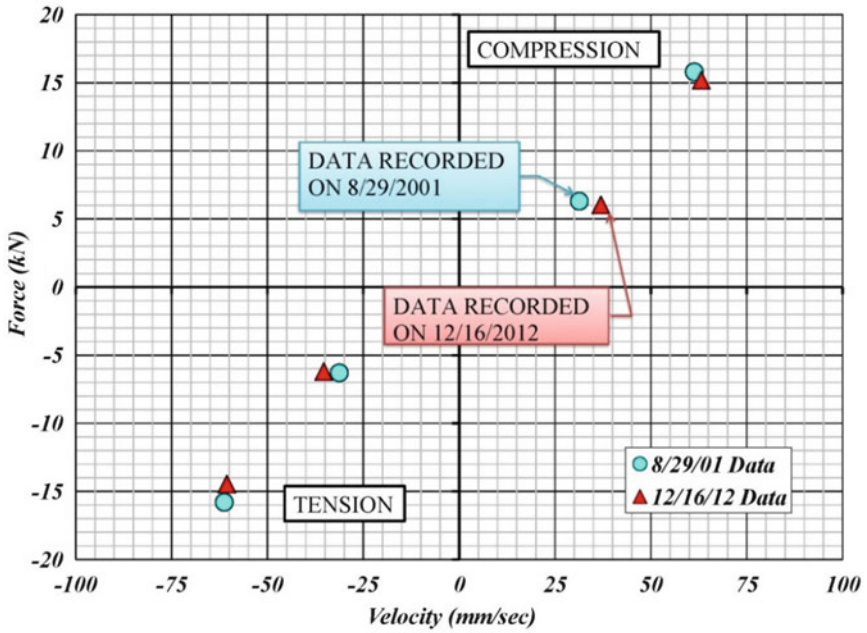


**Fig. 2.12** Force vs. Velocity test results of vertical damper 2001 & 2012

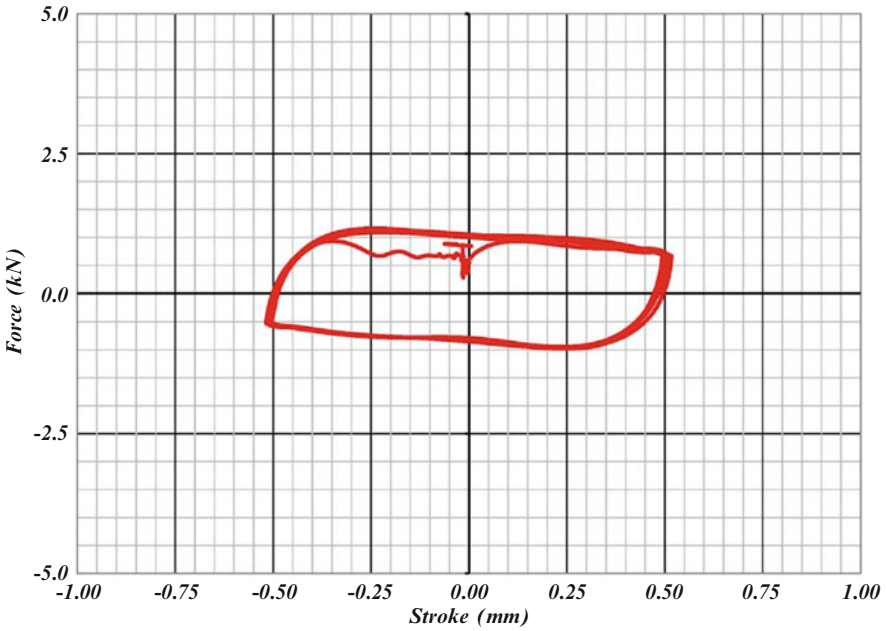


**Fig. 2.13** Low amplitude test results of deck damper 2012

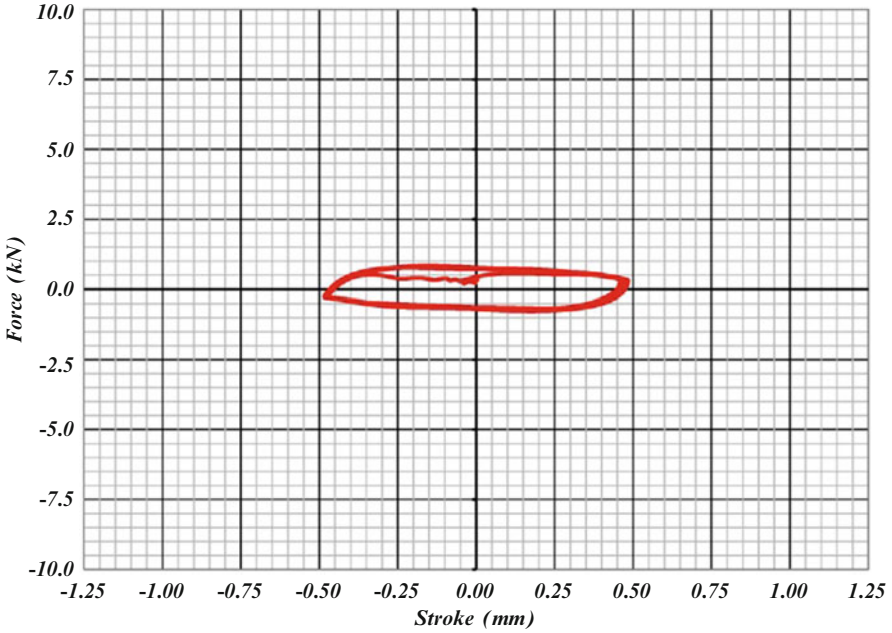


**Fig. 2.14** Low amplitude test results of deck damper 2012

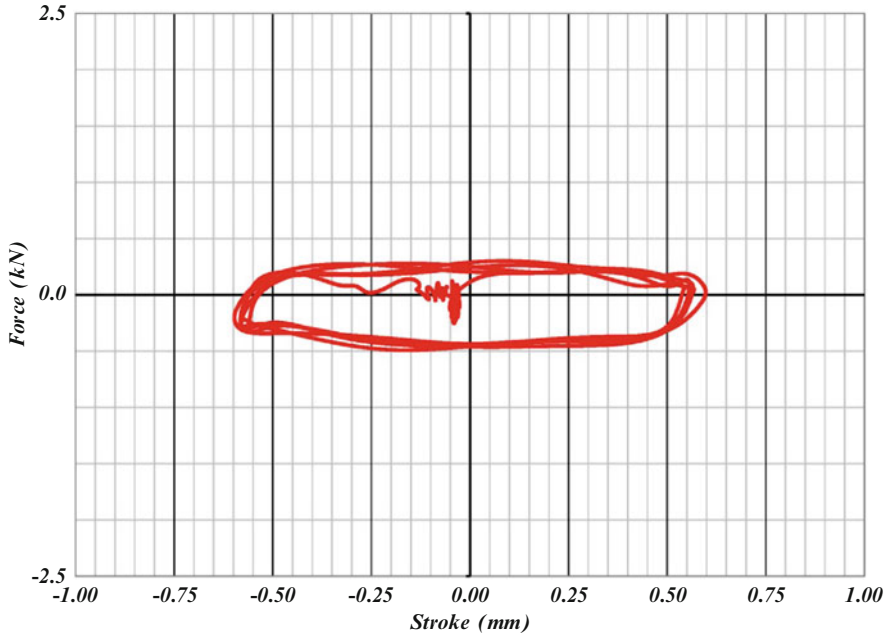


**Fig. 2.15** Low amplitude test results of vertical damper 2012

The dampers were originally designed and built for this nearly constant cycling over a period of more than 50 years, projected to total approximately $2 \times 10^9$ (2 billion) cycles. Due to the fact that the results of the intermediate and principal inspections and testing show no signs of degradation, it is anticipated that the dampers will be able to meet this expected life time as anticipated.

**Acknowledgements** The author would like to thank Craig Winters, Robert Schneider and Sean Frye for their contributions to this paper.

## Reference

1. Taylor, D.: Damper retrofit of the London Millennium Footbridge—a case study in biodynamic design. In: Proceedings of the 73rd Shock and Vibration Symposium, 2002

# Chapter 3
# Analysis of Variation Rate of Displacement to Temperature of Service Stage Cable-Stayed Bridge Using Temperatures and Displacement Data

**Hyun-Joong Kim**

**Abstract** Because stage cable-bridge have long spans and large members, their movements and geometrical changes by temperatures tend to be bigger than those of small or medium-size bridge. Therefore, it is important for maintenance engineers to monitor and assess the effect to temperature on the cable-supported bridges. To evaluate how much the superstructure expands or contracts when subjected to changes in temperature is the first step for the maintenance. Thermal movements of a cable-stayed bridge in service are evaluated by using long-term temperatures and displacements data.

**Keywords** Cable-stayed bridge • Thermal movements • Temperature effect • Correlation analysis

## 3.1 Introduction

Since cable-supported bridges are long and sizable, their movement and transportation amount are quite considerable compared to those of general bridges. Thus, in order for the maintenance of cable-supported bridges, it is important to analyze and evaluate the influence of temperature on the existing bridges; in terms of such temperature evaluation, assessing elastic superstructures of bridges depending on the change in temperature is known to be the most basic analyzing techniques. Recently, there are a variety of ongoing research projects to evaluate the structures more precisely as the existing period of cable-supported bridges getting extended and the amount of their accumulated data is increasing [2–4].

In our research, in order to study the influence of temperature on cable-supported bridges, we employed the previous methods such as using an expansion displacement meter or single measuring method with data gathered from Global Navigation Satellite System (GNSS). Then, based on the cases that evaluated temperature expansion behaviors using different datasets to enhance their statistical reliability, we measured the expansion per unit temperature using the temperature data and the GNSS displacement data of existing cable bridges and confirmed the structural integrity of the bridges through the comparison between our results and theoretical values.

## 3.2 The Subject Bridge and Data Collection Method

### *3.2.1 Subject Bridge*

The bridge used for this research is Cheong-Poong Dae-Kyo (Bridge) located in Jechun, Choong-Cheong-Book-Do, which is a 5-consecutive-span complex cable-stayed bridge with the full length of 472 m (center: 327 m, side span: 57.5 m, abutment: 30 m) and width of 13 m and has RC cross sections for its side spans and composite cross sections consisting of precast concrete floor slap and I-shaped structural steel cross sections for its main spans. Its tower has a H-shaped concrete cross section with the height of 103 m and was completed in May 2012; it is currently under the management of Structural Health Monitoring System (SHMS).

H.-J. Kim (✉)
EJ Tech Co., Ltd., Seokjeong B/D, 10, migeum-ro 33 beon-gil, Bundang-gu, Seongnam-si, Gyeonggi-do, Republic of Korea
e-mail: hjkim@ejtech.net



J. Caicedo, S. Pakzad (eds.), *Dynamics of Civil Structures, Volume 2*, Conference Proceedings
of the Society for Experimental Mechanics Series, DOI 10.1007/978-3-319-54777-0_3

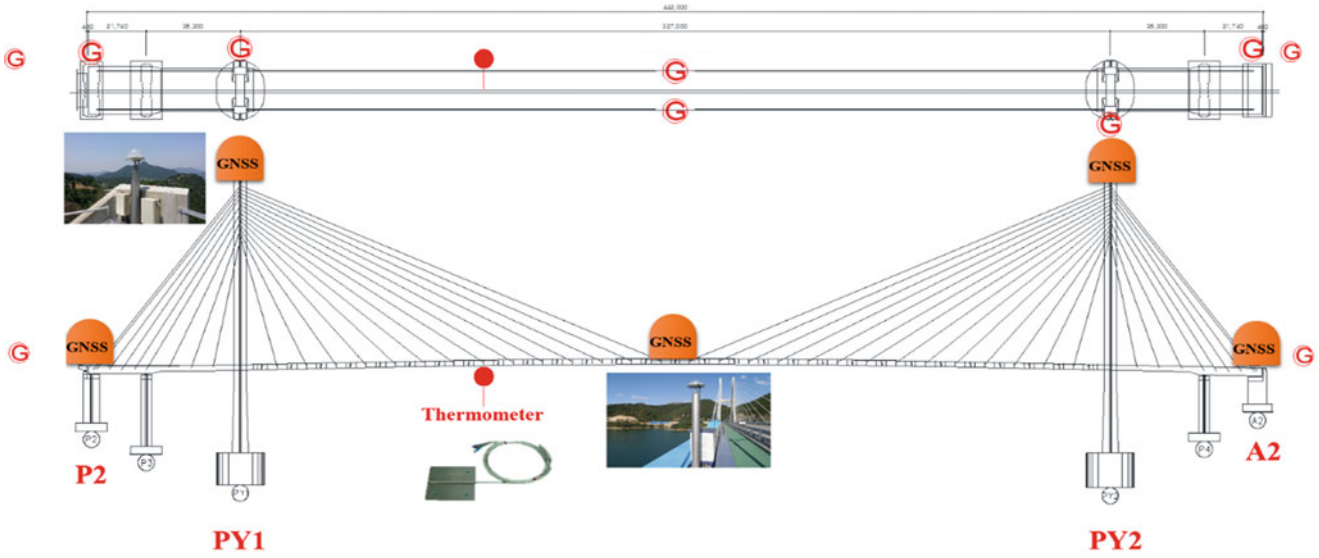


**Fig. 3.1** Installation place of GNSS and thermometer

### *3.2.2 Data Collection Method*

We collected our data using the sensors utilized to measure the expansion of Cheong-Poong Dae-Kyo in the 2 receivers in the central girder and the rest 4 GNSSes except for 2 reference stations among the 8 previously installed GNSS receivers as shown in Fig. 3.1 and also the member thermometer installed at the ¼ location of the stiffner. The duration of our data collection was a year, from January 1st, 2014 to December 31st, 2014, and we performed a correlation analysis of GNSS displacements along the direction of the bridge using the 10-min average data of GNSS. The GNSS data consists of three components, dN, dE, and dH, and we defined directions as "perpendicular" and "corresponding" to the bridge line by turning the azimuth 22° counterclockwise when our Y-axis is due north (N) and X-axis due east (E).

### *3.2.3 The Analysis of Expansion per Unit Temperature*

The amount of expansion due to the temperature change of a structure is calculated as shown in the formula (3.1). Here, $\Delta L$ implies the temperature change, $L$ the expansion length, and $\alpha$ the coefficient of linear expansion of a material. In the formula (3.1), $\alpha$ and $L$ become the values for the boundary conditions depending on the used material and the member length, respectively. We can see that this is a linear relationship between the expansion amount and temperature and define it as the formula (3.2) shown below. $S_T$ is defined as the expansion per unit temperature (mm/°C) [1]

$$\Delta L_T = \alpha \times \Delta T \times L \tag{3.1}$$

$$\Delta L_T / \Delta T = \alpha \times L = S_T \tag{3.2}$$

The calculation of expansion per unit temperature using measured data is to estimate the linear regression (3.3) from the measured values, $\beta_0$, $\beta_1$ of two variables using the least square method (3.4) and its formula is presented below.

$$y = \beta_0 + \beta_1 x \tag{3.3}$$

$$\widehat{\beta}_1 = \frac{\sum \left(x_i - \bar{x}\right)\left(y_i - \bar{y}\right)}{\sum \left(x_i - \bar{x}\right)^2} = \frac{S_{xy}}{S_{xx}} \tag{3.4}$$

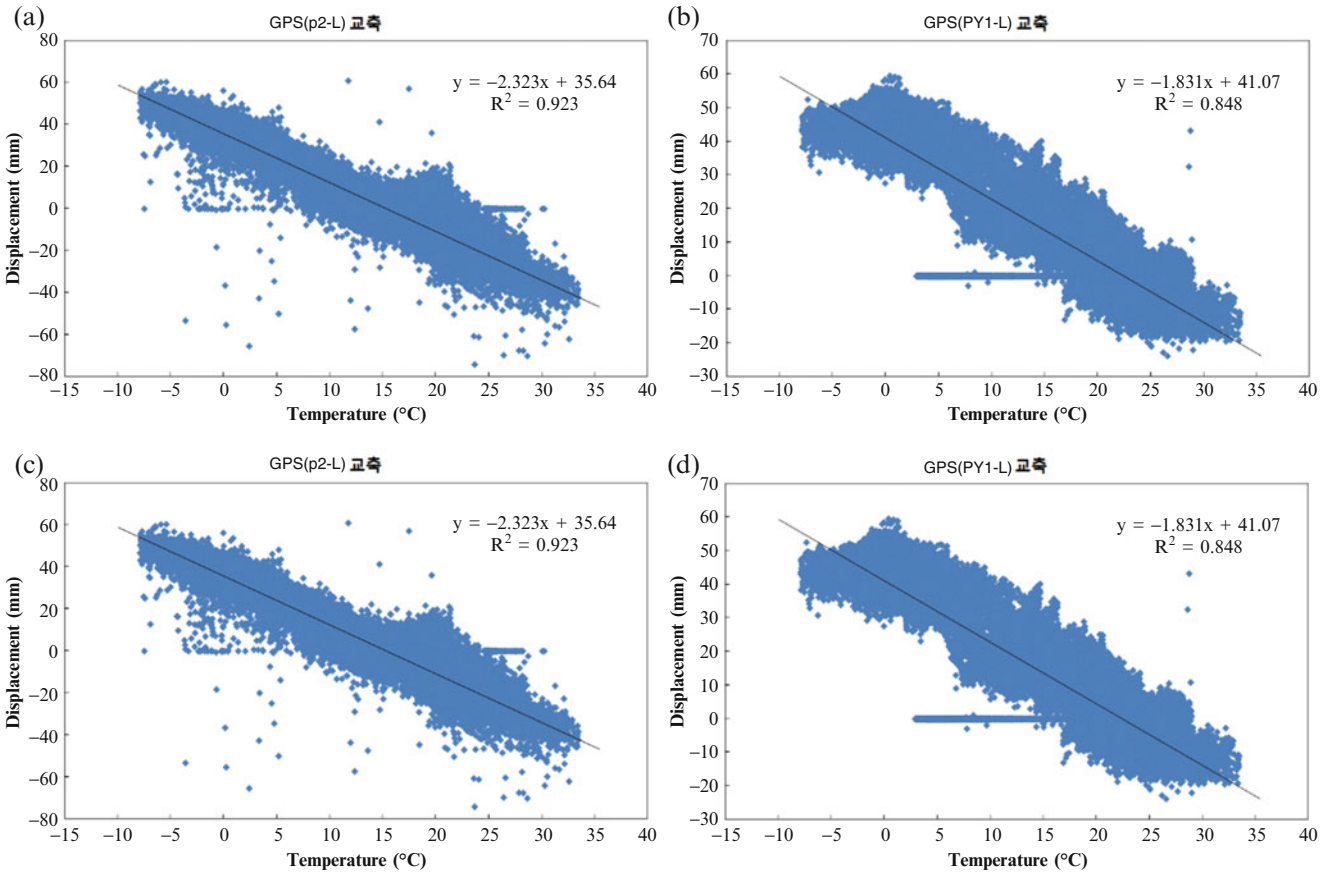


**Fig. 3.2** Relationship between air temperatures and displacement. (**a**) Relationship between air temperatures and P2. (**b**) Relationship between air temperatures and PY1. (**c**) Relationship between air temperatures and PY2. (**d**) Relationship between air temperatures and A2

$$S_{xy} = \sum x_i y_i - \left(\sum x_i\right)\left(\sum y_i\right)/n \tag{3.5}$$

$$S_{xx} = \sum x_i^2 - \left(\sum x_i\right)^2/n \tag{3.6}$$

## 3.3 The Analysis

Through the analysis of measured data, we confirmed a high correlation between two variables as shown in Fig. 3.2 by setting the effective temperature considering expansion directions of bridges and the expansion measured at each location of the bridge as two variables and displayed their distribution [5–8]. We found our coefficient of linear expansion as 0.00001 after calculating the slope of the linear regression equation as displayed in Fig. 3.3. We estimated the theoretical expansion amount per unit temperature as shown in Table 3.1 after applying the coefficient of linear expansion analyzed through our measurement, put it into the formula (3.4), and compared the expansion amounts per unit temperature of temperature and displacement data as presented in Table 3.2.

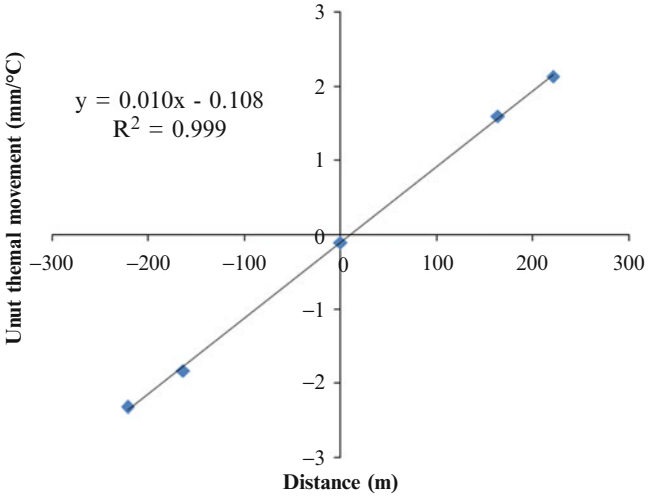


**Fig. 3.3** Relationship between expansion length and $S_T$

**Table 3.1** Analytical comparison of variation rate of displacement to temperature

| | |
|---|---|
| P2 | $\frac{\Delta L_T}{\Delta T} = \alpha \times L_{P2} = 0.0001 \times 221 = 2.21$ mm/°C |
| PY1 | $\frac{\Delta L_T}{\Delta T} = \alpha \times L_{PY1} = 0.0001 \times 163.5 = 1.635$ mm/°C |
| PY2 | $\frac{\Delta L_T}{\Delta T} = \alpha \times L_{PY2} = 0.0001 \times 163.5 = 1.635$ mm/°C |
| A2 | $\frac{\Delta L_T}{\Delta T} = \alpha \times L_{A2} = 0.0001 \times 221 = 2.21$ mm/°C |

**Table 3.2** Comparison of variation rate of displacement to temperature

| Location | P2 | PY1 | PY2 | A2 |
|---|---|---|---|---|
| L (m) | −221 | −163.5 | 163.5 | 221 |
| $S_T$ (mm/°C) | | | | |
| Measurement | −2.323 | −1.831 | 1.593 | 2.13 |
| Theory | 2.21 | 1.635 | 1.635 | 2.21 |

## 3.4 Conclusion

After analyzing correlation (from January 1st, 2014 to December 31st, 2014) through the temperature change and GNSS bridge displacement data, we found a high linear correlation between two variables and confirmed that the coefficient of linear expansion of Cheong-Poong bridge was 1.00*E*-05/°C. In addition, as we compared the theoretical expansion amount per unit temperature with the measured expansion amount, we found a similar result.

After considering the previous research results that a sound structure system showed a linear correlation with strong elastic behaviors depending on the change in temperature and comparing the expansion amount per unit temperature that can evaluate its soundness, we assessed that the structure system and long-term temperature expansion behaviors of Cheong-Poong bridge were quite sound. In order for a precise evaluation of soundness in the future, we expect that a multi-dimensional analysis of different temperature datasets would be necessary.

**Acknowledgments** This work is a part of a research project supported by Ministry of Science, ICT and Future Planning, Institute for Information & communications Technology Promotion (IITP) through Core Research Project No. R-20160216-002659. The authors wish to express their gratitude for the financial support.

## References

1. American Association of State Highway and Transportation Officials (AASHTO): AASHTO LRFD bridge design specifications. Washington (2012)
2. Bae, I.H.: Measurement analysis and management of special bridges. In: Annual Seminar on the Operation and Maintenance of Cable-Supported Bridges in Korea, The New Airport Highway Corporation (in Korean) (2011)

3. Bae, I.H., Choi, B.K., Na, W.C.: Analysis of long-term behaviors and emergency measures of long span cable-supported bridge using the structural health monitoring system. In: Proceedings of Korean Society of Civil Engineers Convention, pp. 876–879 (2013)
4. Naoaki, S.: Long term monitoring in Akashi Kaikyo Bridge. Bridg. Found. (in Japanese). **37**(6), 21–25 (2003)
5. Ni, Y.Q., Hua, X.G., Wong, K.Y., Ko, J.M.: Assessment of bridge expansion joints using long-term displacement and temperature measurement. J. Perform. Constr. Facil. **21**(2), 143–151 (2007)
6. Xu, Y.L., Chen, B., Ng, C.L., Wong, K.Y., Chan, W.Y.: Monitoring temperature effect on a long suspension bridge. Struct. Control. Health Monit. **17**(6), 632–653 (2010)
7. Zhou, Y., Sun, L.: Temperature effects on performance of long-span cable-stayed bridges. In: The 6th World Conference on Structural Control and Monitoring, Barcelona, Spain, pp. 432–444 (2014)
8. Park, J.C.: Evaluation of thermal movements of a cable-stayed bridge using temperatures and displacements data. J. Kor. Soc. Civil Eng. **35**(4), 779–789 (2015)

# Chapter 4
# Triple Friction Pendulum: Does It Improve the Isolation Performance?

**Felix Weber, Peter Huber, Hans Distl, and Christian Braun**

**Abstract** The working philosophy of the triple friction pendulum (FP) is to generate low friction in the region of 1.5–2% combined with high stiffness due to the small effective radii of the articulated slider assembly at low peak ground accelerations (PGAs), to produce medium friction around 3–5% and medium stiffness by simultaneous sliding on surfaces 1 and 4 at PGAs corresponding to the design basis earthquake (DBE), to generate increasing friction with further increasing PGAs up to the maximum credible earthquake (MCE) by the high friction of surface 4 in the region of 10% and, eventually, to produce considerably increased stiffness at PGAs beyond of MCE in order to reduce the maximum required displacement capacity of the triple FP. This study first investigates if this design philosophy results in enhanced isolation of the primary structure compared to the conventional FP. For this, the triple FP according to the above mentioned design concept is numerically tested for several earthquakes that are scaled to various PGAs in order to operate the triple FP within all its sliding regimes with associated isolation efficiencies. These results are compared to those of the conventional non-adaptive double FP with equal friction coefficients on its sliding surfaces and same effective radii as those of concave plates 1 and 4 of the triple FP to ensure equal isolation time periods. The first study demonstrates that the conventional FP outperforms the triple FP for most of the PGAs except for very small PGAs below 1–2 m/s$^2$ depending on the earthquake. This finding is explained by the facts that the small effective radii of the articulated slider assembly reduce the isolation time period and therefore the isolation of the structure and splitting the friction into medium and high values on surfaces 1 and 4 cannot improve the isolation performance since the relative motion amplitudes on surfaces 1 and 4 are reverse whereby the energy dissipation is not enhanced compared to the conventional double FP with equal friction coefficients. The second study shows a way how the triple FP with four friction coefficients, four effective radii and four displacement capacities can be optimized for maximum isolation of the primary structure. This study points out that the optimized triple FP converges to the optimized double FP which explains the similar isolation performances. Thus, the triple FP does not improve the isolation of the structure compared to the conventional friction pendulum.

**Keywords** Curved surface slider • Earthquake • Friction • Isolation • Pendulum • Seismic

## 4.1 Introduction

Conventional spherical friction pendulums (FP) such as single and double FPs are often used isolator. The triple FP with the articulated slider assembly in between of the two main concave sliding surfaces has become famous because it generates displacement amplitude dependent stiffness and friction behaviors [1, 2]. According to [1, 2] the triple FP is intended to produce low friction and high stiffness at small bearing motion amplitudes and peak ground accelerations (PGA), respectively, to exert increasing friction at significantly reduced stiffness at medium bearing displacement amplitudes and PGAs, respectively, due to the design basis earthquake (DBE), to generate further increasing friction at further lowered stiffness at large bearing displacement amplitudes and PGAs, respectively, due to earthquakes between DBE and the

F. Weber (✉)
Maurer Switzerland GmbH, Neptunstrasse 25, 8032 Zurich, Switzerland
e-mail: F.Weber@maurer.eu

P. Huber • C. Braun
MAURER SE, Frankfurter Ring 193, 80807 Munich, Germany
e-mail: P.Huber@maurer.eu; Braun@maurer.eu

H. Distl
Maurer Söhne Engineering GmbH & Co. KG, Frankfurter Ring 193, 80807 Munich, Germany
e-mail: Distl@maurer.eu



J. Caicedo, S. Pakzad (eds.), *Dynamics of Civil Structures, Volume 2*, Conference Proceedings of the Society for Experimental Mechanics Series, DOI 10.1007/978-3-319-54777-0_4

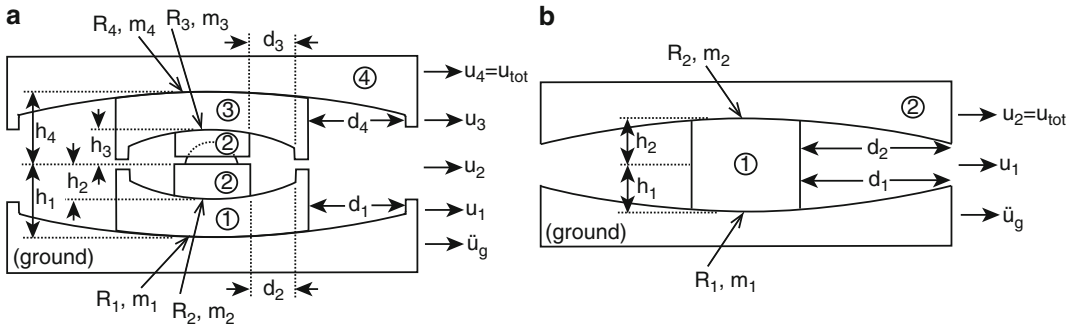


**Fig. 4.1** Sketches of triple FP (**a**) with articulated slider assembly and double FP (**b**) without articulated slider

maximum credible earthquake (MCE), and to exhibit stiffening behavior for earthquakes beyond of MCE to limit the required maximum displacement capacity. This paper investigates if the above mentioned behavior improves the isolation of the structure.

## 4.2 Friction Pendulums Under Consideration

### *4.2.1 Triple Friction Pendulum*

The triple FP consists of the articulated slider assembly with sliding surfaces 2 and 3, the articulated slider in between and the main sliding surfaces 1 and 4 (Fig. 4.1a). The common design is that the effective radii 2 and 3 ($R_{eff-2}$, $R_{eff-3}$) are equal and approx. 8 times smaller than the equal effective radii 1 and 4 ($R_{eff-1}$, $R_{eff-4}$) that determine the isolation time period of the bearing

$$T_{iso} = 2\,\pi\sqrt{\frac{R_{eff-1} + R_{eff-4}}{g}} \tag{4.1}$$

The friction coefficients $\mu_2$ and $\mu_3$ are usually selected to be small in the range of 1.5–2% while $\mu_1$ is designed to produce medium friction around 3–5% and $\mu_4$ high friction in the region of 8–11%. The restrainers on sliding surfaces 2 and 3 are required to initiate sliding on surfaces 1 and 4 and consequently always included in the triple FP. In contrast, the restrainers on surfaces 1 and 4 are not always included but are needed when the intended stiffening behavior due to sliding regime V for earthquakes beyond of MCE is desired and when the structural engineer specifies that the bearing must include end stoppers. For the first study of this paper the triple FP is designed according to the published design [1, 2] which represents a mock-up triple FP: $R_{eff-1} = R_{eff-4} = 0.435$ m, $R_{eff-2} = R_{eff-3} = 0.053$ m, $\mu_1 = 3.1\%$, $\mu_2 = \mu_3 = 1.75\%$ and $\mu_4 = 11.4\%$ where the friction values represent average values identified from testing [2]. The displacement capacities are $d_1 = d_4$=0.064 m and $d_2 = d_3 = 0.019$ m that yield the total displacement capacity $d_{tot} = 0.166$ m. For the second study of this paper the parameters of the triple FP are optimized for minimum absolute structural acceleration which is described in the penultimate section.

### *4.2.2 Double Friction Pendulum*

The conventional, i.e. non-adaptive, double FP is composed of two bearing plates with equal effective radii $R_{eff-1} = R_{eff-2}$ and friction coefficients $\mu_1$ and $\mu_2$ that must be equal because the relative motions on surfaces 1 ($u_1$) and 2 ($u_2$) are coupled due to the non-articulated slider (Fig. 4.1b). For the first study the isolation time period given by the sum ($R_{eff-1} + R_{eff-2}$) is equal to that of the triple FP (1), the equal friction coefficients $\mu_1 = \mu_2$ are tuned by trial and error and $d_{tot}$ is the same as for the mock-up triple FP. For the second study of this paper a double FP with articulated slider is assumed which allows optimizing the double FP by different $\mu_1$ and $\mu_2$.

## 4.3 Assessment Criterion

The isolation performances of the triple FP and the non-adaptive double FP as benchmark are assessed in terms of the extreme value of the absolute acceleration of the structure

$$\max\left(|\ddot{u}_s + \ddot{u}_g|\right) \tag{4.2}$$

where $\ddot{u}_s$ denotes the acceleration of the structure relative to the shaking ground and $\ddot{u}_g$ is the ground acceleration given by the El Centro North-South (NS), the Kobe, the Loma Prieta and the Northridge earthquakes. In order to operate the triple FP within all its sliding regimes with associated different isolation performances the above mentioned accelerograms are scaled to the following PGAs

$$PGA = [0.5 : 0.5 : PGA_{\max}] \tag{4.3}$$

where $PGA_{\max}$ describes this PGA value at which the full displacement capacity of the triple FP is used.

## 4.4 Modelling

### *4.4.1 Approach*

In order to compute the maximum acceleration response of the structure with triple and double FPs the coupled nonlinear (friction damping) equations of motion for the lumped mass of the building and the masses of all bearing plates are formulated. The resulting stiff system of nonlinear differential equations is solved in the time domain in Matlab® using the solver ode15s(stiff/NDF) with maximum relative tolerance 1e-3 and variable step size with upper bound of 1e-5 s. The excitation force is given by the PGA-scaled accelerograms of the aforementioned earthquakes. Subsequent to the dynamic simulations the assessment criterion (4.2) is determined from the time histories of the absolute structural acceleration.

### *4.4.2 Coupled Nonlinear Equations of Motion*

The building with isolator is modelled as a single degree-of-freedom system

$$m_s\,\ddot{u}_s + c_s\,\left(\dot{u}_s - \dot{u}_4\right) + k_s\,\left(u_s - u_4\right) = -m_s\,\ddot{u}_g \tag{4.4}$$

where $m_s$, $c_s$, $k_s$ denote the modal mass, the viscous damping coefficient and the stiffness of the building, $\ddot{u}_s$, $\dot{u}_s$ and $u_s$ denote the acceleration, velocity and displacement of the structure relative to the ground while $\dot{u}_4$ and $u_4$ are the velocity and displacement of the top bearing plate of the triple FP relative to the ground. $c_s$ in (4.4) is computed based on the damping ratio $\zeta_s = 1\%$. For study with the mock-up triple FP $k_s$ is selected so that the isolation time period (1), which is 1.87 s, is two times higher than the natural period of the non-isolated structure; for the second study the isolation time period is set to the typical value of 3.5 s in order to shift the structure out of the frequency range of most earthquakes and the natural period of the non-isolated structure is set to the typical value of 1.2 s. The equation of motion of concave plate 4 of the triple FP with mass $m_4$ becomes

$$m_4\,\ddot{u}_4 + f_{h-4} + \frac{W}{R_{eff-4}}\,\left(u_4 - u_3\right) + f_{r-4} = c_s\,\left(\dot{u}_s - \dot{u}_4\right) + k_s\,\left(u_s - u_4\right) - m_4\,\ddot{u}_g \tag{4.5}$$

where $f_{h-4}$ is the friction force of the curved sliding surface, $W/R_{eff-4}$ is the restoring stiffness due to the vertical load $W = 9.81\,m_s$ on the bearing and the effective radius $R_{eff-4} = R_4 - h_4$; $\dot{u}_3$ and $u_3$ are the velocity and displacement of bearing plate 3 of the triple FP relative to the ground. The force $f_{h-4}$ is modelled by the hysteretic damper modelling approach [3]

$$f_{h-4} = \begin{cases} k_{h-4}\,\left(u_4 - u_3\right) & : pre-sliding \\ \mu_4\,W\,sign\left(\dot{u}_4 - \dot{u}_3\right) & : \quad sliding \end{cases} \tag{4.6}$$

where $k_{h-4}$ is the pre-sliding stiffness that is selected two orders of magnitude greater than $W/R_{eff-4}$. The force of the restrainer of concave plate 4 is assumed as linear stiffness force if it is triggered

$$f_{r-4} = \begin{cases} k_{r-4}\ (|u_4 - u_3| - d_4)\ sign\,(u_4 - u_3) & : |u_4 - u_3| \geq d_4 \\ 0 & : |u_4 - u_3| < d_4 \end{cases} \tag{4.7}$$

where $k_{h-4}$ denotes the restrainer stiffness which is also assumed to be two orders of magnitude greater than $W/R_{eff-4}$. The equations of motion of concave plate 3 ($i = 3$) and slider mass 2 ($i = 2$) have the same form

$$m_i\,\ddot{u}_i + f_{h-i} + \frac{W}{R_{eff-i}}\,(u_i - u_{i-1}) + f_{r-i} = f_{h-(i+1)} + \frac{W}{R_{eff-(i+1)}}\,(u_{i+1} - u_i) + f_{r-(i+1)} - m_i\,\ddot{u}_g \tag{4.8}$$

where the friction and restrainer forces $f_{h-i}$ and $f_{r-i}$ are formulated analogically with (4.6) and (4.7). The equation of motion of concave plate 1 is given by Eq. (4.8) with $i = 1$ and $u_{i-1} = \dot{u}_{i-1} = 0$. The equation of motion of concave plate 2 of the double FP is given analogically with (4.5) and the equation of motion of the slider (index 1) of the double FP is given by (4.8) with $i = 1$ and $u_{i-1} = \dot{u}_{i-1} = 0$.

## 4.5 Isolation Performance of Mock-Up Triple Friction Pendulum

The isolation results of the triple FP that is designed according to the literature [1, 2] and of the double FP with same isolation time period and equal friction coefficients $\mu_1 = \mu_2$ that are tuned by trial and error are depicted in Figs. 4.2 and 4.3 for the four chosen accelerograms. The following main observation can be made:

- The triple FP generates a worse isolation of the structure for most of the PGAs ($PGA \geq 2.2$ m/s$^2$ for El Centro NS, $PGA \geq 0.59$ m/s$^2$ for Kobe, $PGA \geq 0.85$ m/s$^2$ for Loma Prieta, $PGA \geq 1.12$ m/s$^2$ for Northridge) than the double FP whose equal friction coefficients are tuned by trial and error (suboptimal tuning).
- The isolation due to the triple FP deteriorates dramatically when sliding regime V is triggered due to the stiffening behavior at reduced friction of sliding regime V [4].
- The fact that the restrainers of the double FP with same total displacement capacity are triggered at larger PGAs than in case of the triple FP demonstrates that the double FP does not only generate better isolation of the structure but also that the total bearing displacement is smaller.

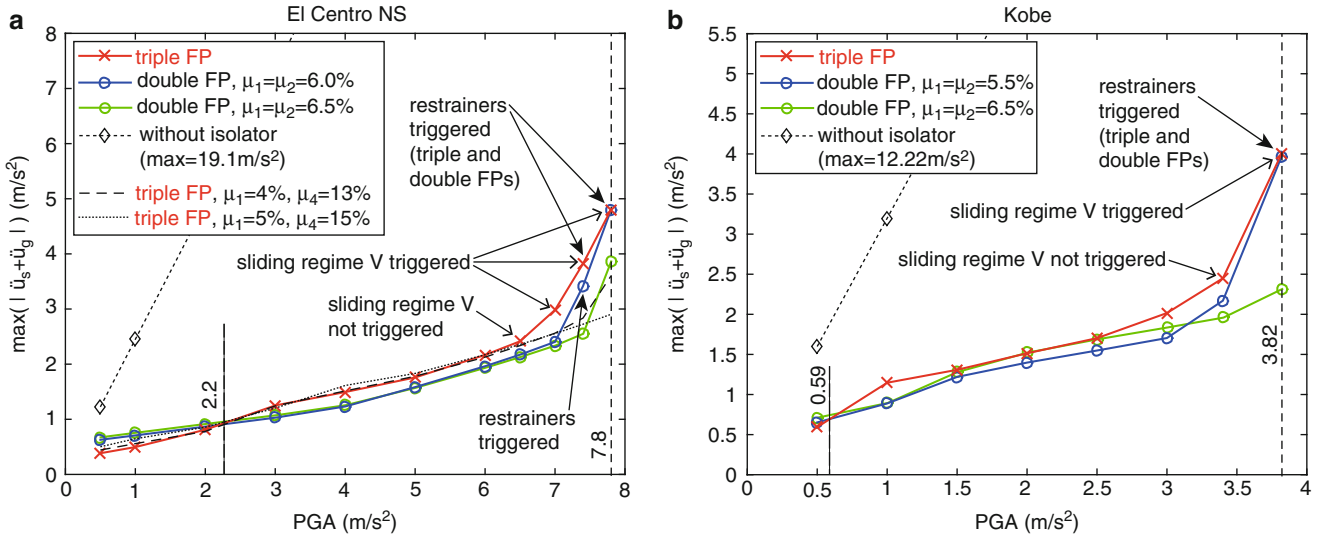


**Fig. 4.2** Isolation performances of triple FP according to literature and conventional double FP tuned by trial and error for El Centro NS (**a**) and Kobe (**b**) accelerograms

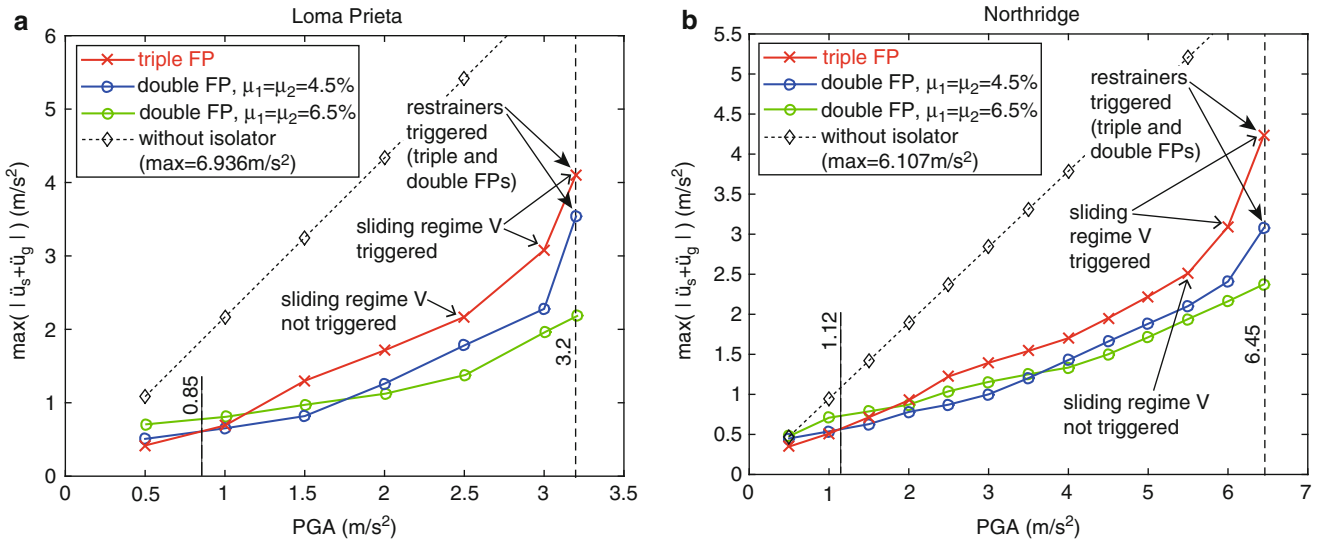


**Fig. 4.3** Isolation performances of triple FP according to literature and conventional double FP tuned by trial and error for Loma Prieta (**a**) and Northridge (**b**) accelerograms

As Fig. 4.2a shows also two triple FPs with slightly different friction tunings of the main sliding surfaces 1 and 4 are computed. These simulations show that increased friction on the main sliding surfaces 1 and 4 avoids that the triple FP is operated in sliding regime V which improves the isolation performance compared to the triple FP according to literature [1, 2]. Nevertheless, these two triple FPs also perform worse compared to the double FP.

## 4.6 Isolation Performance of Optimized Triple Friction Pendulum

### *4.6.1 PGAs of Optimization*

Due to the nonlinearity of friction damping of both FPs their isolation performance depends on their relative motion amplitude [5] and consequently on PGA. Therefore, the optimizations of both FPs must be done for selected PGAs. The following PGAs for optimization are chosen here:

- $PGA_{opt} = 2.5$ m/s$^2$ representing a small DBE,
- $PGA_{opt} = 5$ m/s$^2$ representing a medium to large DBE, and
- $PGA_{opt} = 7.5$ m/s$^2$ representing a large DBE.

### *4.6.2 Isolation Time Period*

The optimizations of both FPs are made for the typical situation where the fundamental time period of the non-isolated structure is 0.83 s (1.2 Hz), the vertical load $W$ is 12 MN, $\zeta_s = 1\%$ and the selected isolation time period is 3.5 s in order to shift the isolated structure into the time period range of good isolation. This leads to effective radii $R_{eff-1} = R_{eff-4} = 1.522$ m for the triple FP and $R_{eff-1} = R_{eff-2} = 1.522$ m for the double FP.

### *4.6.3 Articulated Slider Assembly of Triple FP*

As the intention of the articulated slider assembly of triple FP is to trigger relative motion in the bearing at even very small PGAs the friction coefficients $\mu_2 = \mu_3$ are assumed to be 1.75% similar to the published data. According to the design

philosophy of the triple FP the effective radii $R_{eff-2} = R_{eff-3}$ are designed to be smaller than $R_{eff-1} = R_{eff-4}$ so that sliding regime II is activated without force step due to triggered restrainers on concave plates 1 and 3. In order to comply with this design methodology, $R_{eff-2} = R_{eff-3}$ are selected to be eight times smaller than $R_{eff-1} = R_{eff-4}$ as $R_{eff-1}/R_{eff-2} = 8$ is in accordance to the design given in [1, 2]. The displacement capacities $d_2 = d_3$ are scaled by approx. the same factor as the effective radii which yields $d_2 = d_3 = 0.07$ m.

### 4.6.4 Restrainers 1 and 4

The previous study demonstrated that the activation of sliding regime V due to restrainers 1 and 4 worsens the isolation of the structure dramatically. The previous study further demonstrated that the isolation deteriorates completely when the full displacement capacity of the bearing is used, i.e. all restrainers are triggered. Therefore, restrainers 1 and 4 are omitted for the optimization of the triple FP.

### 4.6.5 Optimization Parameters

Due to the definition of the isolation time period of 3.5 s whereby $R_{eff-1}$ and $R_{eff-4}$ of the triple FP are given, due to the design of the articulated slider assembly of the triple FP which is in agreement with the common design philosophy of the triple FP and due to the neglect of restrainers 1 and 4 of the triple FP in order to avoid bad isolation of the structure due to sliding regime V and when all restrainers are triggered the triple FP can be optimized for minimum acceleration response of the structure (2) by variation of the friction coefficients $\mu_1$ and $\mu_4$. Similarly, the double FP with same isolation time period as the triple FP and without end stoppers on sliding surfaces 1 and 2 is optimized for minimum acceleration response of the structure (2) by variation of the friction coefficients $\mu_1$ and $\mu_2$. As $\mu_1$ and $\mu_2$ can be different a double FP with articulated slider is assumed.

### 4.6.6 Optimization Results

Exemplarily for all optimization cases, i.e. four earthquakes scaled to three $PGA_{opt}$, two optimization results are plotted in Figs. 4.4 and 4.5. The following can be observed:

- The optimal friction coefficients of the triple and double FPs and the resulting absolute structural acceleration are very similar.
- The optimal friction coefficients can be different (El Centro NS, Fig. 4.4) or equal (Loma Prieta, Fig. 4.5); if they are different it is not relevant which one is higher (valid for triple and double FPs).

### 4.6.7 Isolation Performance of Optimized Triple FP

The isolation performances of the optimized triple and double FPs are computed for the El Centro NS, the Kobe, the Loma Prieta and the Northridge accelerograms that are scaled to PGAs ranging from 0.25 m/s$^2$ up to 150% of $PGA_{opt}$ assuming that the FPs are optimized at the PGA corresponding to DBE and that the PGA of MCE is around 150% of the PGA of DBE. The isolation performances accompanied by the total bearing displacement as an important economical parameter are depicted in Figs. 4.6, 4.7, 4.8, and 4.9 for $PGA_{opt} = 5$ m/s$^2$; showing also the results due to the optimizations at 2.5 and 7.5 m/s$^2$ is not possible due to the limited number of pages of the manuscript but the results are qualitatively similar. It is seen that the optimized triple and double FPs approximately yield the same absolute structural accelerations and total bearing displacements. This outcome is explained by the fact that the triple FP mutates to a double FP by the optimization which

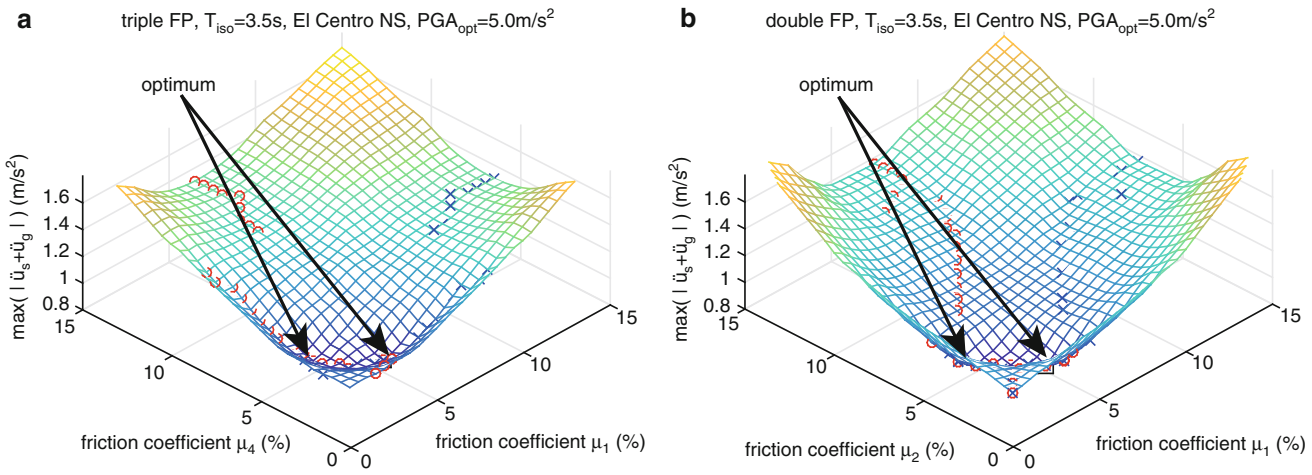


**Fig. 4.4** Optimization results for triple (**a**) and double (**b**) FPs for the El Centro NS accelerogram scaled to 5 m/s$^2$

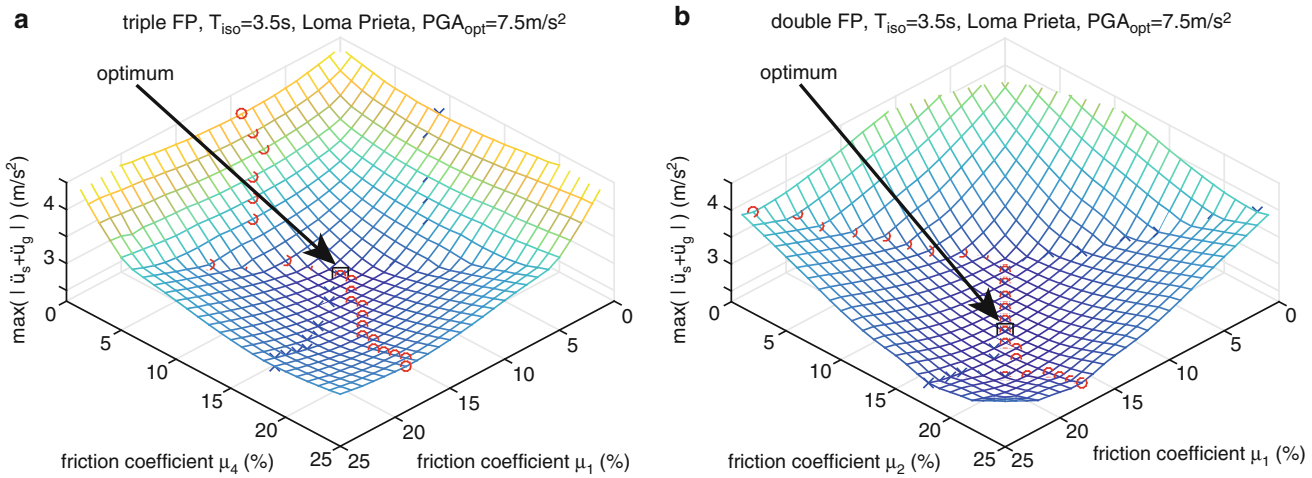


**Fig. 4.5** Optimization results for triple (**a**) and double (**b**) FPs for the Loma Prieta accelerogram scaled to 7.5 m/s$^2$

means that $\mu_1$ and $\mu_4$ must be designed similar to $\mu_1$ and $\mu_2$ of the optimal double FP and that the articulated slider assembly is not beneficial for maximum isolation due to its high stiffness which is equivalent to a low isolation time period. From Fig. 4.6 it is also evident that the conventional design of the triple FP [1, 2] is far from optimal and that the suboptimal solutions with equal friction coefficients perform almost as well as their optimal counterparts.

## 4.7 Summary

First, the isolation performance in terms of absolute structural acceleration of the triple friction pendulum (FP) with parameters from literature is compared to that of the conventional double FP. Second, the triple and double FPs are optimized for minimum absolute structural acceleration and their isolation performances are compared subsequently. The first study demonstrates that the triple FP designed according to literature performs worse than the conventional double FP with suboptimal friction tuning. The second investigation demonstrates that both optimized FPs generate similar structural acceleration responses and total bearing displacements due to the fact that the triple FP mutates to the double FP due to the optimization.

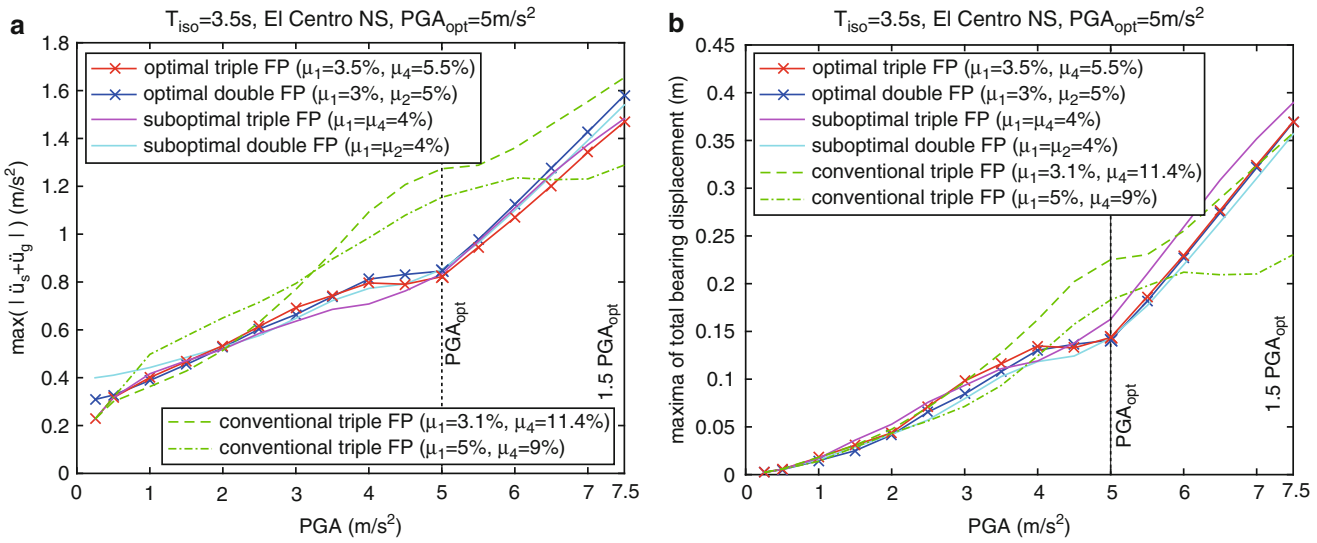


**Fig. 4.6** Isolation performance (**a**) and total bearing displacement (**b**) of triple and double FPs optimized for El Centro NS accelerogram scaled to 5 m/s$^2$

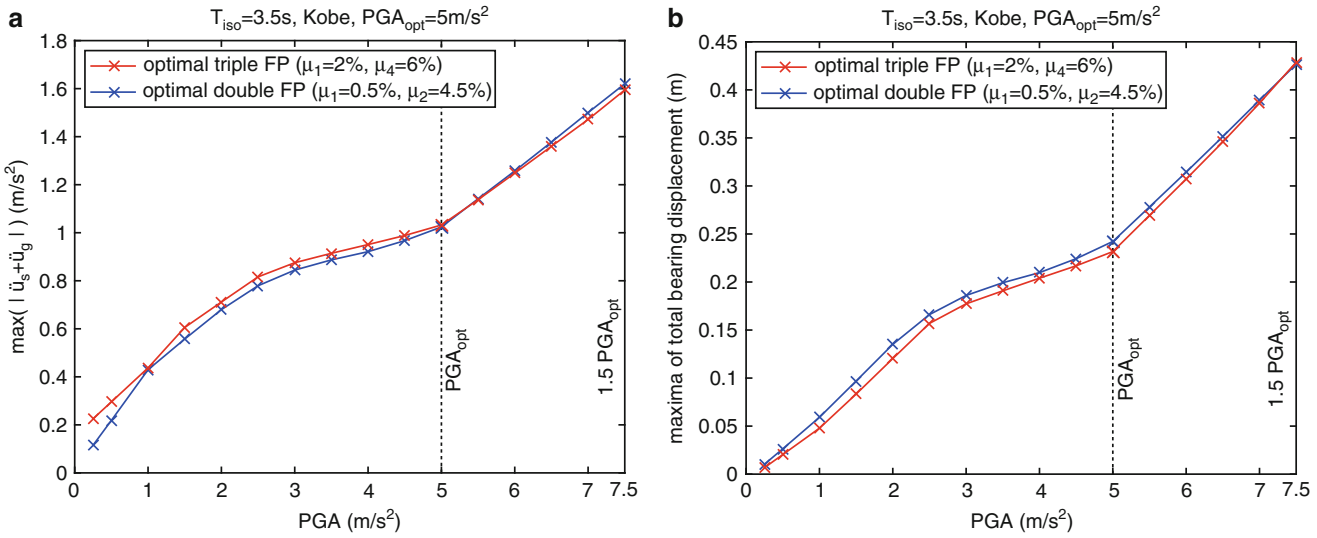


**Fig. 4.7** Isolation performance (**a**) and total bearing displacement (**b**) of triple and double FPs optimized for Kobe accelerogram scaled to 5 m/s$^2$

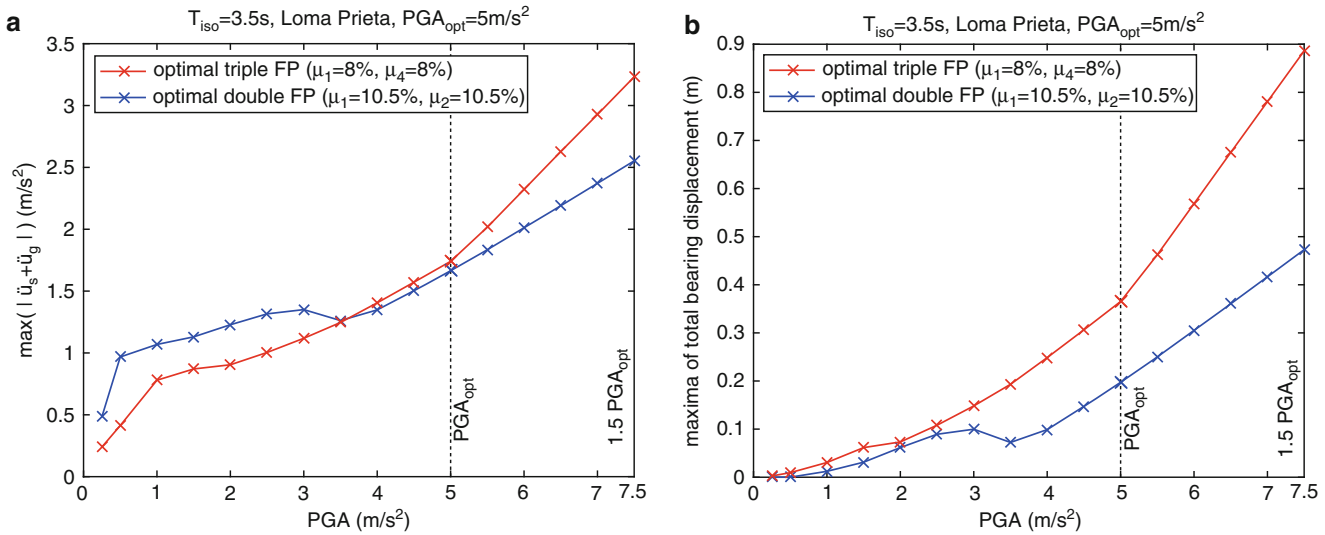


**Fig. 4.8** Isolation performance (**a**) and total bearing displacement (**b**) of triple and double FPs optimized for Loma Prieta accelerogram scaled to 5 m/s$^2$

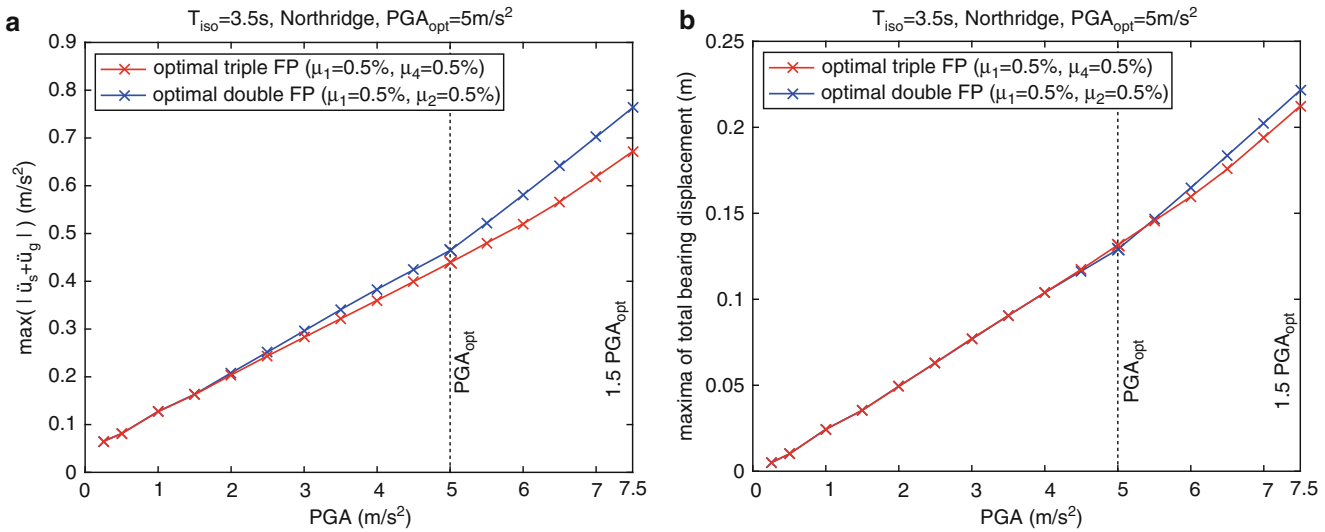


**Fig. 4.9** Isolation performance (**a**) and total bearing displacement (**b**) of triple and double FPs optimized for Northridge accelerogram scaled to 5 m/s$^2$

**Acknowledgements** The authors gratefully acknowledge the financial support of MAURER SE.

## References

1. Fenz, D.M., Constantinou, M.C.: Spherical sliding isolation bearings with adaptive behavior: theory. Earthq. Eng. Struct. Dyn. **37**, 163–183 (2008)
2. Fenz, D.M., Constantinou, M.C.: Spherical sliding isolation bearings with adaptive behavior: experimental verification. Earthq. Eng. Struct. Dyn. **37**, 185–205 (2008)
3. Ruderman, M.: Presliding hysteresis damping of LuGre and Maxwell-slip friction models. Mechatronics. **30**, 225–230 (2015)
4. Weber, F., Distl, H., Braun, C.: Dynamic characterization and isolation performance of triple friction pendulum. In: Proceedings of the 8th World Congress on Joints, Bearings and Seismic Systems for Concrete Structures (IJBRC), Atlanta (GA, USA), 25–29 September 2016
5. Weber, F., Boston, C.: Energy based optimization of viscous-friction dampers on cables. Smart Mater. Struct. **19**, 045025 (11pp) (2010)

# Chapter 5
# Experimental Investigation of the Dynamic Characteristics of a Glass-FRP Suspension Footbridge

**Xiaojun Wei, Justin Russell, Stana Živanović, and J. Toby Mottram**

**Abstract** Due to high strength- and stiffness-to-weight ratios, good durability performance in a variety of environments and quick installation, fibre reinforced polymers have increasingly been utilised for construction of highway and pedestrian bridges. Their relatively low mass and stiffness make these bridges potentially susceptible to vibration serviceability problems, which are increasingly governing the design. Currently, a lack of experimental data on the dynamic characteristics of polymeric composite structures is hindering their wider application and the development of design guidance. To fully exploit the benefits of using these structural materials in bridge engineering requires a better understanding of their dynamic behaviour. The aim of this paper is to utilise ambient vibration measurements to experimentally identify the dynamic characteristics (i.e., natural frequency, damping ratio and mode shape) of a glass fibre reinforced polymer deck suspension footbridge in the UK. It is found that the Wilcott footbridge possesses a relatively high density of vibration modes in the low frequency range up to 5 Hz and has damping ratios of most of these modes >1%.

**Keywords** FRP suspension footbridge • Dynamic characteristics • Ambient vibration testing • Peak picking method • Stochastic subspace identification method

## 5.1 Introduction

Since the first Fibre Reinforced Polymer (FRP) road bridge was built in Miyun, China in 1982 [1], thousands of bridges with FRP components have been built around the World [2]. The driver for this practice is this structural materials' favourable properties, including: high strength- and stiffness-to-weight ratios, good durability and short installation time. FRP construction is typically employed for short-to-medium span bridges. The longest span to date is 63 m, achieved with the Aberfeldy footbridge that was constructed in Scotland in 1992 [3], using the same construction system as for the Wilcott footbridge. The benefits of using FRP as the structural material would be more prominent if longer bridge spans could be executed.

Due to the lightweight and relatively low stiffness of glass FRPs, FRP bridges may be very lively and potentially suffer excessive vibration, causing user discomfort and affecting the bond in joints and between surfacing and the FRP superstructure [4]. Vibration serviceability is increasingly found to govern the design of FRP structures. A sound knowledge and understanding of their dynamic characteristics is therefore important for us having robust serviceability design procedures. Owing to a lack of experimental data on the dynamic characteristics we find that existing design guidance used in conventional material designs is usually employed. This approach may produce a conservative solution and compromise the benefits of using FRP in the first place. For example, in the AASHTO Guide Specifications for Design of FRP Pedestrian Bridges (1st Ed.) [5], a damping ratio of 2–5% is recommended. A damping ratio of at least 1% is expected to be present in every FRP structures, whilst such a high value as 5% is rarely achieved with pedestrian bridges made of other structural materials, such as steel, steel-concrete composite, aluminium and, even, concrete. In Prospect for New Guidance in the Design of FRP [6] the damping ratio is specified to be 1.5% for a conservative estimate in design analysis, and higher damping values may be used if these have been substantiated by representative experimental data. Given that the above recommendations for damping ratios are not necessarily based on extensive and comprehensive data from as-built FRP

X. Wei (✉) • J. Russell • S. Živanović • J.T. Mottram
School of Engineering, University of Warwick, Coventry, CV4 7AL, UK
e-mail: x.wei.3@warwick.ac.uk



J. Caicedo, S. Pakzad (eds.), *Dynamics of Civil Structures, Volume 2*, Conference Proceedings of the Society for Experimental Mechanics Series, DOI 10.1007/978-3-319-54777-0_5

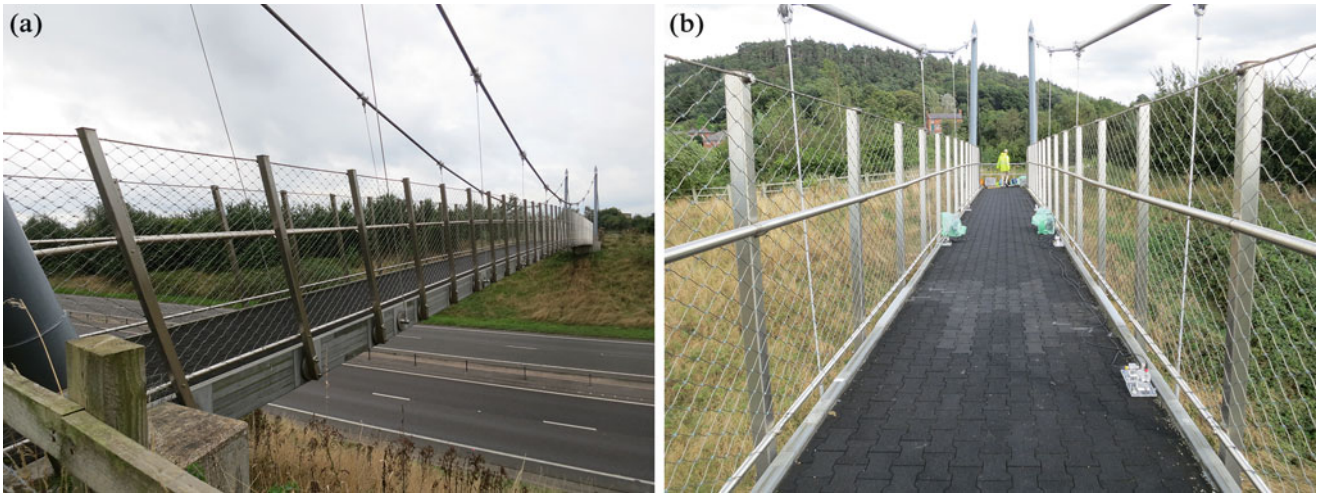


**Fig. 5.1** The Wilcott Bridge

structures there is a need to experimentally determine them. This paper contributes to this goal by providing a rare insight into the dynamic features of suspension footbridge near to the village of Nesscliffe, Shropshire, UK (Google Earth co-ordinates 52° 45′54.89″ N and 2° 55′04.68″W).

The paper starts with a description of the FRP bridge in Sect. 5.2, followed by a description of the ambient-based modal testing in Sect. 5.3. Identified modal parameters are reported in Sect. 5.4 with conclusions from their evaluation made in Sect. 5.5.

## 5.2 Bridge Description

The Wilcott Bridge, shown in Fig. 5.1, is a single span suspension footbridge over the Nesscliffe A5 bypass road. The bridge has a width of 2.1 m and a span of 51.3 m. It consists of a lightweight glass FRP deck, two pairs of steel pylons, two steel cables with a span of 57.89 m, and four steel backstays and 20 steel hangers (10 per side). The FRP deck is constructed from pultruded components of E-glass fibre embedded in an isophthalic polyester matrix, which are adhesively bonded together to form an integral box section. The pultruded construction system is known today as Composolite, and is supplied by the American pultruder Strongwell. Ballast is employed to increase the mass of the deck. The deck was built in three units of approximately equal length that are connected by bonded interlocking splice joints and was integrally connected to the foundation, without the need for movement joints.

## 5.3 Ambient Vibration Testing

To provide a precise and reliable characterization for the dynamic characteristics of the Wilcott footbridge an ambient testing programme was conducted by the authors from the University of Warwick, UK, on 09 September 2016. Acceleration responses of the deck were measured under the natural excitation of wind and road traffic passing underneath the bridge on a main truck road. During data recording the bridge was closed to pedestrian traffic.

To identify the first few modes of the bridge we used the measurement grid in Fig. 5.2, having 26 measurement stations on top of the deck. These measurement locations included anchoring points of each hanger, the mid-span points and supports at the two span ends. Vertical accelerations only were recorded on the North side, whilst both vertical and horizontal accelerations were acquired on the South side. Figure 5.3 shows the accelerometers at a location on the South side. The measurement campaign was divided into seven set-ups. In each set-up we had eight Honeywell accelerometers QA750 (of nominal sensitivity of 1300 mV/g). A lateral accelerometer and a vertical accelerometer at measurement station 55 were used as reference vibration sensors, whilst the other six accelerometers are the roving transducers.

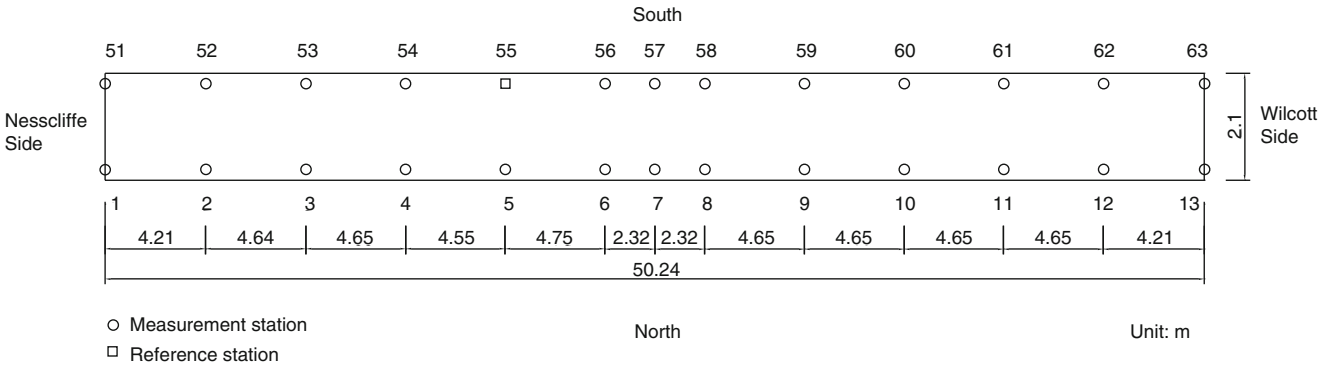


**Fig. 5.2** Measurement grid on the deck

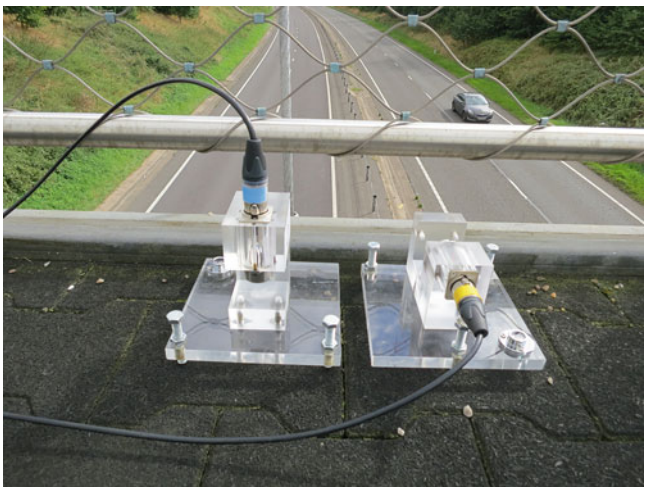

**Fig. 5.3** Vertical and lateral accelerometers on the deck

The test programme was started from the Nesscliffe side of the bridge and progressed to the Wilcott side. The duration for each measurement set-up was 20 min. The sampling frequency was 256 Hz. Typical vertical and lateral acceleration time histories at the reference station (No. 55) in one of the seven set-ups are plotted in Fig. 5.4. The ambient vibration response level exhibited little variation between the seven different set-ups.

## 5.4 Modal Parameter Identification

To identify the modal parameters of the Wilcott footbridge we employed the frequency-domain peak-picking method and the time-domain stochastic Sub-Space Identification (SSI) method. Whilst the peak-picking method was chosen to identify natural frequencies only, the SSI method was employed to identify natural frequencies, damping ratios and mode shapes.

### *5.4.1 Peak-Picking Method*

Since certain modes may not be observable in the power spectrum density at a particular measurement station, the Averaged Normalised Power Spectral Densities (ANPSD) [7, 8] of all the measurement stations can be used to identify all natural frequencies. The ANPSDs of the vertical and lateral accelerations are plotted in Figs. 5.5 and 5.6, respectively. The natural frequencies of the bridge are inferred from the peaks in the ANPSD curves. From the results in Fig. 5.5 there are six dominant peaks in the vertical direction, at frequencies of 0.94, 1.52, 2.22, 2.72, 3.20 and 3.89 Hz, and a less pronounced

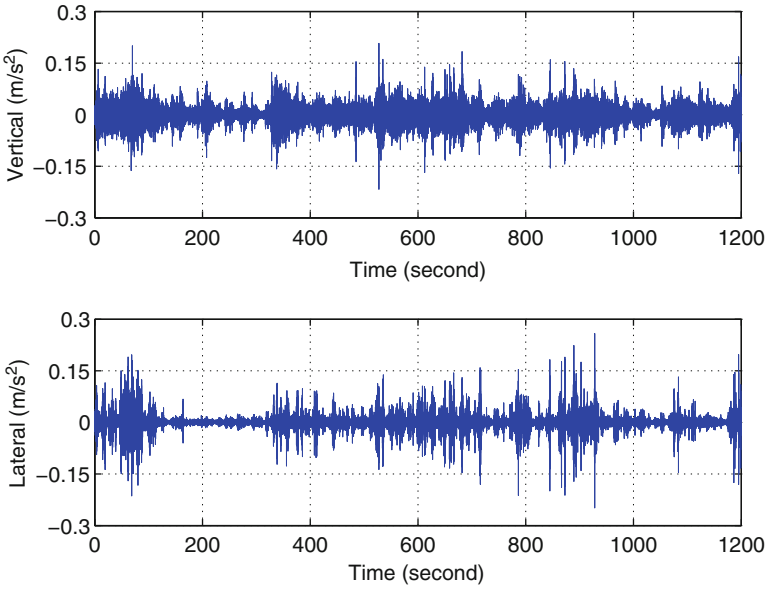


**Fig. 5.4** Acceleration time histories measured at the reference station (No. 55)

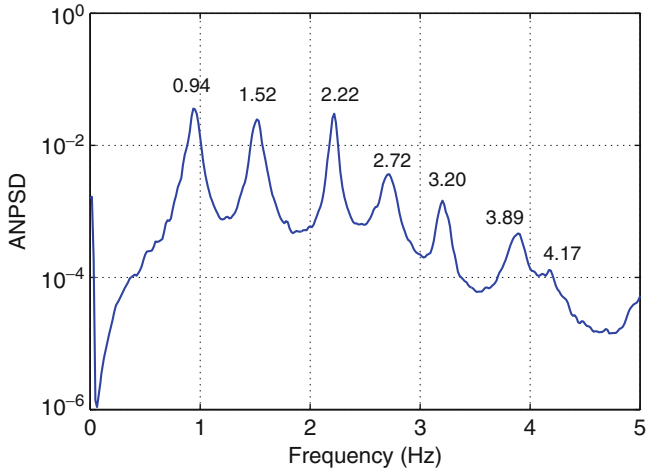


**Fig. 5.5** ANPSD for vertical acceleration records

peak at 4.17 Hz. As for the lateral direction with results in Fig. 5.6, the three dominant peaks are observed at 1.08, 1.55 and 4.19 Hz, with two smaller peaks at 2.19 and 3.20 Hz. In addition, there are two close frequency peaks at 2.47 and 2.58 Hz. It is seen that frequencies at certain peaks in the vertical direction are close to those observed in the lateral direction. This finding shows that there is uncertainty in interpreting whether the close peaks in the two orthogonal directions correspond to distinct modes or that they represent the same mode having both lateral and vertical components. The SSI method presented in Sect. 5.4.2 is used to further analyse these.

### *5.4.2 Stochastic Subspace Identification*

A reference-based data-driven stochastic SSI algorithm, built in the Matlab toolbox MACEC 3.2 (by K.U.LEUVEN Research & Development [9–12]), was applied for data pre-processing and modal parameter identification. The measured data were first de-trended, such that the DC components were removed. Then the data were filtered using a low-pass filter with a cut-off frequency of 20.48 Hz and resampled at 25.60 Hz.

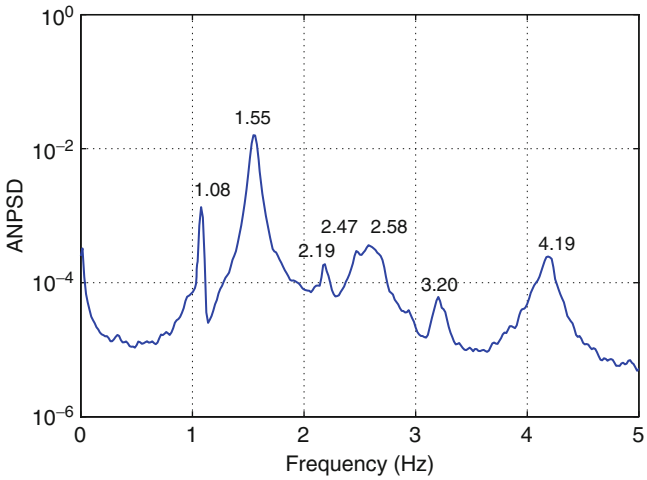


**Fig. 5.6** ANPSD for lateral acceleration records

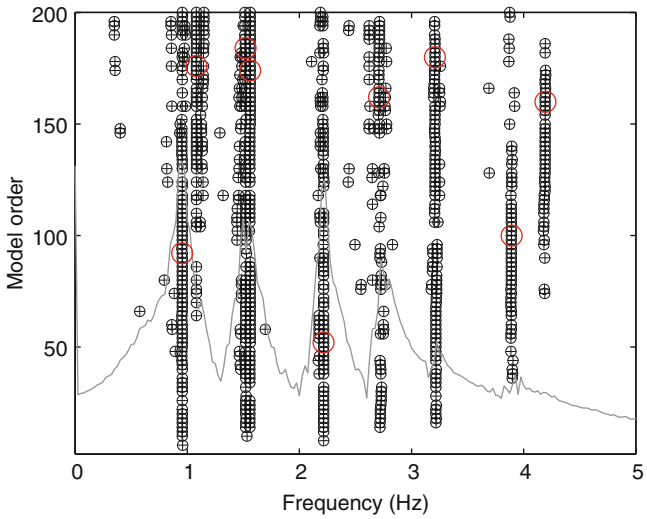


**Fig. 5.7** The stabilization diagram of one of the setups

The vertical and lateral accelerations from all the sensors were used for modal parameter identification, with the model order parameter set to 200. The two channels corresponding to the reference stations (No. 55) were chosen as the reference channels. The stabilisation criteria were set to 1% for frequency, 5% for damping, 1% for modal assurance criterion and 0.8 for the low bound of the modal phase collinearity. Shown in Fig. 5.7 is a stabilisation diagram from one of the data set-ups, with the power spectral density of all the signals superimposed. Only the frequency content, up to 5 Hz, is presented in the figure, since this is the most relevant frequency range for pedestrian structures. Stable poles are presented by big red circles. It can be seen that the stable poles for natural frequencies are clearly identified, except for the one around 2.70 Hz. There are in total nine dominant modes identified, including three lateral bending, five vertical bending and one torsional mode. These nine mode shapes are illustrated in Figs. 5.8, 5.9, 5.10, 5.11, 5.12, 5.13, 5.14, 5.15 and 5.16.

It can be observed that a majority of the modes found by the peak-picking method are identified by the SSI method. The only discrepancy is that two modes appear from peak-picking in the frequency range of 2.40–2.70 Hz, whereas Fig. 5.7 for SSI shows that there is only one consistent stable pole around 2.70 Hz. Moreover, the mode shapes of the identified lateral bending modes in Figs. 5.9, 5.11 and 5.16 are not very smooth. These findings might be due to the fact that the vertical acceleration signals are stronger than those in the lateral direction, and consequently the noise in vertical accelerations might be spoiling or hiding some lateral bending dominated modes [13].

The identified modes are summarised in Table 5.1. There is a relatively high mode density in the frequency range 0–5 Hz. From the first harmonic dynamic force generated from pedestrian walking the two vertical bending modes at the natural frequencies of 1.51 and 2.21 Hz and a lateral mode at 1.08 Hz are potentially excitable. The damping ratios of all vertical bending modes in Table 5.1 are not <0.96%, whilst the damping ratios of all lateral bending modes are >1%, except for

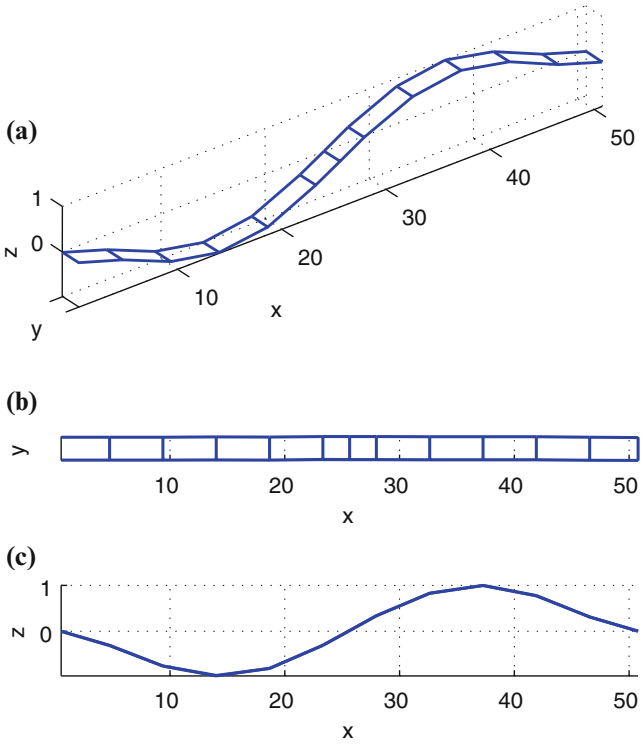


**Fig. 5.8** The first vertical bending dominated mode ($f = 0.96$ Hz, $\zeta = 2.49\%$)

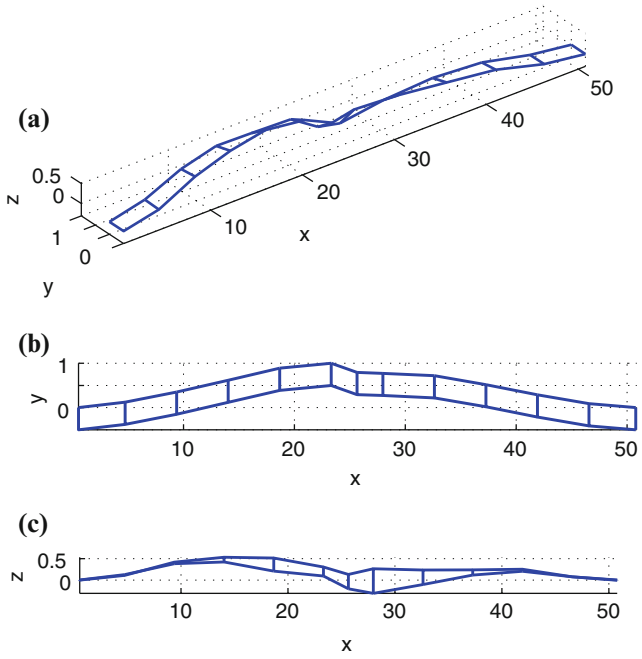


**Fig. 5.9** The first lateral bending dominated mode ($f = 1.08$ Hz, $\zeta = 0.31\%$)

the first of these modes, which has an exceptionally low damping ratio of 0.31%. Despite the potential for a number of modes being excited by pedestrians we find the bridge's vibration performance to be satisfactory. Contributing to this good serviceability performance is the reasonable level of damping in almost every mode and the potential interaction between simultaneously excited modes. The vibration response of the bridge to a range of human actions is going to be subject to new work by the University of Warwick team.

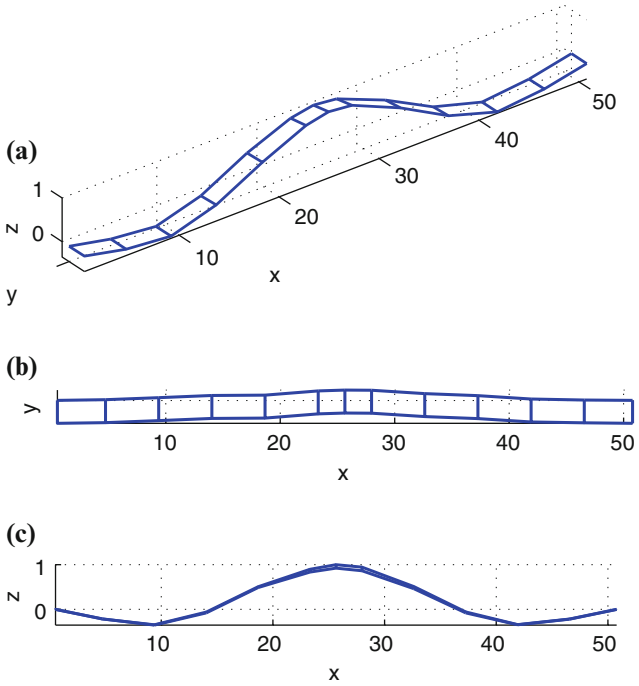


**Fig. 5.10** The second vertical bending dominated mode ($f = 1.51$ Hz, $\zeta = 1.91\%$)

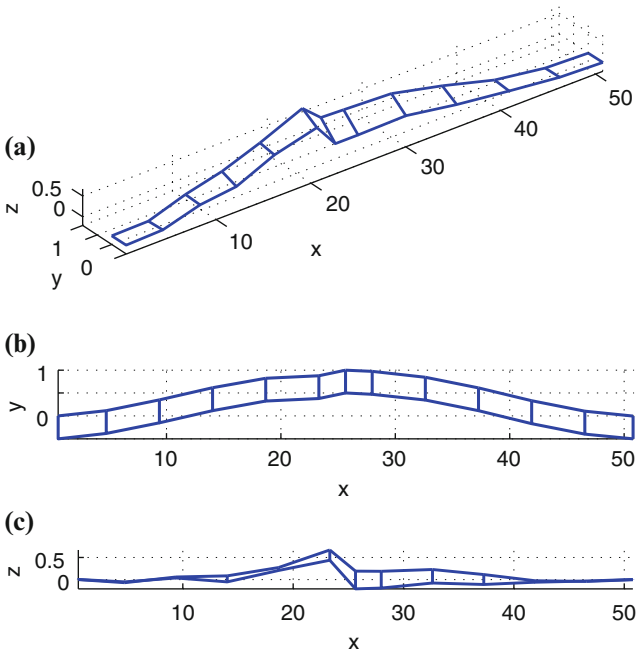


**Fig. 5.11** The second lateral bending dominated mode ($f = 1.56$ Hz, $\zeta = 1.67\%$)

## 5.5 Conclusions

Ambient testing of a suspension pedestrian bridge made with fibre reinforced polymer components was conducted to identify modal properties. The method of peak picking of the averaged normalised power spectral densities in the frequency-domain was employed to identify the natural frequencies, whilst the stochastic subspace identification method, in the time-domain, was employed to the identify natural frequencies, damping ratios and mode shapes. The combined use of the two independent analysis techniques led to identifying of as many as nine dominant vibration modes in the low frequency range of 0–5 Hz.

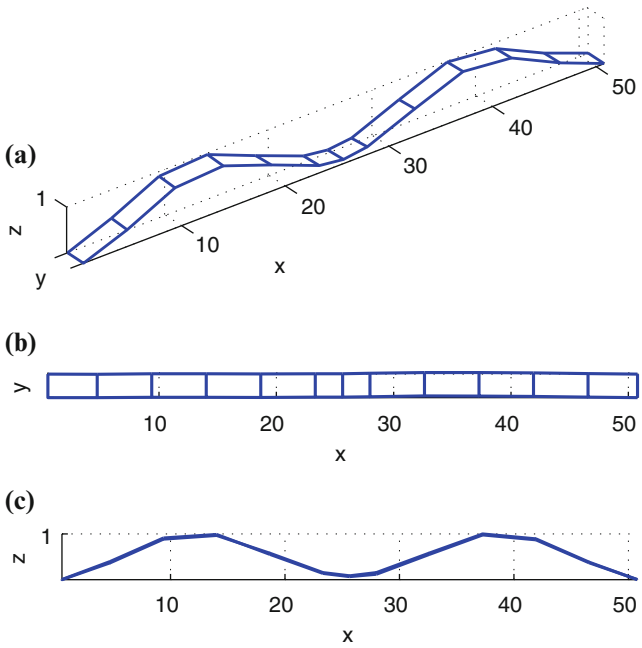


**Fig. 5.12** The third vertical bending dominated mode ($f = 2.21$ Hz, $\zeta = 0.96\%$)

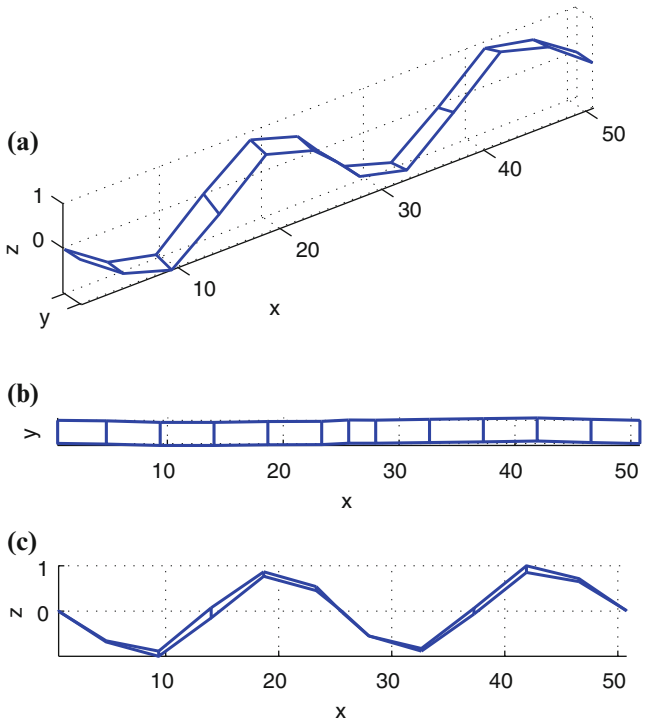


**Fig. 5.13** The fourth vertical bending dominated mode ($f = 2.71$ Hz, $\zeta = 1.89\%$)

These nine modes include three lateral bending, five vertical bending and one torsional. The damping ratios of most modes were found to be >1%, and this provided evidence to justify a recommendation in vibration serviceability design to have the damping ratio at 1% or higher. Despite some vibration modes having natural frequencies excitable in resonance by human walking actions the relatively high damping in the Wilmott footbridge ensures satisfactory serviceability performance.

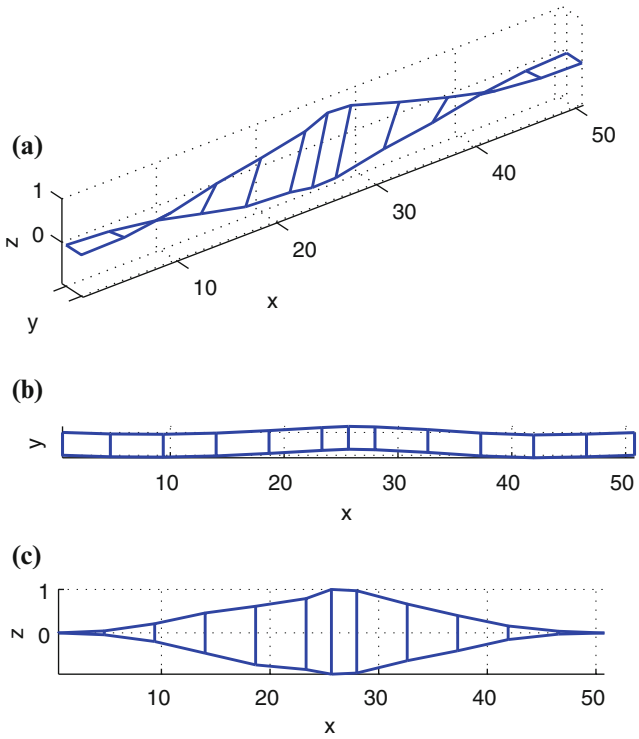


**Fig. 5.14** The first torsional mode ($f = 3.22$ Hz, $\zeta = 0.82\%$)

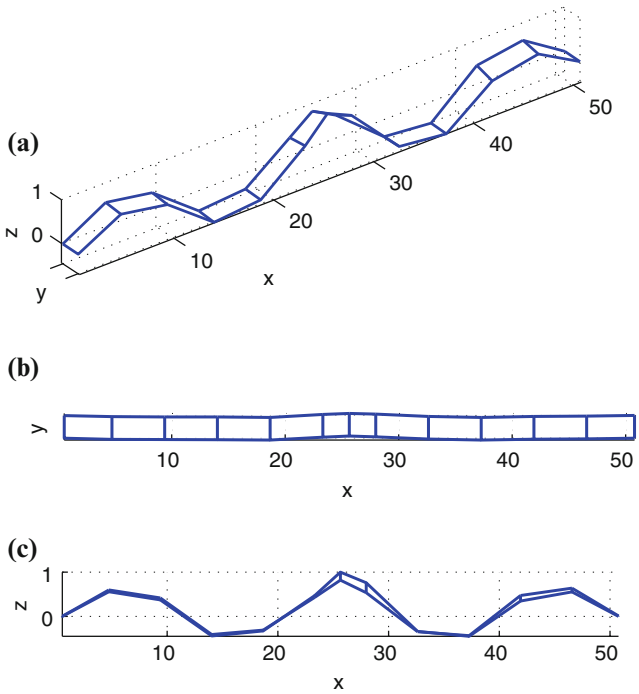


**Fig. 5.15** The fifth vertical bending dominated mode ($f = 3.86$ Hz, $\zeta = 1.41\%$)

**Acknowledgements** This research work was supported by the UK Engineering and Physical Sciences Research Council [grant number EP/M021505/1: Characterising dynamic performance of fibre reinforced polymer structures for resilience and sustainability].

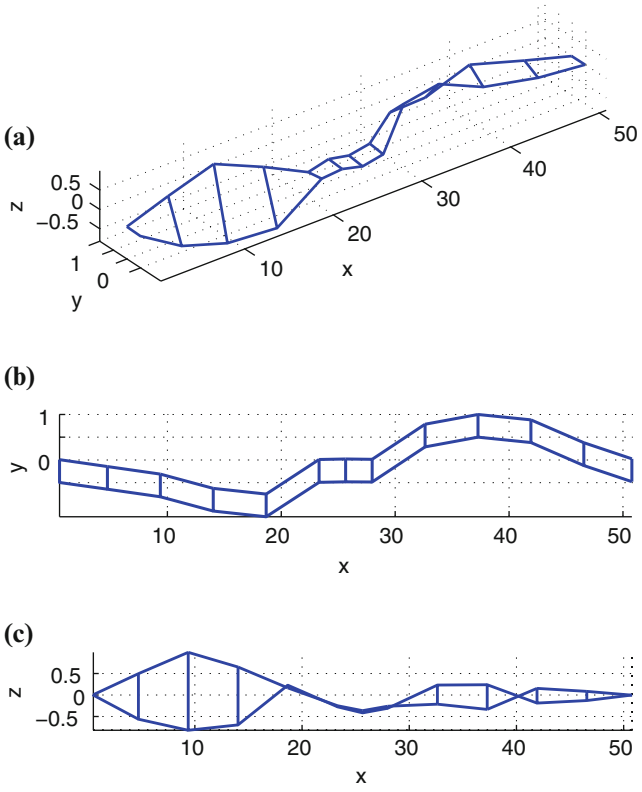


**Fig. 5.16** The third lateral bending dominated mode ($f = 4.11$ Hz, $\zeta = 1.34\%$)

**Table 5.1** Identified modal parameters of the Wilcott Bridge

| No. | Mode description | SSI | | Peak-picking |
|---|---|---|---|---|
| | | Frequency (Hz) | Damping (%) | Frequency (Hz) |
| 1 | 1st VD | 0.96 | 2.49 | 0.94 |
| 2 | 1st LD | 1.08 | 0.31 | 1.08 |
| 3 | 2nd VD | 1.51 | 1.91 | 1.52 |
| 4 | 2nd LD | 1.56 | 1.67 | 1.56 |
| 5 | 3rd VD | 2.21 | 0.96 | 2.22 |
| 6 | 4th VD | 2.71 | 1.89 | 2.72 |
| 7 | 1st T | 3.22 | 0.82 | 3.20 |
| 8 | 5th VD | 3.86 | 1.41 | 3.89 |
| 9 | 3rd LD | 4.11 | 1.34 | 4.19 |

*VD* vertical bending dominated mode, *LD* lateral bending dominated mode, *T* torsional mode

## References

1. Ye, L.P., Feng, P., Zhang, K., Lin, L., Hong, W.H., Yue, Q.R.: FRP in civil engineering in China: research and applications. In: Proceedings of Fiber Reinforced Polymer: Reinforcement for Concrete Structures, pp. 1401–1412. Singapore (2003)
2. Wan, B.: Using fiber-reinforced polymer (FRP) composites in bridge construction and monitoring their performance: an overview. Advanced Composites in Bridge Construction and Repair, pp. 3–28 (2014)
3. Burgoyne, C., Head, P.: Aberfeldy Bridge–an advanced textile reinforced footbridge. In: Techtextil Syposium, pp. 1–9 (1993)
4. BD 49/01 Design Rules for Aerodynamic Effects on Bridges. In: Design Mannual for Roads and Bridges, vol. 1, Section 3, Part 17. ed: Highways England (2001)
5. AASHTO: Guide Specifications for Design of FRP Pedestrian Bridges, 1st edn. American Association of State Highway and Transportation Officials, Washington (2008)
6. Ascione, L., Caron, J.-F., Godonou, P., IJselmuijden, K.v., Knippers, J., Mottram, T., et al.: Prospect for New Guidance in the Design of FRP. EUR 27666 EN, 2016
7. Felber, A.J.: Development of a hybrid bridge evaluation system. PhD Thesis, The University of British Columbia (1994)

8. Ren, W.-X., Peng, X.-L., Lin, Y.-Q.: Experimental and analytical studies on dynamic characteristics of a large span cable-stayed bridge. Eng. Struct. **27**, 535–548 (2005)
9. Reynders, E., Schevenels, M., Roeck, G.D.: MACEC 3.2: A Matlab Toolbox for Experimental and Operational Modal Analysis. Department of Civil Engineering, KU Leuven (2014)
10. Peeters, B., De Roeck, G.: Reference-based stochastic subspace identification for output-only modal analysis. Mech. Syst. Signal Process. **13**, 855–878 (1999)
11. Peeters, B., De Roeck, G.: Stochastic system identification for operational modal analysis: a review. J. Dyn. Syst. Meas. Control. **123**, 659–667 (2001)
12. Reynders, E., Roeck, G.D.: Reference-based combined deterministic–stochastic subspace identification for experimental and operational modal analysis. Mech. Syst. Signal Process. **22**, 617–637 (2008)
13. Brownjohn, J.M.W., Magalhaes, F., Caetano, E., Cunha, A.: Ambient vibration re-testing and operational modal analysis of the Humber Bridge. Eng. Struct. **32**, 2003–2018 (2010)

# Chapter 6
# Vibration-Based Occupant Detection Using a Multiple-Model Approach

**Yves Reuland, Sai G. S. Pai, Slah Drira, and Ian F. C. Smith**

**Abstract** Sensor-based occupant detection has the potential to make an important contribution to the development of structures of the future. Applications that may benefit from robust occupant detection include patient detection in hospitals, senior citizen housing facilities, personnel localization in emergencies as well as user behavior studies. In this contribution, an occupant detection and localization methodology based on recorded vibration time-series is outlined. The movement of an occupant on a floor generates vibrations that can be recorded by accelerometers. However, measured vibrations contain measurement noise and are contaminated by ambient sources of vibration such as machinery and nearby traffic. This contribution relies on using filtered vibration time-series to detect events of moving occupants and subsequently perform model-based localization of occupants using error-domain model falsification. The error-domain model-falsification methodology utilizes multiple models to deal with ambiguity related to the inverse problem of occupant localization. By explicitly incorporating uncertainty from various sources using engineering heuristics, error-domain model falsification provides a set of candidate locations based on measurements obtained through a coarse sensor configuration. The results from this methodology provide in a binary manner the presence or absence of an occupant and subsequently candidate locations of the occupant on the floor of a 200 $m^2$ hall that is equipped with only four accelerometers.

**Keywords** Human detection • Structural vibrations • Multiple model • Error-domain model falsification • Robust localization

## 6.1 Introduction

Recent advances in sensing and computing technology have made available reliable sensors at reduced cost and tools for processing this data are leading the way for development of structures of the future. Sensor-based human detection requires availability of data from sensors and robust methods for interpretation of this data in presence of ambiguity. Human detection using sensor data has the potential to increase the safety of building occupants, security and general knowledge of building use. For example, this technology may be applied for patient detection in hospitals and senior-citizen housing facilities, security systems for banks, personnel localization in emergencies, energy management and user-behavior studies.

Fall detection of elderly and patients in healthcare facilities is particularly likely to benefit from this technology. Current state-of-the-art fall detectors include community alarms, wearable detectors and cameras, which are a potential impedance to functioning of patients and undermine their privacy [1, 2]. An alternative approach for human detection and localization relies on the use of vibration data from sensors. Unlike the use of cameras and to a lesser extent, motion sensors for occupant detection, retrieval of vibration data from sensors does not infringe on the privacy of building occupants.

Localization of an occupant has been proposed by Schloemann et al. [3] using vibration measurements from 241 sensors. Lam et al. [4] proposed an occupant detection methodology taking into consideration structural behavior to determine thresholds on classifying vibrations from occupant activities. Pan et al. [5] presented a building occupancy estimation system wherein data from low-resolution vibration sensors was used for occupant detection. They were able to distinguish between occupant activity and noise from ambient vibrations leading to tracking of occupants entering a room, their position and number of occupants in a room. Mirshekari et al. [6] used high energy components of signals and time-difference-of arrival to accurately localize human presence. Floor vibration measurement has even been used for gender classification of occupants

Y. Reuland (✉) • S.G.S. Pai • S. Drira • I.F.C. Smith
Applied Computing and Mechanics Laboratory, Swiss Federal Institute of Technology (EPFL), Lausanne 1015, Switzerland
e-mail: yves.reuland@epfl.ch



J. Caicedo, S. Pakzad (eds.), *Dynamics of Civil Structures, Volume 2*, Conference Proceedings
of the Society for Experimental Mechanics Series, DOI 10.1007/978-3-319-54777-0_6

based on vibration characteristics [7]. However, most of the research in this domain has focused on using a high-density sensor layout, which is unrealistic for monitoring systems of most smart-buildings and which might induce unnecessary costs.

Current human detection and localization methodologies are model-free, meaning that they rely only on processing and analyzing measurement data. Coupling the measured response with a structural behavior model of the building has the potential to reduce the number of sensors necessary for human localization. However, predictions of the structural response for vibrations induced by human footsteps are prone to multiple sources of uncertainty including material properties, geometry and boundary conditions. Therefore, a model-based data-interpretation methodology that is robust in presence of uncertainty is needed to perform human localization using vibration measurements from a sparse sensor configuration.

In this paper, a procedure for human detection and localization is presented using floor vibration data. First a methodology to detect the presence of an occupant is described. Once the presence of an occupant is established, localization is carried out using error-domain model falsification (EDMF) [8], which is a model-based data interpretation methodology that has already been employed successfully for improving knowledge of the behavior of bridges [9, 10], water-supply-networks [11] and wind around buildings [12].

## 6.2 Methodology

### *6.2.1 Human Detection*

Detection of human presence on a floor is achieved through on a two-step procedure [4]. In the first step, structural characteristics of the floor slab are derived from prior ambient vibration measurements. Two types of information are obtained from these baseline measurements, the dominant frequencies of the slab at the measured locations as well as the level of vibrations that characterize ambient conditions (due to factors such as outside traffic). With the ambient signal taken as a Gaussian white noise process, the signal statistics that are obtained from the initial measurements, mainly the standard deviation of the signal, are calculated. With knowledge of the ambient vibration level, thresholds are set and then used to detect "anomalies" such as human steps.

As a human step can be conceptualized to be an impact load, measurable levels of energy are carried by the shockwaves that are close to the dominant frequencies of the structure. Based on this observation, and in order to improve the signal-to-noise ratio for human detection, the recorded signals are bandpass-filtered around the dominant frequencies. A classic sixth-order Butterworth filter is used to filter the signals. Various recordings of several minutes taken on several days are then used to compute detection thresholds based on the standard deviation of the bandpass-filtered ambient-vibration accelerations. Human detection is achieved when two consecutively measured samples exceed the detection threshold.

### *6.2.2 Error-Domain Model Falsification*

Popper [13] asserted that data cannot be used to validate correct models, rather to falsify wrong models. Motivated through this assertion, error-domain model falsification was proposed by Goulet et al. [8] as a multiple model methodology, where wrong models are falsified using thresholds, which are defined by the uncertainties associated with the system. The EDMF methodology has been applied to fourteen full-scale systems [14]. In this paper, the application of this methodology is extended to human localization using acceleration data.

Assume $g(\theta)$ is a model with $n$ identification parameters $\theta_i$. The response of such a physics-based model is subjected to uncertainty from many sources such as model fidelity, geometric simplifications, material property and boundary conditions. Many of these uncertainty sources cannot be approximated using zero-mean independent Gaussian distributions. Moreover, some of these uncertainties are systematic in nature with unknown correlation between measurement locations. Let the combination of all these uncertainties at a measurement location $i$ be $\varepsilon_{mod,i}$. If $m$ such measurement locations are present, then $\mathbf{y} = [y_1, y_2 \ \ldots \ y_m]^{\mathrm{T}}$ is the vector of measured structural responses at $m$ locations. The uncertainty associated with each measurement is $\varepsilon_{meas,i}$. If $Q_i$ is the true (unknown) structural response at a measurement location then it can be represented as the difference between model prediction and model error or the difference between measurement and measurement error as shown in Eq. (6.1)

$$Q_i = g_i\left(\theta^*\right) - \varepsilon_{mod,i} = y_i - \varepsilon_{meas,i} \tag{6.1}$$

where, $\theta^*$ is the vector of model parameter values and $g_i(\theta^*)$ is the predicted structural response at measurement location $i$. By rearranging Eq. (6.1), the residual between the model prediction and measurements is equal to the combined uncertainty at a measurement location, $\varepsilon_{c,i}$. In a probabilistic approach, these errors $\varepsilon_{mod,i}$, $\varepsilon_{meas,i}$ and $\varepsilon_{c,i}$ are represented as random variables $U_{mod,i}$, $U_{meas,i}$ and $U_{c,i}$, respectively.

Thresholds are defined using the combined uncertainty $U_{c,i}$. For a target reliability of identification $\phi \in \{0,1\}$, the falsification thresholds, $T_{high,i}$ and $T_{low,i}$, are computed as shown in Eq. (6.2)

$$\phi^{1/m} = \int_{T_{low,i}}^{T_{high,i}} f_{U_{c,i}}(\varepsilon_{c,i})\ d\varepsilon_{c,i} \tag{6.2}$$

where, $f_{U_{c,i}}$ is the PDF of the combined uncertainty and $\phi$ is the target reliability of identification. Due to small number of measurements available, the target reliability of identification is corrected using the term $1/m$, called as Šidák correction for multiple hypotheses testing [15].

In EDMF, the user generates model response for multiple values of model parameters $\theta$. Then the residual at each measurement location is calculated as the difference between model prediction and measurement. For all measurement locations, model instances whose residuals lie outside the thresholds are falsified, as represented by Eq. (6.3).

$$\forall i \in \{1, .., m\} \quad T_{low,i} \leq g_i(\theta) - y_i \leq T_{high,i} \tag{6.3}$$

All model instances not falsified using Eq. (6.3) are accepted into the candidate model set [16–18]. Due to the lack of information of the true uncertainty distributions, all candidate models are treated as equally probable. The localization challenge is treated as an inverse problem where the primary parameter to be identified is the location of the load.

## 6.3 Test Setup

The application of human detection and localization has been performed on a continuous reinforced concrete slab that forms the entrance hall of a building on the EPFL campus. The slab is 24 cm thick, which is typical for buildings in Northern Europe. In addition to the high stiffness of the slab, a dense network of structural and non-structural walls underneath the slab results in relatively short spans of the slab (see Fig. 6.1). Most structural walls are in reinforced concrete, while non-structural walls are built in unreinforced masonry. In combination with the rigid slab, the coarse sensor network makes the tested setup an unconventionally complex one. Therefore, the results obtained demonstrate a lower limit of the efficiency of human detection and localization with a multiple model approach.

Roctest Actimon-X1 sensors are used to record accelerations in all three directions. The sensors have a measurement range of 1.5 g and a resolution of 0.05 mg. The frequency response of the sensor ranges from 0 to 200 Hz and the maximum sampling rate is 2000 Hz. The sensors are attached underneath the slab using screws.

## 6.4 Results

Prior information of the vibration characteristics of the building are obtained from ambient-vibration measurements performed on 4 days. As described above, the most important features that are obtained are the fundamental frequency of the structure and the baseline level of ambient vibrations. The fundamental frequency of the slab is 18 Hz, while at sensor location 4, more energy is present around 24 Hz. Based on the mean level of measured ambient vibrations, thresholds are calculated for detection of occupants. In order to increase the signal-to-noise ratio, and accounting for the measured fundamental frequencies, the measured signal is bandpass-filtered using a sixth order Butterworth filter between 16 and 25 Hz. Best results are obtained if thresholds for human detection are set to six standard deviations of the filtered ambient signals. Comparison with raw signal, wavelet transforms (Mexican hat wavelet) and short-term average over long-term average (STA/LTA) ratios showed that for this application, a comparatively simple technique such as bandpass filtering provides the best results for human detection.

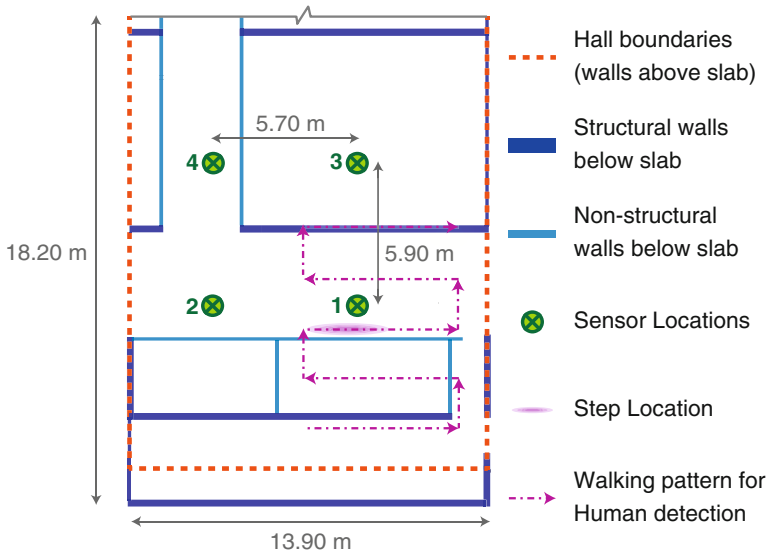


**Fig. 6.1** Schematic view of the tested slab with sensor locations and walking pattern

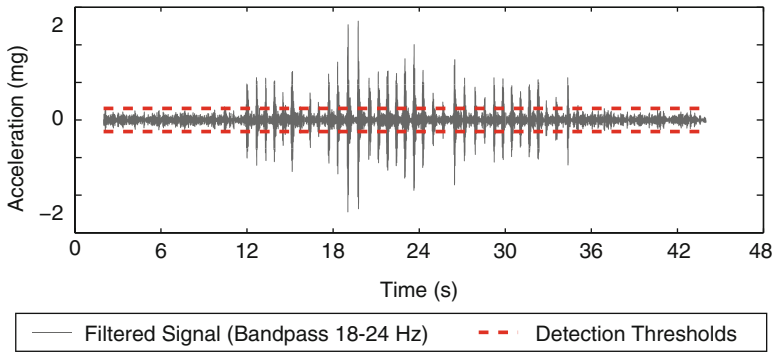


**Fig. 6.2** Successful human detection from sensor 1

The feasibility of human detection is shown for a tested walking pattern (see Fig. 6.1) on the slab. For the filtered signal of sensor 1 (see Fig. 6.2), footsteps that are close enough to the sensor, and that are not damped out by a structural wall underneath the slab, can be successfully detected. This example shows that even for a stiff slab having short spans, an accelerometer is able to measure the impact of a human step (person of approximately 85 kg) in a radius of more than 4 m.

It is also interesting to note that steps that are done in different directions do not have the same amplitude. This might be linked to path-length dependent gates and is a promising feature for user behavior studies.

As shown in Fig. 6.3, all four sensors (see Fig. 6.1 for sensor locations) showed the single footstep that is subsequently used for localization. Sensor 1 is closest to the footstep and logically recorded the highest acceleration. The amplitude of filtered acceleration for sensor 2 is comparable due to the absence of walls supporting the slab between the two sensors. Sensors 3 and 4 show a slight exceedance of the triggering thresholds, which shows that steps can be detected even if supporting walls are between the step source and the sensor. However, this observation is not true for all the steps that were analyzed and therefore, the sensor configuration that is necessary for robust human detection may need to take into account the walls and other types of supports underneath floor slabs.

Localizing the presence of a human walking on the floor is treated as an inverse problem. The recorded vibration data is used to update knowledge about location of the occupant on a slab using EDMF. In this application, the only model parameter that is intended to be identified using EDMF is the location of an occupant.

For application of EDMF, a finite element model of the hall is developed using ANSYS. Using the location of an occupant as a variable, a unit load is applied along a grid on the model and the vertical displacement at sensor locations is recorded. The model response is subjected to uncertainties from many sources, such as modulus of elasticity of the concrete deck, locations and stiffness of boundary conditions. Also, uncertainties arise from processing the measured vibration data using numerical integration in order to obtain displacements, as well as from the weight of the occupant and dynamic amplification

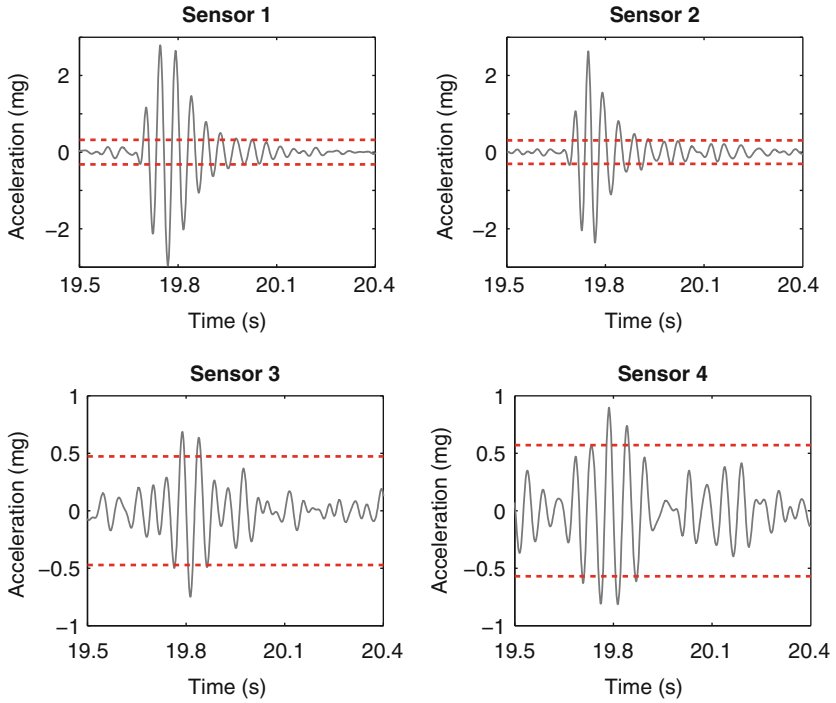


**Fig. 6.3** Signals induced by one footstep (see Fig. 6.1) recorded on the 4 sensors

**Table 6.1** Uncertainty sources and distribution

| Source | Distribution | Min/Mean | Max/Std dev |
|---|---|---|---|
| Measurement uncertainty (%) | Gaussian | 0 | 3 |
| Modelling uncertainty (%) | Uniform | −35 | 85 |
| Sensor 1 location uncertainty (mm) | Uniform | −0.0006 | 0.0006 |
| Sensor 2 location uncertainty (mm) | Uniform | −0.0006 | 0.0005 |
| Sensor 3 location uncertainty (mm) | Uniform | −0.0010 | 0.0010 |
| Sensor 4 location uncertainty (mm) | Uniform | −0.0004 | 0.0004 |

of structural response due to this loading. These uncertainty sources are synthesized as modelling uncertainty. In addition, measurement uncertainty that is provided by the sensor manufacturer is taken into account. Finally, the uncertainty related to the exact position of sensors on the slab are derived from a parametric analysis using the finite element model, by changing the sensor location by ±250 mm. The estimated distribution of these three uncertainty sources is shown in Table 6.1.

The uncertainties are subsequently combined using a Monte Carlo simulation to obtain the combined uncertainty distribution. Once the combined uncertainty distribution is obtained, the thresholds of the error-domain are computed using Eq. (6.2) for a target reliability of identification of 0.95.

In EDMF, a model instance is falsified if the residual between model prediction and measurement lies outside the threshold bounds. In this application, the model prediction is the vertical displacement at sensor locations for a unit load applied at various locations on the grid multiplied by the weight of the occupant and a dynamic amplification value that is taken equal to 1.3. For measurement response, a single step of a human being detected (see Fig. 6.3) is considered. The maximum displacement experienced for a step, obtained through numerical integration using the trapezoidal integration scheme, is considered to be the measurement response. The difference between measured and predicted vertical displacement response is then calculated for all possible occupant locations.

Figure 6.4 shows the residuals calculated for sensor location 1. Falsified location instances that fall between thresholds for sensor 1 are falsified by another sensor.

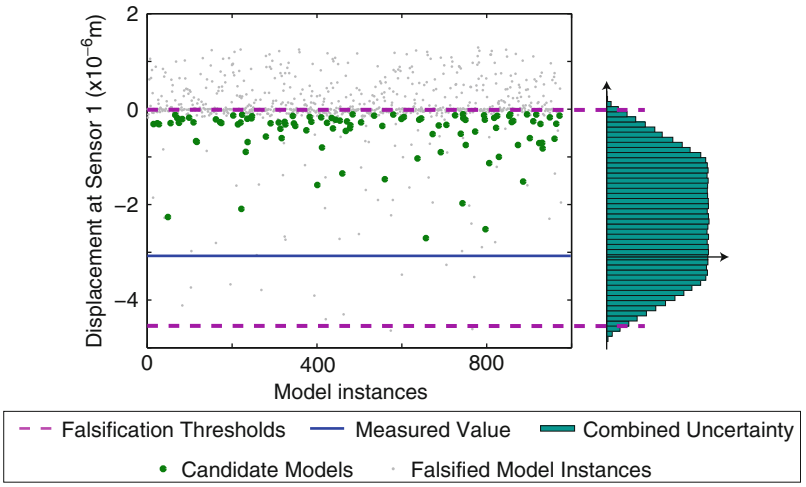


**Fig. 6.4** Falsification plot for sensor 1 based on the maximum displacement induced by a footstep signal

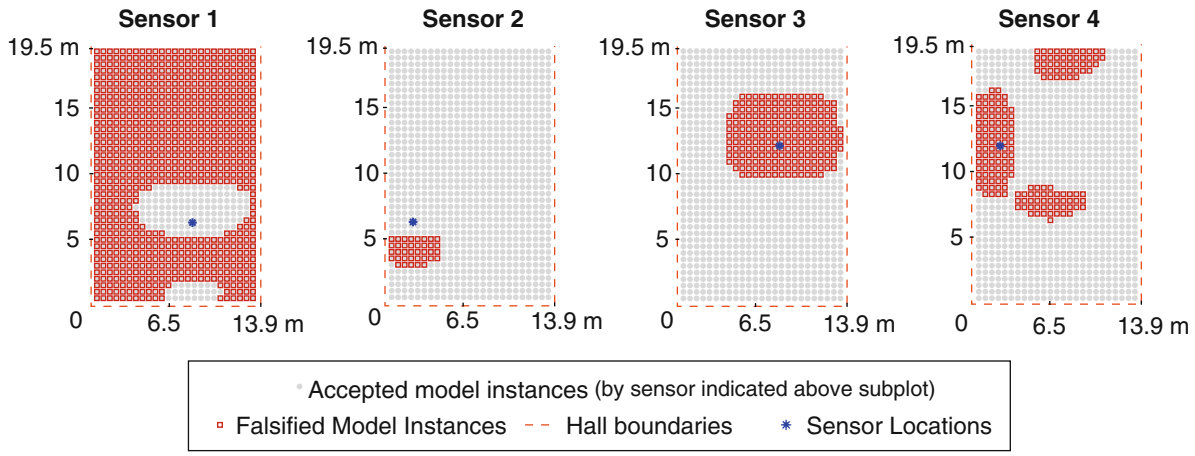


**Fig. 6.5** Instances of human locations that are falsified by each sensor

Similarly, locations of the occupant are falsified using measurement data from all four sensors as shown in Fig. 6.5. From the figure, it can be seen that sensor 1, which is closest to the true location of the person, falsifies most locations of the occupant and is most informative of all sensors.

In EDMF, the final candidate location set is comprised of locations not falsified by any of the sensors. Therefore, combining the information from all four sensors, the candidate location set is obtained and shown in Fig. 6.6. This set of candidate locations includes the true location of the step taken by the occupant.

From Fig. 6.6, it can be seen that there are locations not falsified at the periphery of the hall and between sensor locations indicating a more comprehensive study of the sensor layout configuration might be useful in improving the accuracy of identifying candidate locations. Entropy-based justification will help in determining the usefulness of additional sensors for falsifying locations at the periphery. A detailed study of the model class required for localization might be useful in improving the robustness of candidate occupant locations obtained. Structural parameters such as support stiffness and material properties such as density and Young's modulus were treated as deterministic and known values.

## 6.5 Discussion

In this paper, a methodology has been presented for human detection and localization that can explicitly take into consideration ambiguities of the inverse problem. The methodology utilizes error-domain model falsification for updating knowledge regarding the presence and location of an occupant in a hall using vibration data. The methodology is

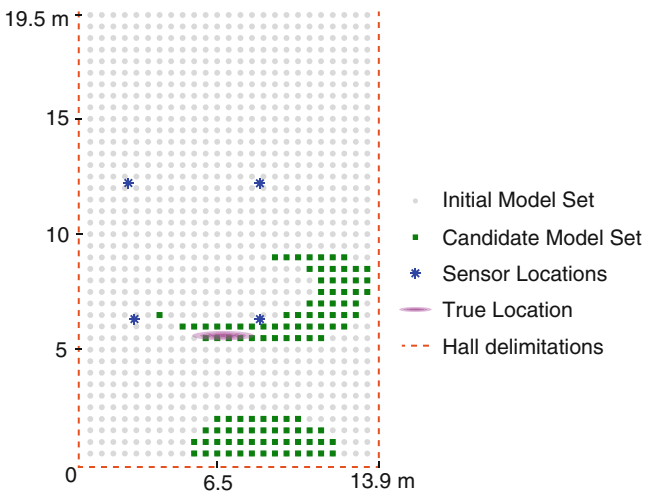


**Fig. 6.6** Candidate locations (*green*) for the human presence derived from EDMF and 4 sensors compared the true location of a person

demonstrated to provide a set of possible locations that include the true location of an occupant on a comparatively stiff slab using a sparse configuration of commercially available sensors.

In order to improve model-based localization of human presence, a refined model that includes other parameters and their uncertainty and allows simulation of the dynamic response of the slab to human induced footsteps is needed. Also, an enhanced model would allow the engineer to select the optimal number and location of sensors to improve detection and localization of human presence. Finally, the automatic detection of footsteps and the localization of multiple consecutive steps will further decrease the uncertainty on human location since impossible walking patterns can be falsified.

**Acknowledgments** This work was funded by the Swiss National Science Foundation under Contract No. 200020_169026.

## References

1. Alwan, M., Rajendran, P.J., Kell, S., Mack, D., Dalal, S., Wolfe, M., Felder, R.: A smart and passive floor-vibration based fall detector for elderly. In: 2006 2nd International Conference on Information & Communication Technologies, IEEE, pp. 1003–1007 (2006)
2. Yu, X.: Approaches and principles of fall detection for elderly and patient. In: 10th International Conference on e-health Networking, Applications and Services, 2008. Health Com 2008, IEEE, pp. 42–47 (2008)
3. Schloemann, J., Malladi, V.S., Woolard, A.G., Hamilton, J.M., Buehrer, R.M., Tarazaga, P.A.: Vibration event localization in an instrumented building. In: Experimental Techniques, Rotating Machinery, and Acoustics, vol. 8, pp. 265–271. Springer (2015)
4. Lam, M., Mirshekari, M., Pan, S., Zhang, P., Noh, H.Y.: Robust occupant detection through step-induced floor vibration by incorporating structural characteristics. In: Dynamics of Coupled Structures, vol. 4, pp. 357–367. Springer (2016)
5. Pan, S., Bonde, A., Jing, J., Zhang, L., Zhang, P., Noh, H.Y.: Boes: building occupancy estimation system using sparse ambient vibration monitoring. In: SPIE Smart Structures and Materials+ Nondestructive Evaluation and Health Monitoring, pp. 90611O–90611O. International Society for Optics and Photonics (2014)
6. Mirshekari, M., Pan, S., Zhang, P., Noh, H.Y.: Characterizing wave propagation to improve indoor step-level person localization using floor vibration. In: SPIE Smart Structures and Materials+ Nondestructive Evaluation and Health Monitoring, pp. 980305–980305. International Society for Optics and Photonics (2016)
7. Bales, D., Tarazaga, P., Kasarda, M., Batra, D.: Gender classification using under floor vibration measurements. In: Allen, M., Mayes, R.L., Rixen, D (eds.) Dynamics of Coupled Structures, Conference Proceedings of the Society for Experimental Mechanics Series, vol. 4, pp. 377–383. Springer International Publishing (2016)
8. Goulet, J.-A., Coutu, S., Smith, I.F.C.: Model falsification diagnosis and sensor placement for leak detection in pressurized pipe networks. Adv. Eng. Inform.. Elsevier **27**(2), 261–269 (2013)
9. Pasquier, R., Goulet, J.-A., Acevedo, C., Smith, I.F.C.: Improving fatigue evaluations of structures using in-service behavior measurement data. J. Bridge Eng.. American Society of Civil Engineers **19**(11), 4014045 (2014)
10. Pasquier, R., Angelo, L.D., Goulet, J.-A., Acevedo, C., Nussbaumer, A., Smith, I.F.C.: Measurement, data interpretation, and uncertainty propagation for fatigue assessments of structures. J. Bridge Eng.. American Society of Civil Engineers **21**(5), 04015087 (2016)
11. Moser, G., Paal, S.G., Smith, I.F.: Performance comparison of reduced models for leak detection in water distribution networks. Adv. Eng. Inform. **29**, 714–726 (2015)
12. Vernay, D.G., Raphael, B., Smith, I.F.C.: A model-based data-interpretation framework for improving wind predictions around buildings. J. Wind Eng. Ind. Aerodyn.. Elsevier **145**, 219–228 (2015)

13. Popper, K.: The Logic of Scientific Discovery. Routledge (1959)
14. Smith, I.F.C.: Studies of sensor-data interpretation for asset management of the built environment. Front. Built Environ.. Frontiers **2**, 8 (2016)
15. Šidák, Z.: Rectangular confidence regions for the means of multivariate normal distributions. J. Am. Stat. Assoc.. Taylor & Francis Group **62**(318), 626–633 (1967)
16. Goulet, J.-A., Kripakaran, P., Smith, I.F.C.: Multimodel structural performance monitoring. J. Struct. Eng.. American Society of Civil Engineers **136**(10), 1309–1318 (2010)
17. Goulet, J.-A., Smith, I.F.C.: Structural identification with systematic errors and unknown uncertainty dependencies. Comput. Struct.. Elsevier **128**, 251–258 (2013)
18. Goulet, J.-A., Michel, C., Smith, I.F.C.: Hybrid probabilities and error-domain structural identification using ambient vibration monitoring. Mech. Syst. Signal Process. **37**(1), 199–212 (2013)

# Chapter 7
# Vibration Assessment and Control in Technical Facilities Using an Integrated Multidisciplinary Approach

**Nicholas Christie, James Hargreaves, Rob Harrison, and Francois Lancelot**

**Abstract** Scientific research is advancing rapidly in several fields including materials science, applied physics, life sciences, bio and nanotechnology. This research often brings with it specialist imaging requirements to resolve ever finer details over time. The equipment needed to perform this imaging is often very sensitive to vibration in addition to factors including acoustic coupling, electromagnetic, thermal and airflow effects. This paper discusses the application of end-to-end vibration engineering to address these low vibration challenges. Using measurement data from the site and surrogate locations combined with advanced simulations allows a deeper understanding of the specific project implications and reduces risk and cost. This paper also illustrates how Arup deployed such an integrated multidisciplinary approach to assess and control vibration at the planning and design stages and contributed to the delivery of some of the most advanced scientific and industrial low vibration environment facilities in the world.

**Keywords** Vibration • Technical facility • Laboratory • Assessment • Survey • Mitigation • Foundation • Ground • Structure • Passive control • Active control

## 7.1 Introduction

Microscopy is one of the key aspects of scientific research and is continuously evolving to enable higher resolution powers to be achieved which then enables smaller detail sizes to be resolved. Electron based microscopy has enabled images to be produced for particle, then atomic and, in the future, sub-atomic matter with sub-Angstrom resolution considered to be the state-of-the-art. The performance of the microscope itself, however, depends on the environment within which it is located. This is typically an imaging suite in a university or other research building and while ideally this building would be located in a relatively quiet environment, in reality this is not necessarily possible. Environmental factors that can influence the microscope performance include structural vibration, acoustics, electromagnetic fields, thermal performance and air flow. In this paper the effects of structural vibration on electron and similar microscope performance will be presented and discussed in the context of a new building design. This will include criteria selection, vibration survey methods, modelling and analysis methods to guide the design and vibration mitigation to control or minimize the influence of structural vibration.

## 7.2 Structural Vibration

Structural vibration is vibration that is transmitted through a building structure and eventually arrives at the floor plate structure of the imaging suite and then is transmitted to the microscope equipment. The sources of such vibration are many and varied but can be classified as internal or external. Internal vibration sources are those sources which lie within the

N. Christie • F. Lancelot (✉)
Arup North America Limited, Advanced Technology & Research, 560 Mission Street, Suite 700, San Francisco, CA, USA
e-mail: nicholas.christie@arup.com; francois.lancelot@arup.com

J. Hargreaves
Ove Arup & Partners UK, Advanced Technology & Research, The Arup Campus, Solihull, UK
e-mail: james.hargreaves@arup.com

R. Harrison
Ove Arup & Partners UK, Advanced Technology & Research, 3 Piccadilly Place, Manchester, UK
e-mail: rob.harrison@arup.com



J. Caicedo, S. Pakzad (eds.), *Dynamics of Civil Structures, Volume 2*, Conference Proceedings of the Society for Experimental Mechanics Series, DOI 10.1007/978-3-319-54777-0_7

project boundary and include footfall, MEP plant, elevators as well as other equipment, machinery and in some cases test rigs. For a new building project, structural vibration from internal sources can be influenced and controlled to some degree by design or through facility management. External vibration sources are those sources which lie outside the project boundary and include surface and underground railway, highway, construction and demolition. Typically the vibration is transmitted from the sources through the ground to the new building foundation in the form of waves. These sources are not within the control of the project but the vibration transmitted from them to the new project must be somehow controlled and managed. Structural vibration has several characteristics which need to be considered in design: frequency, amplitude, wavelength, direction, temporal and spatial. The sources and transmission paths can be complex and the evaluation of vibration and its characteristics requires survey methods as well as modelling and analysis.

## 7.3 Criteria

Criteria for vibration are essentially limits on vibration magnitude above which it is considered that the equipment or process performance might be impaired. Criteria can take the form of generic criteria published in [1, 2] and discussed in [3]. Generic criteria cover general classes of process and vibration sensitive equipment including electron microscopes and are relevant at the planning and even design stages where it may still be too early for specific manufacturer's equipment to be identified with any confidence. The VC criteria are presented in [3] and shown in Fig. 7.1.

The VC criteria have a number of aspects to consider. The VC vibration magnitudes are $\leq$100.0 μm/s, which is also the average threshold of human vibration perception so the criteria are relevant to small vibrations which are generally sub-perceptible. The VC criteria are defined over a specific frequency range, namely 1–80 Hz. The format of the vibration is the RMS velocity in the 1/3rd octave band, although as discussed below there are a number of methods in which this can be evaluated. The criteria apply to vibration along the vertical or two horizontal axes. The criteria in [1] are applicable to "vibration measured on the building structure" and similarly in [2], however it is actually the vibration transmitted to the equipment that will be determinative of overall vibration performance. According to the above guidance, the criteria VC-D and VC-E might apply to electron and similar microscope equipment. Manufacturer's criteria are intended to define limits

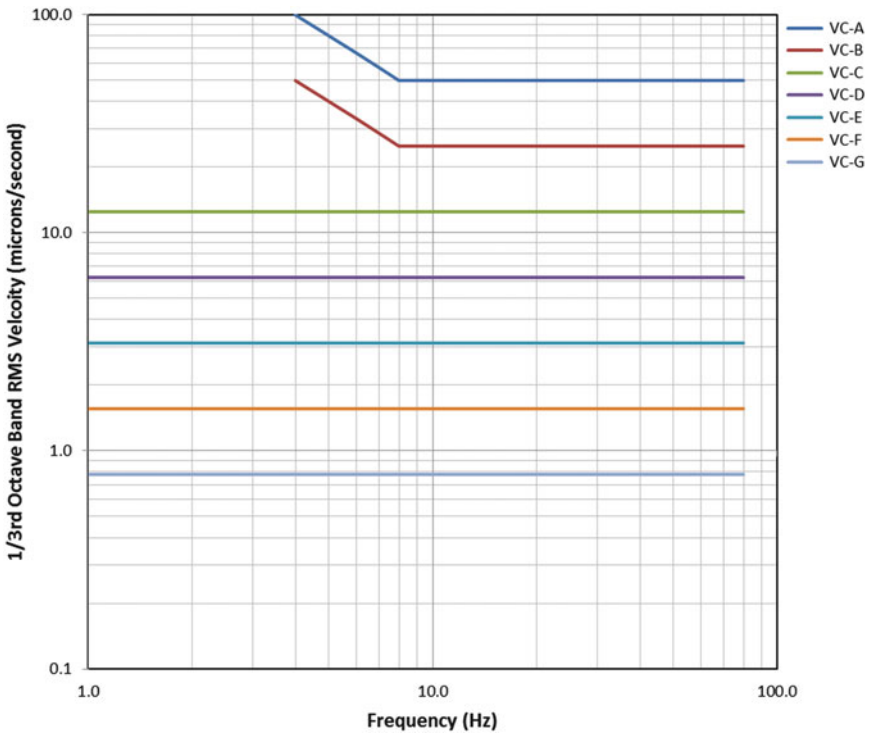


**Fig. 7.1** VC criteria for vibration sensitive equipment

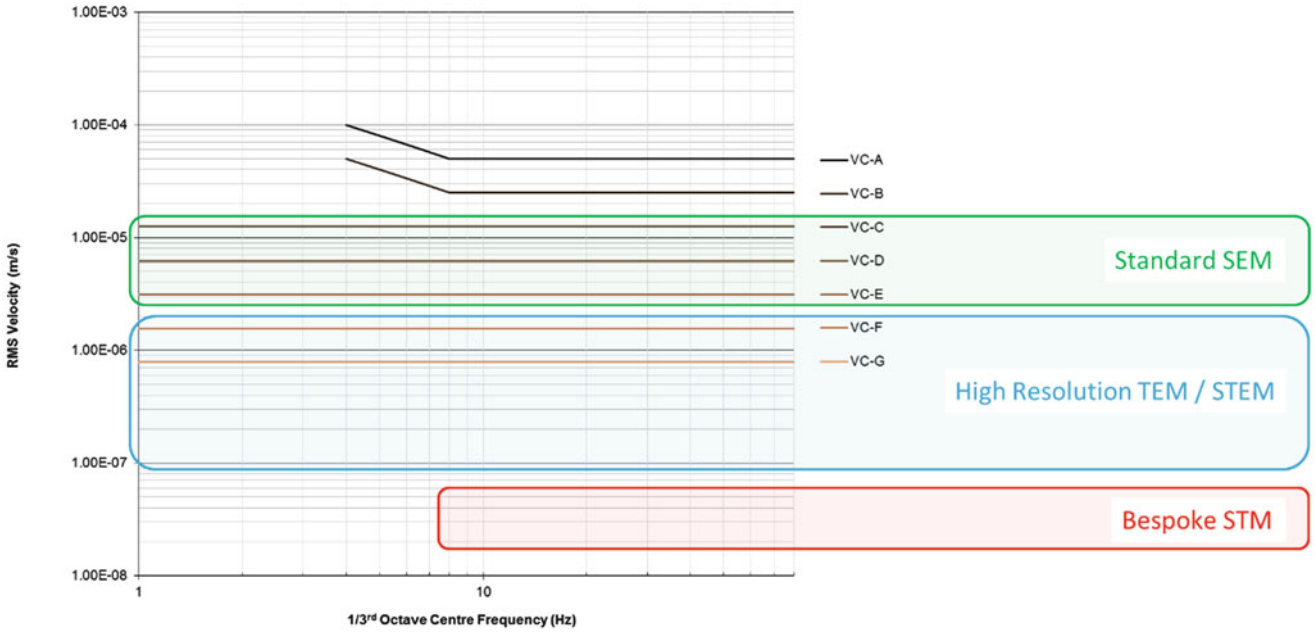


**Fig. 7.2** Manufacturers' criteria ranges for electron microscopy and VC criteria

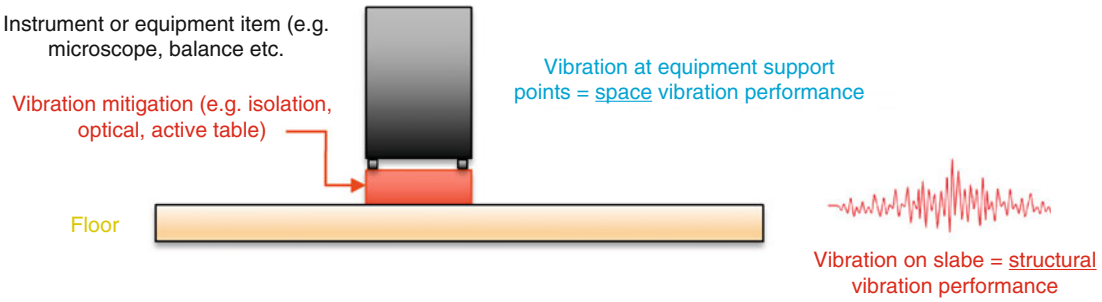


**Fig. 7.3** Structural vibration and space vibration performance

for vibration for a specific product or item of equipment. Such criteria might be defined with reference to the VC criteria or might be defined using an alternative format. A selection of manufacturer's criteria is presented in Fig. 7.2 (SEM = Scanning Electron Microscope, TEM = Transmission Electron Microscope, STEM = Scanning Transmission Electron Microscope, STM = Scanning Tunnelling Microscope). In project work it is necessary to consult the manufacturer to confirm the format in which the criteria are defined.

For project sites and buildings vibration generally varies with time leading to a need for some sort of metric, average and maximum to give the most common examples, to evaluate. Hence there are two key aspects of the criteria that need to be defined: the vibration limit and metric. The limit is simply the magnitude of vibration above which the equipment or process function starts to become impaired. The metric defines precisely how the temporal vibration must be evaluated before a comparison with the limit is made. Vibration in this context might be vibration measured during a survey or it might be a prediction from a computational model. Another key consideration with criteria is whether it is considered feasible, or even possible, to achieve them through structural design. Where some of the more demanding criteria such as VC-G, VC-F and VC-E might not realistically be achieved through structural design, it is necessary to introduce mitigation and to consider vibration transmission to the equipment rather than the structure. Enhancing the structural vibration performance with mitigation can produce a **space vibration performance** that is better than that of the structure and which does meet the criteria (see Fig. 7.3).

## 7.4 Vibration Survey

Vibration surveys enable the vibration performance of a site to be evaluated directly and are a key aspect of the development of technical building projects from the planning stage right through to commissioning. In this paper, attention is focused mainly on survey work at the planning stage where a proposed project site requires evaluation. The site is in an urban location with a main highway to the east and west of the site boundary and with a smaller road to the south [4]. This borehole is at a location that will be indicative of the future characterisation suite performance. The instrumentation at a typical measurement location is shown in Fig. 7.4 and comprises a steel canister (see inset image) placed at the base of a borehole in the ground and containing a tri-axial accelerometer arrangement connected to the data acquisition system. In this way vertical and horizontal ground vibration, at the building foundation elevation, is measured over a 24 h time period. The vertical vibration signal output from this test is shown in Fig. 7.5.

The main source of vibration is highway traffic comprising cars, vans, trucks and buses and is generated by the interaction of vehicle dynamics with highway surface irregularity. The two most common metrics, namely average and maximum would be reported in most if not all projects. However, average would not typically be selected unless consultation with the user and manufacturer established that this would give a good indication of the vibration that might be disruptive in research practice. The maximum is by definition the worst case and needs to be evaluated and reported, however, in cases where there a very few instances in time when this occurs it can be less useful. The exceedence metric is a useful way of expressing temporal vibration performance and the 1% exceedence vibration is shown in Fig. 7.4 and indicates performance of VC-E compared to VC-D using maximum. 1% exceedence as a metric needs to be agreed with the project in the context of the equipment and methods being used but it typically means that VC-E would be exceeded for just a few minutes in each day and may be acceptable. In cases where image capture is not a process that can be quickly and easily repeated then several minutes of exceedence might be a concern.

**Fig. 7.4** Borehole vibration survey

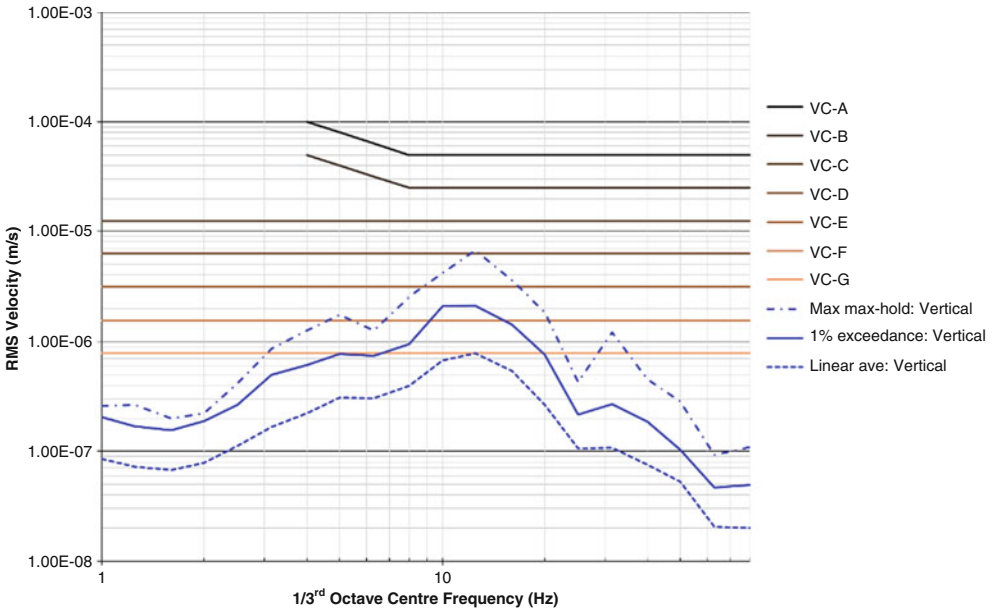


**Fig. 7.5** Measured borehole vibration vs. VC-criteria

## 7.5 Computational Methods

During the design stage of a building project the structural performance attributes need to be evaluated and the design steered to meet the respective criteria. For low vibration environment projects it is quite common for the strength design to be developed further to meet the vibration criteria with particular attention needed to the grid size, suspended slab thickness and the foundation structure. Computational methods such as finite element analysis (FEA) are a useful means of predicting structural vibration performance for the various dynamic loads associated with internal and external sources of vibration. Footfall is often the most critical dynamic loads for suspended slab structures, i.e. laboratory floors, and it is not normally possible to meet criteria such as VC-A with a strength design alone and without careful consideration of grid size and slab thickness. The effects of footfall on the structural design can be evaluated using published industry methods such as [5, 6]. An example of floor plate FEA using the GSA analysis software [7] is shown in Fig. 7.6.

In this case the floor plate supports a typical laboratory space function with criteria VC-A. Footfalls in circulation areas, corridors and laboratory spaces need to be considered. As with test data processing, some consideration of the occurrence of peak events is necessary. Footfall induced vibration can produce resonant and impulsive response types. Resonant response involves a build-up of vibration with each footfall and occurs because one or more of the load harmonics align with a structural mode for a given walking speed. This occurs with so-called low frequency slab designs, with fundamental vertical natural frequencies of 10 Hz or less. High frequency floors exhibit impulsive response where each footfall produces a decaying impulse response. When comparing with the VC criteria it is necessary to evaluate the maximum RMS velocity in the 1/3rd octave band. A rough estimate of 1/3rd octave band RMS can be obtained by taking 70% of the whole signal RMS. However, this can be calculated by passing the predicted vibration time-history though the ANSI 1/3rd octave band filters [8] or by modal response based on modes within the 1/3rd octave bands.

The predicted response of the floor plate in Fig. 7.6 is within VC-A for more than 90% of the floor plate area. The vibration response is higher than VC-A in some small areas and is lower in others. Floor plate areas around columns are clearly less mobile and in this case have a vibration performance of VC-B to VC-C or better. This makes it possible to realise more vibration performance out of a structure designed to the VC-A criteria and enables equipment that might require VC-B or VC-C to be used on the floor plate subject to feasibility constraints.

FEA can be used to assess the vibration performance of foundation structures which is the part of the building structure where ground vibration transmitted from external sources such as railway and highway traffic, first arrives. An example is shown in which a ground bearing or raft foundation design has been proposed which requires a thickness of 350 mm to meet the strength performance requirements. The objective of the FEA study in this case is to determine whether this slab thickness would enable the vibration criteria to be met or whether it would need to be increased. A review of the principles of soil structure interaction in a low vibration environment context is available in [9]. The structural dynamics of the foundation

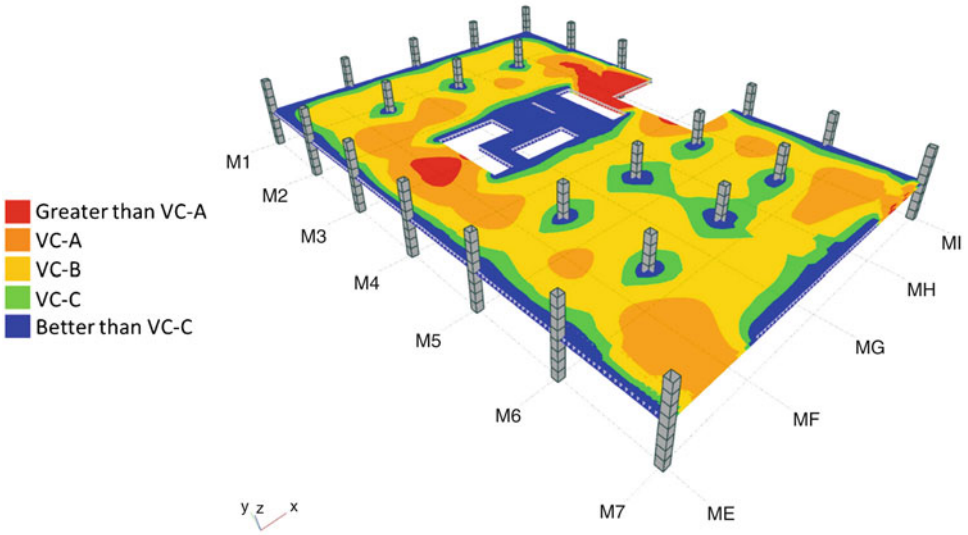


**Fig. 7.6** FEA analysis of footfall induced vibration on a suspended floor plate

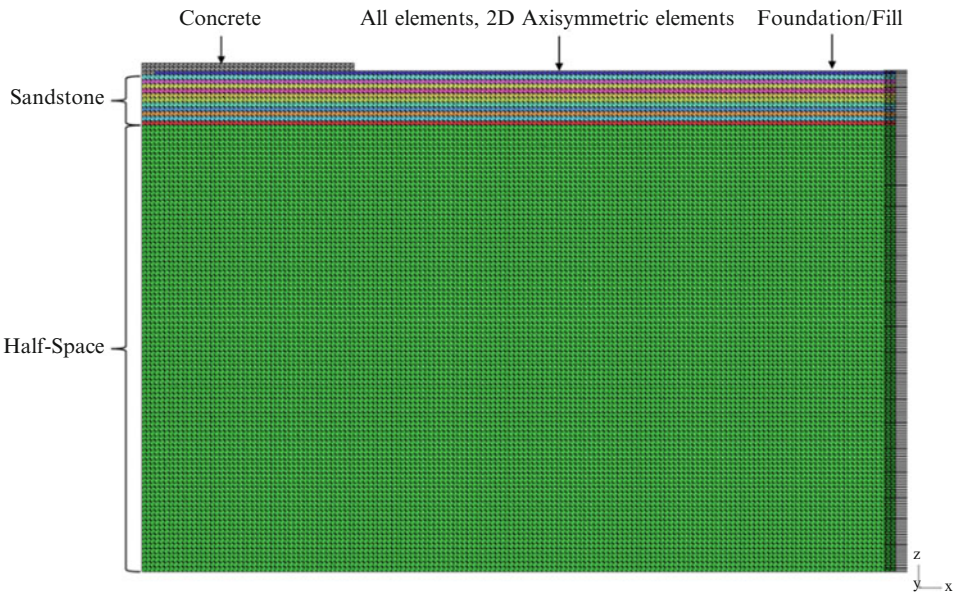


**Fig. 7.7** FEA analysis of ground and foundation structure

depend on several parameters: slab mass, slab stiffness, slab structural damping, column take down loads, soil stiffness, soil hysteretic damping, radiation damping, soil stiffness, soil mass and soil-structure interaction. These parameters combined with the wave behaviour of the vibration in the ground result in relatively complex dynamic behaviour for which some simplification is necessary in order to apply FEA in a pragmatic way at the design stage. On this basis an axisymmetric model of the foundation structure and ground has been developed and used in conjunction with measured vibration data, see Fig. 7.7.

In this case the axis of the model is aligned with the foundation pad centreline and a finite radius of foundation slab concrete is modelled. The take-down load of the columns is included as discrete mass centred on the model axis. The upper layers of soil are modelled discretely with the deep soil layers all simplified to an elastic half-space type continuum. Viscous dampers are applied to the vertical edge of the model in the horizontal and vertical directions. These dampers are known as Lysmer dampers and represent the radiation damping of the ground [10]. This model has been analysed using the MSC.NASTRAN finite element direct frequency response solver [11]. The external sources generate vibration in the ground which is transmitted to the foundation structure as an enforced motion. The first step in the analysis is to use the

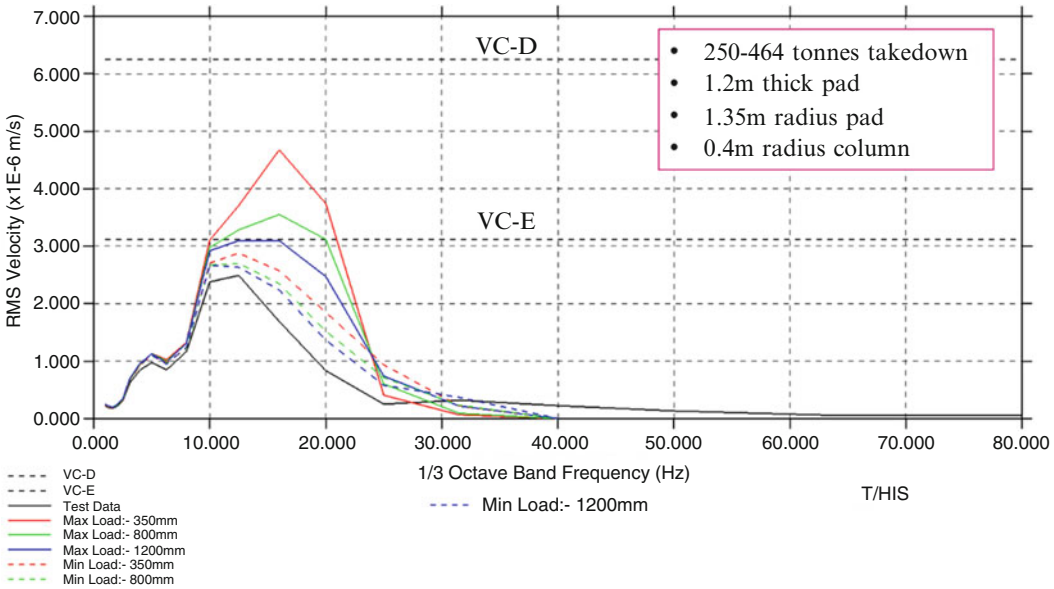


**Fig. 7.8** Predicted foundation slab vibration using FEA model and measured data

reciprocity principle [12] to determine forces acting on the ground boundary that would produce the measured vibration on the foundation structure. This first step is necessary to enable a forced response analysis to be carried out which can enable the vibration response for various design assumptions to be evaluated, something that would not be possible with an enforced motion loading. An example of the output from this analysis is shown in Fig. 7.8 for the given structural configuration but assuming three slab thicknesses 350, 800 and 1200 mm and two different column take-down loads.

In this case increasing the foundation thickness from 350 mm would be of marginal benefit, barely reducing the response by one full VC band from a baseline performance of VC-D, which meets the performance requirements. Where mitigation is being considered, as is the case here, this analysis needs to be combined with transmissibility data to estimate the slab vibration performance including mitigation. This is discussed in Sect. 7.6 below.

## 7.6 Mitigation

Mitigation is a common aspect of technical facility design and arises because often structural vibration needs to be enhanced to meet the equipment criteria, especially where the more demanding criteria, such as VC-E and more onerous, are concerned. Mitigation might also be a more efficient means of achieving the required space performance or it may be more desirable, for example, where some amount of future-proofing is needed; not uncommon where research equipment is being continuously developed and a facility might be operational for 25 years or more. Mitigation systems can be grouped into passive or active types. Passive systems comprise relatively simple, unpowered systems which exploit basic physical principles. Common examples are low vibration bases and keel slabs. It should be noted that passive isolation systems are often designed into the equipment itself. Sometimes this is called internal isolation and care is needed when specifying keel slab systems to avoid "stacking" the isolation, i.e. where the internal and keel slab isolation frequencies are close or align. Active systems comprise devices that use computer controlled electro-mechanical actuators to deliver a dynamic force which minimises the vibration transmitted to the sensitive imaging and other equipment. The input to active systems is the floor vibration and the control system is designed to minimise this vibration using actuator arrays to deliver a platen vibration that meets the required criteria over a given frequency range, normally 1–80 Hz. One advantage of active control is that it is not based on a spring mass system and hence does not have an amplification region around the isolation frequency. This leads to better low frequency performance and also means it can work in the presence of internal isolation. The performance of both passive and active control systems needs to be specified and realised in design and manufacture. The vibration transmitted to the equipment from keel slab passive and two typical active control systems using the measured bore hole vibration can be estimated using theoretical transmissibility for each control system as shown in Fig. 7.9.

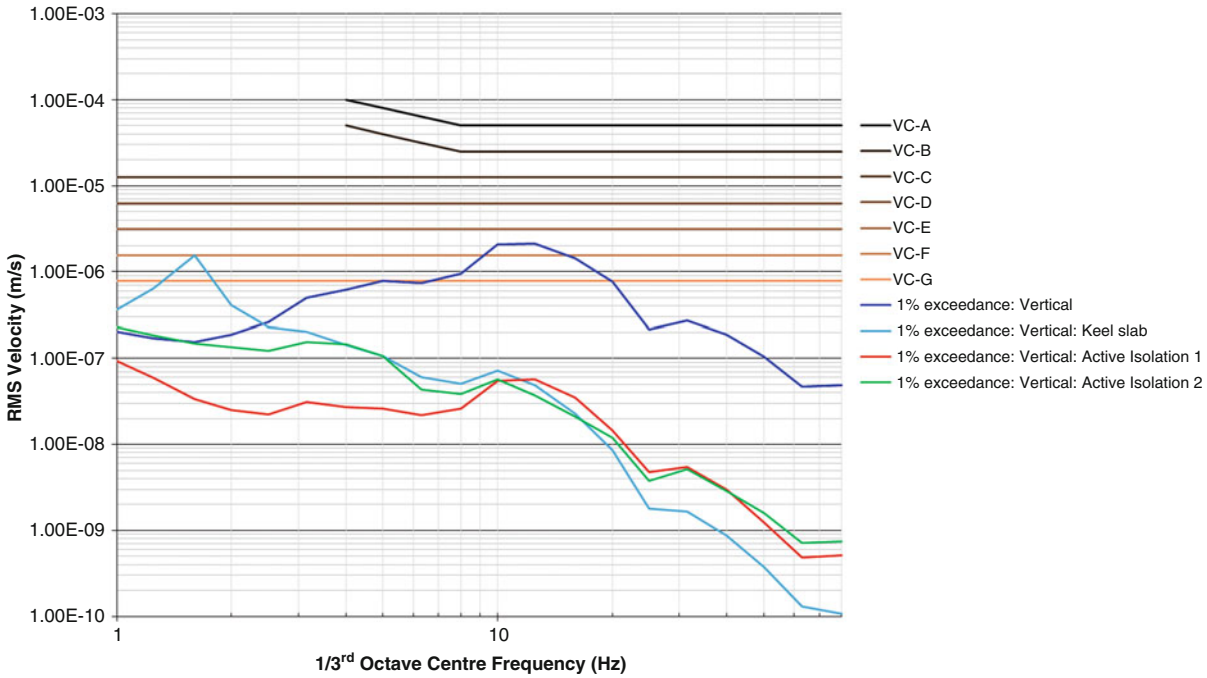


**Fig. 7.9** Predicted effect of active control system using measured bore hole vibration

## 7.7 Summary

Successful technical facility design involves the management of internal and external sources of vibration from the start of the project, through the design stages and on to completion. The site vibration performance is one of the fundamental inputs to the vibration engineering aspects of the project and requires specific methods, equipment and results interpretation to enable advice of value to be provided. Computational methods are another important aspect of the design process which enables the structural vibration performance to be evaluated and compared with the criteria at the design stage. Examples have been presented of how FEA has been applied to footfall induced vibration on suspended slabs and, in conjunction with survey data, how a foundation design should be checked for vibration performance. An overview of passive and active vibration control has been provided and an illustration of how passive and active control can enhance structural vibration has been given.

## References

1. 2015 ASHRAE Handbook, Heating Ventilating and Air-Conditioning Applications SI Edition
2. Institute of Environmental Sciences and Technology, IEST-RP-CC012.2 Considerations in Cleanroom Design (2007)
3. Amick, H., Gendreau, M., Busch, T., Gordon, C.: Evolving criteria for research facilities: I – vibration. Reprinted from SPIE Conference 5933: Buildings for Nanoscale Research and Beyond, San Diego, CA, 31 July 2005 to 1 August 2005
4. Manchester Engineering Campus Development (http://www.mecd.manchester.ac.uk/)
5. Willford, M., Young, P.: A Design Guide for Footfall Induced Vibration of Structures. Concrete Centre, December (2006)
6. Murray et al. Structural Design Guide – Section 11. American Institute of Steel Constructors (1997)
7. www.oasys-software.com/GSA
8. ANSI-S1.11: Specification for Octave-Band and Fractional-Band Digital Filters. American National Standards Institute
9. Amick, H., Xu, T., Gendreau, M.: The role of buildings and slabs-on-grade in the suppression of low-amplitude ambient ground vibrations. In: 11th International Conference on Soil Dynamics & Earthquake Engineering
10. Lysmer, J., Kulmeyer, R.L.: Finite dynamic model for infinite media. J. Eng. Mech. ASCE. **95**, 859–875 (1969)
11. MSC.NASTRAN v2014 User Manual
12. Richart, F.E., Hall, J.R., Woods, R.D.: Vibration of Soils and Foundations. Prentice-Hall, Englewood Cliffs (1969)

# Chapter 8
# Iterative Pole-Zero Model Updating Using Multiple Frequency Response Functions

**M. Dorosti, R.H.B. Fey, M.F. Heertjes, M.M.J. van de Wal, and H. Nijmeijer**

**Abstract** For accurate positioning of motion systems having an accurate yet low-order dynamic model from actuators to sensors and to unmeasured performance variables is crucial. A (reduced) Finite Element (FE) dynamic model may be a good candidate. However, a FE model in practice has limited accuracy in describing the dynamic behavior of the system for nano positioning performance. This can be either due to the simplifications in the FE modeling or due to system variations. To improve the dynamic properties of the (reduced) FE model toward dynamic properties of the real system, an Iterative Pole-Zero (IPZ) model updating procedure that updates poles and zeros of a single Frequency Response Function (FRF) was recently proposed. Using more FRFs from different actuator/sensor configurations helps to better improve the dynamic properties of the (reduced) FE model. In this paper, an extension of IPZ model updating to use multiple FRF measurements is presented. The proposed method is verified using a simulated experiment of a pinned-sliding beam structure.

**Keywords** FE modeling • Model updating • Least square optimization • Unmeasured performance variables

## 8.1 Introduction

Model updating techniques are well-known tools to improve the accuracy of a FE model. In principle there are two types of model updating techniques: direct methods [1] and iterative methods [2]. Within the iterative methods, there are two categories. The first category contains modal-based techniques concerned with updating modal properties such as poles, zeros, and mode shapes in an attempt to reduce the residuals between numerical and measured modal quantities [2–4]. Recently, an IPZ model updating technique is introduced that tries to update both the poles and the zeros of a single FRF of the system in an iterative manner. The second category attempts to reduce the residuals between numerical and measured FRFs directly [5, 6].

In model updating, it is sometimes clear which (physical) model parameter values are uncertain. Often, however, for example in geometrically complex structures with many mechanical connections, it may be far from trivial to identify which physical parameters are causing differences between the numerical and experimental target quantities. In those situations, generic parameters may be better candidates for model updating. Most of the modal-based model updating techniques are concerned with updating the resonance frequencies [2]. Recently, some effort has been dedicated to include the effect of zeros (antiresonances) in the model updating, see [7, 8]. However, all of these model updating techniques are based on updating physical design parameters, while in IPZ model updating, the eigenvalues of the stiffness and/or damping matrix of the (sub)structure are introduced to be the design parameters. This is done because errors in stiffness/damping modeling are more likely to occur than errors in mass modeling.

In general, IPZ model updating tries to improve a reduced FE model by minimizing residuals between the numerical and the experimental values of poles and zeros of an FRF. This is done by iteratively updating the eigenvalues of the

M. Dorosti (✉) • R.H.B. Fey • H. Nijmeijer
Mechanical Engineering Department, Eindhoven University of Technology, 5600 MB Eindhoven, The Netherlands
e-mail: M.Dorosti@tue.nl; R.H.B.Fey@tue.nl; H.Nijmeijer@tue.nl

M.F. Heertjes
Mechanical Engineering Department, Eindhoven University of Technology, 5600 MB Eindhoven, The Netherlands

ASML, De Run 6501, 5504 DR Veldhoven, The Netherlands
e-mail: M.F.Heertjes@tue.nl

M.M.J. van de Wal
ASML, De Run 6501, 5504 DR Veldhoven, The Netherlands
e-mail: Marc.van.de.Wal@asml.com



J. Caicedo, S. Pakzad (eds.), *Dynamics of Civil Structures, Volume 2*, Conference Proceedings
of the Society for Experimental Mechanics Series, DOI 10.1007/978-3-319-54777-0_8

stiffness/damping matrix of the (sub)structure as generic parameters. In this paper, IPZ model updating is extended to incorporate multiple FRFs. Using multiple FRFs from different actuator/sensor configurations helps to better improve the overall accuracy of the reduced FE model toward the real system since more information on the eigenmodes is used. The remainder of the paper is organized as follows. IPZ model updating using multiple FRFs is discussed in Sect. 8.2. In Sect. 8.3, as a case study, a simulated pinned-sliding beam structure is introduced on which the IPZ model updating technique using multiple FRFs is verified. Finally, some conclusions are drawn in Sect. 8.4.

## 8.2 IPZ Model Updating Using Multiple FRFs

Updating a full FE model is computationally expensive. In addition, the physical parameters causing the difference between the model and the real system may not be known. In this case, updating a reduced-order FE model using generic parameters becomes useful. Using a model reduction technique based on eigenmodes and residual flexibility modes, consider the following reduced-order dynamic equation of an FE model:

$$\mathbf{M}_r\ddot{\mathbf{q}}_r + \mathbf{B}_r\dot{\mathbf{q}}_r + \mathbf{K}_r\mathbf{q}_r = \mathbf{f}_r, \tag{8.1}$$

where $\mathbf{q}_r$ is a set of desired DOFs including actuators, sensors, and unmeasured performance variables DOFs. $\mathbf{M}_r, \mathbf{B}_r, \mathbf{K}_r \in \mathbb{R}^{r\times r}$ are the reduced order mass, damping, and stiffness matrices and $\mathbf{f}_r \in \mathbb{R}^{r\times 1}$ is the reduced external load column. Using the reduced-order dynamic equation in (8.1), the FRF corresponding to a sensor at DOF $i$ and an actuator at DOF $j$ can be described as

$$\mathbf{G}_{ij}(\omega) = \frac{\det(-\omega^2\mathbf{M}_s + j\omega\mathbf{B}_s + \mathbf{K}_s)}{\det(-\omega^2\mathbf{M}_r + j\omega\mathbf{B}_r + \mathbf{K}_r)}, \tag{8.2}$$

where $\mathbf{M}_s, \mathbf{B}_s, \mathbf{K}_s$ are the so-called substructure matrices which are constructed from the reduced-order matrices $\mathbf{M}_r, \mathbf{B}_r, \mathbf{K}_r$ respectively, by eliminating the $i$th row and the $j$th column corresponding to the sensor and actuator DOFs. Therefore, $\mathbf{K}_r$ can be written as

$$\mathbf{K}_r = \mathbf{K}_{r,s} + \Delta\mathbf{K}_r, \tag{8.3}$$

where $\mathbf{K}_{r,s}$ is partitioned such that

$$\mathbf{K}_{r,s} = \left[\begin{array}{c|c|c} \mathbf{K}_{s,1} & 0 & \mathbf{K}_{s,2} \\ \hline 0 & 0 & 0 \\ \hline \mathbf{K}_{s,3} & 0 & \mathbf{K}_{s,4} \end{array}\right], \tag{8.4}$$

and

$$\Delta\mathbf{K}_r = \left[\begin{array}{c|c|c} 0 & \Delta\mathbf{k}_{r,1} & 0 \\ \hline \Delta\mathbf{k}_{r,2} & \Delta k_{r,3} & \Delta\mathbf{k}_{r,4} \\ \hline 0 & \Delta\mathbf{k}_{r,5} & 0 \end{array}\right], \tag{8.5}$$

$\mathbf{K}_s$ is derived from (8.4), i.e.

$$\mathbf{K}_s = \left[\begin{array}{c|c} \mathbf{K}_{s,1} & \mathbf{K}_{s,2} \\ \hline \mathbf{K}_{s,3} & \mathbf{K}_{s,4} \end{array}\right]. \tag{8.6}$$

In IPZ model updating, a selected number of the eigenvalues of the stiffness matrix $\mathbf{K}_r$ and the substructure stiffness matrix $\mathbf{K}_s$ are introduced to represent the design parameters $\boldsymbol{\theta}_p$ and $\boldsymbol{\theta}_z$ for updating poles and zeros, respectively. The poles of the system ($\boldsymbol{\lambda}_p$) are the roots of the denominator in (8.2), while the zeros of FRF $G_{ij}$ ($\boldsymbol{\lambda}_z$) are the roots of the numerator.

Now assume that $m$-FRF measurements from different actuator/sensor configurations are available. In IPZ model updating using multiple FRFs, the quadratic pole-zero error functional

$$\epsilon_i(\boldsymbol{\theta}) = \left( \begin{bmatrix} \boldsymbol{\lambda}_{p,e} \\ \boldsymbol{\lambda}_{z_1,e} \\ \vdots \\ \boldsymbol{\lambda}_{z_m,e} \end{bmatrix} - \begin{bmatrix} \boldsymbol{\lambda}_{p,n}(\boldsymbol{\theta}) \\ \boldsymbol{\lambda}_{z_1,n}(\boldsymbol{\theta}) \\ \vdots \\ \boldsymbol{\lambda}_{z_m,n}(\boldsymbol{\theta}) \end{bmatrix}_i \right)^H \mathbf{W}_\lambda \left( \begin{bmatrix} \boldsymbol{\lambda}_{p,e} \\ \boldsymbol{\lambda}_{z_1,e} \\ \vdots \\ \boldsymbol{\lambda}_{z_m,e} \end{bmatrix} - \begin{bmatrix} \boldsymbol{\lambda}_{p,n}(\boldsymbol{\theta}) \\ \boldsymbol{\lambda}_{z_1,n}(\boldsymbol{\theta}) \\ \vdots \\ \boldsymbol{\lambda}_{z_m,n}(\boldsymbol{\theta}) \end{bmatrix}_i \right), \tag{8.7}$$

is iteratively minimized by updating the generic parameters $\boldsymbol{\theta}^T = [\boldsymbol{\theta}_p^T, \boldsymbol{\theta}_{z_1}^T, \ldots, \boldsymbol{\theta}_{z_m}^T]$, where the subscripts $e$ and $n$ indicate experimentally and numerically obtained quantities, respectively. $\boldsymbol{\lambda}_{z_1}, \ldots, \boldsymbol{\lambda}_{z_m}$ stand for the set of zeros from the first up to the $m$th-FRF measurement, respectively. The diagonal weighting matrix $\mathbf{W}_\lambda \succ 0$ is applied in order to have equal contributions of the relative errors from each pole and zero. In a linear time invariant (LTI) system, pole locations are identical in any FRF measurement of the system. Therefore, in (8.7), pole residuals is used once, whereas the zero residuals are repeated for each FRF measurement since zero locations vary per actuator/sensor configuration.

Replacing the entries $\boldsymbol{\lambda}_{p,n}(\boldsymbol{\theta})$ and $\boldsymbol{\lambda}_{z_1,n}(\boldsymbol{\theta})$ up to $\boldsymbol{\lambda}_{z_m,n}(\boldsymbol{\theta})$ in (8.7) by their first-order Taylor series approximations around $\boldsymbol{\theta}_i$ results in the approximation of the error functional, or

$$\epsilon_i^*(\boldsymbol{\theta}) = \Delta\mathbf{r}_i^H(\boldsymbol{\theta})\mathbf{W}_\lambda\Delta\mathbf{r}_i(\boldsymbol{\theta}), \tag{8.8}$$

where

$$\Delta\mathbf{r}_i(\boldsymbol{\theta}) = \underbrace{\begin{bmatrix} \boldsymbol{\lambda}_{p,e} \\ \boldsymbol{\lambda}_{z_1,e} \\ \vdots \\ \boldsymbol{\lambda}_{z_m,e} \end{bmatrix} - \begin{bmatrix} \boldsymbol{\lambda}_{p,n}(\boldsymbol{\theta}) \\ \boldsymbol{\lambda}_{z_1,n}(\boldsymbol{\theta}) \\ \vdots \\ \boldsymbol{\lambda}_{z_m,n}(\boldsymbol{\theta}) \end{bmatrix}_i}_{\Delta\boldsymbol{\lambda}_i} - \underbrace{\begin{bmatrix} \frac{\partial\boldsymbol{\lambda}_{p,n}(\boldsymbol{\theta})}{\partial\boldsymbol{\theta}_p} & 0 & \ldots & 0 \\ 0 & \frac{\partial\boldsymbol{\lambda}_{z_1,n}(\boldsymbol{\theta})}{\partial\boldsymbol{\theta}_{z_1}} & \ldots & 0 \\ \ldots & \ldots & \ldots & \ldots \\ 0 & 0 & \ldots & \frac{\partial\boldsymbol{\lambda}_{z_m,n}(\boldsymbol{\theta})}{\partial\boldsymbol{\theta}_{z_m}} \end{bmatrix}_i}_{\mathbf{S}_i} \underbrace{\begin{bmatrix} \Delta\boldsymbol{\theta}_p \\ \Delta\boldsymbol{\theta}_{z_1} \\ \vdots \\ \Delta\boldsymbol{\theta}_{z_m} \end{bmatrix}_i}_{\Delta\boldsymbol{\theta}_i}. \tag{8.9}$$

$\mathbf{S}_i$ in (8.9) represents the sensitivity matrix which includes the sensitivity of each pole denoted by

$$\frac{\partial\lambda_{p,n}(\theta_p)}{\partial\theta_p} = \frac{\boldsymbol{\psi}_p{}^T \frac{\partial\mathbf{K}_r}{\partial\theta_p}\boldsymbol{\psi}_p}{2\lambda_{p,n}\boldsymbol{\psi}_p{}^T\mathbf{M}_r\boldsymbol{\psi}_p + \boldsymbol{\psi}_p{}^T\mathbf{B}_r\boldsymbol{\psi}_p}, \tag{8.10}$$

together with the sensitivity of each zero

$$\frac{\partial\lambda_{z,n}(\theta_z)}{\partial\theta_z} = \frac{\boldsymbol{\psi}_z{}^T \frac{\partial\mathbf{K}_s}{\partial\theta_z}\boldsymbol{\psi}_z}{2\lambda_{z,n}\boldsymbol{\psi}_z{}^T\mathbf{M}_s\boldsymbol{\psi}_z + \boldsymbol{\psi}_z{}^T\mathbf{B}_s\boldsymbol{\psi}_z}. \tag{8.11}$$

The number of design parameters is generally equal or lower than the number of measured poles and zeros. Therefore, the optimization problem is (over)determined; hence, a least squares approach is applied. Minimizing (8.8) with regard to $\Delta\boldsymbol{\theta}_i$, and requiring that $\partial\epsilon_i/\partial\Delta\boldsymbol{\theta}_i = 0$, leads to the following equation [9]:

$$\mathrm{Re}\left(\mathbf{S}_i^H\mathbf{W}_\lambda\mathbf{S}_i\right)\Delta\boldsymbol{\theta}_i = \mathrm{Re}\left(\mathbf{S}_i^H\mathbf{W}_\lambda\Delta\boldsymbol{\lambda}_i\right). \tag{8.12}$$

The iteration process will be terminated using the following stop criterion:

$$|\epsilon_i - \epsilon_{i-1}| \leq \delta, \tag{8.13}$$

where $\delta$ is a sufficiently small number.

In summary, the proposed IPZ model updating algorithm using multiple FRFs will be given as follows:

1. Preparation

   (a) Choose the frequency range of interest; identify the experimental values of the poles and zeros in this range.

(b) Select the desired physical DOFs $\mathbf{q}_r$ including the actuators, sensors, and unmeasured performance variables DOFs; then apply the model reduction step.
(c) Match the experimental poles and zeros with their numerical counterparts from the reduced FE model.
(d) Select the stop criterion parameter $\delta$ in (8.13).

2. IPZ model updating

(a) Select a number of (lowest) eigenvalues of the reduced stiffness matrix $\mathbf{K}_r$ and the substructure reduced stiffness matrices $\mathbf{K}_{s_1}, \ldots, \mathbf{K}_{s_m}$, corresponding to the first up to the $m$th FRF, respectively, as the generic parameters $\boldsymbol{\theta}_p, \boldsymbol{\theta}_{z_1}, \ldots, \boldsymbol{\theta}_{z_m}$.
(b) Calculate the sensitivity matrix $\mathbf{S}_i$ in (8.9) based on (8.10), (8.11) and calculate $\Delta\boldsymbol{\lambda}_i$ in (8.9).
(c) Calculate $\Delta\boldsymbol{\theta}_i$ according to (8.12), then update the design parameter $\boldsymbol{\theta}_i$ with $\Delta\boldsymbol{\theta}_i$.
(d) Incorporate the updated generic parameters $\boldsymbol{\theta}_p$, $\boldsymbol{\theta}_{z_1}, \ldots, \boldsymbol{\theta}_{z_m}$ into $\mathbf{K}_r, \mathbf{K}_{s_1}, \ldots, \mathbf{K}_{s_m}$, respectively, to calculate the updated structure and substructure stiffness matrices $\mathbf{K}_r^u$ and $\mathbf{K}_{s_1}^u, \ldots, \mathbf{K}_{s_m}^u$, respectively.
(e) Use (8.3)–(8.6) to replace $\mathbf{K}_{s_1}^u$ into $\mathbf{K}_r^u$ and construct the updated stiffness matrix $\mathbf{K}_{r,s_1}^u$; this process repeats until the replacement of $\mathbf{K}_{s_m}^u$ in $\mathbf{K}_{r,s_{m-1}}^u$ to construct the final updated stiffness matrix $\mathbf{K}_{r,s_m}^u$.

3. Stop criterion check

(a) Calculate $\epsilon_i$ in (8.7) using the updated stiffness $\mathbf{K}_{r,s_m}^u$ instead of $\mathbf{K}_r$; check whether the stop criterion in (8.13) is satisfied; if not, return to step 2 (c) using $\mathbf{K}_{r,s_m}^u$ instead of $\mathbf{K}_r$; the iteration process stops when the stop criterion in (8.13) is satisfied.

## 8.3 Case Study: 2D Pinned-Sliding Beam

To verify the IPZ model updating using multiple FRFs consider a 2D finite element model of a pinned-sliding aluminum beam, see Fig. 8.1, with properties listed in Table 8.1. In the model, twelve Euler beam elements of equal size are used. Each element has two nodes and each node has two DOFs: transversal ($w$) and rotational ($r$) displacement. Modal damping of 0.1% is added to all modes. This model is referred to as the original model $G_n$.

Assume that the original model $G_n$ differs from the experimental structure $G_e$ in the 12th element which in reality has $3.0 \times 10^{-2}$ m thickness, and $4.0/3.0 \times 10^{-2}$ m width. Therefore, the original and experimental model have identical mass. A force actuator $u$ is located on the transversal DOF of the third node. Two displacement sensors are located on the transversal DOF of the fourth ($y_1$) and the fifth ($y_2$) node, while the unmeasured performance variable ($z$) is represented by the transversal DOF of the seventh node. The following FRFs are introduced: $G_1 = Y_1/U$, $G_2 = Y_2/U$, and $G_3 = Z/U$. In reality, the performance variables cannot be measured directly. However, in this simulated experiment, the quality of the updated performance variable ($G_3$) can be assessed since the "experimental" $G_{e,3}$ can be calculated. It will be assumed that in a real experiment all the experimental poles and zeros can be estimated from the measured FRFs by applying modal parameter fit procedures. In the simulated experiment, they can simply be calculated. Note that the complex poles/zeros are assumed to occur in complex conjugated pairs since weak damping is assumed. In what follows, only the poles/zeros with positive imaginary parts will be used.

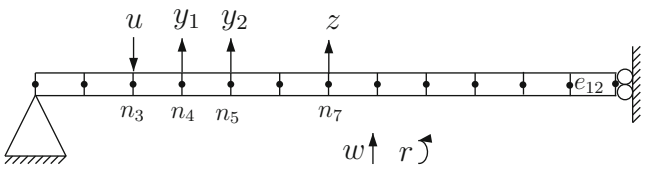


**Fig. 8.1** 2D Pinned-Sliding aluminum beam

**Table 8.1** Properties of the beam

| Property | Value | Unit |
|---|---|---|
| Young's modulus | 69 | GPa |
| Mass density | $2.7 \times 10^3$ | kg m$^{-3}$ |
| Thickness | $2.0 \times 10^{-2}$ | m |
| Width | $2.0 \times 10^{-2}$ | m |
| Length of the beam | 1.0 | m |

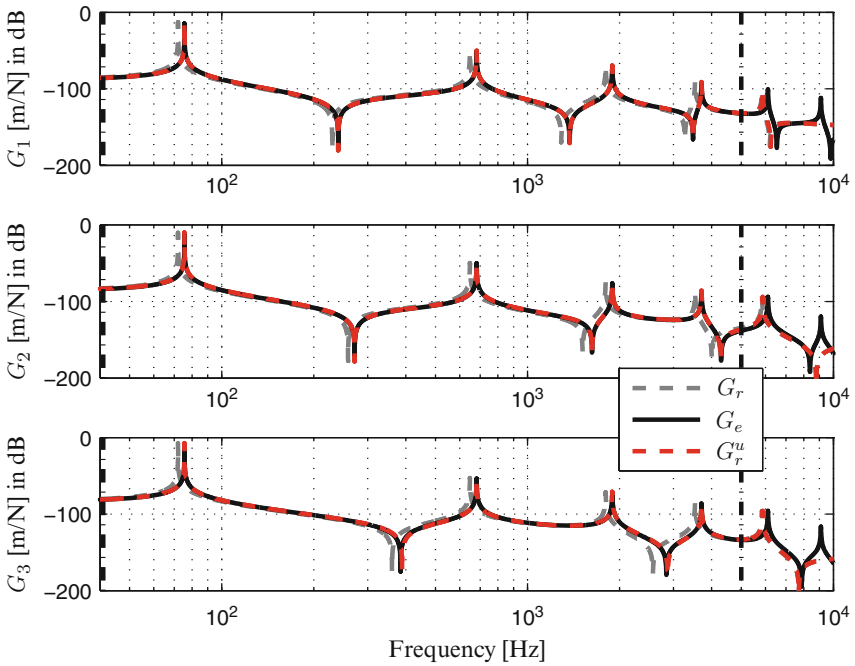


**Fig. 8.2** Original, experimental, and updated $G_1$ (*top*), $G_2$ (*middle*), and $G_3$ (*bottom*)

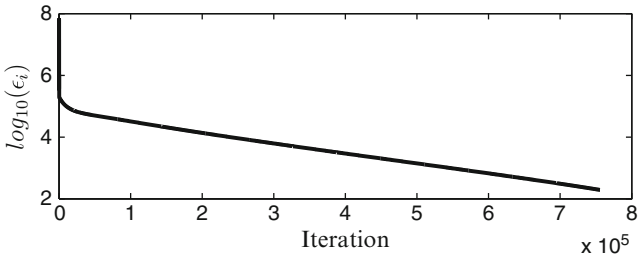


**Fig. 8.3** $\log_{10}(\epsilon_i)$ for IPZ model updating using $G_1$ and $G_2$

It is assumed that $G_{e,1}$ and $G_{e,2}$ are available and that the frequency range of interest is $[40, 5000]$ Hz. Therefore, the original model $G_n$ will be reduced to $G_r$ considering the first five eigenmodes plus one residual flexibility mode for the truncated modes (modes: $6, \ldots, 24$). A coordinate transformation is applied so that the reduced model is expressed in terms of the desired DOFs $q_r = [w_4, w_6, w_8, w_{12}, w_{16}, w_{20}]$; containing the actuator, sensors, and the unmeasured performance variables DOFs. The goal is to match the poles and the zeros of the reduced-order $G_{r,1}$ and $G_{r,2}$ with the poles and the zeros of the experimental $G_{e,1}$ and $G_{e,2}$, respectively, in the frequency range of interest. According to Fig. 8.2, the first four poles of $G_{e,1}$ and $G_{e,2}$, the first three zeros of $G_{e,1}$, and the first two zeros of $G_{e,2}$ lay within the frequency range of interest, hence are assumed to be extracted from the measurements. The first four poles of $G_{r,1}$ and $G_{r,2}$ are updated using the first four (real) eigenvalues of the reduced-order stiffness matrix $\mathbf{K}_r$, i.e. $[\theta_{p,1}, \ldots, \theta_{p,4}]$. Furthermore, the first three zeros of $G_{r,1}$ and the first two zeros of $G_{r,2}$ are updated using the (real) eigenvalues $[\theta_{z_1,2}, \ldots, \theta_{z_1,4}]$ and $[\theta_{z_2,3}, \theta_{z_2,4}]$ of the substructure reduced-order stiffness matrices $\mathbf{K}_{s_1}$ and $\mathbf{K}_{s_2}$, respectively.

Using the discussed IPZ model updating algorithm with $\delta = 10^{-5}$, the algorithm converged to $\epsilon_i = 244.58$ in $i = 755{,}634$ iterations. Although many iterations are needed, the required calculation time is limited because a reduced-order model is used. Note that the number of iterations also depends on the value of the stop criterion parameter $\delta$. It can be seen from Fig. 8.3 that $\epsilon_i$ decreased rapidly during the first iterations, but it takes many iterations to fulfill the convergence criterion of (8.13) with $\delta = 10^{-5}$. Convergence of the IPZ model updating toward a (local) minima of (8.7), results in the updated reduced model $G_u$ composed of $\mathbf{M}_r$, $\mathbf{B}_r$, and $\mathbf{K}^u_{r,s_2}$. Figure 8.2 shows that $G_{u,1}$ and $G_{u,2}$ match very well in terms of both poles and zeros with the poles and the zeros of $G_{e,1}$ and $G_{e,2}$ in the frequency range of interest. Moreover, $G_{u,3}$ which resembles the unmeasured performance variable also matches very well in terms of both the poles and the zeros with those from $G_{e,3}$.

**Table 8.2** Correlations in the frequency range of interest before/after IPZ model updating using $G_1$ and $G_2$

| | $G_{n,1}$ vs. $G_{e,1}$ | $G^u_{r,1}$ vs. $G_{e,1}$ | $G_{n,2}$ vs. $G_{e,2}$ | $G^u_{r,2}$ vs. $G_{e,2}$ | $G_{n,3}$ vs. $G_{e,3}$ | $G^u_{r,3}$ vs. $G_{e,3}$ |
|---|---|---|---|---|---|---|
| $X_S$ | 0.025 | 0.999 | 0.025 | 0.991 | 0.026 | 0.669 |
| $X_A$ | 0.004 | 0.994 | 0.004 | 0.993 | 0.004 | 0.994 |

**Table 8.3** Correlations in the frequency range of interest before and after IPZ model updating using only $G_1$

| | $G_{n,1}$ vs. $G_{e,1}$ | $G_{u,1}$ vs. $G_{e,1}$ | $G_{n,3}$ vs. $G_{e,3}$ | $G_{u,3}$ vs. $G_{e,3}$ |
|---|---|---|---|---|
| $X_S$ | 0.025 | 0.946 | 0.026 | 0.336 |
| $X_A$ | 0.004 | 0.950 | 0.004 | 0.954 |

Furthermore, the shape ($X_S$) and amplitude ($X_A$) correlation measures [6], listed in Table 8.2, show significant improvement after IPZ model updating not only for the FRFs which are used in the model updating ($G_1$ and $G_2$), but also for the unmeasured FRF ($G_3$). Correlation measures for the case where only $G_1$ is included in the model updating process is listed in Table 8.3. The results indicate that correlations for both $G_1$ and $G_3$ are higher when an extra FRF $G_2$ is used in the model updating process. This means the reduced FE model is indeed better improved, when more FRFs are included the model updating process.

## 8.4 Conclusion

In this paper, the IPZ model updating technique is extended to enable the use of multiple FRFs so that more information of eigenmodes can be used. The IPZ model updating using multiple FRFs is verified based on a simulated experiment of a pinned-sliding beam. It was shown that using more FRF measurements, from different actuator/sensor configurations, helps to better improve the reduced FE model toward the (simulated) real system. After IPZ model updating, the numerical FRFs match very well with the experimental FRFs. This not only holds for the two experimental FRFs which were used in the model updating procedure, but also for the third FRF related to an unmeasured performance variable.

Although the method seems promising, there are still unresolved issues in the proposed model updating method which need further investigation: (1) a proof of convergence to a local minimum, although the convergence behavior shown in Fig. 8.3 is promising, a rigorous proof is lacking and (2) after model updating the stiffness matrix shows a small amount of asymmetry.

## References

1. Yang, J., Ouyang, H., Zhang, J.-F.: A new method of updating mass and stiffness matrices simultaneously with no spillover. J. Vib. Control **22**(5), 1181–1189 (2016)
2. Mottershead, J.E., Link, M., Friswell, M.I.: The sensitivity method in finite element model updating: a tutorial. Mech. Syst. Signal Process. **25**, 2275–2296 (2011)
3. Jaishi, B., Ren, W.-X.: Finite element model updating based on eigenvalue and strain energy residuals using multiobjective optimisation technique. Mech. Syst. Signal Process. **21**, 2295–2317 (2007)
4. Dorosti, M., Fey, R., Heertjes, M., van de Wal, M., Nijmeijer, H.: Finite element model reduction and model updating of structures for control. In: 19th World Congress The International Federation of Automatic Control, Cape Town (2014)
5. Arora, V., Adhikari, S., Friswell, M.: FRF-based finite element model updating method for non-viscous and non-proportional damped system. In: International Conference on Structural Engineering Dynamics, Lagos (2015)
6. Dorosti, M., Heck, F., Fey, R., Heertjes, M., van de Wal, M., Nijmeijer, H.: Frequency response sensitivity model updating using generic parameters. In: American Control Conference (ACC) (2016)
7. Arora, V.: Constrained antiresonance frequencies based model updating method for better matching of FRFs. Inverse Prob. Sci. Eng. **22**(6), 873–888 (2014)
8. D'Ambrogio, W., Fregolent, A.: Results obtained by minimising natural frequency and antiresonance errors of a beam model. Mech. Syst. Signal Process. **17**(1), 29–37 (2003)
9. de Kraker, B.: A Numerical-Experimental Approach in Structural Dynamics. Shaker, Maastricht (2013)

# Chapter 9
# Vision-Based Concrete Crack Detection Using a Convolutional Neural Network

**Young-Jin Cha and Wooram Choi**

**Abstract** The prominent methods for monitoring structures to date rely on analyzing data measured from contact sensors that are physically attached to a structure. However, these approaches have the high possibility of false alarms due to noises, sensor malfunctions, and complex environmental effects. Under those circumstances, engineers have to conduct on-site investigations to confirm that damage has occurred. To address this challenge, this paper proposes a new vision-based approach for detecting concrete cracks using a convolutional neural network (CNN). Images are firstly taken under uncontrolled situations to collect widely varying crack features. Second, the raw images are divided into 40K images to build training and validation sets. Lastly, the prepared datasets are fed into a deep CNN architecture with eight layers including convolution, pooling, ReLU, and softmax. The trained classifier consequently records 98% of accuracies in both training and validation.

**Keywords** Concrete crack detection • Convolutional neural network • Structural health monitoring • Vision-based • Machine learning

## 9.1 Introduction

The deterioration of civil structures is an inevitable process occurring from the beginning stage of the use. Considering a single damaged member can cause significant changes [1] in their systems, structural health monitoring (SHM) cannot be overvalued. Therefore, structural safety has become a major issue, and routine inspections are regularized [2] as a result. However, heavy reliance on human-conducted on-site inspection arises the following problems. First, the considerable number of structures hinders frequent inspections due to limited human-resources [3]. Second, evaluation results by human-inspectors differ dependent on their physical ability, knowledge, and experience [3, 4]. Hence, developing automated and reliable inspection methods is necessary.

In order to overcome the above issues, contact-sensor approaches have been developed [5, 6]. One of the particular works focused on monitoring the global behavior of a suspension bridge was conducted by Kurata et al. [7]. Wireless sensors, including tri-axial accelerometers, potentiometers, and climate stations, collected data from each sensor node to extract seven mode shapes of the bridge. Although these research articles are highlighted as accurate measurements in the field, the complex requirements, such as installing multiple sensors, integration of each data and maintenance of sensors, remains as challenges. Obtaining adequate data is also known as one of the toughest issues due to environmental variations [8, 9] especially temperature and humidity. This aspect may require extra efforts to identify modal properties accurately [10].

Vision-based approaches have emerged as the alternatives because the results provide intuitively comprehensive information compared to sensor-based methods. Several modal identification methods using high-speed cameras have been proposed [11, 12]. However, further tests for massive structures are required to completely substitute sensor-based monitoring systems. While the main purpose of the aforementioned studies is lying on observing the global behaviors of structures, several research projects that mainly dedicate to detecting local damages from images have been proposed [13, 14]. Although the vision-based damage detection partly overcome some limitations of sensor-based approaches, it is still challenging to create methods that actually works in real-world situations.

Y.-J. Cha (✉)
Department of Civil Engineering, University of Manitoba, Winnipeg, MB, R3T 5V6, Canada
e-mail: young.cha@umanitoba.ca

W. Choi
Department of Civil Engineering, University of Manitoba, Winnipeg, MB, R3T 6B3, Canada
e-mail: choiw@myumanitoba.ca



J. Caicedo, S. Pakzad (eds.), *Dynamics of Civil Structures, Volume 2*, Conference Proceedings of the Society for Experimental Mechanics Series, DOI 10.1007/978-3-319-54777-0_9

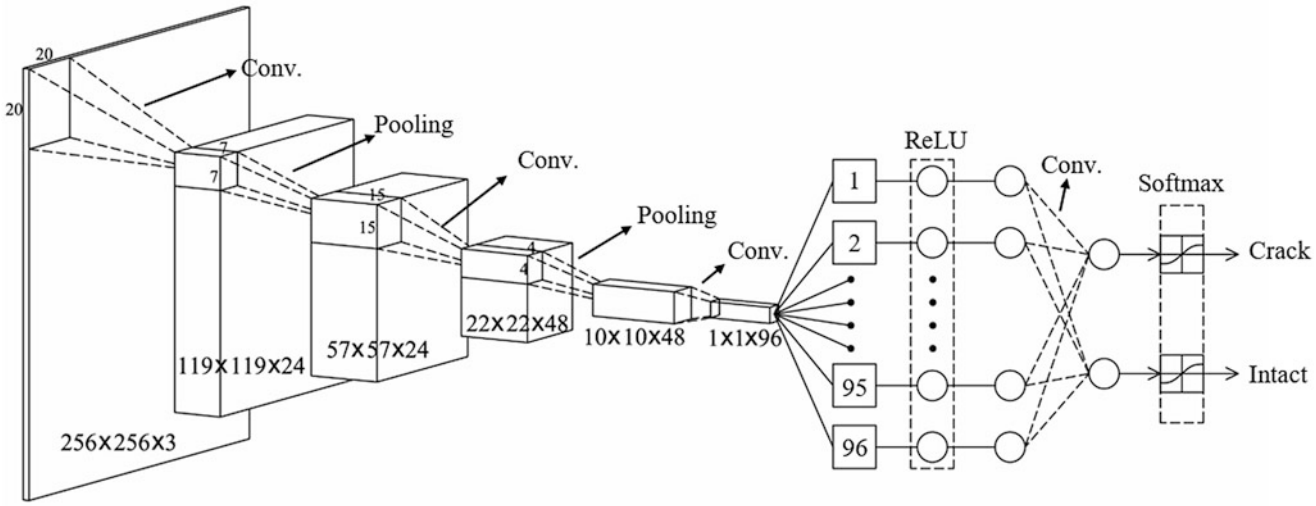


**Fig. 9.1** Overall architecture

A possible breakthrough is the implementation of artificial neural networks [15]. Especially, convolutional neural networks (CNNs) have received a great attention in image classification due to the excellent performance [16]. In addition, extremely fast computations by the conjugation of graphic process units (GPUs) enable CNNs to have deeper architectures that can learn a vast amount of features from datasets [17]. In this study, a deep CNN architecture is proposed for detecting concrete cracks, and two GPUs (Nvidia Geforce Titan X × 2ea) are used [18].

## 9.2 Overall Architecture of the Proposed CNN and the Results

The designed architecture is depicted in Fig. 9.1 representing how an input data is generalized by passing through the designed architecture. Overall, input images with 256 × 256 × 3 pixel resolutions are generalized to the vector with 96 elements in training, and the vector is consequently classified to crack or intact after rectified linear unit (ReLU), the last convolution, and softmax layers. During the training process, pooling layers simply pool features from previous layers. These operations may reduce computational cost significantly. Convolution layers conduct element by element multiplications between inputs of each layer and receptive fields, where the values of receptive fields are given by random numbers and tuned in stochastic gradient descent. The proposed CNN trained on 32K images and 8K extra images are used in validation, in which the images were cropped from raw images taken under uncontrolled conditions to generate a dataset with extensively varying features of cracks. As a result, the designed architecture records 98.25 and 98.04% of accuracies in training and validation respectfully. It is anticipated that the trained CNN classifier works very well in testing with images that are taken under uncontrolled situations because the generated training dataset includes extensively varying crack images, and the accuracies reach to about 98%. In the future, the trained CNN will be combined with a sliding window technique and autonomously flying drones.

## 9.3 Conclusion

A vision-based method for detecting concrete cracks using a deep CNN was proposed. To generate the dataset with extensively varying crack features, images were taken under uncontrolled circumstances, and they cropped into small images of 256 × 256. The generated image database was fed into the designed CNN. Consequently, 98% of accuracies in training and validation were recorded. In the future, we will combine the trained CNN with a sliding window technique and autonomously flying drones to develop an advanced framework.

## References


1. Begg, R.D., et al.: Structural integrity monitoring using digital processing of vibration siqnals. In: Offshore Technology Conference: Offshore Technology Conference (1976)
2. Administration, F.H. [cited 2016 September 21]; Available from: https://www.fhwa.dot.gov/bridge/
3. Chang, P.C., Flatau, A., Liu, S.: Review paper: health monitoring of civil infrastructure. Struct. Health Monit. **2**(3), 257–267 (2003)
4. Phares, B.M., et al.: Reliability of visual bridge inspection. Public Roads. **64**(5), (2001)
5. Rice, J.A., et al.: Flexible smart sensor framework for autonomous structural health monitoring. Smart Struct. Syst. **6**(5–6), 423–438 (2010)
6. Jang, S., et al.: Structural health monitoring of a cable-stayed bridge using smart sensor technology: deployment and evaluation. Smart Struct. Syst. **6**(5–6), 439–459 (2010)
7. Kurata, M., et al.: Internet-enabled wireless structural monitoring systems: development and permanent deployment at the New Carquinez Suspension Bridge. J. Struct. Eng. **139**(10), 1688–1702 (2012)
8. Xia, Y., et al.: Temperature effect on vibration properties of civil structures: a literature review and case studies. J. Civ. Struct. Heal. Monit. **2**(1), 29–46 (2012)
9. Cornwell, P., et al.: Environmental variability of modal properties. Exp. Tech. **23**(6), 45–48 (1999)
10. Behmanesh, I., et al.: Hierarchical Bayesian model updating for structural identification. Mech. Syst. Signal Process. **64**, 360–376 (2015)
11. Dorn, C.J., et al.: Automated extraction of mode shapes using motion magnified video and blind source separation. In: Topics in Modal Analysis & Testing. Springer, Cham/Heidelberg (2016)
12. Chen, J.G., et al.: Modal identification of simple structures with high-speed video using motion magnification. J. Sound Vib. **345**, 58–71 (2015)
13. Abdel-Qader, I., Abudayyeh, O., Kelly, M.E.: Analysis of edge-detection techniques for crack identification in bridges. J. Comput. Civ. Eng. **17**(4), 255–263 (2003)
14. Cha, Y.-J., You, K., Choi, W.: Vision-based detection of loosened bolts using the Hough transform and support vector machines. Autom. Constr. **71**, 181–188 (2016)
15. LeCun, Y., et al.: Gradient-based learning applied to document recognition. Proc. IEEE. **86**(11), 2278–2324 (1998)
16. LeCun, Y., Bengio, Y., Hinton, G.: Deep learning. Nature. **521**(7553), 436–444 (2015)
17. Steinkrau, D., Simard, P.Y., Buck, I.: Using GPUs for machine learning algorithms. In: 8th International Conference on Document Analysis and Recognition. IEEE, Seoul, Korea (2005)
18. Cha, Y.-J., Choi, W.: Deep learning-based crack detection using convolutional neural networks. Comput. Aided Civ. Infrastruct. Eng. **32**(3) (2017). doi:10.1111/mice.12263

# Chapter 10
# Analytical and Experimental Analysis of Rocking Columns Subject to Seismic Excitation

**Ryan Kent Giles and Thomas John Kennedy**

**Abstract** Structures of ancient Mediterranean cultures that have survived numerous earthquakes over the span of millennia relied on multifaceted rocking columns to dissipate seismic energy. Rocking columns are again emerging as an effective mechanism in modern structural systems; understanding the rocking behavior can provide insight into how to best design this type of system. This study examines the analytical and experimental rocking behavior of a rectangular column. Equations of motion that describe the rocking behavior of the polygonal columns are derived and analytical energy dissipation methods compared. A high-speed 3D motion capture system, providing noncontact measurement of the column motion, is used in a series of experiments on a uniaxial shake table to validate the analytical model. These experiments show variation indicating stochastic behavior during the excitation phase. The damping ratio and coefficient of restitution are calculated from the experimental results. The experimental results and analytical solution are compared.

**Keywords** Rocking columns • Coefficient of restitution • Impact damping • 3D metrology • Seismic excitation

## 10.1 Introduction

The ability of ancient Greek temples and other structures to survive seismic events is due to the rocking motion of their columns. When stripped of their architectural adornments and cultural significance, columns are slender, rigid blocks. Many researchers have derived the equations of motion for slender, rigid blocks in two dimensions [1–8] and performed analytical analysis of their behavior under various sources of base excitation [9–13]. The effects of friction and shape of the initiation of rocking or sliding have also been well studied analytically [14]. There has been some extension of the rocking problem to three dimensions accounting for cylinders [4] and general three-dimensional structures with a rectangular base [15, 16]. Fewer studies have experimentally confirmed these analytical equations [2]. This paper presents an experimental validation of the equations of motion of a slender rigid body under seismic excitation. The results draw attention to the typical analytical assumptions for the coefficient of restitution and the probabilistic nature of experiments.

## 10.2 Background

For the case of two-dimensional rocking (see Fig. 10.1), the block is assumed to be located on a rigid base. The column has a height of $2h$ and a width of $2b$. We define a slender column as one where:

$$\frac{h}{b} > \frac{1}{\sqrt{1 + I_O}} \tag{10.1}$$

given $I_O$ is the moment of inertia of the block about $O$ or $O'$ which for a rectangle is equal to $(4/3)mR^2$. The slenderness of the block controls whether, on impact, the rigid block will switch its rotation point from $O$ or $O'$ or bounce back and continue to rotate about $O$. The behavior of interest for structural columns is the switching of the rotation point upon impact.

R.K. Giles (✉) • T.J. Kennedy
Department of Civil Engineering, Stony Brook University, 2426 Computer Science, Stony Brook, NY, 11794-4424, USA
e-mail: ryan.giles@stonybrook.edu



J. Caicedo, S. Pakzad (eds.), *Dynamics of Civil Structures, Volume 2*, Conference Proceedings
of the Society for Experimental Mechanics Series, DOI 10.1007/978-3-319-54777-0_10

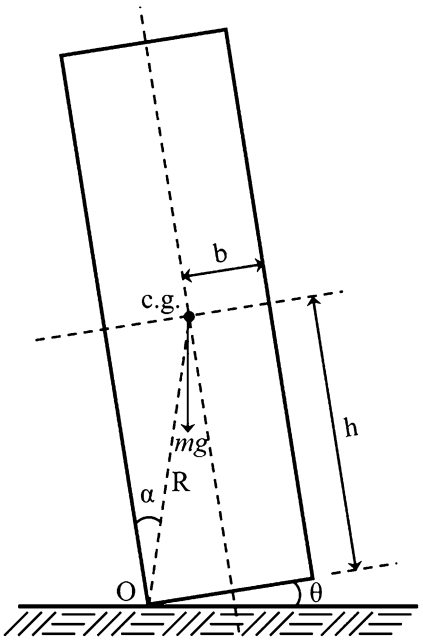


**Fig. 10.1** Rigid rectangular block freely rocking on a rigid base

The derivations also assume that the coefficient of friction between the column and the rigid base is sufficient to prevent sliding. Therefore, the horizontal ground motion ($\ddot{u}_g$) may cause either rigid motion with the column or rocking of the column. If rocking initiates, as in Fig. 10.1, the block will move about the center of rotation ($O$) with an angle of rotation ($\theta$). The equations of motion [1, 2, 10, 12] on the block are:

$$I_O\ddot{\theta} + mgR\sin(-\alpha - \theta) = -mR\cos(-\alpha - \theta)\,\ddot{u}_g \tag{10.2}$$

when the block is in rotation about $O$. When it is rocking about the opposite corner, ($O'$), then the equation of motion becomes:

$$I_O\ddot{\theta} + mgR\sin(\alpha - \theta) = -mR\cos(\alpha - \theta)\,\ddot{u}_g \tag{10.3}$$

In both equations, $\alpha$ is equal to $\tan^{-1}(b/h)$ and $R$ is equal to $\sqrt{(b^2 + h^2)}$. Both of these equations can be combined taking advantage of the signum function and solving for the angular acceleration.

$$\ddot{\theta} = -p^2\left\{\sin(\alpha sgn[\theta] - \theta) + \frac{\ddot{u}_g}{g}\cos(\alpha sgn[\theta] - \theta)\right\} \tag{10.4}$$

where $p$ is $\sqrt{(3g/4R)}$ and a dynamic characteristic related only to the block's geometry.

When the column impacts with the base (i.e. $\theta = 0$), there must be a conservation of momentum but there is also an opportunity for energy loss in the system. Yim et al. [1] derived a coefficient of restitution, $e$, such that:

$$e = \dot{\theta}^+ \Big/ \dot{\theta}^- \tag{10.5}$$

where $\dot{\theta}^-$ and $\dot{\theta}^+$ are the angular velocity just before and after impact. The properties of the rectangular column are such that the coefficient of restitution can be analytically calculated to be

$$e = 1 - \frac{3}{2}sin^2\alpha \tag{10.6}$$

The energy loss due to impact is therefore $1-e^2$ and the higher the coefficient of restitution, the smaller the energy loss and the less damping takes place in the system. Equation (10.6), as written depends solely on the geometry of the column. More recently, Calio and Marletta [6] gave an alternative expression for the coefficient of restitution:

$$e = {}^{h}\!/_{R} \tag{10.7}$$

Again, Eq. (10.7) is dependent solely on the geometry. However, Aslam et al. [2], in their experimental results, purposely did not formally derive or give any expression for the coefficient of restitution. Instead, they stated that the coefficient of restitution would depend on $\dot{\theta}^{-}$ and the material properties of the column. This research considers the coefficient of restitution to be a primary parameter for matching the experimental and analytic results.

## 10.3 Analytical Model

The equation of motion for the rocking column (Eq. (10.4)) was programmed into MATLAB using its explicit Runge-Kutta method based on the Dormand-Price (4,5) pair. To model the impact conditions, the event finder in the method was used such that when $\theta = 0$, the solver would stop, reduce the angular velocity by the coefficient of restitution, and restart the solver with the updated initial conditions ($\theta = 0$ and $\dot{\theta}^{+} = e\dot{\theta}^{-}$). The coefficient of restitution was not programmed explicitly to be either Eq. (10.6) or Eq. (10.7). Instead, it was left as a parameter that could be changed to allow the model to be updated according to the experimental results.

## 10.4 Experimental Method

The column used in this study was a 2.50 cm × 2.50 cm × 25.4 cm (0.985 in × 0.985 in × 10.0 in) machined steel rod weighing 1.238 kg (2.729 lbs). The column was painted with a series of tracking points on one side at regular 6 cm intervals starting 4 cm from the bottom of the column, as seen in Fig. 10.2. One end was marked to indicate the top of the column. A uniaxial Quanser Shake Table II provided the horizontal base excitation. A sheet of 400 grit sand paper was mounted on the shake table to increase the coefficient of friction between the shake table surface and the column. The increased coefficient of friction prevented sliding and rocking-sliding motion. The column was placed at the center of the shake table and aligned so that the axis of the shake table was perpendicular to the sides of the rectangular column using a carpenter's square.

The excitation commanded by the shake table was a modified East-West strong motion record for the 1986 Kalamata earthquake. The record was scaled to initiate rocking in the column but not topple the column. The record was clipped as the first part of the record provides essentially one large pulse and one smaller pulse in the displacement of the table as seen in Fig. 10.3a. Artificial pulses have been previously used in analytical evaluations of rocking columns [13]. Figure 10.3b shows the corresponding accelerations the command displacement produced.

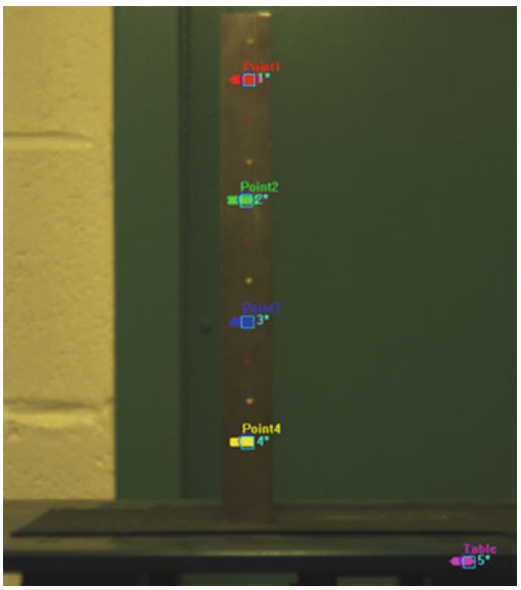


**Fig. 10.2** Experimental setup showing steel column and the tracking results of four points on the column and one on the shake table

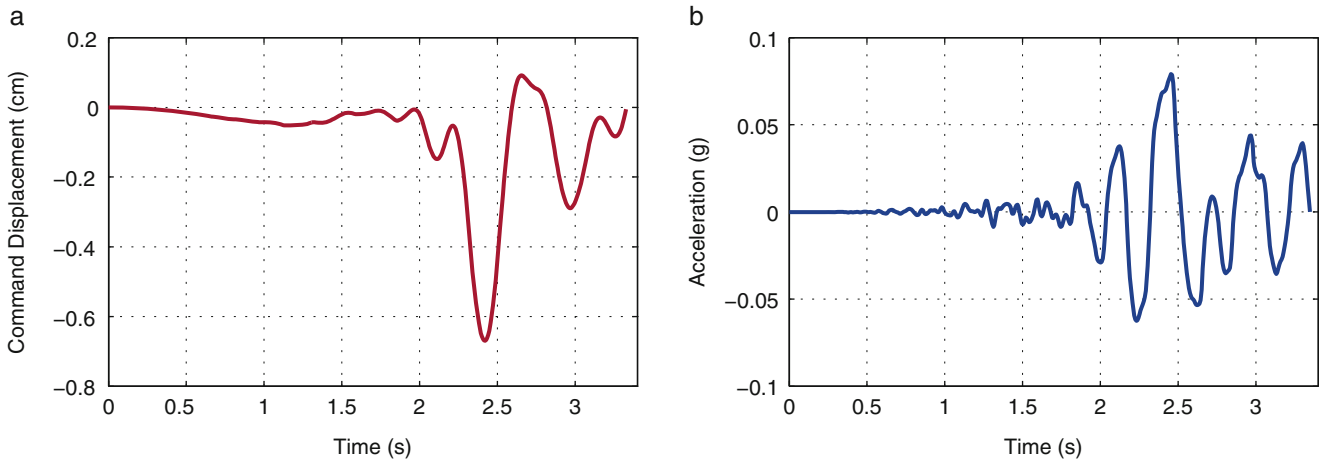


**Fig. 10.3** (**a**) Command displacement (cm) for the Quanser Shake Table II. (**b**) Corresponding command accelerations (g)

Noncontact, three-dimensional measurement of the column motion was performed using a three-camera Xcitex ProCapture system. The cameras were arranged to capture the three-dimensional movement of the column. Each camera operated at a sampling speed of 125 frames per second. Recordings were individually calibrated within Xcitex ProAnalyst software to remove lens distortion and merged in pairs to allow for the two-dimensional images to be interpreted as three-dimensional measurements. The ProAnalyst software is able to track each point individually over the entire length of the record. Four points on each column and a fixed point on the shake table were tracked for each trial. Figure 10.2 shows the four column points and the table point tracked and overlaid on the image of the column at rest. An accelerometer on the shake table was synchronized to the image data to confirm the desired command accelerations.

Positional data was exported from the ProAnalyst software and displacement measurements of the column relative to the shake table surface were calculated. The data was also filtered using an eight pole elliptical filter with a 50 Hz cutoff frequency. The filter served to reduce the small amount of jitter inherently present due to the motion tracking. Anti-alias filtering is not possible with optical systems and therefore oversampling above the expected behavior of the rocking is required to produce accurate results.

## 10.5 Results and Discussion

Thirty-two experiments were performed and processed for this analysis. As the cameras are located in fixed positions external to the shake table system, the motion of the table was removed from the motion of the column to generate displacement values relative to the shake table. Figures 10.4, 10.5, 10.6 and 10.7 show typical results for the tracking of the top tracking point (i.e. Point 1 in Fig. 10.2) in all three directions—**x** is the axis of the table motion, **y** is the gravitational axis, and **z** is out of plane. These figures have been plotted in the same scale to emphasize the differences between the records. The tracked motion of the table is shown in each plot for reference. The rocking motion in the x-axis is greater than the other directions as expected from the desired experimental focus on rocking in one direction.

To investigate the differences apparent in the experiments, the free rocking of each record was examined further. The rocking records were processed to determine when the forced motion of the table ended and free rocking began. The value for the angular displacement and angular velocity were determined for the initiation of the free rocking. These values served as initial conditions for comparison to the analytical free rocking model. The values for the angular displacement and angular velocity at the end of the table motion showed great variety. Each experiment was excited using the same command displacements as confirmed by the tracking of the table during each trial. Nevertheless, the excitation had varied effects on the forced motion of the column in each trial. The differences are due to slight, uncontrollable, experimental conditions.

However, the free rocking of the columns shows similar behavior once it begins. After determining the start of free rocking, the peaks of the motion were located. The initial six peaks were used to calculate the damping ratio using the logarithmic decrement method. A histogram of the damping ratios is presented in Fig. 10.8. Figure 10.9 plots the calculated damping ratio against a lognormal distribution. Both Figs. 10.8 and 10.9 indicate that four of the experiments do not fall within the same distribution of damping coefficients. These four do however appear similar to one another and Fig. 10.6

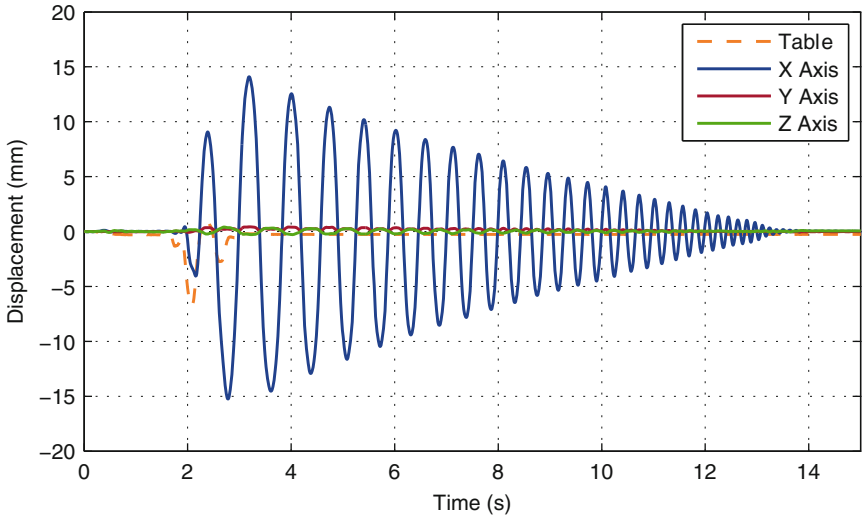


**Fig. 10.4** Representative sample data characterized by a long period of free rocking

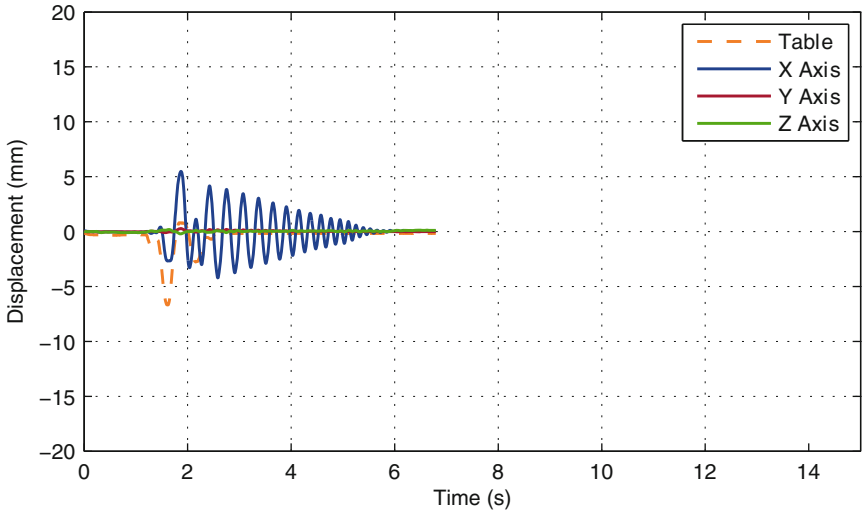


**Fig. 10.5** Representative data characterized by a medium length free rocking period

represents this group. They are characterized by a rocking motion that is arrested by the last movement of the table causing a very small initial angle and velocity at the start of free rocking phase. The rocking is quickly damped out by the impacts.

The free rocking phases of the experimental results were compared to the results from the analytical model. For the steel column used in the experiments, Eq. (10.6) would yield a coefficient of restitution of 0.9857; Eq. (10.7) would yield a coefficient of restitution of 0.9952; and Aslam et al. [2] found a coefficient of restitution of 0.9250 for their concrete block. Because the damping ratio varied among the samples, so did the coefficient of restitution that best matched the analytical and experimental models. For the data presented in Fig. 10.5, a coefficient of restitution of 0.9750 produced the best result and the comparison in presented in Fig. 10.10. At the start of this plot, there is excellent correlation between the experimental and analytical results as the orange and blue lines lay on top of each other. However, as the column continues to rock, the frequency of its rocks increases as the amplitude of the rock decreases suddenly. At this point, the analytical and experimental results diverge. The analytical results, with a constant coefficient of restitution, continues to dampen at a steady rate. This type of result is typical for all the comparisons between the analytical and experimental results. It is indicative that the coefficient of restitution for a rocking column is a function of the rocking period and the angular velocity.

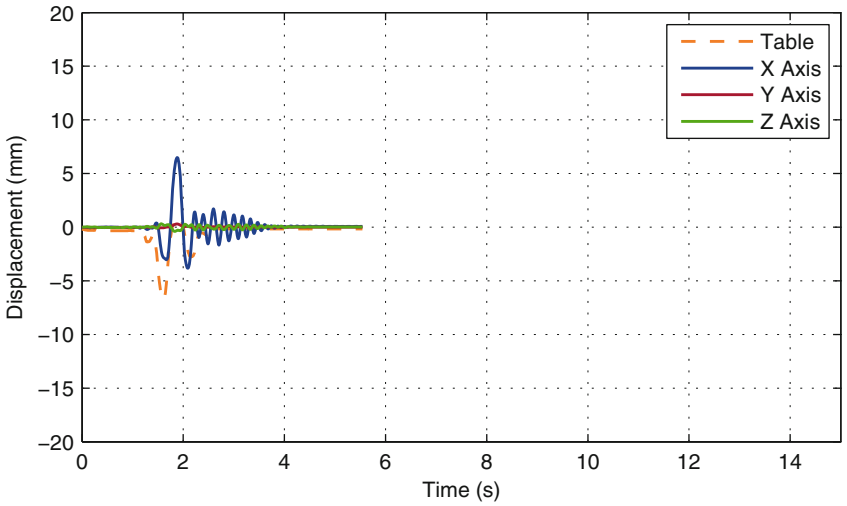


**Fig. 10.6** Representative data characterized by a short free rocking period starting with a small amplitude

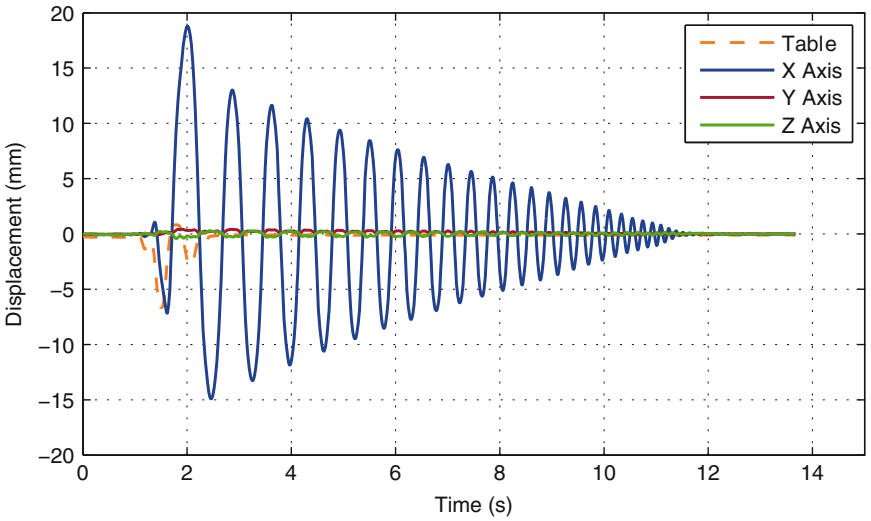


**Fig. 10.7** Representative data showing a very large displacement in the forced phase followed by an extended period of free rocking

**Fig. 10.8** Histogram of the calculated damping ratios during free rocking of the columns

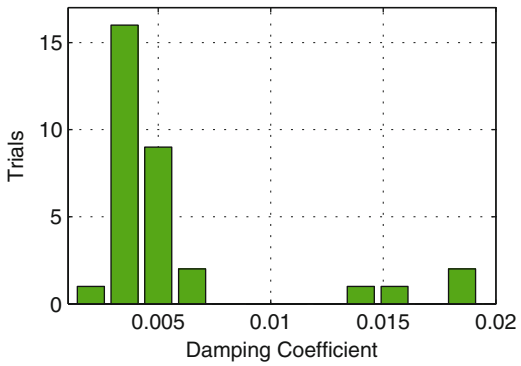

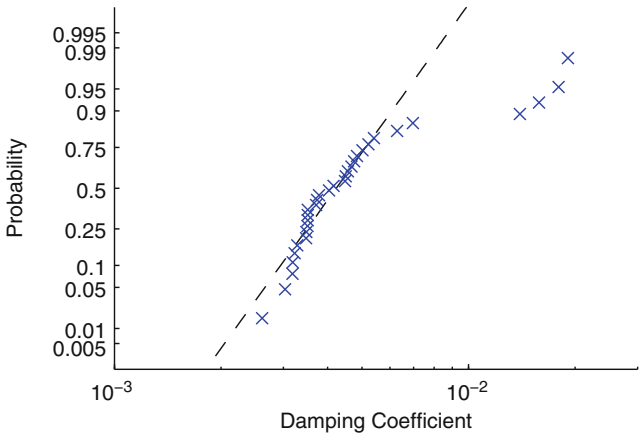


**Fig. 10.9** Lognormal probability plot of the calculated damping ratios during the free rocking of the columns

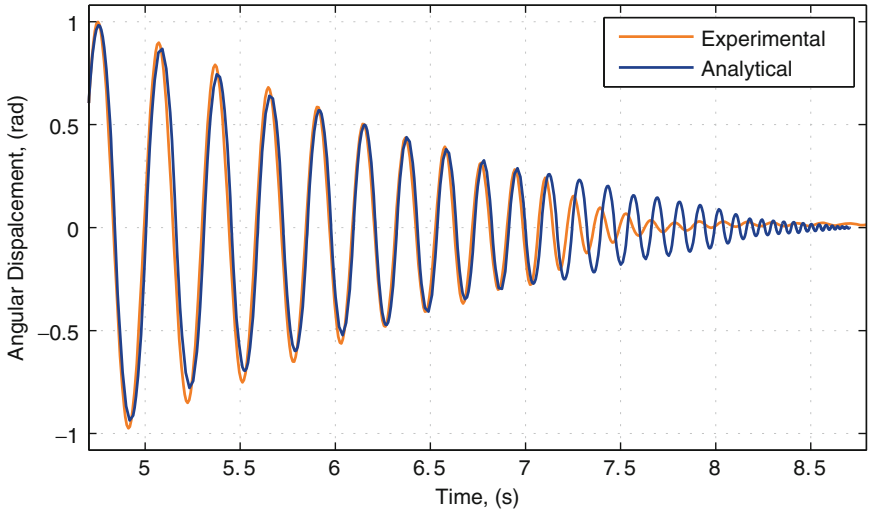


**Fig. 10.10** Comparison between the experimental and analytical results with an optimized coefficient of restitution

## 10.6 Conclusion

The invention of motion tracking software has made the experimental verification of the analytical solutions of the rocking column possible. The speed and accuracy at which images can be processed has dramatically increased since Aslam et al. performed a few motion capture experiments using hand digitization. The data collected in this study confirmed the conclusions that the coefficient of restitution is not constant, is likely dependent on the angular velocity, and is significantly less than the theoretical derivation. The coefficient of restitution calculated for a steel column in this study is greater than that calculated by Aslam for their concrete blocks. The elastic properties of the two materials, and the geometry of the two columns, can account for the primary differences. Future research will continue to investigate the coefficient of restitution by further classifying the collected data by the relevant parameters at the start of the free rocking. More data will be collected to provide a larger statistical sample that can better accommodate the variation inherent to the experimental process. The analytical solution will be modified to account for the stochastic nature of the excitation phase. The modified analytical model, and its range of results, will be compared to all the collected data.

## References


1. Yim, C.-S., Chopra, A.K., Penzien, J.: Rocking response of rigid blocks to earthquakes. Earthq. Eng. Struct. Dyn. **8**(6), 565–587 (1980)
2. Aslam, M., Scalise, D.T., Godden, W.G.: Earthquake rocking response of rigid bodies. J. Struct. Div. **106**(2), 377–392 (1980)
3. Psycharis, I.N., Jennings, P.C.: Rocking of slender rigid bodies allowed to uplift. Earthq. Eng. Struct. Dyn. **11**(1), 57–76 (1983)
4. Koh, A., Mustafa, G.: Free rocking of cylindrical structures. J. Eng. Mech. **116**(1), 35–54 (1990)
5. Andreaus, U., Casini, P.: On the rocking-uplifting motion of a rigid block in free and forced motion: influence of sliding and bouncing. Acta Mech. **138**(3–4), 219–241 (1999)
6. Caliò, I., Marletta, M.: Passive control of the seismic rocking response of art objects. Eng. Struct. **25**(8), 1009–1018 (2003)
7. Apostolou, M., Gazetas, G., Garini, E.: Seismic response of slender rigid structures with foundation uplifting. Soil Dyn. Earthq. Eng. **27**(7), 642–654 (2007)
8. Contento, A., Di Egidio, A.: Investigations into the benefits of base isolation for non-symmetric rigid blocks. Earthq. Eng. Struct. Dyn. **38**(7), 849–866 (2009)
9. Spanos, P., Koh, A.: Rocking of rigid blocks due to harmonic shaking. J. Eng. Mech. **110**(11), 1627–1642 (1984)
10. Hogan, S.J.: On the dynamics of rigid-block motion under harmonic forcing. Proc. R. Soc. Lond. A. **425**(1869), 441–476 (1989)
11. Hogan, S.J.: The many steady state responses of a rigid block under harmonic forcing. Earthq. Eng. Struct. Dyn. **19**(7), 1057–1071 (1990)
12. Makris, N., Roussos, Y.S.: Rocking response of rigid blocks under near-source ground motions. Géotechnique. **50**(3), 243–262 (2000)
13. Zhang, J., Makris, N.: Rocking response of free-standing blocks under cycloidal pulses. J. Eng. Mech. **127**(5), 473–483 (2001)
14. Shenton III, H.: Criteria for initiation of slide, rock, and slide-rock rigid-body modes. J. Eng. Mech. **122**(7), 690–693 (1996)
15. Egidio, A.D., Zulli, D., Contento, A.: Comparison between the seismic response of 2D and 3D models of rigid blocks. Earthq. Eng. Eng. Vib. **13**(1), 151–162 (2014)
16. Zulli, D., Contento, A., Di Egidio, A.: 3D model of rigid block with a rectangular base subject to pulse-type excitation. Int. J. Non Linear Mech. **47**(6), 679–687 (2012)

# Chapter 11
# Extending the Fixed-Points Technique for Optimum Design of Rotational Inertial Tuned Mass Dampers

**Abdollah Javidialesaadi and Nicholas Wierschem**

**Abstract** The fixed-points technique is an approximate version of H-infinity optimization and one of the most common methods used for the design of tuned vibration absorbers. The fixed-points technique is based on the existence of fixed points on the system's frequency response curve that are independent of the system's damping level and are thus at the same location during both the zero and infinite damping conditions. Optimum tuning parameter of tuned mass dampers (TMDs) have been obtained by equalizing the magnitude of the response at these fixed-points. This technique has been previously investigated for the optimal design of conventional TMDs and extended for various types of other TMDs. Recently, by replacing the damper in the TMD with combination of a tuning spring, viscous damper, and a small physical mass connected to a mechanism which converts translational motion to the rotational motion of that small mass, rotational tuned mass dampers (RITMDs) have been developed. However, the fixed-points technique has not been extended previously for RITMDs, which have one additional degree-of-freedom compared to TMDs. In this paper, the fixed-points technique is extended, via algebraic solution, for selecting the optimum tuning and damping values of RITMDs. Comparison of the response of the system with the optimum design values determined from the proposed method and numerical results in the literature demonstrates the validity of the assumptions and procedures of the proposed optimization method. Additionally, the performance of the system, in comparison to a conventionally optimized TMD via the fixed-points technique, shows that the RITMDs can be more effective at reducing the underlying system's maximum displacement response.

**Keywords** Vibration absorber • Tuned mass damper • Fixed-points method • Optimum design • Rotational inertia damper

## 11.1 Introduction

Fixed-points techniques have been proposed and utilized for finding the optimum tuning frequency and damping ratio of tuned mass dampers (TMDs) [1] (Fig. 11.1) as an approximate version of H-infinity optimization. In addition, the fixed-points method has been used for optimum design of damped non-traditional TMDs [2], developed for TMDs attached to multi-degree of freedom primary systems [3], and generalized for global vibration control [4].

Utilizing the inerter [5], which produces inertial mass through transferring the translational motion of the primary structure to the rotational motion of the inerter, different configurations of rotational mass dampers have been proposed and developed to control the response of the primary structure they are attached to and reduce the physical mass of the absorber [6–9]. As inerter based devices, rotational inertia tuned mass dampers (RITMD) (Fig. 11.2), which consist of a TMD modified with the addition of a tuned of rotational inertia device (RID) such as rack and pinion or ball and screw mechanism, have been introduced and optimized numerically [10]. However, the fixed-point technique has not been developed for optimum design of RITMD. In this paper, a fixed-points technique is developed for optimum design of a RTIMD attached to an undamped SDOF primary structure.

A. Javidialesaadi • N. Wierschem (✉)
Department of Civil and Environmental Engineering, The University of Tennessee, Knoxville, TN, USA
e-mail: ajavidia@vols.utk.edu; nwiersch@utk.edu



J. Caicedo, S. Pakzad (eds.), *Dynamics of Civil Structures, Volume 2*, Conference Proceedings
of the Society for Experimental Mechanics Series, DOI 10.1007/978-3-319-54777-0_11

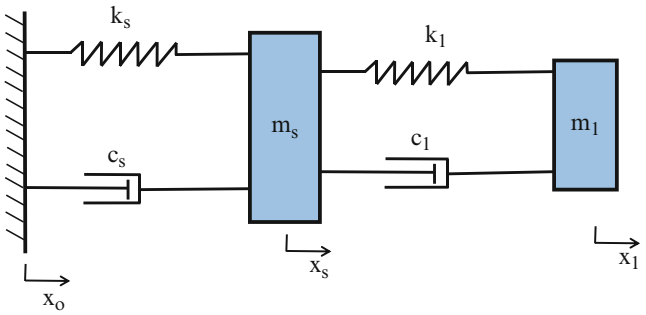


**Fig. 11.1** TMD

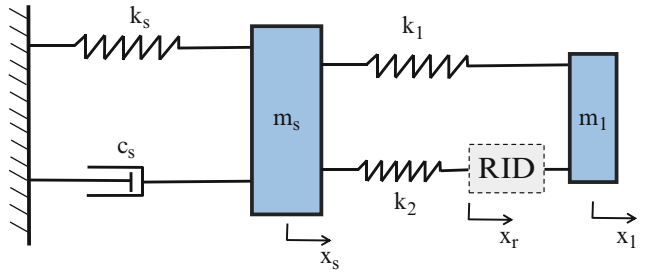


**Fig. 11.2** RITMD

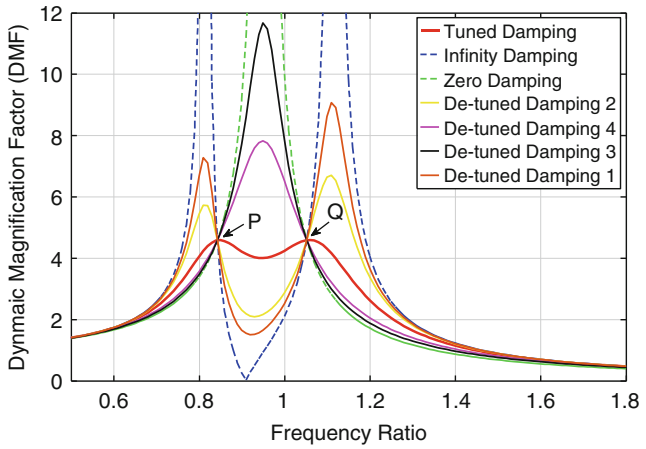


**Fig. 11.3** Fixed-points in the TMD's frequency response curves

## 11.2 Fixed-Point Technique for RITMD

For traditional TMDs, there are always two fixed-points $(P, Q)$ in the frequency response curve for case of damping equal to zero or infinity [1] (Fig. 11.3). In other words, these points are independent from the damping level of the absorber $(c)$, therefore, the primary structure frequency response curves always passed through these two points. The fixed-points can be found by setting the zero and infinity damping transfer functions equal to each other ($\|H\|_{c=0} = \|H\|_{c=\infty}$). The optimum frequency ratio can be obtained by setting the magnitude of the two fixed points equal. This provides an optimization condition in which the curve has a peak at these points [1]. By putting the partial derivative of frequency response function respect to damping equal to zero at optimum frequency points, two optimum damping are achieved and the final optimum damping is the average of two damping values.

Since the RITMD is a three degree-of-freedom system with two optimum frequency ratios, four fixed-points $(P_1, P_2, Q_1, Q_2)$ in the frequency response curves of the primary structure are observed (Fig. 11.4). This observation can be support mathematically by solving the equation of zero-infinity damping in the RITMD ($\|H\|_{c=0} = \|H\|_{c=\infty}$),

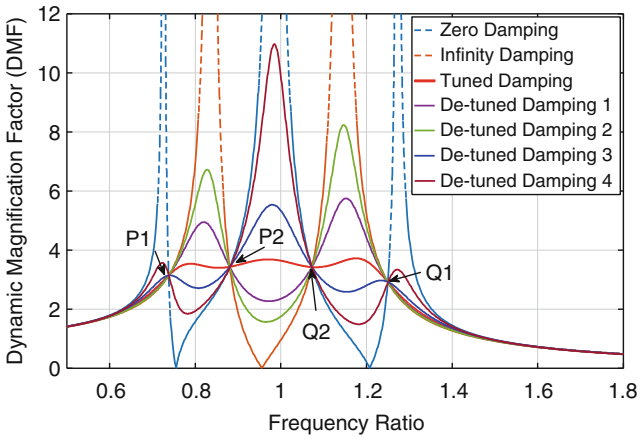


**Fig. 11.4** Fixed-points in the RITMD's frequency response curves

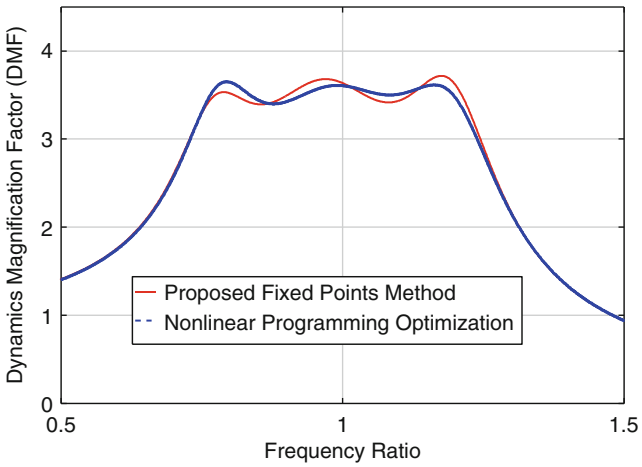


**Fig. 11.5** Extended Fixed-Point Method vs Numerical Optimization; m1 = 10% ms (rotational mass = 15% m1)

which is a forth degree polynomial with four real positive roots. Extending the fixed-points method, we assumed the optimum frequencies condition occurs in the case of a pair equality of the primary structure response magnitude in the fixed-points ($\|H_{P1}\| = \|H_{Q1}\|; \|H_{p2}\| = \|H_{Q2}\|$). This assumption leads to two high-order nonlinear equations which are solved numerically to find the optimum frequency ratios. In the final step, the optimum damping can be found by putting the maximum response magnitude of one of two frequency ratios equal to response magnitude of the other optimum frequency ratio.

## 11.3 Results and Discussion

To examine the proposed extended fixed-points technique accuracy, the frequency response of the primary system with optimum design values from the proposed method is compare with the optimum H-infinity design utilizing an numerical nonlinear programming optimization method [10] (Fig. 11.5). The propose method is an approximate method, thus there are small difference in comparison to the exact H-infinity optimization utilizing nonlinear programming; however, the results from the proposed method are close, which demonstrates the accuracy of the assumptions in the extended proposed method. In addition, the response of the primary structure of both RITMD and TMD systems with the same secondary mass ratio (10%) and optimized with the fixed point method is shown in Fig. 11.6. It can be observe that the RITMD exhibits superior performance in reducing the vibration amplitude of the primary system in compare to the TMD.

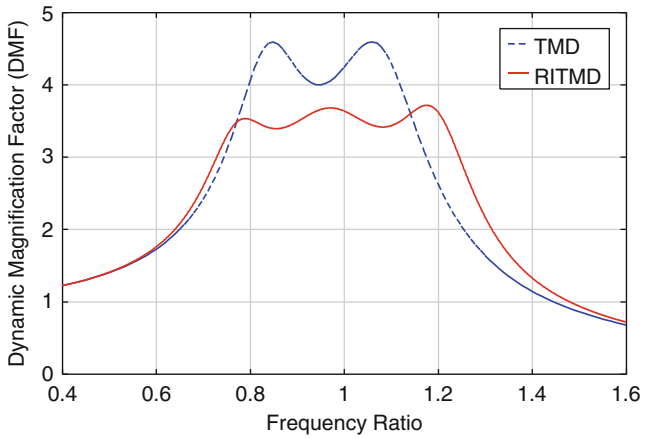


**Fig. 11.6** TMD vs RITMD Response; m1 = 10% ms (rotational mass = 15% m1)

## References

1. Den Hartog, J.: Mechanical Vibrations, 4th edn. McGraw-Hill, New York (1956)
2. Liu, K., Liu, J.: The damped dynamic vibration absorbers: revisited and new result. J. Sound Vib. **284**(3–5), 1181–1189 (2005)
3. Ozer, M.B., Royston, T.J.: Extending Den Hartog's vibration absorber technique to multi-degree-of-freedom systems. J. Vib. Acoust. **127**(4), 341 (2005)
4. Dayou, J.: Fixed-points theory for global vibration control using vibration neutralizer. J. Sound Vib. **292**(3–5), 765–776 (2006)
5. Smith, M.C.: Synthesis of mechanical networks: the inerter. IEEE Trans. Autom. Control. **47**(10), 1648–1662 (2002)
6. Hwang, J.-S., Kim, J., Kim, Y.-M.: Rotational inertia dampers with toggle bracing for vibration control of a building structure. Eng. Struct. **29**(6), 1201–1208 (2007)
7. Ikago, K., Saito, K., Inoue, N.: Seismic control of single-degree-of-freedom structure using tuned viscous mass damper: the tuned viscous mass damper. Earthq. Eng. Struct. Dyn. **41**(3), 453–474 (2012)
8. Hu, Y., Chen, M.Z.Q.: Performance evaluation for inerter-based dynamic vibration absorbers. Int. J. Mech. Sci. **99**, 297–307 (2015)
9. Lazar, I.F., Neild, S.A., Wagg, D.J.: Using an inerter-based device for structural vibration suppression: using an inerter-based device for structural vibration suppression. Earthq. Eng. Struct. Dyn. **43**(8), 1129–1147 (2014)
10. Garrido, H., Curadelli, O., Ambrosini, D.: Improvement of tuned mass damper by using rotational inertia through tuned viscous mass damper. Eng. Struct. **56**, 2149–2153 (2013)

# Chapter 12
# Temperature Effects on the Modal Properties of a Suspension Bridge

**Etienne Cheynet, Jonas Snæbjörnsson, and Jasna Bogunović Jakobsen**

**Abstract** The paper studies temperature effects on the modal parameters of a suspension bridge across a Norwegian fjord. The approach used is a full-scale ambient vibration testing, where an automated Covariance-Driven Stochastic Subspace Identification (SSI-COV) method is used to identify the modal parameters. The bridge site, the bridge structure and the monitoring system are presented, followed by a summary of the data analysis procedure and the parameters used for the automated SSI-COV method applied. The operational modal analysis is based on 6 months of continuous acceleration records providing seasonal and diurnal variations of the natural frequencies of the bridge and the modal damping ratios. Temperature effects were observed with details that are scarcely available in the literature. In particular, the pronounced daily fluctuations of natural frequencies and seasonal effects are documented.

**Keywords** Suspension bridge • Full-scale • Ambient vibrations • Modal parameters • Temperature effects

## 12.1 Introduction

Ambient Vibration Testing (AVT) has become the "default procedure" for modal parameter identification of cable-supported bridges [3]. AVT is particularly attractive for studying environmental effects on the modal parameters, such as the evolution of the modal damping ratios of suspension bridge with the mean wind velocity [2, 4, 9, 13]. Other environmental effects, such as daily and seasonal fluctuations of temperature, are also known to influence the eigen-frequencies of concrete bridges [11, 14] and suspension bridges [6, 8]. During the last few years, several studies have focused on modelling the thermal behaviour of the entire bridge structure [5, 18, 22] and on measuring the static displacements induced by thermal loading [20, 21]. On the other hand, relatively few studies have been dedicated to the investigation of temperature effects on the modal properties of suspension bridges using AVT, based on large amount of ambient vibration data.

The present paper illustrates the influence of daily temperature fluctuations on the eigen frequencies and modal damping ratios of the Lysefjord bridge, which is located at the inlet of a fjord in Norway. The automated Covariance-Driven Stochastic Subspace Identification (SSI-COV) algorithm developed by Magalhães et al. [11] has been used to identify the modal parameters of the bridge. This algorithm was applied by e.g. Magalhães and Cunha [10] on an arch bridge using more than 2 years of data and by Brownjohn et al. [3] on a long-span suspension bridge using only a couple of days of data. The present study therefore complements the study of Magalhães and Cunha [10] and Brownjohn et al. [3] by utilising 6 months of continuous vibration measurements conducted on a long-span suspension bridge.

The present paper is organised as follows: first, the bridge site and instrumentation are presented, followed by a short summary of the parameters used with the automated SSI-COV algorithm. Then the influence of the daily temperature fluctuations on the bridge eigen-frequencies is demonstrated and discussed. Finally, the evolution of the modal damping ratios with temperature variations are investigated.

E. Cheynet (✉) • J.B. Jakobsen
Department of Mechanical and Structural Engineering and Materials Science, University of Stavanger, N-4036 Stavanger, Norway
e-mail: etienne.cheynet@uis.no

J. Snæbjörnsson
Department of Mechanical and Structural Engineering and Materials Science, University of Stavanger, N-4036 Stavanger, Norway

School of Science and Engineering, Reykjavik University, Menntavegur 1, 101 Reykjavík, Iceland



J. Caicedo, S. Pakzad (eds.), *Dynamics of Civil Structures, Volume 2*, Conference Proceedings
of the Society for Experimental Mechanics Series, DOI 10.1007/978-3-319-54777-0_12

## 12.2 Instrumentation and Methods

### *12.2.1 The Bridge Site*

The Lysefjord Bridge, positioned at the narrow inlet of a fjord in the South-West part of the Norwegian coast, is used as a case study. Its main span is 446 m, with the central part 55 m above the sea level. The bridge is entrenched between two steep hills with slopes ranging from 30 to 45° and a maximum altitude of 350 m to the North and 600 m to the South. The bridge is exposed to winds that may descent from mountains nearby or follow the fjord over a longer path. The West side of the bridge is exposed to a more open and levelled area.

Since 2013, the bridge has been instrumented with seven sonic anemometers installed on the West side of the bridge deck and four pairs of accelerometers located inside the deck (Fig. 12.1). GPS timing is used to synchronize the wind- and acceleration data, acquired locally with separate data logging units. Although the highest sampling frequency of the accelerometers and anemometers is 200 Hz and 32 Hz respectively, the data are acquired with a sampling frequency of 50 Hz and decimated to 20 Hz to facilitate data handling. Finally, a 3G router enables wireless data access and transfer via a mobile network. A more detailed description of the bridge instrumentation is given in e.g. [4]. Temperature measurements are provided by a Vaisala weather transmitter WXT520 located on hanger 10, denoted H-10, whereas the accelerometers are located near hangers 9, 18, 24 and 30, where hanger 18 corresponds to the mid-span position.

### *12.2.2 Automated SSI-COV Procedure*

The automated SSI-COV method developed by Magalhães et al. [11] is applied on 6 months of acceleration records obtained from July 2015 to December 2015. For the sake of brevity, the automated SSI-COV method used will not be described explicitly in this paper but the details can be found in e.g. [10, 11]. The parameters used to calibrate this automated SSI-COV method are summarized in Table 12.1. The minimal and maximal order of the system for the calculation of the stabilization diagram are denoted $N_{\min}$ and $N_{\max}$ respectively, whereas $\tau_{\max}$ is the maximal time lag used to compute the cross-covariance matrix. The three accuracy thresholds for the identified eigen-frequencies, modal damping ratios and modal assurance criterion [1] are denoted $\epsilon_{\text{fn}}$, $\epsilon_{\zeta}$ and $\epsilon_{\text{MAC}}$ respectively. Finally, the threshold accuracy for the cluster analysis is $\epsilon_{\text{d}}$.

The mode shapes and eigen-frequencies of the Lysefjord Bridge were successfully identified by the automated SSI-COV method used in the present study [4]. The modal parameters are hereby denoted using the code XYZ, where $\text{X} = \{\text{H}, \text{V}, \text{T}\}$ represents the lateral (H), vertical (V) and torsional (T) bridge motion. $\text{Y} = \{\text{S}, \text{A}\}$ is the symmetric (S) or asymmetric (A) mode shape, and Z the mode number. For example HS1 refers to the first symmetric horizontal mode shape, and TA2 refers to

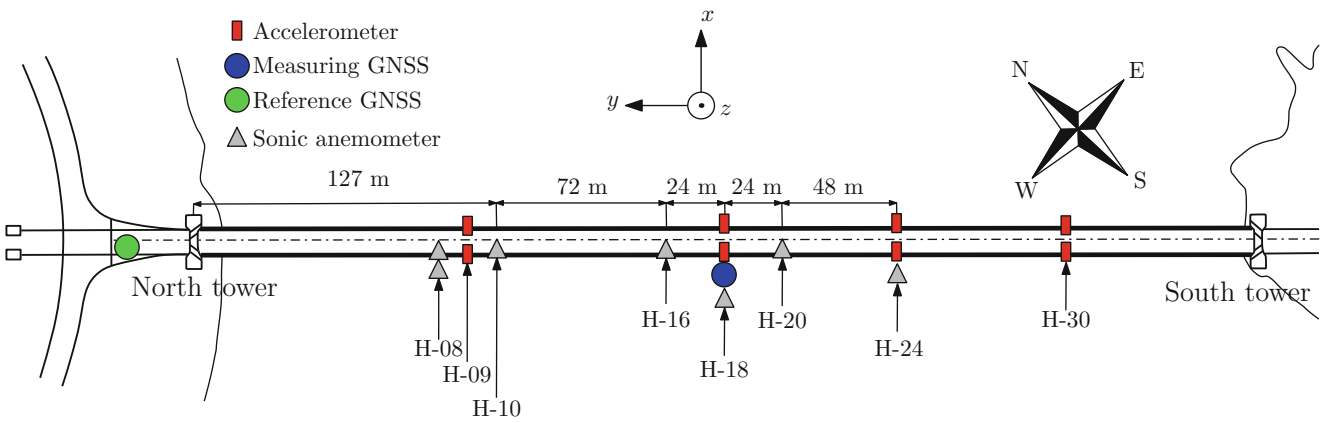


**Fig. 12.1** Wind and structural health monitoring system installed on the Lysefjord Bridge

**Table 12.1** Parameters used in the SSI-COV method applied on Lysefjord bridge acceleration data

| $\tau_{\max}$ (s) | $N_{\min}$ | $N_{\max}$ | $\epsilon_{\text{fn}}$ | $\epsilon_{\zeta}$ | $\epsilon_{\text{MAC}}$ | $\epsilon_{\text{d}}$ |
|---|---|---|---|---|---|---|
| 15 | 3 | 30 | 5e−3 | 3e−2 | 5e−3 | 2e−2 |

**Table 12.2** Eigen-frequencies estimated from the measurement data using the SSI-COV algorithm in comparison to the values based on the SBM method and the Abaqus model

| | SSI-COV | SBM | | Abaqus | |
|---|---|---|---|---|---|
| Modes | Hz | Hz | % | Hz | % |
| HS1 | 0.136 | 0.130 | −4.41 | 0.128 | −6.19 |
| HA1 | 0.444 | 0.442 | −0.45 | 0.431 | −2.90 |
| HS2 | 0.577 | 0.556 | −3.51 | 0.533 | −7.56 |
| HA2 | 0.626 | 0.597 | −4.61 | 0.583 | −6.81 |
| HS3 | 0.742 | 0.830 | 11.90 | 0.833 | 12.31 |
| HA3 | 1.011 | 1.000 | −1.03 | 0.974 | −3.69 |
| VA1 | 0.223 | 0.205 | −8.10 | 0.214 | −3.91 |
| VS1 | 0.294 | 0.319 | 8.35 | 0.302 | 2.72 |
| VS2 | 0.408 | 0.439 | 7.63 | 0.407 | −0.25 |
| VA2 | 0.587 | 0.585 | −0.39 | 0.583 | −0.68 |
| VS3 | 0.853 | 0.864 | 1.31 | 0.856 | 0.34 |
| VA3 | 1.163 | 1.194 | 2.72 | 1.191 | 2.36 |
| TS1 | 1.237 | 1.215 | −1.78 | 1.238 | 0.026 |
| TA1 | 2.184 | 2.186 | 0.09 | 2.122 | −2.85 |

the second asymmetric torsional mode shape. To increase the identification speed of the lower modes, the sampling frequency of the lateral and vertical acceleration records were reduced to 2 Hz. The sampling frequency of the torsional acceleration response remained at 20 Hz. This allowed the SSI-COV algorithm to be applied to more than 50,000 acceleration records of 10 min duration in less than half a day.

A Finite element (FE) model created by Steigen [15], using the Abaqus software, and improved by Tveiten [17] was used to evaluate a numerical prediction of the mode shapes and eigen-frequencies of the Lysefjord Bridge. The eigen-frequencies and the mode shapes of the Lysefjord Bridge were also approximated by using harmonic series expansions following Sigbjörnsson and Hjorth-Hansen [12] for the lateral motion and Strømmen [16] for the vertical and torsional ones. In the following, the latter method is referred to as the "Simplified Bridge Model" denoted SBM. The eigen-frequencies evaluated using the two different models and the SSI-COV algorithm are listed in Table 12.2.

## 12.3 Results

### *12.3.1 Influence of Temperature Variations on the Eigen-Frequencies*

As stated by Xia et al. [19], a higher temperature leads in general to decreased values of vibration frequencies, mainly due to the temperature dependency of the materials Young's modulus. Such variations of the eigen-frequencies are visible in Fig. 12.2, except for temperatures over 20 °C where the number of samples was probably too low to provide reliable results. The influence of temperature variations on the first lateral mode HS1 is rather small. The frequency drops from 0.139 to 0.135 Hz when the temperature increases from 0 to 20 °C. For a similar temperature change, the frequency associated with VA1 decreases only from 0.227 to 0.220 Hz. The most dramatic frequency change occurs for the mode TS1 where the frequency decreases from 1.25 to 1.23 Hz. The scatter of the eigen-frequencies observed on Fig. 12.2 is due to the influence of other parameters such as traffic and wind excitation. The daily fluctuations of the eigen-frequencies can be visualized by studying few days of data. This is done in Fig. 12.3, where 10 days of data recorded in October 2015 are displayed. The first lateral eigen-frequency HS1 fluctuates between 0.132 Hz for diurnal data and 0.145 Hz for nocturnal data. These fluctuations are relatively small compared to those from VA1 which ranges from 0.217 Hz during day time to almost 0.230 Hz during the night. For the torsional motion, TS1 fluctuates between 1.25 Hz down to 1.23 Hz.

As suggested by Kim et al. [7], heavy traffic is likely to be responsible for a decrease in the estimated eigen-frequencies of the bridge deck. The effects of the temperature and traffic on the bridge eigen-frequencies are therefore expected to superimpose and be responsible for larger frequency variations. At night time, the lower temperature and the reduced traffic leads to higher eigen-frequencies whereas at day time, the increase of the temperature and traffic leads to lower eigen-frequencies. This appears clearly on Fig. 12.3, where a pseudo-period of 24 h is visible. The periodical pattern is clearly visible for the vertical bridge motion, but it is more noisy for the lateral and torsional motions. This can be partly explained by the higher signal to noise ratio measured for the vertical motion.

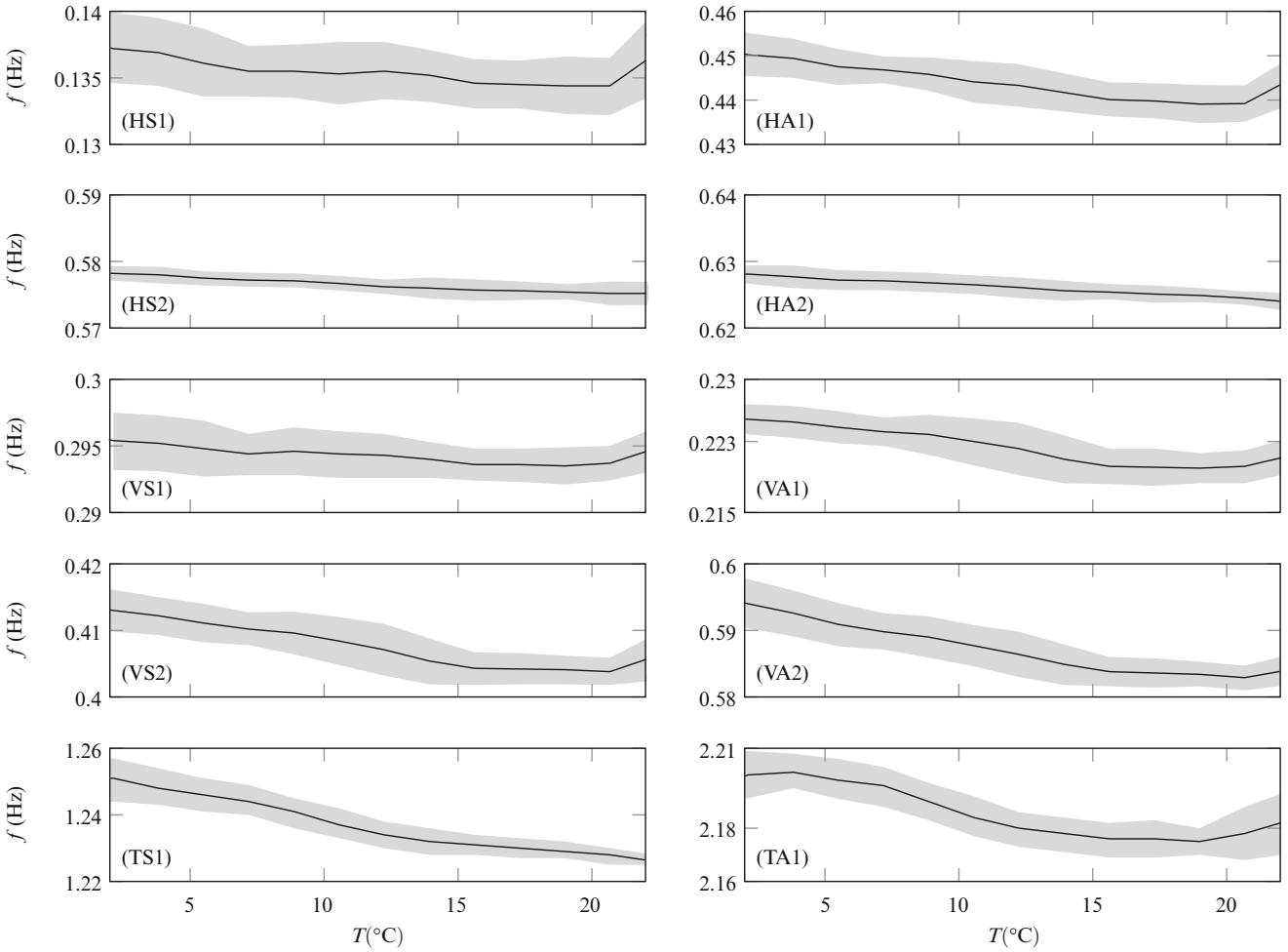


**Fig. 12.2** Evolution of the first four lateral and vertical and the first two torsional eigen-frequencies with the temperature. The data set comprises 6 months of acceleration and temperature records (July–December 2015)

Temperature fluctuations seem to have a larger influence on the variation of the eigen-frequencies than the traffic loading. The attenuation of the daily periodicity of the eigen-frequency in November and December (Fig. 12.4) cannot simply be explained by a reduction of heavy traffic for example. The periodicity pattern appears to be almost entirely modulated by temperature changes. For example, we observed that the sinusoidal pattern was elongated at the bottom part in July (longer day) but elongated at the top part in October (shorter day), without strong variations in the amplitude of the fluctuations.

### *12.3.2 Influence of Temperature Variations on the Modal Damping Ratios*

The estimation of the modal damping ratios is one of the most crucial step in studying accurately the buffeting response of a suspension bridge. Unfortunately, such studies are a rarity in full scale. In general, the aerodynamic damping ratios are obtained with a large dispersion in full-scale [2, 13]. This requires a statistically significant amount of data, which is rarely presented in the literature. In this subsection, the total damping is considered for various wind conditions, using a considerable amount of data. The evolution of the modal damping ratios with the mean wind velocity has been described in e.g. Cheynet et al. [4] and is therefore not recalled here.

Temperature effects on the modal damping ratios remain mostly unexplored and are therefore briefly investigated in the following. The variation of the modal damping ratios with temperature is displayed in Fig. 12.5, for the first four lateral and vertical modes as well as the first two torsional modes.

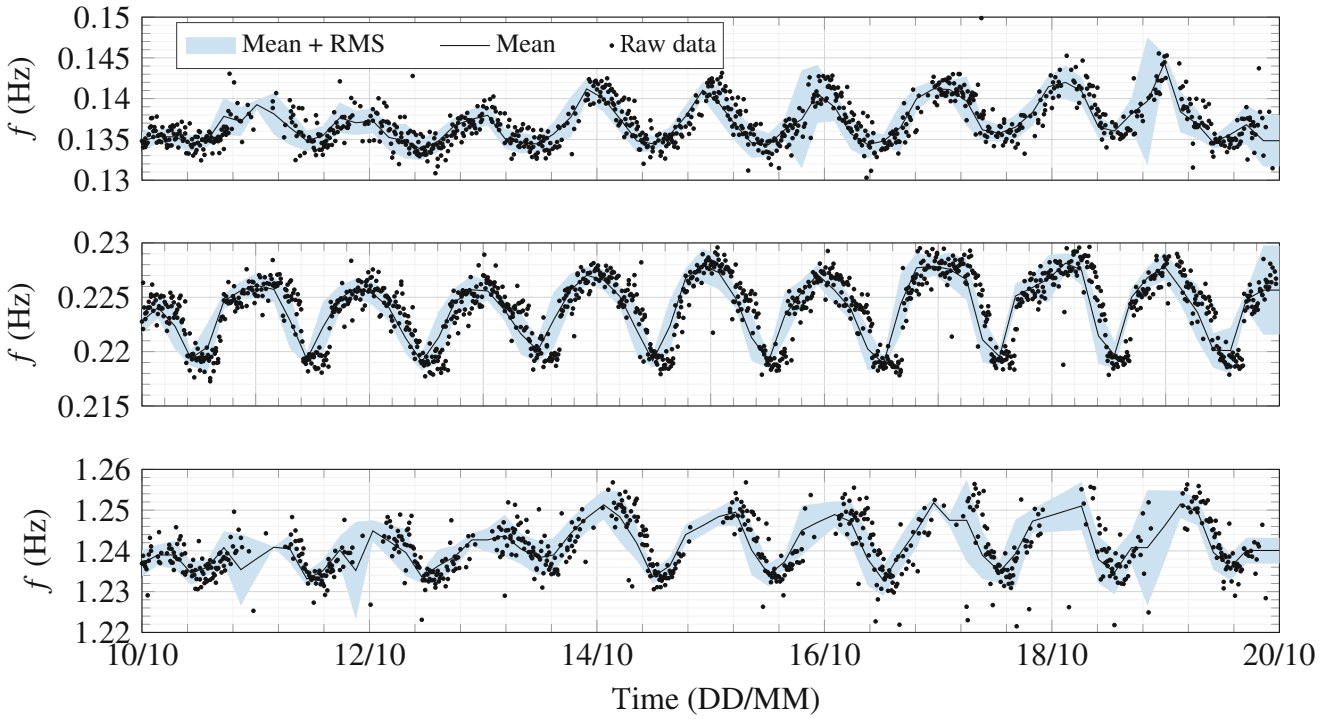


**Fig. 12.3** Evolution of HS1 (*top*), VA1 (*middle*) and TS1 (*bottom*) between the 20/09/2015 and 30/09/2015. Data binning has been applied to better estimate the fluctuating mean value and RMS of the eigen-frequencies

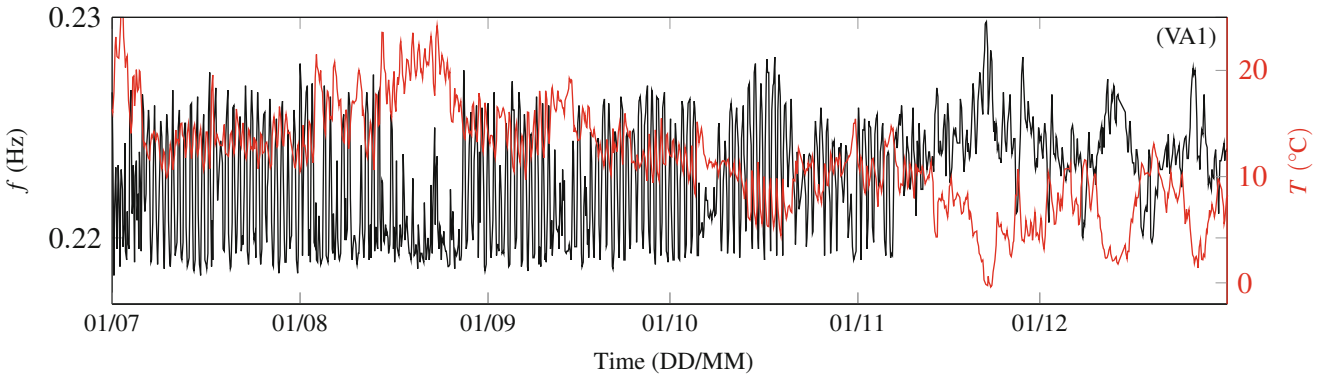


**Fig. 12.4** Evolution of the temperature and the frequency of the mode VA1 from July 2015 to December 2015

As expected, the damping ratios for HS1, HS2, HA2, VS1, VA1 and TA1 fluctuate little with the temperature. For a given temperature, multiple wind velocities are recorded. Because the total modal damping ratios increase with the wind velocity, due to added aerodynamic damping, a large variety of total modal damping ratios are recorded for a given temperature. Consequently, a large dispersion is expected when the modal damping ratios are expressed as a function of the temperature alone. On Fig. 12.5, VS1 and VA1 have an averaged modal damping ratios of about 0.75% and 1% respectively and are characterized by a considerable spreading. This is not surprising given that the modal damping ratios associated with VS1 and VA1 are highly affected by the wind induced aerodynamic damping effect [4].

A reduction in modal damping with increasing temperatures and the underlying reduction in wind speed is generally expected. This is in particular the case for the vertical modes for which the aerodynamic damping can be relatively high. The highest damping values are still observed for temperatures between 5 °C and 10 °C at which the strongest winds occur.

The decrease in the damping ratios of TS1 for increasing temperatures is somewhat more distinct. As already pointed out, lower temperatures are typically associated with higher wind speeds, for which a weakly increasing TS1 damping ratio has been observed [4]. It is however a bit surprising that the corresponding contribution of the aerodynamic damping, which is much stronger for the vertical modes, is not so obvious in the average damping estimates presented. To improve the reliability of these results, an analysis using at least 1 year of temperature, velocity and acceleration data is required.

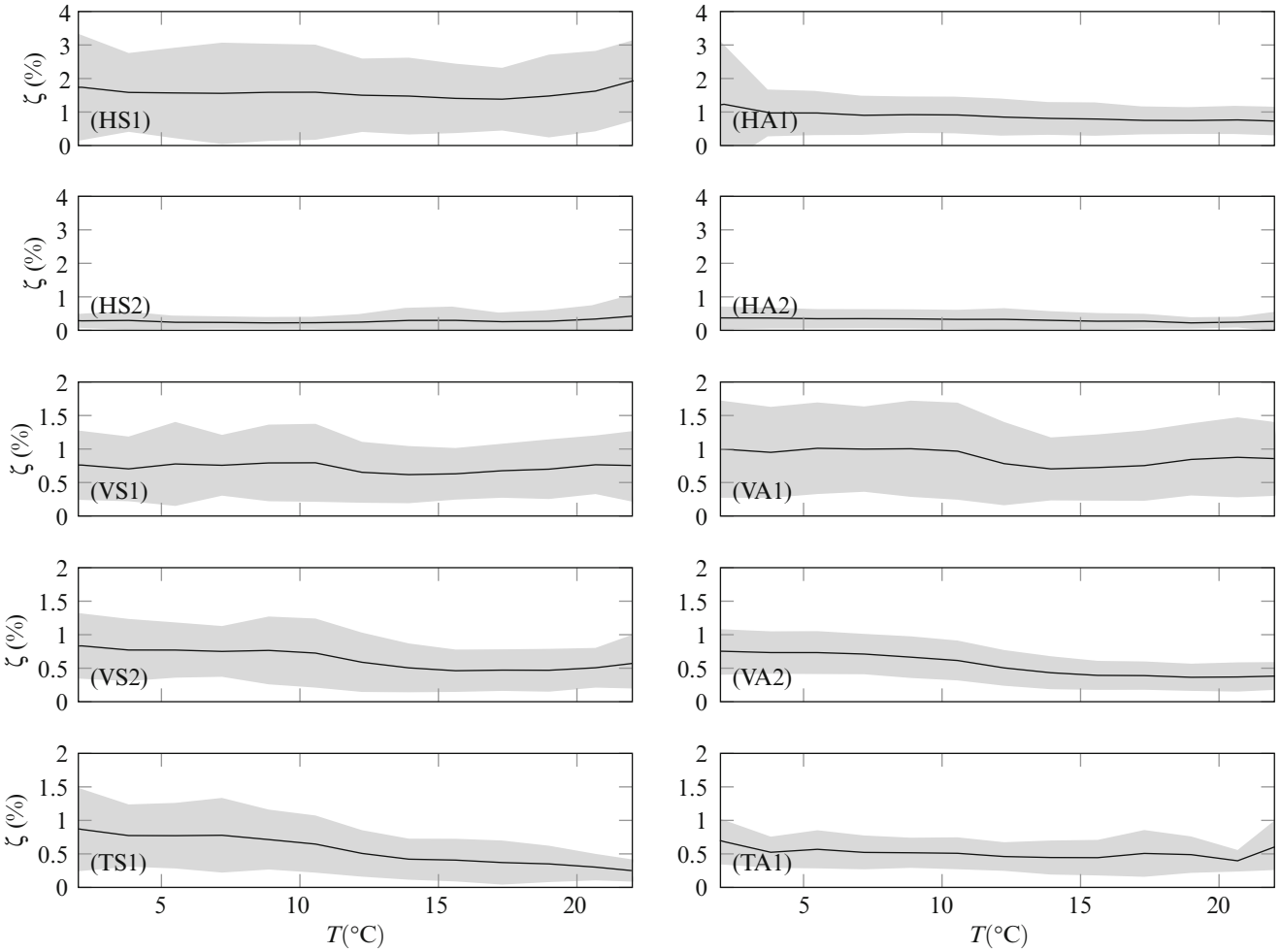


**Fig. 12.5** Modal damping ratios expressed as a function of the temperature for the first four lateral and vertical modes and the first two torsional modes, based on acceleration data recorded from July 2015 to December 2015

## 12.4 Conclusions

The modal parameters of the Lysefjord bridge have been identified using AVT based on an automated SSI-COV procedure relying on several months of continuous acceleration records. Environmental effects were observed with a level of details that is scarcely available in the literature. In particular, the daily fluctuations of the eigen-frequencies were remarkably well captured as was the possible temperature-dependency of the modal damping ratios. A relatively large amount of acceleration data was accumulated, so that a statistical description of the influence of the mean wind velocity on the modal damping ratios could be achieved. The application of OMA using the automated SSI-COV method on other suspension bridges may provide a better general understanding of environmental influence on the modal parameters of such structures.

The good agreement between the computed natural frequencies and the measured ones is encouraging for further investigation of full-scale measurement data using the automated SSI-COV method. The modal analysis also documented the non-linearity of the modal damping ratios and a possible non-negligible role of temperature effects on the modal parameters of the bridge. Further analysis will consider at least 1 year of full-scale measurements, and a more severe segregation of wind samples characterized by unusually high turbulence intensity indicating non-stationary fluctuations in excitation and response.

**Acknowledgment** The authors are grateful to the Norwegian Public Road Administration for the support of and the assistance during the measurement campaign at the Lysefjord Bridge.

## References


1. Allemang, R.J., Brown, D.L.: A correlation coefficient for modal vector analysis. In: Proceedings of the 1st International Modal Analysis Conference, SEM, Orlando, vol. 1, pp. 110–116 (1982)
2. Brownjohn, J.M.W., Dumanoglu, A.A., Severn, R.T., Taylor, C.A.: Ambient vibration measurements of the Humber Suspension Bridge and comparison with calculated characteristics. Proc. Inst. Civil Eng. **83**(3), 561–600 (1987)
3. Brownjohn, J.M.W., Magalhaes, F., Caetano, E., Cunha, A.: Ambient vibration re-testing and operational modal analysis of the Humber Bridge. Eng. Struct. **32**(8), 2003–2018 (2010). doi:10.1016/ j.engstruct. 2010.02.034
4. Cheynet, E., Bogunovic' Jakobsen, J., Snæbjörnsson, J.: Buffeting response of a suspension bridge in complex terrain. Eng. Struct. **128**, 474–487 (2016). doi:10.1016/ j.engstruct.2016.09.060
5. de Battista, N., Brownjohn, J.M.W., Pink Tan, H., Koo, K.-Y.: Measuring and modelling the thermal performance of the Tamar Suspension Bridge using a wireless sensor network. Struct. Infrastruct. Eng. **11**(2), 176–193 (2015). doi:10.1080/ 15732479.2013.862727
6. Ding, Y., Li, A.: Temperature-induced variations of measured modal frequencies of steel box girder for a long-span suspension bridge. Int. J. Steel Struct. **11**(2), 145–155 (2011). doi:10.1007/ s13296- 01120044
7. Kim, C.-Y., Jung, D.-S., Kim, N.-S., Kwon, S.-D., Feng, M.Q.: Effect of vehicle weight on natural frequencies of bridges measured from traffic-induced vibration. Earthquake Eng. Eng. Vib. **2**(1), 109–115 (2003). doi:10.1007/ BF02857543
8. Koo, K.Y., Brownjohn, J.M.W., List, D.I., Cole, R.: Structural health monitoring of the Tamar suspension bridge. Struct. Control Health Monit. **20**(4), 609–625 (2013)
9. Macdonald, J.H.G.: Evaluation of buffeting predictions of a cable-stayed bridge from full-scale measurements. J. Wind Eng. Ind. Aerodyn. **91**(12–15), 1465–1483 (2003). doi:10.1016/ j.jweia.2003.09.009. ISSN:0167-6105
10. Magalhães, F., Cunha, À.: Explaining operational modal analysis with data from an arch bridge. Mech. Syst. Signal Process. **25**(5), 1431–1450 (2011). doi:10.1016/ j.ymssp.2010.08.001. ISSN: 0888-3270
11. Magalhães, F., Cunha, À., Caetano, E.: Online automatic identification of the modal parameters of a long span arch bridge. Mech. Syst. Signal Process. **23**(2), 316–329 (2009). doi:10.1016/ j.ymssp.2008.05.003. ISSN: 0888-3270
12. Sigbjörnsson, R., Hjorth-Hansen, E.: Along-wind response of suspension bridges with special reference to stiffening by horizontal cables. Eng. Struct. **3**(1), 27–37 (1981)
13. Siringoringo, D.M., Fujino, Y.: System identification of suspension bridge from ambient vibration response. Eng. Struct. **30**(2), 462–477 (2008). doi:10.1016/ j.ymssp.2008.05.003
14. Sohn, H., Dzwonczyk, M., Straser, E.G., Kiremidjian, A.S., Law, K.H., Meng, T.: An experimental study of temperature effect on modal parameters of the Alamosa Canyon Bridge. Earthquake Eng. Struct. Dyn. **28**(8), 879–897 (1999). ISSN: 1096-9845
15. Steigen, R.O.: Modeling and analyzing a suspension bridge in light of deterioration of the main cable wires. MA thesis. University of Stavanger (2011)
16. Strømmen, E.N.: Eigenvalue calculations of continuous systems. In: Structural Dynamics, pp. 89–159. Springer International Publishing, Cham (2014). doi: 10.1007/ 9783319018027_3. ISBN: 978-3-319-01802-7
17. Tveiten, J.: Dynamic analysis of a suspension bridge. MA thesis. University of Stavanger (2012)
18. Westgate, R., Koo, K.-Y., Brownjohn, J.: Effect of solar radiation on suspension bridge performance. J. Bridge Eng. **20**(5), 04014077 (2014). doi:10.1061/ (ASCE)BE.19435592.0000668
19. Xia, Y., Chen, B., Weng, S., Ni, Y.Q., Xu, Y.L.: Temperature effect on vibration properties of civil structures: a literature review and case studies. J. Civ. Struct. Health Monit. **2**(1), 29–46 (2012). doi:10.1007/ s13349- 01100157
20. Xia, Y., Chen, B., Zhou, X.Q., Xu, Y.L.: Field monitoring and numerical analysis of Tsing Ma Suspension Bridge temperature behavior. Struct. Control Health Monit. **20**(4), 560–575 (2013). doi:10.1002/ stc.515
21. Xu, Y.L., Chen, B., Ng, C.L., Wong, K.Y., Chan, W.Y.: Monitoring temperature effect on a long suspension bridge. Struct. Control Health Monit. **17**(6), 632–653 (2010). doi:10.1002/ stc.340
22. Zhou, L., Xia, Y., Brownjohn, J.M.W., Young Koo, K.: Temperature analysis of a long-span suspension bridge based on field monitoring and numerical simulation. J. Bridge Eng. **21**(1), 04015027 (2016). doi:10.1061/ (ASCE)BE.19435592.0000786

# Chapter 13
# Mass Scaling of Mode Shapes Based on the Effect of Traffic on Bridges: A Numerical Study

**M. Sheibani, A.H. Hadjian-Shahri, and A.K. Ghorbani-Tanha**

**Abstract** In order to derive mass normalized mode shapes from Operational Modal Analysis (OMA) techniques, additional experiments have to be conducted in the interest of scaling the determined mode shapes. Various investigations have been carried out based on the deterministic perturbed mass matrix, also known as the mass change method. However, the conventional form of this method requires a number of rather costly and sometimes impractical experiments on the structure. In this article, it is intended to use traffic as a stochastic source of mass change to calculate mass scaling factors. Adequate traffic stream on bridges can affect the Eigen properties of the structure efficiently. The vehicles on the bridge are only considered to affect the mass properties, and vehicle-bridge interaction is neglected. A simplified structural model of a bridge is considered and the traffic is modeled as lognormal distribution. Nodal masses induced by the vehicles are converted to time histories to avoid difficulties based on the moving mass problem. Consequently, a method is proposed to produce the modified mass matrix which can be used in the scaling factor equations. Finally, scaling factors of mode shapes are proposed by comparing the unperturbed structure and the perturbed mass matrix structure.

**Keywords** Mass change strategy • Mode shape scaling • Traffic induced • Lognormal distribution • Modified mass matrix

## 13.1 Introduction

Operational Modal Analysis (OMA) techniques have been widely used during the recent decades and have nearly made Experimental Modal Analysis (EMA) obsolete. The advantages of OMA, such as elimination of the need for heavy shakers and the ability to perform tests without interruption of normal structure service, have made this method a reliable substitution for the EMA technique. However, certain drawbacks exist in every approach of OMA. As these methods consider the input force to be the unknown ambient noise, there is not a direct method available to normalize the extracted mode shapes and additional steps need to be taken [1]. Mass scaled modes are essential in numerous applications of modal analysis such as structural response simulation, damage detection, health monitoring applications, model updating, etc. [2, 3]. Several methods have been proposed to overcome this issue and they all share the notion that a controlled perturbation to the dynamics of the structure is the key element in obtaining scale factors of the mode shapes. The most promising methods have been found to be mass change techniques, in which known masses are added to the structure and the tests are performed before and after the addition of masses. The scale factors, consequently, can then be calculated by comparing the results.

Parloo et al. proposed a sensitivity based method for obtaining scale factors of each mode shape. Mass change method was first introduced and validated by comparing the scale factors derived from forced vibration test, with those from repeated in-operation test considering different locations of the added mass [4]. Parloo et al. further evaluated the normalization method by employing it in a full-scale bridge test. Heavy concrete blocks were added to specific locations of the bridge in order to provide sufficient frequency shifts that are desired for the mass change method [5]. Brinker and Andersen further studied the method and derived a formula based on the equation of motion to estimate the scale factors [6]. Other studies investigated the best mass change setups and sources of error [2, 7]. Aenlle et al. offered optimized strategies regarding the method and studied the best mass ratios, optimized locations and uncertainties relating the method. It was shown that the best mass change scenarios were those which induced uniform mass changes to the entire structure and consequently prevented alteration of the mode shapes. Furthermore, the ratios of added masses to the entire structure were recommended to be high

M. Sheibani (✉) • A.H. Hadjian-Shahri • A.K. Ghorbani-Tanha
School of Civil Engineering, College of Engineering, University of Tehran, P.O. Box: 11155-4563, Tehran, Iran
e-mail: mr.sheibani@ut.ac.ir



J. Caicedo, S. Pakzad (eds.), *Dynamics of Civil Structures, Volume 2*, Conference Proceedings
of the Society for Experimental Mechanics Series, DOI 10.1007/978-3-319-54777-0_13

enough to produce frequency shifts desired for the method, and low enough to avoid significant changes of mode shapes [8]. Mass-stiffness change method was also proposed to change the first modes of vibration more significantly [9].

The growing accuracy of modal analysis testing equipment and precise methods which have made obtaining the modal parameters possible, as well as the difficulties associated with placing heavy masses on the structure when using the conventional mass change methods, has revealed the need for more convenient and efficient methods. In this article a new method is proposed to exploit the traffic load as the required change in the mass of the structures. The heavy traffic jams or congested traffic situations observed in big cities has appealing characteristics which makes it useful for utilization in the mass change method. Vehicle traffic induces a sufficiently uniform load on the bridges in the case of congested traffic and this condition can be assumed almost time independent for the required time period concerning OMA. Equally distributed mass change strategy is suggested to be the optimum approach in the literature and is provided by the traffic load. On the other hand, there are various urban bridges which are constructed using light-weight materials that promise sufficient frequency shifts desired for the mass change method provided by the traffic stream. Near-congestion traffic has been shown to be best represented by shifted lognormal distribution [10, 11].

To demonstrate, a bridge-like structure is simulated by a finite-element model of a simply-supported Euler-Bernoulli beam. The beam model has been subjected to artificial traffic generated from lognormal distribution and the proposed method has been evaluated. Mass change is applied to the mass matrix of the beam in each time-step to represent the actual case of traffic, and responses of the structure has been determined by the Newmark method. The car-bridge interaction is ignored since vehicles in congested traffic conditions have negligible dynamic interactions with bridges, and therefore a decoupled bridge-vehicle system is considered [12]. The response-only analysis method that is used in this study is the Natural Excitation Technique-Eigensystem Realization Algorithm (NExT-ERA) which has shown promising results [13] and can be exploited for repetitive tests needed in this study. Unscaled mode shapes are derived from response-only modal analysis and the corresponding scale factors are calculated based on the traffic induced mass modification. These scale factors are then compared with the scale factors obtained from finite-element model.

## 13.2 Theory

### *13.2.1 Output-Only Modal Identification*

The method which is used for modal analysis purposes is NExT-ERA. The prevailing assumptions made in this method are that the structure behaves within a linear range, the structure is time-invariant, and the forces applied to the system are uncorrelated to the response of the structure [15]. In this method, response of the structure based on ambient excitation is used for estimating the cross-correlation functions. These functions can represent the impulse response functions of the structure which are used in classical modal analysis. The direct procedure for obtaining the cross-correlation functions between two channels of acceleration $i$ and $j$ is used to this end. In discrete time approach, the correlation function (CF) matrix can be estimated using the formula [14]

$$R_{\ddot{y}_i,\ddot{y}_j}(k\Delta t) = \frac{1}{N-k}\sum_{s=1}^{S-k}\ddot{y}_i(s)\ddot{y}_j(s+k) \tag{13.1}$$

In which $S$ is the total number of data points of the acceleration record and $\Delta t$ is the time step.

The ERA method is based on the state-space representation of a discrete system. The procedure to obtaining modal parameters from ERA method starts with formation of the Hankel matrix using correlation functions which are calculated by Eq. (13.1). Singular value decomposition (SVD) is then performed and modal parameters are derived with the help of specific equations and guidelines which are described in [15, 16].

### *13.2.2 Mass Scaling*

In order to obtain mass normalized mode shapes from OMA techniques, additional steps are required. The unscaled mode shape vector $\boldsymbol{\psi}_i$ have to be scaled in the interest of modal analysis applications mentioned in the introduction. The scaled mode shapes can be obtained from unscaled modes using the following equation [8]

$$\boldsymbol{\varphi}_i = \alpha_i . \boldsymbol{\psi}_i \tag{13.2}$$

where $\alpha_i$ is the scaling factor of mode shape $i$. The proposed methods existing in the literature for determining the scaling factors, are based on the eigenvalue changes of the structure before and after the addition of the masses. The eigenvalue problem of equation of motion in the absence of damping is

$$\mathbf{m}.\boldsymbol{\varphi}_0.\omega_0^2 = \mathbf{k}.\boldsymbol{\varphi}_0 \tag{13.3}$$

where $\mathbf{m}$ and $\mathbf{k}$ are mass and stiffness matrices of the structure, respectively, $\varphi_0$ is the mass normalized mode shape and $\omega_0$ is the natural frequency. Added masses are often considered lumped masses for simplification purposes and thus the mass change matrix $\Delta\mathbf{m}$ becomes in general diagonal. The eigenvalue problem of equation of motion in the presence of additional masses is in the following form

$$(\mathbf{m} + \Delta\mathbf{m}) . \boldsymbol{\varphi}_1 . \omega_1^2 = \mathbf{k}.\boldsymbol{\varphi}_1 \tag{13.4}$$

in which $\varphi_1$ and $\omega_1$ are modal parameters of the modified structure. It has been shown that the scaling factors of unscaled mode shapes can be derived from the following equation [8]

$$\alpha = \sqrt{\frac{\left(\omega_0^2 - \omega_1^2\right)}{\omega_1^2 . \boldsymbol{\psi}^T . \Delta\mathbf{m} . \boldsymbol{\psi}}} \tag{13.5}$$

However, according to [3], if a full set of modes is used, the exact scale factors can be derived from the following equation and this equation is fulfilled for each value of $i$

$$\alpha_j = \sqrt{\frac{\left(\omega_{0j}^2 - \omega_{1i}^2\right) . B_{ji}}{\boldsymbol{\psi}_{0j}{}^T . \left(\omega_{1i}^2 . \Delta\mathbf{m}\right) . \boldsymbol{\psi}_{1i}}} \tag{13.6}$$

in which matrix $\mathbf{B}$ can be produced by the equation

$$\widehat{\mathbf{B}} = \widehat{\boldsymbol{\psi}}_0^{-1} . \boldsymbol{\psi}_1 \tag{13.7}$$

where $\widehat{\boldsymbol{\psi}}_0^{-1}$ is the pseudo-inverse of $\boldsymbol{\psi}_0$.

### 13.2.3 Modeling the Traffic Excitation

Traffic load is shared between nodes of the system using a physics-based traffic excitation model. In this method, every vehicle induces a moving load when it is traversing the bridge and this load can be assumed to affect each node of the structure with a time history load [17].

Concentrated and constant vehicle forces are represented by $P$ during vehicle movement over the bridge. The governing equation of motion for vertical deflection of the bridge is

$$\overline{m}\frac{\partial^2}{\partial t^2} y_b(x,t) + \overline{c}\frac{\partial}{\partial t} y_b(x,t) + \overline{EI}\frac{\partial^4}{\partial x^4} y_b(x,t) = -\delta(x - vt) P \tag{13.8}$$

in which, $\overline{m}$, $\overline{c}$, $\overline{E}$ and $\overline{I}$ are the mass per unit length, the damping coefficient, the Young's modulus and the cross-sectional moment of inertia of the beam, respectively, and $v$ is the velocity of the vehicle while $y_b$ is the vertical deflection of the bridge from the equilibrium position. Horizontal position of the forces is shown by $x$ as illustrated in Fig. 13.1. Considering the forces induced by multiple vehicles on the bridge as a summation and assuming a lognormal distribution for the headways of the successive arrivals of the vehicles, one can replace the right hand side of Eq. (13.8) by


**Fig. 13.1** Model of moving load on the bridge [18]

$$F_x(t) = -\sum_{i=1}^{N(t)} P_i \delta\left[x - v\left(t - \tau_i\right)\right] \tag{13.9}$$

where $F_x(t)$ is the time history of traffic excitation at location $x$ on the bridge, $N(t)$ is the number of vehicles on the bridge at the time $t$, and $\tau_1, \tau_2, \ldots \tau_i, \ldots \tau_N$ are the sequence of headway times. The shifted lognormal distribution is used to model headway times in various studies and in this study is used to generate headway times of the artificial traffic [10]. The probability distribution equation is

$$f\left(t|\beta,\mu,\sigma\right) = \frac{1}{\sigma\left(t-\beta\right)\sqrt{2\pi}} \times \exp\left(-\frac{\left(\ln\left(t-\beta\right)-\mu\right)^2}{2\sigma^2}\right); t > \tau \tag{13.10}$$

in which $t$ is the time headway, $\beta$ is the shift value in seconds, and $\mu$ and $\sigma$ are parameters of lognormal distribution; location and scale parameter, respectively.

Dynamic nodal loading (DNL) is used to convert time-varying moving forces into load histories at each node of the Finite Element Method (FEM) model based on the equivalent nodal forces (ENFs) method [18]. The bridge is modeled by beam elements and each node of the beam has two degrees of freedom; $y_i$, the transvers displacement and $\theta_i$, the in-plane rotation. The vertical force $P$ is then applied to nodes of the structure as nodal shear $W_i^Q$ and nodal moment $W_i^M$ using the following equations

$$W_i^Q(t) = \begin{cases} 0 & \left(t \le \frac{x_i - l_{i-1}}{v}\right) \\ \frac{\left(l_{i-1} - x_i + vt\right)^2}{l_{i-1}^2}\left[1 + \frac{2\left(x_i - vt\right)}{l_{i-1}}\right] & \left(\frac{x_i - l_{i-1}}{v} < t \le \frac{x_i}{v}\right) \\ \frac{\left(l_i + x_i - vt\right)^2}{l_i^2}\left[1 + \frac{2\left(vt - x_i\right)}{l_i}\right] & \left(\frac{x_i}{v} < t \le \frac{x_i + l_i}{v}\right) \\ 0 & \left(\frac{x_i + l_i}{v} < t\right) \end{cases} \tag{13.11}$$

$$W_i^M(t) = \begin{cases} 0 & \left(t \le \frac{x_i - l_{i-1}}{v}\right) \\ -\frac{\left(l_{i-1} - x_i + vt\right)^2}{l_{i-1}^2}\left(x_i - vt\right) & \left(\frac{x_i - l_{i-1}}{v} < t \le \frac{x_i}{v}\right) \\ \frac{\left(l_i + x_i - vt\right)^2}{l_i^2}\left(vt - x_i\right) & \left(\frac{x_i}{v} < t \le \frac{x_i + l_i}{v}\right) \\ 0 & \left(\frac{x_i + l_i}{v} < t\right) \end{cases} \tag{13.12}$$

in which $v$, $l_i$ and $l_{i\text{-}1}$ are illustrated in Fig. 13.2, and $x_i$ is the coordinate of node $i$. Therefore, the equivalent forces at node $i$ are presented by

$$F_i^Q(t) = -\sum_{j=1}^{N(t)} P_j W_i^Q\left(t - \tau_j\right) \tag{13.13}$$

$$F_i^M(t) = -\sum_{j=1}^{N(t)} P_j W_i^M\left(t - \tau_j\right) \tag{13.14}$$

These forces are then used to simulate the traffic excitation for each node.

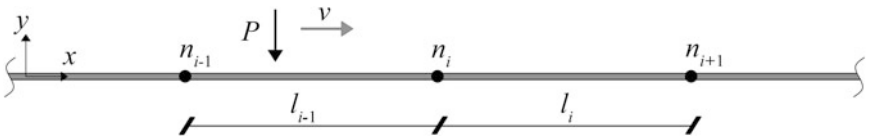


**Fig. 13.2** FEM model of the bridge [18]

### *13.2.4 Estimation of the Mass loading of Traffic*

In this article, the mass loading of traffic on the bridge is considered as the perturbation to the mass matrix of the structure, instead of additional lumped masses. The OMA techniques assume that the dynamic response of the structure is stationary in the testing period. Similarly, the effect of mass loading of traffic stream on the bridge in case of stationary traffic and sufficiently long observation periods, can also be assumed stationary. Accordingly, one can assume the average mass loading of the traffic to affect the structure with a uniform distribution during the test period. For that reason, expected value of the induced mass loading of traffic has been calculated for each node during the period of each test, and is used as the mass change needed in the Eqs. (13.5, 13.6). The expected value of the mass loading of traffic is related to several parameters such as traffic headway distribution, vehicle masses and velocities, driving behavior, etc. Nevertheless, different headway distributions and vehicle velocities have been studied in this article and other factors are neglected for simplicity of the method.

In order to apply the mass changes due to traffic stream, shear values which are calculated for vehicle loads from Eq. (13.13) are transformed to mass quantities using Eq. (13.15) and moment values are assumed to have insignificant effect on the mass of the structure.

$$M_i(t) = F_i^Q(t)/\mathrm{g} \tag{13.15}$$

where $M_i$ $(t)$ is the nodal mass of traffic in time $t$ and g is the acceleration of gravity. The aim of this study is to propose a method to produce the $\Delta\mathbf{m}$ matrix used in scaling factor Eqs. (13.5, 13.6) based on traffic characteristics. Accordingly, a reasonable range of traffic conditions which is virtually the case of congested traffic situations reported in [10] has been considered and artificial traffic is generated using Eq. (13.10). The following conditions has been considered

$$\mu_p = 1.35 + \frac{p}{20} \quad p = 1, 2, \ldots, 20 \tag{13.16}$$

$$v_q = 12 + \frac{q}{10}\,(\mathrm{km/h}) \quad q = 1, 2, \ldots, 100 \tag{13.17}$$

Shift value $\beta$ is considered to be 0.12 s and $\sigma$ is assumed to be 0.9. Expected value of the time history of nodal masses which were mentioned earlier are then calculated for each traffic condition using the equation

$$\Delta m_{i,\mu,v} = \mathrm{E}\left[M_{i,\mu,v}(t)\right] \tag{13.18}$$

However, since the velocity of the vehicles are constant during each simulation and the testing period has been considered long enough, we can assume that

$$\Delta m_{i,\mu,v} \simeq \Delta m_{j,\mu,v} \simeq \Delta m_{\mu,v} \tag{13.19}$$

These values are normalized with respect to the total mass of the structure and a quadratic surface is fitted through them, as can be seen in Fig. 13.3. The governing polynomial is determined by Eq. (13.20) and the corresponding coefficients are presented in Table 13.1.

$$\Delta m_{\mu,v} = h(\mu, v) = a + b \times v + c \times \mu + d \times v^2 + e \times v \times \mu + f \times \mu^2 \tag{13.20}$$

In order to use values generated from Eq. (13.20) in the scaling factor formulas, the $\Delta\mathbf{m}$ matrix has to be constructed. However, due to the assumption that the average traffic mass loading is applied uniformly to the structure and it is converted to

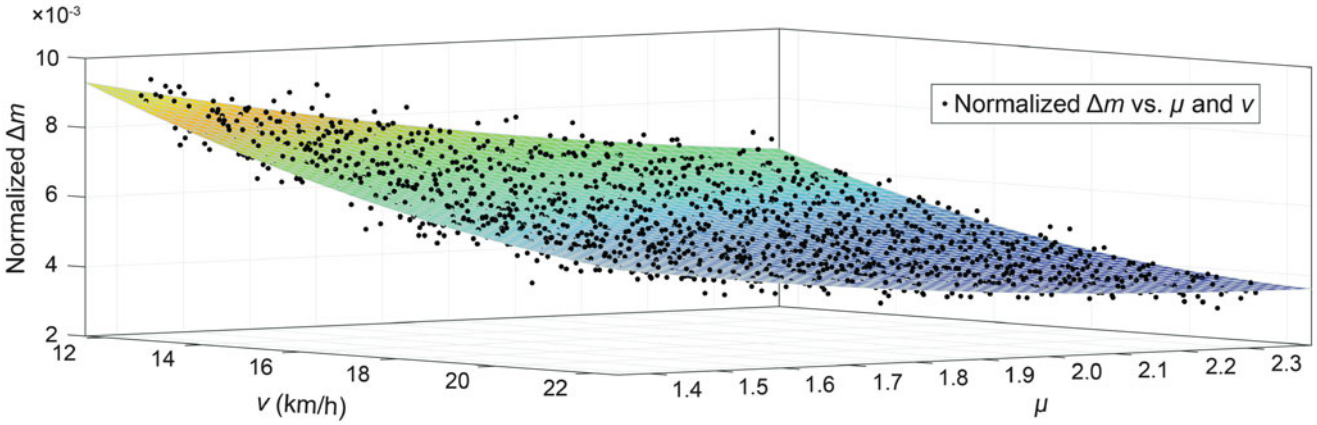


**Fig. 13.3** Surface fitted based on the $\mu$ and $v$ values

**Table 13.1** Polynomial coefficients

| $a$ | $b$ | $c$ | $d$ | $e$ | $f$ |
|---|---|---|---|---|---|
| 0.02853 | −0.001208 | −0.008903 | 1.919e−5 | 1.202e−4 | 1.294e−3 |

lumped masses assigned to each node, the estimated matrix $\Delta\widehat{\mathbf{m}}$ will be diagonal and can be constructed using the following equation for each traffic situation.

$$\Delta\widehat{\mathbf{m}}_{\mu,v} = h\,(\mu, v) \times \overline{m}L \times \mathbf{I} \tag{13.21}$$

in which $\mathbf{I}$ is identity matrix and $L$ is the length of the entire beam.

## 13.3 Numerical Case Study

A simply supported Euler-Bernoulli beam has been considered in order to simulate the bridge structure. The beam is consisted of 8 identical elements and each node has 2 degrees of freedom; transverse displacement and in-plane rotation. The mass matrix is assembled using consistent-mass matrices for each element, the stiffness matrix is assembled using cubic shape functions, and damping is neglected. The beam has one traffic lane and the vehicle velocities are the same during each simulation. Furthermore, each vehicle is assumed to impose a concentrated load on the beam and vehicle masses are the same and are assumed to be equal to 2% of the bridge mass. Natural frequencies of the FEM model are presented in Table 13.2.

Two different conditions of the traffic has been considered. First, a free flow of the traffic is considered which has minor effects on the mass of the structure and can be assumed as the unmodified structure in the classical methods, and second, congested traffic situation is used which has significant effects on the mass properties and can be assumed as the modified structure [19]. Time period is 300 s for each simulation in which the traffic stream can be assumed stationary [10] and 0.001 s is taken as time step. Vehicle loads are then shared between successive nodes using Eqs. (13.11, 13.12) for each time step. A sample time history of excitation is depicted in Fig. 13.4 for one node of the structure

The mass loading of the vehicles are applied to the global mass matrix of the finite element model in each time step. Since these quantities are shared between nodes and can be assumed to be lumped masses, they can be added to diagonal elements of the mass matrix that correspond with transvers degrees of freedom, i.e. the odd columns and rows of the mass matrix. The time-variant mass matrix will then be in the following form

**Table 13.2** FEM model natural frequencies

| Mode no. | 1 | 2 | 3 |
|---|---|---|---|
| Natural frequency $\omega_0$—(rad/s) | 12.8 | 51.4 | 115.8 |

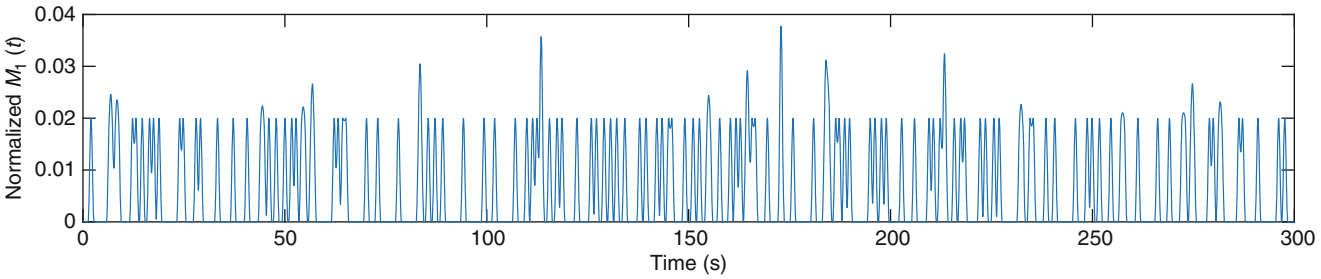


**Fig. 13.4** Time history of traffic assigned to node 1 under specific traffic conditions: $\mu = 1.85$, $\sigma = 0.9$, $v = 15$ (km/h)

**Table 13.3** Traffic characterestics

| Case no. | Front headway | | Velocity—$v$ (km/h) |
|---|---|---|---|
| | $\mu$ | $\sigma$ | |
| 1 | 1.97 | 0.9 | 15.1 |
| 2 | 1.94 | 0.94 | 15.9 |
| 3 | 1.69 | 0.96 | 21.2 |
| 4 | 1.55 | 0.87 | 23.2 |

$$\mathbf{m}(t) = \begin{bmatrix} m_{11} + M_1(t) & & \cdots & & m_{1,2n} \\ & m_{22} & & & \\ \vdots & & \ddots & & \\ & & & m_{2i-1,2i-1} + M_i(t) & \\ & & & & \ddots \\ m_{2n,1} & & & & m_{2n,2n} \end{bmatrix} \tag{13.22}$$

where $n$ is number of nodes. It should be noted that since the traffic excitation is stationary and time period is long enough, there are no concerns regarding the use of time-variant mass matrix in the modal analysis techniques.

In order to evaluate the validity of the proposed method for estimating mass changes, four near congestion real traffic scenarios for front headway of passenger cars are acquired from [10] and are tested using the method. The details of the traffic conditions are presented in Table 13.3.

Therefore, in the interest of imposing artificial traffic excitation, lognormal distribution parameters presented in Table 13.3 are considered and headway times between vehicles are generated using the lognormal distribution from Eq. (13.10). Response of the structure is then determined by Newmark method. Shears forces and moments which are determined using Eqs. (13.13, 13.14) are used as input for the system with the addition of Gaussian white noise. The sensors are assumed to be located on all of the nodes, and acceleration of each node is recorded during the time period for each simulation, and then low-pass filtered to have the signal in the frequency range of the desired mode shapes. Fast Fourier Transform (FFT) method is used for filtering to avoid phase and amplitude errors [14]. Correlation function matrix of the acceleration response is then constructed using Eq. (13.1) and is then used in the NExT-ERA process for output-only modal identification of the structure.

The mass change matrix is created using Eq. (13.21) for each traffic condition and is subsequently used in the scaling factor equations. Equation (13.6) is used to obtain scale factors and the modal parameters extracted from the free flow condition and the values extracted from the mentioned congested traffic conditions are used as inputs for this equation. A hundred simulations are performed for each traffic setup and the calculated scale factors are normalized to the exact scale factors obtained from FEM model which are shown for the first three modes of vibration in Figs. 13.5, 13.6, 13.7 and 13.8:

The mean value and standard deviation regarding each case for the first three modes are calculated. Mean values of normalized scale factors and Coefficients of Variations (CV), along with average frequency shifts are presented in Table 13.4. The results show that values of CVs are lower than 5% for all cases of traffic situations and frequency shift is 2% for each case identically. However, there is an inclination in mean values which indicate that mass changes produced by Eq. (13.21) are slightly overestimated.

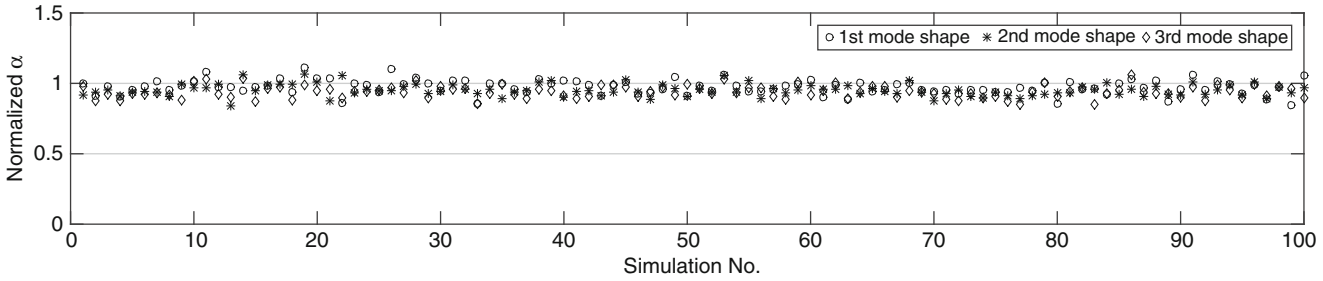


**Fig. 13.5** Normalized scale factors—Traffic case 1

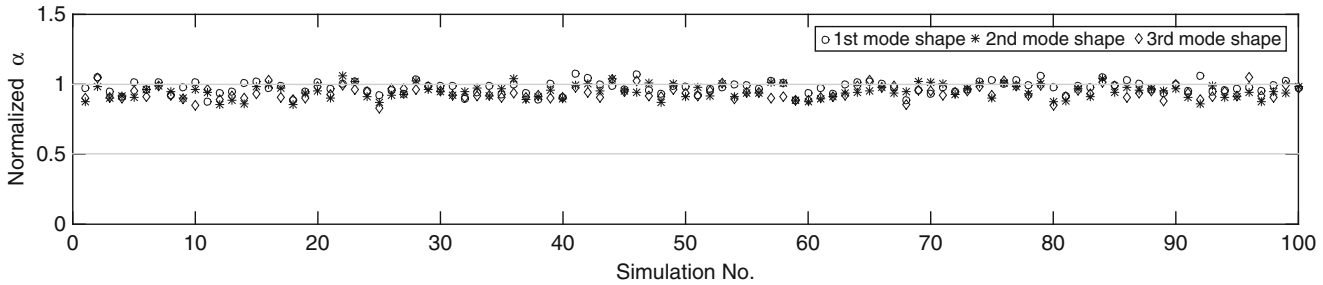


**Fig. 13.6** Normalized scale factors—Traffic case 2

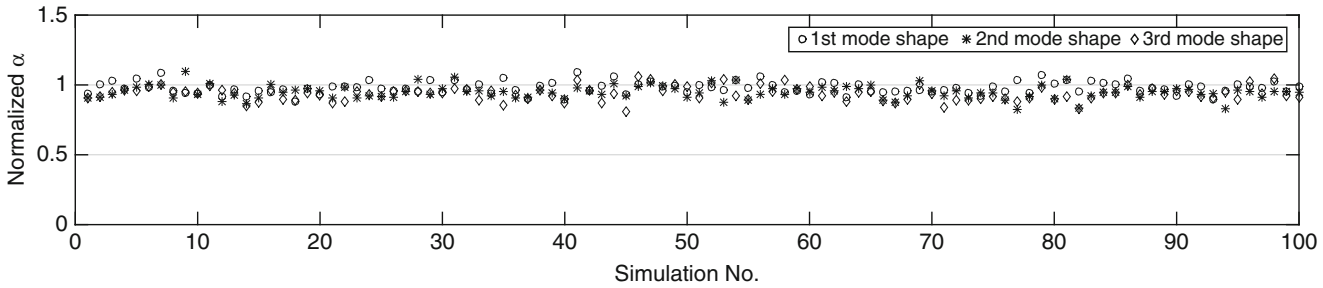


**Fig. 13.7** Normalized scale factors—Traffic case 3

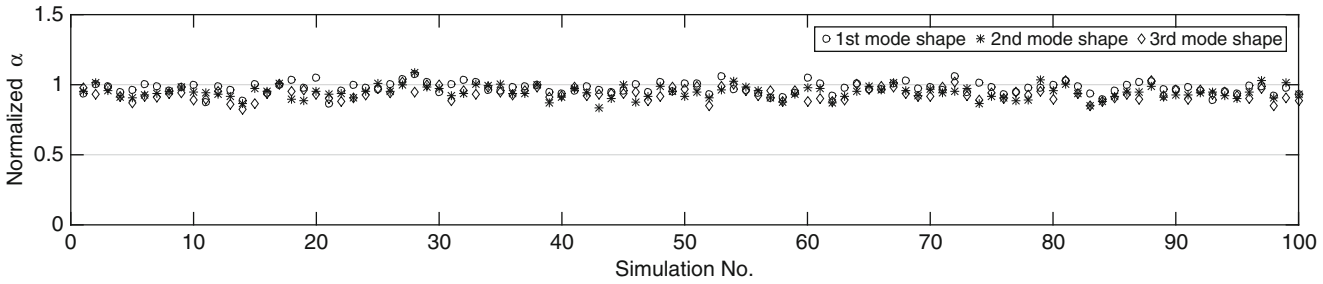


**Fig. 13.8** Normalized scale factors—Traffic case 4

The unscaled mode shapes which are extracted from the free flow traffic condition, the scaled modes using scale factors obtained by the proposed method, and the exact modes calculated using FEM model are shown in Fig. 13.9 for the first three modes of the first traffic case for one random simulation. It should be noted that in order to compare mode shapes extracted from modal tests and the FEM extracted mode shapes, the size of mass and stiffness matrices are reduced using the Guyan reduction technique [20].

The scaled mode shapes extracted from OMA and the corresponding modes calculated by FEM model are also compared using Modal Assurance Criterion (MAC). Figure 13.10 shows the complete correlation of these two conditions.

**Table 13.4** Statistical parameters of scale factors regarding each traffic case

| Case no. | Mode shape no. | Mean value of frequency $\omega_1$ (rad/s) | Mean frequency shift (%) | Mean value of normalized $\alpha$ | Coefficient of variation (CV) |
|---|---|---|---|---|---|
| Case 1 | 1 | 12.57 | 2 | 0.974 | 0.052 |
| | 2 | 50.35 | 2 | 0.951 | 0.044 |
| | 3 | 113.38 | 2 | 0.939 | 0.047 |
| Case 2 | 1 | 12.57 | 2 | 0.977 | 0.044 |
| | 2 | 50.36 | 2 | 0.947 | 0.051 |
| | 3 | 113.37 | 2 | 0.940 | 0.047 |
| Case 3 | 1 | 12.57 | 2 | 0.979 | 0.043 |
| | 2 | 50.36 | 2 | 0.948 | 0.049 |
| | 3 | 113.38 | 2 | 0.937 | 0.052 |
| Case 4 | 1 | 12.57 | 2 | 0.976 | 0.041 |
| | 2 | 50.37 | 2 | 0.945 | 0.047 |
| | 3 | 113.40 | 2 | 0.935 | 0.046 |

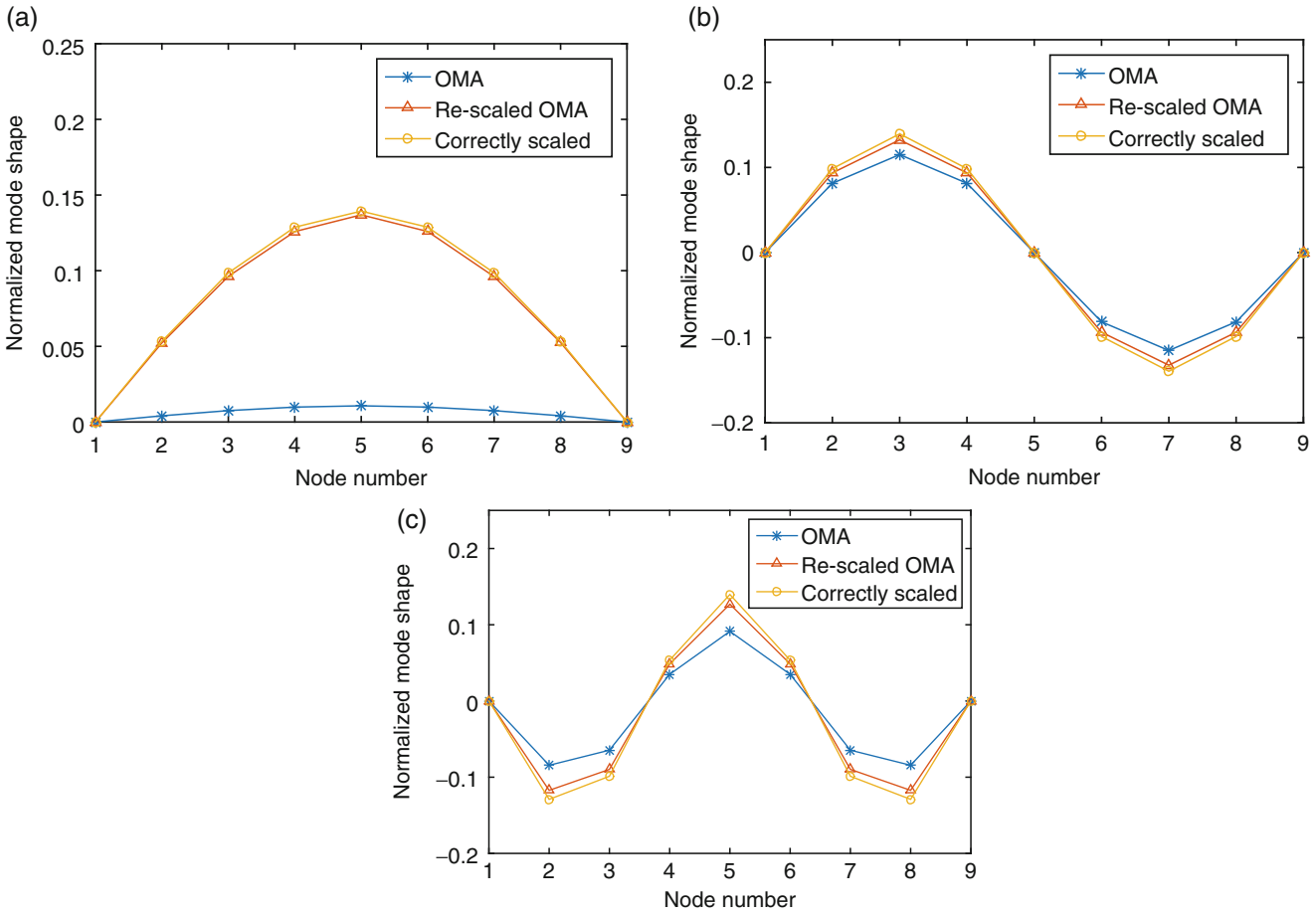


**Fig. 13.9** Comparison of unscaled OMA mode shapes and re-scaled modes with correctly scaled mode shapes from FEM model for a typical simulation of the first traffic case. (**a**) Mode 1. (**b**) Mode 2. (**c**) Mode 3

Modal Scaling Factor (MSF) error is then calculated using Eq. (13.23) between the scaled mode shapes and FEM mode shapes [9]. Maximum and average error values are shown in Fig. 13.11 for each traffic case.

$$Error_i = 100 \times \left| 1 - \frac{\alpha_i^2 . \boldsymbol{\psi}_{0i}^T . \boldsymbol{\psi}_{0i}}{\boldsymbol{\varphi}_i^T . \boldsymbol{\varphi}_i} \right| \tag{13.23}$$

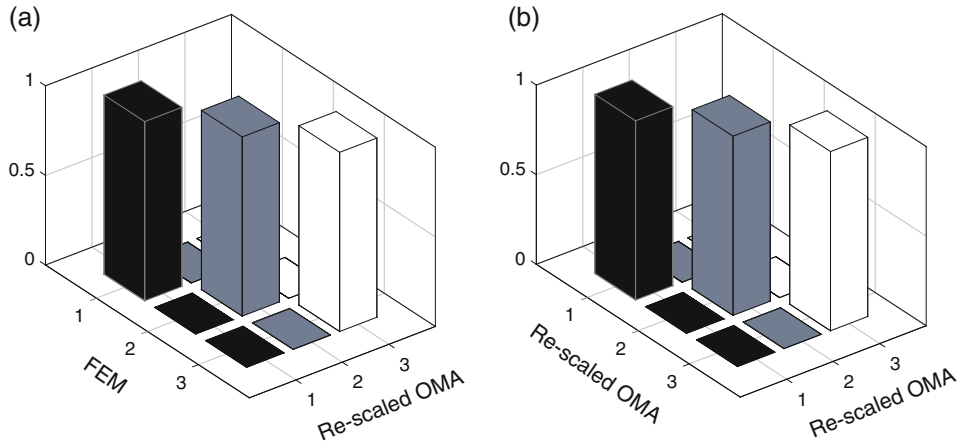


**Fig. 13.10** Comparison of MAC values

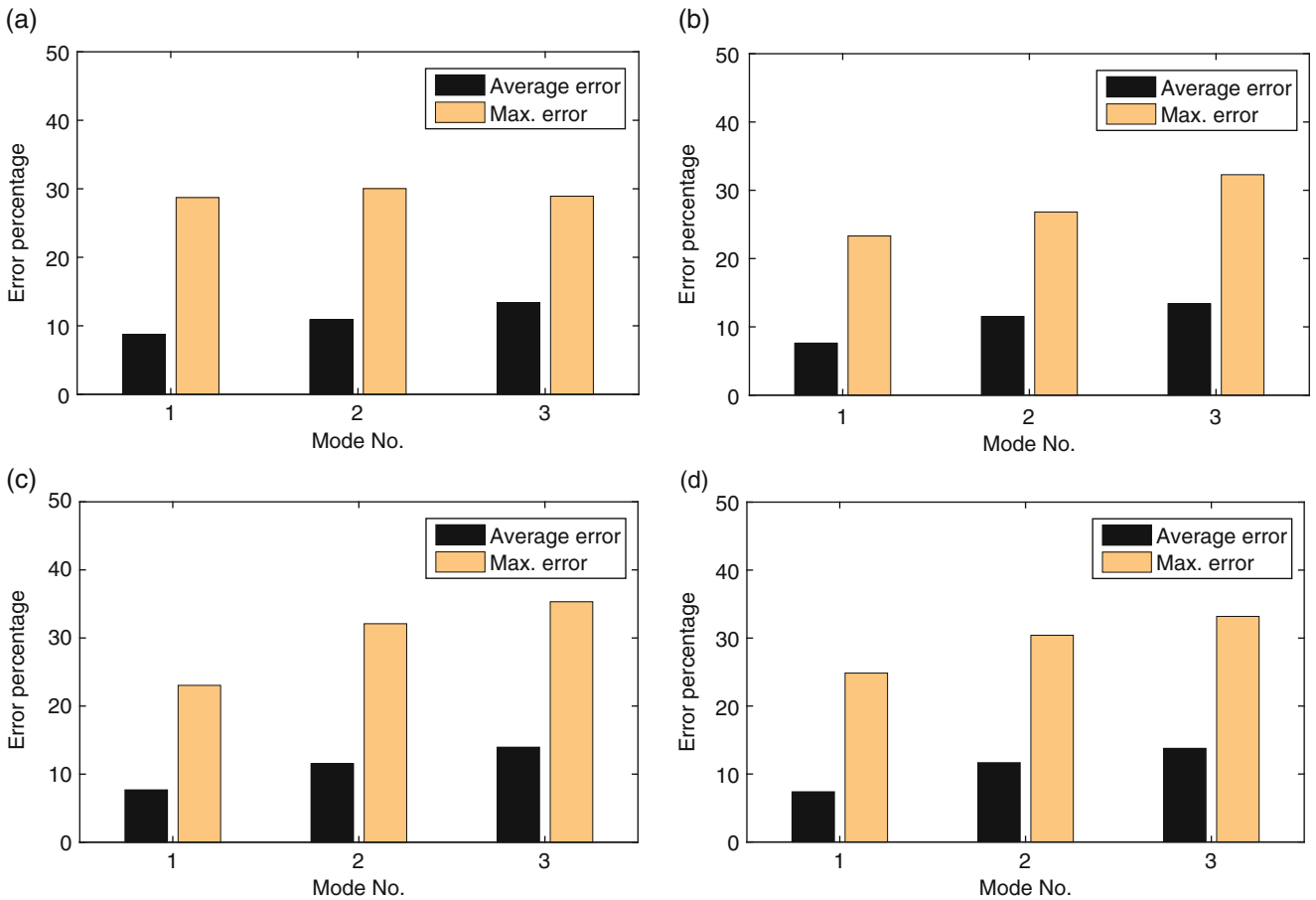


**Fig. 13.11** Average and maximum MSF values regarding each traffic case. (**a**) Case 1. (**b**) Case 2. (**c**) Case 3. (**d**) Case 4

The MSF values indicate that in each traffic scenario, average error is in an acceptable range below 15% and the maximum error value is as high as the conventional mass change method for specific frequency shifts [9]. Moreover, both maximum and average error percentages increase with the mode shape number. Therefore, if desired traffic conditions are satisfied and distribution of traffic headway times are known, with the help of repetitive tests, the scale factors can be calculated with promising accuracy.

## 13.4 Conclusion

In this article, traffic induced mass change is considered to provide the required mass modification. The average mass loading of traffic is calculated for a range of near congestion traffic and a polynomial surface is fitted through the values to calculate the mass change matrix needed in the scaling factor equations. Therefore, in case of traffic conditions which satisfy the lognormal distribution of headways, the mass change matrix can be constructed using the proposed procedure. A finite-element model of a bridge is considered and the method is evaluated for the first three modes of vibration of the structure using iterative tests and four real traffic conditions. The results indicate that for each traffic scenario, scale factors can be calculated with promising accuracy and the coefficients of variations are lower than 5%. Furthermore, the mean value of MSF errors are lower than 15% and the maximum MSF errors are as low as the conventional mass change methods. Therefore, it can be concluded that in cases of near congestion traffic streams which can be assumed stationary and are able to produce sufficient frequency shifts, the method can be used to derive the scale factors of the mode shapes. However, there are several assumptions made to simplify the problem in this study which are not present in the real situations. Nevertheless, the method can be further developed to account for different uncertainties and more robust modal identification approaches.

## References

1. Magalhães, F., Cunha, A.: Explaining operational modal analysis with data from an arch bridge. Mech. Syst. Signal Process. **25**(5), 1431–1450 (2011)
2. López Aenlle, M., Brincker, R., Fernández Canteli, A.C.: Some methods to determine scaled mode shapes in natural input modal analysis. In: Proceedings of the IMAC-XXIII: Conference & Exposition on Structural Dynamics – Structural Health Monitoring (2005)
3. López-Aenlle, M., Brincker, R., Pelayo, F., Canteli, A.F.: On exact and approximated formulations for scaling-mode shapes in operational modal analysis by mass and stiffness change. J. Sound Vib. **331**(3), 622–637 (2012)
4. Parloo, E., Verboven, P., Guillaume, P., Van Overmeire, M.: Sensitivity-based operational mode shape normalization. Mech. Syst. Signal Process. **16**(5), 757–767 (2002)
5. Parloo, E., Cauberghe, B., Benedettini, F., Alaggio, R., Guillaume, P.: Sensitivity-based operational mode shape normalisation: application to a bridge. Mech. Syst. Signal Process. **19**(1), 43–55 (2005)
6. Brincker, R., Andersen, P.: A way of getting scaled mode shapes in output only modal testing. In: Proceedings of the IMAC-XXI: International Modal Analysis Conference, Kissimmee, FL, p. 141 (2003)
7. López Aenlle, M., Brincker, R., Fernández Canteli, A.C., Villa García, L.M.: Scaling factor estimation by the mass change method. In: Proceedings of the International Operational Modal Analysis Conferencee (IOMAC), Copenhagen, Denmark (2005)
8. López Aenlle, M., Fernández Fernández, P., Brincker, R., Fernández Canteli, A.C.: Scaling factor estimation using an optimized mass change strategy, part 1: theory. In: Proceedings of the 2nd International Operational Modal Analysis Conference (2007)
9. Khatibi, M.M., Ashory, M.R., Malekjafarian, A., Brincker, R.: Mass–stiffness change method for scaling of operational mode shapes. Mech. Syst. Signal Process. **26**, 34–59 (2012)
10. Moridpour, S.: Evaluating the time headway distributions in congested highways. J. Traffic Logist. Eng. **2**(3), 224–229 (2014)
11. Abtahi, S.M., Tamannaei, M., Haghshenash, H.: Analysis and modeling time headway distributions under heavy traffic flow conditions in the urban highways: case of Isfahan. Transport. **26**(4), 375–382 (2011)
12. Ding, L., Hao, H., Zhu, X.: Evaluation of dynamic vehicle axle loads on bridges with different surface conditions. J. Sound Vib. **323**(3), 826–848 (2009)
13. Cimellaro, G.P., De Stefano, A.: Ambient vibration tests of XV century Renaissance Palace after 2012 Emilia earthquake in Northern Italy. Struct. Monit. Maint. **1**(2), 231–247 (2014)
14. Brincker, R., Ventura, C.: Introduction to Operational Modal Analysis. Wiley, Chichester (2015)
15. Caicedo, J.M.: Practical guidelines for the natural excitation technique (NExT) and the eigensystem realization algorithm (ERA) for modal identification using ambient vibration. Exp. Tech. **35**(4), 52–58 (2011)
16. Juang, J.N., Pappa, R.S.: An eigensystem realization algorithm for modal parameter identification and model reduction. J. Guid. Control. Dyn. **8**(5), 620–627 (1985)

17. Chen, Y., Tan, C.A., Feng, M.Q.: Physics-based traffic excitation models for highway bridges. In: Smart Structures and Materials. International Society for Optics and Photonics, pp. 377–388 (2004)
18. Chen, Y., Feng, M.Q., Tan, C.A.: Modeling of traffic excitation for system identification of bridge structures. Comput. Aided Civ. Inf. Eng. **21**(1), 57–66 (2006)
19. Kim, C.Y., Kim, N.S., Yoon, J.G., Jung, D.S.: Effect of vehicle mass on the measured dynamic characteristics of bridges from traffic-induced vibration test. In: Proceedings of the International Society for Optical Engineering, vol. 2, pp. 1106–1111 (2001)
20. Guyan, R.J.: Reduction of stiffness and mass matrices. AIAA J. **3**(2), 380–380 (1965)

# Chapter 14
# Covariance-Driven Stochastic Subspace Identification of an End-Supported Pontoon Bridge Under Varying Environmental Conditions

**Knut Andreas Kvåle, Ole Øiseth, and Anders Rönnquist**

**Abstract** The Bergsøysund Bridge is currently being extensively monitored with accelerometers, anemometers, wave radars and GNSS sensors. By applying Covariance-driven Stochastic Subspace Identification (Cov-SSI), the modal parameters of the bridge are estimated. The results are interpreted in the context of the environment, represented by significant wave heights. The problem is characterized by the fact that modes are closely spaced in frequency and have high damping. Two weighting algorithms for the Cov-SSI are applied, to assess their performance for application on structures with these characteristics.

**Keywords** Floating bridge • Stochastic subspace identification • Environmental influence • Wave excitation • High damping

## 14.1 Introduction

For decades, floating bridges served mainly as a military asset, for temporary crossings of rivers and straits. Floating bridges were first applied as critical links in modern road networks in the middle of the twentieth century, with exception of the Galata floating bridge in Istanbul finished in 1912 [1]. The continuous box girder design has shown great success in the State of Washington, USA, where most of the existing floating bridges are located. For straits highly affected by current and wave action, floating bridges relying on separate and discretely distributed pontoons may be beneficial. By using such a design, the waves will excite the structure merely in the points where the pontoons are located, and the correlation of the excitation will influence the response in a manner more sensitive to changes in the wave field. This will be of particular importance when the spans of the bridges increase. Currently, limited experience about the behavior of such floating bridges is available, and a thorough study of existing structures will be valuable. There exist only two end-supported floating bridges in the world that rely on discretely distributed pontoons, both located in Norway. The Bergsøysund Bridge is one of them, and it is currently extensively monitored to study its behavior upon wave and wind excitation. Operational modal analysis (OMA) is a highly valuable tool in the study of the behavior of the bridge. The covariance-driven stochastic subspace identification (Cov-SSI) algorithm is amongst the methods considered most robust and accurate [2–5] and performs very well for traditionally tested civil structures, such as suspension bridges and high-risers. The performance of the Cov-SSI algorithm applied on the Bergsøysund Bridge has previously been studied by [6]. In the current study, it is applied on recordings of acceleration of the bridge, to evaluate how it is affected by variations in the environmental conditions. The performances of various weighting algorithms are also assessed. The results are compared with modal parameters obtained from the eigenvalue solution of an model-updated version of the numerical prediction model presented in [7].

## 14.2 Covariance-Driven Stochastic Subspace Identification

The applied implementation of the Cov-SSI algorithm is based on the description given by Herman and van Der Auweraer [8], and the reader is referred to the mentioned paper for specifics. Only the most important details are repeated here. The starting point for the analysis is the block-Hankel matrix, $[H_i]$, which is constructed with sub-matrices representing the

K.A. Kvåle (✉) • O. Øiseth • A. Rönnquist
Department of Structural Engineering, Faculty of Engineering Science and Technology, NTNU, Norwegian University of Science and Technology, Trondheim, Norway
e-mail: knut.a.kvale@ntnu.no



J. Caicedo, S. Pakzad (eds.), *Dynamics of Civil Structures, Volume 2*, Conference Proceedings of the Society for Experimental Mechanics Series, DOI 10.1007/978-3-319-54777-0_14

correlation between all the measurement channels $l$, with varying time shifts, as follows:

$$[H_i] = \begin{bmatrix} [R_1] & [R_2] & \dots & [R_i] \\ [R_2] & [R_3] & \dots & [R_{i+1}] \\ \vdots & \vdots & \ddots & \vdots \\ [R_i] & [R_{i+1}] & \dots & [R_{2i+1}] \end{bmatrix} \tag{14.1}$$

Here, $2i$ corresponds to the maximum number of time lags, or equally valid, $i$ corresponds to the number of block rows. The correlation matrices are formally defined as:

$$[R_k] = \mathrm{E}\left(\{y_{n+k}\}\{y_n\}^T\right) \tag{14.2}$$

where the vector $\{y_n\}$ corresponds to the monitored quantities (accelerations) from all channels, for sample $n$. The sample-shift $k$ is related to the time lag through $\Delta t = kf_s^{-1}$, where $f_s$ is the sampling rate and $\Delta t$ represents the time lag. The cross-correlation matrices may be efficiently computed based on FFT and IFFT, as is how the `xcorr` function built-in to MATLAB is functioning.

The block-Hankel matrix can be decomposed into the corresponding observability and controllability matrices as follows:

$$[H_i] = [\mathscr{O}_i][\mathscr{C}_i] \tag{14.3}$$

which further are defined as follows:

$$[\mathscr{O}_i] = \begin{bmatrix} [C] \\ [C][A] \\ [C][A]^2 \\ \vdots \\ [C][A]^{i-1} \end{bmatrix}, \qquad [\mathscr{C}_i] = \begin{bmatrix} [G] & [A][G] & \dots & [A]^{i-1}[G] \end{bmatrix} \tag{14.4}$$

The matrices $[A]$ and $[C]$ refer to the discrete state matrix and discrete output matrix, respectively, from the stochastic state space model describing the problem:

$$\{z_{n+1}\} = [A]\{z_n\} + \{w_n\} \tag{14.5}$$

$$\{y_n\} = [C]\{z_n\} + \{v_n\} \tag{14.6}$$

where $\{z_n\}$, $\{y_n\}$, $\{w_n\}$, and $\{v_n\}$ correspond to the state vector, output vector, process noise and measurement noise, respectively. The matrix $[G]$ is formally defined as follows:

$$[G] = \mathrm{E}\left(\{z_{n+1}\}\{y_n\}^T\right) \tag{14.7}$$

After pre-multiplication with $[W_1]$ and post-multiplication with $[W_2]^T$, the block-Hankel matrix is decomposed using singular value decomposition (SVD), and thereafter truncated, as follows:

$$[W_1][H_i][W_2]^T = \begin{bmatrix} [U_1] & [U_2] \end{bmatrix} \begin{bmatrix} [\Sigma_1] & [0] \\ [0] & [\Sigma_2] \end{bmatrix} \begin{bmatrix} [V_1]^T \\ [V_2]^T \end{bmatrix} \tag{14.8}$$

$$\approx \begin{bmatrix} [U_1] & [U_2] \end{bmatrix} \begin{bmatrix} [\Sigma_1] & [0] \\ [0] & [0] \end{bmatrix} \begin{bmatrix} [V_1]^T \\ [V_2]^T \end{bmatrix} \tag{14.9}$$

$$= [U_1][\Sigma_1][V_1]^T \tag{14.10}$$

The truncation above represents an approximation due to noise and imperfections in the system; a system of finite order will have non-zero values for $[\Sigma_2]$ in practice, and a manual specification of the order has to be made. The optimal order is not known a priori, and a stabilization plot is used to distinguish physical poles from spurious ones, using multiple truncation

levels (orders). A pole is deemed physical and stable, as opposed to spurious and unstable, if certain criteria for deviance of modal quantities are fulfilled. One possible implementation of this is discussed in the sub-section below.

By combining Eqs. (14.3) and (14.8), the following estimate of the observability matrix is established:

$$[\mathscr{O}_i] = [W_1]^{-1}[U_1][\Sigma_1]^{1/2} \tag{14.11}$$

Then, the state matrix can be computed as follows:

$$[A] = [\mathscr{O}_{\text{down}}]^{\dagger}[\mathscr{O}_{\text{up}}] \tag{14.12}$$

where the matrices $[\mathscr{O}_{\text{down}}]$ and $[\mathscr{O}_{\text{up}}]$ both are subsets from $[\mathscr{O}_i]$, without the first or last $l$ rows, respectively, and † denotes the pseudo-inverse. The output matrix $[C]$ is required to establish the physical mode shapes, and is retrieved from the first $l$ rows of the observability matrix, as follows:

$$[C] = [\mathscr{O}_i]_{1:l} \tag{14.13}$$

By performing an eigenvalue decomposition of the discrete state matrix $[A]$, the discrete eigenvalues $\hat{\lambda}_r$ and the system eigenvectors $[\Psi]$ are established, which thereafter are transformed to continuous eigenvalues and to eigenvectors with coordinates referring to the sensor coordinates as follows:

$$\lambda_r = \ln\left(\hat{\lambda}_r\right) \cdot f_s^{-1}, \quad [\Phi] = [C][\Psi] \tag{14.14}$$

where the modal transformation matrix $[\Phi]$ has columns that refer to the identified mode shapes $\{\phi_r\}$, where $r$ is the mode index.

### 14.2.1 Selection of Weighting Matrices

There are two traditional options for the weighting matrices $[W_1]$ and $[W_2]$ for Cov-SSI, namely the canonical variate analysis (CVA) weighting and the balanced realization (BR) weighting.

The CVA weighting is commonly interpreted as the weights ensuring balanced energy levels for all the system modes (see e.g. [8]). The following two Toeplitz-structured matrices are used as a starting point:

$$[R^+] = \begin{bmatrix} [R_0] & [R_1]^T & \dots & [R_{i-1}]^T \\ [R_1] & [R_0] & \dots & [R_{i-2}]^T \\ \vdots & \vdots & \ddots & \vdots \\ [R_{i-1}] & [R_{i-2}] & \dots & [R_0] \end{bmatrix}, \qquad [R^-] = \begin{bmatrix} [R_0] & [R_1] & \dots & [R_{i-1}] \\ [R_1]^T & [R_0] & \dots & [R_{i-2}] \\ \vdots & \vdots & \ddots & \vdots \\ [R_{i-1}]^T & [R_{i-2}]^T & \dots & [R_0]^T \end{bmatrix} \tag{14.15}$$

The weights are thereafter defined as follows:

$$[W_1] = [L^+]^{-1}, \quad [W_2] = [L^-]^{-1} \tag{14.16}$$

where $[L^+]$ and $[L^-]$ are established from the Cholesky decomposition of $[R^+]$ and $[R^-]$, respectively. This weighting is reported to yield a better identification of less excited modes. The Cholesky decomposition is not straightforward to perform due to the poor conditioning of the input matrices. The authors observed that the block-Cholesky decomposition algorithm described in [9], modified to use Gaxpy-rich Cholesky factorization, was rather robust.

BR weighting is analogous to using unit matrices for $[W_1]$ and $[W_2]$.

### *14.2.2 Efficient Stabilization Analysis*

To determine if poles corresponding to analyses with different orders corresponds to the same mode, a modal indicator is used, which in the current study is the modal assurance criterion (MAC) number. The MAC number between poles $p$ and $q$ are computed as follows:

$$\mathrm{MAC}_{p,q} = \frac{|\{\phi_q\}^T\{\phi_p\}|^2}{\{\phi_q\}^T\{\phi_q\} \cdot \{\phi_p\}^T\{\phi_p\}} \tag{14.17}$$

where the $\bar{\cdot}$ is the complex conjugate operator. The poles from the current order are identified to correspond to the poles from the previous order by finding the maximum value of the MAC between the poles in the different orders. The most common choice for a modal indicator is the frequency, but because the modes are closely spaced in frequency, the MAC number is a better choice for the current study. For a pole from a analysis with a higher order to be considered stable, it has to fulfill the following criteria when compared to a previous reference pole: it has to deviate a maximum amount in frequency and damping, and their mode shapes have to yield a MAC value above a certain threshold. To increase the clarity of the stabilization plots, the parameter *stability level* is introduced. For a stability level of $s$, the above requirements have to be fulfilled with all poles corresponding to calculations with 1-$s$ orders lower than the queried pole.

## 14.3 The Bergsøysund Bridge

The Bergsøysund Bridge is a pontoon bridge with total length 931 m and main span 845 m, located on the northwestern coast of Norway. It consists of a steel truss supported by seven concrete pontoons (Fig. 14.1). The bridge is arc-shaped to reduce the bending moments due to lateral wave forces. The bridge is only supported in the ends, as no side-mooring is present. An extensive monitoring system is currently operating on the bridge (Fig. 14.2). Three-dimensional anemometers are capturing winds 7 m above the deck level at locations spread across the deck, while wave radars are monitoring the sea surface elevation near the center of the bridge. Furthermore, the response of the bridge is measured by means of two triaxial accelerometers on each pontoon and a single Global Navigation Satelite Systems (GNSS) displacement sensor located at midspan on top of the deck. The reader is referred to Kvåle et al. [10] for a more in-detail description of the monitoring system.

**Fig. 14.1** The Bergsøysund Bridge. Photograph by NTNU/K. A. Kvåle

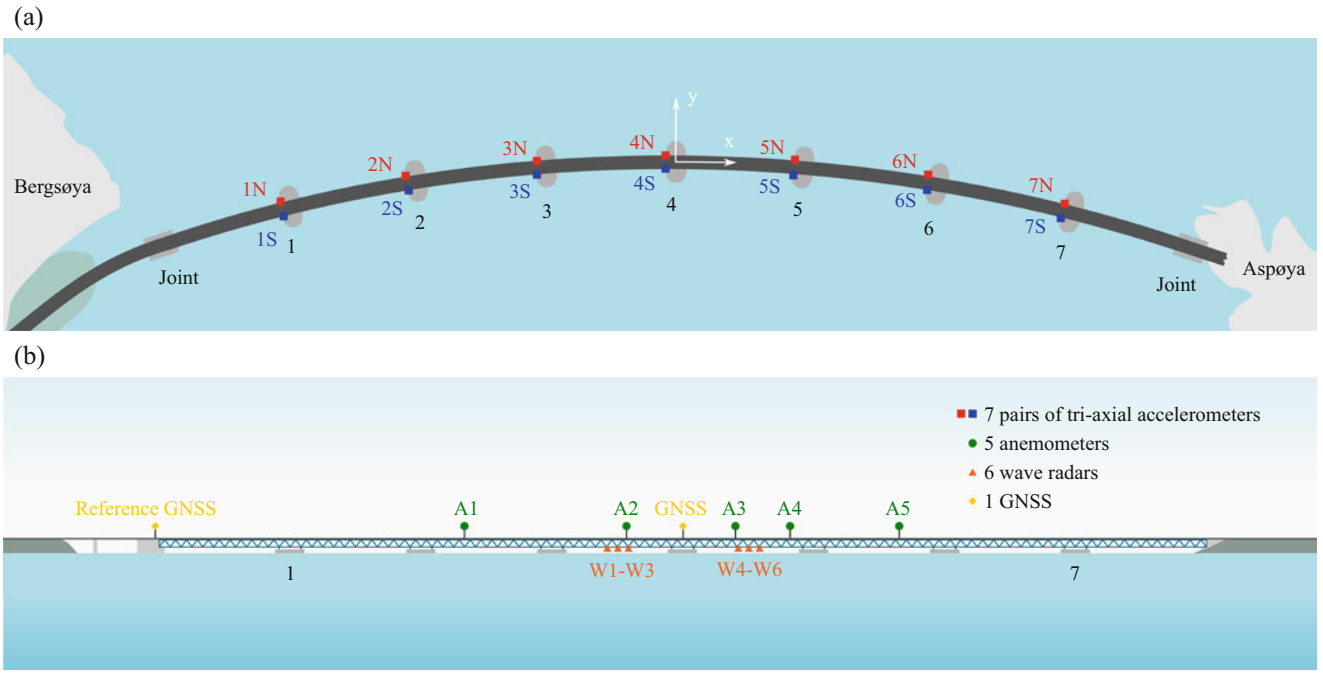


**Fig. 14.2** Monitoring system. (**a**) *Top view*, including coordinate system definition. (**b**) *Side view*

**Table 14.1** Vital statistics of the selected recording, initiated 06:47 on December 26, 2015, with a duration of 30 min

| | Waves | | Horizontal wind | | Acceleration[a] | |
|---|---|---|---|---|---|---|
| Position | SWH [cm] | Pontoon water level [cm] | Speed [m/s] | Direction [°] | Lateral [mg] | Vertical [mg] |
| Center (pontoon 4) | 34.8 | 407 | 12.4 | 264.7 | 1.8 | 0.5 |
| Quarter (pontoon 2) | – | – | 12.3[b] | 262.7[b] | 1.4 | 0.5 |

The indicated wind direction corresponds to the angle of origin of the wind, where 0° corresponds to winds along the x-axis indicated in Fig. 14.2 and increases in an clockwise manner.
[a] g is used as acceleration unit, and refers to the gravitational constant ($g = 9.81\ \mathrm{m/s^2}$).
[b] Reported wind statistics refer to anemometer A1, positioned close to pontoon 2. See Fig. 14.2.

## 14.4 Operational Modal Analysis

The following stability criteria were used: maximum frequency deviance of 1%, maximum damping deviance of 5%, and a minimum MAC value of 95%. The stability level was chosen as $s = 8$ for the analyses of which all presented results are based on. By investigating the statistical properties of captured recordings, a suitable time series was identified. In particular, a recording with perpendicular winds and decent excitation levels was sought after. A recording made 06:47 on December 26, 2015, fits these requirements. Some vital statistics related to this recording are found in Table 14.1. Modal analyses were performed both with BR and CVA weighting. The resulting stabilization plots are shown in Fig. 14.3, for both cases. It is clear that the CVA weighting does help in identifying the less excited modes for the current analysis. However, it is observed to behave rather erratically, and is very sensitive to input parameters, such as the number of block rows. The agreement with an updated version of the numerical prediction model in [7] is indicated with lines in the stabilization plot from the CVA analysis. To assess the effect of the increased stability level ($s = 8$), the stabilization plot from the analysis with CVA weighting is also shown with $s = 1$ in Fig. 14.4. Increased stability level results in a better readability and clarity of the stabilization plot. Table 14.2 shows the modal parameters of the CVA analysis together with modal parameters obtained from the eigenvalue solution of the numerical prediction model. The corresponding mode shape comparison is found in Fig. 14.5. Overall, a decent agreement is observed. The damping levels are not satisfactory, especially for modes 2, 4 and 5. The next sub-section indicates large variability of the damping ratios. Because the modes are closely spaced, they are prone to switch their ordering in frequency with small changes in the excitation. Furthermore, the complex, coupled and environment-dependent dynamic behavior is believed to make the appearance of the mode shapes more variable.

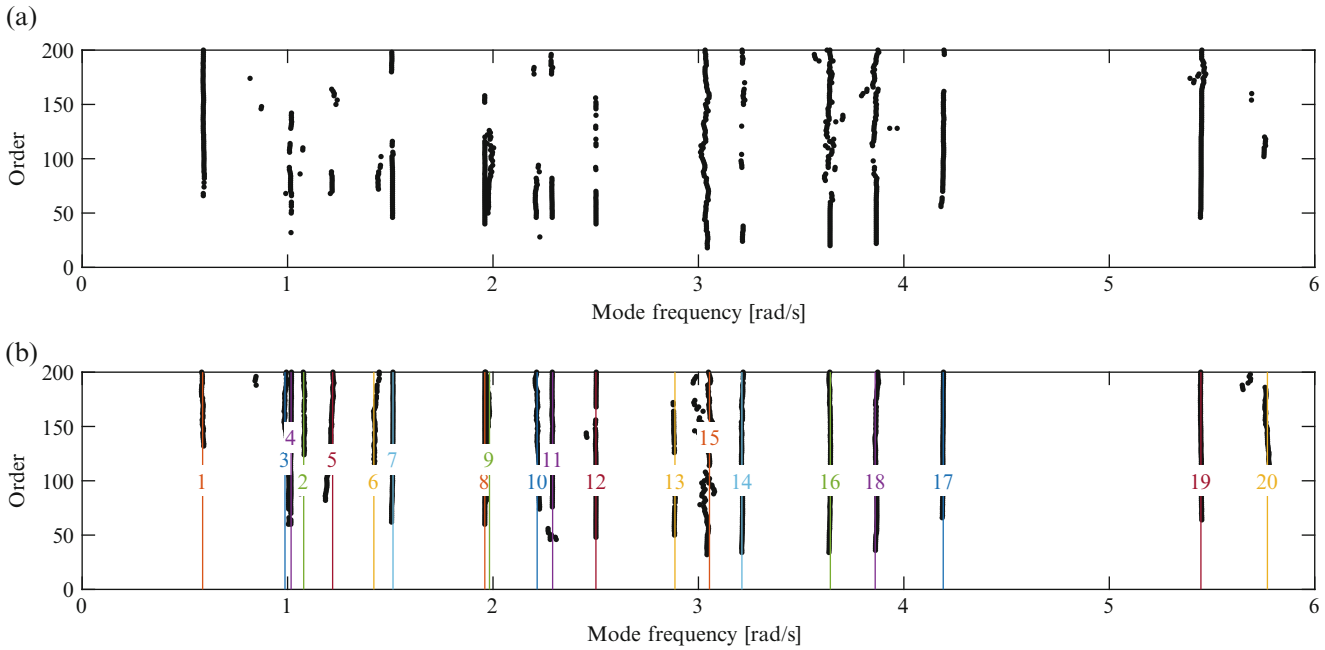


**Fig. 14.3** Stabilization plot from Cov-SSI analyses of the selected recording. Stabilization level $s = 8$. (**a**) BR weighting. (**b**) CVA weighting. The *lines* indicate identified modes, with numbers corresponding to the modes from the numerical prediction model

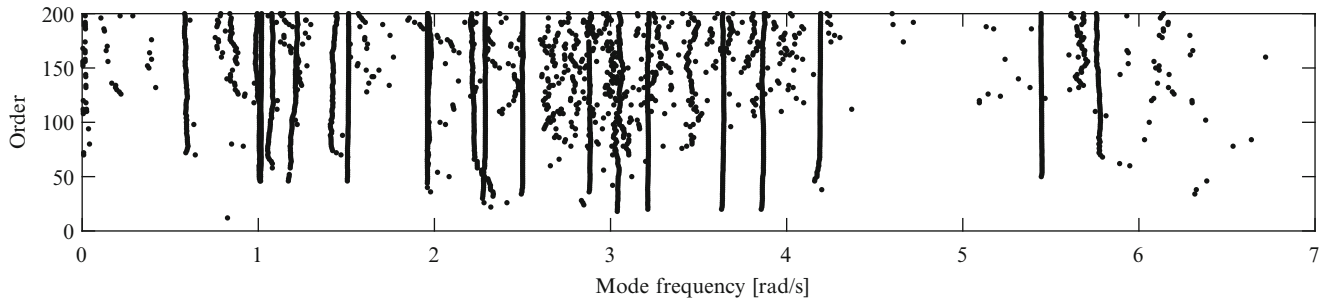


**Fig. 14.4** Stabilization plot from Cov-SSI analysis of the selected recording with CVA weighting. Stabilization level $s = 1$

**Table 14.2** Identified modal parameters compared with modal parameters from eigenvalue solution of numerical prediction model

| | Natural frequency, $\omega_r$ [rad/s] | | Damping ratio, $\xi_r$ [%] | | |
|---|---|---|---|---|---|
| Mode number | Prediction | Cov-SSI/CVA | Prediction | Cov-SSI/CVA | MAC |
| 1 | 0.58 | 0.59 | 1.63 | 5.16 | 0.94 |
| 2 | 0.99 | 1.08 | 12.25 | 4.47 | 0.32 |
| 3 | 1.03 | 0.99 | 11.24 | 11.62 | 0.86 |
| 4 | 1.05 | 1.02 | 5.00 | 2.53 | 0.53 |
| 5 | 1.17 | 1.22 | 7.67 | 4.88 | 0.95 |
| 6 | 1.38 | 1.42 | 5.91 | 6.93 | 0.78 |
| 7 | 1.44 | 1.51 | 3.28 | 2.65 | 0.98 |
| 8 | 1.87 | 1.96 | 1.07 | 0.96 | 0.67 |
| 9 | 1.95 | 1.98 | 3.62 | 3.15 | 0.90 |
| 10 | 2.23 | 2.21 | 0.43 | 1.86 | 0.89 |

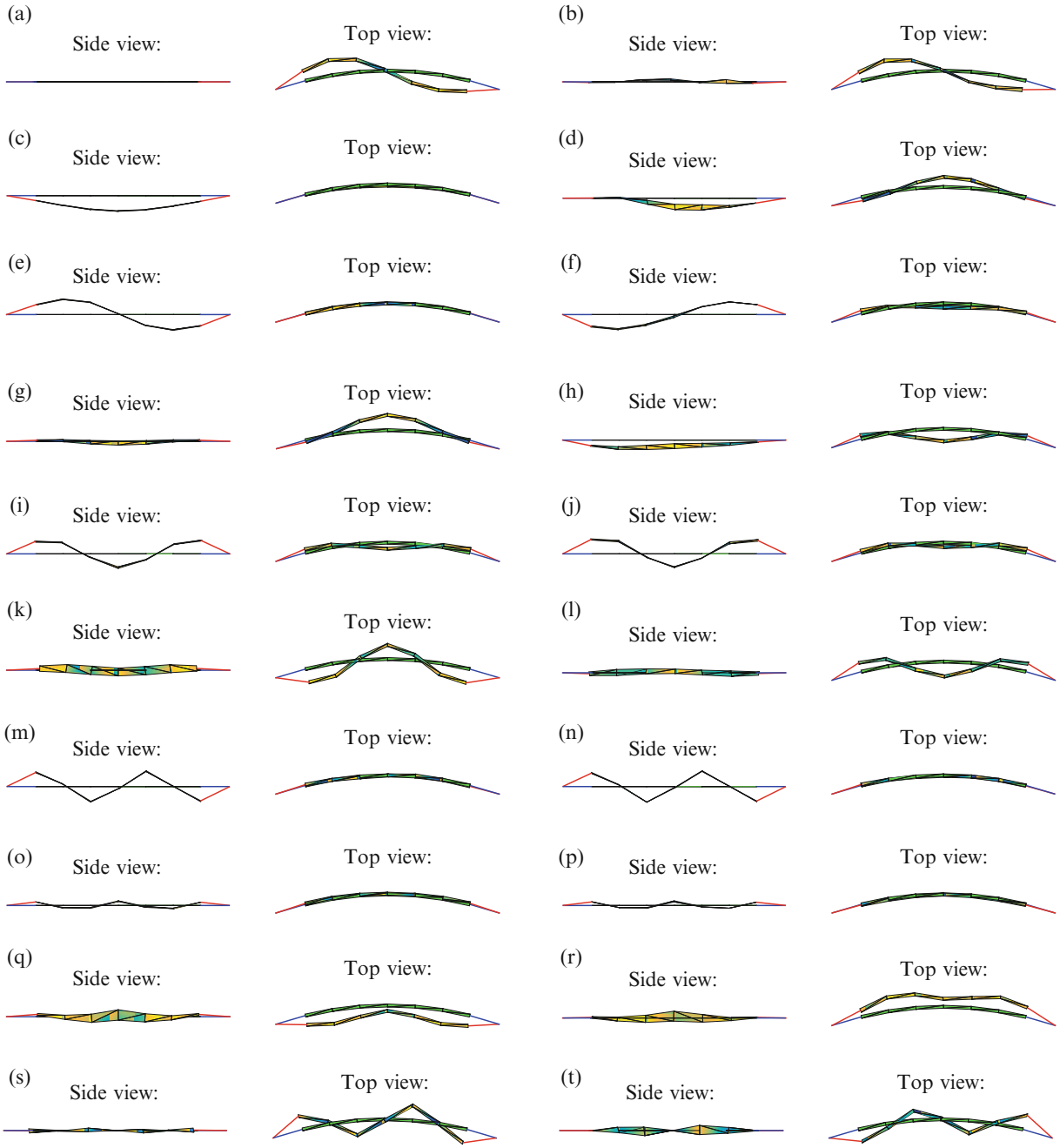


**Fig. 14.5** *Mode shapes* from eigenvalue solution of numerical prediction model and identified from Cov-SSI/CVA. The numbering refers to the numerical prediction. (**a**) Mode 1: numerical prediction. (**b**) Mode 1: Cov-SSI/CVA. (**c**) Mode 2: numerical prediction. (**d**) Mode 2: Cov-SSI/CVA. (**e**) Mode 3: numerical prediction. (**f**) Mode 3: Cov-SSI/CVA. (**g**) Mode 4: numerical prediction. (**h**) Mode 4: Cov-SSI/CVA. (**i**) Mode 5: numerical prediction. (**j**) Mode 5: Cov-SSI/CVA. (**k**) Mode 6: numerical prediction. (**l**) Mode 6: Cov-SSI/CVA. (**m**) Mode 7: numerical prediction. (**n**) Mode 7: Cov-SSI/CVA. (**o**) Mode 8: numerical prediction. (**p**) Mode 8: Cov-SSI/CVA. (**q**) Mode 9: numerical prediction. (**r**) Mode 9: Cov-SSI/CVA. (**s**) Mode 10: numerical prediction. (**t**) Mode 10: Cov-SSI/CVA

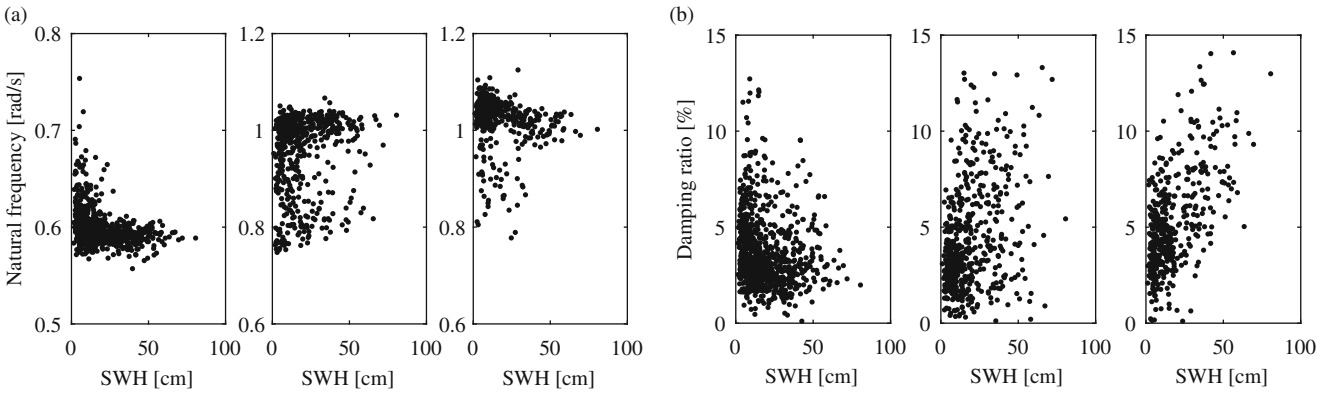


**Fig. 14.6** Effects on modal parameters from changing significant wave height. (**a**) Effect on natural frequency. (**b**) Effect on critical damping ratio

### *14.4.1 Automatic OMA and the Effect of Varying Environment*

By using the eigenvalue solution from the predictive numerical model as reference, the natural frequencies and critical damping ratios are automatically identified for various environmental conditions. The numerical prediction model is described in [7]. The MAC numbers between the predicted and measured mode shapes were required to have a value above 0.7, for storing as an identified mode. For the automatic OMA, the BR weighting is utilized due to higher robustness than the CVA weighting. The natural frequency and critical damping coefficients of mode 1, 2 and 3 are compared to the significant wave height (SWH) in Fig. 14.6. The SWH is defined as $H_s = 4\sigma_\eta$, where $\sigma_\eta$ is the standard deviation of the wave elevation process. Large variability in the modal parameters, in particular the damping ratios, are observed. The plots indicate that the damping ratio is increasing for increased SWH. Increased SWH affects the three presented natural frequencies differently. Furthermore, the scatter of the natural frequencies are reduced for increasing SWH, i.e., increased excitation levels. This tendency is explained by the fact that a larger amount of the excitation is accounted for when the SWH is larger.

## 14.5 Concluding Remarks

The Cov-SSI method is successfully applied with different weighting schemes on the Bergsøysund Bridge, an end-supported pontoon bridge in current operation, to identify the structure's modal parameters. Damping ratios and MAC-values are poor for certain modes. The CVA weighting scheme improves the clarity of the stabilization plot to a great extent. When the CVA weighting is used in conjunction with a high stability level, the resulting stabilization plots become quite clear. On the other hand, the CVA weighting implementation used is observed as very sensitive to the input time series and parameters, and less robust than an unweighted analysis, i.e., BR weighting. The OMA procedure is made automatic by using the eigenvalue solution from a predictive numerical model as reference, which shows that the bridge's natural frequencies' variability is reduced when the excitation, represented by the SWH, is increased. Both mean value and variance of the damping ratios are in general increased as a consequence of increasing SWH.

**Acknowledgements** The research was funded by the Norwegian Public Roads Administration. The authors gratefully acknowledge this support.

## References

1. Watanabe, E.: Floating bridges: past and present. Struct. Eng. Int. **13**(2), 128–132 (2003)
2. Brownjohn, J.M.W., Magalhaes, F., Caetano, E., Cunha, A.: Ambient vibration re-testing and operational modal analysis of the Humber Bridge. Eng. Struct. **32**, 2003–2018 (2010)
3. Magalhães, F., Cunha, Á., Caetano, E.: Dynamic monitoring of a long span arch bridge. Eng. Struct. **30**, 3034–3044 (2008)
4. Farrar, C., James, G.: System identification from ambient vibration measurements on a bridge. J. Sound Vib. **205**, 1–18 (1997)

5. Peeters, B., De Roeck, G.: One-year monitoring of the Z24-Bridge: environmental effects versus damage events. Earthq. Eng. Struct. Dyn. **30**, 149–171 (2001)
6. Kvåle, K.A., Øiseth, O., Rønnquist, A., Sigbjörnsson, R.: Modal analysis of a floating bridge without side-mooring. In: Dynamics of Civil Structures, Volume 2, vol. 2, pp. 127–136. Springer, Berlin (2015)
7. Kvåle, K.A., Sigbjörnsson, R., Øiseth, O.: Modelling the stochastic dynamic behaviour of a pontoon bridge: a case study. Comput. Struct. **165**, 123–135 (2016)
8. Hermans, L., Van der Auweraer, H.: Modal testing and analysis of structures under operational conditions: industrial applications. Mech. Syst. Signal Process. **13**, 193–216 (1999)
9. Golub, G.H., Van Loan, C.F., Matrix Computations, vol. 3. JHU Press, Baltimore (2012)
10. Kvåle, K.A., Øiseth, O.: Structural monitoring of an end-supported pontoon bridge. Mar. Struct. **52**, 188–207 (2017). Available at: http://linkinghub.elsevier.com/retrieve/pii/S0951833916300284

# Chapter 15
# Probabilistic Analysis of Human-Structure Interaction in the Vertical Direction for Pedestrian Bridges

**Federica Tubino**

**Abstract** This paper deals with the quantification of the effects of human-structure interaction in the vertical direction for footbridges. Analyses are based on the study of a coupled system of the footbridge, modeled as a continuous dynamic system, and pedestrians, schematized as moving single-degree-of-freedom systems, characterized by random dynamic properties. The equivalent dynamic properties of the coupled system are estimated based on a state-space approach. Results of Monte Carlo simulations show that pedestrians can strongly modify the dynamic properties of the footbridge, especially regarding the damping ratio. A numerical application to some literature examples shows that the model is able to reproduce experimental findings on real footbridges.

**Keywords** Footbridges • Human-structure interaction • Monte Carlo simulations • Probabilistic analysis • Serviceability

## 15.1 Introduction

Modern footbridges are very slender structures with low damping characteristics, and they are often characterized by natural frequencies falling within the range of typical human step frequencies. Thus, the can be very sensitive to human-induced vibrations and their serviceability assessment is becoming a central step in their design. Recent guidelines [1–5] and research papers (e.g. [6]) provide simplified procedures to deal with their serviceability analyses. The author of the paper has introduced an equivalent spectral model for human-induced forces on footbridges in unrestricted pedestrian traffic [7], which has been validated both experimentally [8] and numerically [9]. Then, the model has been generalized in order to taken into account pedestrian interaction in crowded conditions [10]. All these procedures are based on simplified expressions of pedestrian-induced forces, which neglect human-structure interaction.

Recent literature has recognized that human-structure interaction could have a determinant role in the assessment of human-induced vibrations of footbridges. Concerning vibrations in the lateral direction, it is widely recognized that synchronization between pedestrians and footbridge motion may lead to instability problems (e.g. the London Millennium Bridge). Many models have been introduced in the literature in order to model lateral synchronization. Dealing with vibrations in the vertical direction, experimental measurements on real structures seem to demonstrate that human-structure interaction is beneficial, providing an equivalent additional damping to the footbridge [11–13]. Thus, experimental tests in laboratory conditions have been carried out on scaled footbridges, confirming the results on real structures [14]. Analogous findings have been reported for staircases [15, 16]. Different models have been proposed in the literature to deal with human-structure interaction in the vertical direction, mainly representing pedestrians as equivalent single-degree-of-freedom or multi-degree-of-freedom systems [17–19], as an inverted pendulum [20], or as a bipedal walking model with damped compliant legs [21, 22]. In the analysis of grandstands and stadia occupied by humans, some researchers have been modeling sitting or standing humans as single- or multi- degree-of-freedom systems and analyzed the properties of the coupled system from a deterministic [23] or probabilistic [24] point of view. The main issue in the analysis of human-structure interaction in footbridges is the representation of pedestrian motion both in terms of the dynamic characterization of moving pedestrians (experimental measurements available in the literature mainly deal with sitting or standing humans) and in the analysis of the dynamic properties of the coupled dynamic system composed by the footbridge and the moving pedestrians. Within this framework, two papers have been recently published where pedestrians have been modelled as moving SDOF systems with random dynamic properties [25, 26]. In [25], the interaction among pedestrians is neglected, and an application to a specific footbridge with fixed dynamic characteristics is shown. In [26], a modelling framework based on a microscopic model of

F. Tubino (✉)
Department of Civil, Chemical and Environmental Engineering, University of Genova, Via Montallegro 1, 16145, Genova, Italy
e-mail: federica.tubino@unige.it



J. Caicedo, S. Pakzad (eds.), *Dynamics of Civil Structures, Volume 2*, Conference Proceedings
of the Society for Experimental Mechanics Series, DOI 10.1007/978-3-319-54777-0_15

multiple pedestrian traffic and schematizing pedestrians as moving single-degree of freedom systems with random dynamic properties has been introduced [26]. Due to the complexity of the model, a limited number of numerical simulations are carried out on four ideal footbridges with the same natural frequency and damping ratio and different modal mass, subjected to three traffic scenarios have been reported. Furthermore, the effect of human-structure interaction is quantified through the analysis of the footbridge dynamic response.

The objective of this paper is to provide a general overview of the effect of human-structure interaction on the dynamic properties of a footbridge. The dynamic properties of the coupled system of the footbridge, modeled as a continuous dynamic system, and pedestrians, schematized as moving single-degree-of-freedom systems, characterized by random dynamic properties, are studied. The adopted dynamic model is the same as in [25], but, in order to get general results valid for any specific structure, the equations of motion of the coupled system are written in non-dimensional form and the main non-dimensional parameters governing the behavior of the coupled system are identified. The equivalent dynamic properties of the coupled system are estimated based on a state-space approach through Monte Carlo simulations taking into account the randomness of the dynamic properties of pedestrians. Results are provided both in terms of mean values and standard deviations and they are provided for different combinations of the non-dimensional parameters identified. It is shown that pedestrians can strongly modify the dynamic properties of the footbridge, especially regarding the damping ratio. Furthermore, the model is applied to the study of human-structure interaction for real footbridges, demonstrating that the model is able to reproduce experimental findings.

## References


1. FIB: Bulletin 32—Guidelines for the Design of Footbridges, International Federation for Structural Concrete. Sprint-Digital-Druck, Stuttgart (2005)
2. SETRA: Footbridges—Assessment of Vibrational Behaviour of Footbridges Under Pedestrian Loading. Technical Department for Transport, Roads and Bridges Engineering and Road Safety, Ministry of Transport and Infrastructure, Paris (2006)
3. ISO10137: Bases for Design of Structures—Serviceability of Buildings and Walkways Against Vibration. International Organization for Standardization, Geneva (2007)
4. BSI: UK National Annex to Eurocode 1: Actions on Structures—Part 2: Traffic Loads on Bridges. NA to BS EN 1991-2:2003. British Standards Institution (2008)
5. HIVOSS: Design of footbridges guideline. Human induced vibrations of steel structures. http://www.stb.rwth-aachen.de/projekte/2007/HIVOSS/download.php RFS2-CT-2007-00033, 2009
6. Piccardo, G., Tubino, F.: Simplified procedures for the vibration serviceability analysis of footbridges subjected to realistic walking loads. Comput. Struct. **87**, 890–903 (2009)
7. Piccardo, G., Tubino, F.: Equivalent spectral model and maximum dynamic response for the serviceability analysis of footbridges. Eng. Struct. **40**, 445–456 (2012)
8. Tubino, F., Carassale, L., Piccardo, G.: Human-induced vibrations on two lively footbridges in Milan. J. Bridg. Eng. ASCE. **21**(8), C4015002 (2016)
9. Tubino, F., Piccardo, G.: Serviceability assessment of footbridges in unrestricted pedestrian traffic condition. Struct. Infrastruct. Eng. **12**(12), 1652–1662 (2016)
10. Ferrarotti, A., Tubino, F.: Generalized equivalent spectral model for pedestrian-induced forces on footbridges. J. Bridg. Eng. ASCE **21**(12) (2016). doi:10.1061/(ASCE)BE.1943-5592.0000963
11. Zivanovic, S., Pavic, A., Ingolfsson, E.T.: Modeling spatially unrestricted pedestrian traffic on footbridges. J. Struct. Eng. ASCE. **136**, 1296–1308 (2010)
12. Van Nimmen, K., Lombaert, G., Jonkers, I., De Roeck, G., Van den Broeck, P.: Characterisation of walking loads by 3D inertial motion tracking. J. Sound Vib. **333**, 5212–5226 (2014)
13. Dang, H.V., Zivanovic, S.: Modelling pedestrian interaction with perceptibly vibrating footdbridges. FME Trans. **41**, 271–278 (2013)
14. Shahabpoor, E., Pavic, A., Racic, V.: Identification of mass-spring-damper model of walking humans. Structures. **5**, 233–246 (2016)
15. Busca, G., Cappellini, A., Manzoni, S., Tarabini, M., Vanali, M.: Quantification of changes in modal parameters due to the presence of passive people on a slender structure. J. Sound Vib. **333**, 5641–5652 (2014)
16. Cappellini, A., Manzoni, S., Vanali, M., Cigada, A.: Evaluation of the dynamic behaviour of steel staircases damped by the presence of people. Eng. Struct. **115**, 165–178 (2016)
17. Matsumoto, Y., Griffin, M.J.: Dynamic response of the standing human body exposed to vertical vibration: influence of posture and vibration magnitude. J. Sound Vib. **212**(1), 85–107 (1998)
18. Matsumoto, Y., Griffin, M.J.: Mathematical models for the apparent masses of standing subjects exposed to vertical whole-body vibration. J. Sound Vib. **260**, 431–451 (2003)
19. Alexander, N.A.: Theoretical treatment of crowd-structure interaction dynamics. Proc. ICE Struct. Build. **159**(SB6), 329–338 (2006)
20. Bocian, M., Macdonald, J., Burn, J.: Biomechanically-inspired modelling of pedestrian-induced vertical self-excited forces. ASCE J. Bridg. Eng. **18**(12), 1336–1346 (2012)
21. Qin, J.W., Law, S.S., Yang, Q.S., Yang, N.: Finite element analysis of pedestrian-bridge dynamic interaction. J. Appl. Mech. **81**, 041001, 1–15 (2014)
22. Yang, Q.S., Qin, J.W., Law, S.S.: A three-dimensional human walking model. J. Sound Vib. **357**, 437–456 (2015)

23. Sachse, R., Pavic, A., Reynolds, P.: Parametric study of modal properties of damped two-degree-of-freedom crowd-structure dynamic systems. J. Sound Vib. **274**, 461–480 (2004)
24. Agu, E., Kasperski, M.: Influence of the random dynamic parameters of the human body on the dynamic characteristics of the coupled system of structure–crowd. J. Sound Vib. **330**, 431–444 (2011)
25. Caprani, C., Ahmadi, E.: Formulation of human-structure interaction system models for vertical vibration. J. Sound Vib. **377**, 347–367 (2016)
26. Venuti, F., Racic, V., Corbetta, A.: Modelling framework for dynamic interaction between multiple pedestrians and vertical vibrations of footbridges. J. Sound Vib. **379**, 245–263 (2016)

# Chapter 16
# Effects of Seismic Retrofit on the Dynamic Properties of a 4-Storey Parking Garage

**Ilaria Capraro and Carlos E. Ventura**

**Abstract** This paper presents the results of an Ambient Vibration Test (AVT) conducted in March 2015 on the Health Sciences Parkade at the University of British Columbia in Vancouver, Canada. A similar test was conducted in March 2014 before the Parkade was subjected to different interventions for seismic retrofit purpose between July and October 2014.

Natural frequencies, modal damping and mode shapes were identified with the Frequency Domain Decomposition (FDD), the Enhanced Frequency Domain Decomposition (EFDD) and the Stochastic Subspace Identification (SSI) techniques. Results showed good agreement between the different methods and confirmed the ones obtained from the 2014 data analysis.

Six modes were identified up to a frequency of 8.4 Hz, showing a slight increase of the frequency values with respect to the 2014 results, with a maximum of about 10% for the fundamental mode. In addition to the previous test, it was also possible to identify the site period, which corresponded to a frequency of 0.64 Hz. The effects of the retrofit on the values of natural frequencies are further discussed in the paper.

**Keywords** Ambient vibration test • Modal analysis • Seismic retrofit • Operational conditions • Site period

## 16.1 Introduction

This paper presents the results of an Ambient Vibration Test on the Health Science Parkade at the University of British Columbia in Vancouver, Canada. The test was conducted during the spring 2015 after the Parkade was subjected to significant interventions for seismic upgrade. The purpose of the test was to compare the results and to understand how and in what extent such interventions affected the natural properties of the structure.

The Health Sciences Parkade can be considered as a combination of two 4-storey reinforced concrete buildings which are interconnected by sets of three ramps each level. The principal lateral force resisting systems is composed by internal shear walls which work jointly with a reinforced concrete moment frame. The north building has also a basement to which is allocated extra parking space. At basement level, external shear walls and additional internal walls are present, providing additional stiffness to the structure at that level. A picture of the Health Science Parkade is given in Fig. 16.1.

## 16.2 Seismic Upgrade

The Health Sciences Parkade was built in 1979. After the first Ambient Vibration Test, the Parkade was subjected to different structural interventions during the summer of 2015. These interventions aimed to improve the structural performance of the Parkade to seismic loads. The works of seismic upgrade affected several locations of the Parkade, which was kept operational during the interventions. The principal shear walls have been reinforced at each end with additional reinforced concrete columns and the application of fibre reinforced polymer (FRP) composites. Some details of these interventions are shown in Figs. 16.2 and 16.3. Moreover, new foundation at the ground floor have been constructed with the installation of anchor bolts and mini-piles. Similar technique involving FRP composites was applied to strengthen some of the slabs at the upper floors. The external perimeter of the basement has been walled up with a new reinforced concrete shear wall on

I. Capraro (✉) • C.E. Ventura
Department of Civil Engineering, The University of British Columbia, 6250 Applied Science Lane, Vancouver, BC, V6T 1Z4, Canada
e-mail: icapraro@civil.ubc.ca



J. Caicedo, S. Pakzad (eds.), *Dynamics of Civil Structures, Volume 2*, Conference Proceedings
of the Society for Experimental Mechanics Series, DOI 10.1007/978-3-319-54777-0_16


**Fig. 16.1** North elevation of the Parkade from East Mall and Hospital Ln

**Fig. 16.2** Additional RC columns to shear walls, under construction

four locations on the longitudinal edges of the parking ramps (Figs. 16.4 and 16.5). A further intervention was performed on the internal timber bumpers, which have been substituted with reinforced concrete curbs at all levels, as shown in Figs. 16.6 and 16.7.

## 16.3 Ambient Vibration Test

The ambient vibration test was performed on Saturday March14th, 2015 at the Health Sciences Parkade at the University of British Columbia in Vancouver by a group of five graduate students. During this period, the Parkade was experiencing a lower level of traffic than a regular weekday. A total of nine Tromino sensors [1] have been used to perform the ambient vibration test. One sensor was kept as reference at the second floor, while the remaining eight sensors were placed at the corners of the slabs and on the ramps of the structure. These roving sensors were arranged in a total of five different setups

**Fig. 16.3** Anchor bolts on internal shear walls, under construction

**Fig. 16.4** External shear wall and short columns, before upgrade

as to capture the response of the structure at the most significant locations. Detailed illustration of the sensors locations and their orientation is provided in Fig. 16.8. The sampling frequency was kept as constant to 128 Hz. The recorded data was synchronized into ASCII file via computer program Grilla [1].

The natural properties of the structure, such as natural frequency, mode shapes and damping have been identified with different Operational Modal Analysis techniques. The analyses have been carried out with computer program ARTeMIS Modal v3.0 [2]. The data collected during the test were preprocessed and decimated to a frequency range of 0–16 Hz, considering ten projection channels and the resolution set to 1024.

The Frequency Domain Decomposition (FDD) technique allowed to estimate the first 6 natural modes up to a frequency of 8.5 Hz. The plot for singular values of the spectral density matrix in Fig. 16.9. For sake of comparison, a similar plot obtained through the test run in 2014 before seismic upgrade is given in Fig. 16.10. The fundamental mode has been found to be a first bending mode in the longitudinal N–S direction and occurred at 3.05 Hz. The second natural mode was identified as a first mode in torsion and corresponded to a frequency of about 3.8 Hz. The remaining modes involve bending in both N–S and E–W and torsion, which sometimes occurred coupled to a bending mode. With the FDD method it was also possible to identify the site period, which corresponded to a frequency of about 0.6 Hz.

**Fig. 16.5** New external shear walls, during construction


**Fig. 16.6** Timber bumpers, before seismic upgrade


**Fig. 16.7** New reinforced concrete beam, under construction

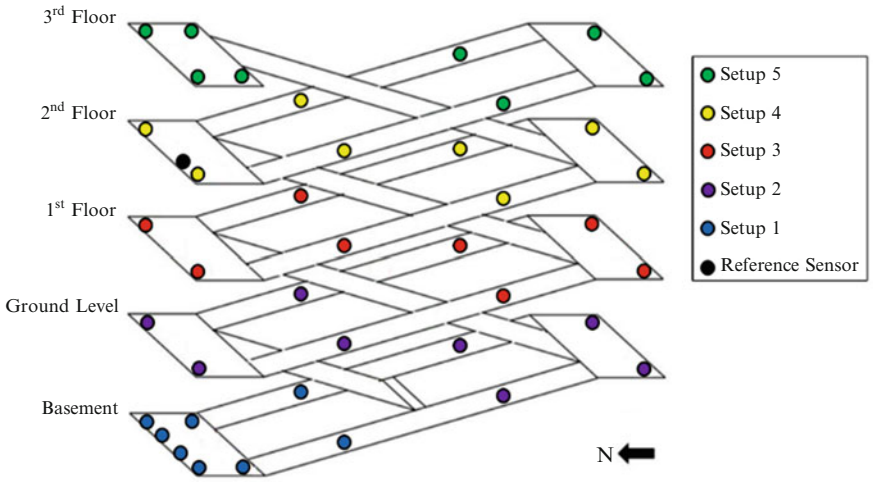


**Fig. 16.8** Sensor location and orientation, setup configuration

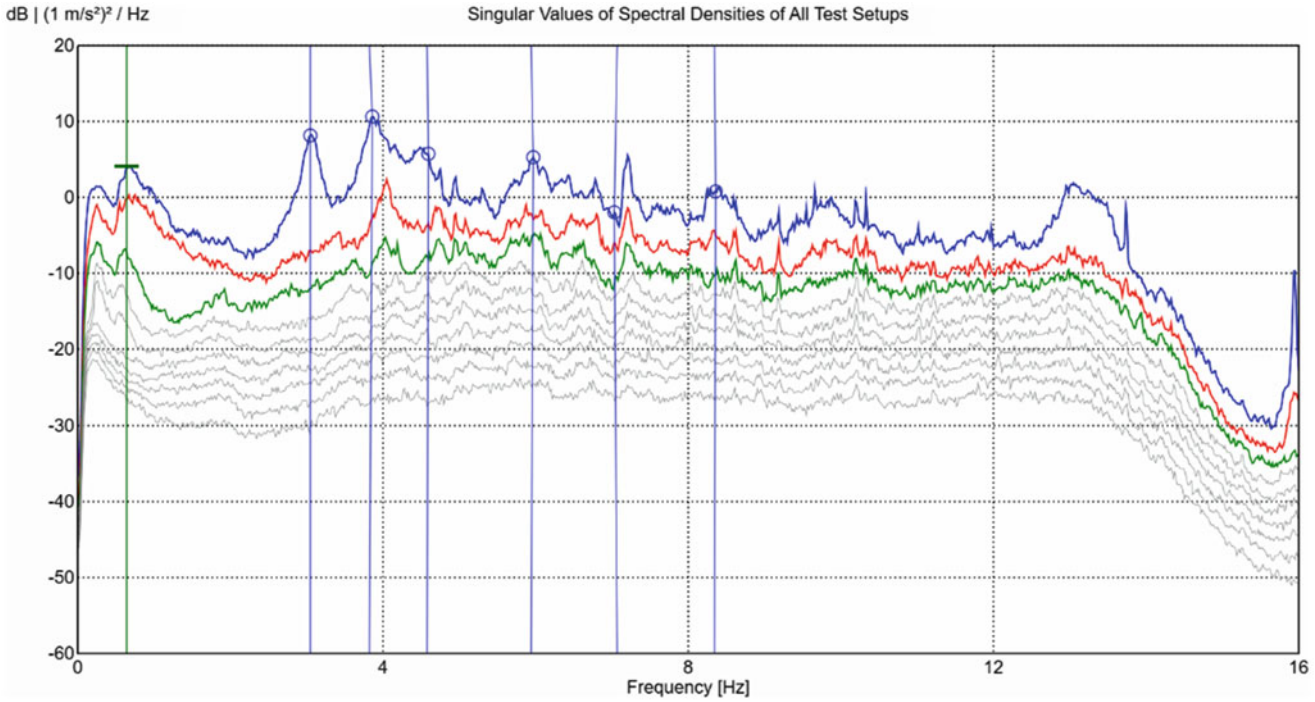


**Fig. 16.9** Singular values of the spectral densities, 2015 results (after seismic upgrade)

The analysis was repeated also with the Enhanced Frequency Domain Decomposition (EFDD) technique, as to estimate the value of natural damping for each mode. This analysis confirmed the frequency values obtained by the previous analysis and the damping values were found to be between 0.2 and 3.3% for the different modes.

In order to further confirm the results obtained via frequency domain, the data was analyzed with the Stochastic Subspace Identification (SSI-PC) method. The analysis in the time domain led to results which correlated very well to the ones obtained in the frequency domain in terms of natural frequency values. As for the damping values, the results agreed very well for the first fundamental mode, while they slightly diverged for the higher modes. The six mode shapes are illustrated in Figs. 16.11, 16.12, 16.13, 16.14, 16.15, 16.16 and the site period is illustrated in Fig. 16.17.

A detailed summary of the natural frequencies, damping values and description of the modes is given in Table 16.1.

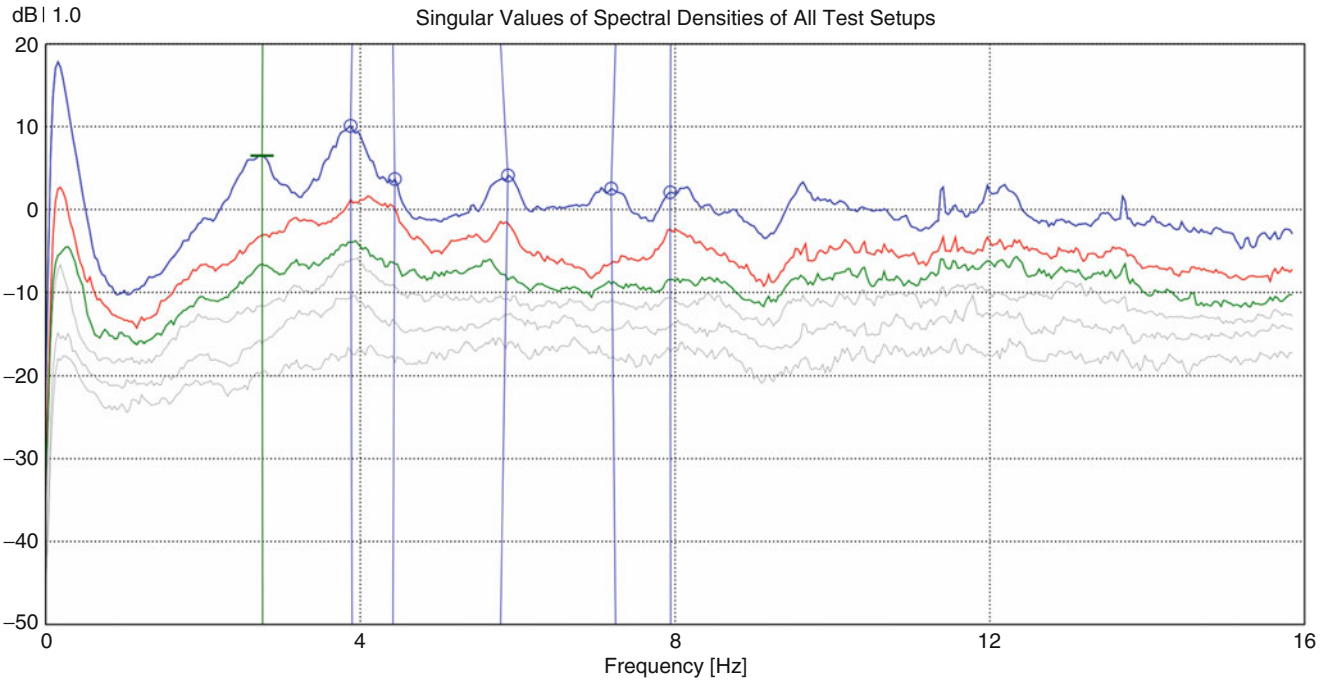


**Fig. 16.10** Singular values of the spectral densities, 2014 results (before seismic upgrade)

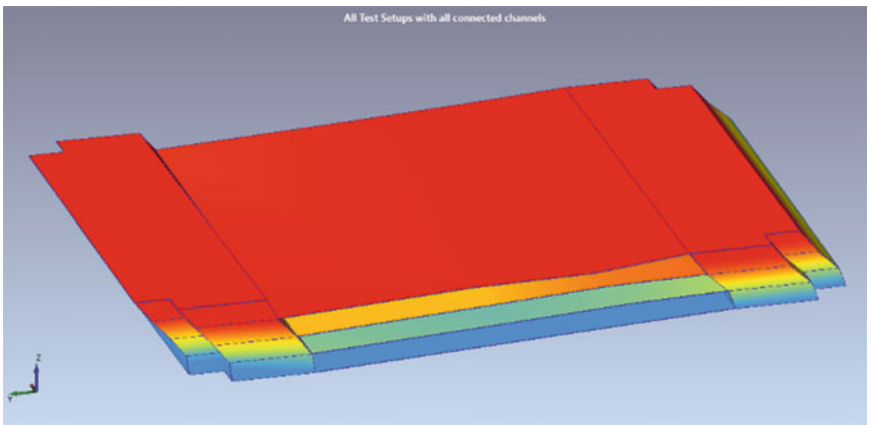


**Fig. 16.11** Mode 1, 1st N–S longitudinal at 3.05 Hz

## 16.4 Comparison with the Results Before Seismic Retrofit

Another Ambient Vibration Test was carried out in March 2014, before the seismic upgrade interventions. Details on the test and the results can be found in literature [3, 4]. The results in terms of natural frequencies are summarized and compared in Table 16.2.

After the structural upgrade, the increase in frequency is found to be around 10% for the fundamental mode. This pattern does not hold for the higher modes, where a clear trend cannot be recognized and the results of the second test do not differ significantly from the ones obtained during the first test.

The two ambient tests were planned according a similar method, the only condition that changed was the traffic volume experienced by the Parkade. The first test was conducted during a weekday, when the operational condition is higher level of traffic, while the second test was performed on a Saturday and less vehicles were present in the structure. Provided that a common trend for the change in values cannot be determined, the difference in frequency is expected to be the result of the seismic upgrade interventions only, or however, that the traffic conditions do not represent a significant variable in this study.

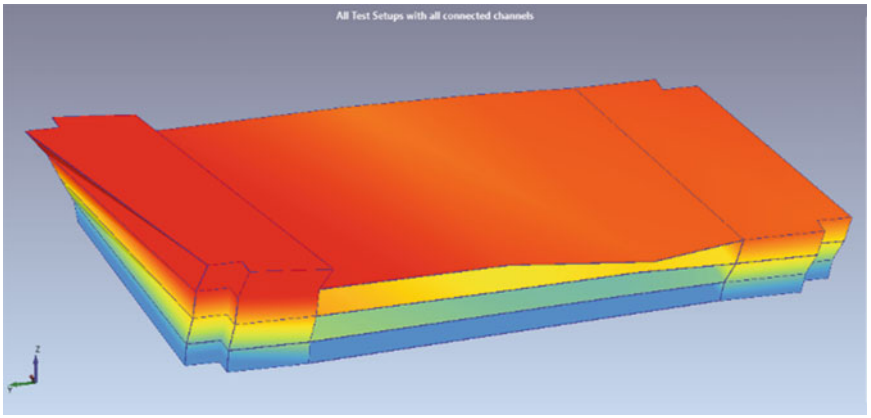


**Fig. 16.12** Mode 2: 1st torsion at 3.82 Hz

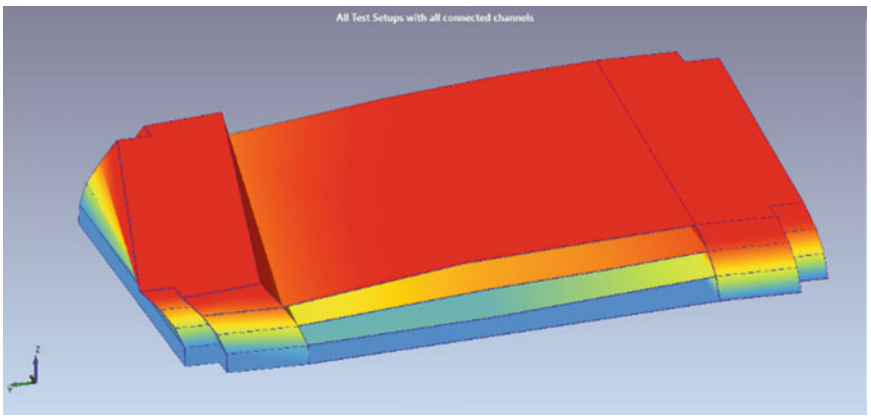


**Fig. 16.13** Mode 3: 1st torsion and 1 E–W transversal at 4.58 Hz

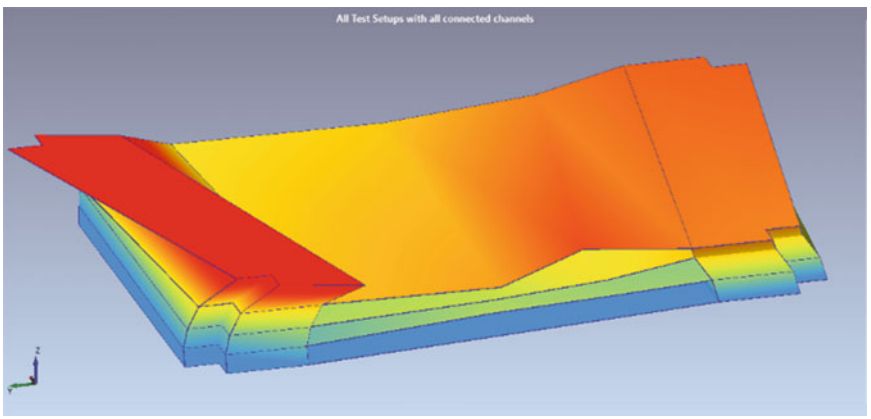


**Fig. 16.14** Mode 4: 2nd torsion at 5.94 Hz

## 16.5 Conclusions

As a result of the Ambient Vibration Test, six modes have been identified up to a frequency of about 8.5 Hz. The fundamental mode occurs at 3.05 Hz and corresponds to a first bending mode in the N–S longitudinal direction. The results obtained with the different techniques in frequency and time domain agree reasonably well with each other. The presence of the mode shapes identified before the structural interventions was also confirmed by the second test.

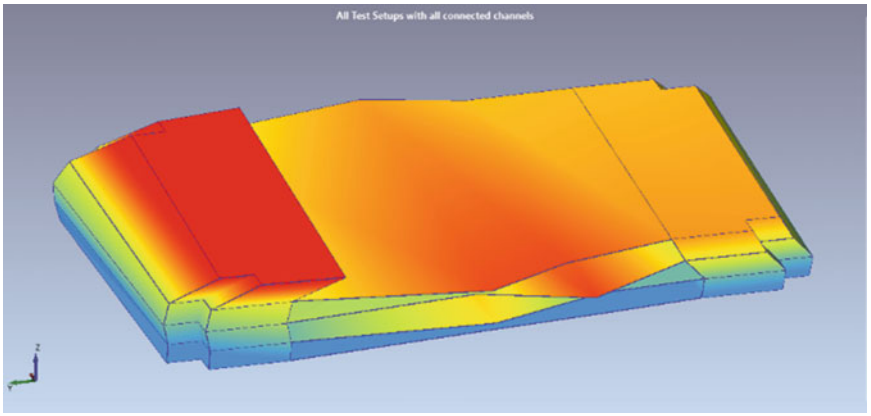


**Fig. 16.15** Mode 5: 2nd N–S longitudinal at 7.07 Hz, antisymmetric mode

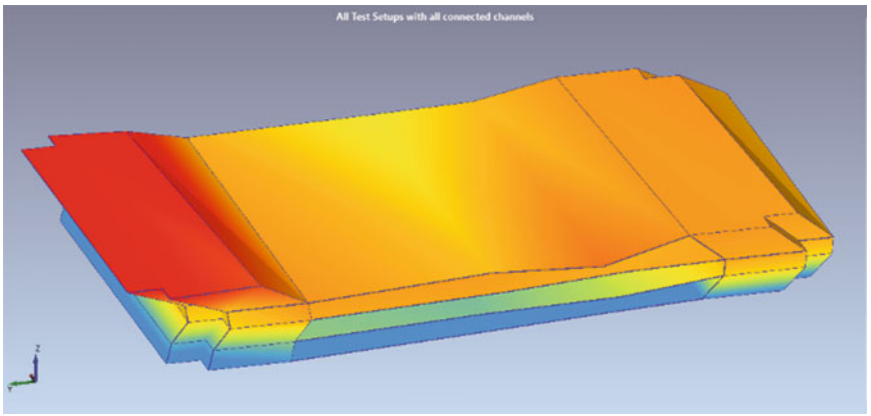


**Fig. 16.16** Mode 6: 3rd N–S longitudinal at 8.34 Hz, symmetric mode

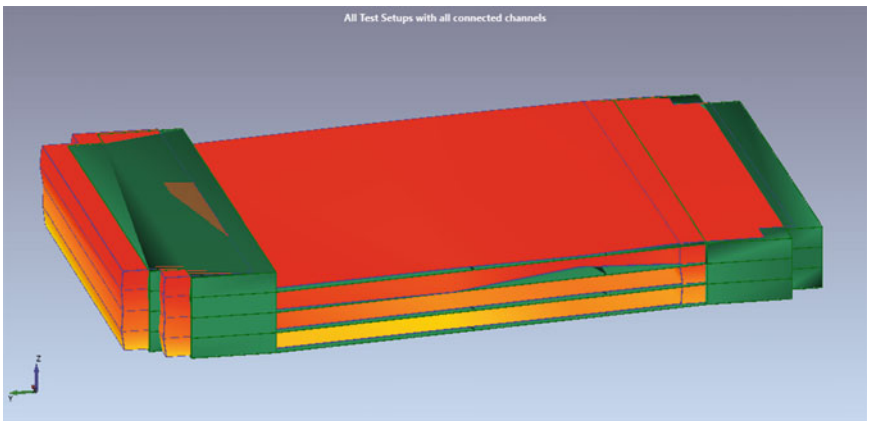


**Fig. 16.17** Site period at 0.64 Hz, undeformed configuration in *solid green color*

The comparison of the results between the two tests led to an increase of the first fundamental frequency of about 10%, which results into an increase of roughly 20% on the overall stiffness of the structure. A similar trend could not be recognized for the higher frequencies in the longitudinal direction, nor for the transversal and torsional modes of vibration. These findings were confirmed by the interventions for seismic upgrade, as they were made mainly on the lower floor and they were expected to modify significantly the stiffness in the longitudinal direction.

In addition to what found with the 2014 test, with the test preformed in 2015 after the structural interventions was also possible to clearly identify the site period at a frequency of about 0.64 Hz.

**Table 16.1** Summary of the results of the ambient vibration test of March 2015

| | Frequency [Hz] | | | Damping [%] | | |
|---|---|---|---|---|---|---|
| Mode | FDD | EFDD | SSI-PC | EFDD | SSI-PC | Comment |
| Site period | 0.641 | 0.651 | – | 3.52 | – | Site period |
| 1 | 3.047 | 3.064 | 3.059 | 3.24 | 3.272 | 1st N–S longitudinal |
| 2 | 3.822 | 3.904 | 3.897 | 2.37 | 3.617 | 1st torsional |
| 3 | 4.578 | 4.48 | 4.36 | 1.48 | 5.502 | 1st torsional + 1st E–W transversal |
| 4 | 5.941 | 5.914 | 5.949 | 1.08 | 2.395 | 2nd torsional |
| 5 | 7.069 | 7.09 | 7.184 | 0.24 | 3.438 | 2nd N–S longitudinal antisymmetric |
| 6 | 8.344 | 8.318 | 8.499 | 0.40 | 2.671 | 3rd N–S longitudinal symmetric |

**Table 16.2** Comparison of the results before and after the seismic upgrade

| Mode | 2014 FDD results | 2015 FDD results | Difference [Hz] | Difference [%] |
|---|---|---|---|---|
| 1 | 2.756 | 3.047 | 0.291 | 10.56% |
| 2 | 3.875 | 3.822 | −0.053 | −1.37% |
| 3 | 4.413 | 4.578 | 0.165 | 3.74% |
| 4 | 5.781 | 5.941 | 0.16 | 2.77% |
| 5 | 7.25 | 7.069 | −0.181 | −2.50% |
| 6 | 7.931 | 8.344 | 0.413 | 5.21% |

**Acknowledgements** The authors would like to acknowledge the technical and financial support of the Earthquake Engineering Research Facility (EERF) at the University of British Columbia, in Vancouver. The authors wish to acknowledge Amir Deris, Jesper Pedersen, Louis Moskven and Matthew Liman, graduate students at UBC, for their help during the Ambient Vibration Test and the data acquisition process. The help of Dr. Tim White is greatly appreciated, for providing the authors with information about the seismic upgrade interventions on the Parkade. The authors would like to thank Mr. André Harrmann, Associate Project Manager of Infrastructure Development, Project Services at UBC for providing access and information about the Parkade. Finally, the authors would like to thank Dr. Palle Andersen of Structural Vibration Solutions A/S for providing a special license of ARTeMIS Modal.

## References

1. MoHo s.r.l.: MOHO Sience and Technology. Venice
2. Structural Vibration Solutions A/S: Artemis. Software for Operational Modal Analysis. Aalborg
3. Capraro, I., Pan, Y., Rollins, K., Gao, W., Ventura, C.E.: Ambient vibration testing of a 4-storey parking garage. In: IMAC XXXIII, Orlando (2015)
4. Capraro, I., Ventura, C.E.: Model updating of a 4-storey parking garage using ambient vibration measurements. In: 11th Canadian Conference on Earthquake Engineering, Victoria (2015)

# Chapter 17
# Analytical and Experimental Study of Eddy Current Damper for Vibration Suppression in a Footbridge Structure

**Wai Kei Ao and Paul Reynolds**

**Abstract** Eddy current damping has been extensively developed in recent years and is widely used in the mechanical engineering sector, for example, in railway and turbine braking systems as well as in car vibration control systems. Vibration control approaches for civil engineering structures still usually rely on more traditional approaches, such as viscous and tuned mass dampers. The use of novel Eddy current damping devices has the potential to complement these traditional approaches and is the focus of the work presented here.

The Eddy current damper (ECD), which is a kind of electromagnetic induction damper, comprises a permanent magnet, a conductor and framing components. In this study, an ECD is developed and investigated to provide an alternative to viscous dampers that often exhibit undesirable non-linear characteristics arising from friction. Since the moving components of an ECD are not in contact, the influence of friction is negligible. A finite element model is initially used to evaluate the ECD damping properties and employed on a footbridge structure. The finite element and analytical results demonstrate satisfactory augmentation of damping effect under both random and harmonic signal input.

**Keywords** Eddy current damper (ECD) • Permanent magnet • Conductive material • Electromagnetic forces • Method of image

## 17.1 Introduction

The research work described here focuses on improving the vibration serviceability performance of civil engineering structures, for example, buildings, floors and footbridges subjected to different types of dynamic excitation. This is required since increasing problems with vibrations have been observed as a consequence of the increased use of very slender and flexible structures with low inherent damping.

Previously, there have been many approaches used to tackle vibration serviceability problems, including passive (e.g. tuned mass dampers (TMD), viscoelastic dampers (VE) and friction dampers), active (e.g. active mass dampers) and semi-active (e.g. magnetorheological dampers) techniques.

As an alternative to traditional vibration suppression devices, Eddy current damping (ECD) devices have been proposed to suppress system vibrations in the mechanical sector. The concept of passive ECD is to utilise relative motion between a permanent magnet and a conductor to create a resistance force. For a braking system [1], a cylindrical magnet and conductor plate of arbitrary shape were chosen to provide Eddy current damping according to their relative motion. After that, a simple theoretical study of rectangular magnet and conductor geometry ([2] and [3]) was developed. It included a calculation of induced electrical intensity during the conductive plate passed through a rectangular geometry magnet. Coulomb's law was used and assumed the magnet had an infinite boundary.

A simple example of ECD is shown in [4], which considers the example of a neodymium magnet dropping through a conductive tube. In this example, the magnet is slowed as a result of resistance forces developed by the induced Eddy currents in the tube. This simple model illustrates resistance to motion, which can be used to generate vibration damping via fundamental electromagnetic induction theory.

Some other examples have been used in a small scale structure [5] and [6], where a non-contact Eddy current damper was applied to perform vibration suppression on a small scale cantilever beam. These are just some of a large number of previous ECD studies that illustrate the use of this induced resistance force to attenuate vibration.

W.K. Ao (✉) • P. Reynolds
Vibration Engineering Section, College of Engineering, Mathematics and Physical Sciences, University of Exeter, North Park Road, Exeter EX4 4QF, UK
e-mail: wka203@exeter.ac.uk; p.reynolds@exeter.ac.uk



J. Caicedo, S. Pakzad (eds.), *Dynamics of Civil Structures, Volume 2*, Conference Proceedings of the Society for Experimental Mechanics Series, DOI 10.1007/978-3-319-54777-0_17

Large scale classical tuned mass dampers (TMD) can be employed to provide an effective solution to mitigate vibration problems in civil engineering structures. Usually, viscous dampers are utilised to achieve the required damping in the TMDs. Whilst the design of such dampers tends to be simple, they have several disadvantages. These include oil leakage and the fact that the magnitude of damping cannot usually be adjusted after installation, leading to sub-optimal TMD performance. Therefore, an ECD design was investigated [7] to provide Eddy current damping to an optimally designed large scale TMD. In [8], the basic theoretical and experimental analysis of a magnetically damped TMD was presented and a laboratory scale ECD was implemented to perform vibration suppression on a small mock-up bridge structure.

This paper describes firstly the fundamental electromagnetic induction theory, which can be utilised to calculate the analytical damping force of an ECD involving the classical infinite and finite (method of image) boundary of a conductor. Next, a case study of a footbridge structure is presented, which uses a TMD design with Eddy current damping element. This work includes a finite element (FE) model that can be compared to the analytical calculation.

## 17.2 Fundamental Electromagnetic Induction Theory

The basic law of electromagnetism is Faraday's law or electromagnetic induction. The relative motion between a magnetic field and a conductor can induce an electromotive force (emf) and hence a current within the conductor (Eddy current). This represents an electric generator converting mechanical energy into electrical energy. In this study, this induced energy is being utilised to provide the non-contact Eddy current damping.

### *17.2.1 Modelling Eddy Currents and Electromagnetic Force of ECD*

Figure 17.1 shows a rectangular conductive plate which is assumed to have infinite dimension size [9] and [10]. On the conductive plate, there is a finite sized permanent magnet. The dimension of the magnet is $2a$ in length, $2b$ in width and $t$ in thickness. Note that the magnet is rectangular in shape.

The magnetic flux density is directed into the page as shown in Fig. 17.1. Therefore, the magnetic flux density is in the negative $z$ direction. The vector of magnetic flux density $\boldsymbol{B}$ can then be expressed as

$$\boldsymbol{B} = B_x \boldsymbol{i} + B_y \boldsymbol{j} + (-B_z)\boldsymbol{k} \tag{17.1}$$

where $B_x$, $B_y$ and $B_z$ are the individual components of magnetic flux density $\boldsymbol{B}$ in the $x$, $y$ and $z$ directions, respectively. Note that in this case the magnetic flux density of the $x$ and $y$ components is zero, and hence only the $z$ direction component contributes to the electromagnetic force.

In Fig. 17.1c, the conductive plate is assumed to move in the positive horizontal direction. The velocity vector $\boldsymbol{v}$ can be written as

$$\boldsymbol{v} = v_x \boldsymbol{i} + v_y \boldsymbol{j} + v_z \boldsymbol{k} \tag{17.2}$$

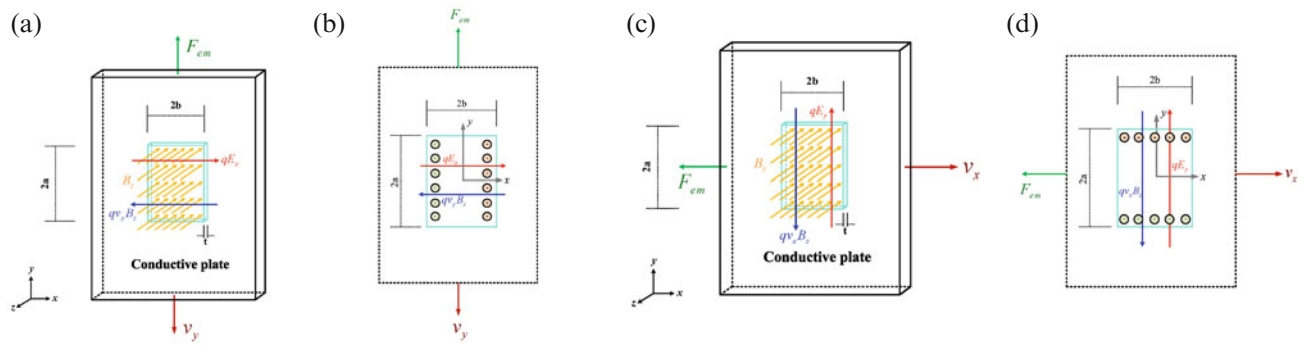


**Fig. 17.1** Concept of generation of electromagnetic force via moving plate in a magnetic field. (**a**) *3D view* of vertically moving conductive plate. (**b**) *Front view* with electrical charge moving in $V_y$. (**c**) *3D view* of horizontally moving conductive plate. (**d**) *Front view* with electrical charge moving in $V_x$

which can be re-written as

$$\boldsymbol{v} = v_x \boldsymbol{i} + (-v_y)\boldsymbol{j} + v_z \boldsymbol{k} \tag{17.3}$$

Figure 17.1a shows the conductive plate $v_y$ moving in the negative $y$ direction, whilst the other directional components have no contribution. In addition, all of these values are time-invariant.

In general, several basic electromagnetic theories can now be used to calculate the electromagnetic damping force.

The magnetic field $\boldsymbol{B}$ is defined in terms of the force $\boldsymbol{F_B}$ acting on a test particle with charge $q$ moving through the field with velocity $\boldsymbol{v}$. Therefore, the magnetic force or Lorentz's force on the charge $q$ can be obtained as follows:

$$\boldsymbol{F_{em}} = q\boldsymbol{v} \times \boldsymbol{B} = \oint i d\boldsymbol{l} \times \boldsymbol{B} = \oint \frac{i}{\boldsymbol{A}} \boldsymbol{A} \cdot d\boldsymbol{l} \times \boldsymbol{B} = \int \frac{i}{\boldsymbol{A}} d\boldsymbol{V} \times \boldsymbol{B} = \int \boldsymbol{J} \times \boldsymbol{B} d\boldsymbol{V} \tag{17.4}$$

where $i$ is the electric current, $\boldsymbol{A}$ is an outward normal unit area vector, $\boldsymbol{V}$ is a volume of magnetic pole projection, and $\boldsymbol{J}$ can be defined as the current density, which stands for current per area. However, the current density can also be defined by multiplying the conductivity of the material and the electric field, as follows:

$$\boldsymbol{J} = \sigma \boldsymbol{E} \tag{17.5}$$

The total electric field intensity induced on the conductive plate can be calculated as

$$\boldsymbol{E} = \boldsymbol{E_{ind}} + \boldsymbol{E_v} = \boldsymbol{E_{ind}} + \boldsymbol{v} \times \boldsymbol{B} \tag{17.6}$$

where $\boldsymbol{E}$ is total electric field intensity, $\boldsymbol{E_{ind}}$ is the induced electric field intensity of the electric charged particle, and $\boldsymbol{E_v}$ is an electric field intensity caused by the magnetic field in addition to that of the electric charged particle, which is also the cross product of velocity and magnetic flux density. Equation (17.5) can now be rewritten as follows:

$$\boldsymbol{J} = \sigma \left(\boldsymbol{E_{ind}} + \boldsymbol{E_v}\right) \tag{17.7}$$

## 17.3 The Method of Image Current

The previous section was developed based on a conductive plate with infinite $x$ and $y$ dimensions. In this section, the method of image ([11] and [12]) is presented to calculate the ECD electromagnetic force, using finite $x$ and $y$ dimensions, which cause the Eddy currents to be zero at the edges of the conductive plate.

The solid line in Fig. 17.2 shows the infinite boundary condition of Eddy current density $J^{(p)}$. The two tails of the curve extend infinitely in the positive and negative directions. Due to the finite actual dimensions of the plate, the curve does not exactly express the real current flowing, which potentially might cause a calculation error.

To solve this problem, the tails of the profile of $\boldsymbol{J^{(P)}}$ are reflected about axes of symmetry corresponding with the edges of the conductive plate. In this case, the image current density on the left-hand edge ($\boldsymbol{J^{i_{left}}}$) is reflected to the right and the right-hand edge $\boldsymbol{J^{i_{right}}}$ is reflected to the left. Hence, the edge effect can be eliminated.

From this point of view, when the conductive plate moves in the $y$ direction, the mathematical expression of the primary and image current density shows the following relationship

$$\boldsymbol{J'_x} = J'_x \boldsymbol{i} = J_x^{(P)} \boldsymbol{i} - J_x^{(i_{right})} \boldsymbol{i} - J_x^{(i_{left})} \boldsymbol{i} \tag{17.8}$$

The image Eddy current density is symmetrical to the primary Eddy current density. Looking at the $y$ movement of the conductive plate, $\boldsymbol{J^{i_{left}}}$ can be expressed in terms of $\boldsymbol{J^{(P)}}$ using a coordinate transformation, as given by

$$J_x^{(i_{right})} \boldsymbol{i} = J_x^{(P)}(2B - x, y)\boldsymbol{i} = \sigma \left\{ -\frac{v_y B_z}{2\pi} \left[ \tan^{-1}\left(\frac{y-a}{2B-x-b}\right) - \tan^{-1}\left(\frac{y+a}{2B-x-b}\right) + \tan^{-1}\left(\frac{y+a}{2B-x+b}\right) - \tan^{-1}\left(\frac{y-a}{2B-x+b}\right) \right] \right\} \boldsymbol{i} \tag{17.9}$$

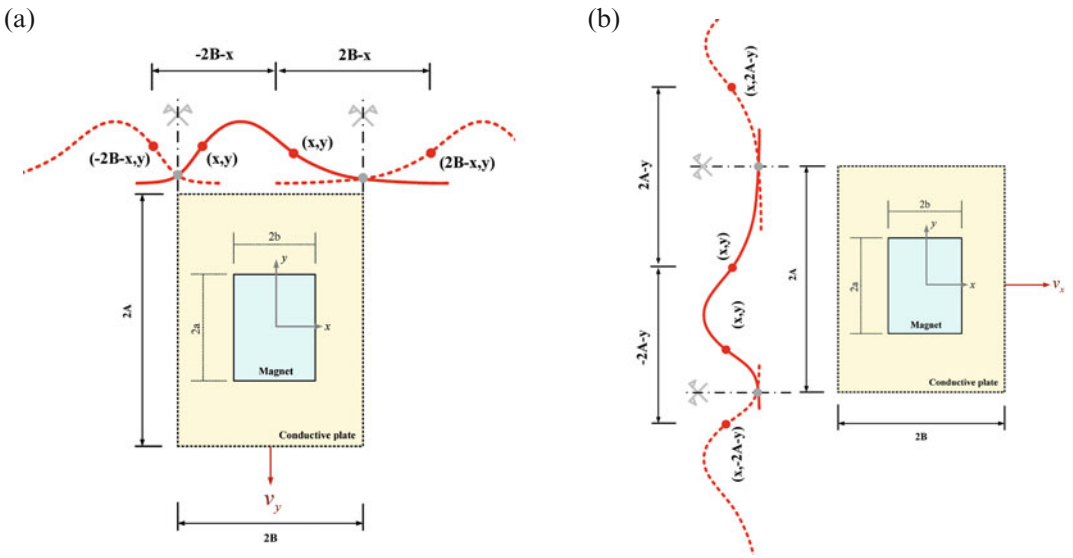


**Fig. 17.2** Eddy current density using method of image for moving conductive plate in $y$ and $x$ direction. (**a**) Single magnetic pole projections moving conductive plate in $y$ direction. (**b**) Single magnetic pole projections moving conductive plate in $x$ direction

The same method can be used to express $\boldsymbol{J}^{i_{right}}$ in terms of $\boldsymbol{J}^{(P)}$, as given by

$$\begin{aligned} J_x^{(i_{left})}\boldsymbol{i} &= J_x^{(P)}(-2B-x,y)\,\boldsymbol{i} \\ &= \sigma\left\{-\frac{v_y B_z}{2\pi}\left[\tan^{-1}\left(\frac{y-a}{-2B-x-b}\right)-\tan^{-1}\left(\frac{y+a}{-2B-x-b}\right)+\tan^{-1}\left(\frac{y+a}{-2B-x+b}\right)-\tan^{-1}\left(\frac{y-a}{-2B-x+b}\right)\right]\right\}\boldsymbol{i} \end{aligned} \tag{17.10}$$

When the updated Eddy current density is obtained, it can be substituted into Eq. (17.4) to calculate the electromagnetic force by $\boldsymbol{J}'_{\boldsymbol{x}}$. Hence, the force can be written as

$$\boldsymbol{F}_{\boldsymbol{em,y}} = F_{em,y}\boldsymbol{j} = -\int J_x' \times B_z dVj = -t\int_{-a}^{a}\int_{-b}^{b}\left(J_x{}^{(P)} - J_x{}^{(i_{right})} - J_x{}^{(i_{left})}\right)B_z dxdy\boldsymbol{j} \tag{17.11}$$

Similarly, moving the conductive plate in the $x$ direction as shown in Fig. 17.2b, the method of image can also be used. Therefore, the total updated Eddy current density in the $y$ component can be shown as follows

$$\boldsymbol{J}'_{\boldsymbol{y}} = J'_y\boldsymbol{j} = J_y^{(P)}\boldsymbol{j} - J_y^{(i_{right})}\boldsymbol{j} - J_y^{(i_{left})}\boldsymbol{j} \tag{17.12}$$

where coordinate transformations can again be used to shift the primary Eddy current density $\boldsymbol{J}_{\boldsymbol{y}}^{(\boldsymbol{P})}$ to locations $(x, 2A-y)$ and $(x, -2A-y)$, as given by Eqs. (17.13) and (17.14), respectively

$$\begin{aligned} J_y^{(i_{right})}\boldsymbol{j} &= J_y^{(P)}(x,2A-y)\boldsymbol{j} \\ &= \sigma\left\{-\frac{v_x B_z}{2\pi}\left[\tan^{-1}\left(\frac{x-b}{2A-y-a}\right)-\tan^{-1}\left(\frac{x+b}{2A-y-a}\right)+\tan^{-1}\left(\frac{x-b}{2A-y+a}\right)-\tan^{-1}\left(\frac{x+b}{2A-y+a}\right)\right]\right\}\boldsymbol{j} \end{aligned} \tag{17.13}$$

$$\begin{aligned} J_y^{(i_{left})}\boldsymbol{j} &= J_y^{(P)}(x,-2A-y)\boldsymbol{j} \\ &= \sigma\left\{-\frac{v_x B_z}{2\pi}\left[\tan^{-1}\left(\frac{x-b}{-2A-y-a}\right)-\tan^{-1}\left(\frac{x+b}{-2A-y-a}\right)+\tan^{-1}\left(\frac{x-b}{-2A-y+a}\right)-\tan^{-1}\left(\frac{x+b}{-2A-y+a}\right)\right]\right\}\boldsymbol{j} \end{aligned} \tag{17.14}$$

Hence, the total Eddy current density in the $x$ direction can be calculated by combining $J_y^{(P)}\boldsymbol{j}$, $J_y^{(i_{right})}\boldsymbol{j}$ and $J_y^{(i_{left})}\boldsymbol{j}$ and then the result can be used to calculate the electromagnetic force, as given by

$$\boldsymbol{F_{em,x}} = F_{em,x}\boldsymbol{i} = -\int J_y' \times B_z dVi = -t\int_{-a}^{a}\int_{-b}^{b}\left(J_y{}^{(P)} - J_y{}^{(i_{right})} - J_y{}^{(i_{left})}\right)B_z dxdy\boldsymbol{i} \tag{17.15}$$

## 17.4 ECD Application to Tuned Mass Damper Design for a Footbridge

In this section a real footbridge is used as a case study. Figure 17.3 shows a footbridge located in the UK. The structure is very slender and has three long spans between two column supports. An ECD is considered as a damping element within a TMD to achieve the required damping for the project.

Figure 17.4a shows the results of modal analysis carried out by the bridge designer. It can be seen that the second mode shape of this structure shows significant vertical bending.

A vibration serviceability assessment of the bridge was carried out by Full Scale Dynamics Ltd (FSDL). For application of the excitation scenarios from the NA to BS EN 1991-2:2003, Fig. 17.4b and c show responses calculated due to a group of people jogging and a crowd of people walking. For the response analysis, modal damping ratios were assumed in all modes of vibration to be 0.2%. It was assumed that the maximum allowed peak acceleration was 1.0 m/s$^2$ and the walking path was along the centreline of the bridge.

For both cases of group jogging and crowd walking, the responses exceeded the allowed limits in the second span of the footbridge, which represented a potential vibration serviceability problem on this structure. Hence, the use of a tuned mass damper (TMD) box (as shown in Fig. 17.5) was considered to overcome the vibration problem.

The basic components of a TMD are tuning mass, stiffness element and damping device. An ECD can be chosen to provide a damping element for the TMD. Because the ECD is an non-contact damper, it does not have any additional Coulomb's friction contribution. The space available for the ECD is 640 × 260 × 88 mm. From the TMD design, the required damping coefficient is 2.4 × 10$^3$ Ns/m, the maximum velocity is ±0.48 m/s and the required stroke is ±30 mm.

Section 17.2.1 showed the copper plate moving in the vertical direction. The horizontal magnetic pole projection can be used for ECD design to achieve the required damping. Therefore, the layout shown in Fig. 17.6 can be utilised.

The clearance space between the TMD mass block and bridge structure is 88 mm, including the moving stroke ±30 mm. The magnet height is designed to have 28 mm height. Figure 17.6b and c show the relative dimensions of the ECD design. The ECD has a volume of 350 × 182 × 56.5 mm and the copper plate has 4 mm thickness with height 30 mm.

Figure 17.7a shows the FEM meshing of the ECD. As the copper plate moves with velocity 0.48 m/s, the damping force calculation is shown in Fig. 17.7b. The vertical component of the output force is the target design damping force. The maximum value achieved is 1260 N and the average value is 1150 N, which meets the design requirement. The damping

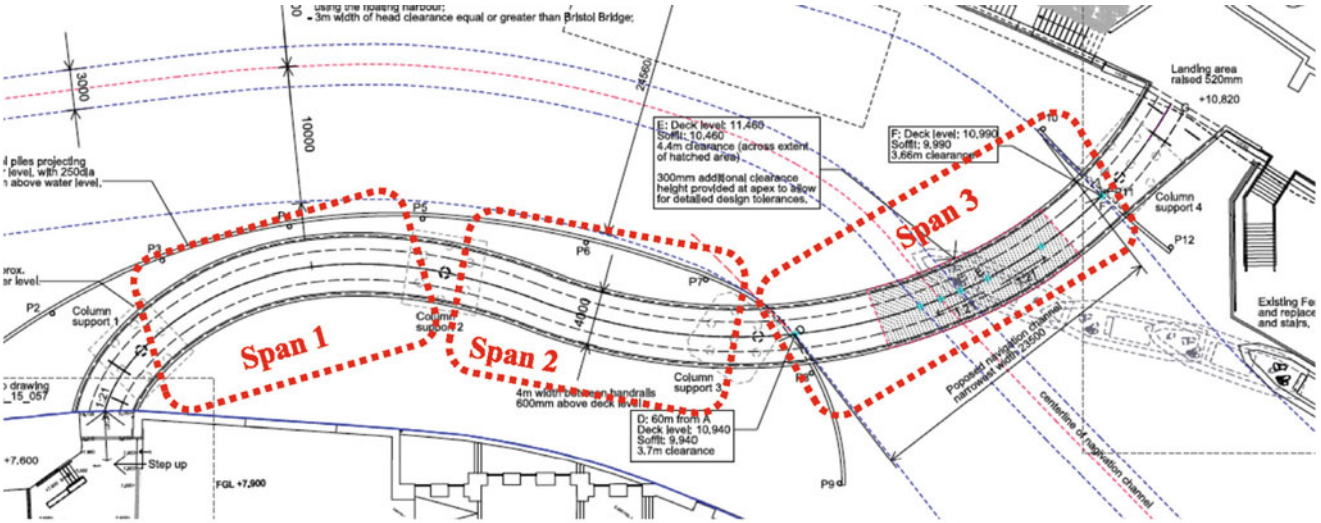


**Fig. 17.3** Case study footbridge

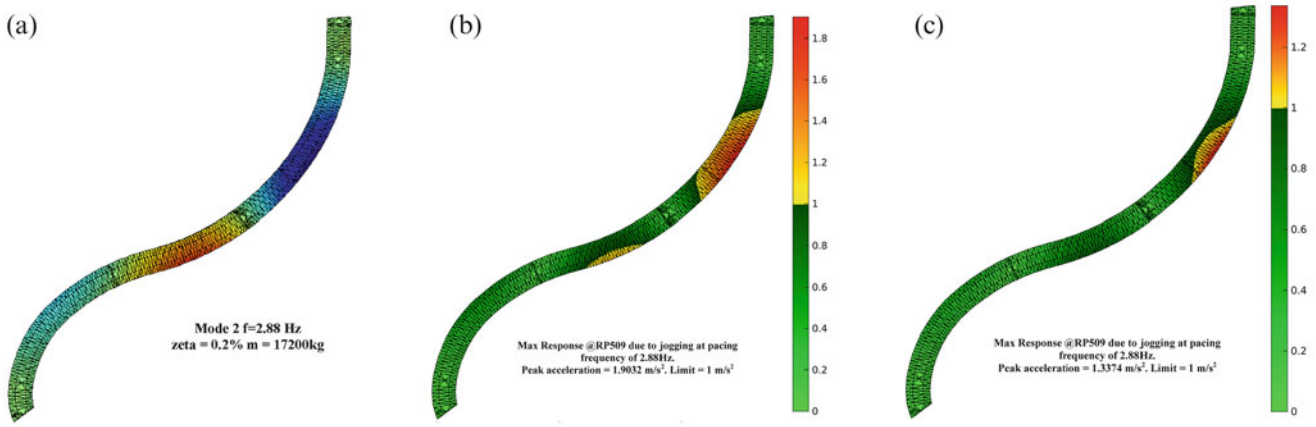


**Fig. 17.4** Case study footbridge vibration serviceability assessment. (**a**) Second mode shape. (**b**) Group jogging 0.2% damping. (**c**) Crowd walking 0.2% damping

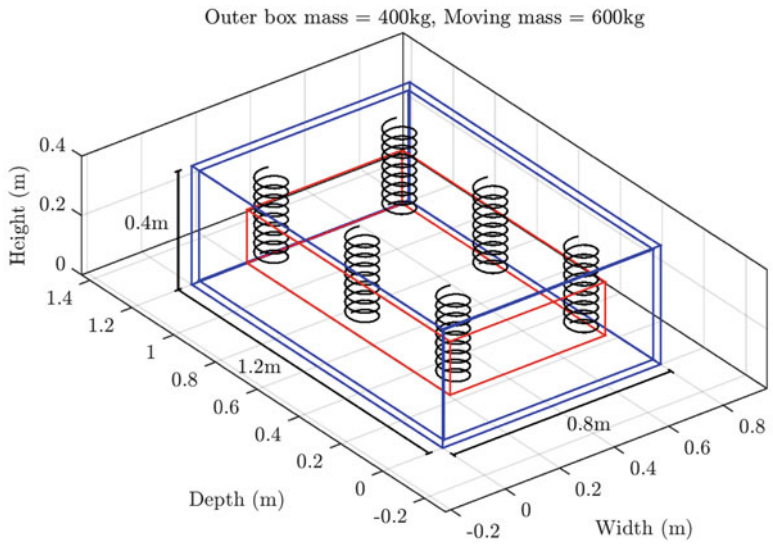


**Fig. 17.5** Schematic 3D view of the TMD box

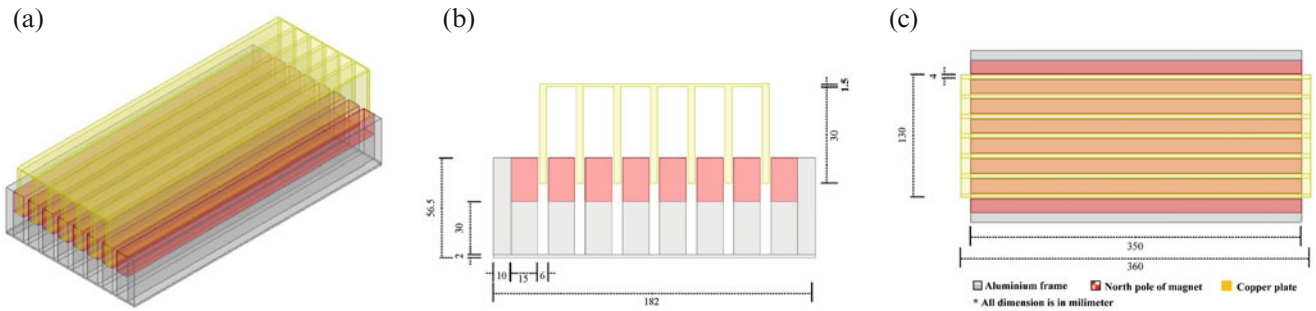


**Fig. 17.6** Case study footbridge Eddy current damper design. (**a**) Conceptual Eddy current damper. (**b**) *Front view*. (**c**) *Top view*

force from FEM can be compared to the analytical calculation. Using infinite boundary condition, the damping force is 1398 N, while when using the method of image, the force is 1233 N. It can see that the analytical calculation is higher than the FEM results, which might be caused by the assumption of uniform magnetic field distribution and other directional edge effect of the ECD analytical calculation. However, further discussion is not included here.

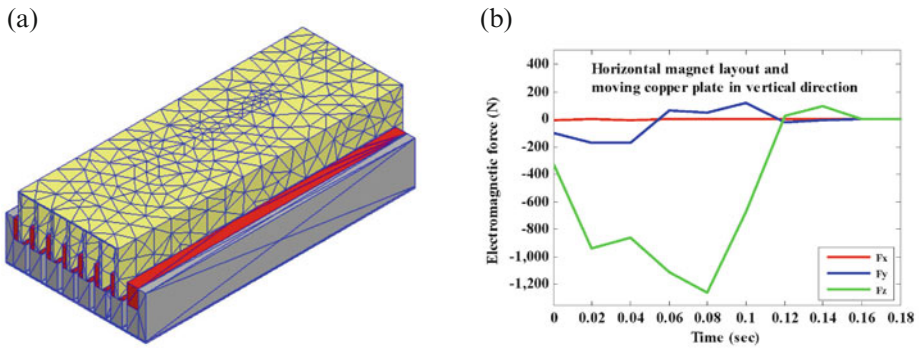


**Fig. 17.7** Finzels Reach footbridge FEM and damping force outcome. (**a**) Meshing of ECD. (**b**) ECD damping force

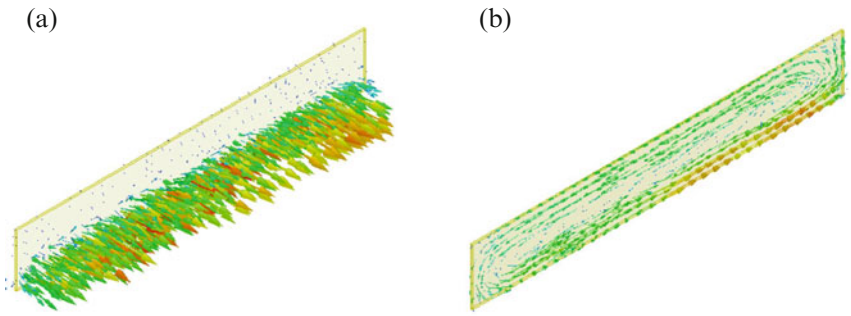


**Fig. 17.8** ECD of Finzels Reach footbridge magnetic flux density and current density of one copper plate demonstration. (**a**) Magnetic flux density. (**b**) Current density

On the other hand, the relative magnetic flux density can be shown in Fig. 17.8a. The vector plot demonstrates the orientation of magnet flux density points in a single direction. The current density is shown in Fig. 17.8b, where it can be seen that the flowing current tends to loop in one direction. The above vector plots are selected for an instantaneous time. However, the distribution of the parameters at different time steps can change over time. This shows that the uniformity assumption might not be appropriate, but it is good enough to perform a preliminary design of the ECD.

## 17.5 Discussion and Conclusions

This study has investigated an alternative damping source for inclusion in a TMD to mitigate vibration of a footbridge structure. Therefore, an electromagnetic damper (EMD) or Eddy current damper (ECD) has been considered for this application. Based on this idea, electromagnetic induction theory was presented, including the method of image to find out the electromagnetic damping force analytically.

After the introduction of the ECD, a footbridge structure was used as a case study. The vibration serviceability assessment of the footbridge illustrated that it had a potential problem over the second and third span, and the adoption of a TMD was recommended to deal with this circumstance. An ECD was considered as the damping element of the TMD, in contrast to the use of traditional viscous damping. After the design process, a projection panel of ECD with eight single magnetic poles was presented. The FEM and analytical simulation results showed that such a damper can match the design requirement in this case.

**Acknowledgements** The authors acknowledge the financial assistance of the UK Engineering and Physical Sciences Research Council (EPSRC) through a Leadership Fellowship Grant (Ref. EP/J004081/2) entitled “Advance Technologies for Mitigation of Human-Induced Vibration”.

## References


1. Nagaya, K., Kojima, H., Karube, Y., Kibayashi, H.: Braking forces and damping coefficients of eddy current brakes consisting of cylindrical magnets and plate conductors of arbitrary shape. IEEE Trans. Magn. **6**, 2136–2145 (1984)
2. Heald, M.A.: Magnetic braking: improved theory. Am. J. Phys. **6**, 521 (1988)
3. Cadwell, L.H.: Magnetic damping: analysis of an eddy current brake using an airtrack. Am. J. Phys. **7**, 917 (1996)
4. Hahn, K.D., Johnson, E.M., Brokken, A., Baldwin, S.: Eddy current damping of a magnet moving through a pipe. Appl. Math. Mech. **12**, 1066 (1998)
5. Sodano, H.A., Inman, D.J.: Non-contact vibration control system employing an active eddy current damper. J. Sound Vib. **4–5**, 596–613 (2007)
6. Yang, Y., Xu, D., Liu, Q.: Milling vibration attenuation by eddy current damping. Int. J. Adv. Manuf. Technol. **81**(1–4), 445 (2015)
7. Wang, Z., Chen, Z., Wang, J.: Feasibility study of a large-scale tuned mass damper with eddy current damping mechanism. J. Dyn. Syst. Meas. Control **3**, 391–401 (2012)
8. Bourquin, F., Caruso, G., Peigney, M., Siegert, D.: Magnetically tuned mass dampers for optimal vibration damping of large structures. Smart Mater. Struct. **8**, 085009 (2014)
9. Lee, K., Park, K.: Modeling eddy currents with boundary conditions by using Coulomb's law and the method of images. IEEE Trans. Magn. **38**(2), 1333–1340 (2002)
10. Zuo, L., Chen, X., Nayfeh, S.: Design and analysis of a new type of electromagnetic damper with increased energy density. J. Vib. Acoust. **133**(4), 041006 (2011)
11. Bae, J.-S., Kwak, M.K., Inman, D.J.: Vibration suppression of a cantilever beam using eddy current damper. J. Sound Vib. **284**(3–5), 805–824 (2005)
12. Pluk, K.J.W., Member, S., Beek, T.A.V., Jansen, J.W., Lomonova, E.A., Member, S.: Modeling and measurements on a finite rectangular conducting plate in an Eddy current damper. IEEE Trans. Ind. Electron. **61**(8), 4061–4072 (2014)

# Chapter 18
# Nonlinear Damping in Floor Vibrations Serviceability: Verification on a Laboratory Structure

**Onur Avci**

**Abstract** Damping is a critical parameter in dynamics of structures which has been proven to be dependent on the amplitude of the applied force on the structure. This is known as nonlinear damping or amplitude-dependent damping. While the nonlinear characteristics of damping have been studied thoroughly for earthquake and wind loading excitations; it has not been comprehensively studied for floor vibration serviceability applications.

This paper focuses on a laboratory structure in an attempt to shed some light on obtaining and verifying the modal damping ratio with experimental and analytical studies. Finite element models were built and updated per static and dynamic tests conducted in laboratory environment. The nonlinear damping behavior of the laboratory structure is verified for different amplitudes of sinusoidal excitations.

**Keywords** Floor vibrations • Serviceability • Damping • Nonlinear damping • Amplitude dependent damping

## 18.1 Introduction

Damping is a critical parameter in structural dynamics. Dealing with damping has been a challenge for floor vibrations researchers as the acceleration predictions are very sensitive to damping ratio values. While the nonlinear nature of damping is extensively researched for seismic and wind excitations [1–13], it is not studied in great detail for floor vibrations applications. Damping has been reported to have a material and non-material components. Material damping is due to the energy dissipation capacities of the structural materials. Non-material damping on the other hand, is due to the surroundings of the vibrating structure. Material damping has three components: Coulomb damping, viscous damping and radiation damping.

This paper focuses on the amplitude depending characteristics of damping based on the experiments conducted on a laboratory footbridge structure. The structure was studied extensively with static and dynamic tests; 3D finite element (FE) models were created. There has been numerous static and dynamics tests conducted on the structure, all of which were used to fine-tune the three-dimensional finite element model for various bottom chord extension configurations [14–21]. This paper is presenting the results of a study on the nonlinear damping behavior of the structure.

## 18.2 Experimental Modal Testing on the Laboratory Structure

The laboratory structure dimensions are 2.2 m by 9.2 m. The cold-formed deck is 38 mm deep and concrete slab depth is 114 mm resulting in a total slab depth of 152 mm. The slab is supported on two parallel 30 K7 × 9.2 m joist members at 1.2 m on center (Fig. 18.1).

Vibration testing is done for two different bottom chord extension configurations to determine the modal parameters (natural frequencies, mode shapes and modal damping ratios). Stage 1 is the configuration for bottom chords being extended to the supports and Stage 2 is the configuration for the bottom chords extensions are removed from the structural system. Individual FRF results, MEScope curve fitting approximations and FE model predictions are presented in Table 18.1 [15]. According to Table 18.1, removing the bottom chord extensions from the system (Stage 2) results in a 14% decrease in the natural frequency of the first bending mode (the frequency dropped from 8.08 Hz to 6.95 Hz). Stage 1 natural frequency

O. Avci (✉)
Department of Civil and Architectural Engineering, Qatar University, Doha, Qatar
e-mail: oavci@vt.edu



J. Caicedo, S. Pakzad (eds.), *Dynamics of Civil Structures, Volume 2*, Conference Proceedings of the Society for Experimental Mechanics Series, DOI 10.1007/978-3-319-54777-0_18

**Fig. 18.1** Laboratory structure, 2.2 m × 9.2 m

**Table 18.1** First bending mode natural frequencies and damping ratios for the footbridge [15]

| | First bending mode frequency, $f_n$ (Hz) | | | Modal damping ratio ($\xi$) | | |
|---|---|---|---|---|---|---|
| Stage | Individual FRF | Curve fitting of vibration data (MEScope) | FE model (SAP2000) | Half-power method (Individual FRF) | Curve fitting of vibration data (MEScope) | Time domain decay curves (filtered to capture first mode only) |
| 1 | 8.00 | 8.08 | 7.99 | 0.00284 | 0.00451 | 0.01300 |
| 2 | 6.95 | 6.95 | 7.03 | 0.00453 | 0.00448 | 0.02200 |

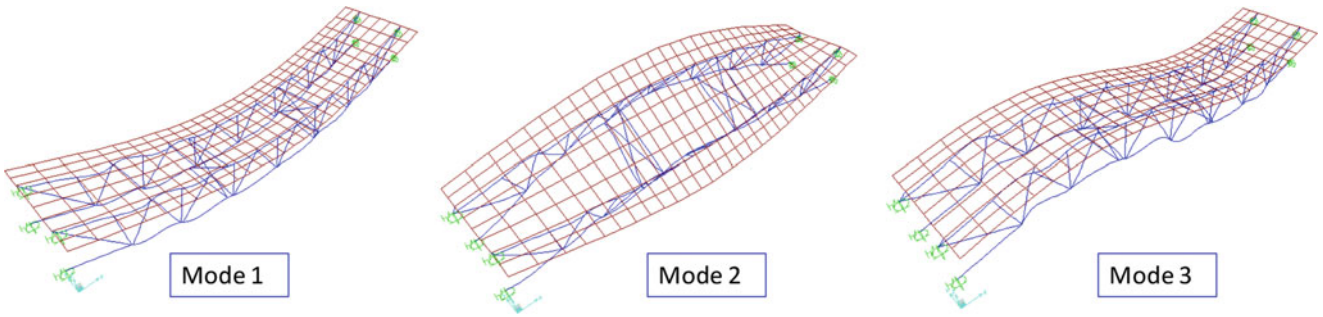


**Fig. 18.2** Mode shapes with commercial FE software

of the first mode is higher than the Stage 2 natural frequency which means the bottom chord extensions provided stiffness to the structure. From Table 18.1, it can be observed that the curve fitted MEScope and FE model (SAP2000) frequency predictions are in very good agreement (within 2%). Moreover, according to Table 18.1, the frequency domain methods for the prediction of modal damping ratio (half-power method and MEScope curve fits) do not agree [22]. The time domain method (simple decay curves) results in a higher damping ratio than the frequency domain method predictions.

As a result of the inconsistency in the modal damping ratio values of Table 18.1, it is not clear what to use for the damping values in the FE models. In order to overcome the modal damping ratio inconsistency, sinusoidal excitations are applied to the structure to put the system in resonance. By doing so, the effective mass procedure can be followed for the structure in resonance to find the modal damping ratios. FE model mode shapes are shown in Fig. 18.2.

## 18.3 Resonance of the Structure

### *18.3.1 Stage 1 Configuration*

For Stage 1, the structure was put in resonance by a shaker placed at the midspan, at three levels of excitation amplitudes. The results are shown in Table 18.2.

**Table 18.2** Test and FE model results for Stage 1

| Sine excitation amplitude at 8 Hz frequency | | Acceleration response amplitude (Test) | Calculated damping ratio ($\xi$) using Me = 0.470 M | Acceleration response amplitude SAP2000 | Acceleration response amplitude ratio: SAP2000/Test |
|---|---|---|---|---|---|
| (N) | (lbs) | (%g) | | (%g) | |
| 56.5 | 12.7 | 0.14 | 0.00690 | 0.135 | 0.964 |
| 118.8 | 26.7 | 0.26 | 0.00781 | 0.252 | 0.969 |
| 198.8 | 44.7 | 0.36 | 0.00944 | 0.348 | 0.967 |

**Table 18.3** Test and FE model results for Stage 2

| Sine excitation amplitude at 6.95 Hz frequency | | Acceleration response amplitude (Test) | Calculated damping ratio ($\xi$) using Me = 0.502 M | Acceleration response amplitude SAP2000 | Acceleration response amplitude ratio: SAP2000/Test |
|---|---|---|---|---|---|
| (N) | (lbs) | (%g) | | (%g) | |
| 33.8 | 7.6 | 0.12 | 0.00451 | 0.1226 | 1.022 |
| 53.4 | 12.0 | 0.17 | 0.00503 | 0.1736 | 1.021 |
| 120.1 | 27.0 | 0.24 | 0.00801 | 0.2453 | 1.022 |
| 195.7 | 44.0 | 0.32 | 0.00979 | 0.3271 | 1.022 |

### *18.3.2 Stage 2 Configuration*

For Stage 2, the structure was put in resonance again by a shaker placed at the midspan, at four levels of excitation amplitudes. The results are shown in Table 18.3.

## 18.4 Damping Ratio Back-Calculations Using Effective Mass

When the structure is in resonance, the resulting peak acceleration amplitude can be used to calculate the effective mass of the specific mode. The relationship between the effective mass, peak acceleration amplitude, the input excitation amplitude and the modal damping ratio can be derived.

It is known that for harmonic vibration with viscous damping:

$$m\ddot{u} + c\dot{u} + ku = p_0 \sin \omega t \tag{18.1}$$

$$u(t) = u_c(t) + u_p(t) \tag{18.2}$$

The transient decay component is:

$$u_c(t) = e^{-\xi\omega_n t}\left[A \cos \omega_D t + B \sin \omega_D t\right] \tag{18.3}$$

The steady-state response component is:

$$u_p(t) = C \sin \omega t + D \cos \omega t \tag{18.4}$$

$$\text{For } \omega = \omega_n; C = 0 \text{ and } D = \frac{-(u_{st})_0}{2\xi} \tag{18.5}$$

For $\omega = \omega_n$ and zero initial conditions;

$$\text{A} = \frac{(u_{st})_0}{2\xi} \text{ and } B = \frac{(u_{st})_0}{2\sqrt{1-\xi^2}} \tag{18.6}$$

$$(u_{st})_0 = \frac{p_0}{k} \tag{18.7}$$

$$u_0 = \frac{(u_{st})_0}{2\xi} \tag{18.8}$$

$$\omega_D \cong \omega_n \tag{18.9}$$

Therefore,

$$u(t) \cong \frac{(u_{st})_0}{2\xi}\left(e^{-\xi\omega_n t} - 1\right)\ cos\ \omega_n t \tag{18.10}$$

$$u(t) = e^{-\xi\omega_n t}\left[A\ cos\ \omega_D t + B sin\omega_D t\right] + C sin\omega t + D\ cos\ \omega t \tag{18.11}$$

$$u(t) = (u_{st})_0 \cdot \frac{1}{2\xi}\left[e^{-\xi\omega_n t}\left(\ cos\ \omega_D t + \frac{\xi}{\sqrt{1-\xi^2}} sin\omega_D t - \ cos\ \omega_n t\right)\right] \tag{18.12}$$

$$u(t) = (u_{st})_0 \cdot \frac{1}{2\xi} \cdot e^{-\xi\omega_n t}\left(\ cos\ \omega_D t + \frac{\xi}{\sqrt{1-\xi^2}} sin\omega_D t\right) - (u_{st})_0 \cdot \frac{1}{2\xi}\ cos\ \omega_n t \tag{18.13}$$

$$A = \frac{(u_{st})_0}{2\xi} \tag{18.14}$$

$$B = \frac{(u_{st})_0}{2\xi} \cdot \frac{\xi}{\sqrt{1-\xi^2}} = \frac{(u_{st})_0}{2\sqrt{1-\xi^2}} \tag{18.15}$$

For lightly damped structural systems;

$$\frac{\xi}{\sqrt{1-\xi^2}} sin\omega_D t \to 0 \tag{18.16}$$

Also, since

$$\omega_D \cong \omega_n \tag{18.17}$$

Then, Eq. (18.13) can be written as:

$$u(t) = (u_{st})_0 \frac{1}{2\xi}\left(e^{-\xi\omega_n t} - 1\right)(\ cos\ \omega_n t) \tag{18.18}$$

$$u_0 = \frac{(u_{st})_0}{2\xi} \to \frac{u(t)}{(u_{st})_0} = \frac{1}{2\xi} \tag{18.19}$$

$$\frac{u(t)}{p_0/k} = \frac{1}{2\xi} \to \frac{u(t)}{p_0} = \frac{1}{2\xi k} \tag{18.20}$$

Multiplying both sides with $(2\pi f)^2$:

$$\frac{u(t)}{p_0/k}(2\pi f)^2 = \frac{1}{2\xi k}(2\pi f)^2 = \frac{\omega^2}{2\xi k} \to \frac{u(t)}{p_0/k}\omega^2 = \frac{\omega^2}{2\xi k} \to \frac{\ddot{u}(t)}{p_0/k} = \frac{\omega^2}{2\xi} \tag{18.21}$$

Then,

$$\frac{\ddot{u}(t)}{p_0} = \frac{\omega^2}{2\xi k} \tag{18.22}$$

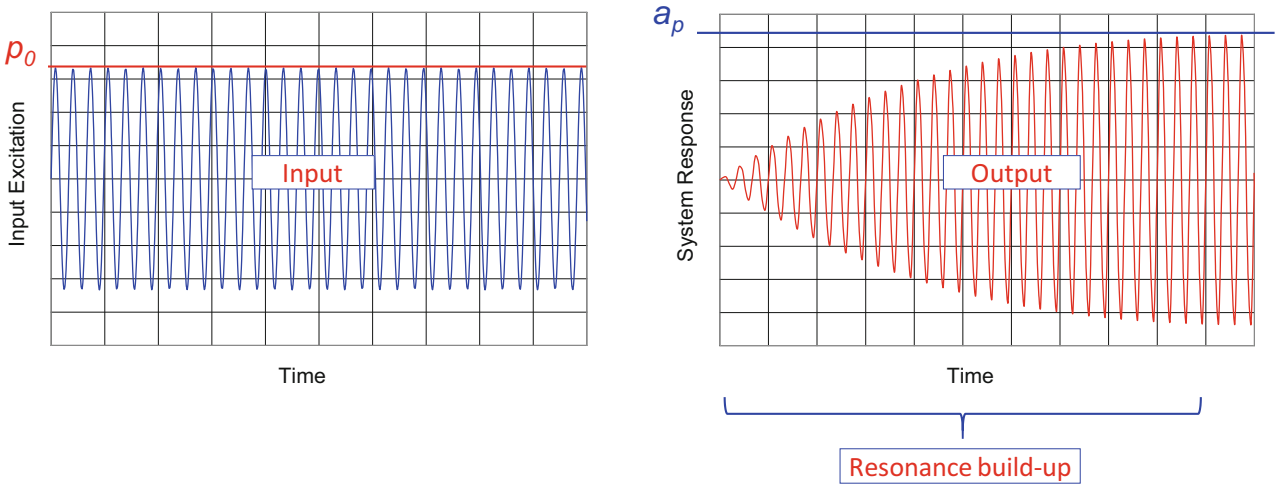


**Fig. 18.3** Input excitation and system response at resonance

**Table 18.4** Effective mass for the first bending mode

| Stage | Effective mass calculations per MEScope mode shapes |
|---|---|
| 1 | 0.470 M |
| 2 | 0.502 M |

Therefore,

$$\frac{\ddot{u}(t)}{p_0} = \frac{k/m}{2\xi k} = \frac{1}{2\xi m} \tag{18.23}$$

Equation (18.22) can also be written as;

$$\ddot{u}(t) = \frac{p_0}{2\xi m} \tag{18.24}$$

When both sides are divided by gravitational acceleration;

$$\frac{\ddot{u}(t)}{g} = \frac{p_0}{2\xi mg} = \frac{p_0}{2\xi W_e} \tag{18.25}$$

$$a_p = \frac{p_0}{2\xi M_e} \tag{18.26}$$

For Eq. (18.26), $a_p$ is the peak acceleration; $p_0$ is the excitation amplitude of the sinusoidal forcing function (Fig. 18.3); $\xi$ is the modal damping ratio and $M_e$ is the effective mass for the first bending mode. Equation (18.26) will be used for determining the modal damping ratios of the laboratory structure when the structure was in resonant condition.

While effective mass is basically an indication of mass sensitivity to a dynamic excitation, it can be calculated if the mode shapes are available. The mode shapes for the laboratory structure are calculated experimentally by using the modal data collected with accelerometers. When each accelerometer location is assigned as a lumped mass, data for each lumped mass location can then be loaded into a commercial vibration analysis software (MEScope) and the mode shapes can be formed. Since the mode shape of a structure is known, the effective mass for that specific mode can be calculated. This is how the mode shape vectors for the first bending mode are determined for both stages of the structure. Each mode shape vector was normalized and effective mass for the first bending mode was calculated (Table 18.4). As shown in Table 18.4, Stage 1 resulted in an effective mass of 0.470 M for the first bending mode. Likewise, Stage 2 resulted in 0.502 M for the effective mass of the first bending mode. The effective mass value is about 7% higher for the Stage 2 than the Stage 1. This make sense since Stage 1 is structurally stiffer than Stage 2. The amount of vibrating effective mass would be less for a stiffer structure.

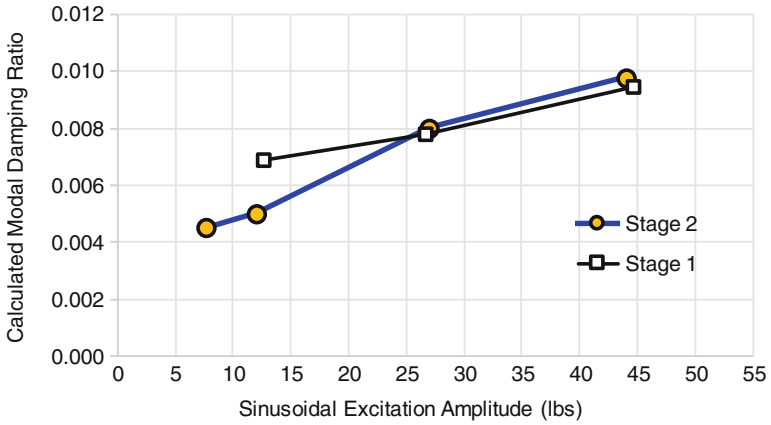


**Fig. 18.4** Nonlinear damping behavior for both stages of the laboratory structure

For the back-calculations of the modal damping ratios, when the effective weight values of 0.470 W and 0.502 W are used for Stages 1 and 2, respectively, the corresponding damping ratios are found for each sinusoidal test run, using Eq. (18.26). Table 18.2 presents the calculated damping ratios for Stage 1 and Table 18.3 presents the calculated damping ratios for Stage 2. Studying the results of Tables 18.2 and 18.3 it is observed that as the sine excitation amplitude is increasing, the damping ratio value is also increasing. This is the nonlinear behavior of the damping and it is plotted in Fig. 18.4. It must be emphasized that the damping ratio values for Stage 1 and 2 are very close and showing the same trend for the amplitude dependent behavior. It is shown that for very low excitations, the damping ratio value can go as low as 0.5% while for increased excitations, the damping ratio value is around 1%.

## 18.5 Verification of Nonlinear Damping

After the amplitude dependent characteristics of damping has been shown in the previous sections, the finite element models can be re-run for the acceleration responses. The sinusoidal excitations of Stages 1 and 2 are simulated in the FE software with the calculated modal damping ratios presented in Tables 18.2 and 18.3. The corresponding acceleration predictions by the FE model are also shown in Tables 18.2 and 18.3. It is observed that the modal damping ratios introduced for different level of excitations result in very good correlation with the FE model acceleration predictions and measured accelerations. The acceleration predictions are within 4% of the measured data for Stage 1 and within 3% for Stage 2.

Since matching the test acceleration responses with the FE model predictions has been a challenge in floor vibrations research, the successful verification of the nonlinear damping in the laboratory environment builds more confidence in FE models for matching the measured accelerations.

## 18.6 Conclusions

The amplitude dependent nature of damping is investigated in this paper based on experimental and analytical work conducted on a laboratory structure. Damping values per various excitation levels are verified; as a result, measured acceleration values matched the FE model predictions utilizing the effective mass calculations for resonant cases. This strengthens the existing confidence on FE models for acceleration predictions in floor vibrations serviceability.

## References

1. Jeary, A.P.: The description and measurement of nonlinear damping in structures. J. Wind Eng. Ind. Aerodyn. **59**, 103–114 (1996). doi:10.1016/0167-6105(96)00002-5
2. Li, Q.S., Yang, K., Wong, C.K., Jeary, A.P.: The effect of amplitude-dependent damping on wind-induced vibrations of a super tall building. J. Wind Eng. Ind. Aerodyn. **91**, 1175–1198 (2003). doi:10.1016/S0167-6105(03)00080-1

3. Li, Q., Liu, D., Fang, J., Jeary, A., Wong, C.: Damping in buildings: its neural network model and AR model. Eng. Struct. **22**, 1216–1223 (2000). doi:10.1016/S0141-0296(99)00050-4
4. Fang, J.Q., Jeary, A.P., Li, Q.S., Wong, C.K.: Random damping in buildings and its AR model. J. Wind Eng. Ind. Aerodyn. **79**, 159–167 (1999). doi:10.1016/S0167-6105(97)00295-X
5. Tamura, Y., Suganuma, S.: Evaluation of amplitude-dependent damping and natural frequency of buildings during strong winds. J. Wind Eng. Ind. Aerodyn. **59**, 115–130 (1996). doi:10.1016/0167-6105(96)00003-7
6. Middleton, C.J., Brownjohn, J.M.W.: Response of high frequency floors: a literature review. Eng. Struct. **32**, 337–352 (2010). doi:10.1016/j.engstruct.2009.11.003
7. Díaz, I.M., Reynolds, P.: Acceleration feedback control of human-induced floor vibrations. Eng. Struct. **32**, 163–173 (2010). doi:10.1016/j.engstruct.2009.09.003
8. Díaz, I.M., Reynolds, P.: On-off nonlinear active control of floor vibrations. Mech. Syst. Signal Process. **24**, 1711–1726 (2010). doi:10.1016/j.ymssp.2010.02.011
9. Brownjohn, J.M.W., Pavic, A.: Experimental methods for estimating modal mass in footbridges using human-induced dynamic excitation. Eng. Struct. **29**, 2833–2843 (2007). doi:10.1016/j.engstruct.2007.01.025
10. Taillon, J.-Y., Légeron, F., Prud'homme, S.: Variation of damping and stiffness of lattice towers with load level. J. Constr. Steel Res. **71**, 111–118 (2012). doi:10.1016/j.jcsr.2011.10.018
11. Casini, P., Giannini, O., Vestroni, F.: Effect of damping on the nonlinear modal characteristics of a piecewice-smooth system through harmonic forced response. Mech. Syst. Signal Process. **36**, 540–548 (2013). doi:10.1016/j.ymssp.2012.10.001
12. Jang, T.S.: A method for simultaneous identification of the full nonlinear damping and the phase shift and amplitude of the external harmonic excitation in a forced nonlinear oscillator. Comput. Struct. **120**, 77–85 (2013). doi:10.1016/j.compstruc.2013.02.008
13. Daoulatli, M.: Rate of decay of solutions of the wave equation with arbitrary localized nonlinear damping. Nonlinear Anal. Theory Methods Appl. **73**, 987–1003 (2010). doi:10.1016/j.na.2010.04.026
14. Avci, O.: Retrofitting steel joist supported footbridges for improved vibration response, In: Structures Congress 2012 – Proceedings of the 2012 Structures Congress 2012 2012. doi:10.1061/9780784412367.041
15. Avci, O.: Amplitude-dependent damping in vibration serviceability: case of a laboratory footbridge. J. Archit. Eng. **22**, (2016). doi:10.1061/(ASCE)AE.1943-5568.0000211
16. Avci, O.: Modal parameter variations due to joist bottom chord extension installations on laboratory footbridges. J. Perform. Constr. Facil. **29**, (2015). doi:10.1061/(ASCE)CF.1943-5509.0000635
17. Avci, O., Davis, B.: A study on effective mass of one way joist supported systems. In: Structures Congress 2015 – Proceedings of the 2015 Structures Congress (2015). doi:10.1061/9780784479117.073
18. Avci, O., Murray, T.M.: Effect of bottom chord extensions on the static flexural stiffness of open-web steel joists. J. Perform. Constr. Facil. **26**, (2012). doi:10.1061/(ASCE)CF.1943-5509.0000262
19. Avci, O., Setareh, M., Murray, T.M.: Effects of bottom chord extensions on the static and dynamic performance of steel joist supported floors. In: Proceedings of the AEI 2008 Conference—AEI 2008 Building Integration Solutions (2008)
20. Avci, O., Setareh, M., Murray, T.M.: Vibration testing of joist supported footbridges. In: Structures Congress 2010 2010. doi:10.1061/41130(369)80
21. Barrett, A.R., Avci, O., Setareh, M., Murray, T.M.: Observations from vibration testing of in-situ structures. In: Proceedings of the Structures Congress Expo. (2006). doi:10.1061/40889(201)65
22. Avci, O.: Effects of bottom chord extensions on the static and dynamic performance of steel joist supported floors. Ph.D. Dissertation, Virginia Polytechnic Institute and State University, Blacksburg, VA (2005)

# Chapter 19
# Addressing Parking Garage Vibrations for the Design of Research and Healthcare Facilities

**Brad Pridham, Nick Walters, Luke Nelson, and Brian Roeder**

**Abstract** The urban setting of many research and healthcare facilities often results in challenging stacking arrangements that require unique solutions to vibration control issues. A condition for which design guidance is limited is the multi-level parking garage that stacks above or below vibration-critical spaces. This situation is becoming increasingly common in urban areas where the cost of land imposes small building footprints, and owners must build 'up' rather than 'out'. Design solutions often include appropriate separation between vibration-critical spaces and parking areas and/or de-tuning of stacked floor structures to limit the efficiency of vibration transmission. However, these solutions are not universally applicable and in some cases, alternative approaches to vibration control must be developed.

In this paper we discuss approaches to addressing vibrations from parking garages during the design of vibration-sensitive facilities. A case study is presented involving a Medical Office Building that features multi-level parking stacked above an ambulatory surgical clinic located on the ground floor. Concerns included noise and vibration disturbance to patients and staff, as well as potential disruptions to overhead equipment in Operating Rooms (ORs). Numerical reviews early in design were complemented with measurements of vehicle vibrations during construction. The results from the measurements and modeling were used for the development of secondary structural support systems to limit vibration disturbances in the surgical clinic.

**Keywords** Vehicle-induced vibration • Floor vibration • Parking garage • Operating rooms

## 19.1 Introduction

The densification of urban education and healthcare campuses is driving the development of taller buildings housing state-of-the-art technologies and treatments to service growing enrollments and an aging population. One result of 'building up' is the challenge of co-location of traditionally incompatible spaces from a noise and vibration perspective. Examples include mid-level mechanical floors above or below acoustically-sensitive areas; vibration-sensitive equipment (e.g., MRIs, electron microscopes) above ambulance or loading bays; and parking garages sharing structure with noise and vibration sensitive spaces. Each of these situations requires a careful assessment of building systems for development of suitable noise and vibration controls.

This paper address approaches to addressing vibrations from parking garages that share structural systems with noise and vibration sensitive spaces. Despite being a common condition in many mid-to-high rise research and healthcare facilities, the topic has received limited attention in technical publications. References on the topic generally focus on human and industrial occupancies, for which noise disturbance and tactile perception by occupants are the primary concerns [1, 2]. The problem of parking garage vibrations in sensitive occupancies is mentioned in design guides and standards; however, the reader is typically deferred to 'more detailed analysis', without specific direction on means and methods for control [3, 4]. In this contribution we provide discussion on the parking garage vibration issue together with a practical example of how it may be addressed in design and construction.

B. Pridham (✉) • N. Walters
Novus Environmental Inc., 150 Research Lane, Suite 105, Guelph, ON, N1G4T2, Canada
e-mail: bradp@novusenv.com

L. Nelson
Datum Engineers, 5929 Balcones Drive # 100, Austin, TX, 78731, USA

B. Roeder
Page Southerland Page, Inc., 400 W. Cesar Chavez Street Suite 500, Austin, TX, 78701, USA



J. Caicedo, S. Pakzad (eds.), *Dynamics of Civil Structures, Volume 2*, Conference Proceedings of the Society for Experimental Mechanics Series, DOI 10.1007/978-3-319-54777-0_19

This paper first investigates the source of vehicle forces and common control strategies for parking garage vibrations. This is followed by a case study on the vibration design of an ambulatory surgical clinic located below a multi-level parking garage. The case study includes a discussion on recommended design criteria, preliminary numerical assessments of the issue, and the results from measurements on the built structure and detailed modelling for development of design solutions.

## 19.2 Vehicle Vibrations in Parking Garages

Vehicle-induced vibrations in parking garages are caused by the dynamic interaction that occurs between the tires, suspension system and sprung mass, and irregularities in the roadway surface. The magnitude of the forces are a function of the stiffness and damping of the suspension system, the speed of travel, and the roughness of the roadway surface. A stiffer, more heavily damped vehicle suspension will generally create higher dynamic forces than a 'soft' suspension on an equivalent surface. Additionally, fast moving vehicles on rough surfaces will generally create higher dynamic forces than slow-moving vehicles on smooth surfaces.

The dynamic loads are associated with two classes of vibration modes: 'body bounce' or cabin motion typically located at frequencies between 0–2 Hz, and 'axle hop' or wheel motions typically located at frequencies between 10–15 Hz. The axle hop modes are the primary concern for vibration-sensitive building structures (both ground-borne from roadways and structure-borne from parking garages and connected ramps), since floor modal frequencies are normally well above 2 Hz in these types of structures. Figure 19.1 is an example of dynamic load spectra for a car and heavy truck computed using the quarter car model (QCM). The loads are normalized by the amplitude of surface displacement/roughness, h, and tire stiffness $k_t$, based on the analytical procedure presented in [5]. The peaks in the spectrum are the location of the vehicle system resonances, i.e., body and axle modes. This model is useful for screening models of vehicle-induced vibrations on parking garage structures.

The axle hop forces are characterized by a transient temporal signature, having a peak at the first point of tire impact followed by a train of reduced amplitude forces (wheel hops) that decay quickly. In parking garages these transient forces are generated by vehicles traversing irregularities such as speed bumps, expansion joints and drainage grates.

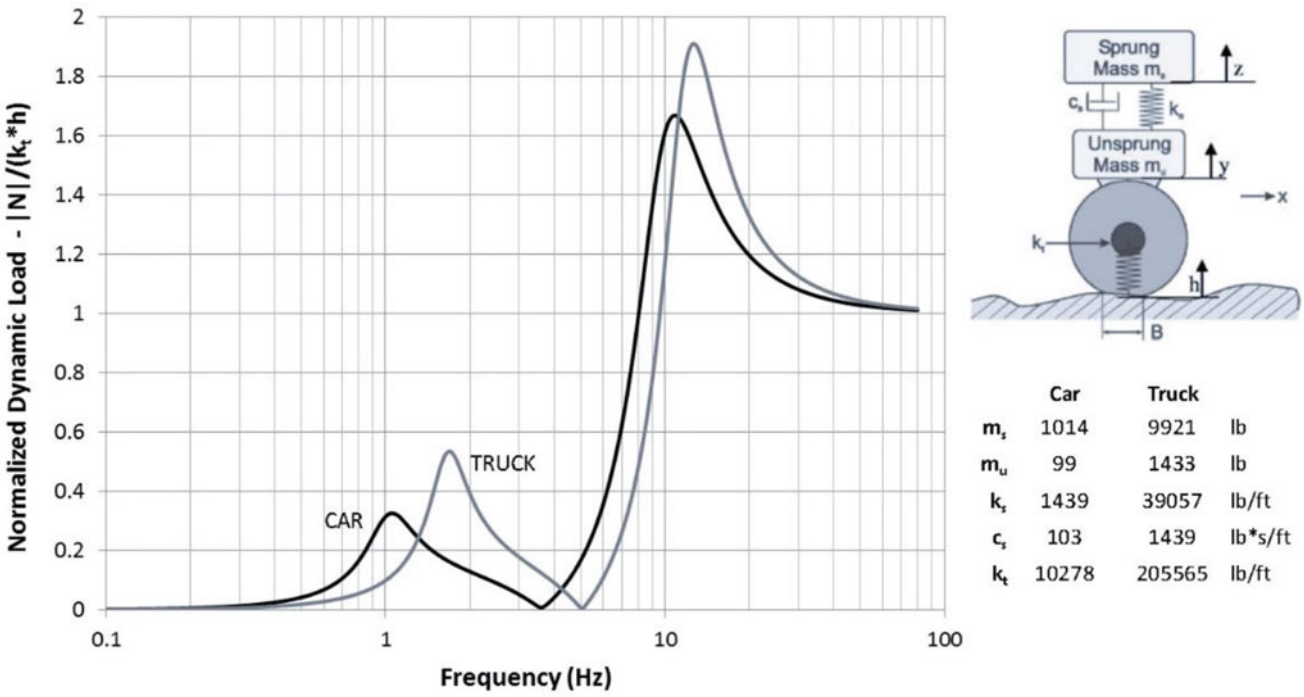


**Fig. 19.1** Example of dynamic load spectra computed with the QCM [5]

## 19.3 Control Strategies

Design strategies to limit vibration impacts from parking garages typically involve a combination of source, path and receiver control measures. Source controls address the vehicle and associated forces on the structure; path controls address the transmission medium (i.e., the building systems); and receiver controls address isolation/decoupling of the vibration receptor. The applicability and effectiveness of each strategy will differ for a new build versus renovation or re-use scenarios.

### *19.3.1 Source Control*

Considering the parameters that determine the forces imparted to the parking structure, options for source control include:

- speed restrictions;
- restriction on vehicle types; and,
- roughness of the driveway surface.

Speed limits are usually posted in parking facilities for safety reasons, but can be difficult to enforce. Typically limits are inherently controlled by the geometry of the space (length of open laneways and layout of parking spaces, turning points, ramp placement etc.), and while there are no design 'rules of thumb' for speed limits, vibration levels on a parking slab are typically greater in areas of higher speed vehicle movement (all else being equal). Considering the distribution of forces and parking slab responses is helpful for developing the path and receiver control measures described in the following sections.

Restrictions on vehicle type are usually limited to buses and transport trucks, and are related more to the height and weight of the vehicles and the ability to navigate the garage, than as a vibration control measure. Nonetheless, the anticipated forces used as a basis for design are important to vehicle modelling studies, which should be based on realistic loads. A plausible recommendation from such studies could include restrictions on the types of vehicles permitted in certain areas.

Controlling the roughness of the driveway surface is an effective means of source control. Expansion joint covers and drainage grates should be specified as smooth as possible, and care taken during construction to avoid large steps in the driveway surface at these locations. Settlement and creep over time can change the surface geometry at these areas and joint/drain coverings should be designed or specified to perform under expected conditions. Locations and placement of the expansion joints should be determined in coordination with the planned use of the building and finish out requirements. Speed bumps and other traffic calming obstructions should generally be avoided in parking garages that share structure with, or are in close proximity to, vibration-sensitive uses.

Source control strategies would generally be applicable to new build scenarios; however, changes to the parking program and retrofit of the driveway surface may also be considerations for renovations and re-use scenarios.

### *19.3.2 Path Control*

Controls that target the vibration path include space layouts, isolation, and the selected structural scheme. The first line of defense against vibration disturbances is space planning. Vibration-sensitive spaces that are well-separated from parking will usually be less susceptible to disturbances from vehicles than spaces in close proximity, or spaces that share a floor plate with moving vehicles. While there are no universally applicable guidelines, experience has shown that separations of two or more floors is effective. There should be a minimum of three bays of separation between the driveway surface and sensitive spaces sharing the floor plate. Ultimately the separation will depend on the specifics of the structural scheme and level of sensitivity of the receptor, and greater setbacks may be necessary. Electromagnetic interference from moving vehicles is a critical consideration for many vibration-sensitive research and medical imaging tools, and control of this element may be the controlling factor, warranting greater setbacks than those associated with noise and vibration control.

Decoupling or interrupting the transmission path is important for controlling both noise and vibration disturbances. Severing the path using structural breaks is most effective, but may not be feasible. Including resilient isolation elements at connections between architectural, mechanical and plumbing and the base building structure at strategic locations can limit secondary movement that results in noise radiation. Critical areas located below driveway surfaces may require secondary/isolated structural systems that effectively lengthen the travel path of vibration energy and amount of dissipation, prior to arrival at the sensitive receptor.

Reviews of the dynamics of proposed designs during planning can be helpful for identifying areas of the structure that will have limited participation in the vibration modes associated with laneways. Similarly, finite element modelling can be helpful for development of de-tuning strategies, such as modifications to framing to alter and effectively de-couple the dynamic response at laneways and sensitive occupancies. Ultimately there may be physical limitations on what can be done with the base parking structure to arrive at the design criteria for the facility. Adding sufficient mass to the system to suppress the impulsive response associated with axle hop may not be possible. Other factors, such as cost, schedule, constructability and space limitations may rule out change to structure such that other strategies must be considered.

Path control strategies are usually applicable to new build scenarios since they can involve changes to layouts and structure, which can be addressed early in design. In a retrofit or re-use scenario, a vibration survey is required to carefully assess the proposed site(s) of planned spaces, the nature and frequency of disturbances and control measures appropriate to planned occupancy. In a retrofit, controls might include renovations to existing architectural, mechanical and plumbing systems, which can be costly.

### *19.3.3 Receiver Control*

The third component addresses vibration controls at the receiver space. This might include isolation of equipment within the space and/or isolation of the space itself. There are numerous passive and active vibration control systems commercially available for a wide range of research and medical tools—see [6–9]. Design or selection of the correct isolation system usually includes measurements to determine the temporal and spectral characteristics of the parking vibrations (among other sources), at planned equipment locations. Some customization of the isolation system is typically required to accommodate unique toolsets, space constraints etc.

Whole-room isolation may be required for ultra-sensitive spaces located near, or sharing structure with the parkade. The general concept is to build an isolated box around the room that effectively decouples the space from the noisy surroundings. This approach requires structural and acoustic treatments that prevent or suppress incoming vibrations with isolation elements (springs, flex connections etc.), secondary support structures isolated from the base building and, where necessary, sound isolation elements (masonry and/or double-stud walls, drywall ceilings etc.), for control of noise.

Receiver control strategies are applied to new builds and renovation/re-use scenarios. In some cases, receiver isolation may be sufficient to satisfy vibration criteria; however, the authors caution the use of this strategy as the first line of defense. A holistic solution that includes a combination of source, path and receiver controls should always be considered.

## 19.4 Case Study: Ambulatory Surgical Clinic Located on the Ground Floor of a Multi-Story Mixed Occupancy Building

The approaches to vibration control discussed in Sect. 19.3 were applied during the design of a surgical clinic located on the ground floor of a multi-story concrete parking garage. Some of the key observations and results from this work are presented in this section as a case study on how parking garage vibrations can be addressed in vibration-sensitive facilities.

### *19.4.1 Facility Description*

The case study involves a ten-story medical office building (plus mechanical penthouse), constructed as part of a new medical campus located in a major urban center. The first floor of the building is dedicated to ambulatory care and ambulatory surgery use, levels two through six are a concrete parking structure and levels seven through ten are pan joist concrete structure to be occupied by a mix of administrative and clinical uses. Some photos of the partially completed building and architectural plans for levels one and two are shown in Fig. 19.2. Note the location of an expansion joint spanning top-to-bottom of the plans at the mid-point of the parking structure.

The use and occupancy of the first floor have undergone several iterations that included varying degrees of vibration sensitivity. During the detailed design phase of the project the area was designated as shelled space, with the possibility of future use for general surgery and radiosurgery (cancer treatment). Screening level studies of vibration performance were


**Fig. 19.2** Photos and plan layouts of Levels 1 and 2 of the case study building

conducted during this phase that included reviews of baseline test data collected early in the project, as well as structural modelling to identify areas of concern.

As the facility entered the construction phase, planning for the level one space evolved to include an ambulatory surgery clinic featuring patient bed space and operating rooms. A second phase of detailed design followed to address fit-out of the space. This included vibration measurements on the constructed building and detailed numerical modelling for solution development.

### *19.4.2 Design Criteria*

Specification of appropriate vibration criteria for the surgical clinic required consideration of the following vibration disturbances:

- tactile motion of the level one floor that could result in discomfort of occupants;
- motions at the supports of medical equipment that could degrade functionality and interrupt surgical procedures; and,
- motions of the superstructure that could result in audible noise or perceptible vibration from equipment such as lighting or screens and monitors.

Criteria relating to items #1 and #2 are specified based on published guidance by the Facilities Guidelines Institute [10], criteria related to research facilities that have evolved over the past ten years [11, 12], and experience with design of similar facilities.

Due to the complex nature of vibration-induced (structure-borne) noise there are no commonly applied vibration criteria to limit noise disturbances caused by structural motions. Recommendations were developed based on thresholds related to ground-borne noise disturbances in acoustically sensitive areas (i.e., ground motions causing noise emissions from building elements). See for example [13].

Table 19.1 is a summary of the vibration criteria applied to the design. As is customary for the design of research and healthcare facilities, the criteria are specified as root-mean-square vibration velocities in one-third octave bands between 1 and 80 Hz.

Separate criteria are proposed for the ground floor slab on level one and for the overhead ceiling structure supporting equipment and building services (ductwork, lighting, plumbing etc.). The design criteria for the ground on level one relates to comfort of patients and staff, whereas criteria for the superstructure relate to vibration-sensitive ceiling-mounted devices and generation of noise. The criteria are applicable to any plane of motion.

Some additional notes to Table 19.1 are as follows:

- the 2000 micro-in./s lower bound criterion for Patient Care is associated with a background noise level of 25 dBA and the 6000 micro-in./s upper bound is based on a 45 dBA background noise level. The FGI recommends a 45 dBA background noise threshold for patient rooms. As such, the lower bound would be appropriate if actual sound levels in these spaces were closer to 25 dBA.
- the 4000 micro-in./s criterion recommended for the ground in level one ORs is based on general surgical use. Specialized surgical procedures featuring floor-mounted microscopes and lasers require a lower threshold.
- The 1000 micro-in./s threshold recommended for the overhead structure in ORs and Procedure Rooms addresses mounting of surgical microscopes to the ceiling structure. This criterion was proposed in [14] and has been shown to be appropriate in field tests [15].

In the early stages of the project, when the space was planned to be shelled, the criteria for ORs and Procedure Rooms were applied to the results of a screening-level review.

**Table 19.1** Summary of vibration criteria applied during detailed design

| Space | Level 1 ground | Superstructure/Ceiling support |
|---|---|---|
| Patient care area | 6000 micro-in./s (ISO-residential night) | 2000–6000 micro-in./s (Class A—ISO residential night) |
| ORs and procedure rooms | 4000 micro-in./s (ISO-operating theatre) | 1000 micro-in./s (Class B) |

### *19.4.3 Screening Level Assessment: Design Phase*

During design of the base building a screening level review was conducted to determine compatibility of the site with surgical use. Finite element models (FEM) were constructed for a review of system dynamics. The models were used to establish preferred locations for placement of operating rooms on level one, and to confirm the potential for motions of the parking slab to exceed design criteria during use.

A numerical study was conducted to compare the dynamic forces from a typical heavy truck travelling at a speed of 15 mph in the garage (the speed limit), with the vehicle forces required to excite the structure at a response equal to the design criteria. Vehicle loads were estimated using the quarter car model, with parameters as specified in Fig. 19.1. The amplitude of surface irregularities (h), which are required to compute the vehicle forces, were specified based on the roughness profiles defined in ISO 8608 [16]. Three degrees of surface roughness were examined: 'very good', 'average' and 'very poor'. These were considered representative of varying levels of obstructions such as expansion joints, drainage grates etc. The height of irregularities for these profiles ranges approximately between 2 mm (very good) and 35 mm (very poor).

The estimated vehicle loads were compared to the force amplitudes required to excite each mode of vibration at a response level equal to the design criteria. These response amplitude for the *ith* mode was computed as follows:

$$F_i = V_{crit} \cdot 2\pi f_i \cdot \sqrt{2} \cdot M_i \tag{19.1}$$

Where $F_i$ is the modal force amplitude; $V_{crit}$ is the root-mean-square vibration velocity; $f_i$ is the frequency of the *ith* mode of the FEM; and, $M_i$ is the generalized (modal) mass of the *ith* mode of the FEM. Note that the estimate computed in Eq. (19.1) is conservative as it neglects any dynamic interaction between the vehicle and parking surface, and it is assumed that the vehicle forces are applied at the maximum mode shape coordinate. In reality, responses are reduced by the interaction between the vehicle and parking slab systems and the load varies in space and time as the vehicle traverses the garage.

An example of the results from the screening level assessment is shown in Fig. 19.3. The modal force amplitudes for the first 100 modes of the FEM of the north (left) half of level two of the garage are shown together with the truck forces estimated using the QCM. The modal force amplitudes were estimated using Eq. (19.1), assuming a critical velocity of 1000 micro-in./s. Modal force amplitudes that fall below the vehicle force curves indicate modes of vibration that may be excited by vehicle forces. The results illustrate that even for very good roadway conditions, forces from trucks traversing the garage may result in vibration levels above 1000 micro-in./s.

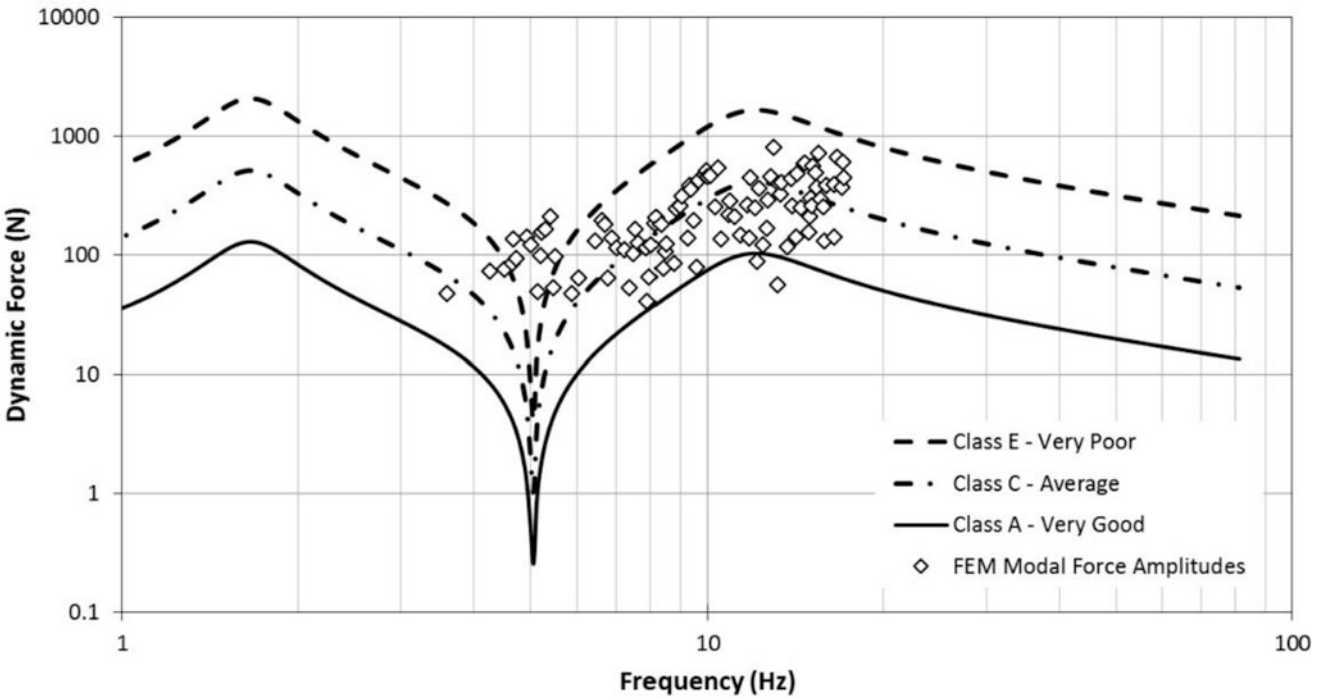


**Fig. 19.3** Vehicle force curves and modal force amplitudes associated with the 1000 micro-in./s criterion

The results from Fig. 19.3 were reviewed together with the dynamic deflection characteristics of the FEM to identify 'quiet' areas of the level two garage floor structure where a smooth surface and slower vehicle speeds are expected. Following the recommendations, the design evolved to include patient rooms and multiple surgical suites, and a more detailed study was proposed during the construction phase of the project.

### *19.4.4 Detailed Assessment: Construction Phase*

Detailed design of the surgical clinic commenced following completion of construction of the parking garage. Consequently, it was possible to conduct vibration testing on levels one and two as part of the design process. Testing was completed with a Chevrolet Silverado Pickup truck travelling at a maximum speed of 15 mph. Three test setups were completed:

- Setup #1: truck traversing level two ramp up to level 3 (above future ORs);
- Setup #2: truck traversing level 1 speed ramp up to level 2 turn (above patient area); and
- Setup #3: truck traversing level 2 turn area, through small parking zone (above patient area).

Setups #1 and #2 included recordings of vibrations caused by the truck traversing the expansion joint.

Vibration acceleration data was collected for three axes of motion for each test (vertical, north–south, and east–west). Data was recorded concurrently on the level two slab, building columns and on ground on level one. The measurement locations are shown in Fig. 19.4. The locations are labelled according to setup, e.g., location 1.2 is measurement location two, for setup #1. Some key vertical axis measurement results from setups #1 and #2 are summarized in Fig. 19.5.

A summary of key results from the tests is as follows:

- Structural resonances due to vehicle movements occur at frequencies between 7 and 12 Hz.
- Level two slab motions during vehicle movements were as much as 100× greater than recommended vibration criteria for ceiling-mounted surgical equipment and as much as 12× greater than recommended vibration criteria for ceilings in patient care areas.
- Measured vibrations on the slab in ramp areas (1.6, 2.5 and 3.2) were 5× to 10× greater than levels measured at location 2.8. This is a result of higher possible speeds and the presence of the expansion joint (surface roughness).
- Motions at the columns satisfied the recommend thresholds for patient care areas but marginally exceed recommended thresholds for ceiling-mounted surgical/procedure equipment at the planned OR locations (see Table 19.1).
- Vibrations on ground on level one satisfied all recommended vibration criteria during the testing.

Based on these observations the team was advised against mounting of medical equipment to the underside of slab or to the building columns. To avoid visual cues of parking garage motions and disturbance to occupants, the team was advised against support of lighting fixtures, screens and monitors from the underside of the slab. Finally, a high risk of structure-borne noise was identified in the areas near the speed ramp and the team was advised to avoid connection of building services or architectural elements in this area.

### *19.4.5 Vibration Control Solutions*

Following a review of the results from the testing the Design Team and Owner adopted the following strategies to control noise and vibration disturbances from the parkade:

- speed bumps were not permitted in the parking structure (*source control*);
- secondary steel grillage was added between columns in the level one ceiling space to support building services and architectural elements (*path control*); and,
- framework 'cages' supported off an isolated floor slab were added to the ORs and Procedure Room on level one (*receiver control*).

The vibration design of the overhead grillage and OR cages was developed during detailed design. Finite element models of the systems were constructed using the SAP2000 package for use in dynamic analyses. The measurements obtained from the site testing were applied as inputs to response simulations, and changes to framing proposed to arrive at systems satisfying the design criteria. Given the small footprint of the ORs, the response of the systems were estimated using a uniform base excitation applied to the supports. The response of the grillage system was estimated using a multiple-support excitation

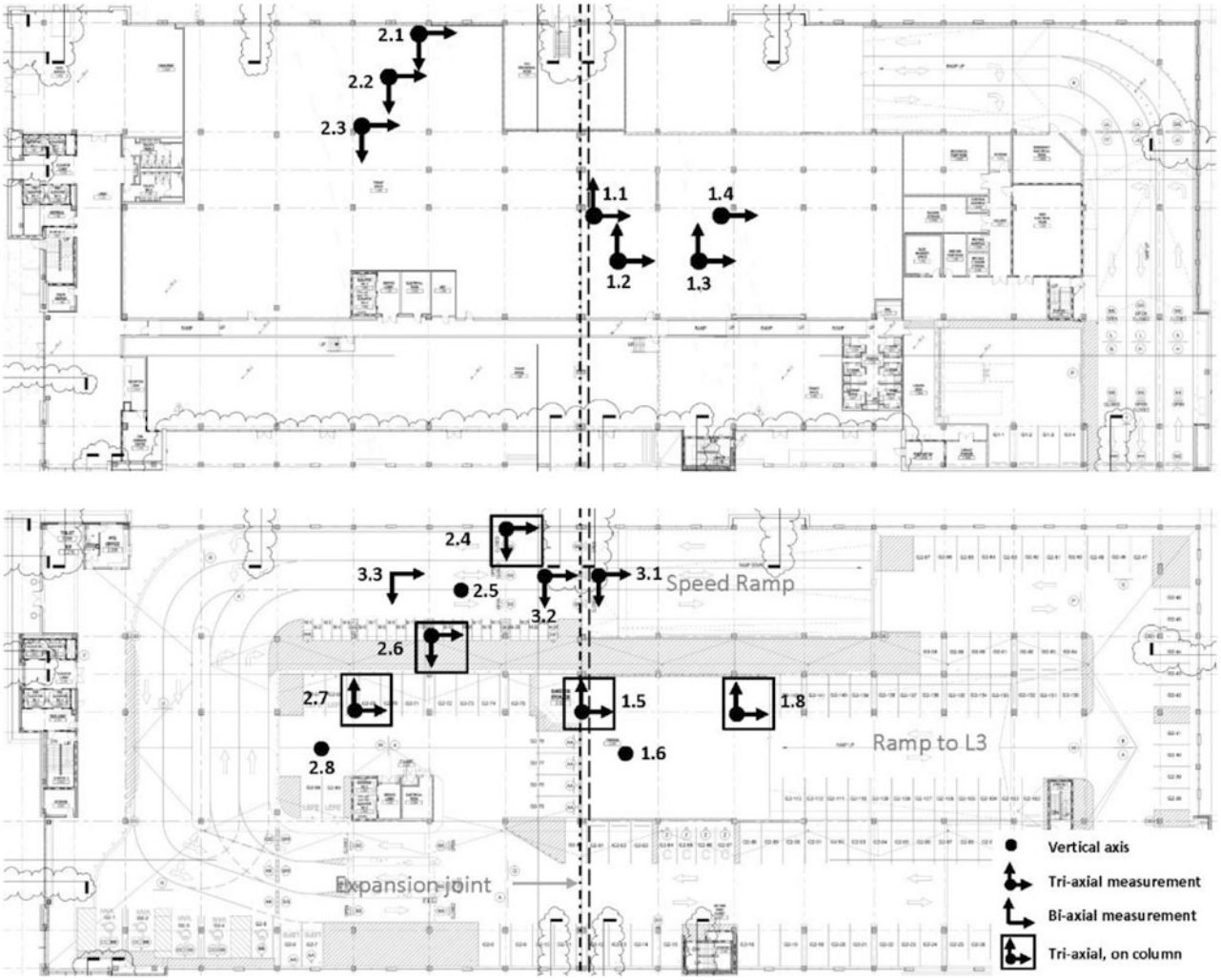


**Fig. 19.4** Vibration measurement locations on level one (*top*) and level two (*bottom*)

in which the measured column responses from the site testing were applied to the connection points between grillage and building structure. Dynamic interaction between the two systems was omitted (i.e., the base building was not included in the model). Screen shots of the final framing configurations are shown in Fig. 19.6.

## 19.5 Concluding Remarks

Approaches to control of vibrations from parking garages address source, path and receiver elements of the system. Although there is no universally applicable solution, strategies that include control measures for each element are recommended. Control at the source should address the quality of the driveway surface and planned traffic calming measures. Control on the vibration path should address proximity through space planning, opportunities for isolation breaks and secondary structural systems that can effectively lengthen the transmission path. Control at the receiver should address vibration isolation supports for equipment or the space as a whole.

At the time of completion of this paper, further planning revisions to the case study building are in development. Additional operating rooms are anticipated, which will require review of the applicability of the control concepts developed in other areas of the ground floor. Performance measurements will be conducted at the request of the Owner following construction for verification of the design and are expected to be helpful for the design of other facilities featuring similar vibration challenges, in the future.

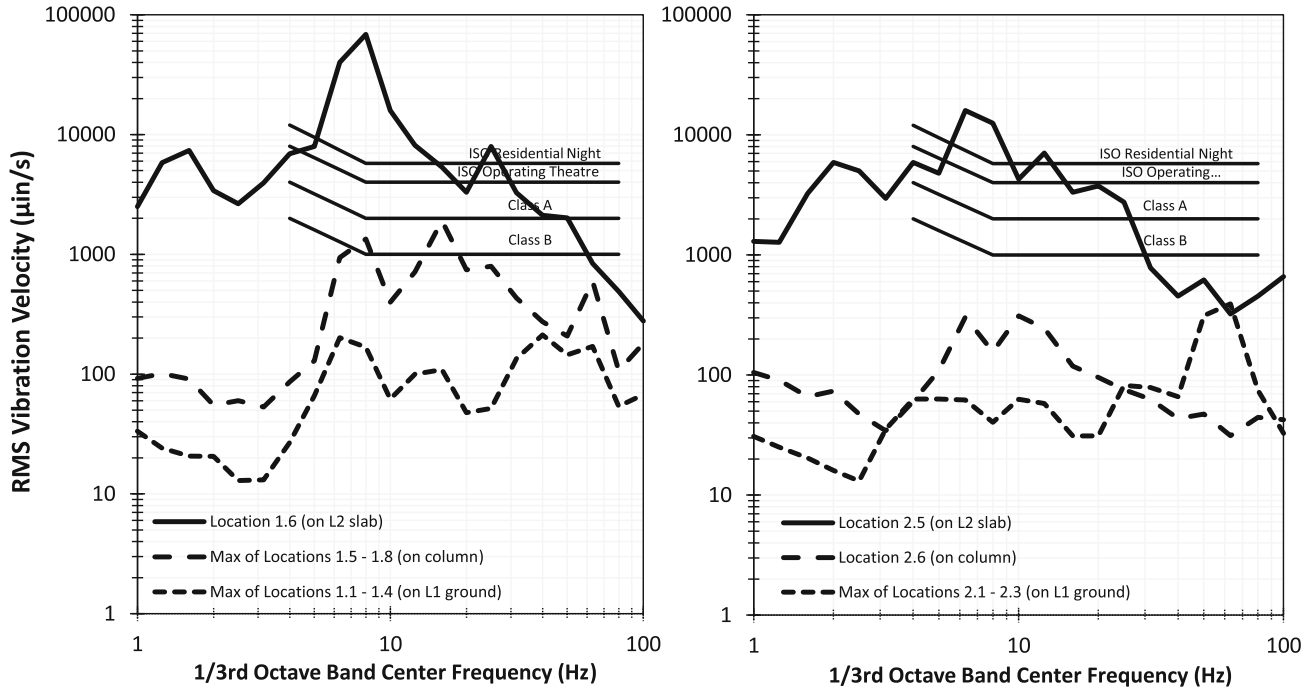


**Fig. 19.5** Vertical axis measurement results for test setup #1 (*left*) and setup #2 (*right*)

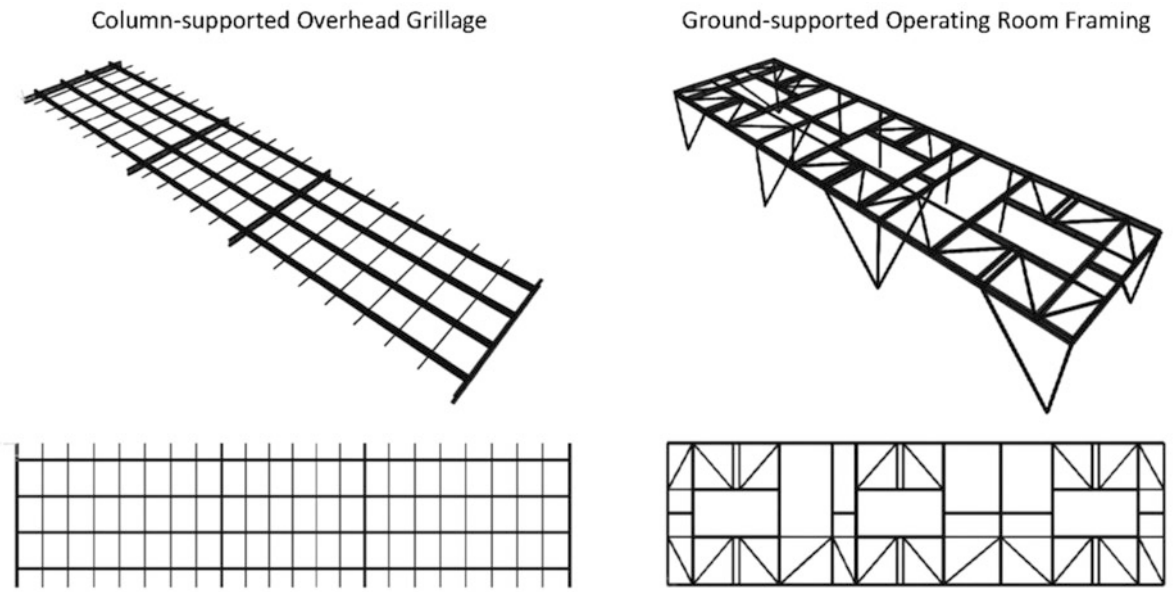


**Fig. 19.6** Framework designs for control of parking garage vibrations in the ambulatory surgical clinic

## References

1. Evans, J.B.: Garage structure vibration transmission to human occupied spaces. In: Proceedings of the 13th International Congress on Sound and Vibration, Vienna, 2006
2. Pan, T.C., Mita, A., Li, J.: Vehicle-induced floor vibrations in a multistory factory building. J. Perform. Constr. Facil. **15**(2), 52–61 (2001)
3. ISO 10137: Basis for design of structures–serviceability of buildings and walkways against vibrations, International Organization for Standardization, 2007
4. Naeim, F.: Design practice to prevent floor vibrations. Structural Steel Education Council (1991). http://www.steeltips.org/steeltips/tip_details.php?id=62

5. Agostinacchio, M., Ciampa, D., Olita, S.: The vibrations induced by surface irregularities in road pavements – a Matlab approach. Eur. Transp. Res. Rev. **6**(3), 267–275 (2014)
6. Mecal: Advanced platform OEM products. http://www.active-vibration-isolation.com/
7. Minus K: Technology, negative stiffness system. http://www.minusk.com/
8. Technical Manufacturing Corporation: Active and passive control systems. http://www.techmfg.com/
9. Newport Corporation: Active and passive control systems. https://www.newport.com/
10. Guidelines for Design and Construction of Hospitals and Outpatient Facilities. Facilities Guidelines Institute, Dallas (2014)
11. Amick, H., Gendreau, M., Busch, T.: Evolving criteria for research facilities: I. Vibration. In: Proceedings of SPIE Conference 5933, San Diego (2005)
12. Watch, D.: Building Type Basics for Research Laboratories, 2nd edn. John Wiley & Sons, Hoboken, NJ (2005)
13. Transit Noise and Vibration Impact Assessment, Federal Transit Administration (FTA), Technical Report No. FTA-VA-90-1003-06, May 2006
14. Ungar, E.: Vibration criteria for healthcare facility floors, Sound and Vibration, Sept 2007
15. Tigli, O.F.: Floor vibrations on healthcare facilities: a case study on a surgical microscope. In: Proceedings of the 32nd International Modal Analysis Conference, Orlando (2014)
16. ISO 8608:1995 Mechanical vibration–Road surface profiles–Reporting of measured data. International Organization for Standardization (1995)

# Chapter 20
# Modeling and Measurement of a Pedestrian's Center-of-Mass Trajectory

**Albert R. Ortiz, Bartlomiej Blachowski, Pawel Holobut, Jean M. Franco, Johannio Marulanda, and Peter Thomson**

**Abstract** This paper presents the measurement and model updating of a pedestrian's center of mass trajectory. A mathematical model proposed by the authors is updated using the actual trajectory of a pedestrian. The mathematical model is based on the principle that a human's control capability tries to maintain balance with respect to the pedestrian's center of mass (CoM), independently of the surface type. In this research, the human is considered as a mass point concentrated at CoM. The parameters of the models are updated using experimental identification of the human walking trajectory on a rigid surface. The proposed measurement technique uses a depth sensor, which enable skeletal tracking of the pedestrian walking on rigid or flexible structures. Experiments were performed using a mobile platform with the time-of-flight commercial camera Microsoft Kinect for Windows 2.0. The velocity of the mobile platform is set to maintain a 1 m separation from the pedestrian in order to provide high resolution. The results of the measurement technique allowed the identification of the human's CoM trajectory. The results of the model updating process present the probability density function of the parameters which could be used for modeling the CoM's trajectory of the pedestrian.

**Keywords** Human-structure interaction • Pedestrian's trajectory • Human-induced vibrations • MS kinect sensor

## 20.1 Introduction

After an incident related to excessive oscillations which occurred in 2000 on the opening day of the Millennium Bridge in London, researchers and engineers started to pay more attention to the phenomenon called Human-Structure Interaction (HSI). Since that time a number of papers have been published introducing a variety of mathematical models of this phenomenon. However, there is still insufficient understanding of the physics which is behind the phenomenon and governs this interaction [1, 2].

This paper presents an experimental verification of the model described earlier by Blachowski et al. [3]. The essential part of this model relies on the accurate knowledge of the trajectory of the pedestrian's center of mass (CoM). This work is a first step in a bigger project which is intended to develop a better understanding of the influence of a vibrating structure on the movement of pedestrians on it. Here, we focus on the experimental part and selection of a feasible measurement technique which would allow to identify the pedestrian's CoM during walking on a rigid surface.

There is a rich literature related to experimental human movement analysis, in which authors suggest different measurement systems for that purpose. One of the pioneering works in that field is a book by Braune and Fisher [4]. The Authors begun their original research at the end of the nineteenth century and used a technique called two-sided chronophotography. This technique requires two cameras to be opened and shut at short intervals at precisely the same time. To illuminate different parts of the human body the Authors used tubes, which were filled with rarefied nitrogen.

Modern techniques for measuring human movement can be classified as either motion capture using optoelectronic cameras or inertial motion tracking using a set of accelerometers. The work by Whittle [5] belongs to the first class of

A.R. Ortiz (✉)
Department of Civil and Environmental Engineering, Universidad del Norte, Barranquilla, Colombia
e-mail: oalbert@uninorte.edu.co

B. Blachowski • P. Holobut
Institute of Fundamental Technological Research, Polish Academy of Sciences, Warsaw, Poland
e-mail: bblach@ippt.pan.pl; pholob@ippt.pan.pl

J.M. Franco • J. Marulanda • P. Thomson
School of Civil Engineering and Geomatics, Universidad del Valle, Cali, Colombia
e-mail: jean.franco@correounivalle.edu.co; johannio.marulanda@correounivalle.edu.co; peter.thomson@correounivalle.edu.co



J. Caicedo, S. Pakzad (eds.), *Dynamics of Civil Structures, Volume 2*, Conference Proceedings
of the Society for Experimental Mechanics Series, DOI 10.1007/978-3-319-54777-0_20

techniques. The Author used a kinematic gait analysis system to determine the three dimensional motion of the center of the pelvis during walking. The measurement of the center of the pelvis was synchronized with a force platform, and these data were integrated to eventually determine the motion of the center of gravity of the body. Recently, Dang and Zivanovic in 2015 [6] used a more advanced motion capture system, which consists of twelve video-based optoelectronic cameras and sensors that were used to capture displacements of 34 markers attached to human anatomical landmarks. The Authors considered four different markers' arrangement to increase accuracy of the estimation of such parameters of walking as: the pacing frequency, step length, step width, attack angle, end-of-step angle, trunk rotation and first harmonic of the dynamic loading factor.

An example of an application of an inertial motion tracking system for the analysis the walking behavior of pedestrians is the paper by van Nimmen et al. [7]. The Authors used the Xsens MTw Development Kit measurement system, which consisted of multiple wireless inertial units incorporating 3D accelerometers. The system consisted of six sensors, one of which was placed close to the body's CoM located at the level of the fifth lumbar vertebra. To estimate the trajectory of the pedestrian's center of mass during walking the above-mentioned measurement system has to be combined with appropriate computational algorithms. Usually, two types of methods are utilized: dynamic or kinematic. The kinematic methods can be further subdivided into minimalistic marker methods and segmental analysis methods. The latter suffer from uncertainties arising from missing information about limb motion. The former, on the contrary, require full-body marker sets and calculate the CoM trajectory by assuming the masses and CoM locations of each segment [8]. The accuracy of the dynamic methods is limited by the precision of the measured forces and the precision of the integration constants.

It was observed by Maus et al. [9] that inaccuracies in each method, dynamic or kinematic, are related to different parts of the Fourier spectrum. As a result of this, they proposed a new approach to compute CoM motion based on a reliable frequency range of force and kinematic measurements. An extension of the previous method has been presented by Carpentier et al. [10]. The modification was related to adding information about the center of pressure, also called Zero Moment Point (ZMP). However, according to the Authors' conclusion, the proposed filtering approach with the ZMP measure does not improve the vertical component of the CoM, because ZMP provides only two-dimensional information.

Recently, researchers started to consider infrared cameras combined with video cameras as an alternative to the above-mentioned marker-based systems. An example of this new measurement technology is the Microsoft Kinect sensor. After finding its popularity among gamers, MS Kinect has received a lot of attention from biomechanical, mechanical and civil engineers.

Jun et al. [11] performed a comparative analysis of motion data from two alternative human motion-capture systems (Vicon vs Kinect). They employed an 8-camera Vicon MX system that was synchronized with the Kinect system via a video synchronizer (Kistler 5610). They concluded that direct application of the Kinect system to clinical or research work (without post-processing of raw data) tends to be limited. However, they pointed out that with suitable post processing there is a potential for clinically relevant use.

Another paper related to the accuracy of the MS Kinect was published by Galna et al. [12]. They proposed to use MS Kinect as a potentially low-cost solution for clinical and home-based assessment of movement symptoms in people with Parkinson's disease. Another application of the MS Kinect sensor was proposed by Seer et al. [13]. In their study, the Authors proposed an algorithm for human detection and tracking. The algorithm is based on agglomerative clustering of Kinect depth data captured from an elevated view in contrast to the lateral view used for gesture recognition in Kinect's gaming applications. They combined measurement signals from three different Kinect sensors.

Yet another comparison of MS Kinect with a marker-based motion capture system was presented by Zerpa et al. [14]. The Authors used both Vicon Peak Motus version 9 and the Microsoft Kinect system with customized skeleton software to collect data about a subject sitting on a platform moving horizontally at the speed of 2.4 m/min. The results of their study support the findings in literature and indicate that the Kinect system has a potential to be used as a tool to measure and analyze human movement kinematics. The last example of an application of MS Kinect to human movement analysis is the paper by Chen et al. [15]. In their article, the Authors proposed an efficient pedestrian detection approach for crowded scenes by fusing the RGB and depth images from the Kinect. First they extracted pedestrian contour regions from the RGB images using background subtraction and then, they applied a region clustering algorithm to extract pedestrians from the contour regions using depth information. Finally, a tracking and counting algorithm was employed to acquire pedestrian volumes.

All the above examples indicate that a depth sensor combined with a video camera can be an attractive alternative to the classical expensive motion capture measurement systems.

The present paper is organized as follows: Sect. 20.2 presents the model used for describing the trajectory of the pedestrian and offers an introduction to the probabilistic model updating technique, which is the tool used in this paper for updating the parameters of the trajectory model. Section 20.3 describes the experimental setup to obtain the trajectory of a pedestrian walking on a rigid surface as well as the mobile sensor developed on MS Kinect technology. Section 20.4 presents the experimental trajectory and the parameters obtained after being updated. Conclusions and future work are detailed in Sect. 20.5.

## 20.2 Background

### *20.2.1 Model of Pedestrian's Motion*

The purpose of this paper is to present a simple closed-form description of the motion of the pedestrian and verify it against experimental data. In this paper, a pedestrian walking on a rigid surface. The analytical description is intended for use in Human Structure Interaction (HSI) modeling, as proposed earlier in [3]. The focus is therefore on simplicity. Since one may roughly assume that the subtleties of motion of the human body, like hand movement, do not have a significant impact on structural vibrations during HSI, we disregard them. We shall only consider the "first order" characteristics of human walking, which can be represented by the trajectory of the human's CoM. This trajectory describes the position of the CoM at a given time instant with respect to the surface, on which the human walks. The main assumptions about/features of the motion can be summarized as:

1. For the purpose of an HSI analysis, a human can be adequately represented as a mass point, placed at the human's CoM and having three translational degrees of freedom.
2. During constant-speed walking, the CoM's trajectory is a periodic function of time (except in the longitudinal direction).
3. The vertical, $z(t)$, and lateral, $y(t)$, components of the trajectory, as well as the longitudinal velocity $v(t) = \dot{x}(t)$, have the same phase.
4. The frequency of $z(t)$ and $v(t)$ are equal, and is twice the frequency of $y(t)$.

*Remark.* During walking, the ground reaction force (GRF) and its placement result from the balance of forces acting on the mass centered at the CoM. If one assumes, for simplicity, that the double-support phase of walking is negligibly short, then: (1) GRF is equal to the sum of the forces of gravity and inertia acting at the CoM during its movement along the prescribed trajectory. (2) The position of the supporting foot's center of pressure is the spot on the ground from which the GRF points towards the CoM.

In the remainder of the paper, we will use the below—example—form of the trajectory [3], for comparison with experimental results. Its free parameters are: step length $a_x$, lateral sway amplitude $a_y$, vertical sway amplitude $a_z$, mean vertical position $z_0$, maximum longitudinal velocity $v_0$, and amplitude of longitudinal velocity $a_v$. The parameters should be adjusted to fit experimental data.

1. Longitudinal velocity of the CoM:

$$\dot{x}(t) = v(t) = v_0 - |a_v \sin(ft)|, \tag{20.1}$$

   where $f = (v_0\pi - 2a_v)/a_x$.
2. Longitudinal position of the CoM, obtained by integrating $\dot{x}$ between 0 and $t$:

$$x(t) = v_0 t - \frac{a_v}{f}\left(2\left\lfloor\frac{ft}{\pi}\right\rfloor + 1 - \cos(ft \bmod \pi)\right). \tag{20.2}$$

3. Lateral and vertical positions of the CoM:

$$y(t) = a_y \sin\left(\frac{\pi}{a_x}x(t)\right), \tag{20.3}$$

$$z(t) = z_0 - a_z \cos\left(\frac{2\pi}{a_x}x(t)\right). \tag{20.4}$$

### *20.2.2 Bayesian Model Updating*

The trajectory of the pedestrian can be idealized following the model presented in the previous section. The trajectory depends on six parameters ($a_x$, $a_y$, $a_z$, $a_v$, $v_0$ and $z_0$). In this paper, Bayesian inference is used to update the parameters of the model based on experimental data [16, 17]. Bayesian inference is based on the Bayes theorem:

$$P(\Theta|D, M_j) \propto P(D|\Theta, M_j)P(\Theta|M_j) \tag{20.5}$$

where $P(\Theta|D, M_j)$ is the posterior probability density function (PDF) of the parameters $\Theta$, for model $M_j$, given the observation $D$. $P(\Theta|M_j)$ is the prior PDF of the parameters $\Theta$ and it represents the knowledge of the parameters before updating. $P(D|\Theta, M_j)$ is the likelihood of the occurrence of the measurement $D$ given the vector of parameters $\Theta$ and model $M_j$. $M_j$ is the model presented in Sect. 20.2.1

In this research, samples of the posterior are obtained to derive statistics of the parameters. The samples are generated using the Markov chain Monte Carlo (MCMC) methodology [18–20]. The MCMC is a derivation of the Monte carlo sampling algorithm, where the samples distribution is based on an equilibrium condition. The Markov chain algorithm defines the probability of the next step based on the probability of the current step. Further details about model updating of human-structure interaction models using this approach can be found in Ortiz 2016 [21].

## 20.3 Experimental Setup

The identification of the trajectory of the pedestrian's CoM involves the use of an infrared video camera. In order to track the trajectory, the artificial vision system needs to move along the distance that the pedestrian walks, keeping an optimal distance, otherwise images will not have the same resolution. Therefore, the experimental measurement of the human body is performed using a mobile platform Microsoft Kinect V2 for Windows and a Laptop, as seen in Fig. 20.1.

The mobile platform is located in front of the human body. Acquisition of the depth images of the Kinect sensor is performed once the mobile platform is moving at constant velocity. The relative velocity of the human to the mobile platform is measured using depth images. The velocity of the mobile platform is measured using two integrated quadrature encoder which provide a resolution of 64 counts per revolution of the motor shaft. This resolution corresponds to 4480 counts per revolution of the gearbox's output shaft. Therefore, synchronization of the velocity signals is required to calculate the actual velocity of the pedestrian. Figure 20.2 shows a picture of the test. The camera and the computer are on the mobile platform ahead of the pedestrian. The mobile platform is on rails in order to reduce the noise generated by surface irregularities.

The acquisition and processing of depth images is performed using own developed algorithms in Matlab [22]. The developed algorithm performs a calibration of the depth images in order to obtain a rectified point cloud of the scene in front of the Kinect V2. The scene acquired on the depth images is complex since it includes all the surroundings. The surroundings are removed using a spatial threshold volume. As a result of the inclination angle of the Kinect V2 depth camera, the orientation of the segmented human body needs to be corrected. The ground floor surface is also identified (assumed constant) and the angle $\alpha$ is obtained. This surface is used for correction of the inclination angle. A rigid transformation of

**Fig. 20.1** Picture of the mobile platform carrying the computer and the MS Kinect sensor (at the top)

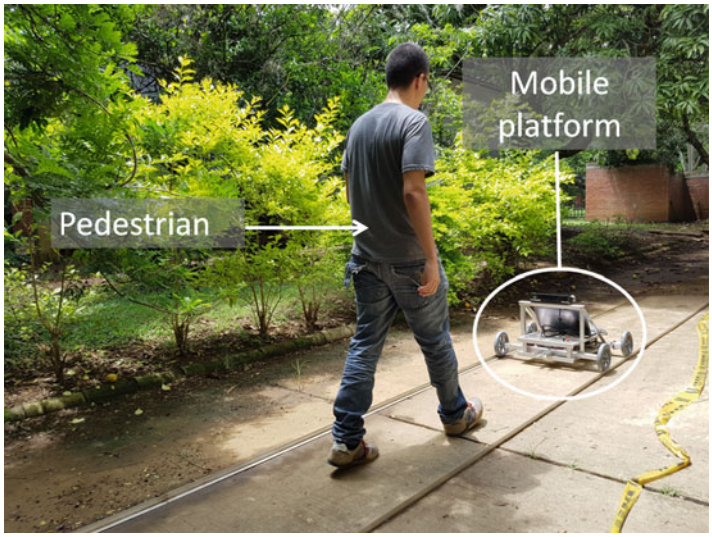


**Fig. 20.2** Picture of a test. The pedestrian walking in front of the mobile platform. MS Kinect and a laptop are on the mobile platform taking images at approximately 30 fps

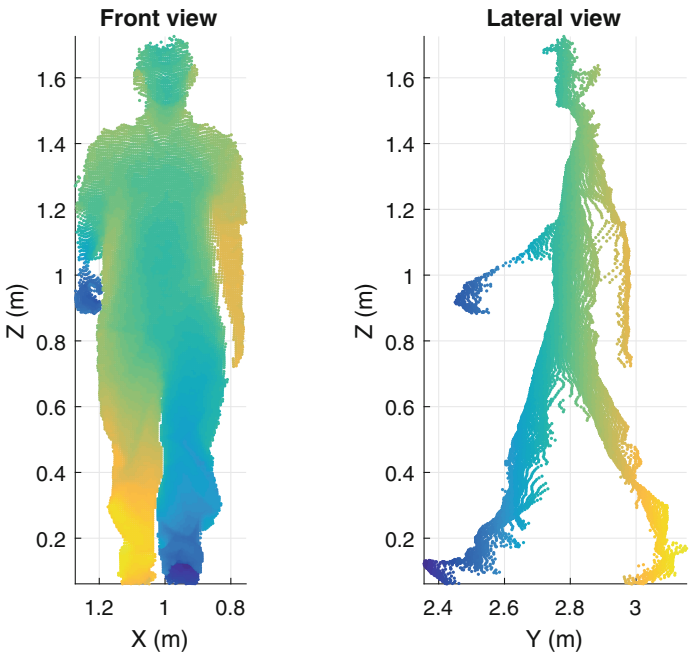


**Fig. 20.3** Segmented human body

the point clouds to a proper orientation is performed using Eq. (20.6). Figure 20.3 shows the cloud of points for the pedestrian body. A geometric 3D centroid is calculated and tracked on all the point clouds.

$$T(x,a) = \begin{bmatrix} 1 & 0 & 0 & 0 \\ 0 & cos(\alpha) & -sin(\alpha) & 0 \\ 0 & -sin(\alpha) & cos(\alpha) & 0 \\ 0 & 0 & 0 & 1 \end{bmatrix} \tag{20.6}$$

## 20.4 Results

The pedestrian's Center of Mass (CoM) is identified and traced for the pedestrian walking along a 9 m pathway. The pathway is a rigid ground slab, stiff enough to avoid the human-structure interaction phenomenon. The pedestrian is a man, 29 years old, with a mass of 69 kg. Axial ($x_r$), transversal ($y_r$) and vertical ($z_r$) components of the tracked trajectory are shown in Fig. 20.4.

The velocity of the pedestrian is approximately constant as can be seen in the slope of the first plot in Fig. 20.4. The total distance recorded by the Kinect sensor is around 6.0 m. The vertical and transversal movement of the pedestrian is shown in the last two plots of Fig. 20.4. The movement of the pedestrian's CoM is somehow following sinusoidal functions where the main frequency of the vertical movement ($z_r$) is around twice the main frequency of the transversal movement ($y_r$). This is in accordance with the assumption of the model described in section two, however there is not a unique frequency, fact notably seen in the vertical component.

The analytical model used for modeling the pedestrian's trajectory (described by Eqs. (20.2)–(20.4)) is updated based on the experimental data showed in Fig. 20.4. Model's parameters are updated using a probabilistic approach based on Bayesian theory as described in the methodology section. The prior distributions $P(\Theta|M_j)$ of the parameters $\{\Theta = a_x, a_y, a_z, a_v, v_0$ and $z_0\}$ are presented in Table 20.1. Figure 20.5 shows the marginals histogram of each parameter (along the diagonal) and the relation between parameters (plots outside the diagonal). A total of 100,000 samples were used. Other 400,000 were used for thinning as burning samples.

Figure 20.5 shows a strong correlation between the parameters $a_v$ and $v_0$. This means that the model could be reduced to five parameters using a relation between $a_v$ and $v_0$. Beyond this correlation, parameters look independent to each other's.

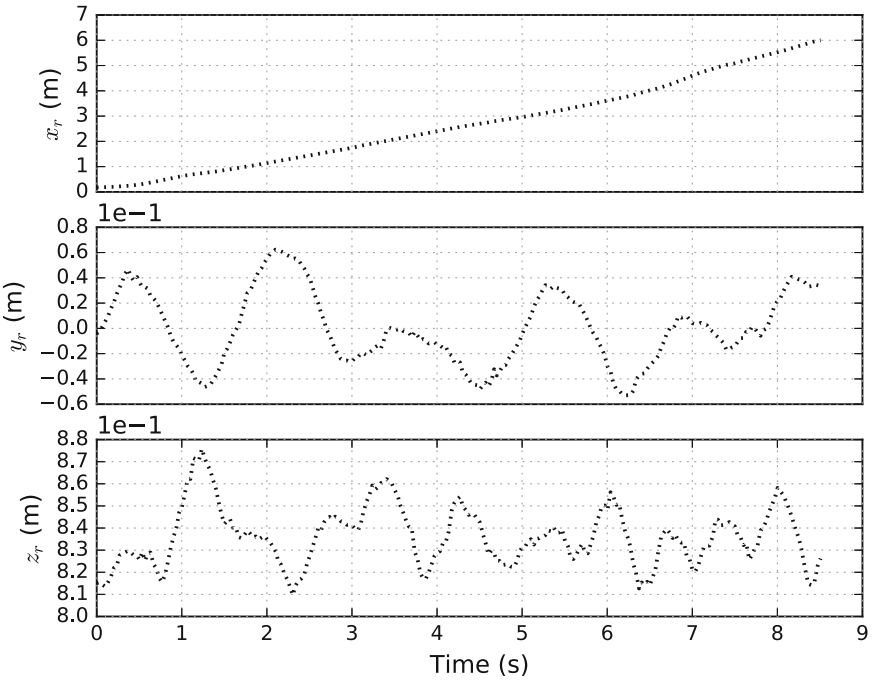


**Fig. 20.4** CoM trajectories of the pedestrian

**Table 20.1** Prior PDFs used for updating the parameters

| Parameter | Units | PDF | Parameters |
|---|---|---|---|
| $a_x$ | m | Uniform | $lower = 0.3$, $upper = 1.0$ |
| $a_y$ | m | Normal | $\mu = 0.02$, $\sigma = 0.005$ |
| $a_z$ | m | Normal | $\mu = 0.02$, $\sigma = 0.005$ |
| $a_v$ | m/s | Normal | $\mu = 0.3$, $\sigma = 0.07$ |
| $v_0$ | m/s | Normal | $\mu = 1.0$, $\sigma = 0.25$ |
| $z_0$ | m | Uniform | $lower = 0.8$, $upper = 0.9$ |

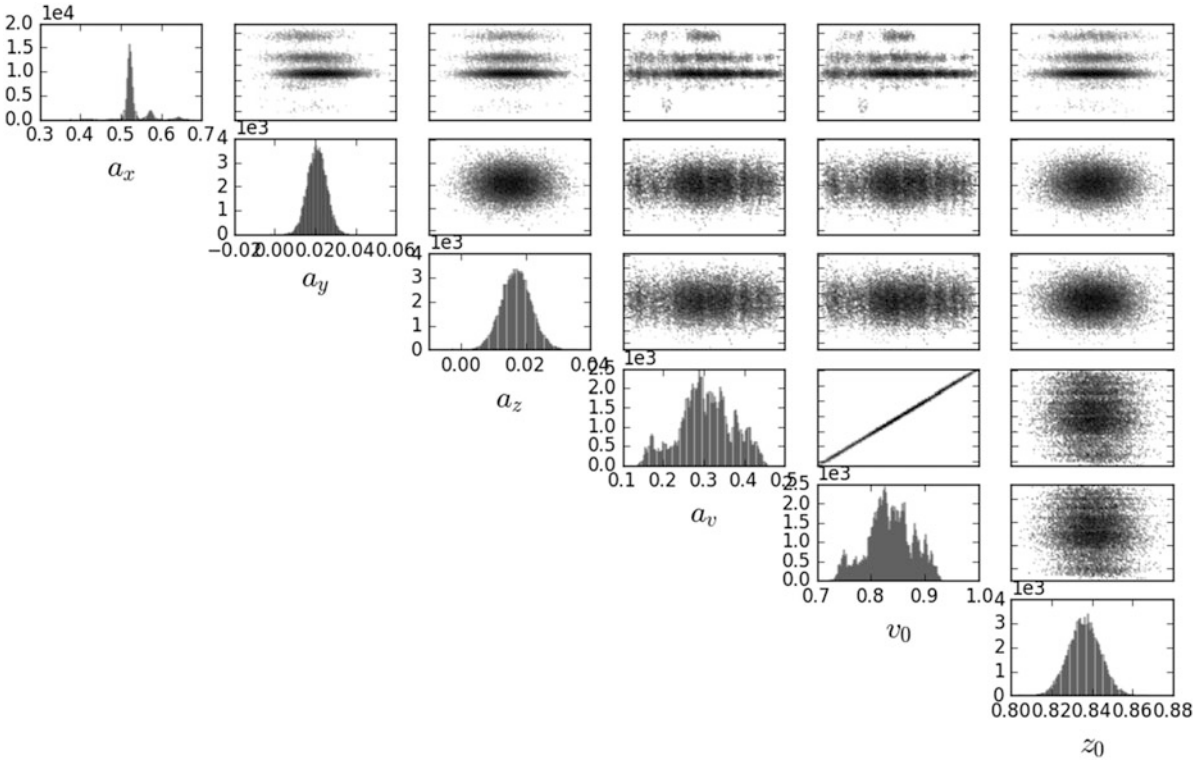


**Fig. 20.5** Marginal histograms of parameters describing the CoM trajectory of the pedestrian after being updated

**Table 20.2** Moments of variables describing the parameters of the model

| Parameter | $a_x$ [m] | $a_y$ [m] | $a_z$ [m] | $a_v$ [m] | $v_0$ [m/s] | $z_0$ [m] |
|---|---|---|---|---|---|---|
| Mean | 0.531 | 0.021 | 0.017 | 0.305 | 0.834 | 0.836 |
| STD | 0.028 | 0.004 | 0.005 | 0.067 | 0.042 | 0.0.008 |
| 95% HPD | (0.500, 0.588) | (0.011, 0.030) | (0.008, 0.026) | (0.165, 0.426) | (0.746, 0.913) | (0.819, 0.851) |

Table 20.2 shows the statistical moments of the parameters after updated. Figure 20.6 presents a comparison between the experimental data and the analytical model when the maximum probability values are used.

Figure 20.6 shows that after using the most probable values, the model tracks well the velocity of the pedestrian. However, the model is not good for tracking the variation of the amplitude of the transversal component (plot in the middle), and the frequency of the vertical component (third plot). This difference between the model and the experimental data is due to two reasons: first, the model assumes a basic trigonometric trajectory, meaning that the human's trajectory could be modeled as something more complicated; and second, the experimental data includes noise which could induce additional frequency components to the CoM of the pedestrian.

Figure 20.7 presents the pedestrian induced forces corresponding to one step cycle. The force is scaled and presented by single arrows. Each arrow starts around supporting foot's positions.

## 20.5 Conclusions

The focus of this research is to update the parameters of a model that describes the trajectory of a pedestrian when walking on a rigid platform. Within this model, the forces exerted by the pedestrian to the ground can be modeled. This is a significant advance for future works seeking to understand the variation of the trajectory given different surfaces' conditions.

The model of the trajectory was updated using experimental data of a pedestrian walking. The experimental trajectory was obtained using a MS Kinect sensor adapted on a mobile platform. The platform moves in the same direction of the pedestrian and it is tracking the trajectory of the person as a cloud of points. The MS Kinect on the mobile platform is an economic

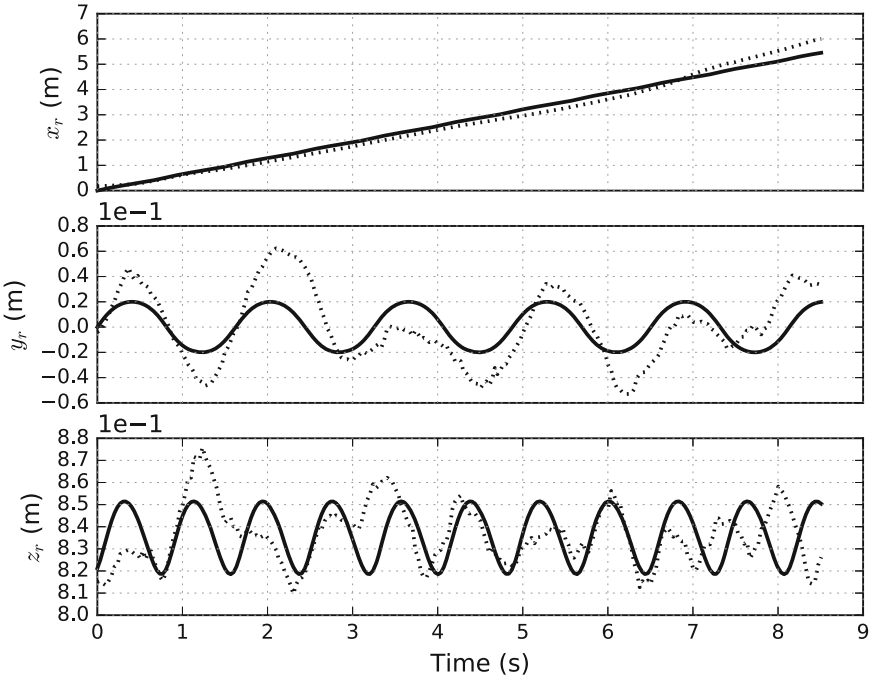


**Fig. 20.6** CoM's Trajectory of the pedestrian: the *dash line* is the trajectory obtained in the experiment. The *solid line* is the trajectory of the model using the maximum probable values of the parameters

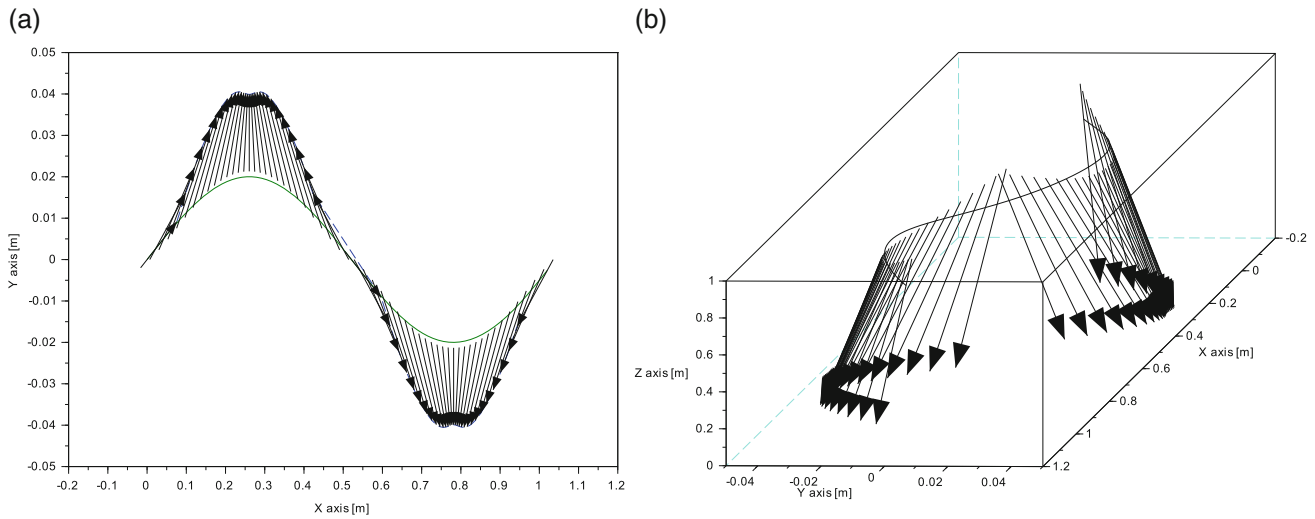


**Fig. 20.7** Pedestrian induced forces for the CoM's trajectory: top view (**a**) and 3D view (**b**). The *arrows* are normalized so that the length of the longest is 1

solution for the identification of large trajectories. Additional work should be done to reduce frequency components included in the experimental data which are produced by the vibration of the car and the resolution of the MS Kinect.

This research shows that there is a high correlation between two parameters of the model, which means that a less number of parameters could be used for modeling the trajectory of the pedestrian. The longitudinal and transversal components of the trajectory show good approximation respect to the maximum probabilistic values, however there is still high standard deviations in the probability density functions of parameters as the amplitude of the velocity, $a_v$, and the maximum longitudinal velocity, $v_0$. This uncertainty is affecting the performance of the model. More tests, a better mobile platform, and a better definition of the part of the body used to identify the trajectory of the CoM could reduce the uncertainty in these parameters.

Future work will focus in tracking and comparing the trajectory of a human walking on rigid and flexible surfaces. Differences will help to understand the response of the body and the influence of the surface in the human-structure interaction phenomenon.

## References


1. Yang, Q., Qin, J., Law, S.: A three-dimensional human walking model. J. Sound Vib. **357**, 437–456 (2015)
2. Sánchez, J., Gómez, D., Thomson, P.: Análisis de la interacción humano-estructura en puentes peatonales de santiago de cali. Dyna **80**(177), 86–94 (2013)
3. Blachowski, B., Holobut, P., Ortiz, A., Caicedo, J.: Simple human-structure interaction model of walking on a flexible surface. In: ISMA2016 International Conference on Noise and Vibration Engineering, USD2016 International Conference on Uncertainty in Structural Dynamics, pp. 559–570, Leuven, Belgium (2016)
4. Braune, W., Fischer, O.: The Human Gait. Springer, Berlin (1987)
5. Whittle, M.W.: Three-dimensional motion of the center of gravity of the body during walking. Hum. Mov. Sci. **16**(2), 347–355 (1997)
6. Dang, H.V., Živanović, S.: Experimental characterisation of walking locomotion on rigid level surfaces using motion capture system. Eng. Struct. **91**, 141–154 (2015)
7. Van Nimmen, K., Lombaert, G., Jonkers, I., De Roeck, G., Van den Broeck, P.: Characterisation of walking loads by 3d inertial motion tracking. J. Sound Vib. **333**(20), 5212–5226 (2014)
8. Winter, D.A.: Biomechanics and Motor Control of Human Movement. Wiley, New York (2009)
9. Maus, H.-M., Seyfarth, A., Grimmer, S.: Combining forces and kinematics for calculating consistent centre of mass trajectories. J. Exp. Biol. **214**(21), 3511–3517 (2011)
10. Carpentier, J., Benallegue, M., Mansard, N., Laumond, J.-P.: A kinematics-dynamics based estimator of the center of mass position for anthropomorphic system – a complementary filtering approach. In: 2015 IEEE-RAS 15th International Conference on Humanoid Robots (Humanoids), pp. 1121–1126. IEEE, New York (2015)
11. Jun, S.-K., Zhou, X., Ramsey, D.K., Krovi, V.N.: A comparative study of human motion capture and computational analysis tools. In: The 2nd International Digital Human Modeling Symposium, Citeseer (2003)
12. Galna, B., Barry, G., Jackson, D., Mhiripiri, D., Olivier, P., Rochester, L.: Accuracy of the microsoft Kinect sensor for measuring movement in people with Parkinson's disease. Gait Posture **39**(4), 1062–1068 (2014)
13. Seer, S., Brändle, N., Ratti, C.: Kinects and human kinetics: a new approach for studying pedestrian behavior. Transp. Res. C **48**, 212–228 (2014)
14. Zerpa, C., Lees, C., Patel, P., Pryzsucha, E., Patel, P.: The use of microsoft Kinect for human movement analysis. Int. J. Sports Sci. **5**(4), 120–127 (2015)
15. Chen, X., Henrickson, K., Wang, Y.: Kinect-based pedestrian detection for crowded scenes. Comput. Aided Civ. Inf. Eng. **31**(3), 229–240 (2016)
16. Beck, J., Katafygiotis, L.S.: Updating models and their uncertainties i: Bayesian statistical framework. J. Eng. Mech. **124**, 455–461 (2009)
17. Cheung, S.H., Beck, J.: Bayesian model updating using hybrid Monte Carlo simulation with application to structural dynamic models with uncertain parameters. J. Eng. Mech. **135**, 243–225 (2009)
18. Robert, C., Casella, G.: Monte Carlo Statistical Methods. Springer, New York (2013)
19. Hastings, W.K.: Monte carlo sampling methods using Markov chains and their applications. Biometrika **57**(1), 97–109 (1970)
20. Metropolis, N., Ulam, S.: The Monte Carlo method. J. Am. Stat. Assoc. **44**(247), 335–341 (1949)
21. Ortiz, A.R.: Modeling human-structure interaction using a controller system. Ph.D. Thesis, University of South Carolina (2016)
22. MATLAB: version 7.10.0 (R2010a). The MathWorks Inc., Natick (2010)

# Chapter 21
# Evaluation of Mass-Spring-Damper Models for Dynamic Interaction Between Walking Humans and Civil Structures

**Ahmed S. Mohammed and Aleksandar Pavic**

**Abstract** Dynamic interaction between walking humans and vibrating flexible structures is one of the main challenges when simulating human-induced vibrations. To account for this interaction, several mass-spring-damper (MSD) models featuring different parameters have recently been proposed. This paper compares the performance of six experimentally-based MSD models of walking humans available in the literature. The simulated vibration responses of these models were compared with experimental measurements of four human test subjects walking on a full-scale flexible footbridge. Numerical simulations were carried out for two cases: non-interactive and interactive models using the above mentioned MSD models. Moreover, for each case two models of walking forces were used: previously measured continuous walking forces (from a treadmill test) for the corresponding test subjects and a deterministic walking force function from design guidelines. It is demonstrated that neglecting human-structure interaction in the simulations can result in a significant overestimation of the vibration responses. By utilising any of the interactive models of walking people, the accuracy of the vibration response predictions can be improved. The best performance was obtained when both the measured walking forces and the interactive model were used.

**Keywords** Human-structure interaction • Human-induced vibrations • Walking forces • Mass-spring-damper • Footbridge

## 21.1 Introduction

The advancements of structural materials and design techniques have enabled engineers to design more slender and longer span civil structures such as footbridges, floors and grandstands. While the strength requirements are usually assured, the structural design of such structures has been increasingly governed by vibration serviceability criteria related to human dynamic excitation including walking and running [1].

There is a growing number of cases of structures which are either over- or under-designed for vibration serviceability according to current design methods. This indicates a lack of reliable methods for prediction and assessment of human-induced vibration [2]. For lightweight slender structures, one of the main challenges in developing such methods is the complexity of the dynamic interaction between walking people and their accommodating structure [3, 4]. To consider using this interaction in a design method, recently, there has been proliferation of walking-related human-structure interaction (HSI) models [5]. The performance of these models have not been compared with each other, and therefore, there is a need to evaluate their performance using experimental measurements.

This paper compares the performance of six experimentally-developed HSI models for walking humans [6–11]. Experimental measurements pertinent to four people walking on a full-scale slender footbridge were used for this purpose. Furthermore, two models of walking forces were utilised in the analysis: measured walking forces (from nominally identical treadmill walking test for corresponding test subjects) and the traditional walking force model based on Fourier series representation.

A.S. Mohammed (✉) • A. Pavic
Vibration Engineering Section, College of Engineering, Mathematics and Physical Sciences, University of Exeter, Kay Building, North Park Road, Exeter, EX4 4QF, UK
e-mail: asm221@exeter.ac.uk



J. Caicedo, S. Pakzad (eds.), *Dynamics of Civil Structures, Volume 2*, Conference Proceedings of the Society for Experimental Mechanics Series, DOI 10.1007/978-3-319-54777-0_21

## 21.2 Human-Structure Interaction Models of Walking Humans

The existence of walking people is proven to have an effect on the dynamic behaviour of their accommodating structure. This effect can be mainly observed as an increased modal damping and a change in natural frequency due to the coupling between the walking people and supporting structure during walking [1, 5, 12].

HSI models of walking humans can generally be divided into three groups according to their approaches: mass-spring-damper (MSD) models, inverted-pendulum models and more complex models of the human body. This paper considers only the first group, as it is the most widely used and user-friendly approach in the vibration serviceability community. It comprises either a single or multiple MSDs attached to the supporting structure, replicating the dynamic behaviour of a walking human, as shown in Fig. 21.1.

In this study, the performance of six experimentally-developed MSD models of a single person walking [6–11] were compared. These models represent nominally identical human walking and the only difference between them is the parameters of the mass, stiffness and damping. Table 21.1 presents MSD parameters of eight experimentally-developed models of HSI of walking humans available in the literature.

The model presented by Lou et al. [13] is excluded from the comparison, as the suggested range of natural frequency of the walking human is considerably below the range reported of other models. The model presented by Silva [14] is also excluded from the comparison. It was originally developed for crowds of walking people based a model of a single walking human [8]. These two models [8, 14] have relatively close MSD parameters so the model presented in [14] is excluded.

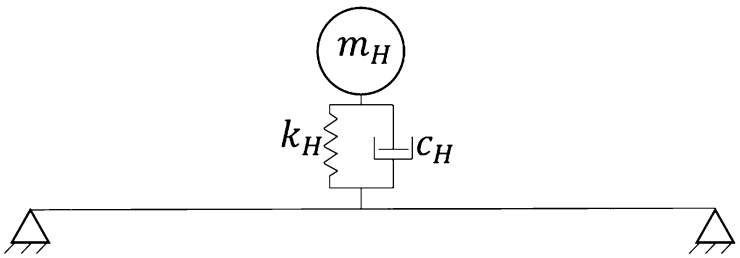


**Fig. 21.1** MSD representation of a walking human on a simply supported footbridge beam

**Table 21.1** Experimentally developed MSD parameters for walking human model available in the literature

| No. | Study | Natural frequency ($f$) (Hz) | Mass ($m$) (kg) | Stiffness ($k$) (N/m) | Damping | |
|---|---|---|---|---|---|---|
| | | | | | Damping coefficient ($c$) (N s/m) | Damping ratio (%) |
| 1 | Jiménez-Alonso and Sáez [6] | 2.75 | 84% of body mass ( $M$) | – | – | 47 |
| 2 | Lou et al. [13] | 1.25–1.60 | 100% of body mass ( $M$) | – | – | 37–50 |
| 3 | Shahabpoor et al. [7] | 2.75–3.0 | 100% of body mass ( $M$) | – | – | 27.5–30 |
| 4 | Silva and Pimentel [8] | – | $97.082 + 0.275\,M - 37.518\,f_p$ | $30351.744 - 50.26\,c + 0.035\,c^2$ | $29.041\,m^{0.883}$ | – |
| 5 | Silva et al. [14] | – | $97.082 + 0.275\,M - 37.518\,f_p$ | $5758.441 + 11.103\,c$ | $107.455 + 16.208\,m$ | – |
| 6 | Toso et al. [9] | – | [a] | [b] | [c] | – |
| 7 | Van Nimmen et al. [10] | 2.5–4.0 | 95% of body mass | – | – | 20–40 |
| 8 | Zhang et al. [11] | 1.85 | 100% of body mass | – | – | 30 |

[a] $m = -231.34 + 3.69\,M + 145.06\,f_p - 1.97\,M\,f_p + 0.005\,M^2 - 15.25\,f_p^2$

[b] $k = 75601.45 - 1295.32\,M - 33786.75 f_p + 506.44\,M\,f_p + 3.59\,M^2 + 539.39\,f_p^2$

[c] $c = -1115.69 + 92.56\,M - 108.94\,m + 2.91\,M\,m - 1.33\,M^2 - 1.30\,m^2$

## 21.3 Method

The performance of the six HSI models of walking people mentioned in Sect. 21.2 is evaluated by comparing the simulated vibration response using each model with their experimental counterpart of a human walking on a full-scale footbridge. The work explained in this study can be divided into three stages: identification of dynamic properties of the test structure, walking tests and simulations of vibration responses.

### *21.3.1 Test Structure*

The walking tests were carried out on a laboratory footbridge located in the Structures Lab at the University of Exeter. The footbridge is 15 m long and 2.5 m wide. It consists of Sandwich Plate System (SPS) plates connected by thin plates and supported by perimeter steel beams using steel bolts.

A preliminary modal test was carried out to identify the modal properties of the test structure. The natural frequency and mode shapes of the first, second and third bending modes are presented in Fig. 21.2.

Since the natural frequency of the second vertical bending mode is much higher than the range of the fundamental natural frequency of walking human models (Table 21.1), only the fundamental mode of the test structure is considered in this study. Moreover, since the structure is flexible and can have relatively high vibration response due to human walking, it is expected that the nonlinear effects are not negligible. Therefore, the amplitude-dependent damping ratio and fundamental frequency were investigated. A series of tests by a single person bouncing on the middle on the structure were carried out to obtain the freely decaying response. For each test, the person was bouncing with the same frequency (controlled by a metronome) as the fundamental frequency of the footbridge (3.81 Hz) to achieve a resonant vibration response before jumping off the footbridge. In this way, the decaying response of the bare structure can be measured without interference from the excitation source, which was the bouncing person in this case. The decaying vibration response is considered from the moment the bouncing person jumps off the footbridge. To achieve this, two synchronised wireless Inertial Measurement Units (IMUs) were utilised, one was fixed on the leg of the person and the other one was fixed on the mid-span of the footbridge. In this way, it was possible to define the moment when the jumping person leaves the footbridge. A low-pass filter was then applied to the measured vibration responses, before the cycle by cycle curve fitting was used to determine the amplitude-dependent damping ratio and fundamental frequency, as shown in Fig. 21.3.

The modal mass was estimated from another test. A sinusoidal driving force was applied on the structure using a shaker at the same frequency as the frequency of the first bending mode (3.81 Hz). The driving force and the resulting vibration responses were measured during the test.

Numerical simulations of a single degree of freedom (SDOF) system representing the first bending mode were carried out. The identified amplitude-dependent natural frequency and damping ratio and the measured driving force of the shaker were utilised in these simulations. A range of modal masses were used and for each simulation the simulated and measured responses were compared. It was possible to identify the modal mass (5100 kg) by trial and error when the simulated response matches the measured response.

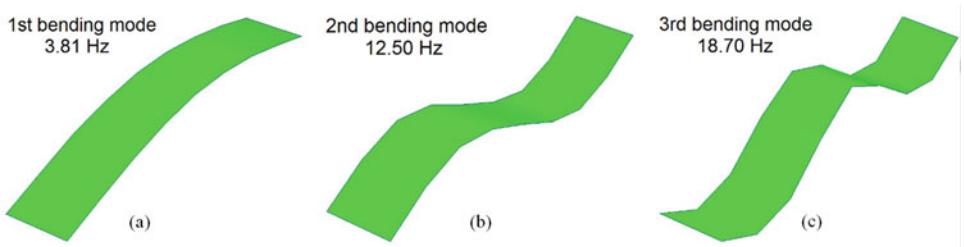


**Fig. 21.2** (**a**) First, (**b**) second and (**c**) third bending modes of the test structure

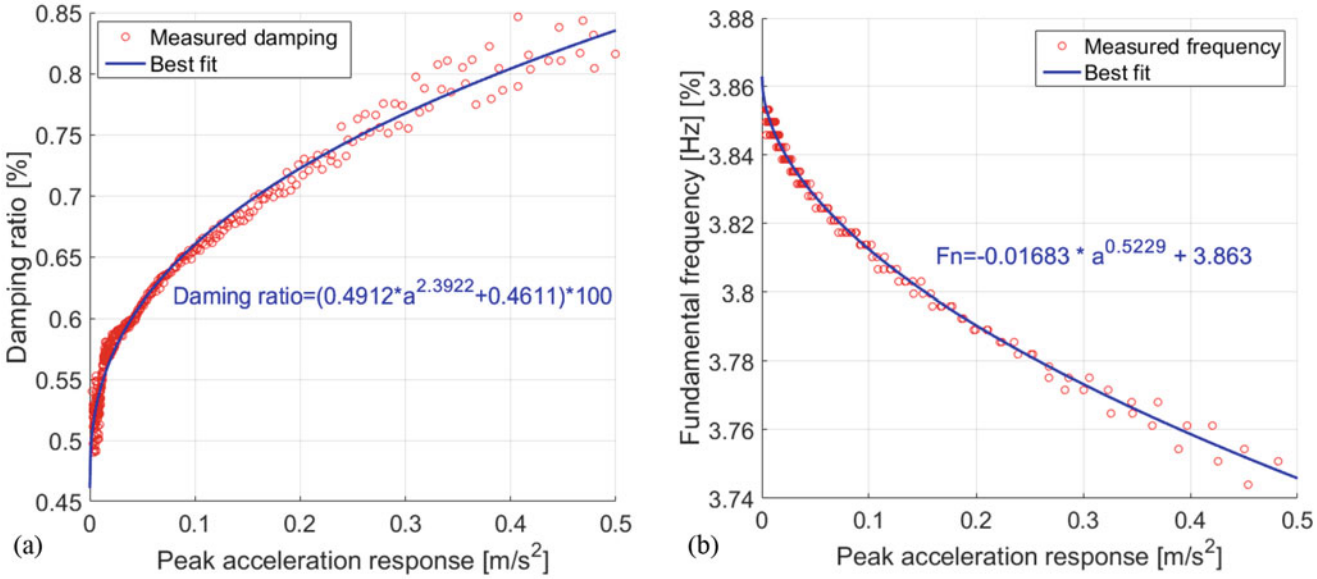


**Fig. 21.3** Amplitude-dependent values of (**a**) damping ratio and (**b**) fundamental frequency of the test structure

### *21.3.2 Walking Tests*

Walking tests were carried out individually by four male test subjects. Their weight range between 820 and 900 N and they were denoted as (TS1, TS2, TS3 and TS4). To take into account the intra-subject variability, each TS performed six walking tests at two pacing frequencies: 1.90 Hz and 2.05 Hz (12 walking tests in total). The second harmonic of the former pacing frequency excites the first bending mode of the footbridge and produces a resonant response. The later pacing frequency is chosen to obtain a non-resonant response. All walking tests were controlled by a metronome and each TS had to wait for about 10 s (at the location of one of the supports) between every two successive tests to allow for the vibration decay. The vibration response for each case was measured at the anti-node of the first vibration mode (mid-span of the footbridge).

### *21.3.3 Simulation of Vibration Responses*

The identified dynamic properties of the first bending mode (Sect. 21.3.1) were utilised in the simulations of vibration responses. A MATLAB script was developed to take into account the amplitude-dependent damping ratio and fundamental frequency. The values of these parameters were updated after each cycle of the simulated vibration responses.

The simulations carried out in this study can be classified into two groups:

- Non-interactive models, for which HSI is neglected and only the walking force is applied on the oscillator of the vibration mode, and
- Interactive models, which include the HSI of walking people (as discussed in Sect. 21.2).

For each group, two types of walking forces are utilised:

- Measured walking forces for corresponding test subjects, and
- Deterministic walking force function based on Fourier series representation which can be mathematically described in Eq. (21.1):

$$F(t) = W\left(1 + \sum_{n=1}^{N} \alpha_n \sin\left(2n\pi f_p + \varnothing_n\right)\right), \tag{21.1}$$

where $t$ is time (s), $F(t)$ is the walking force (N), $W$ is the static weight of the subject (kg), $n$ is the harmonic number, $N$ is the total number of harmonics, $\alpha_n$ is the Fourier coefficient of the $n$th harmonic, which is also known as dynamic load factor (DLF), $f_p$ is pacing frequency and $\varnothing_n$ is the phase shift of the $n$th harmonic.

Based on the above mentioned simulation groups, nine cases of simulations are considered in this study:

- Deterministic force and non-interactive model (DF-N).
- Measured force and non-interactive model (MF-N).
- Deterministic force and Silva's model [8] of walking people (DF-Si).
- Measured force and Alonso's model [6] of walking people (MF-A).
- Measured force and Shahabpoor's model [7] of walking people (MF-Sh).
- Measured force and Silva's model [8] of walking people (MF-Si).
- Measured force and Toso's model [9] of walking people (MF-T).
- Measured force and Van Nimmen's model [10] of walking people (MF-V).
- Measured force and Zhang's model [11] of walking people (MF-Z).

It is worth mentioning that the simulated vibration responses are repeated six times to replicate the experimentally measured vibration responses.

## 21.4 Results and Discussion

### *21.4.1 Results*

In this section, the simulated vibration responses described in Sect. 21.3.3 are compared with their experimental counterparts. Two approaches are utilised for comparison, and as follows:

- Maximum 1-second Root Mean Square (RMS).
- Statistical comparison of vibration responses.

The process of comparing the simulations is schematically illustrated in Fig. 21.4 and the description of each procedure is presented in this section.

The maximum 1-second RMS is calculated for each measured and simulated vibration response. There are six walking tests/simulations for each case (i.e. six maximum 1-second RMS), and the average value is calculated and considered for comparison. This average value is normalised by its experimental counterpart and the results are presented in Fig. 21.5.

The maximum 1-second RMS does not provide a clear description of the overall vibration responses, as it is based on the maximum 1-second of the vibration response only. The cumulative distribution of the vibration responses can provide more informative description. Hence, it is used to compare the measured and simulated vibration responses. Figure 21.6 presents the cumulative distribution function (CDF) of the experimental and simulated vibration responses for a test subject at two pacing frequencies.

The concept of fractiles is utilised to compare the CDF of the measured and simulated vibration responses. In this study, a certain fractile of a vibration signal refers to the proportion of vibration signal with magnitude up to that value. The fractile related to any probability of non-exceedance (0–100%) can be extracted from the CDF plots. Figure 21.7 compares the fractiles of two simulations with their experimental counterparts. Interestingly, the fractiles of up to 90% probability of non-exceedance of all simulation cases follow almost a linear line which does not necessarily slope at 45° (Fig. 21.7). This means there is a trend of over- or under-estimation of vibration responses for vibration magnitudes with probability of non-exceedance up to 90%. Hence, the ratio of simulated/measured fractiles for this range is utilised to estimate the slope of the best linear line that passes through them (Fig. 21.7). This slope is the ratio of the vertical/horizontal components of the line. A slope of 1.1, for example, indicates an overestimation for vibration response for up to 90% of the vibration signal. This feature is used to compare the measured and simulated responses for all simulation cases, and the values of the slope for all simulation cases are presented in Table 21.2. The overall performance of each model is demonstrated by calculating the average absolute difference (from 1.0) of each fractile ratio as shown in the last row in Table 21.2.

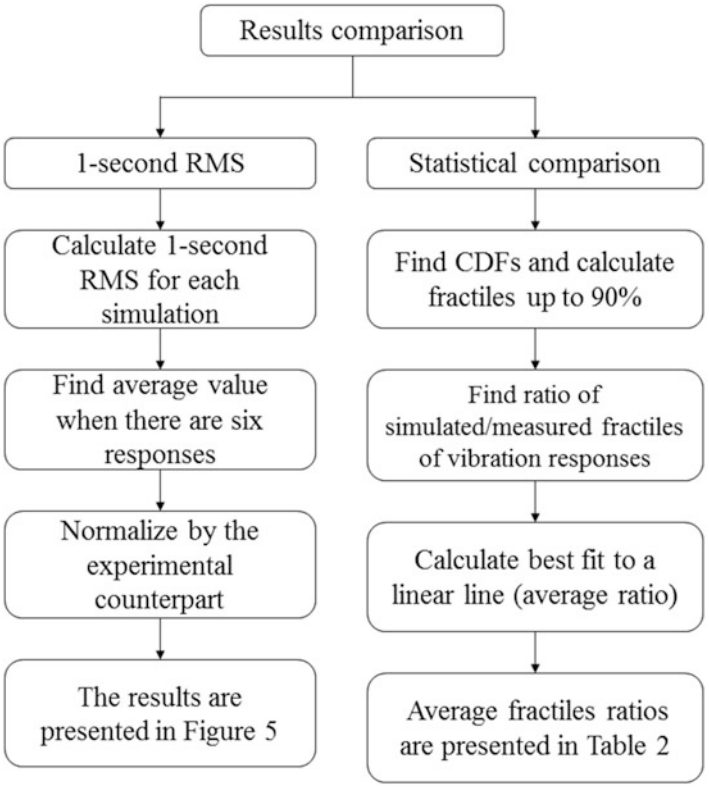


**Fig. 21.4** Schematic overview of the results comparison approaches

### *21.4.2 Discussion*

Section 21.4.1 provided comparison between the measured and simulated vibration responses in terms of vibration magnitudes up to 90% probability of non-exceedance and the maximum 1-second RMS. Hence, they can be used to describe the performance of the simulated models.

Simulated vibration responses for all non-interactive models are found to significantly overestimate the measured vibration responses in most of the cases, especially for the resonant responses (Fig. 21.5 and Table 21.2). Less conservative vibration responses are generally obtained when any of the interactive models are used. This is in line with previous findings that neglecting the interaction between walking people and the supporting structure can result in overestimation of vibration responses [4, 15]. Interestingly, none of the utilised HSI models of walking people performed particularly better than the others. However, the models presented by Silva [8] and Alonso [6] appear to perform slightly better than the others in most of the simulation cases (Fig. 21.5 and Table 21.2).

It is worth mentioning that the simulated vibration responses using any of the HSI models has less difference from the measured responses in the non-resonant cases (when pacing frequency is 2.05 Hz) than in the resonant case (1.90 Hz). This could indicate sensitivity to damping or amplitude-dependent parameters of the HSI models of walking humans. Another possible source of error is the variability of walking human model parameters between different people (inter-subject variability). This could be better addressed by repeating the test and simulations for a larger number of people.

The utilised measured walking forces model appears to have a non-negligible effect on the accuracy of the simulated vibration responses (Fig. 21.5 and Table 21.2). Therefore, despite the improved accuracy of the simulated responses, when any of the HSI models of walking humans is used, it can be even more improved when a more realistic walking forces model is used (the measured forces). This emphasises the importance of utilising a narrow-band near-periodic walking force model instead of the traditional periodic walking force model. Figure 21.8 shows an example of measured and simulated vibration responses when a measured force and an interactive model are used.

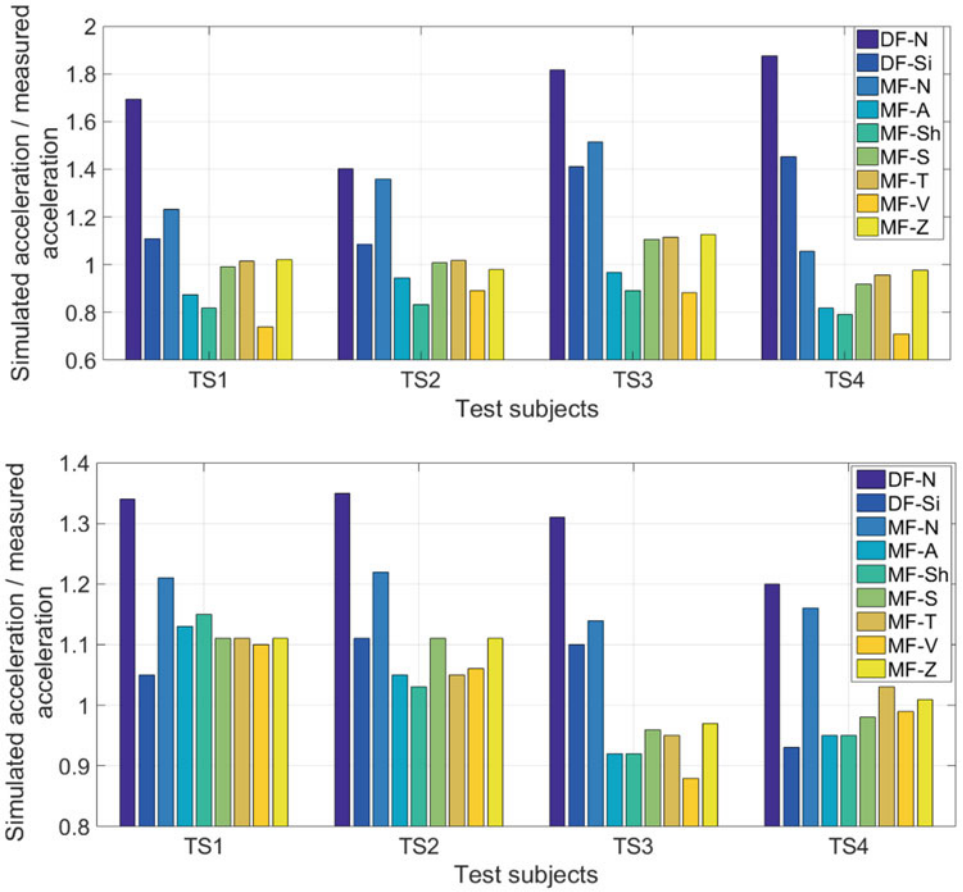


**Fig. 21.5** Comparison of 1-second RMS of simulated and measured vibration responses for pacing frequencies (**a**) 1.9 Hz and (**b**) 2.05 Hz

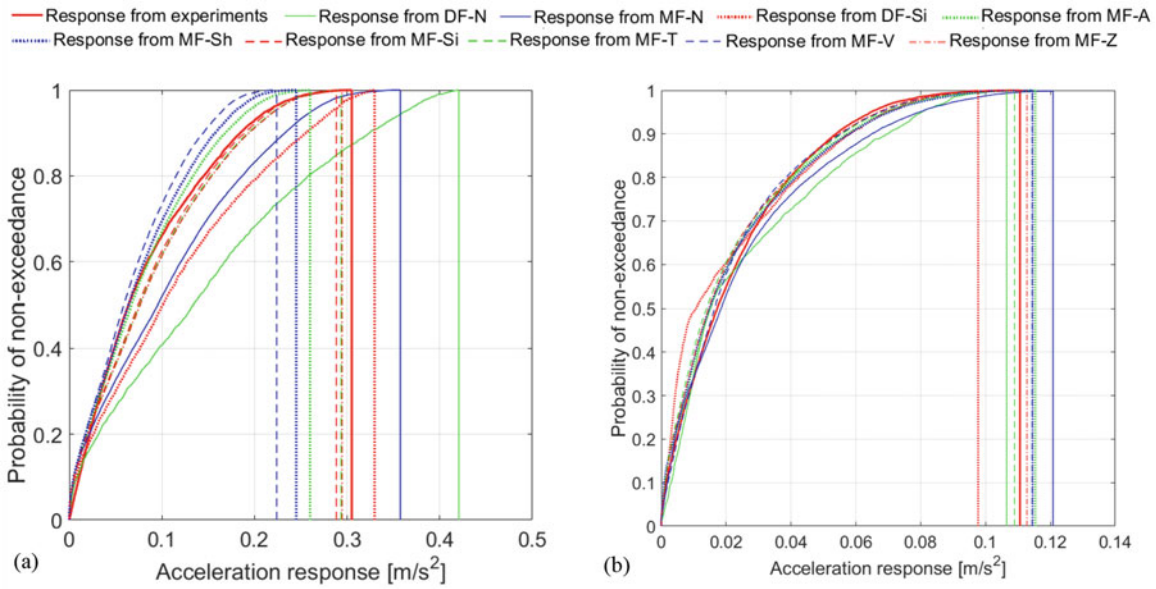


**Fig. 21.6** Cumulative distribution function of vibration responses for TS1 using the model MF-Sh for pacing frequencies (**a**) 1.90 Hz and (**b**) 2.05 Hz

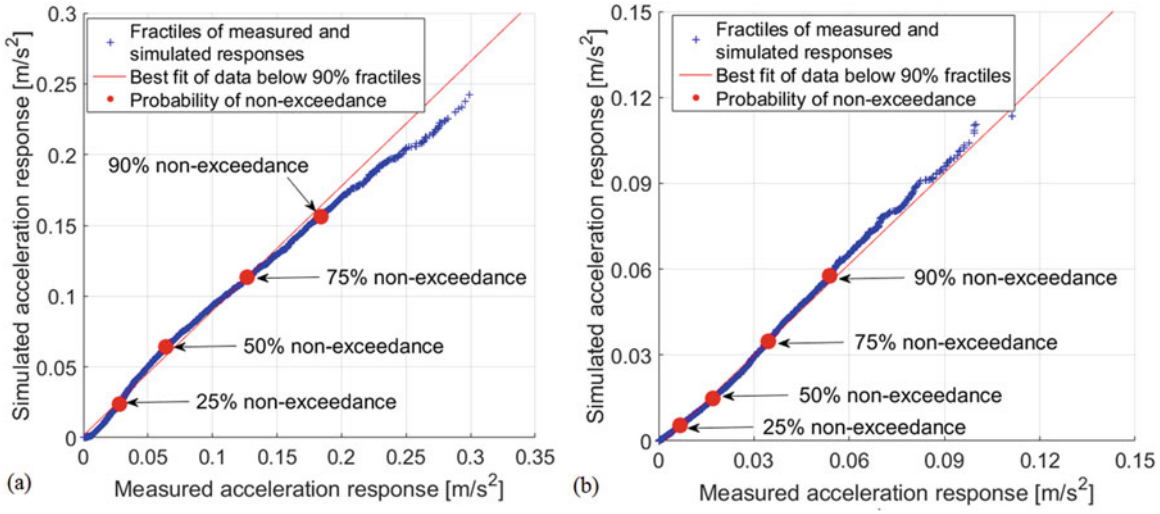


**Fig. 21.7** Fractiles of measured and simulated vibration responses for TS1 using MF-Sh model for pacing frequencies (**a**) 1.90 Hz and (**b**) 2.05 Hz

**Table 21.2** Average ratio of simulated/measured fractiles of vibration responses

| Pacing frequency | Test subjects | Non-interactive models | | Interactive models | | | | | | |
|---|---|---|---|---|---|---|---|---|---|---|
| | | Force function | Measured force | Force function | Measured force | | | | | |
| | | | | Silva [8] | Alonso [6] | Shahabpoor [7] | Silva [8] | Toso [9] | Van Nimmen [10] | Zhang [11] |
| 1.9 Hz | TS1 | 1.84 | 1.33 | 1.44 | 0.94 | 0.88 | 1.06 | 1.08 | 0.80 | 1.09 |
| | TS2 | 1.40 | 1.31 | 1.10 | 0.88 | 0.77 | 0.92 | 0.91 | 0.90 | 0.87 |
| | TS3 | 2.03 | 1.66 | 1.60 | 1.09 | 1.02 | 1.23 | 1.24 | 0.99 | 1.26 |
| | TS4 | 2.08 | 1.17 | 1.62 | 0.89 | 0.88 | 0.96 | 1.03 | 0.78 | 1.06 |
| 2.05 Hz | TS1 | 1.29 | 1.20 | 1.08 | 1.06 | 1.06 | 1.02 | 1.03 | 1.01 | 1.01 |
| | TS2 | 1.35 | 1.24 | 1.21 | 0.96 | 0.92 | 1.02 | 0.94 | 0.98 | 1.01 |
| | TS3 | 1.76 | 1.15 | 1.38 | 0.94 | 0.95 | 0.98 | 0.96 | 0.90 | 0.99 |
| | TS4 | 1.31 | 1.23 | 1.14 | 0.99 | 0.95 | 1.02 | 1.04 | 0.98 | 1.06 |
| Average difference | | **0.633** | **0.286** | **0.321** | **0.069** | **0.091** | **0.061** | **0.076** | **0.085** | **0.079** |

Blue and red cells refer to overestimated and underestimated responses, respectively

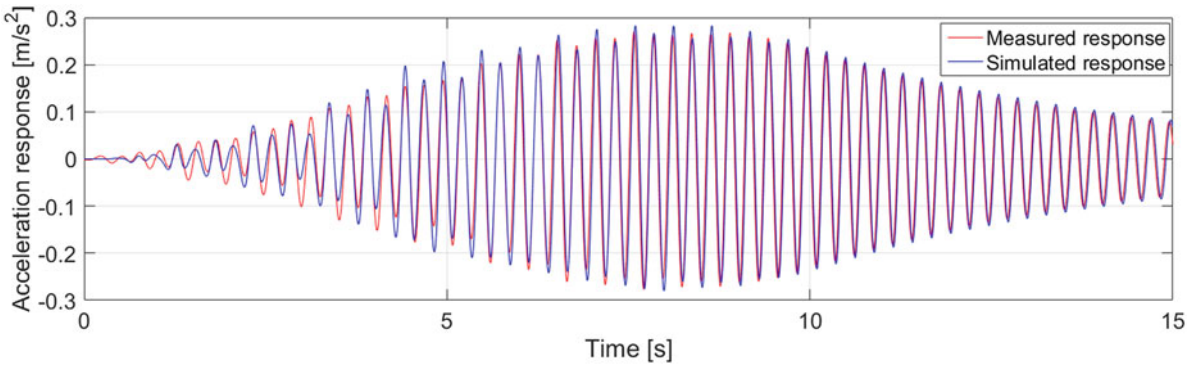


**Fig. 21.8** Measured and simulated vibration responses for TS1 using MF-Sh model for pacing frequency 1.90 Hz

## 21.5 Conclusions

This paper, compares the performance of six experimentally-developed HSI models of walking people available in the literature. The simulated vibration responses are compared with measured vibration responses pertinent to four test subjects walking on a full-scale laboratory footbridge. It is concluded that utilising any of these models can improve considerably the accuracy of the vibration responses, and some of them performed slightly better than the others. It is found also that utilising a HSI model of walking people with a reliable walking force model can produce even better accuracy.

**Acknowledgements** The authors are grateful for the College of Engineering, Mathematics and Physical Sciences in the University of Exeter for the financial support they provided for the first author and his PhD programme. The authors would also like to acknowledge the financial support provided by the UK Engineering and Physical Sciences Research Council (EPSRC) for grant reference EP/E018734/1 ('Human Walking and Running Forces: Novel Experimental Characterization and Application in Civil Engineering Dynamics').

## References

1. Zivanovic, S., Pavic, A., Reynolds, P.: Vibration serviceability of footbridges under human-induced excitation: a literature review. J. Sound Vib. **279**(1–2), 1–74 (2005)
2. Brownjohn, J.M.W., Racic, V., Chen, J.: Universal response spectrum procedure for predicting walking-induced floor vibration. Mech. Syst. Signal Process. 1–15 (2015)
3. Pavic, A., Zivanovic, S.: Key elements for probabilistic framework for estimation of structural vibration due to human-structure dynamic interaction. In: Third International Conference on Structural Engineering, Mechanics and Computation (2007)
4. Živanović, S.: Modelling human actions on lightweight structures: experimental and numerical developments. In: Feltrin, G. (ed.) EVACES 2015, p. 1005 (2015)
5. Shahabpoor, E., Pavic, A., Racic, V.: Interaction between walking humans and structures in vertical direction: a literature review. Shock Vib. **2016**, 12–17 (2016)
6. Jiménez-Alonso, J.F., Sáez, A.: A direct pedestrian-structure interaction model to characterize the human induced vibrations on slender footbridges. Inf. Constr. **66**(1), 1–9 (2014)
7. Shahabpoor, E., Pavic, A., Racic, V.: Identification of mass–spring–damper model of walking humans. Structures. **5**, 233–246 (2016)
8. da Silva, F.T., Pimentel, R.L.: Biodynamic walking model for vibration serviceability of footbridges in vertical direction. In: Eurodyn 2011, pp. 1090–1096 (2011)
9. Toso, M.A., Gomes, H.M., da Silva, F.T., Pimentel, R.L.: Experimentally fitted biodynamic models for pedestrian–structure interaction in walking situations. Mech. Syst. Signal Process. 1–17 (2015)
10. Van Nimmen, K., Maes, K., Živanović, S., Lombaert, G., De Roeck, G., Van den Broeck, P.: Identification and Modelling of Vertical Human-Structure Interaction, pp. 319–330. Springer, New York (2015)
11. Zhang, M., Georgakis, C.T., Qu, W., Chen, J.: SMD Model Parameters of Pedestrians for Vertical Human-Structure Interaction, pp. 311–317. Springer International Publishing, New York (2015)
12. Brownjohn, J.M.W., Fok, P., Roche, M., Omenzetter, P.: Long span steel sedestrian bridge at Singapore Changi Airport—part 2: crowd loading tests and vibration mitigation measures. Struct. Eng. **82**(16), 28–34 (2004)
13. Lou, J., Zhang, M., Chen, J.: Identification of Stiffness, Damping and Biological Force of SMD Model for Human Walking, pp. 331–337. Springer, New York (2015)
14. da Silva, F., Fernandes, B., Pimentel, R.: Modeling of crowd load in vertical direction using biodynamic model for pedestrians crossing footbridges. Can. J. Civ. Eng. **40**, 1196–1204 (2013)
15. Zivanovic, S., Pavic, A., Ingolfsson, E.T.: Modeling spatially unrestricted pedestrian traffic on footbridges. J. Struct. Eng. **136**, 1296–1308 (2010)

# Chapter 22
# Numerical Model for Human Induced Vibrations

**Marcello Vanali, Marta Berardengo, and Stefano Manzoni**

**Abstract** This paper proposes a new model for describing the effect of people on the dynamic behaviour of slender structures. The influence of people is described by using the so-called ground reaction forces. These are split into two types: passive ground reaction forces and active ground reaction forces. This enables to model the influence of both passive and active people occupying the structure.

The experimental tests carried out on two different test-case structures allowed to validate the proposed approach, proving its reliability as well as its accuracy.

**Keywords** Human structure interaction • Ground reaction force • Dynamics • Vibration • Slender structure

## 22.1 Introduction

The dynamic behaviour of structures occupied by people is studied since a lot of time. Particular attention has been devoted to the vibration serviceability issues of civil structures, with special focus on human induced vibrations and Human-Structure Interaction (HSI) [1–5]. Staircases [6, 7], footbridges [8–14], and more generally pedestrian structures [15–17], have been deeply investigated and many other research works focus on stadia serviceability issues [18–20]. Furthermore, international standards and codes [21–25] have been developed to the aim of both designing and evaluating the structure dynamics under the crowd action and they are the natural reference when vibration serviceability is assessed. Unlike other standards, the recent guidance [26] (Joint Working Group, 2008) regarding dynamic performance requirements for permanent grandstands subjected to crowd action recommends to consider human structure interaction.

Many works proposed models to describe/predict the HSI effects on the structure dynamics (e.g., [9, 15, 16]). This work proposes a model where the action of each single person on the structure is taken into account and the structure is considered as a multi-degrees-of-freedom system. Therefore, even structures with coupled modes can be considered when computing the structural response due to people walking.

The paper is structured as follows: Sect. 22.2 describes the theoretical approach and explains how to use the model proposed to predict structural vibrations in presence of people; Sect. 22.3 describes the experimental tests carried out for model validation.

## 22.2 Theoretical Model

When a person is in contact with a point of a structure, he/she produces a Ground Reaction Force (GRF). The GRF is the total force exchanged between the person and the structure. The GRF can be split into passive GRF (PGRF) and active GRF (AGRF) [7]. The PGRF is a force generated by structural movement; when an external force acts on the structure, it vibrates and excites the person. If the person is considered as a dynamic system, it starts to vibrate as well. Therefore, a force is exerted by the person on the structure. Such a force is named PGRF. The AGRF is due to the active force generated by the person's active movement. The AGRFs do not depend on (and are not generated by) the vibration of the structure behind the

M. Vanali (✉) • M. Berardengo
Dipartimento di Ingegneria e Architettura, Università degli studi di Parma, Parma, Italy
e-mail: marcello.vanali@unipr.it

S. Manzoni
Dipartimento di Meccanica, Politecnico di Milano, Milan, Italy



J. Caicedo, S. Pakzad (eds.), *Dynamics of Civil Structures, Volume 2*, Conference Proceedings
of the Society for Experimental Mechanics Series, DOI 10.1007/978-3-319-54777-0_22

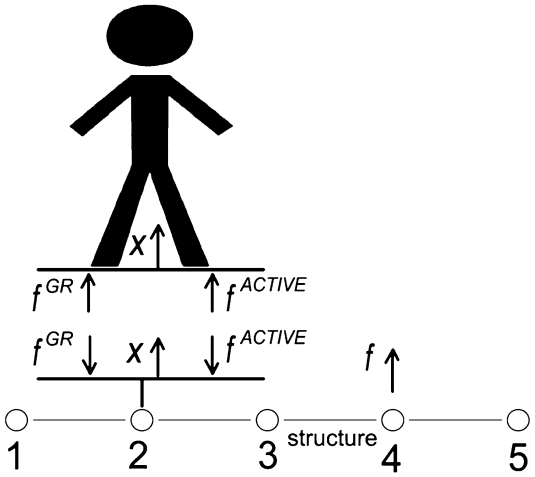


**Fig. 22.1** Human-structure interaction: PGRFs ($f^{GR}$) and AGRFs ($f^{ACTIVE}$)

person and are only due to the active movement of the person. The AGRF can be described as the force exerted by a moving person on a structure with an infinite stiffness.

To sum up, the PGRF depends on the dynamic features of the person and on the motion of the structure. Conversely, the AGRF is produced by an active movement which is not related to the dynamics of the structure.

According to Fig. 22.1, the following equation describes the dynamics of the structure occupied by people:

$$\mathbf{x}(\boldsymbol{\omega}) = \mathbf{G}(\boldsymbol{\omega})\left(-\mathbf{f}^{\mathbf{ACTIVE}}(\boldsymbol{\omega}) - \mathbf{f}^{\mathbf{GR}}(\boldsymbol{\omega}) + \mathbf{f}(\boldsymbol{\omega})\right) \tag{22.1}$$

where $\mathbf{x}$ is the vector of the degrees-of-freedom in which the structure has been discretised, $\mathbf{G}$ is the matrix containing the frequency response functions (FRF) of the empty structure, $\mathbf{f}$ is the vector of the external forces, $\mathbf{f}^{\mathbf{ACTIVE}}$ is the vector of the AGRFs and $\mathbf{f}^{\mathbf{GR}}$ is the vector of the PGRFs. The expression of $\mathbf{G}$ is [27, 28]:

$$\mathbf{G}(\omega) = \sum_{j=1}^{n} \frac{\boldsymbol{\phi}_j \boldsymbol{\phi}_j^{\mathrm{T}}}{\omega_j^2 - \omega^2 + 2\mathrm{i}\zeta_j \omega \omega_{\mathrm{j}}} \tag{22.2}$$

where $\omega_{\mathrm{j}}$ is the jth eigenfrequency, $\zeta_j$ is the associated non-dimensional damping ratio and $\boldsymbol{\phi}_j$ is the jth mode shape vector (scaled to the unit modal mass) measured/evaluated at discrete points (the superscript T indicates transposition). Finally, $n$ is the (arbitrary) number of considered modes, $\omega$ is the circular frequency and i is the imaginary unit. Since the eigenvectors are known at discrete ($m$) points, the matrix $\mathbf{G}(\omega)$ is the $m \times m$ matrix containing the FRFs for these points.

We can now take into account two different situations:

1. passive people (i.e., people who is not moving) on the structure;
2. active people (i.e., people who is moving) on the structure.

The two following subsections will show how to use the model of Eq. (22.1) to describe the dynamics of the whole system in the two listed cases.

### *22.2.1 The Case of Passive People*

In the case of passive people the AGRFs are null. As for the PGRFs, they can be described by the apparent mass of each person. The apparent mass $M^*(\omega)$ is the ratio between the force at the interconnection with the structure and the acceleration of the connection point $\ddot{x}_i$:

$$f_i^{\mathrm{GR}}(\omega) = M^*(\omega)\,\ddot{x}_i(\omega) = -M^*(\omega)\,\omega^2 x_i(\omega) = H(\omega)\,x_i(\omega) \tag{22.3}$$

If we consider more than one person, all the $f_i^{\mathrm{GR}}$ functions can be expressed in matrix form $\mathbf{H}$ and Eq. (22.1) becomes:

$$\left[\mathbf{G}^{-1}(\omega) + \mathbf{W}\mathbf{H}\mathbf{W}^{\mathrm{T}}\right]\mathbf{x}(\omega) = \mathbf{G}_{\mathrm{H}}^{-1}(\omega)\,\mathbf{x}(\omega) = \mathbf{f}(\boldsymbol{\omega}) \tag{22.4}$$

where $\mathbf{W}$ is a matrix representing the connection of $m$ subjects to the structure (i.e., it is a matrix composed by 0 and 1 elements [6]).

According to the Woodbury matrix identity [29], the new matrix $\mathbf{G_H}$ of the FRFs of the new system composed by the structure and the people is:

$$\mathbf{G_H} = \left[\mathbf{G}^{-1} + \mathbf{WHW^T}\right]^{-1} = \mathbf{G} - \mathbf{GW}\left(\mathbf{H}^{-1} + \mathbf{W^T GW}\right)^{-1}\mathbf{W^T G} \tag{22.5}$$

To find the expression of $\mathbf{G_H}$, the $H$ functions must be known for all the people. It is possible to use measured $H$ functions as well as approximated models available in literature [30, 31].

### 22.2.2 The Case of Active People

In the case of active people the AGRFs are non-null. Equation (22.1) can be used to estimate the structural response due to people movement on the structure. To this purpose, we need an estimation of the AGRFs and PGRFs.

As for the AGRFs, it is possible to build a database of forces for the considered kind of movement (e.g., as in [7] for people ascending and descending staircases). Figure 22.2 shows some examples of the collected AGRF time-histories for people ascending and descending staircases.

As for PGRFs, we can still use Eq. (22.3), but we have to keep in mind that in this case the function $H$ changes with time because people change posture during the movement. Furthermore, people move over the structure so that the PGRFs change point of application in time. As for the former point, an equivalent apparent mass $M^*_{eq}$ is defined taking into account many different postures of the subject during the motion. Basically, each step is split into different positions ($P$ positions) and the apparent mass $M^*_{a,i}$ is estimated (e.g., with experimental tests as in [7]) for each of these postures. Actually, each $M^*_{a,i}$ is the average of the apparent mass of different people in the given posture. Then, $M^*_{eq}$ is calculated as:

$$M^*_{eq}(\omega) = \sum_{i=1}^{P} \alpha_i M^*_{a,i}(\omega) \tag{22.6}$$

where the $\alpha_i$ coefficients are the weights. They are chosen in order to describe properly the amount of time spent by the people in the corresponding posture within the cycle time $T$ (i.e., the time of a single step). In other words, we freeze $P$ postures within the movement cycle and we treat each of them as a static posture.

In this scenario, each person produces a PGRF related to the apparent mass $M^*_{eq}$. Then, the PGRFs can be applied to the structure in two different ways:

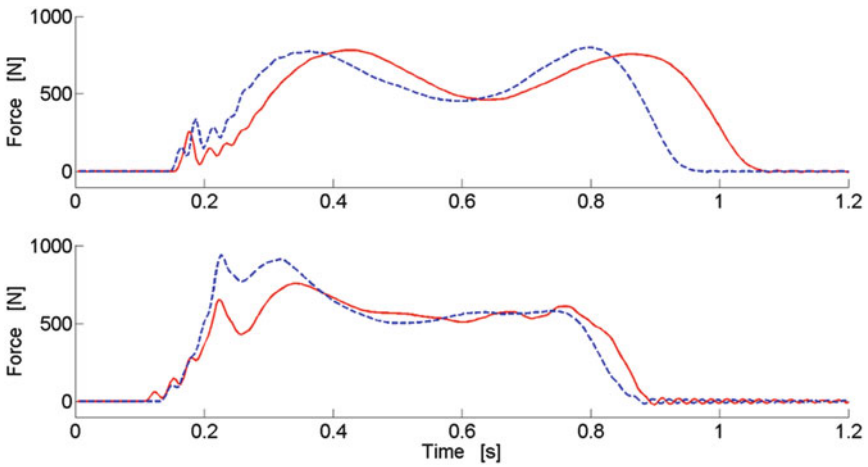


**Fig. 22.2** Two examples of recorded AGRF time-histories for people ascending a staircase (*up*) and two examples of recorded AGRF time-histories for people descending a staircase (*down*)

1. each PGRF (i.e., one for each person on the structure) is considered as a moving excitement. Hence, the equivalent matrix $\mathbf{G_H}(\omega)$ (see Eq. 22.4) changes in time;
2. a fraction of the apparent mass $m^*_{fr}(\omega)$ is calculated:

$$m^*_{fr}(\omega) = \frac{m}{n_d} M^*_{eq}(\omega) \tag{22.7}$$

where $m$ is the number of people on the structure and $n_d$ is the number of points in which the structure is discretised. Then, $m^*_{fr}(\omega)$ is applied to each of the $n_d$ points. Thus, the PGRF in each point can be expressed as:

$$f_i^{\mathrm{GR}}(\omega) = m^*_{fr}(\omega)\,\ddot{x}_i(\omega) = -m^*_{fr}(\omega)\,\omega^2 x_i(\omega) \tag{22.8}$$

In terms of the full displacement vector $\mathbf{x}(\omega)$, $\mathbf{f}^{\mathrm{GR}}$ becomes:

$$\mathbf{f}^{\mathrm{GR}}(\omega) = \mathbf{W_n H W_n^T x}(\omega) = -\omega^2 m^*_{fr}(\omega)\,\mathbf{W_n x}(\omega) \tag{22.9}$$

where $\mathbf{W_n}$ is a $n_d$ x $n_d$ identity matrix, $\mathbf{H}(\omega)$ is a $n_d$ x $n_d$ diagonal matrix containing the fractions of the equivalent apparent mass (i.e. $\mathbf{H}(\omega) = -\mathbf{W_n}\omega^2 m^*_{fr}(\omega)$). Substituting Eq. (22.9) into Eq. (22.1), we obtain (neglecting $\mathbf{f}$):

$$\left[\mathbf{G}^{-1}(\omega) + \omega^2 m^*_{fr}(\omega)\,\mathbf{W_n}\right]\mathbf{x}(\omega) = \mathbf{G}_{\mathrm{H}}^{-1}(\omega)\,\mathbf{x}(\omega) = -\mathbf{f}^{\mathbf{ACTIVE}}(\omega) \tag{22.10}$$

where $\mathbf{G_H}(\omega)$ is the $n_d \times n_d$ matrix representing the equivalent set of FRFs describing the dynamic behaviour of the joint system composed by the structure and the people. Obviously, the behaviour of this joint system is an average behaviour because $m^*_{fr}$ is employed.

The second approach of the previous list assumes a fixed form of $\mathbf{G_H}(\omega)$ in time. Therefore, this assumption makes the simulation of the structure response fast and easy under the computational point of view. Moreover, when the number of people on the structure is increases, the accuracy of this easy-to-apply approach is expected to increase as well.

Finally, the response of the structure to the movement of people can be calculated as the convolution between the AGRFs and the unit impulse response functions of the joint system. These unit impulse response functions can be achieved by applying the inverse Fourier transform to the FRFs composing $\mathbf{G_H}(\omega)$. As for the AGRFs to be applied, Fig. 22.3 provides an example of how to build them by using the database of AGRFs mentioned previously. Such an example refers to a person ascending a staircase and the forces depicted are related to the force exerted by this person on three consequent steps.

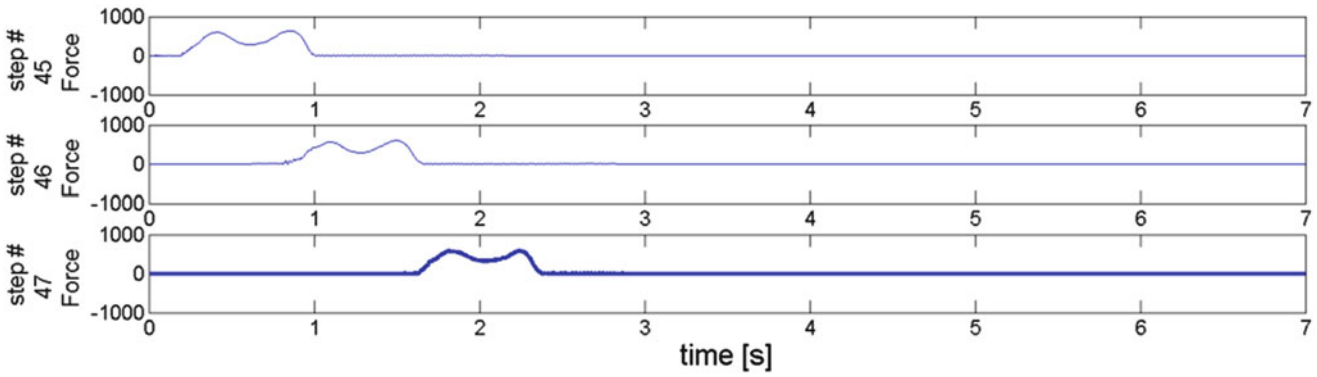


**Fig. 22.3** Simulation of the AGRFs exerted by a person ascending a staircase on three consequent steps. The portion of the time-histories where the forces are not null are recorded AGRFs like those of Fig. 22.2. The force signals are in Newton

## 22.3 Experimental Tests

This section describes the experimental campaign carried out to validate the model presented in Sect. 22.2. Two staircases were used as test-structures. One, named S1, is made up of steel and marble, its length is 12.03 m, its width is 1.80 m and the height is 5.22 m. The second one, named S2, is made up of steel and has marble sheets on the steps, its length is 13.30 m, its width is 1.80 m and the height is 5.60 m. The modal parameters of the empty structures were identified by means of experimental modal analysis [32] and the values of the eigenfrequencies and non-dimensional damping ratios are gathered in Tables 22.1 and 22.2. The modes taken into account are those in the frequency range 0–15 Hz, which is the frequency band where the humans are mostly able to influence the dynamics of the structures.

### *22.3.1 Tests with Passive People*

This subsection presents some results related to the validation of the model of Sect. 22.2.1, developed to model the influence of passive people on the dynamic behaviour of the hosting structure. Different people were asked to stay in given points of the staircases. Then, the structure was excited by using an electro-dynamic shaker laid down on the staircase and moving a mass. Therefore, the excitement was provided employing the inertial effect (more details about the way to excite the structure can be found in [6, 7]). Finally, the FRFs of the structure were estimated by measuring the structural response by means of accelerometers. Figure 22.4a, b show the FRFs (for some tests and points of the structure chosen as examples) in a given point of S1 and S2, respectively. The experimental results match the numerical expectations for both the structures, proving the reliability and accuracy of the proposed approach. Other tests gave a similar level of accordance between experiments and simulations. Therefore, they are not shown here for sake of conciseness.

**Table 22.1** Modal data identified experimentally for S1 in the frequency range 0–15 Hz (empty structure)

| Mode number | $\omega_j/(2\pi)$ [Hz] | $\zeta_j$ [%] |
|---|---|---|
| 1 | 7.84 | 0.33 |
| 2 | 8.89 | 0.43 |

**Table 22.2** Modal data identified experimentally for S2 in the frequency range 0–15 Hz (empty structure)

| Mode number | $\omega_j/(2\pi)$ [Hz] | $\zeta_j$ [%] |
|---|---|---|
| 1 | 6.70 | 0.33 |
| 2 | 9.55 | 0.28 |
| 3 | 10.75 | 0.29 |
| 4 | 11.21 | 0.17 |

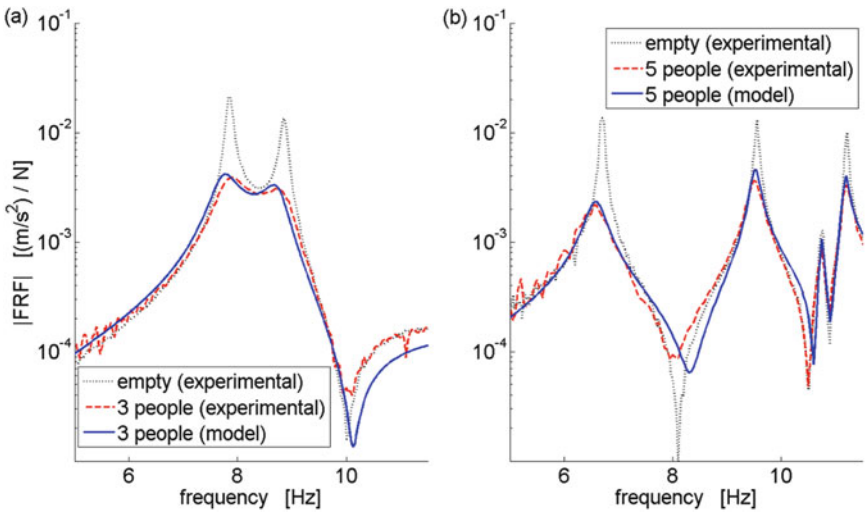


**Fig. 22.4** FRF for S1 (**a**) and S2 (**b**)

### 22.3.2 Tests with Active People

This subsection shows that the use of the model presented in Sect. 22.2.2 allows to improve the prediction of the structural response due to people moving. The tests were carried out by asking a given number of people to walk freely and all together on S1/S2. The acceleration responses of the structures were measured by means of accelerometers. The newly proposed approach is compared here to the experiments and to the use of the model of the empty structure directly excited by the AGRFs.

The mentioned comparison is carried out in terms of root mean square (RMS) of the time-responses. Here, the resulting RMS values are related to the point of maximum response for both S1 and S2. The RMSs are calculated in the frequency range 0–15 Hz.

The RMS values coming from the use of the models is represented as a mean value plus/minus twice the standard deviation. Indeed, since the AGRFs are sampled from a database of AGRFs (see Sect. 22.2.2), the result of a single simulation depends upon the AGRFs extracted from the database. Therefore, each case (i.e., a given number of people walking on either S1 or S2) was simulated 100 times to achieve a statistical reliability of the results by building of the resulting RMS values distributions (which were found to have a Gaussian trend).

Figure 22.5a, b show the results related to the tests on S1 with three and nine people walking on the staircase, respectively. Figure 22.5c, d show the results related to the tests on S2 with five and ten people walking on the staircase, respectively. These plots demonstrate that the model proposed in Sect. 22.2.2 allows to satisfactorily estimate the experimental results. Furthermore, the use the FRF matrix $\mathbf{G_H}$ as described in Sect. 22.2.2 allows to achieve results more accurate than the direct application of the AGRFs to the model of the empty structure (i.e., using $\mathbf{G}$).

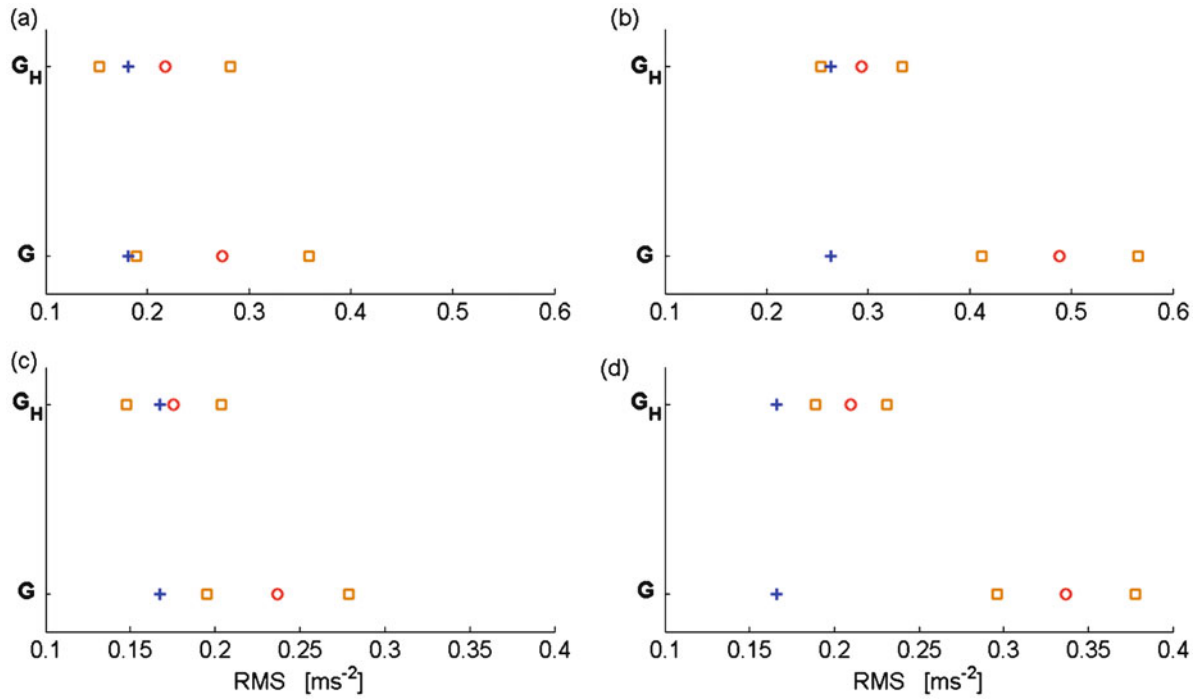


**Fig. 22.5** Resulting RMS values: S1 with three people walking (**a**), S1 with nine people walking (**b**), S2 with five people walking (**c**) and S2 with ten people walking (**d**). The symbol $G_H$ on the vertical axis refers to the results related to model presented in Sect. 22.2.2, while the symbol G is related to the application of the AGRFs to the model of the empty structure. *Plus symbols* are related to experimental results, *circle symbols* are related to the mean value of the simulations results and *square symbols* are related to the mean value of the simulations results plus/minus twice the standard deviation of the simulation results

## 22.4 Conclusion

This paper has dealt with a new approach to model the coupling between a slender structure and people occupying it. The proposed approach shows to be accurate and reliable when considering both passive and active people. Such a result is achieved by splitting the influence of each person as the sum of a passive ground reaction force and an active one.

The model has been validated by means of experimental tests performed on two different staircases showing a good agreement with experiments in terms of the predicted vibration levels and highlighting the fact that considering the empty structure response always leads to a consistent overestimation of the human induced vibrations.

## References

1. Sachse, R., Pavic, A., Reynolds, P.: Human-structure dynamic interaction in civil engineering dynamics: a literature review. Shock Vib. Dig. **35**, 3–18 (2003)
2. Živanović, S., Pavic, A., Reynolds, P.: Vibration serviceability of footbridges under human-induced excitation: a literature review. J. Sound Vib. **279**, 1–74 (2005)
3. Racic, V., Pavic, A., Brownjohn, J.M.W.: Experimental identification and analytical modelling of human walking forces: literature review. J. Sound Vib. **326**, 1–49 (2009)
4. Alexander, N.A.: Theoretical treatment of crowd–structure interaction dynamics. Proc. Inst. Civ. Eng. Struct. Build. **159**, 329–338 (2006)
5. Sim, J., Blakeborough, A., Williams, M.: Modelling of joint crowd-structure system using equivalent reduced-DOF system. Shock Vib. **14**, 261–270 (2007)
6. Busca, G., Cappellini, A., Manzoni, S., Tarabini, M., Vanali, M.: Quantification of changes in modal parameters due to the presence of passive people on a slender structure. J. Sound Vib. **333**, 5641–5652 (2014)
7. Cappellini, A., Manzoni, S., Vanali, M., Cigada, A.: Evaluation of the dynamic behaviour of steel staircases damped by the presence of people. Eng. Struct. **115**, 165–178 (2016)
8. Venuti, F., Bruno, L., Bellomo, N.: Crowd dynamics on a moving platform: mathematical modelling and application to lively footbridges. Math. Comput. Model. **45**, 252–269 (2007)
9. Venuti, F., Racic, V., Corbetta, A.: Modelling framework for dynamic interaction between multiple pedestrians and vertical vibrations of footbridges. J. Sound Vib. **379**, 245–263 (2016)
10. Van Nimmen, K., Lombaert, G., De Roeck, G., Van den Broeck, P.: Vibration serviceability of footbridges: evaluation of the current codes of practice. Eng. Struct. **59**, 448–461 (2014)
11. Figueiredo, F.P., da Silva, J.G.S., de Lima, L.R.O., Vellasco, P.C.G.d.S., de Andrade, S.A.L.: A parametric study of composite footbridges under pedestrian walking loads. Eng. Struct. **30**, 605–615 (2008)
12. Mashaly, E.S., Ebrahim, T.M., Abou-Elfath, H., Ebrahim, O.A.: Evaluating the vertical vibration response of footbridges using a response spectrum approach. Alex. Eng. J. **52**, 419–424 (2013)
13. Ingólfsson, E.T., Georgakis, C.T.: A stochastic load model for pedestrian-induced lateral forces on footbridges. Eng. Struct. **33**, 3454–3470 (2011)
14. Piccardo, G., Tubino, F.: Equivalent spectral model and maximum dynamic response for the serviceability analysis of footbridges. Eng. Struct. **40**, 445–456 (2012)
15. Toso, M.A., Gomes, H.M., Da Silva, F.T., Pimentel, R.L.: Experimentally fitted biodynamic models for pedestrian-structure interaction in walking situations. Mech. Syst. Signal Process. **72–73**, 590–606 (2016)
16. Caprani, C.C., Ahmadi, E.: Formulation of human–structure interaction system models for vertical vibration. J. Sound Vib. **377**, 346–367 (2016)
17. Setareh, M.: Vibrations due to walking in a long-cantilevered office building structure. J. Perform. Constr. Facil. **26**, 255–270 (2012)
18. Sachse, R., Pavic, A., Reynolds, P.: Parametric study of modal properties of damped two-degree-of-freedom crowd-structure dynamic systems. J. Sound Vib. **274**, 461–480 (2004)
19. Reynolds, P., Pavic, A., Ibrahim, Z.: Changes of modal properties of a stadium structure occupied by a crowd. In: Proceedings of XXII International Modal Analysis Conference (IMAC), Orlando, FL, USA, 2004
20. Cappellini, A., Cattaneo, A., Manzoni, S., Scaccabarozzi, M., Vanali, M.: Effects of people occupancy on the modal properties of a stadium grandstand. In: Proceedings of XXXIII International Modal Analysis Conference (IMAC), Orlando, FL, USA, 2015
21. EN1990-Eurocode: Basis of Structural Design (2002)
22. Sètra: Technical guide—assessment of vibrational behaviour of footbridges under pedestrian loading. Service d'Etudes techniques des routes et autoroutes (2006)
23. ISO10137: International Organization for Standardization—bases for design of structures—serviceability of buildings and walkways against vibration (2007)
24. Caprioli, A., Reynolds, P., Vanali, M.: Evaluation of serviceability assessment measures for different stadia structures and different live concert events. In: Proceedings of XXV International Modal Analysis Conference (IMAC), Orlando, FL, USA, 2007
25. Caprioli, A., Vanali, M.: Comparison of different serviceability assessment measures for different events held in the G. Meazza stadium in Milano. In: Proceedings of XXVII International Modal Analysis Conference (IMAC), Orlando, FL, USA, 2009
26. Institution of Structural Engineers: Dynamic performance requirements for permanent grandstands subject to crowd action: recommendations for management, design and assessment (2008)
27. Ewins, D.J.: Modal Testing: Theory, Practice and Application. Research Studies Press Ltd., Baldock (2000)

28. Brandt, A.: Noise and Vibration Analysis—Signal Analysis and Experimental Procedures. Wiley (2011)
29. Woodbury, M.A.: Inverting Modified Matrices. Princeton, NJ, USA (1950)
30. Matsumoto, Y., Griffin, M.J.: Dynamic response of the standing human body exposed to vertical vibration: influence of posture and vibration magnitude. J. Sound Vib. **212**, 85–107 (1998)
31. Matsumoto, Y., Griffin, M.J.: Mathematical models for the apparent masses of standing subjects exposed to vertical whole-body vibration. J. Sound Vib. **260**, 431–451 (2003)
32. Peeters, B., Van Der Auweraer, H., Guillaume, P., Leuridan, J.: The PolyMAX frequency-domain method: a new standard for modal parameter estimation? Shock Vib. **11**, 395–409 (2004)

# Chapter 23
# Dynamic Testing on the New Ticino Bridge of the A4 Highway

**Elena Mola, Franco Mola, Alfredo Cigada, and Giorgio Busca**

**Abstract** The dynamic tests on the two separate viaducts constituting the bridge over the Ticino river offered the chance to start a thorough identification process consisting in numerical simulation, experimental activity and model updating, to gather a deeper knowledge of the bridge behavior. In addition, this series of tests has offered a good benchmark to prove the actual strengths and weaknesses of the Italian standards for dynamic testing. The two viaducts are identical and made up of a series of equal length spans, making modal identification a more complex task, since it has to be performed in the presence of dense spectra with a number of closely spaced peaks, belonging to quite similar mode shapes. Operational Modal Analysis (OMA) was performed and is scheduled to be repeated in the future to assess any eventual on-going damage. The paper will present the results of the experimental activity compared to the numerical predictions and the model tuning activity.

**Keywords** Operational modal analysis • Composite bridges • Eigenvalue analysis • Model tuning • Monitoring

## 23.1 Introduction

The study of the dynamic performance of civil infrastructures, such as bridges and viaducts, is a very important matter both in the academic research community and for the Institutions, since their security and reliability are deeply related to casualties, resilience and strategic performance in case of events such as earthquakes.

The importance of correctly assessing the dynamic behavior of strategic infrastructures is reflected in most European normative documents, with different levels of detail, depending on the Country. In Italy, there are prescriptions enforced by the Italian Code, i.e. D.M. 14 Jan 2008 [1], for strategic flyovers, bridges or otherwise significant structures that need to guarantee increased performance levels in case of an emergency. For these cases, the design and construction validation protocol needs to include dynamic experimental analysis of some sort, through which at least the first natural frequency of the structure can be estimated and compared to that predicted by the numerical analysis during the design phase. Unfortunately, the current version of the Code does not specify what kind of dynamic tests must be carried out, but the only requirement is the identification of at least the first vibration frequency, and its comparison to the one predicted by the numerical model. For modal identification and model tuning to be effective, though, it is definitely necessary to identify and compare a full set of modal parameters and mode shapes, rather than one single value of frequency: in this way, thorough correlation and cross-correlation tests can be performed between the experimental and the numerical results.

In the case at hand, the Owner of the highway A4, SATAP Spa, required a thorough experimental modal analysis of the Ticino Bridge, which was carried out by the staff of Politecnico di Milano. The experimentally dynamic properties were then compared to the numerical analyses carried out by the staff of ECSD Srl, in charge of the final design and construction validation.

It is well known that modal identification can usually be performed in two ways: Operational Modal Analysis (OMA) [2] and Experimental Modal Analysis [3]. If the dynamic tests are mainly meant as a design validation tool, then operational modal analysis is often preferred. It provides sufficiently accurate information on the modal properties of the infrastructures with reduced global costs with respect to an experimental modal analysis requiring forced excitation. When using OMA,

E. Mola (✉)
ECSD Srl, Via Carlo Goldoni, 22 20129, Milan, Italy
e-mail: elena.mola@ecsd.it

F. Mola
ABC Department, Politecnico di Milano, Piazza Leonardo da Vinci, 32 20133, Milan, Italy

A. Cigada • G. Busca
Mechanical Engineering Department, Politecnico di Milano, Via Giuseppe La Masa, 34 20156, Milan, Italy



J. Caicedo, S. Pakzad (eds.), *Dynamics of Civil Structures, Volume 2*, Conference Proceedings
of the Society for Experimental Mechanics Series, DOI 10.1007/978-3-319-54777-0_23

though, natural frequencies and modal damping coefficients can still be obtained, but mode shapes can not be mass- scaled since the excitation force is unknown. A very important advantage of OMA is the fact that it does not require disruption of use, which is very important for a bridge, so it can be easily repeated over time under operational conditions to monitor the evolution of the dynamic properties, for both monitoring and early damage detection purposes. This, together with its reduced costs, was the main reason why the Owner chose to perform OMA tests only, in view of a future monitoring protocol to be implemented for the bridge, including periodic repetitions of OMA tests in operating conditions.

The modal parameter identification methods based on Operational Modal Analysis can be classified into frequency domain methods and time domain methods. In this paper, the Poly-reference Least Squares Complex Frequency Domain method is adopted to modal parameter identification for operational data, which is a polyreference version of the LSCF method, using a so-called right matrix-fraction model [4].

In the following, the numerical analysis and the experimental activity carried out on the bridge will be presented and the results compared and discussed.

## 23.2 Description of the Bridge

The Ticino Bridge is part of A4 highway which connects the two main cities in Italy (Milan and Turin respectively) and it is one of the oldest and most important European motorways. Therefore, it is of great significance and importance.

The bridge is designed so that the two ways (MI-TO and TO-MI), consisting of three lanes each, are separated. Each way consists of 16 reinforced concrete piers supporting a continuous steel beam deck of 17 spans without joints. The steel girder sections of the deck, composed by four main beams and horizontal braces, which support a reinforced concrete slab (Fig. 23.1a), were assembled and launched by pushing them independently at both the river banks for optimizing and reducing construction time (Fig. 23.1b). The TO-MI way is 16.9 m wide while the MI–TO way is 18.4 m due to an additional pedestrian lane. In order to guarantee the necessary seismic performance of the bridge, as well as the compensation of the thermal deformations, the deck rests on friction pendula allowing a relative displacement in the horizontal direction.

## 23.3 Structural Analysis and Modelling Assumptions

The dynamic properties of the Ticino Bridge were numerically predicted by means of a finite element (FE) model that was developed using the commercial software for structural analysis Midas Gen v.2014 (Fig. 23.2).

The friction pendulum damping devices between the piers and the deck elements were modeled considering their force displacement curve provided by producers and reported in Fig. 23.3a.

The horizontal stiffness of these devices, k, is function of vertical load, V, and is higher for small displacements ($<d_1 = 2$ mm) and lower for large displacements, as reported in Fig. 23.3a). For the analysis of the dynamic properties of the flyover to be compared with the experimental results from operational modal analysis, the horizontal stiffness of each friction pendulum was taken equal to $ki = \mu V/d_1$, where $\mu = 0.025$ is the friction coefficient, V is the vertical load on the device (actually in place during the dynamic tests), $d_1 = 2$ mm is the limit value of the displacement for which the slope of the bi-linear curve representing the stiffness of the bearing changes, as can be observed in Fig. 23.3a). In order to correctly represent the boundary conditions and distribute the stiffness of the bearing on the beams, nine nodal isolators were modeled by means of nine springs acting on the beam (Fig. 23.3b). The value of the horizontal stiffness of these springs was taken equal to $k_i^* = k_i/9$ as a function of the vertical load.

The bridge substructure, consisting of reinforced concrete piers, was not included in the numerical model since its contribution to the dynamic vibration characteristics of the deck was judged negligible, mainly because the stiffness of the piers is much higher than those of the friction pendulum bearings. Moreover, because most of the mass of a bridge is in the deck, the first modes usually involve mainly the deck and not the piers. As a matter of fact, the deck can thus be considered restrained to the ground by means of systems of two springs in series, one corresponding to the isolator with low stiffness and the other to the pier with much higher stiffness. Therefore, for very different stiffness values, the global stiffness of the series springs is dominated by the lower value and the higher one could be neglected. The model has been accordingly limited to the deck and the supporting isolating system. The developed finite element model is three-dimensional and was implemented using a refined mesh of shell elements. This choice allows a realistic description of the deck geometry (Fig. 23.2) and of the mass and loads distribution together with a more reliable definition of the mode shapes, especially those involving the torsional behavior of the bridge deck. All shell elements have four node rectangular shapes, adopting meshing

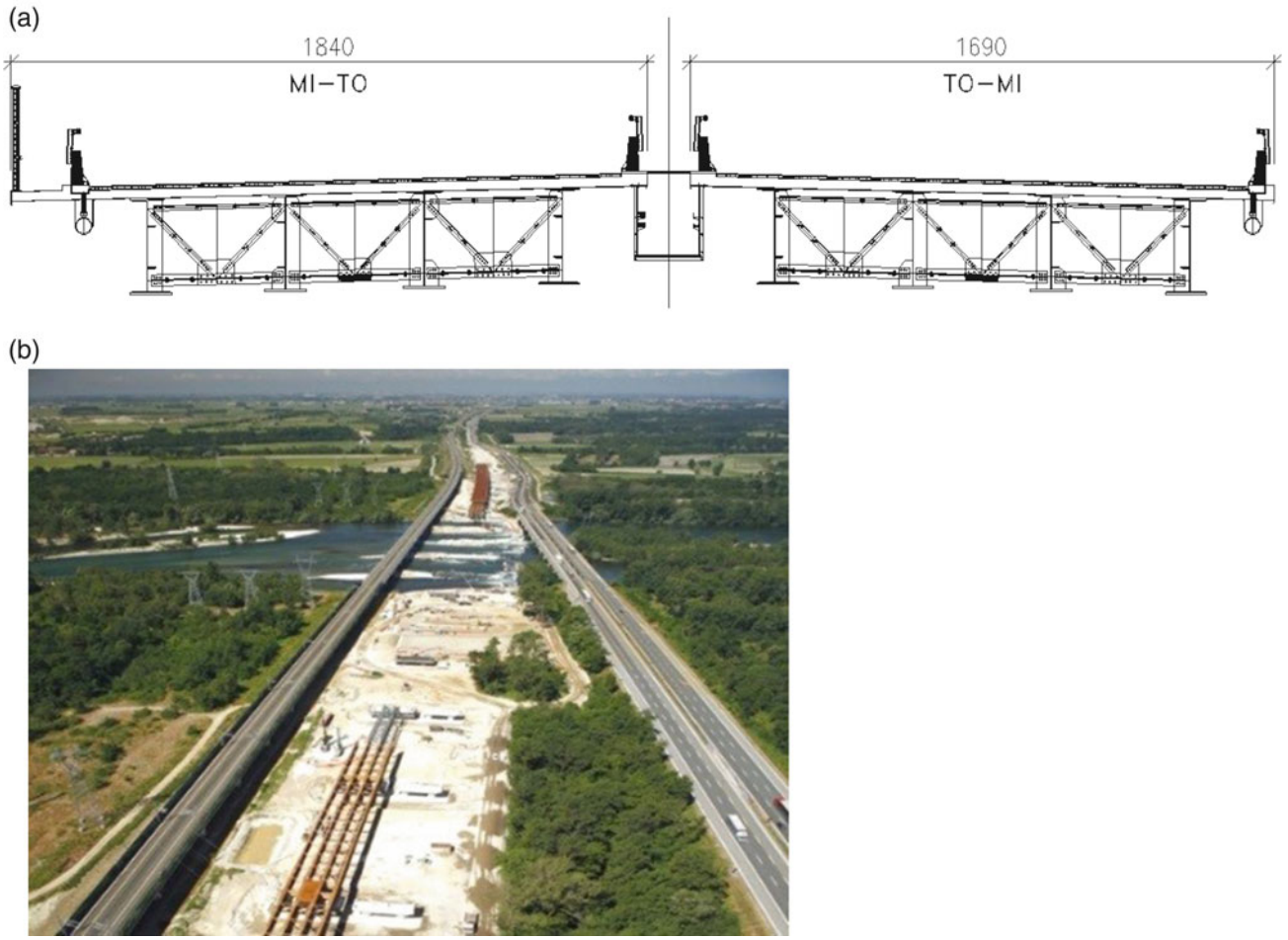


**Fig. 23.1** (**a**) Scheme of the cross section of the bridge deck and (**b**) the bridge under construction

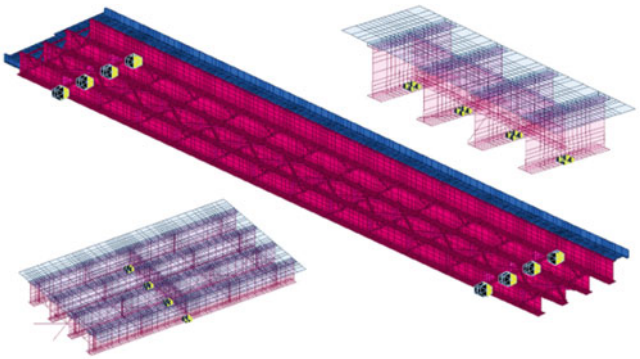

**Fig. 23.2** Details of the FEM of the bridge—cross sections and friction bearings modeled with four springs

criteria such as low aspect ratio, avoidance of small or large angles in elements and avoidance of small to large element transitions.

The modes obtained from modal analysis are typically similar to a static wave with close frequency values. For instance, Modes 1, 2 and 3 are similar vertical modes, while 8, 9 and 10 are similar torsional modes. These mode shapes and frequencies will be compared to those derived from preliminary operational analysis in the next section. The frequencies and mode shapes are slightly different for the two travelling ways, due to the presence of the additional pedestrian way on the MI-TO side, but the same, very closely spaced, modes appear in both cases. In Table 23.1, the first 14 natural frequencies and mode shapes of the MI–TO way, identified by numerical linear modal analysis, are shown.

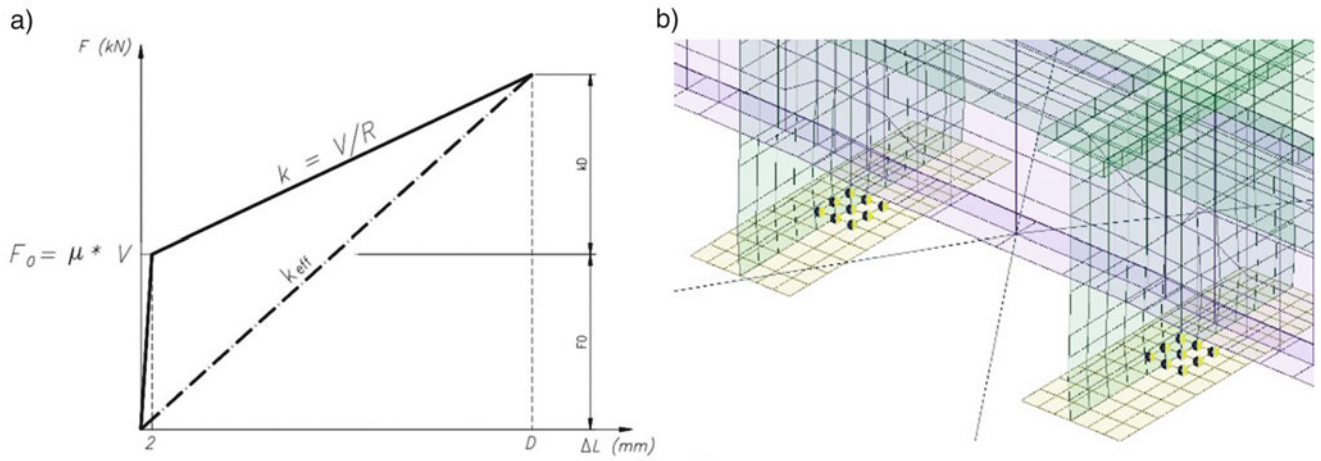


**Fig. 23.3** (**a**) Force-displacement diagram of a friction pendulum device under seismic conditions; (**b**) Friction pendulum bearing modelled by nine springs

**Table 23.1** Linear modal analysis results: modal frequencies MI–TO way

| Mode | f (Hz) | Vibration mode of the whole MI-TO way | Vibration mode of the investigated spans | Mode | f (Hz) | Vibration mode of the whole MI-TO way | Vibration mode of the investigated spans |
|---|---|---|---|---|---|---|---|
| 1 | 1.27 | | | 2 | 1.29 | | |
| 3 | 1.32 | | | 4 | 1.37 | | |
| 5 | 1.45 | | | 6 | 1.53 | | |
| 7 | 1.58 | | | 8 | 1.59 | | |
| 9 | 1.61 | | | 10 | 1.63 | | |
| 11 | 1.65 | | | 12 | 1.70 | | |
| 13 | 1.73 | | | 14 | 1.75 | | |

## 23.4 Operational Modal Analysis

Operational modal analysis was applied to process the experimental data: wind, vibrations induced by the surrounding working area, nearby traffic etc. could provide suitable environmental excitation for modal parameters identification. In order to ensure the robustness of the results, the time duration of test was eight hours: this has allowed stabilizing the spectra with a signal/noise ratio good enough to get reliable results in the next modal analysis identification. In addition, it was necessary to check temperature changes to eventually correct any deviation in the modal parameters depending on its value: this dependence was proved to be negligible in this case. The availability of a large amount of data coming from low noise transducers allowed averaging over long time windows, in order to obtain frequency spectra characterized by an acceptable signal to noise ratio.

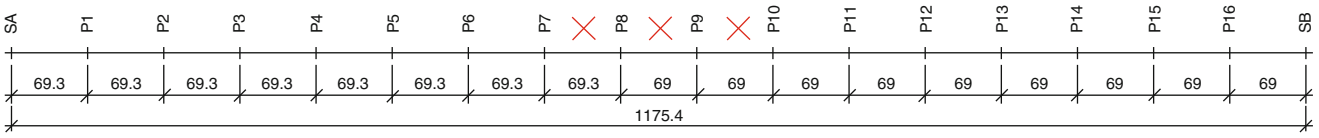


**Fig. 23.4** Investigated spans, dimensions in meters

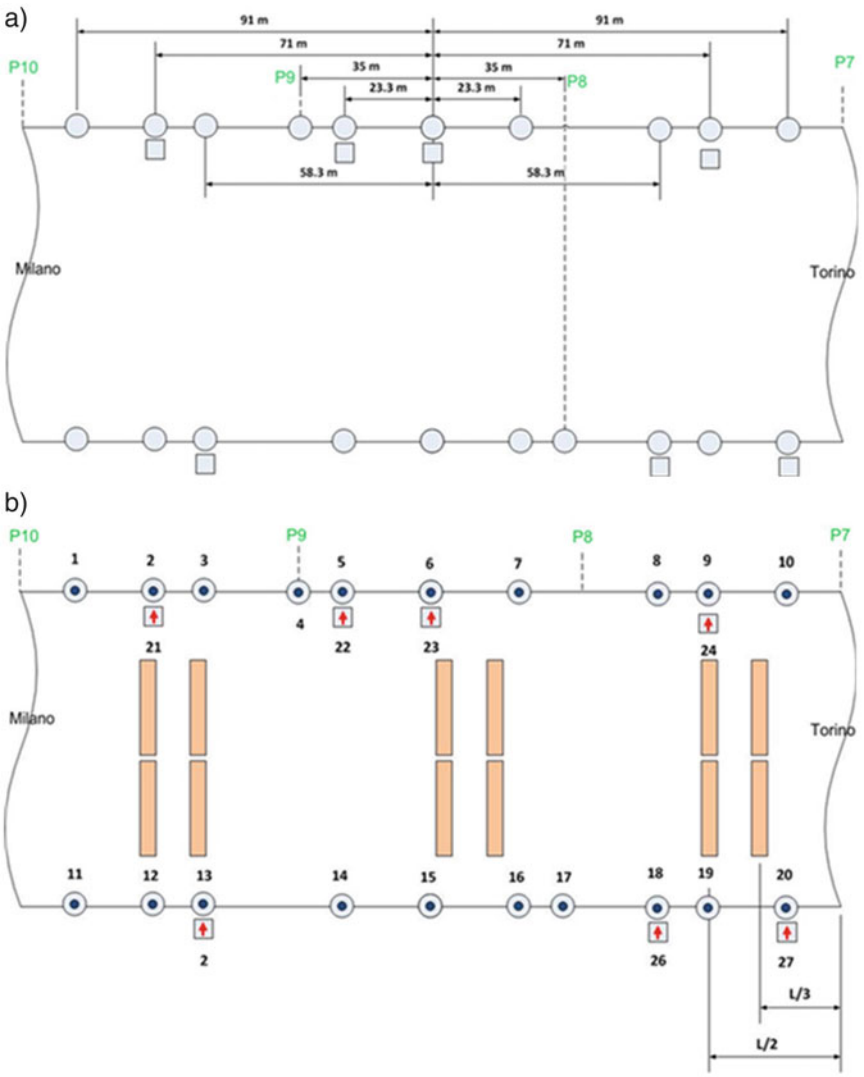


**Fig. 23.5** Measurement grid: (**a**) locations and (**b**) channel numbers

### *23.4.1 Description of the Tests*

The measurement mesh and dimensions of investigated spans are shown in Figs. 23.4 and 23.5. The response of the bridge was measured at twenty measurement points in the vertical direction and seven in the transverse direction (Fig. 23.5). The sensors placement was based on the numerical model in order to get reliable results for the first mode shapes.

As for the choice of the sensors for measuring the structural response, the accelerometers were piezo-electric sensors used for seismic applications. In fact, this type of sensors ensures excellent sensitivity to vibration and a large enough bandwidth even for low frequencies, granting a high signal to noise ratio even for very low frequencies. More in detail, with reference to the positions shown in Fig. 23.5, the patterns of accelerometer used were:

- accelerometer piezo-electric PCB393B31 (channels 5, 7, 11, 13, 20, 22, 24, 25, 26, 27)
- accelerometer piezo PCB 393A03 (channels 9, 21)
- accelerometer piezo-electric PCB 393B12 (other channels)

All signals were recorded using a 24 bit A/D converter with anti-aliasing filters built inside, with a sampling frequency equal to 2048 Hz.

### *23.4.2 Test Results and Identification Issues*

The technique used for the extraction of modal parameters from the output data only is the Polyreference Least Squares Complex Frequency Domain method. One of the specific advantages of the technique lies in the very stable identification of the system poles and participation factors as a function of the specified system order, leading to easy-to-interpret stabilization diagrams, [4, 5]. Hence it keeps a rather good accurate performance to identify the parameters for small damping and dense modal system by using stabilization diagram. Figure 23.6 shows the stabilization diagram obtained.

Since the first three/four vibration modes are enough for the model validation, a frequency band from 1 to 3 Hz with a rather high mode density was chosen (Fig. 23.6). From the stabilization diagram, the poles marked by arrows are very stable, so these modes can be identified in a reliable and robust way [6, 7].

The averaged Power Spectral Densities (PSD) of Accelerometer 2, 5 and 6 have been computed and showed in Fig. 23.7. It is clear that auto-spectra in Fig. 23.7 have the first significant peaks from 1 to 3 Hz, which reveals that the structure has very closely spaced modes, in some cases just with a 0.05 Hz gap among them.

Because some modes, for instance the two modes marked by arrows in Fig. 23.7, are highly damped and close to the next peaks (1.27 and 1.36 Hz respectively), it is rather challenging to identify these modes. Table 23.2 shows the first identified natural frequencies and corresponding damping ratios. It must be noticed that this table only shows modes for which the identified eigenmodes were reliable. Figure 23.8 shows the mode shapes correctly identified and their corresponding simulations.

Figure 23.8 shows the experimental identified mode shapes and numerical identified mode shapes have a high degree of correspondence and the identified frequencies have a good match with the numerical ones.

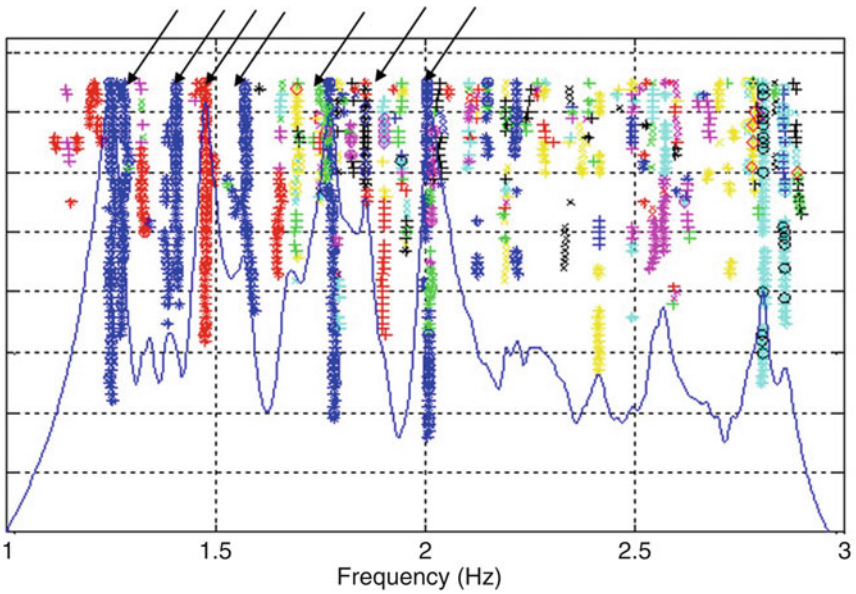


**Fig. 23.6** MI-TO way: stabilization diagram

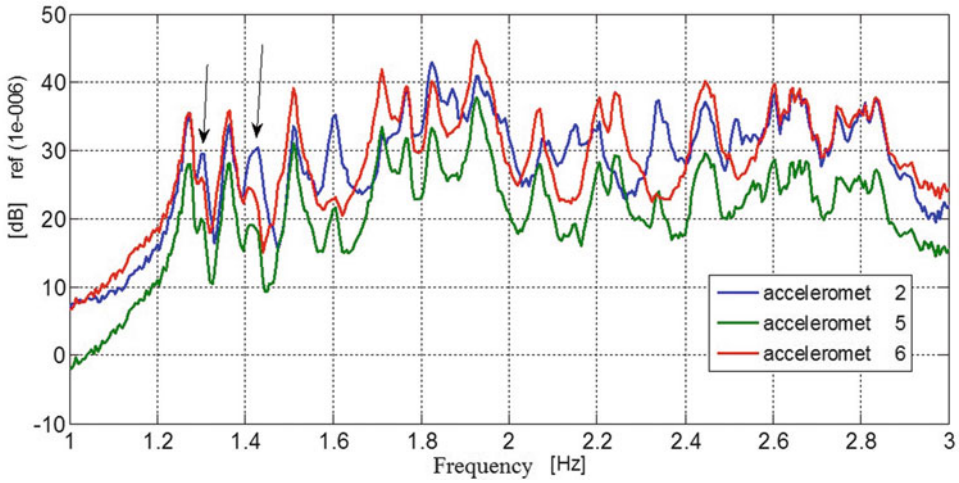


**Fig. 23.7** TO-MI way: PSD, the arrows indicate modes of vibration of lower amplitude of which is difficult to identify reliably the mode shape

**Table 23.2** Modal parameters of TO-MI bridge

| Mode | Frequency (Hz) | Damping ratio (%) |
|---|---|---|
| 1 | 1.27 | 0.52 |
| 2 | 1.36 | 0.51 |
| 3 | 1.51 | 0.52 |
| 4 | 1.71 | 0.45 |
| 5 | 1.77 | 0.71 |
| 6 | 1.82 | 0.43 |
| 7 | 1.92 | 0.42 |
| 8-1 | 2.07 | 0.49 |
| 8-2 | 2.08 | 0.53 |
| 9 | 2.20 | 0.47 |
| 10 | 2.24 | 0.38 |

### *23.4.3 Test Results and Model Tuning Activity*

This good agreement came after some model tuning was performed. In this case, the most important modelling assumption to refine was the behavior of the pendula, because all the rest of the geometry, masses and boundary conditions had been accurately reproduced in the FE model. On the other hand, as discussed before, the real behavior of the pendula in their elastic branch needed to be reproduced in order to be compared with the mode shapes identified at very low levels of vibration. At the beginning of the modelling process, the pendula were considered as fixed restrains to simulate the stiff frictional branch. This assumption caused some modes to disappear and limited the translational vibrations of the bridge along single spans, a fact that was considered non realistic. To overcome this excessive simplification, the correct force-displacement law was introduced, but still the pendulum at one single support were modelled as 'lumped' in one single node of the mesh. This option turned out to be ineffective because in this case in the FE model some additional irregular modes appeared, which were not representative of the physical behavior of a symmetric bridge having regular spans.

Finally, after a few attempts, the number of nine springs for each isolator, each of them having a stiffness of 1/9th of the total and located at nine adjacent nodes of the mesh, gave "smoother" and more realistic numerical results for the mode shapes, as shown in the next section. In fact, these modeling assumptions reflected the behavior of the pendulum, whose physical dimension is much larger than one single node of the mesh chosen for the bridge deck.

**Table 23.3** Percentage differences in frequencies for TO-MI bridge

| Mode | Relative frequencies error (%) |
|---|---|
| 1 | 1.57 |
| 2 | 1.47 |
| 3 | 2.65 |
| 4 | 2.92 |
| 5 | 3.59 |
| 7 | 7.81 |

### *23.4.4 Test Results and Comparison with Tuned Model*

The comparison carried out in the following is carried out by using the numerical mode shapes derived after the model tuning, which are also the ones represented in Table 23.1. In order to illustrate the similarity between the two sets of modes, the relative frequencies error is calculated in Table 23.3. It is clear that percentage differences in frequencies are very low since they are lower than 8% in the worst case.

Modal Assurance Criterion (MAC) is used to assess the correlation between two sets of modes. Herein MAC is used to find the correlation between experimental mode shapes and numerical mode shapes. The formula of MAC is:

$$MAC_{ij} = \frac{\left|\phi_{is}^T \phi_{js}\right|^2}{\left(\phi_{is}^T \phi_{is}\right)\left(\phi_{js}^T \phi_{js}\right)}$$

where $\phi_{is}$, $\phi_{js}$ are values of the *i*th order and *j*th order mode shape corresponding to the degree of freedom s respectively.

The MAC plot between numerical modes and experimental modes for TO-MI way and MI-TO way are shown in Fig. 23.9. The right color-column indicates the MAC level for each color, where 1 indicates perfect correlation, whereas 0 indicates uncorrelated modes. From Fig. 23.9, the diagonal MAC values are all nearly close to 1, which means that numerical modes and experimental modes are pretty closely coincident. It needs to be noticed that high correlation values are also reported for non-corresponding modes. For instance, experimental modes 1, 3 and 5 of TO-MI way have a good matching with simulated modes 1, 2 and 3. From Fig. 23.8 it is clear that these modes have the same shapes for the tested spans, then this high correlation is explained. In order to see a difference among these modes, the number of the spans under test should be increased.

## 23.5 Conclusions

In this paper the numerical model validation of the bridges MI-TO and TO-MI have been achieved.

Considering both results from numerical computation and experimental test, a good agreement between simulation and reality was obtained. The correspondence among the frequency shows a difference lower than 8% for the higher modes and the MAC values among the simulated and experimental modes are close to 100%.

Nevertheless, it is rather difficult to distinguish all the modes in the frequency range 1–3 Hz, because the natural frequencies are very close and the modes are highly damped.

It must be also noticed that the number of spans used for the experimental tests was insufficient to describe completely the modes shapes. Since the two bridges have all the spans of the same length, the mode shapes are similar. The differences among the modes could have been seen only if all the spans would have been instrumented, but it was impossible due to budget limits.

| Num. | Exp. | Mode Shapes TO-MI |
|---|---|---|
| 1 | 1 | |
| 1.29 Hz | 1.27 Hz | |
| **3** | **2** | |
| 1.34 Hz | 1.36 Hz | |
| **5** | **3** | |
| 1.47 Hz | 1.51 Hz | |
| **7** | **4** | |
| 1.66 Hz | 1.71 Hz | |
| **10** | **5** | |
| 1.70 Hz | 1.77 Hz | |
| **12** | **7** | |
| 1.77 Hz | 1.92 Hz | |

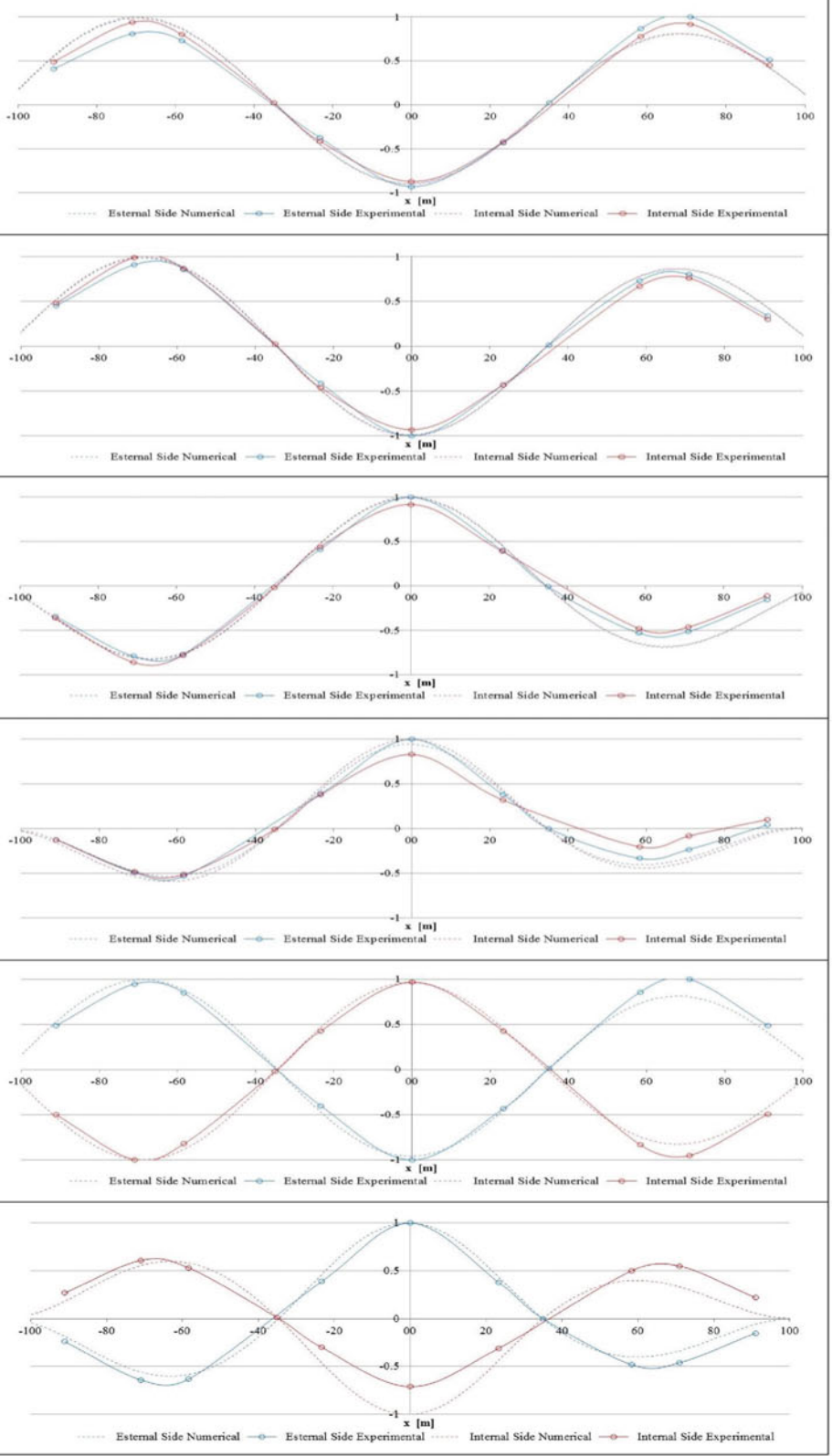


**Fig. 23.8** MI-TO way: numerical and experimental frequency comparison

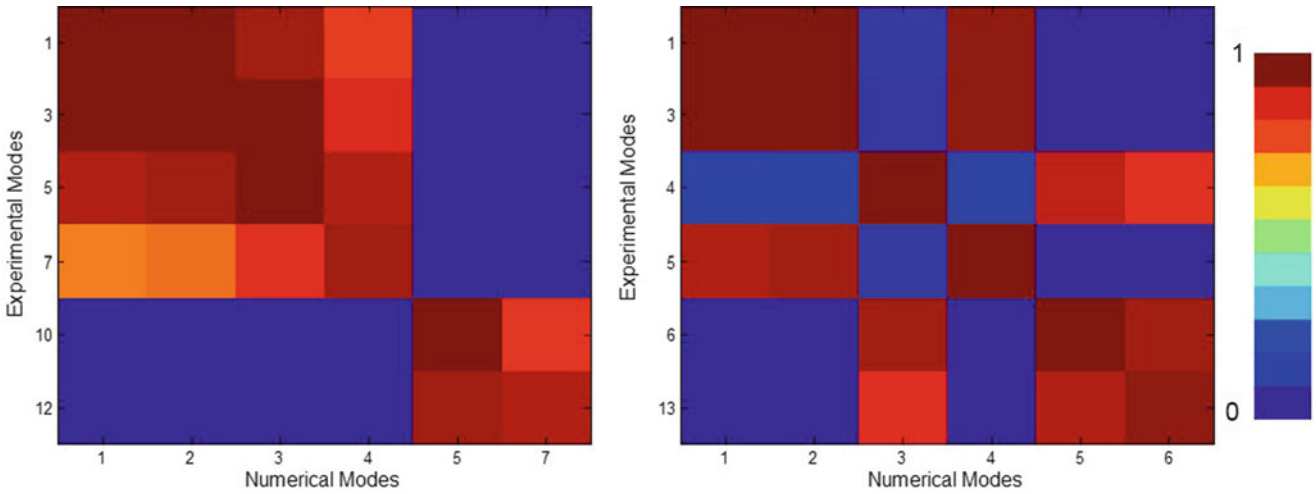


**Fig. 23.9** MAC plot between numerical modes and experimental modes for (**a**) TO-MI way and (**b**) MI-TO way

## References

1. Consiglio Superiore Lavori Pubblici: Nuove Norme Tecniche per le Costruzioni. D.M., Roma, Italy (2008)
2. Caprioli, A., Cigada, A., Gentile, C., Vanali, M.: Comparison of two different OMA techniques applied to vibration data measured on a stadium grandstand. In: Proceedings of International Conference on IOMAC'09—3rd International Operational Modal Analysis Conference, pp. 81–87. IOMAC, Portonovo, Italy (2009)
3. Ewins, J.: Modal Testing: Theory, Practice and Application, 2nd edn. Taylor and Francis Group, London (2001)
4. Peeters, B., Van der Auweraer, H., Guillaume, P., Leuridan, J.: The PolyMAX frequency-domain method: a new standard for modal parameter estimation? Shock Vib. **11**(3–4), 395–409 (2004)
5. Peeters, F., Vanhollebeke, H., Van der Auweraer, H.: Operational PolyMAX for estimating the dynamic properties of a stadium structure during a football game, Proceedings of the International Conference on IMAC XXIII, Orlando, FL, USA, 2005
6. Cigada, A., Caprioli, A., Redaelli, M., Vanali, M.: Numerical modeling and experimental modal analysis of a concrete grand-stand structure to structural health monitoring purposes, Proceedings of the International Conference on IMAC XXVI, Orlando, FL, USA, 2008
7. Cigada, A., Caprioli, A., Redaelli, M., Vanali, M.: Vibration testing at Meazza stadium: reliability of operational modal analysis to health monitoring purposes. J. Perform. Constr. Facil. **22**(4), 228–237 (2008)

# Chapter 24
# Predicting Footbridge Vibrations Using a Probability-Based Approach

**Lars Pedersen and Christian Frier**

**Abstract** Vibrations in footbridges may be problematic as excessive vibrations may occur as a result of actions of pedestrians. Design-stage predictions of levels of footbridge vibration to the action of a pedestrian are useful and have been employed for many years based on a deterministic approach to modeling the action of a pedestrian. The paper employs a probability-based approach to modeling the action of a pedestrian by considering randomness in the behavior of the pedestrian crossing the footbridge. The paper describes the approach and studies implications (sensitivity) of selected decisions made when setting up the probabilistic framework for the predictions of footbridge response.

**Keywords** Footbridge vibrations • Walking loads • Numerical prediction • Serviceability-limit-state • Response prediction

## Nomenclature

| | |
|---|---|
| $a$ | Bridge acceleration |
| $f_s$ | Step frequency |
| $m_1$ | Bridge modal mass |
| $\alpha$ | Dynamic load factor |
| $\sigma$ | Standard deviation |
| $f_1$ | Bridge fundamental frequency |
| $F$ | Walking load |
| $L$ | Bridge length |
| $\zeta_1$ | Bridge damping ratio |
| $\Theta$ | Phase |
| $i$ | Integer |
| $l_s$ | Step length |
| $W$ | Weight of pedestrian |
| $\mu$ | Mean value |
| $\Phi$ | Mode shape |

## 24.1 Introduction

Pedestrians are known to be capable of causing problematic vibrations in footbridges. The London Millennium Bridge incident [1] is well-known and it resulted in increased focus on the modelling of loads generated by pedestrians. Modelling of walking loads is also the topic of this paper.

Deterministic models for walking loads are available in design guides and codes of practise (such as in [2, 3]). However it is known that the locomotion of a pedestrian is not deterministic. Parameters of walking load models (such as step frequency, step length and dynamic load factors) are fundamentally stochastic by nature [4–7] and different pedestrians generate different dynamic forces. This paper will respect this and therefore it will respect that the response of a footbridge

L. Pedersen (✉) • C. Frier
Department of Civil Engineering, Aalborg University, Sofiendalsvej 9-11, DK-9200, Aalborg SV, Denmark
e-mail: lp@civil.aau.dk



J. Caicedo, S. Pakzad (eds.), *Dynamics of Civil Structures, Volume 2*, Conference Proceedings
of the Society for Experimental Mechanics Series, DOI 10.1007/978-3-319-54777-0_24

to the action of a pedestrian is a random variable. This means that the bridge response to the action of a pedestrian is best described by a probability distribution function describing the stochastic nature of bridge response.

When evaluating the vibration serviceability-limit-state of a footbridge, it would often be bridge acceleration levels that would be of concern, and for this paper focus is on the peak midspan acceleration levels of the footbridge generated by single-person pedestrian traffic.

Even when having decided that the footbridge response is to be handled as a random variable, there are decisions to be made related to which walking load model to employ. This is so because not only a single load model is available in literature. There are simple load models that can be used but there are also more advanced load models that can be employed. The difference between the simple and advanced models relates to their way and level of detail in describing the locomotion of a walking person and the load hereby directed to the footbridge. Differences between the models are described in the paper.

The paper examines how different choices made related to modelling the action of a pedestrian will influence predictions of footbridge response. The choices will involve deciding on a load model but there are also decisions to be made in terms of how to model the parameters of the load model. The paper addresses both issues.

Two different bridges are assumed for the study in order to widen the basis for a discussion of results.

The load models assumed are described in Sect. 24.2. Section 24.3 defines the footbridges and Sect. 24.4 presents and discusses results of findings.

## 24.2 The Load Models Considered for the Study

Sections 24.2.1 and 24.2.2 presents the two load models considered for the studies of this paper. Section 24.2.3 presents the assumptions made in terms of input parameters for the models.

### *24.2.1 Load Model I*

This load model, Eq. (24.1), is the one that has been employed for many years for modelling vertical action of a pedestrian and it is for instance suggested in [8–10].

$$F(t) = W \sum_{i=1}^{n} \alpha_i \cos\left(2\pi\, i f_s t + \theta_i\right) \tag{24.1}$$

$W$ is the weight of the pedestrian, $\alpha_i$ is the dynamic load factor for load harmonic no $i$, and $f_s$ is the step frequency of the pedestrian. The value $n$ defines the number of load harmonics assumed for the calculations. For the present studies only the first load harmonic will be considered for this load model as the bridges investigated are such that the load harmonics with values of $i$ above 1 hardly would be able to cause dynamic response of the bridges.

This means that it is not necessary to model phase information between load harmonics; information contained in the parameters $\Theta_i$.

Even though the model is often employed as a deterministic load model, entering model parameters as random variables makes it useful as a stochastic load model. The model is not as advanced as load model II described in the next section.

### *24.2.2 Load Model II*

This load model accounts for the inability of a pedestrian to repeat the same force in each step and that the force generated by a pedestrian is not fully periodic. The load model is introduced in [11] and is seen in Eq. (24.2).

$$F(t) = \sum_{i=1}^{5} F_i(t) + \sum_{i=1}^{5} F_i^S(t), \tag{24.2}$$

Basically the load model is built such that it includes both main harmonics occurring at frequency $if_s$ (see Eq. 24.3) and a set of subharmonics (see Eq. 24.4).

$$F_i(t) = W\alpha_i \sum_{\bar{f}_j=i-0.25}^{i+0.25} \overline{\alpha}_i\left(\bar{f}_j\right)\cos\left(2\pi\bar{f}_j f_s t + \theta\left(\bar{f}_j\right)\right) \tag{24.3}$$

$$F_i^S(t) = W\alpha_i^S \sum_{\bar{f}_j^S=i-0.75}^{i-0.25} \overline{\alpha}_j^S\left(\bar{f}_j^S\right)\cos\left(2\pi\bar{f}_j^S f_s t + \theta\left(\bar{f}_j^S\right)\right) \tag{24.4}$$

For explanation of the parameters of the load model (the parameters included in the two equations above) and for a description of how the model is operated, reference is made to [11]. Here it suffices to mention that load model II includes the main harmonics also considered in load model I. Furthermore load model II includes subharmonics occurring at frequencies in between the main harmonics and it also models a leakage of energy around these frequencies.

### 24.2.3 Parameters of the Models

For the studies of this paper, both load model I and load model II are employed in a way accounting for the fact that different pedestrians will generate different dynamic forces. This is done by modelling at least some of the load model parameters as random variables.

Mean values, $\mu$, and standard deviations, $\sigma$, assumed for step frequency, $f_s$, pedestrian weight, $W$, and step length, $l_s$, are listed in Table 24.1.

The stochastic nature for the load model parameters reported in Table 24.1 are those suggested in [11]. It is seen that the pedestrian weight, $W$, is handled as a deterministic property in that the standard deviation for this parameter, $\sigma$, is set to zero. For the random variables (step frequency and step length) normal distributions are assumed and furthermore step frequency and step length are considered to be independent parameters. Although the step length does not appear in the load models introduced above it defines the position of the pedestrian when crossing the bridge and hereby the modal load generated by the pedestrian.

Apart from the parameters listed above, assumptions are also made about the stochastic nature of dynamic load factors. The mean value of the first dynamic load factor is modelled to depend on step frequency in accordance with Eq. (24.5).

$$\mu_{\alpha_1} = -0.2649f_s^3 + 1.3206f_s^2 - 1.7597f_s + 0.7613 \tag{24.5}$$

This equation models a relationship calibrated in [6], which also suggests a standard deviation, $\sigma$, of $0.16\mu$ for this parameter, which is the stochastic nature of the action assumed for the studies of this paper.

Load model II models load harmonics beyond the first load harmonic, and Table 24.2 shows the numbers assumed for the mean values and standard deviations for these load harmonics.

These load harmonics are not included when employing load model I. However, they form an integrated part of load model II. Phases between the load harmonics are modelled as random variables following a uniform distribution in the range $[-\pi, \pi]$.

For a description of how parameters of load model II not uniquely defined above are computed see [11].

**Table 24.1** Mean values and standard deviations

| | $\mu$ | $\sigma$ |
|---|---|---|
| $f_s$ (Hz) | 1.87 | 0.186 |
| $W$ (N) | 750 | 0 |
| $l_s$ (m) | 0.71 | 0.071 |

**Table 24.2** Mean values and standard deviations [11]

| | $\alpha_2$ | $\alpha_3$ | $\alpha_4$ | $\alpha_5$ |
|---|---|---|---|---|
| $\mu$ | 0.07 | 0.05 | 0.05 | 0.03 |
| $\sigma$ | 0.030 | 0.020 | 0.020 | 0.015 |

**Table 24.3** Modal properties of bridges and bridge length

| Bridge | $f_1$ (Hz) | $\zeta_1$ (%) | $m_1$ ($10^3$ kg) | $L$ (m) |
|---|---|---|---|---|
| A | 1.9 | 0.05 | 43.8 | 45.3 |
| B | 2.85 | 0.05 | 19.5 | 30.2 |

### *24.2.4 A Variation of Study Assumptions*

A central objective of the studies of this paper is to compare the results of footbridge response calculations obtained using load models I and II. Both models handle a number of parameters as random variables. It is considered of interest to study whether one of the walking parameters might as well be handled as a deterministic property without loss in statistical information about relevant footbridge response data.

In load model I as well as in load model II, the step length, $l_s$, is modelled as a random variable. For calculations a scenario is constructed in which the step length is modelled as a deterministic property assuming the mean value (for any outcome of step length), thus not accounting for randomness in outcomes of step length. This in order to compare with results obtained accounting for randomness in step length.

## 24.3 The Footbridges Considered for the Study

It is chosen to consider two-point pinned bridges with the modal properties (natural frequency, damping ratio, and modal mass) of the first vertical bending mode given in Table 24.3.

Although the two bridges will have vertical modes of vibration beyond the first vertical bending mode, these are not considered for the present study, as the natural frequencies of those modes are so high that they are unlikely to be noticeably excited by pedestrian loading.

The natural frequency of bridge A is chosen such that the first harmonic of pedestrian loading is likely to bring bridge A into resonant vibration, as the mean step frequency is fairly close to 1.9 Hz (according to mean values of step frequencies presented in [4, 11]). Bridge B, however, is not very likely to come into vibration due to the first harmonic load component but bridge B might resonate as a result of the first subharmonic above the step frequency.

It can be seen that the bridges are very lightly damped which would suggest that the bridges respond quite lively if subjected to resonant excitation from a pedestrian.

The bridge length, $L$, is not identical for the two bridges. Bridge B is shorter than bridge A, which is meaningful as bridge B is stiffer than bridge A.

## 24.4 Extracting Response Data

Prior to computing bridge response, the load of the pedestrian was conveyed to a modal load acting on the first vertical bending mode of the bridge. This involves accounting for the mode shape of the bridge and the walking velocity of the pedestrian. The walking velocity is calculated based on outcomes of step frequency and step length. The mode shape, $\Phi$, of the first vertical bending mode of the bridges is assumed to have the shape of a half-sine normalized to 1 at the top point.

The footbridge response parameter in focus in this paper is the vertical footbridge acceleration computed at footbridge midspan. During each pedestrian crossing of the bridge, the peak value of accelerations is extracted from a time domain representation of bridge accelerations at this position. The time history of the response is computed using a Newmark time integration approach.

A large number of single person bridge crossings were simulated using the Monte Carlo approach respecting the modelled stochastic nature of parameters in the load models. This approach allows for sorting calculated acceleration response data and finding the probability distribution and then extracting quantiles of the response, hereby respecting that the response is in fact stochastic. The acceleration quantiles focused on in this paper are $a_{95}$, $a_{90}$, and $a_{75}$.

In order to assure confidence in estimates of acceleration response quantiles, 100,000 simulation runs were made for each studied scenario.

## 24.5 Results

Sections 24.5.1 and 24.5.2 presents results of calculations.

### *24.5.1 Influence of Choice of Load Model*

Table 24.4 presents acceleration quantiles derived having applied load models I and II for computing responses of the two bridges (bridges A and B). In both load models, the step length, $l_s$, is handled as a random variable.as defined in Table 24.1.

Focusing on the acceleration quantiles obtained for the 1.9 Hz-bridge (bridge A) it can be seen that there is not much difference between the results obtained employing load model I (the simple load model) and load model II (the advanced load model).

The opposite conclusion is drawn for the 2.85 Hz-bridge (bridge B). For this bridge, the simple load model (model I) underestimates the acceleration response. This is explained by the circumstance that the simple load model does not model subharmonics of load action. Hereby load model I can only excite the 2.85 Hz-bridge as a result of the modelled randomness of step frequency.

That the advanced load model can excite the 2.85 Hz-bridge to resonance is illustrated in Fig. 24.1 which shows a power spectrum of the load generated by a pedestrian.

The frequency representation of the load shown in Fig. 24.1 is constructed by analysing a time history generated by pedestrian forces. The time history was produced assuming that all random variables of the load model assumed their mean value (only the phases between load harmonics have been modelled as a random parameter when producing the time history). It is apparent that this load model contains load energy close to the frequency of bridge B (2.85 Hz) which can put the bridge into resonance vibrations. It is also apparent that the energy that can excite bridge A (1.9 Hz) is higher than that at 2.85 Hz, which explains why the acceleration response of bridge A is higher than that found for bridge B.

Returning to the results for bridge A, it can be observed that for the quantile $a_{75}$, there is a noticeable difference between results obtained assuming load model I and load model II. It is believed that most often it would be the higher quantiles that would be of interest ($a_{95}$ or $a_{90}$). If the task is to produce estimates of these quantiles, the result appears to be insensitive to the choice of load model (i.e. whether the simple or the advanced load model is chosen is not important). This is not the case if the task is to produce estimates of response of a bridge with a natural frequency at about 2.85 Hz. For that bridge, the application of the advanced load model is recommended.

**Table 24.4** Acceleration quantiles

| Bridge | A | | B | |
|---|---|---|---|---|
| Load model | I (m/s$^2$) | II (m/s$^2$) | I (m/s$^2$) | II (m/s$^2$) |
| $a_{95}$ | 0.3524 | 0.3425 | 0.0257 | 0.0754 |
| $a_{90}$ | 0.2764 | 0.2672 | 0.0213 | 0.0672 |
| $a_{75}$ | 0.1099 | 0.1297 | 0.0152 | 0.0560 |

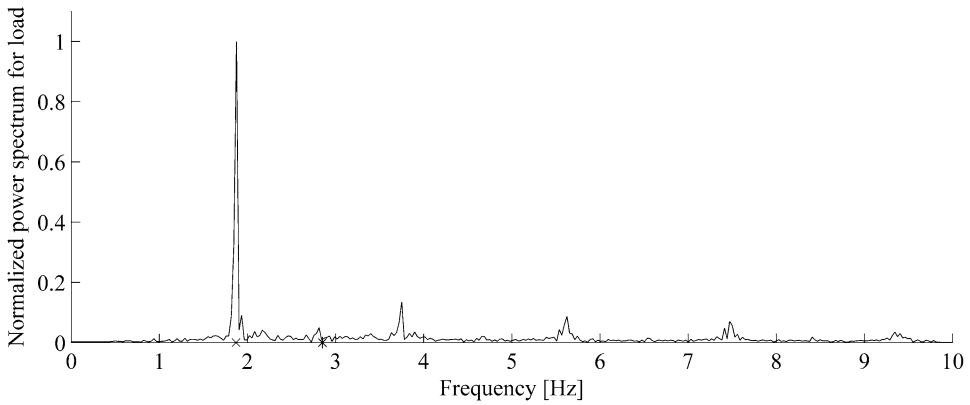


**Fig. 24.1** Normalized power spectrum for load model II. (×: frequency of bridge A, *: frequency of bridge B)

**Table 24.5** Acceleration quantiles

| Bridge | A | | B | |
|---|---|---|---|---|
| Load model | I (m/s$^2$) | II (m/s$^2$) | I (m/s$^2$) | II (m/s$^2$) |
| $a_{95}$ | 0.3537 | 0.3421 | 0.0257 | 0.0754 |
| $a_{90}$ | 0.2770 | 0.2674 | 0.0212 | 0.0670 |
| $a_{75}$ | 0.1095 | 0.1296 | 0.0152 | 0.0559 |

Step length deterministic

### *24.5.2 Influence of Approach for Modelling Step Length*

Table 24.5 presents acceleration quantiles derived having applied load models I and II for the two bridges (bridges A and B). Values for the similar acceleration quantiles were presented in Table 24.4. The only difference is that for the results given in Table 24.5, the step length, $l_s$, was handled as a deterministic property (and not as a random variable as was the case for the results presented in Table 24.4). For the calculations, the step length was set to the mean value, 0.071 m.

A comparison of values of the acceleration quantiles listed in Tables 24.4 and 24.5 reveals that there is a marginal difference in the values. This is the case for both bridges and for both load models.

This suggests that it is not of importance whether the step length is modelled as random parameter or a deterministic property.

## 24.6 Conclusion

Two walking load models have been employed for examining of the stochastic nature of bridge response of two different SDOF bridges in order to compare outcome of results. One bridge was a 1.9 Hz-bridge and the other was a 2.85 Hz-bridge. One of the load models is capable of reproducing forces generated by a pedestrian to a high level of detail. The other load model is not able to replicate the action of pedestrians to a similar level of detail.

It was found that for the 1.9 Hz-bridge, the simple load model provided estimates of bridge acceleration quantiles that where very close to those found when applying a pedestrian load generated by the advanced load model. For the 2.85 Hz-bridge, the estimates of bridge acceleration quantiles did not compare well. This is a result of the fact that the simple load model fails to model energy of pedestrian action correctly at all frequencies, especially in frequency ranges between the main harmonics of the action. Hence, in some cases the simple load model would not be an appropriate choice.

It was found that even though both load models are capable of accounting for stochastic nature of characteristics such as step frequency, dynamic load factor, step length etc., the computed bridge acceleration quantiles are insensitive to whether step length was modelled as a random parameter or as a deterministic property. This was observed for both load models.

It would be of interest to examine whether the conclusions are also valid for other footbridges than those considered for the studies of this paper.

**Acknowledgements** This research was carried out in the framework of the project "UrbanTranquility" under the Intereg V program and the authors of this work gratefully acknowledge the European Regional Development Fund for the financial support.

## References

1. Dallard, P., Fitzpatrick, A.J., Flint, A., Le Bourva, S., Low, A., Ridsdill-Smith, R.M., Wilford, M.: The London Millennium Bridge. Struct. Eng. **79**, 17–33 (2001)
2. Ontario Highway Bridge Design Code, Highway Engineering Division; Ministry of Transportation and Communication, Ontario, Canada, 1983
3. British Standard Institution: Steel, concrete and composite bridges. Specification for loads, BS 5400: Part 2, 1978
4. Matsumoto, Y., Nishioka, T., Shiojiri, H., Matsuzaki, K.: Dynamic design of footbridges, IABSE Proceedings, No. P-17/78, pp. 1–15, 1978
5. Živanovic, S.: Probability-based estimation of vibration for pedestrian structures due to walking, PhD thesis, Department of Civil and Structural Engineering, University of Sheffield, UK, 2006
6. Kerr, S.C., Bishop, N.W.M.: Human induced loading on flexible staircases. Eng. Struct. **23**, 37–45 (2001)
7. Pedersen, L., Frier, C.: Sensitivity of footbridge vibrations to stochastic walking parameters. J. Sound Vib. **329**, 2683–2701 (2009). doi:10.1016/j.jsv.2009.12.022
8. Ellis, B.R.: On the response of long-span floors to walking loads generated by individuals and crowds. Struct. Eng. **78**, 1–25 (2000)

9. Bachmann, H., Ammann, W., Vibrations in structures—induced by man and machines, IABSE Structural Engineering Documents 3e, Zürich, Switzerland, 1987
10. Rainer, J.H., Pernica, G., Allen, D.E.: Dynamic loading and response of footbridges. Can. J. Civil Eng. **15**, 66–78 (1998)
11. Živanovic, S., Pavic, A., Reynolds, P.: Probability-based prediction of multi-mode vibration response to walking excitation. Eng. Struct. **29**, 942–954 (2007). doi:10.1016/j.engstruct.2006.07.004

# Chapter 25
# Flooring-Systems and Their Interaction with Usage of the Floor

**Lars Pedersen, Christian Frier, and Lars Andersen**

**Abstract** Some flooring-system designs might be sensitive to their vibrational performance, as there might be the risk that serviceability-limit-state problems may be encountered. For evaluating the vibrational performance of the flooring-system at the design stage, decisions need to be made by the engineer in charge of computations. On a flooring-system often passive humans and/or furniture are present. Often these masses and their way of interacting with the floor mass are ignored in predictions of vibrational behavior of the flooring-system. The paper explores and quantifies how these masses can influence central parameters describing the dynamic behavior of the flooring-system.

**Keywords** Modal properties of floors • Floor dynamics • Numerical prediction • Serviceability-limit-state • Estimation accuracy

## Nomenclature

| | |
|---|---|
| $f_{(k)}$ | Natural frequency |
| $M_{(k)}$ | Modal mass |
| $E$ | Young's modulus |
| $\mathbf{M}$ | Mass matrix |
| $\zeta_{(k)}$ | Damping ratio |
| $k$ | Mode number |
| $\nu$ | Poisson's ratio |
| $\mathbf{K}$ | Stiffness matrix |
| $\omega_{(k)}$ | Circular natural frequency |
| $n$ | Scenario |
| $\mathbf{\Phi}^{(k)}$ | Mode shape vector |
| $\mathbf{C}$ | Damping matrix |

## 25.1 Introduction

When designing flooring systems in buildings, the main focus often is on assuring that ultimate-limit state requirements are satisfied. For flooring systems this often relates to ensuring that a specified static load is acceptable. However there can be other issues apart from the static problem that can be problematic. This paper addresses vibration issues.

For a floor, vibration problems can occur as a result of internal or external action. Internal actions may originate from humans in motion on the floor (persons walking), or from machinery placed on the floor area. This issue is addressed in [1]. External actions that can cause floor vibrations could be those arising as a result of nearby activities. This could be pile driving, trains running in a nearby metro system [2], road traffic [3] or similarly where structural and/or ground born vibrations end up bringing a floor of a building into vibration.

In any case, the problem can be that humans on the floor can perceive vibration levels as annoying or sensitive equipment on the floor can be exposed to excessive vibrations.

L. Pedersen (✉) • C. Frier • L. Andersen
Department of Civil Engineering, Aalborg University, Sofiendalsvej 9-11, DK-9200, Aalborg SV, Denmark
e-mail: lp@civil.aau.dk



J. Caicedo, S. Pakzad (eds.), *Dynamics of Civil Structures, Volume 2*, Conference Proceedings
of the Society for Experimental Mechanics Series, DOI 10.1007/978-3-319-54777-0_25

The simplest possible basis for a vibration serviceability check by calculation would be to assume that the floor model is constant in time and is represented by the empty floor dynamic characteristics. This approach would rely on the assumption that the floor occupancy (which could be furniture or passive humans) does not influence the floor dynamic characteristics or at least that the influence of floor occupancy masses is neglected for the evaluation. However, it is a known fact that adding humans or non-structural mass will influence modal properties of a floor [4, 5].

The problem matter is that at the design stage often usage of the floor area is only known by the size of the specified life load. The distribution of the masses later to occupy the floor during its service life is generally unknown.

This paper examines different distributions of masses on a floor and how this would influence modal properties of the floor. More specifically, the paper examines the changes occurring in modal properties of a floor when gradually increasing the density of mass added to the floor. Additionally, the paper examines the influence on modal properties occurring when the center of added mass is elevated above the floor midplane. Bookshelves and desks serves as examples of items where the center of mass it elevated above floor midplane. It is assumed that these masses are rigidly attached to the floor. (Some might choose to consider a human mass as a mass rigidly attached to the floor for calculations of floor dynamic behavior. However this might not be appropriate as the human body is not a rigid system [6]).

The influences listed above are examined by numerical calculations and it is chosen to monitor changes in natural frequencies and damping ratios of the first nine modes of floor vibration.

For the investigations, a case study floor is selected. The floor is described in Sect. 25.2 which also describes the finite-element (FE) model of the floor. It is a simple floor in terms of geometry and support conditions in order to keep focus on effects of floor occupancy influences. Scenarios considered for usage of the floor is also outlined in Sect. 25.2 along with methods employed for extracting modal parameters of the floor. Section 25.3 presents and discusses the results. Finally, Sect. 25.4 gives the conclusions of the study.

## 25.2 Methodology

### *25.2.1 Computational Model of the Floor*

The case study concerns a floor with the characteristics described below.

The floor area is assumed rectangular with side lengths of 8 and 9 m. It is assumed that the floor is pinned along all four sides. The floor is made of reinforced concrete with the material characteristics $E = 30$ GPa (Young's modulus), and $\nu = 0.15$ (Poisson's ratio). Based on a brief review of literature these values are considered to be fairly realistic for reinforced concrete, simplifying the composite material consisting of concrete and rebar into a homogeneous, isotropic and linear elastic material. The thickness of the floor is 180 mm and the mass density is 2400 kg/m$^3$. It has been checked that, with these assumptions, it is possible to meet static ultimate-limit-state requirements as well as static serviceability-limit-state requirements, assuming usage as an office floor area.

A FE model of the floor has been constructed using shell elements [7] with five degrees of freedom (d.o.f.) per node, i.e. three displacements and two rotations associated with bending. The element has nine nodes leading to second-order Lagrange interpolation of the displacements and rotations. A small artificial stiffness has been implemented to control the drilling degree of freedom, and selective integration of the stresses has been employed to avoid shear locking.

A 12-by-12-element grid has been employed to model the entire floor. Although not shown here, it has been confirmed by calculation that the model of the empty floor has converged, i.e. decreasing the mesh size will not cause significant improvements in the estimates of frequency and damping characteristics of the empty floor for modes up to 70 Hz. A plate model has also been tested for the empty floor and it gave, as expected, minor differences in floor frequencies compared to those extracted using the shell model. Finally, the MATLAB code has been verified by comparison with an ABAQUS [8] model based on Mindlin-Reissner shell elements with eight nodes and reduced integration. However, a shell model is used for the present study, as the attached masses will be elevated above the horizontal mid plane of the floor, thus influencing the inplane displacement d.o.f's of the shell.

The first mode of the floor is found to have a frequency slightly above 8 Hz. Empty floor frequency and damping values for all modes considered in this paper are listed in a later section.

In terms of damping characteristics, a Rayleigh damping model is assumed:

$$\mathbf{C}_f = a\mathbf{M}_f + b\mathbf{K}_f \tag{25.1}$$

$\mathbf{M}_f$ is the mass matrix and $\mathbf{K}_f$ is the stiffness matrix of the empty floor. The damping matrix $\mathbf{C}_f$ of the empty floor depends on the parameters $a$ and $b$, and these parameters are tuned such that the minimum damping occurs at the frequency associated with the first mode of the empty floor. A minimum damping equivalent to a logarithmic decrement of 0.1 is assumed. This is considered representative for a reinforced concrete floor and entails that the damping ratio of the empty floor, $\zeta$, assumes a value of approximately 0.016.

In the computational model, allowance is made for attaching floor occupancy mass at nodal points of the FE grid.

### *25.2.2 Usage of the Floor*

Usage of the floor area will involve adding masses to the floor. For the studies of this paper, added masses are assumed rigidly attached to the floor and modelled as lumped masses, although this is likely to be a simplification of real-life floor occupancy conditions. Attaching each lumped mass to a single node of the model of the floor is also a simplification of matters. However, the approach is considered reasonable for the purposes of the study.

The scenarios considered for the floor occupancy are outlined in Fig. 25.1. They are denoted by the integer $n$ taking on values of 1, 4, 9 or 16. The figure represents the number of masses placed on the floor in the particular scenario. Each individual mass is of 75 kg. The scenario $n = 0$ represent the empty floor. Lines are added on the floor area in Fig. 25.1 to provide an understanding of the exact positioning of the masses assumed for calculations. The strategy used for placing masses has been to gradually divide the floor into increasing numbers of squares (1, 4, 9, 16) and to place a mass of 75 kg in the center of each square.

As can be seen, the scenarios are arranged such that the floor occupancy mass gradually increases (when moving from scenario $n = 1$ up to $n = 16$).

Initially, the occupancy masses are assumed connected to the floor at the midplane of the floor (in the FE model of the floor at $z = 0$ m defining the horizontal plane of the floor model). For this scenario, the masses are fixed to (only influencing) translational degrees of freedom at nodal points of the FE model of the empty floor.

In order to consider scenarios in which an added mass is elevated above the floor, study scenarios are arranged assuming values of $z$ above zero, were the value of $z$ defines the vertical distance between the horizontal midplane of the floor and the position of the added masses. In the FE model of the floor, the influence of the added mass is modelled such that its contribution to floor dynamics mimics that of an elevated lumped mass attached to a node in the floor model by an interconnecting massless element with infinite axial and bending stiffness. This corresponds, approximately, to the influence of desks, bookshelves or similar furniture where the center of mass is placed at a finite height above the floor.

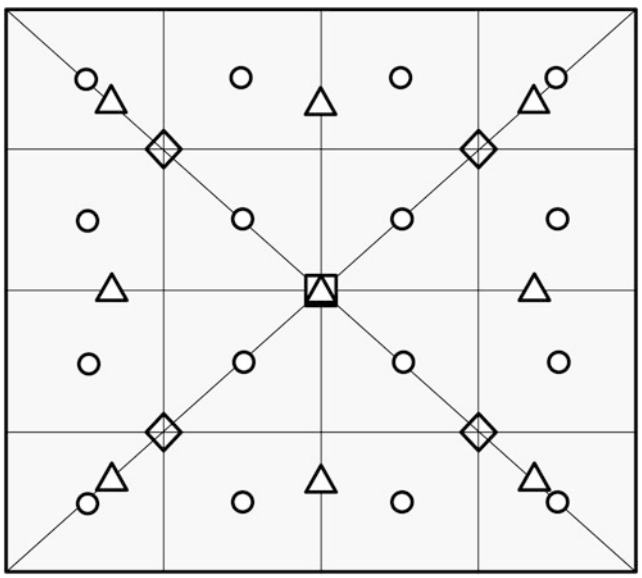

**Fig. 25.1** Layout plan for floor occupancy scenarios. $n = 1$ (*open square*), $n = 4$ (*open diamond*), $n = 9$ (*open triangle*), $n = 16$ (*open circle*)

Values of $z$ of 0, 1, and 2 m are considered in the paper in order to cover a wide range of values of $z$. Although values of $z$ above 2 m are possible they are not considered in the paper. It is emphasized that in the scenarios considered it is assumed that all masses on the floor are elevated to the same height above the midplane of the floor and that the mases are equal in size (75 kg). This will for some floor applications be a simplification of matters. However, it is a useful assumption for providing an overview of the dynamic mechanisms occurring when added masses vibrate together with the floor mass.

### *25.2.3 Extraction of Modal Properties*

For each floor occupancy scenario, natural frequencies $f_{(k)}$ (for mode number $k$) are extracted from the FE model by solving the undamped eigenvalue problem. The problem is solved taking offset in the stiffness matrix, **K**, and the mass matrix, **M**, of the combined system that includes the masses attached to the floor.

Damping ratios, $\zeta_{(k)}$, of the flooring system are extracted as

$$\zeta_{(k)} = \frac{\mathbf{\Phi}^{(k)T}\mathbf{C}\mathbf{\Phi}^{(k)}}{2\omega_{(k)}M_{(k)}}, \quad \omega_{(k)} = 2\pi f_{(k)} \tag{25.2}$$

where $\mathbf{\Phi}^{(k)}$ is the mode shape and $M_{(k)}$ is the modal mass for mode number $k$, and where **C** is the mass matrix.

An eigenvalue solver built into MATLAB was employed for computing natural frequencies, and a sparse approach was used in order to reduce computation time.

## 25.3 Results

This section presents results for floor frequencies (Sect. 25.3.1) and floor damping (Sect. 25.3.2).

### *25.3.1 Floor Frequencies*

For this parameter, the presentation of results is divided into a discussion of results obtained for scenarios in which added masses are attached at floor midplane ($z = 0$ m) not assumed elevated above floor midplane and a discussion of results for scenarios in which elevated positions of added masses are assumed ($z > 0$ m). This is followed by a comparison of results.

#### 25.3.1.1 Masses Attached at Floor Midplane

Results of calculations of floor frequencies are shown in Table 25.1. It displays calculation results obtained assuming the occupancy masses attached at $z = 0$ for the first nine modes of vibration. In the table empty floor frequencies (scenario $n = 0$) are represented by their values in Hz. When masses are attached, scenarios $n = 1$, 4, 9 and 16, the frequencies are normalized by the natural frequency computed for the empty floor, in this particular mode.

**Table 25.1** Floor frequencies $f_{(k)}$ in Hz for the empty floor ($n = 0$) and normalized frequencies for other scenarios ($n > 0$)

| | Mode number ($k$) | | | | | | | | |
|---|---|---|---|---|---|---|---|---|---|
| $n$ | 1 | 2 | 3 | 4 | 5 | 6 | 7 | 8 | 9 |
| 0 | 8.149 | 18.909 | 21.761 | 32.464 | 36.773 | 44.331 | 50.239 | 54.946 | 61.678 |
| 1 | 0.995 | 1.000 | 1.000 | 1.000 | 0.995 | 0.995 | 1.000 | 1.000 | 1.000 |
| 4 | 0.995 | 0.990 | 0.990 | 0.981 | 0.995 | 0.995 | 0.991 | 0.991 | 1.000 |
| 9 | 0.989 | 0.989 | 0.989 | 0.989 | 0.979 | 0.979 | 0.979 | 0.978 | 0.989 |
| 16 | 0.981 | 0.981 | 0.981 | 0.981 | 0.981 | 0.981 | 0.981 | 0.981 | 0.963 |

Floor occupancy masses are attached at $z = 0$ m

First item to mention is that a wide range of modes of vibration are monitored in this study (the first 9 modes of vibration of the floor are included in the table). The quite broad interest in modes of vibration set out above is motivated by the fact that for a floor, the types of excitation may range from low frequency excitation (for instance those caused by pedestrians) to types of excitation were much higher modes of floor vibration might be excited. For instance [2] considered building vibration response to underground train traffic at frequencies up to 110 Hz and evaluated re-radiated noise in the frequency range up to 250 Hz. In a similar manner, [9] assessed the vibroacoustic response of a building to surface rail traffic in the frequency range up to 150 Hz. In the present work modes with frequencies up to 62 Hz are considered.

Looking at Table 25.1, the overall conclusion is that floor frequencies will change when mass is added to the floor. Generally, a decline in frequency is observed when adding occupancy mass (as for scenarios $n > 0$ normalized frequencies attain values less than unity). There are exceptions to this tendency in that some normalized frequencies in the table have values of 1.0, indicating that no change occurs relatively to the unoccupied floor. An inspection of the mode shapes derived by the FE model (not shown in the paper) reveals that the additional masses in these cases are placed at nodes of the associated modes, i.e. at neutral lines of vertical floor vibration. This, combined with the fact that the masses are lumped and placed at floor midplane, i.e. at $z = 0$ m, entails that the masses do not contribute with any inertia in calculations of the floor dynamic behavior.

Returning to the modes in which a decline in frequency is observed, it is found to reduce, at maximum, by a factor of 0.963 for the studied floor-occupancy scenarios (i.e. a reduction of about 4% at maximum). This corresponds to an added mass of $16 \times 75 = 1200$ kg and 3.9% of the mass of the empty floor.

#### 25.3.1.2 Masses Attached at Elevated Positions

The scenario in which masses are attached to the floor at elevated positions is addressed here. Table 25.2 shows results of calculations of floor frequencies for which the lumped masses are placed 2.0 m above floor midplane. The results are presented similarly to Table 25.1.

As in the case of mass attachments at $z = 0$ m, there are scenarios in which a reduction in frequency will not occur when adding a mass; in this case at $z = 2$ m. Such result is observed for mode 4 with a single floor occupancy mass positioned 2 m above the floor midplane, i.e. for the scenario $n = 1$, $k = 4$ (resulting in a normalized frequency of unity). An inspection of floor mode shapes derived by the FE model reveals that the elevated added mass in question is not expected to experience any horizontal translational movements in this mode of vibration (as the mass is placed right above the intersection point of two perpendicular neutral lines for vertical vibration). Since at the same time the mass is not expected to move vertically in this mode of vibration, the mass would not be expected to provide inertia into the system, which explains why the attachment of the mass does not have any influence on floor dynamics.

In some of the other modes (for instance in modes 2 and 3), the elevated mass in question is attached to only a single neutral line of vertical vibration, which would not prevent the elevated mass from vibrating horizontally. The allowance of horizontal vibration of the mass when placed at elevated positions will cause a decline in floor frequency compared to the situation where it cannot move horizontally, as result of rotational inertia of the elevated mass.

Focusing on the maximum influence of adding elevated mass, some scenarios result in a floor-frequency decline by a factor of 0.768, i.e. a reduction of about 23%. This is corresponding to an added mass of $4 \times 75 = 300$ kg and only 1% of the total mass of the floor. Although not shown here, a small number of modes above the ninth mode enter into the 0–62 Hz frequency range for the scenarios studied here.

**Table 25.2** Floor frequencies $f_{(k)}$ in Hz for the empty floor ($n = 0$) and normalized frequencies for other scenarios ($n > 0$)

| | Mode number ($k$) | | | | | | | | |
|---|---|---|---|---|---|---|---|---|---|
| $n$ | 1 | 2 | 3 | 4 | 5 | 6 | 7 | 8 | 9 |
| 0 | 8.149 | 18.909 | 21.761 | 32.464 | 36.773 | 44.331 | 50.239 | 54.946 | 61.678 |
| 1 | 0.995 | 0.989 | 0.986 | 1.000 | 0.995 | 0.995 | 0.946 | 0.835 | 0.897 |
| 4 | 0.990 | 0.984 | 0.985 | 0.981 | 0.954 | 0.936 | 0.883 | 0.846 | 0.768 |
| 9 | 0.978 | 0.960 | 0.955 | 0.929 | 0.958 | 0.954 | 0.862 | 0.842 | 0.768 |
| 16 | 0.962 | 0.936 | 0.930 | 0.904 | 0.890 | 0.868 | 0.854 | 0.838 | 0.917 |

Floor occupancy masses are attached at $z = 2$ m

**Table 25.3** Floor frequency $f_{(9)}$ in Hz for different values of $z$

| $n$ | 0 | 1 | 4 | 9 | 16 |
|---|---|---|---|---|---|
| $f_{(9)}$ ($z = 0$ m) | 61.678 | 61.678 | 61.678 | 61.019 | 59.420 |
| $f_{(9)}$ ($z = 1$ m) | 61.678 | 60.885 | 60.071 | 59.212 | 59.079 |
| $f_{(9)}$ ($z = 2$ m) | 61.678 | 55.330 | 47.367 | 47.379 | 56.550 |

**Table 25.4** Floor damping $\zeta_{(k)}$ in Hz for the empty floor ($n = 0$) and normalized damping ratios for other scenarios ($n > 0$)

| | Mode number ($k$) | | | | | | | | |
|---|---|---|---|---|---|---|---|---|---|
| $n$ | 1 | 2 | 3 | 4 | 5 | 6 | 7 | 8 | 9 |
| 0 | 0.016 | 0.022 | 0.024 | 0.034 | 0.038 | 0.045 | 0.051 | 0.055 | 0.066 |
| 1 | 1.000 | 1.000 | 1.000 | 1.000 | 0.966 | 0.966 | 1.000 | 1.000 | 1.000 |
| 4 | 1.000 | 0.993 | 0.993 | 0.983 | 0.996 | 0.996 | 1.000 | 1.000 | 1.000 |
| 9 | 1.000 | 0.993 | 0.992 | 0.990 | 0.981 | 0.980 | 0.980 | 0.979 | 0.990 |
| 16 | 1.000 | 0.987 | 0.986 | 0.983 | 0.983 | 0.982 | 0.982 | 0.982 | 0.965 |

Floor occupancy masses are attached at $z = 0$ m

#### 25.3.1.3 Comparisons and Supplementary Discussion

Table 25.3 presents floor frequencies computed for mode 9 assuming different elevations of attachment of the floor occupancy masses. Results are also presented for the empty floor ($n = 0$) to be able to follow the change in floor frequency when gradually placing more mass on to the floor.

Noticeably, the frequency drops when the number of masses attached to the floor increases. Exceptions are when floor occupancy mass is attached at floor midplane ($z = 0$ m) when mowing from scenario 0 (empty floor) to scenario 1 (a single mass on the floor), and when moving from scenario 1 to scenario 4 (four masses on the floor). This is explained by the fact that in scenarios 1 and 4, the masses are placed in neutral lines of vertical vibration for these particular modes. On the other hand, in scenarios 9 and 16 the masses are not attached at neutral lines.

Further, for elevated masses positioned 2 m above floor midplane, scenario 16 results in higher floor frequency than scenario 9 (were fewer masses are attached to the floor). This follows from the fact that the masses in scenario 16 mainly move vertically (as attached distant from neutral lines of vertical vibration), whereas masses are attached close to or directly at neutral lines of vertical floor vibration within scenarios 4 and 9. Apparently, this is of more significance in relation to estimating floor frequencies, suggesting that there is a balance point where the rotational inertia associated with the added masses becomes more significant than their contribution to inertia in vertical motion.

Interestingly, when attaching the masses at $z = 1$ m instead of at $z = 0$ m, the frequency drops, however, by far as much as when changing the position of the masses from $z = 1$ m to $z = 2$ m. It might be that it is not that common to see a mass of 75 kg placed at a height of 2 m above floor midplane. However, the results seem to suggest that the rather steep decline in frequency starts somewhere between elevated heights of 1 and 2 m, and the center of mass of a high bookshelf could easily be placed more than 1 m above the floor.

It might be expected that for a low-mass floor (and not the heavy concrete floor considered for this work), the rotational inertia of a bookshelf would contribute even more to floor dynamics. Hence, for such floors, the rather steep decline in floor frequency might start at an elevated height even lower than that found for the concrete floor considered here. Further discussions of results are given in the concluding section of this paper.

Table 25.3 showed how the elevation of the masses attached to the floor influence floor frequency for mode number 9. An inspection of frequency results obtained for the other modes (1–8) reveals that a similar type of frequency decline is found also to occur for mode 6, 7, and 8. The modes 1–5 experience less severe drops in frequency when the value of z increases. It is such the floor modes with frequencies above 40 Hz that are influenced the most by elevating masses to elevations above 1 m.

### *25.3.2 Floor Damping*

This section focuses on damping ratios derived for the various scenarios. The first results to show are those obtained for the scenarios for which the occupancy masses are attached at floor midplane ($z = 0$ m). These results are listed in Table 25.4.

For scenarios $n > 0$ the damping ratios are normalized by the damping ratio of the empty floor of that particular mode.

The damping ratio is 0.016 for the first mode of the empty floor. As the mode number increases so does the damping ratio (see scenario $n = 0$). For some of the modes a slight decline in damping is observed when $n$ increases. The maximum reduction corresponds to about 3.5%. For the scenario where masses are placed at an elevated height of 2 m, the maximum reduction corresponds to about 23%. Results for damping for the scenarios $z = 1$ m and $z = 2$ m will not be shown in the paper. However, it can be mentioned that the relative variations in floor damping follow the overall tendencies observed for the relative variations of floor frequency.

## 25.4 Conclusion

The numerical studies of this paper explored how sensitive modal properties of a $8 \times 9$ m concrete floor are to the usage of the floor area. Simplified assumptions in terms of floor usage were made to provide an initial understanding of the dynamics of the floor occupied by masses rigidly attached to the floor.

As the studies covered monitoring 9 modes of floor vibration, only overall findings are summarized below.

Frequency declines of up to about 4% were observed when adding masses at floor midplane. When masses were attached to the floor at an elevated position corresponding to 2 m above the floor, frequency drops of up to about 23% were observed. Hence, the vertical positioning of the masses can have a significant impact on some of the floor frequencies. For the studied floor a step decline in frequency started when masses reached elevated positions of slightly above 1 m.

Overall the declines in damping ratios perform much like the declines found for frequency.

It would be of interest to examine to which degree the findings would impact serviceability-limit-state evaluations of floors. This step is not taken in the paper. The degree of impact would probably depend on the problem matter and source generating floor vibrations and the frequency range excitations.

Further it would be of interest to study floor occupancy scenarios of less deterministic nature than considered in this paper.

**Acknowledgements** This research was carried out in the framework of the project "Urban Tranquility" under the Intereg V program. The authors of this work gratefully acknowledge the European Regional Development Fund for the financial support.

## References

1. Bachmann, H., Ammann, W.: Vibrations in structures—induced by man and machines, IABSE Structural Engineering Documents 3e, Zürich, Switzerland, 1987
2. Nagy, A.B., Fiala, P., Márki, F., Augusztinovicz, F., Degrande, G., Jacobs, S., Brassenx, D.: Prediction of interior noise in buildings generated by underground rail traffic. J. Sound Vib. **293**, 680–690 (2006)
3. Lombaert, G., Degrande, G., Cloutaeu, D.: Road traffic induced free field vibrations: numerical modelling and in situ measurements. In: Proceedings of the International Workshop Wave, Bochum, Germany, pp. 195–207. Taylor & Francis, Oxfordshire, UK (2000)
4. Ellis, B.R., Ji, T.: Human-structure interaction in vertical vibrations. In: Proceedings of the ICE: Structures and Buildings, vol. 122, pp. 1–9. ICE Publishing, London, UK (1997)
5. Andersen, L.V., Kirkegaard, P.H.: Vibrations in a multi-storey lightweight building structure: influence of connections and nonstructural mass. In: Proceedings of the Fifth International Conference on Structural Engineering, Mechanics and Computation, pp. 131–136. CRC Press LLC, London (2013)
6. Griffin, M.J.: Handbook of Human Vibration. Academic Press, London (1990)
7. Ahmad, S., Irons, B., Zienkiewicz, O.: Analysis of thick and thin shell structures by curved finite elements. Int. J. Numer. Methods Eng. **2**, 419–451 (1970)
8. Abaqus 6.14. Dassault Systèmes Simulia Corporation, Providence, RI, USA: Dassault Systèmes, 2014
9. Fiala, P., Degrande, G., Augusztinovicz, F.: Numerical modelling of ground-borne noise and vibration in buildings due to surface rail traffic. J. Sound Vib. **301**, 718–738 (2007)

# Chapter 26
# Benchmark Problem for Assessing Effects of Human-Structure Interaction in Footbridges

**S. Gómez, J. Marulanda, P. Thomson, J. J. García, D. Gómez, Albert R. Ortiz, S. J. Dyke, J. Caicedo, and S. Rietdyk**

**Abstract** Currently, construction tendencies tend to design flexible structures, such as footbridges, slabs and grandstands, due to the increased resistance of new materials and the regulation gap in building codes. These flexible structures are susceptible of excessive vibrations induced by human activities, producing serviceability failures and, sometimes, collapse. It is essential to improve the understanding of the effect of anthropic loads over the structures to mitigate serviceability problems and the risk of structural damage and, therefore, economic and human loses.

The Human-Structure Interaction (HSI) involves the effect of human activities over a structure and, simultaneously, the effect of the structure's dynamics over the humans. The study of the HSI requires participation of multiple disciplines such as biomechanics and structural dynamics, and expertise in numerical modeling and experimental techniques, usually through finite elements and dynamic shakers or shaking tables. Analytical or numerical models are restricted to solve specific problems and, in most cases, they are not sufficiently detailed to simulate the complex behavior of the coupled human-structure system. Besides, experimental techniques required for HSI studies involve specialized instrumentation and equipment, increasing the cost and time to obtain such measurements.

Because of the current interest in HSI, integrative projects should be formulated regarding this interdisciplinary problem. In 2015, the Universidad del Valle, in collaboration with Purdue University and the University of South Carolina, built the UV HSI footbridge testbed, a testbed for assessing effects of HSI in footbridges. The footbridge has a total length of 12 m and a total width of 1.2 m. Its structure is a simply supported steel truss with a steel-deck platform. Supports are four load cells, two at each end of the bridge. The first six natural frequencies of the bridge are between 3.86 and 25.54 Hz.

The first challenge proposed through the testbed was a Blind Prediction Contest (BPC). Participants of the BPC were encouraged to use their own analytical or numerical HSI models to simulate three different types of experimental tests. The second challenge is a Benchmark problem where experimental data from more than 100 pedestrians walking twice at 10 different frequency gaits are provided. Pedestrians were female and male participants of weights between 50 and 105 kg, and heights between 1.45 and 1.90 m. This paper describes the UV HSI footbridge testbed and the Benchmark problem. Statistical results for the BPC and the Benchmark problem are provided.

**Keywords** Benchmark problem • Human-structure interaction • Footbridges • Human induced vibration • Coupled problems

S. Gómez (✉) • J. Marulanda • P. Thomson • J.J. García
School of Civil Engineering and Geomatics, Universidad del Valle, Cali, Colombia
e-mail: santiago.gomez@correounivalle.edu.co

D. Gómez
School of Civil Engineering and Geomatics, Universidad del Valle, Cali, Colombia

Lyles School of Civil Engineering, Purdue University, West Lafayette, IN 47906, USA

A.R. Ortiz
Department of Civil and Environmental Engineering, Universidad del Norte, Barranquilla, Colombia

S.J. Dyke
Lyles School of Civil Engineering, Purdue University, West Lafayette, IN 47906, USA

Department of Mechanical Engineering, Purdue University, West Lafayette, IN 47906, USA

J. Caicedo
Department of Civil and Environmental Engineering, University of South Carolina, Columbia, SC 29208, USA

S. Rietdyk
Department of Health and Kinesiology, Purdue University, West Lafayette, IN 47906, USA



J. Caicedo, S. Pakzad (eds.), *Dynamics of Civil Structures, Volume 2*, Conference Proceedings
of the Society for Experimental Mechanics Series, DOI 10.1007/978-3-319-54777-0_26

## 26.1 Introduction

In recent years an increasing number of pedestrian bridges experienced problems related with excessive vibrations induced by human activities. Some of the causes are: high structural flexibility, self-weight of the bridge, and use of large spans between supports. As a result, the conditions of serviceability loads due to human activities control the design for this type of structures [1]. Some structures that have reported this condition are: (a) *Millennium bridge* in London, England [2], (b) *Solférino passerelle* in Paris, France [3], (c) *Singapore Changi Airport Footbridge* [4], (d) *Ponte del Mare* in Pescara, Italy [5], (e) *Pedro e Inês footbridge* in Coimbra, Portugal [6], and (f) Goodwill bridge in Brisbane, Queensland, Australia [7] (Fig. 26.1).

Pedestrian-induced vibrations can occur both in the lateral and vertical directions, and may cause discomfort to users. Usually, crowded flexible footbridges may have excessive vibrations in the lateral direction, but in the vertical direction perceptible effects can be induced even by a single pedestrian or by a small number of pedestrians [13]. Unfortunately, some design and construction codes neglect this problem by assuming the pedestrian load as static, ignoring the interaction between human activities and the behavior of the structure. Current design codes and guides which take into account the dynamic effects of the anthropic loads have different criteria to set the limit values of acceleration in structures occupied by people. Generally, those values are subjective and dependent on the fundamental frequency of the structure. Thus, for structures in open places, like footbridges, some international codes, such as ISO-10137, BS-5400, Eurocode, BRO-2004 and SÉTRA, set values for peak acceleration or RMS acceleration as serviceability design criteria; however, some aspects of those criteria differ among codes and, sometimes, are contradictory.

The loads generated by human activities change in time and space, varying considerably the dynamic properties of slabs, pedestrian bridges, stairs and grandstands [14]. Nowadays, it is well known that during vibration of a footbridge some kind of human-structure interaction is almost inevitable. In recent years, some aspects of the Human-Structure Interaction (HIS) have been extensively studied, such as the variation of damping and natural frequency due to pedestrian presence, and the degree of synchronization of movement among pedestrian themselves, and between pedestrian and structure (lock-in effect). However, these researches have been focused, mainly, to the behavior in the lateral direction. On the other hand, the pedestrian-induced effects in the dynamic properties of the structure in the vertical direction, are usually neglected, because the methods for predicting the vertical vibration response remain inaccurate [15]. Even with current advances in load models and response prediction, the responses of the footbridges often differ from predicted response. This gap is mainly due because

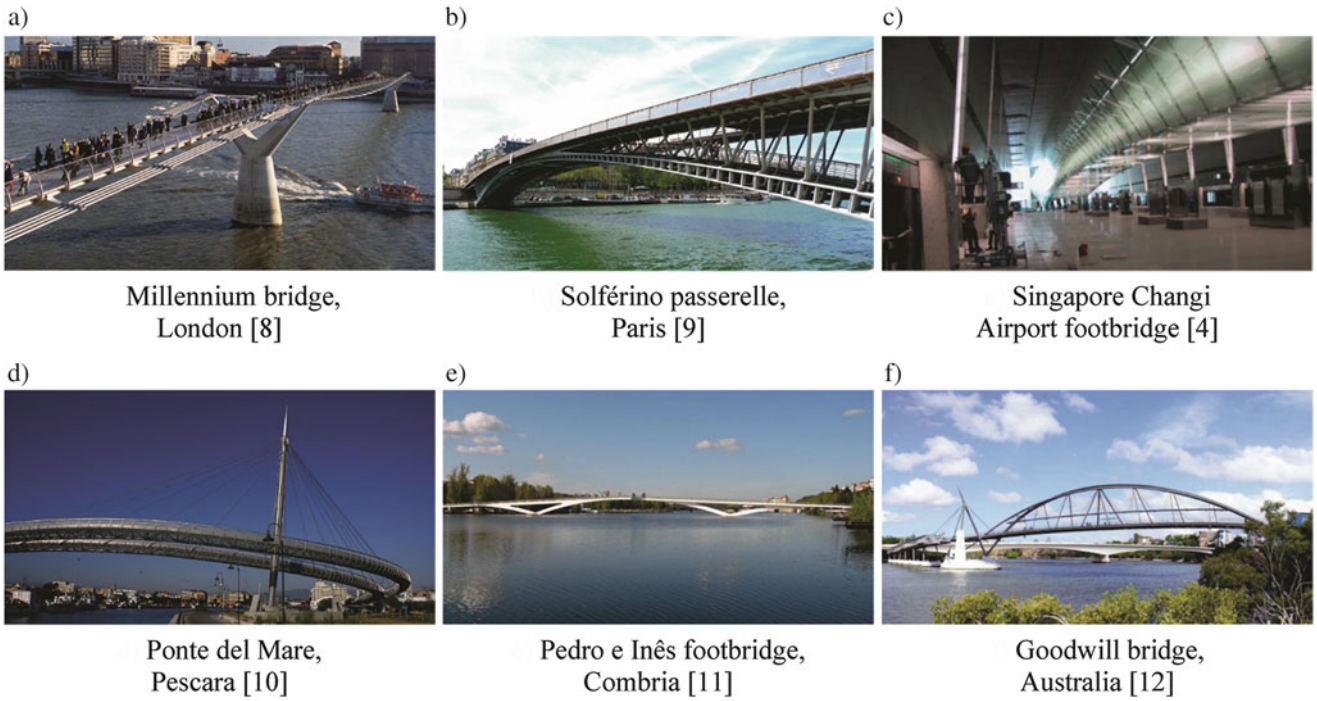


**Fig. 26.1** Footbridges with reported excessive vibration problems

HSI experimental tests in the vertical direction, as well as models of analysis of anthropic load, are not detailed enough to accurately simulate the dynamic interaction between both systems [16].

As a first stage achieving a better understanding of human-induced vibration effects, a full-scale footbridge was built and tested. The testbed structure was instrumented to obtain high-quality response measurements under external forced excitation and ambient excitation. More than 2000 HSI experimental tests were carried out. Trials were conducted over a period of two months in the Earthquake Engineering and Structural Dynamics laboratory at the Universidad del Valle (Colombia). These tests provide a unique dataset of full-scale measurements in a footbridge to support validation of structural, biomechanical and HSI models.

The aim of the Human-Structure Interaction Footbridge Testbed, the Benchmark Problem and the Blind Prediction Contest is to integrate the research community around common purposes regarding the improvement of the understanding of the HIS, comparing analytic and numerical models and sharing experimental information.

## 26.2 UV HSI Footbridge Testbed

Experimental tests were carried out in a testbed structure developed within a research project with participation of the Universidad del Valle (Colombia), University of South Carolina (USA) and Purdue University (USA). The main objective of this research is focused to foster understanding of the HSI effects in foot bridges through reference problems that may be studied by civil and biomechanical engineer. The testbed structure was designed for having the same dynamic behavior of those footbridges that haved experienced vibration problems due to pedestrian actions. Simple supported boundary conditions, at both ends allow neglecting the complexities of system interactions at the supports.

The platform of the footbridge is composed of a steel deck slab. The width, length and thickness of the slab are 1.2 m (3.9 ft), 12 m (39.4 ft) and 0.15 m (0.5 ft), respectively (Fig. 26.2a). The slab is supported by three lattice steel trusses, each one composed by two sub-trusses (Fig. 26.2b). The sub-upper trusses, that directly supports the slab, have welded connections between their elements. The sub-bottom trusses have bolted connections that allow removing some elements, thus the overall stiffness of the structure can be modified to evaluate different structural scenarios for the HSI effects. In this paper only one structural configuration is considered. Supports of the footbridge are two reinforced concrete frames. Four roller supports are used to allow movement in the longitudinal direction of the bridge. In order to guarantee comfort and safety of the users, railings, stairs and approach platform were built.


**Fig. 26.2** Testbed structure: (**a**) general view, (**b**) truss and (**c**) support

Two procedures of experimental modal analysis (EMA) were carried out to identify the dynamic properties of the structure. One procedure consisted in analyzing the dynamic behavior of the structure subject to ambient vibration (Operational Modal Analysis—OMA) and another procedure consisted in analyzing the dynamic behavior of the structure subject to external controlled-forces (Controlled Modal Analysis—CMA). A total of 18 experimental tests were performed, 9 ambient vibration tests and 9 forced-sweep swing vibration tests.

Instrumentation used to record dynamic behavior of the footbridge consists of four seismic accelerometers Wilcoxon Research (WR) model 731A, and four amplifiers WR model P31. The accelerometers' signals are transmitted through BNC connection to a connections box National Intruments (NI) SC-2345, and then to a computer Dell Optiplex-580, which has installed a data acquisition card serie X-NI PCIe-6323, which converts the analog signals to digital format. Finally, for recording digital data, the MATLAB Data Acquisition Toolbox was used.

Forced vibration tests were carried out using an electrodynamic actuator APS400 Electro-Seis (shaker). In order to get the complete modal information of the footbridge, chirp inputs were used to generate samples of a linear swept-frequency signal between 0.5 and 30 Hz during 600 s. The amplitude of the signal command was fixed. The acceleration response was recorded in horizontal and vertical direction using the shaker, leaning 15.9° with respect to the footbridge surface and was placed eccentric to the longitudinal axe. Nine test set-ups were performed, four with vertical sensors, four with horizontal sensors and one configuration to correlation both vertical and horizontal directions. A total of 26 modal coordinates were obtained, 13 vertical and 13 horizontal (Fig. 26.3).

The modal identification through forced vibration tests was carried out using estimation of a set of Frequency Response Functions (FRF), which relate the applied force and the corresponding acceleration responses at different points along the bridge, with enough resolution in spatial and frequency domain. A Hamming window was used overlapped 50% of its length. The modal deformations of the structure were considered linear with respect to generalized coordinates, defined by the orthogonal directions in the points where accelerometers were placed. The results of the modal identification through CMA are shown in Table 26.1. Ambient vibration acceleration records were taken during 300 s. The same configurations of sensors used in the forced vibration tests were implemented. The estimation methods used in the OMA correspond to the Peak Picking (PP) technique, the Natural Excitation Technique (NExT) with the Eigen system Realization Algorithm (ERA), and the Stochastic Subspace Identification (SSI) method. Average results of the OMA are show in Table 26.1.

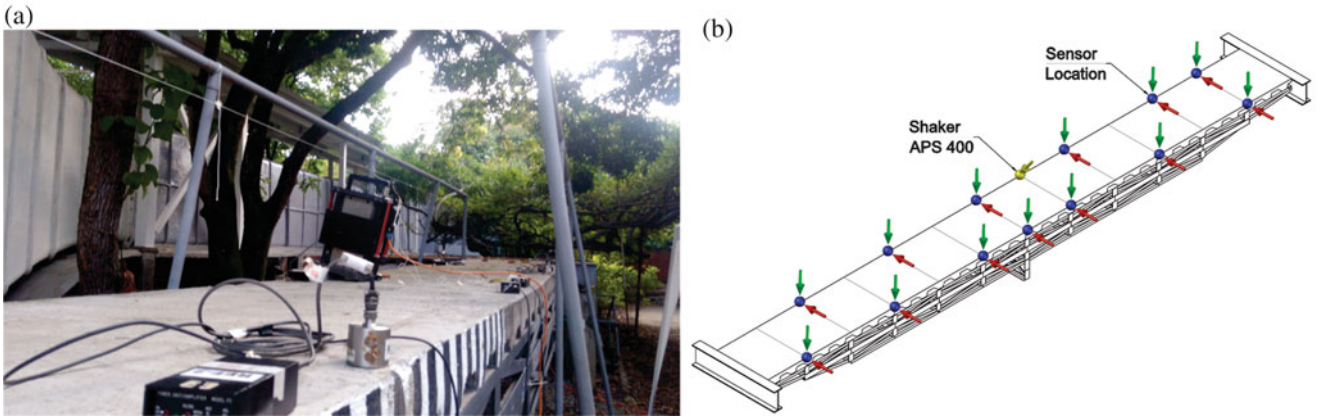


**Fig. 26.3** Test set-up: (**a**) instrumented structure and (**b**) sensors configurations

**Table 26.1** Modal identification results

| | CMA | | | | OMA | | |
|---|---|---|---|---|---|---|---|
| Mode | Frequency (Hz) | ±std. dev. (Hz) | Damping (%) | ±std. dev. (%) | PP | NExT-ERA | SSI |
| 1 | 3.86 | 0.01 | 1.09 | 0.08 | 3.91 | 3.91 | 3.92 |
| 2 | 7.51 | 0.03 | 0.94 | 0.03 | 7.63 | 7.61 | 7.66 |
| 3 | 12.50 | 0.08 | 1.37 | 0.37 | 12.45 | 12.51 | 12.45 |
| 4 | 12.94 | 0.18 | 0.82 | 0.24 | 13.09 | 13.12 | 13.06 |
| 5 | 23.58 | 0.25 | 0.87 | 0.26 | 23.67 | 23.77 | 23.76 |
| 6 | 25.85 | 0.12 | 1.16 | 0.09 | 26.39 | 26.34 | 26.38 |

## 26.3 Benchmark Problem

The protocol of the HSI experimental tests consisted in recording the footbridge dynamic behavior while one person was walking on the structure. The pace of the gait was controlled through a metronome and nine gait frequencies were evaluated (1.5–2.3 Hz), corresponding to ranges of normal walking speed according to different authors [2, 17–19]. The frequencies were sorted in aleatory way in order to avoid predisposition to increase or decrease the walking velocity: 1.7, 2.0, 1.8, 2.3, 1.6, 2.1, 1.9, 1.5 and 2.2 Hz. Additionally, a trial in which the gait frequency was uncontrolled was conducted. Two tests per frequency, including the uncontrolled one, were performed resulting in 20 trials for each person. 100 persons were recorded, therefore, more than 2000 acceleration records and supports reactions due to the effects of HSI were obtained (Fig. 26.4a). In order to evaluate the walking velocity perception of pedestrians, each person was requested to answer if the walking was slow, normal or fast.

Pedestrian-induced vibrations in the testbed structure were recorded at four different points (Fig. 26.4b). The equipment implemented for this purpose was the same used in the process for modal identification of the structure; data was sampled at 256 Hz. A low-pass filter with 30 Hz as cutoff frequency was used. Simultaneous with the acceleration response, pedestrian-induced support reactions were recorded through load cells placed in the four supports of the structure. Representative acceleration and support reaction records are shown in Fig. 26.4c, d. Additionally, the tests were monitored by two video cameras, one placed in the middle of the span, focused to the pedestrian sagittal plane, which allow correlate pedestrian kinematics and the dynamic response of the coupled system; and the second camera placed in one of the footbridge ends, taking a general view of the tests.

The anthropometric characteristics of the pedestrians are show in Fig. 26.5. A total of 100 persons were registered, 72 men and 28 women. The pedestrian heights vary between 142 cm (4.7 ft) and 189 cm (6.2 ft); the pedestrian weights vary between 493.44 and 1007.5 N. The mean height and weight of the women was 162.9 cm (5.3 ft) and 569 N. The mean height and weight of the men was 172.9 cm (5.7 ft) and 701 N. The relationship between height and pedestrian foot length, for men and women, are also shown, and the equations and coefficients of determination ($R^2$) which relate these parameters. The foot length was measured from the heel to the front end of the first metatarsal bone.

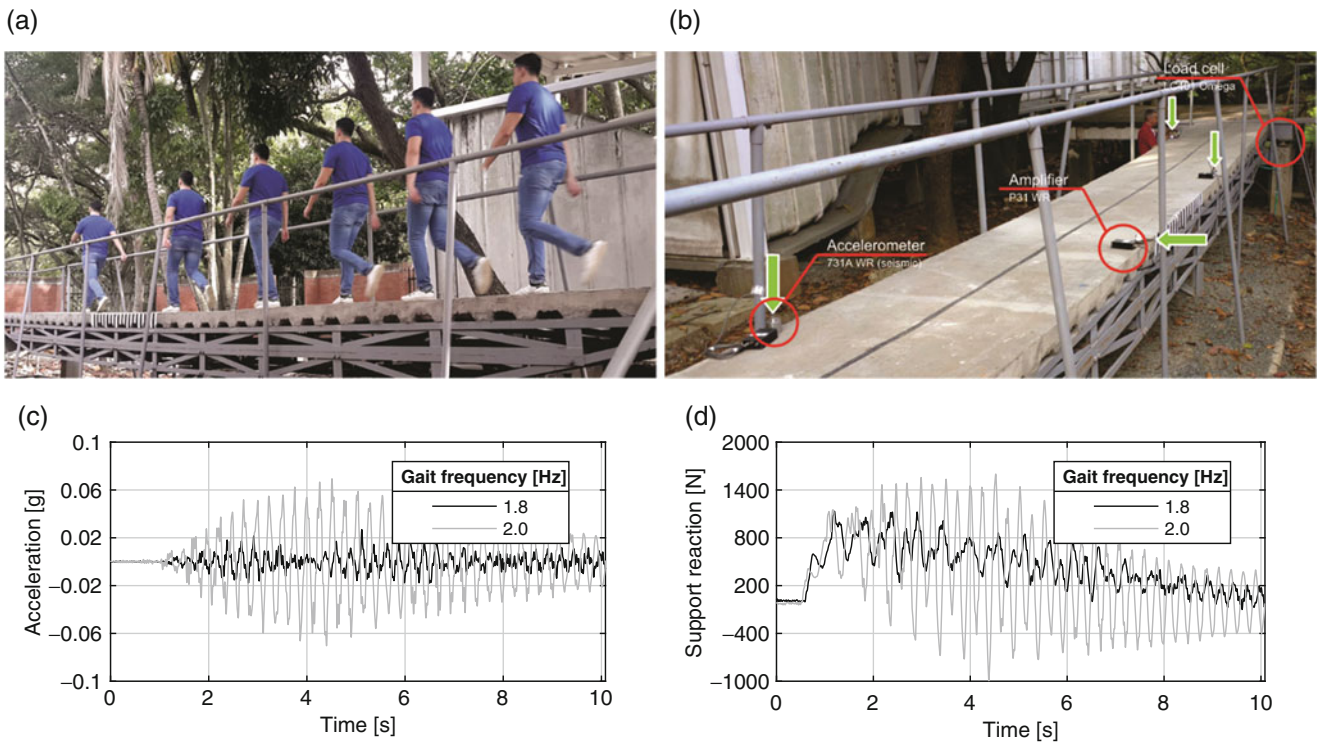


**Fig. 26.4** HSI tests: (**a**) sequence of a person walking along the structure, (**b**) HSI experimental tests set-up, (**c**) pedestrian-induced accelerations at the center of the footbridge, and (**d**) pedestrian-induced support reactions

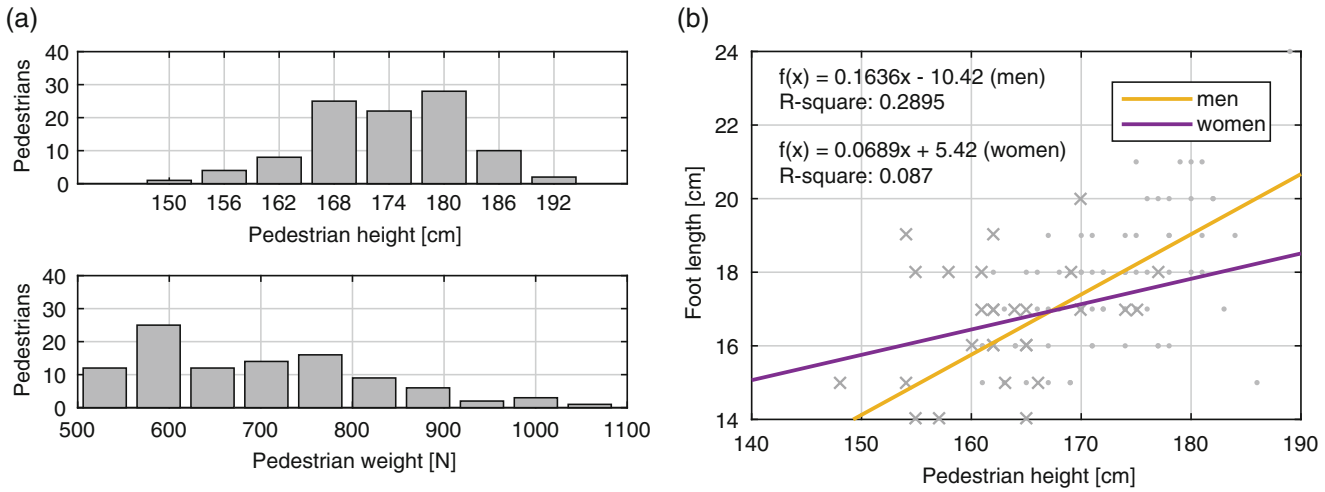


**Fig. 26.5** Anthropometric characteristics of pedestrians: (**a**) pedestrian height and weight distribution, (**b**) pedestrian length and foot length relationship

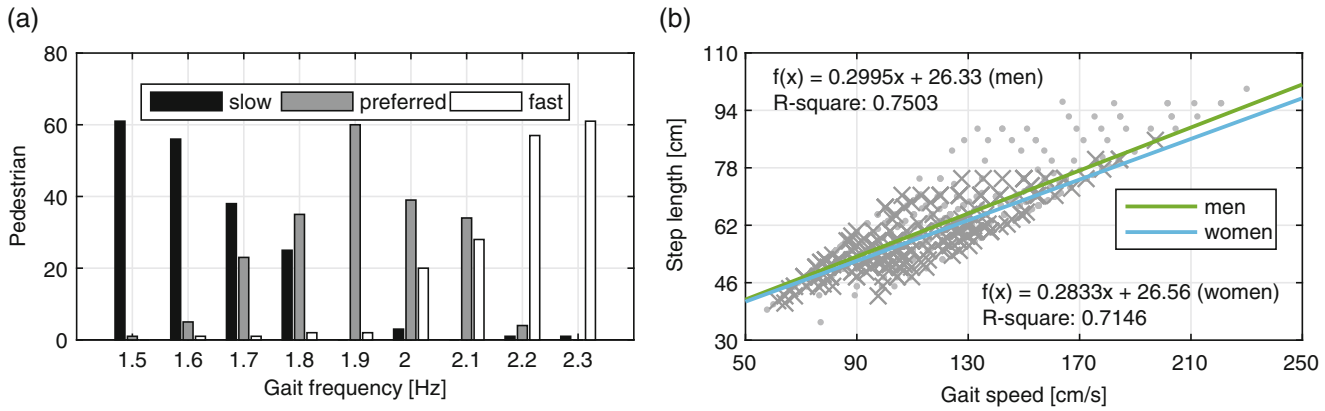


**Fig. 26.6** Gait speed perception: (**a**) perception histogram, and (**b**) pedestrian step length and gait speed relationship

### *26.3.1 Results*

A perception histogram was developed with the speed perception survey (Fig. 26.6a), which bear out the selected frequency range for this analysis. The perception histogram shows that most people consider the frequencies between 1.8 and 2.1 Hz a normal range of walking. Additionally, it appears to be a relationship between the pedestrian gait speed and step length (Fig. 26.6b).

The peak accelerations normalized to the pedestrian weight (Fig. 26.7a) are in a range between 1.02 and 4.02 g/N and higher amplitudes occur in the 1.9–2.2 Hz range. This can be due because in this range the frequency of the second harmonic of the pedestrian-induced pseudo-periodic load walking is similar to the fundamental vertical frequency of the footbridge. This effect is also observed in the RMS accelerations (Fig. 26.7b), peak support reaction normalized to pedestrian weight (Fig. 26.7c), and RMS support reactions (Fig. 26.7d). The peak accelerations and peak support reactions were normalized to pedestrian weight to avoid mass depend trends.

Figure 26.8 shows the predominant vibration frequency associated to the fundamental vertical frequency of the footbridge during each pedestrian walk. The natural frequency of the vertical mode was identified as 3.88 Hz through initial identification tests. The predominant frequency in the course of a pedestrian walk was identified selecting a segment of each acceleration record in which the person remained walking on the bridge. The predominant frequencies have a normal distribution around a 3.991 Hz with a standard deviation $\pm 0.174$ Hz.

The relations between both, the peak accelerations and peak support reactions from uncontrolled gait frequency tests, and the identified gait frequency from acceleration responses were analyzed (Fig. 26.9).

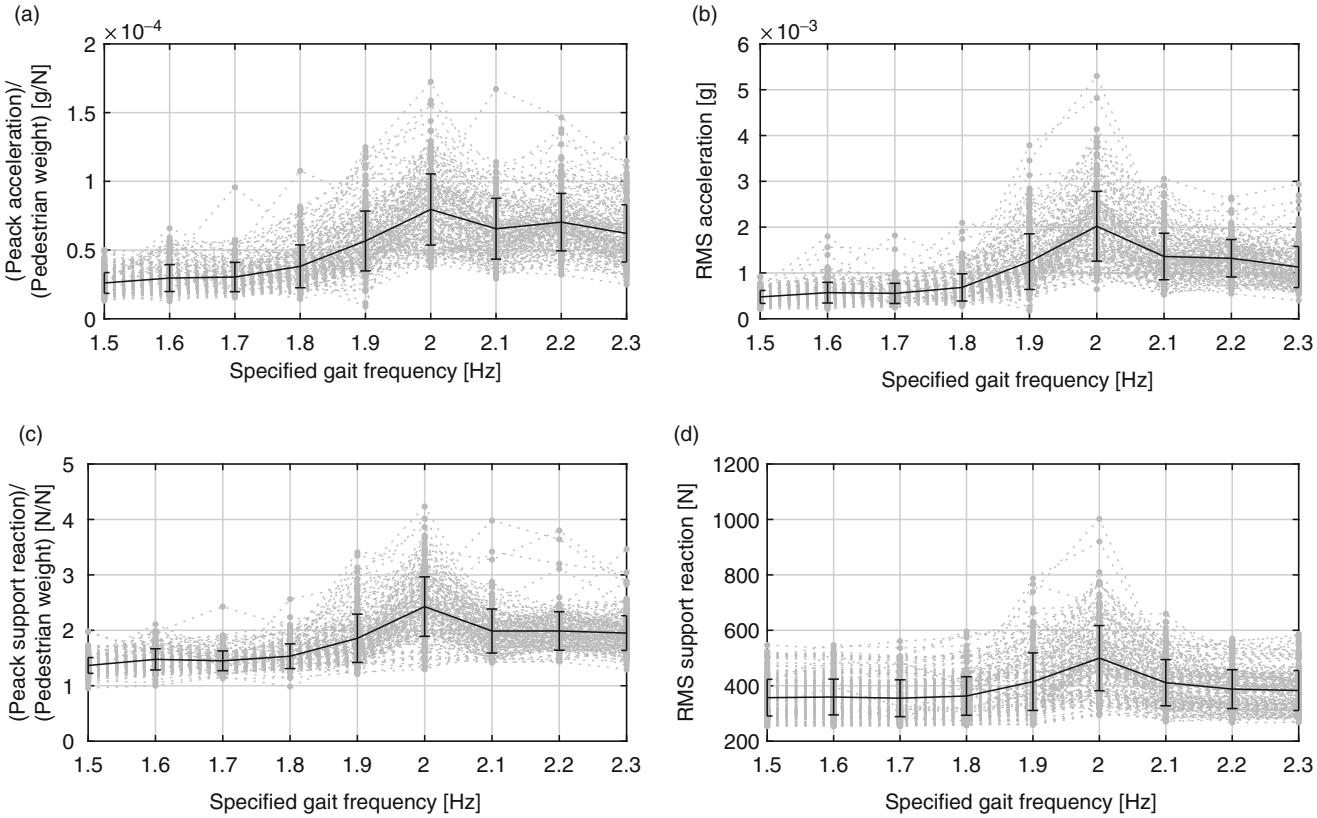


**Fig. 26.7** Controlled gait frequencies results: (**a**) peak accelerations normalized to pedestrian weight, (**b**) RMS accelerations, (**c**) peak support reaction normalized to pedestrian weight, and (**d**) RMS support reactions

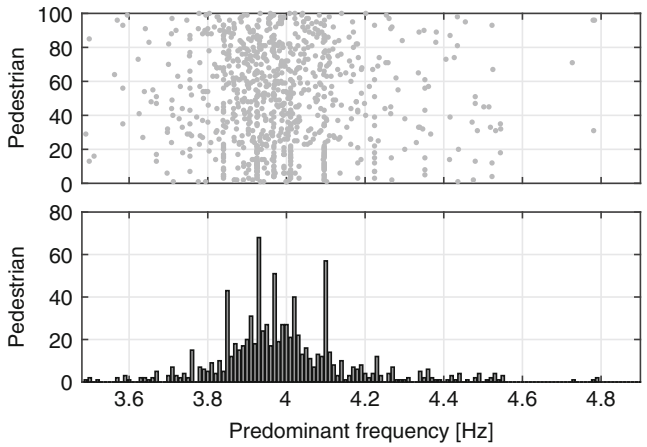


**Fig. 26.8** Predominant vibration frequency of the footbridge during each pedestrian walk

## 26.4 Blind Prediction Contest

A Blind Prediction Contest (BPC) is proposed to encourage the scientific community to compare different HSI models for footbridges. Participants of the BPC are encouraged to use their own analytical or numerical HSI models to simulate three different types of experimental tests. Structural details (plans) and material properties of the footbridge are provided in http://benchmark.univalle.edu.co/. Description of the tests and pedestrian data (weight, height, sex) are also provided. A numerical model of the bridge is not be provided and experimental data is not available for the BPC. Registered participants of the BPC must upload through the webpage two simulated responses of the footbridge for each test: accelerations at the

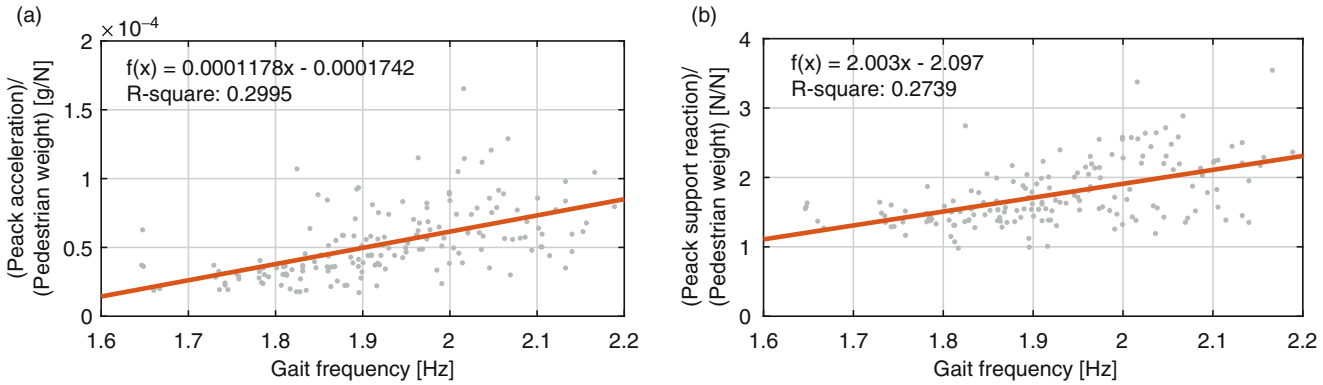


**Fig. 26.9** Uncontrolled gait frequencies results: (**a**) peak accelerations and (**b**) peak support reactions normalized to pedestrian weight and gait frequencies relationship

**Table 26.2** Pedestrian information

| ID | Weight (kg/lb) | Height (m/ft) | Sex (gender) |
|---|---|---|---|
| 0393 | 88.1/194.2 | 1.81/5.94 | Male |
| 3093 | 62.5/137.8 | 1.62/5.31 | Female |
| 1086 | 80.2/176.8 | 1.70/5.58 | Male |
| 8722 | 59.0/130.1 | 1.62/5.31 | Female |
| 2286 | 61.5/135.6 | 1.69/5.54 | Male |
| 7404 | 57.9/127.6 | 1.60/5.25 | Female |

middle of the bridge and support reactions at one end of the bridge. The webpage platform will calculate in real-time the similarity between numerical responses provided by participants and experimental records already taken. The similarity will be measured according to the metrics described as follows.

### *26.4.1 Experimental Data*

The instrumentation used for the experimental tests of the BPC was the same as the instrumentation used for modal analysis of the bridge. The sampling frequency used for all channels was 256 Hz and data records were downsampled to 64 Hz. Participants of the BPC are encouraged to use their own analytical or numerical HSI models to simulate 15 different experimental tests, grouped in three types of experiments:

- Type 1: One pedestrian walks from end B to end A at three different gait frequencies controlled by a metronome: 1.6, 2.0 and 2.2 Hz. Pedestrians are 0393, 3093 and 1086.
- Type 2: Pedestrian 2286 walks from end B to end A at three different gait frequencies controlled by a metronome: 1.6, 2.0 and 2.2 Hz; while pedestrian 7404 walks from end A to end B always at a gait frequency of 1.5 Hz.
- Type 3: Pedestrian 7404 walks from end B to end A at three different gait frequencies controlled by a metronome: 1.6, 2.0 and 2.2 Hz; while pedestrian 8722 stays standing at rest at 5.0 m from end.

Six pedestrians took part in the experimental tests for the BPC. Pedestrian identification code, weight, height and sex are shown in Table 26.2.

### *26.4.2 Metrics*

The uploaded acceleration time-history will be compared to the respective experimental record taken at the middle of the footbridge. For support reactions, only one time-history must be uploaded that will be compared to the sum of the two load cells' records at end A. In real-time, the webpage platform will calculate the similarity between simulated responses provided by participants and experimental records using Eqs. (26.1)–(26.6). The similarity will be measured according to the metrics described forward and will be reported instantly as a Score in the "Ranking page". A score will be provided for each BPC type.

$$A_n^1 = \left[1 - \frac{RMS\left(\mathbf{a_{nref}}\right) - RMS\left(\mathbf{a_n}\right)}{RMS\left(\mathbf{a_{nref}}\right)}\right] * 100 \tag{26.1}$$

$$A_n^2 = \left[1 - \frac{max\left|\mathbf{a_{nref}}\right| - max\left|\boldsymbol{a_n}\right|}{max\left|a_{nref}\right|}\right] * 100 \tag{26.2}$$

$$R_n^1 = \left[1 - \frac{RMS\left(\mathbf{r_{nref}}\right) - RMS\left(\boldsymbol{r_n}\right)}{RMS\left(\mathbf{r_{nref}}\right)}\right] * 100 \tag{26.3}$$

$$R_n^2 = \left[1 - \frac{max\left|\mathbf{r_{nref}}\right| - max\left|\boldsymbol{r_n}\right|}{max\left|\mathbf{r_{nref}}\right|}\right] * 100 \tag{26.4}$$

$$\Delta_n = mean\left(\mathrm{A}_n^1, \mathrm{A}_n^2, \mathrm{R}_n^1, \mathrm{R}_n^2\right) \tag{26.5}$$

$$SCORETYPE\ X = mean\left(\Delta_{1.6}, \Delta_{2.0}, \Delta_{2.2}\right) \tag{26.6}$$

### 26.4.3 BPC Example

A HSI model was developed based in the bipedal model proposed by Whittington and Thelen [20]. The model consists of a point mass supported by spring limbs. Roller feet were incorporated for tracking feet centers of pressure. A simply supported beam, with uniformly distributed mass, was used to simulate the footbridge. Both numerical models were coupled to simulate de HSI effects (Fig. 26.10a). Representative acceleration and support reaction records are also shown in Fig. 26.10b, c. Simulated records were uploaded following the instructions of the webpage (http://benchmark.univalle.edu.co/upload-total). The score for type 1 BPC was 62.02/100 and can be seen in the ranking section of webpage for the user named "BPC Example".

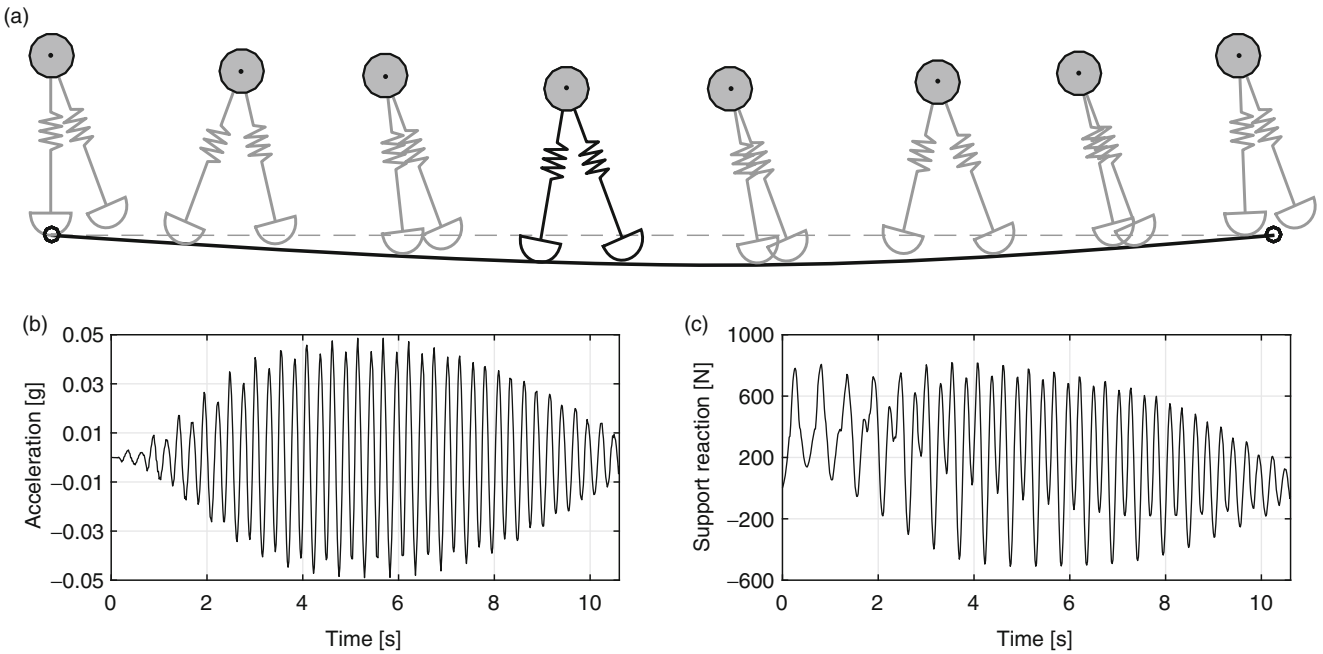


**Fig. 26.10** BPC example: (**a**) HSI model, (**b**) HIS model-induced accelerations at the center of the footbridge, and (**c**) HSI model-induced support reactions

## 26.5 Conclusions

A Human-Structure Interaction Footbridge Testbed, a Benchmark Problem and a Blind Prediction Contest were proposed to integrate the research community around common purposes regarding the improvement of the understanding of the HIS, comparing analytic and numerical models and sharing experimental information. Six modes shapes and the corresponding vibration frequencies and damping ratios of the testbed were identified using controlled and ambient vibration tests. Two thousand tests were performed by 100 pedestrians walking on the bridge at different gait frequencies. Acceleration and support reactions records were taken during each test. One video camera placed at the middle of the bridge was used to calculate the pedestrians' step length and correlate it with the foot length. The gait speed perception survey indicated that normal range frequencies of walking is between 1.8 and 2.1 Hz. The peak accelerations and peak support reactions normalized to pedestrian weight from uncontrolled gait frequency tests were correlated with the corresponding gait frequencies. A HSI model was developed and used for participating in the BPC, obtaining a score 62.02/100 for the type 1 BPC.

## References

1. Sánchez, J.A., Gómez, D., Thomson, P.: Análisis de la interacción humano-estructura en puentes peatonales de santiago de Cali. Dyna. **86–94**, 178 (2014)
2. Živanović, S., Pavić, A., Reynolds, P.: Vibration serviceability of footbridges under human-induced excitation: a literature review. J. Sound Vib. **279**, 1–74 (2005)
3. SETRA: Assessment of vibrational behaviour of footbridges under pedestrian loading, Republique Francaise, 2006
4. Brownjohn, J.M.W., Moyo, P.: Long span steel pedestrian bridge at Singapore Changi Airport—part 1: prediction of vibration serviceability problems. Struct. Eng. **82**, 21–27 (2004)
5. Bonelli, A., Bonora, M., Bursi, O., Santini, S., Vulcan, L., Zasso, A.: Dynamic analysis and vibration control of the twin deck curved suspension foot/cycle bridge "Ponte del Mare". In: Proceedings Footbridge 2008 Conference, Porto, 2004
6. Caetano, E., Cunha, Á., Magalhães, F., Moutinho, C.: Studies for controlling human-induced vibration of the Pedro e Inês footbridge, Portugal. Part 1: assessment of dynamic behaviour. Eng. Struct. **32**(4), 1069–1081 (2010)
7. Ross, J.N.: Human Induced Vibration on Footbridges, Brisbane, 2009
8. London Millennium Footbridge (online) (2000). Available http://www.fosterandpartners.com/media/Projects/0953/img5.jpg
9. Passerelle solférino (online) (2010). Available https://chasetaylorinc.files.wordpress.com/2010/04/p1060666.jpg?w=480&h=270
10. Ponte del mare, Italy, Pescara (online) (2010). Available https://commons.wikimedia.org/wiki/File:Ponte_del_mare,_Italy,_Pescara.jpg
11. Pedro and Inês Bridge, Coimbra (online) (2006). Available https://structurae.net/photos/75988-pedro-and-ines-bridge-coimbra
12. Goodwill Bridge (online) (2015). Available https://briscycle.com/assets/Uploads/_resampled/resizedimage900335-goodwill-bridge.jpg
13. Živanović, S., Pavić, A., Ingólfsson, E.T.: Modelling spatially unrestricted pedestrian traffic on footbridges. ASCE J. Struct. Eng. **136**(10), 1296–1308 (2010)
14. Racic, V., Pavic, A., Brownjohn, J.: Experimental identificacion and analytical modelling of human walking forces: literature review. J. Sound Vib. **326**, 1–49 (2009)
15. Shahabpoor, E., Pavic, A., Racic, V.: Using MSD model to simulate human-structure interaction during walking. In: 31st IMAC, A Conference on Structural Dynamics, 2013
16. Živanović, S.: Benchmark footbridge for vibration serviceability assessment under vertical component of pedestrian load. ASCE J. Struct. Eng. **138**(10), 1193–1202 (2012)
17. Matsumoto, Y., Sato, S., Nishioka, T., Shiojiri, H.: A study on design of pedestrian over-bridges. Trans. JSCE. **4**, 50–51 (1972)
18. Matsumoto, Y., Nishioka, T., Shiojiri, H., Matsuzaki, K.: Dynamic design of footbridges. IABSE Proc. 1–15 (1978)
19. Newland, D.E.: Pedestrian excitation of bridges. Proc. Inst. Mech. Eng., Part C. **218**, 477–492 (2004)
20. Whittington, B.R., Thelen, D.Y.G.: A simple mass-spring model with roller feet can induce the ground reactions observed in human walking. J. Biomech. Eng. **131**, 011013 (2009)

# Chapter 27
# A Discrete-Time Feedforward-Feedback Compensator for Real-Time Hybrid Simulation

**Saeid Hayati and Wei Song**

**Abstract** Real-Time Hybrid simulation (RTHS) is a powerful experimental technique which provides engineers the opportunity of performing cost-effective dynamic tests for large or full scale structures. To carry out a successful RTHS test, the time delay, which is mostly associated with the servo-hydraulic actuator dynamics, needs to be reduced by an appropriate compensator. Model-based feedforward compensators are designed based on the dynamic model of the plant, including both the servo-hydraulic actuator and the specimen attached to it. This dynamic model may not represent the plant accurately during the RTHS, especially when the specimen behaves nonlinearly during the test. As a result, the feedforward compensator/controller which is designed based on this plant model may not work effectively. In this paper, a discrete time feedback controller is introduced, in addition to the feedforward compensator, to provide robustness to the delay compensation. Both numerical and experimental studies will be conducted. The performance of this feedforward-feedback compensator is evaluated through the actuator time delay and the relative Root-Mean-Square (RMS) error between the desired and measured actuator displacement.

**Keywords** Real-time hybrid simulation • Discrete-time feedforward-feedback compensator • Time delay • Servo-hydraulic actuator control • FIR compensator

## 27.1 Introduction

Real-Time Hybrid simulation (RTHS) is a powerful experimental technique which provides engineers the opportunity of performing cost-effective dynamic tests for large or full-scale structures. To carry out a successful RTHS test, the time delay, which is mostly associated with the servo-hydraulic actuator dynamics, needs to be lessened by an appropriate compensator. Horiuchi et al. [1] introduced a polynomial extrapolation technique based on a constant actuator time delay. Darby et al. [2] and Nakashima and Masaoka [3] evolved the polynomial extrapolation technique by introducing interpolation steps into it. More accurate compensators were designed by Darby et al. [4], Ahmadizadeh et al. [5], Jung and Shing [6], and Chen and Ricles [7] where they considered the variation in the actuator time delay during the test. Later, Model-based compensators were designed based on a dynamic model of the plant, mostly includes the actuator and the specimen attached to it. Chen and Ricles [8] introduced the inverse compensation technique by inverting a first order actuator transfer function model. A higher order transfer function model can represent the dynamic of the plant better. Thus, Carrion and Spencer [9] developed their model-based compensator based on a higher order (third or fourth) transfer function of the plant. Recently, Hayati and Song [10] developed a new model-based compensator which can reduce the time delay when the actuator is subjected to inputs with broader frequency bandwidths. Implementing this new compensator enables the RTHS technique to be used for studying the dynamic behavior of those systems which works under inputs with relatively broad frequency bandwidths.

The performance of the model-based compensators such as the FIR compensator can be affected by changing specimen condition, modeling errors and disturbances [11]. Hence, this study aims to improve the robustness of the FIR compensator and reduce the tracking error between the desired and the measured displacement of the actuator. To this end, a feedback controller was designed and integrated to the FIR compensator. The effectiveness of the feedback controller in improving the performance of the FIR compensator will be shown in this extended abstract through the numerical study. Further experimental study needs to be conducted to validate the numerical results.

S. Hayati • W. Song (✉)
Department of Civil, Construction and Environmental Engineering, The University of Alabama, Tuscaloosa, AL, 35487, USA
e-mail: wsong@eng.ua.edu



J. Caicedo, S. Pakzad (eds.), *Dynamics of Civil Structures, Volume 2*, Conference Proceedings
of the Society for Experimental Mechanics Series, DOI 10.1007/978-3-319-54777-0_27

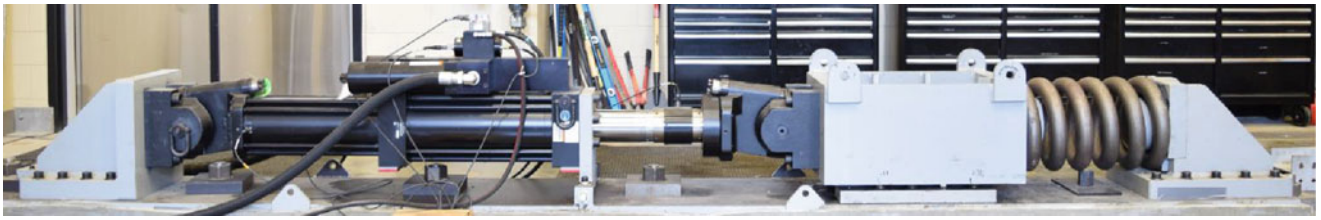

**Fig. 27.1** Experimental setup in the large scale structural laboratory at the University of Alabama

**Fig. 27.2** Implementation of FIR compensator

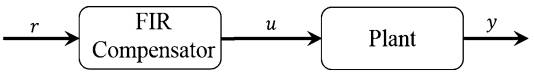


## 27.2 FIR Compensator

Hayati and Song [10] used an Auto-Regressive with Exogenous (ARX) model to represent the plant dynamic accurately. In this study, the plant was comprised of an actuator attached to a mass and a linear spring (see Fig. 27.1).

Then, the inverse of the plant dynamic model was modified by using a Finite Impulse Response (FIR) filter to develop a new model-based compensator. Due to the usage of FIR filter, this compensator was named FIR compensator. Figure 27.2 depicts how the FIR compensator connects in series with the plant (=actuator and the specimen attached to it). In this figure, $r$, $u$ and $y$ are reference signal, compensated signal and measured signal, respectively. Compared to the exciting compensators for RTHS, the FIR compensator can reduce the time delay more effectively when the actuator is subjected to inputs with a wider frequency bandwidth [0 30 Hz] input [10]. Implementing the FIR compensator in an RTHS test makes it a powerful technique to study the dynamic behavior of those systems that work under inputs with high-frequency bandwidth such as suspension system of a vehicle.

Although the FIR compensator can reduce the time delay effectively, its performance can be deteriorated if the dynamic of the plant changes. Therefore, a feedback controller was designed to improve the robustness of the FIR compensator.

## 27.3 Feedforward-Feedback FIR Compensator

In this extended abstract, the FIR compensator [10] is used as a feedforward controller for the actuator. To improve the robustness of the FIR compensator, a feedback controller is designed and combined with it. Then the performance of the combined system, feedforward and feedback controllers, was investigated through the numerical study.

### *27.3.1 Feedback Controller*

The feedback controller places the closed-loop poles of the plant at desirable locations such that the output, $y$, tracks the reference signal, $r$, accurately. In this study, the feedback controller was designed based on the modern control theory. In contrast to the classical control theory which utilizes the transfer function models in the frequency domain, the modern control theory uses the time domain state-space models [12]. For this research, the Linear Quadratic Regulator (LQR) control is used to determine the optimal feedback gain ($K$) by minimizing a cost function shown in Eq. (27.1) [13, 14]

$$J = \frac{1}{2}\int_0^\infty \left(x^T Q x + u^T R u\right) dt \tag{27.1}$$

Where, T is the transpose operator and $Q$ and $R$ are weighting matrixes for states and control signal vectors, respectively. Then, the feedback gain is multiplied by the states of the deviation plant to obtain the feedback control signal as shown in Eq. (27.2). Here, the deviation plant is defined as a plant which its states are the error between the states of the real plant and an ideal plant (more information can be found in [13]).

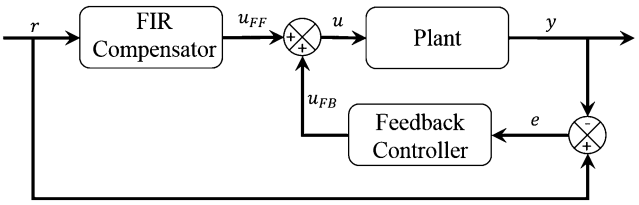


**Fig. 27.3** Implementation of feedforward-feedback FIR compensator

**Table 27.1** Performance study of the feedforward and feedforward-feedback compensators

| RMS of process noise | RMS of measurement noise | $R$ | Relative RMS of the output with respect to the RMS of the process noise (%) | |
|---|---|---|---|---|
| | | | Feedforward compensator | Feedforward-feedback compensator |
| 0.7 | 0.2 | $10^{-2}$ | 37.12 | 34.82 |
| 0.7 | 0.4 | $10^{-2}$ | 61.93 | 61.162 |
| 1 | 0.2 | $10^{-2}$ | 30.99 | 27.84 |
| 1 | 0.4 | $10^{-2}$ | 46.52 | 45.19 |
| 0.7 | 0.2 | $10^{-6}$ | 37.12 | 33.53 |
| 0.7 | 0.4 | $10^{-6}$ | 61.93 | 60.73 |
| 1 | 0.2 | $10^{-6}$ | 30.99 | 25.77 |
| 1 | 0.4 | $10^{-6}$ | 46.52 | 44.19 |

$$u_{FB} = -Kx \tag{27.2}$$

In Eq. (27.2), $x$ indicate the state vector of deviation plant. The only measurable state of the deviation system is the error between the measured displacement ($y$) and the reference signal ($r$). However, all the states are required to calculate the feedback control signal (see Eq. (27.2)). Hence, the Kalman filter was utilized to estimate the unmeasurable states based on one which is measured.

### *27.3.2 Implementing of the Feedforward-Feedback FIR Compensator*

After obtaining the feedback control signal, it will be added to the signal obtained by the feedforward FIR compensator ($u_{FF}$). Then, this new signal ($u = u_{FF} + u_{FB}$) will be sent to the actuator.

Figure 27.3 shows how the feedback controller is integrated into the feedforward controller (in this study FIR compensator) to generate the feedforward-feedback FIR compensator for controlling the actuator movement. Note that in this figure, the plant represents the actuator and a specimen attached to it.

## 27.4 Numerical Study

The performance of the feedforward-feedback FIR compensator in controlling the actuator movement was studied numerically. In this study, the plant was subjected to the process noise (noise introduced in the commanded signal into the actuator) and measurement noise (noise introduced into the measured signal). Also, the effect of $R$ value in the cost function (see Eq. (27.1)), on the performance of the feedforward-feedback FIR compensator was studied. Table 27.1, shows the relative Root-Mean-Square (RMS) of the measured output with respect to the RMS of the process noise for different cases.

## 27.5 Summary and Conclusion

To improve the robustness of the FIR compensator, a feedback controller was designed and was integrated into it. Then, the performance of this new feedforward-feedback FIR compensator was investigated through numerical simulation. Based on the obtained results (see Table 27.1) the following conclusion can be drawn:

1. The performance of the feedforward-feedback FIR compensator is superior to the performance of the feedforward FIR compensator when the actuator is subjected to the different level of process noise and measurement noise.
2. By reducing the $R$ value in Eq. (27.1), the performance of the feedforward-feedback compensator improves.

Further experimental study will be performed to validate the obtained results shown in this extended paper.

## References

1. Horiuchi, T., et al.: Development of a real-time hybrid experimental system with actuator delay compensation. In: Eleventh World Conference on Earthquake Engineering, Acapulco, p. Paper No. 660, 1996
2. Darby, A.P., Blakeborough, A., Williams, M.S.: Improved control algorithm for real-time substructure testing. Earthq. Eng. Struct. Dyn. **30**(3), 431–448 (2001)
3. Nakashima, M., Masaoka, N.: Real-time on-line test for MDOF systems. Earthq. Eng. Struct. Dyn. **28**(4), 393–420 (1999)
4. Darby, A.P., Williams, M.S., Blakeborough, A.: Stability and delay compensation for real-time substructure testing. J. Eng. Mech. **128**(12), 1276–1284 (2002)
5. Ahmadizadeh, M., Mosqueda, G., Reinhorn, A.M.: Compensation of actuator delay and dynamics for real-time hybrid structural simulation. Earthq. Eng. Struct. Dyn. **37**(1), 21–42 (2008)
6. Jung, R.-Y., Benson Shing, P.: Performance evaluation of a real-time pseudodynamic test system. Earthq. Eng. Struct. Dyn. **35**(7), 789–810 (2006)
7. Chen, C., Ricles, J.M.: Improving the inverse compensation method for real-time hybrid simulation through a dual compensation scheme. Earthq. Eng. Struct. Dyn. **38**(10), 1237–1255 (2009)
8. Chen, C., Ricles, J.M.: Analysis of actuator delay compensation methods for real-time testing. Eng. Struct. **31**(11), 2643–2655 (2009)
9. Carrion, J.E., Billie, J., Spencer, F.: Model-Based Strategies for Real-time Hybrid Testing, p. 211. University of Illinois at Urbana-Champaign, Champaign-Urbana (2007)
10. Hayati, S., Song, W.: Discrete-time compensation technique for real-time hybrid simulation. In: IMAC-XXXIV, Orlando, 2016
11. Phillips, B.M., Billie, J., Spencer, F.: Model-Based Feedforward-Feedback Tracking Control for Real-Time Hybrid Simulation, p. 42. University of Illinois at Urbana-Champaign, Champaign-Urbana (2011)
12. Dorf, R.C., Bishop, R.H.: Modern Control Systems, 12th edn. Pearson Prentice Hall, Upper Saddle River (2011)
13. Lewis, F.L., Vrabie, D., Syrmos, V.L.: Optimal Control, 3rd edn. John Wiley & Sons, Hoboken (2012)
14. Phillips, B.M., Billie, J., Spencer, F.: Model-Based Framework for Real-Time Dynamic Structural Performance Evaluation, p. 178. University of Illinois at Urbana-Champaign, Champaign-Urbana (2012)

# Chapter 28
# Sensing and Rating of Vehicle–Railroad Bridge Collision

**Shreya Vemuganti, Ali Ozdagli, Bideng Liu, Anela Bajric, Fernando Moreu, Matthew R. W. Brake, and Kevin Troyer**

**Abstract** Overhead collisions of trucks with low-clearance railway bridges cause more than half of the railway traffic interruptions over bridges in the United States. Railroad owners are required to characterize the damage caused by such events and assess the safety of subsequent train crossings. However, damage characterization is currently visual (subjective) and becomes difficult in remote locations where collisions are not reported and inspections are not performed following the impact. To mitigate these shortcomings, this paper presents a new impact definition and rating strategy for automatically and remotely quantify damage. This research proposes an impact rating strategy based on the information that best describes the consequences of vehicle-railway bridge collisions. A series of representative impacts were simulated using numerical finite element models of a steel railway bridge. Railway owners provided information about the bridge and impact characterization based on railway industry experience. The resulting nonlinear dynamic responses were evaluated with the proposed rating strategy to assess the effect of these impacts. In addition, a neural network methodology was implemented on a simplified numerical model to identify spatial characteristics of the impact damage.

**Keywords** Railway bridges • Structural health monitoring • Finite element model • Impact detection • Neural networks

## 28.1 Introduction

Today nearly half of railway bridge-related service interruptions are attributed to strikes of highway traffic [1]. Out of 8563 reported interruptions in railway services, half are caused by strikes of highway vehicles with railroad bridges (Fig. 28.1). Annual risk created by vehicle-bridge collision is estimated to be as much as $10.2 million for the industry. The consequence of an impact can vary from negligible damage in structural members to disturbance in the alignment due to supports being pushed beyond their capacity limits. In the least serious events, traffic is delayed only until an inspection is conducted. In the most serious cases, destruction of the bridge and even loss of a train may occur.

In general, highway truck impact with the bottom flange of a girder does not have an immediate effect on the structural capacity of the bridge. Nevertheless, after a highway truck collision, bridge inspectors need to conduct a detailed visual inspection to ensure the bridge is safe for subsequent train crossings even when a minor impact is reported. A minimum

Developed at the Nonlinear Mechanics and Dynamics (NOMAD) Research Institute, which was organized by Sandia National Laboratories and hosted by University of New Mexico. Sandia National Laboratories is a multi-mission laboratory managed and operated by Sandia Corporation, a wholly owned subsidiary of Lockheed Martin Corporation, for the U.S. Department of Energy's National Nuclear Security Administration under contract DE-AC04-94AL85000.

S. Vemuganti (✉) • A. Ozdagli • F. Moreu
Department of Civil Engineering, University of New Mexico, Albuquerque, NM, USA
e-mail: shreya.vemuganti@gmail.com

B. Liu
Department of Disaster Prevention Engineering, Institute of Disaster Prevention, Beijing, China

A. Bajric
Department of Mechanical Engineering, Technical University of Denmark, Lyngby, Denmark

M.R.W. Brake
Department of Mechanical Engineering, William Marsh Rice University, Houston, TX, USA

K. Troyer
Component Science and Mechanics Department, Sandia National Laboratories, Albuquerque, NM, USA



J. Caicedo, S. Pakzad (eds.), *Dynamics of Civil Structures, Volume 2*, Conference Proceedings
of the Society for Experimental Mechanics Series, DOI 10.1007/978-3-319-54777-0_28

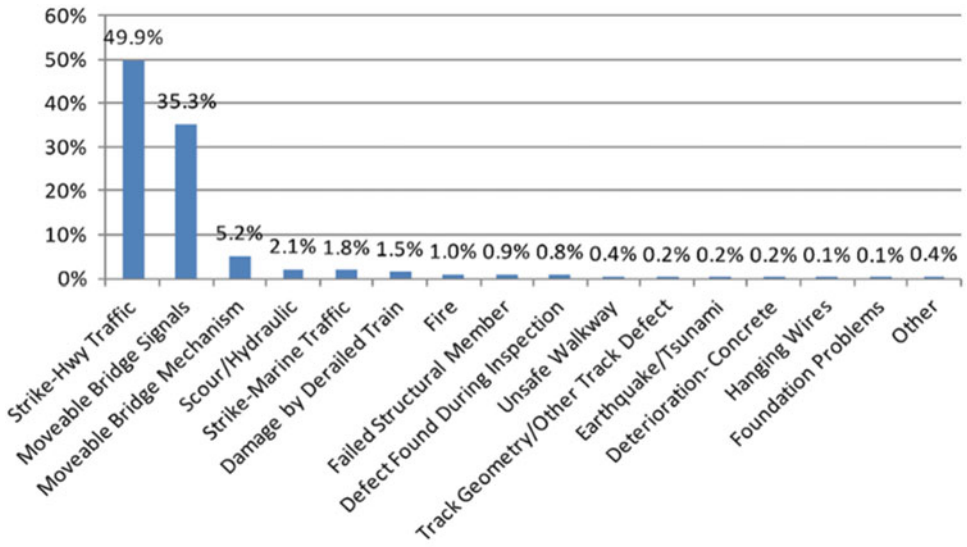


**Fig. 28.1** Frequency of railway reported events causing traffic interruptions [1]

estimated cost for minor service interruption and negligible damage after impact is calculated to be $10,000 [2]. As a result, the railway industry is interested in a method that can rate the damage of vehicle-railway bridge collisions.

With the same interest, three critical objectives of this research are identified as: (a) impact modeling, (b) impact assessment, and (c) impact rating. To achieve these objectives, an extensive literature review has been conducted. Various damage detection techniques and structural health monitoring methodologies [1, 3–13] are studied. Different finite element models focusing on the simulation of impact events have also been reviewed [8, 14–17]. None of the previous literature addressed a realistic vehicle-bridge collision event. Likewise, a consequence-based rating system was overlooked.

In this study, a rating strategy for quantifying damage is proposed. This research develops a three dimensional finite element (FE) model of a railway bridge (ANSYS 17.2) and simulates nonlinear overhead collision events. Results include structural stresses and permanent deformations, and strains under vehicular impacts running at different speeds. Researchers linked the nonlinear dynamic responses with a preliminary rating strategy to assess the effect of impact on the bridge model. In addition, researchers investigated the potential application of neural network systems for impact ratings using a simplified beam model of the bridge.

## 28.2 Impact Modeling

For the impact modeling, this research utilizes a railway bridge owned by one of the Class I railways in North America. This bridge is a single span deck plate girder system that carries one railway track. The bridge is 5 m (16.4 feet) wide and 24 m (78.7 feet) long, crossing over a two lane road. The main structure consists of two plate girders connected with transverse cross beams carrying the train track. Multiple vertical stiffeners are added to the two webs to prevent the web from buckling under heavy train loading. Fig. 28.2 shows the bridge plan and elevation views.

In this study, an FE model of the target structure is constructed using ANSYS/Autodyn software [18] to (1) simulate a vehicle impact with the railway bridge, (2) study resulting nonlinearities on the bridge, and (3) quantify its dynamic deflection characteristics during and after impact. The FE model is developed based on the plans and pictures of the railway bridge. Bridge plans are used to determine the material properties of steel such as Young's modulus, yield stress, tangent modulus and yield strains. All steel components, including the girder web, top and bottom flanges, and the main deck plate, are structural steel with bilinear hysteresis observing elasto-plastic behavior based on American Standard for Testing and Materials (ASTM) A572/A572M [19]. The Cowper-Symonds material deformation law [20] with parameters appropriate for the steel material is utilized for all the structural components. The elastic modulus is estimated to be 200 GPa (29,000 ksi). The geometry of each component such as girders, including web, flange and stiffeners, and the deck plate is modeled in accordance with technical drawings. Those components are meshed automatically with 3-node triangular and 4-node quad shell elements by ANSYS' mesh module. To simplify the modeling procedure, the cross beams are condensed as a continuous

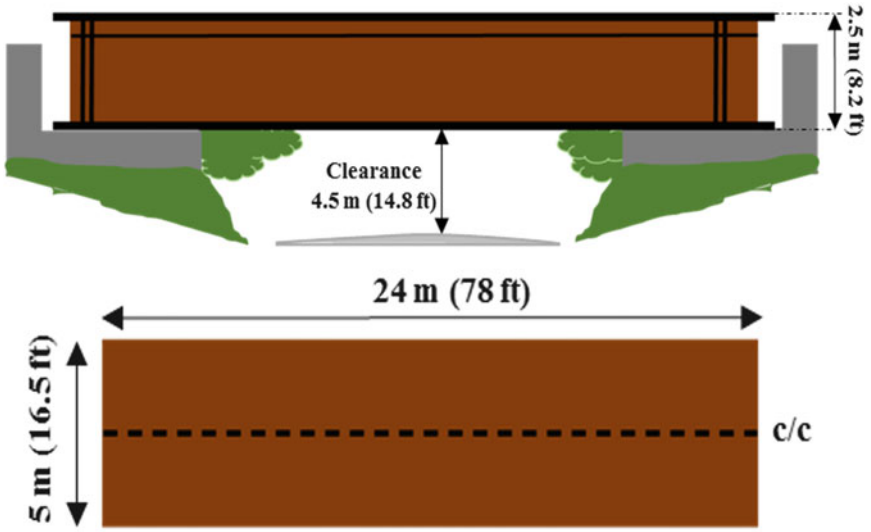


**Fig. 28.2** Plan and elevation of the simulated bridge

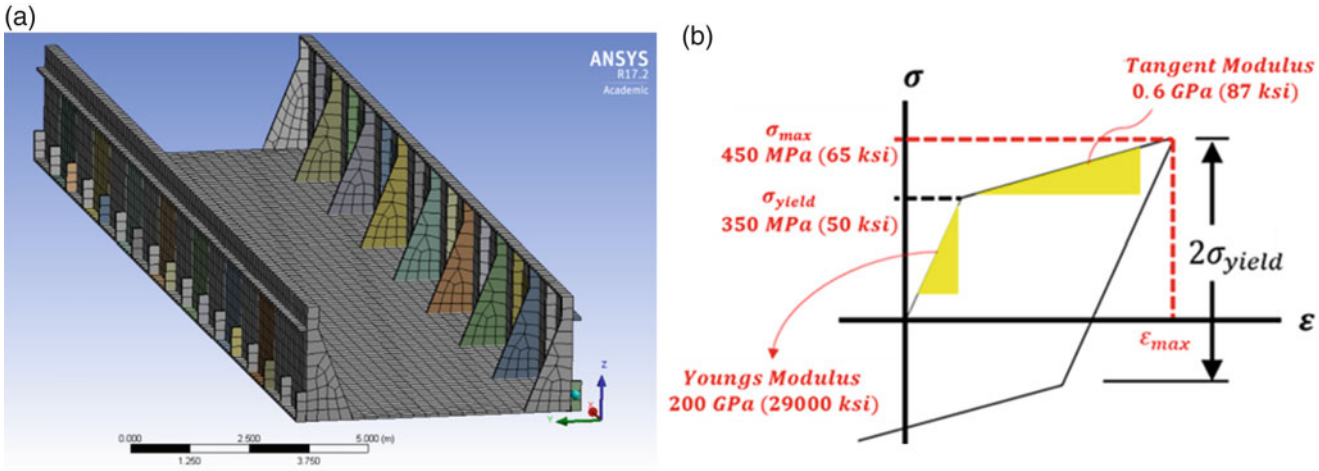


**Fig. 28.3** (**a**) FE model of the railway bridge, and (**b**) the steel stress-strain curve [20]

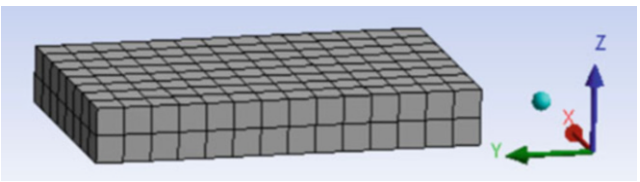


**Fig. 28.4** Finite element mesh for the mass box

diaphragm connecting the two girders in the direction of the impact. Consequently, this approach allows better observation of stresses distributions in the equivalent horizontal plate. The boundary conditions are assumed pin-roller support which is often used in classical single span bridge designs. A typical FE mesh and plot for material properties is shown in Fig. 28.3a, b respectively.

For impact, a semi-trailer truck, simplified as a solid mass box, is modeled with 8-node hexahedron solid elements and impacts are simulated with the bridge. The box, assumed as a steel solid rigid body, has a height of 0.5 m (1.6 feet), length of 3.5 m (11.5 feet) and width of 2 m (6.6 feet). The mass of this box is calculated as 27,475 kg based on the dimensions and the density of steel (7850 kg/m$^3$) which is equivalent to the weight of a representative semi-trailer truck. The surface area facing towards the bridge is calculated as 1 m$^2$. The typical mesh for the mass box is given in Fig. 28.4.

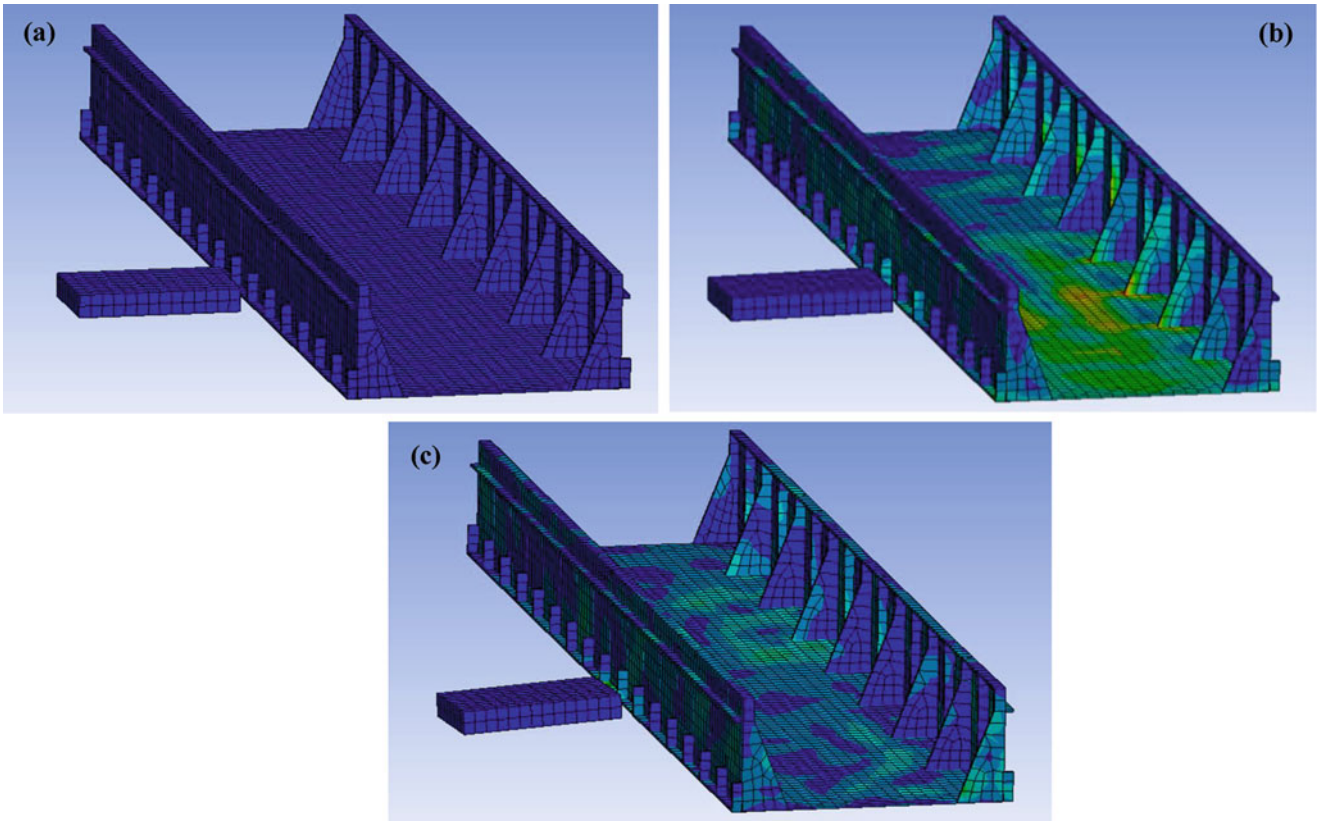


**Fig. 28.5** von Mises equivalent stress patterns for vehicle speed of 40 km/h at impact time of (**a**) 0 s, (**b**) 0.05 s, and (**c**) 0.1 s

## 28.3 Impact Assessment

Autodyn has an explicit numerical solver that yields accurate results for short duration contact problems. Since impact is also a small time step problem, Autodyn is a suitable platform to simulate vehicle-bridge collision event. A series of impact simulations are performed with varying speeds of 20 km/h (12 mph), 40 km/h (24 mph), 40 km/h skewed at a 5-degree angle and 60 km/h (37 mph). The location of impact is 10 m (29.5 feet) from the right end of the bridge. The resulting equivalent (von Mises) stress responses for vehicle speed of 40 km/h are provided at impact times of 0, 0.05, and 0.1 s in Fig. 28.5. The maximum stress observed at the impact location throughout the simulation for a vehicle speed of 40 km/h is determined 337 MPa. Additionally, at the end of each impact, the structure experiences localized equivalent plastic strain (Fig. 28.6).

For all impact events, the bridge experienced nonlinear plastic deformation at varying levels. As shown in Fig. 28.6, visible permanent deformation is observed in the bridge web. The values of permanent deformations compared to the maximum deformations are given in Table 28.1. The presence of permanent deformation is an indication of the severity of damage in a bridge whereas the maximum deformation is considered as a design criteria relevant to the load capacity of the bridge. Since the aim of this study is to improve the serviceability of railroad bridges after impact, permanent deformation is considered for rating which is discussed in the next section.

## 28.4 Impact Rating

To rate the aforementioned impact events, the following consequence based rating system has been proposed. The description of rating categories and the cost of consequences are shown in Table 28.2. The category descriptions have been established in reference to previous literature (severity rating, service interruption, consequence and lost estimate) [2], and discussions of this approach with railroad bridge engineering staff about the threshold limit.

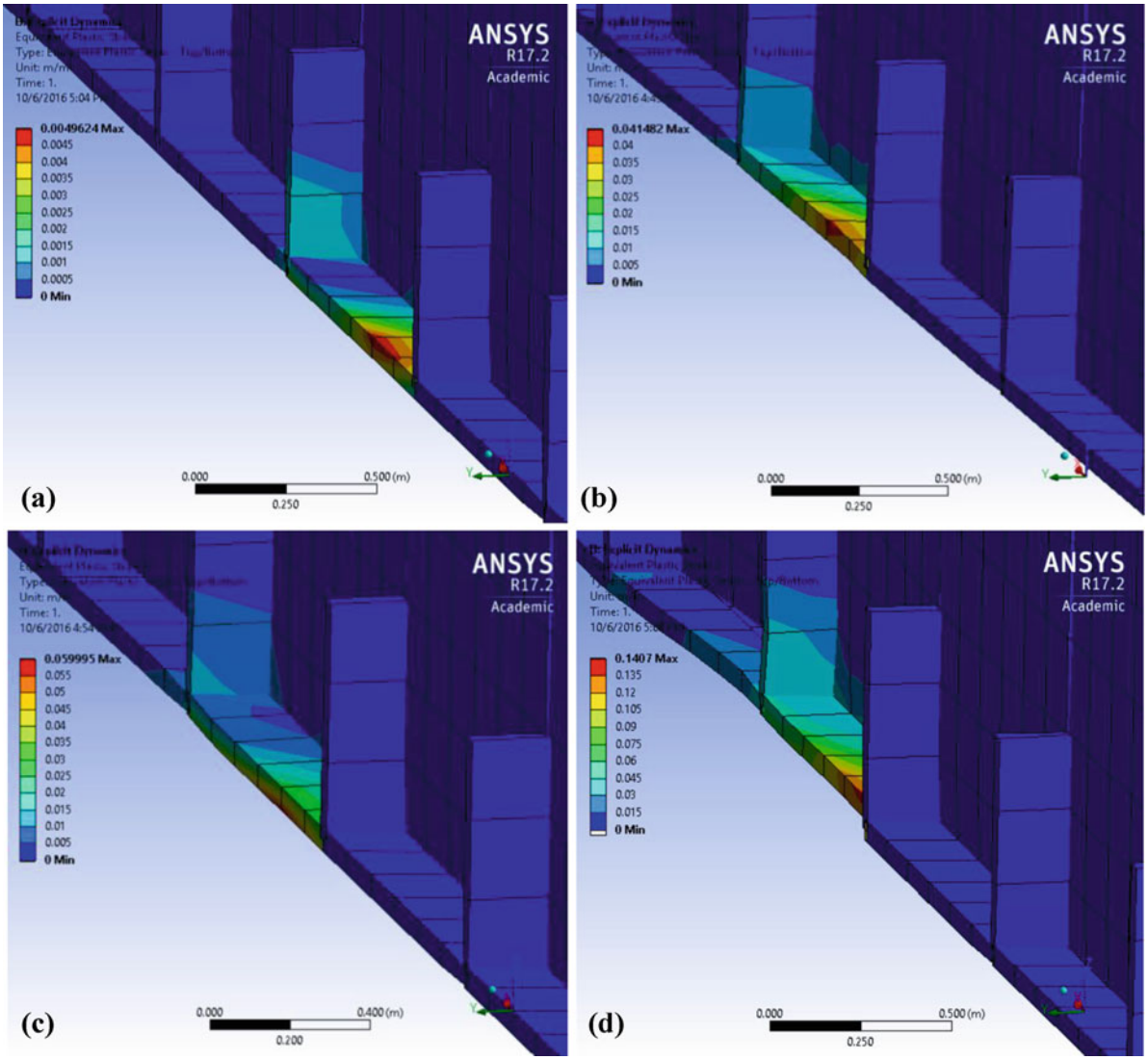


**Fig. 28.6** Equivalent plastic strains at impact speeds of (**a**) 20 km/h (**b**) 40 km/h (**c**) 40 km/h with 5-degree skew and (**d**) 60 km/h

**Table 28.1** Deformation values for series of impacts

| Impact speed (km/h) | Maximum deformation (mm) | Permanent deformation (mm) |
|---|---|---|
| 20 | 9.1 | 2.5 |
| 40 | 26.6 | 14.9 |
| 40-skewed 5-degrees | 27.1 | 16 |
| 60 | 101 | 75 |

**Table 28.2** Description of rating categories

| Rating of impact severity | Level of service interruption | Condition of damage | Threshold limit Permanent disp. | Consequence | Loss estimate |
|---|---|---|---|---|---|
| 1 | No interruption | No damage | 5 mm | No consequence | **$0** |
| 2 | Minor | Negligible | 10 mm | Visual inspection | **$10,000** |
| 3 | Moderate | Repairable | 30 mm | Minor repair | **$100,000** |
| 4 | Major | Significant | 60 mm | Extensive repair | **$300,000** |
| 5 | No service | Bridge collapse | 300 mm | Bridge replacement | **>$1,500,000** |

For preliminary layout of the quantification of impacts and consequences using objective data, the following general scenario is proposed: With truck speeds of 20 km/h, the permanent deformation in the model is observed to be 2.5 mm. For such small deformations, the bridge will still remain in operational condition with no negligible damage. Therefore, this impact is classified as category 1. Due to the increased momentum of vehicle in 40 km/h skewed and non-skewed impact cases, higher deformations are observed in the model. The elevated deformation increases the severity of the collision to category 2. Thus, this bridge would experience some temporary service interruptions such as train speed reduction. A significant permanent deformation of 75 mm is experienced by the bridge in the impact case with truck speed of 60 km/h. With such nonlinearities, the bridge department would have to avoid potential service interruptions, causing permanent train speed reductions until the repair. The severity of this case has therefore been classified as category 4 in the rating system. The trends observed from the results of the numerical simulations indicate that higher velocity impacts have the potential to create impact severity of category 5. These proposed thresholds are the first preliminary effort to "rate" measured consequences with current railroad bridge management decisions. For the application of this theoretical effort to railroad environments and decisions, future research will be conducted in coordination with the railroad departments input, including workshops and small scale tests.

## 28.5 Future Direction: Spatial Identification of Impact Damage

In order to evaluate the severity of a collision after the impact event, the energy inserted into the system must be identified. The level of energy depends on variables such as the speed of the truck and the location of impact. Based on previous studies, which demonstrate the potential of neural networks for detection and characterization of nonlinearities in dynamic systems [21, 22], an effective and simple approach for identification of damage location of bridge-vehicle collisions is proposed here. To demonstrate the identification procedure and represent the dynamic response of a TPG, a simplified FE model of a fixed-pinned beam is considered. Since this response is governed by the six modes, the beam model consists of six elements, where each node has a translational and rotational degree of freedom. The beam has properties representative of the three-dimensional bridge considered above. This has been achieved by adjusting the mass, stiffness and damping matrix. The damping matrix has been computed as Rayleigh damping proportional to the mass and stiffness matrix, respectively. The modal damping ratio of the first mode is tuned to 0.02. The aim is to detect the spatial location of damage. Therefore, the model has been split into six sections as illustrated in Fig. 28.7.

Each of the six elements is given stiffness properties denoted by $k$, with the subscripts 1–6. Damage caused by an impact event is assumed to cause local stiffness reduction. This has been simulated numerically by weakening the stiffness of

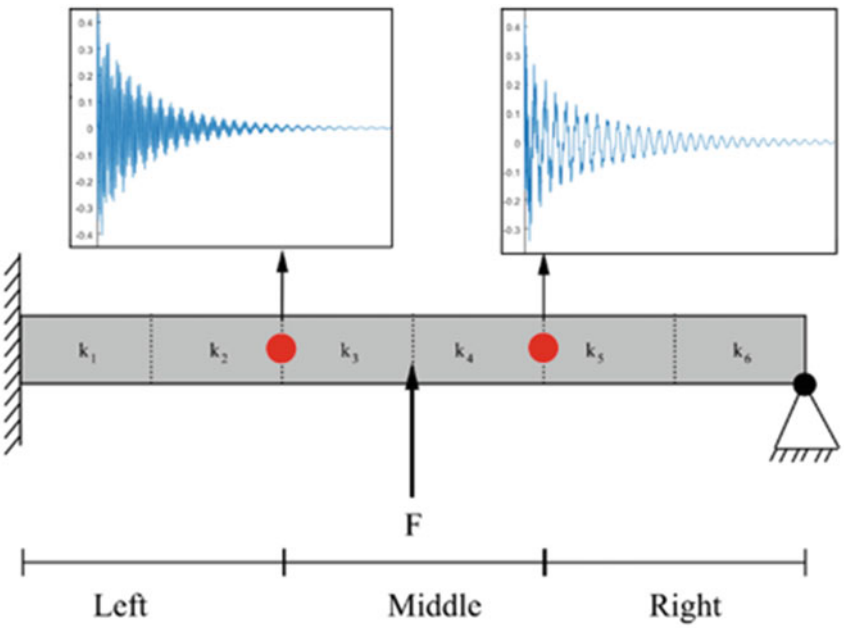


**Fig. 28.7** Simplified beam model of the railway bridge used for the neural networks approach

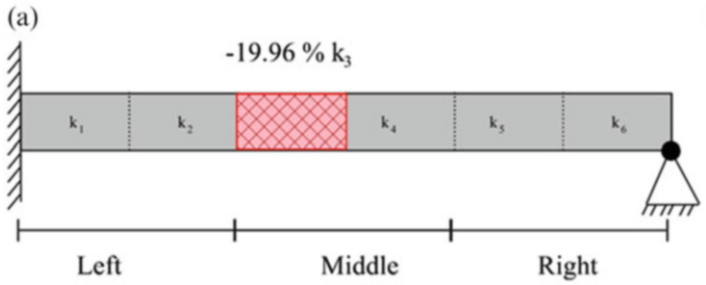


(b)

| Categories | Probability |
|---|---|
| No damage | 0% |
| Left | 0% |
| Middle | 100% |
| Right | 0% |

**Fig. 28.8** (**a**) Beam model of the bridge span, where the *red* element indicates stiffness reduction. (**b**) The probability of the damage location found by the proposed procedure

**Table 28.3** Selection of damage sensitive features of the beam model

| Feature | Damage sensitive features |
|---|---|
| 1 | Difference between displacement time history at reference location |
| 2 | Root-mean-square of reference response |
| 3 | Correlation coefficient of reference response |
| 4 | Mean of reference response |
| 5 | Standard deviation of reference response |
| 6 | Natural frequency, $f_1$ and $f_2$ |
| 7 | Modal damping ratio, $\zeta_1$ and $\zeta_2$ |
| 8 | Euclidian norm of normalized mode shape, $\|\|\phi_1\|\|_2$ and $\|\|\phi_2\|\|_2$ |

subsequent elements. The initial step of the identification is to select the damage sensitive features. These are listed in Table 28.3 and consist of statistical quantities achieved from the dynamic response of the numerical model. The dynamic response is obtained from the two reference signals from the locations indicated in Fig. 28.7. Furthermore, the modal parameters for the first and second mode are selected as features. The patterns of the features selected in response to stiffness reduction have been classified to train and validate the neural network. For training, 230 data sets are simulated by individually reducing the stiffness of $k_1$–$k_6$ by 10, 20, 30, 40, 50, 60, 70, 80 and 90%. The data set contains the features obtained from the impact at the middle of the beam. Forty-nine samples each are employed for validation and testing.

To improve training of the neural network, a feature space reduction step is performed. The space reduction is achieved by applying principal component analysis as in [22]. It is desirable to have the largest possible data set for training of neural networks where the size of the data set grows with an increasing number of features. The training is performed using MATLAB Neural Network Toolbox with nine neurons. A single neuron act as a correspondence to the input-output mapping by regression. The extension to multiple neurons is achieved by establishing a neural network, such that the output of a neuron can be the input of another [22]. The training of the network has been performed to obtain weighting functions that correlate to the features with the damage location. After completion of training, an additional data set has been generated. This data set has been used to test the robustness of the identification procedure. The stiffness in the middle region of the beam has been decreased by 19.96% instead of 20% as in the training data set, shown in Fig. 28.8a. The outcome probability for the damage to be in the middle of the beam model is 100%, as given in Fig. 28.8b. Other combinations of stiffness reduction of the beam elements have also been tested. The true location has been consistently identified with a probability ranging from 80 to 100%. This indicates that the proposed procedure for the spatial identification of damage is reasonable for the developed numerical model. Similar procedure can be adopted for a detailed numerical model, such as the above ANSYS model. This would in particular require an extensive dataset, containing features as proposed in Table 28.3. The extent of this dataset depends on which accuracy of stiffness reduction due to vehicle impact is sought.

## 28.6 Conclusions and Future Work

This paper emphasizes the type of accidents occurring due to impact between highway trucks and railway bridges. In order to study the effects of these impacts and rate them, we developed: (1) a preliminary FE model to understand the deformation processes associated with an impact event, and (2) an idealized neural network model to demonstrate its applicability in

detecting damage. The results presented herein represent an initial attempt to quantify truck-bridge impact phenomena and develop techniques to detect and mitigate future impact events. In our future work, the FE model will be improved by developing a higher fidelity mesh to more accurately capture the internal mechanical behavior of the bridge. In addition, we will develop a more accurate representation of a typical semi-truck. A mesh convergence study will be conducted in order to obtain an accurate and computationally efficient model. Furthermore, a more complex neural network system will be developed to rate the impacts when railway bridges are hit by highway traffic. A hybrid approach will be considered where both the location and the magnitude of the impact detected by neural networks are utilized as inputs to the simulation. Accordingly, structural integrity will be assessed using hybrid simulation results. Additionally, permanent displacements at the supports due to an impact will be evaluated. Finally, the effectiveness of crash beams in protecting the bridge against impacts will be investigated.

**Acknowledgment** The authors of this paper thank the Canadian National Railway and the Canadian Pacific for their help in the development of this research methodology. The authors also thank Duane Otter from the Transportation Technology Center, Inc. TTCI), a wholly owned subsidiary of the Association of American Railroads (AAR) for his constructive feedback and recommendations.

## References

1. Otter, D., Joy, R., Jones, M., Maal, L.: Need for bridge monitoring systems to counter railroad bridge service interruptions. Transp. Res. Rec. J. Transp. Res. Board. **2313**(1), 134–143 (2012)
2. Joy, R., Jones, M.C., Otter, D., Maal, L.: Characterization of Railroad Bridge Service Interruptions. Railroad Bridges (No. DOT/FRA/ORD-13/05), (2013)
3. Bischoff, R., Meyer, J., Enochsson, O., Feltrin, G., Elfgren, L.: Event-based strain monitoring on a railway bridge with a wireless sensor network. In: Proceedings of the 4th International Conference on Structural Health Monitoring of Intelligent Infrastructure, pp. 74–82. Zurich (2009)
4. Staszewski, W.J., Mahzan, S., Traynor, R.: Health monitoring of aerospace composite structures–Active and passive approach. Compos. Sci. Technol. **69**(11), 1678–1685 (2009)
5. Farrar, C.R., Worden, K.: An introduction to structural health monitoring. Philos. Trans. R. Soc. Lond. A Math. Phys. Eng. Sci. **365**(1851), 303–315 (2007)
6. Sohn, H.: Effects of environmental and operational variability on structural health monitoring. Philos. Trans. R. Soc. Lon. A Math. Phys. Eng. Sci. **365**(1851), 539–560 (2007)
7. Moreu, F., Spencer, B.F.: Framework for Consequence-based Management and Safety of Railroad Bridge Infrastructure Using Wireless Smart Sensors (WSS). Newmark Structural Engineering Laboratory. University of Illinois at Urbana-Champaign, Champaign (2015)
8. Yun, H., Nayeri, R., Tasbihgoo, F., Wahbeh, M., Caffrey, J., Wolfe, R., Nigbor, R., Masri, S.F., Abdel-Ghaffar, A., Sheng, L.H.: Monitoring the collision of a Cargo Ship with the Vincent Thomas Bridge. Struct. Control. Health Monit. **15**(2), 183–206 (2008)
9. Coverley, P.T., Staszewski, W.J.: Impact damage location in composite structures using optimized sensor triangulation procedure. Smart Mater. Struct. **12**(5), 795–803 (2003)
10. Sun, Z., Chang, C.C.: Structural damage assessment based on wavelet packet trans-form. J. Struct. Eng. **128**(10), 1354–1361 (2002)
11. Taha, M.M.R., Noureldin, A., Lucero, J.L., Baca, T.J.: Wavelet transform for structural health monitoring: a compendium of uses and features. Struct. Health Monit. **5**(3), 267–295 (2006)
12. Song, G., Olmi, C., Gu, H.: An overheight vehicle–bridge collision monitoring system using piezoelectric transducers. Smart Mater. Struct. **16**(2), 462–468 (2007)
13. Sharma, H., Hurlebaus, S.: Overheight collision protection measures for bridges. In: Structures Congress 2012, pp. 790–797. ASCE (2012)
14. Kurt, E.G., Varma, A.H., Hong, S.: FEM Simulation for INDOT Temporary Concrete Anchored Barrier. Joint Transportation Research Program (2012)
15. Buth, C.E., Williams, W.F., Brackin, M.S., Lord, D., Geedipally, S.R., Abu-Odeh, A.Y.: Analysis of large truck collisions with bridge piers: phase 1. Report of guidelines for designing bridge piers and abutments for vehicle collisions. (No. FHWA/TX-10/9-4973-1), 2010
16. Consolazio, G.R., McVay, M.C., Cowan, D.R., Davidson, M.T., Getter, D.J.: Development of improved bridge design provisions for barge impact loading. (No. UF Project 00051117), 2008
17. Luperi, F.J., Pinto, F.: Structural behavior of barges in high-energy collisions against bridge piers. J. Bridg. Eng. **21**(2), 04015049 (2016)
18. ANSYS Inc., ANSYS Autodyn User's Manual. Cecil Township, PA, 2016
19. ASTM International: ASTM A572-15 Standard Specification for High-Strength Low-Alloy Columbium—Vanadium Structural Steel. (2015)
20. Jones, N.: Structural Impact. Cambridge University Press, Cambridge (1997)
21. Wu, X., Ghaboussi, J., Garrett, J.H.: Use of neural networks in detection of structural damage. Br. J. Surg. **81**(11), 578–581 (2010)
22. Ondra, V., Sever, I.A., Schwingshackl, C.W.: A method for detection and characterization of structural non-linearities using the Hilbert transform and neural networks. Mech. Syst. Signal Process. **83**(2017), 210–227 (2016)

# Chapter 29
# High-Frequency Impedance Measurements for Microsecond State Detection

**Ryan A. Kettle, Jacob C. Dodson, and Steven R. Anton**

**Abstract** This work investigates the use of the electromechanical impedance (EMI) method at high frequencies for application in state detection in highly dynamic systems; a key aspect of which is the excitation and measurement of PZT impedance at higher frequency bands than those typically used in structural health monitoring, in ranges greater than 1 MHz. The use of impedance analyzers, which are typically used in EMI measurements, are not considered for this work due to their slow measurement speeds, large size, heavy weight, and high cost. Instead, an alternative impedance measurement approach from the literature will be leveraged. The alternative method, which allows impedance measurements to be made using standard data acquisition devices, was originally developed to present a low-cost solution to impedance measurement. The focus of this work, however, is the adaptation of the alternative measurement approach to allow accurate impedance measurements at frequency ranges in excess of 1 MHz. The accuracy of the alternative system's impedance measurements will be verified by comparison with theoretical models. First, the impedance response of a simple RLC circuit with well understood dynamics will be experimentally tested and then the resulting measurements will be compared to analytical solutions of the circuit impedance to validate the measurement system. This alternative measurement system is then used to perform high frequency impedance measurements on a piezoelectric wafer embedded in a structure in order to detect structural damage. The long-term goal of this research is the deployment of an impedance measurement system using high-speed real-time hardware, such as field-programmable gate array technology which has significantly higher sampling rates and calculation speeds compared to traditional data acquisition systems, to enable microsecond state detection of structures operating in highly dynamic environments using the EMI method. Microsecond state detection has a number of potential applications, such as in aerospace technology, the mining industry, and civil architecture.

**Keywords** Structural health monitoring (SHM) • Electromechanical impedance (EMI) method • Piezoelectric materials • Microsecond state detection • Dynamic systems

## 29.1 Introduction

The goal of this research is to develop a system capable of microsecond state detection in highly dynamic environments. In this work, a structure's state refers to any change to its physical properties that affects its dynamic response which includes mass, stiffness, boundary conditions, etc. Microsecond state detection has a staggeringly wide array of potential applications. This includes the monitoring of drill strings used in mining, monitoring fluid flow around hypersonic aircraft for better flight handling, deployment in civil structures for rapid structural assessment and blast mitigation, and monitoring critical structures that are part of complex assemblies such as those commonly found in the automotive and aerospace industries.

This work directly builds off of the foundation of knowledge created by researchers in the field of structural health monitoring. Structural health monitoring can be described as a range of techniques and tools to detect the development of damage in structures. In particular, the structural health monitoring technique known as the electromechanical impedance method is used in this work for state detection. The electromechanical impedance method is an active sensing method, meaning the structure is actively "interrogated" instead of relying on passive excitation [1]. This effect is achieved by the electromechanical coupling exhibited by piezoelectric (PZT) materials, which allows them to act as both a sensor and an actuator simultaneously. The electromechanical coupling also means that the electrical impedance of a piezoelectric

R.A. Kettle (✉) • S.R. Anton
Department of Mechanical Engineering, Tennessee Technological University, Cookeville, TN, 38505, USA
e-mail: rakettle42@students.tntech.edu

J.C. Dodson
Air Force Research Laboratory (AFRL/RWMF), Eglin AFB, FL, 32542-5430, USA



J. Caicedo, S. Pakzad (eds.), *Dynamics of Civil Structures, Volume 2*, Conference Proceedings
of the Society for Experimental Mechanics Series, DOI 10.1007/978-3-319-54777-0_29

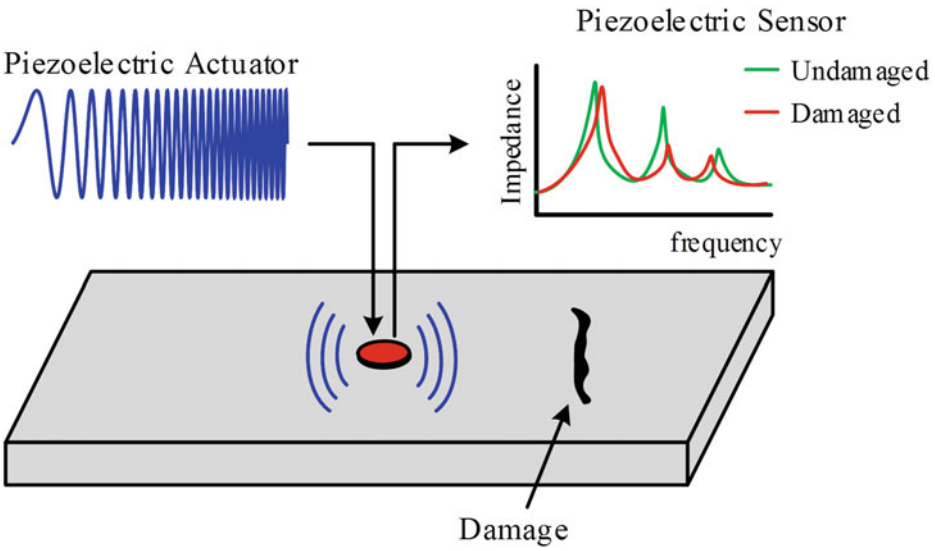


**Fig. 29.1** The electromechanical impedance method being used to detect damage in a structure

material bonded to a structure becomes a function of the mechanical impedance of the host structure. If the properties of the piezoelectric material are assumed to remain constant, then any changes in the in the electrical impedance of the piezoelectric material can be attributed to a change in the mechanical impedance of the structure [2]. To perform state detection, the electrical impedance signature of the structure in a known, healthy state is used as a baseline. As the structure is being monitored, the measured data is continuously compared to the baseline and any significant deviation between the two is attributed to a state change in the structure. The process of using the electromechanical impedance to detect damage in a structure is illustrated in Fig. 29.1.

To achieve state detection at the microsecond timescale, high frequency excitation signal are required, on the order of 1 MHz or higher [3], which is a significant increase over the 30–400 kHz normally used [1]. A further break from the norm that is required for microsecond state detection is a change in the hardware utilized to make the electrical impedance measurement. Normally, an impedance analyzer, such as an HP4194A, is used to make impedance measurements. However, these devices have several drawbacks, which include being large ($16'' \times 14'' \times 24''$), heavy (81.4 lbs), expensive ($40,000), and the fact that they use a slow stepped sinewave method of measurement. These issues have been noted by previous researchers, with the biggest concern being cost. Because of this there have been a multitude of attempts to create new, low-cost impedance measurement devices which include the use of an FFT analyzer [4], a digital signal processor (DSP) [5], an AD5933 impedance analyzer IC chip [6, 7], and a data acquisition device (DAQ) [8, 9]. The method employing the FFT analyzer utilizes a measurement circuit to calculate an approximation of the unknown impedance. This measurement is based on the value of a known resistance placed in the circuit with the assumption that this resistor does not make a significant impact on the impedance measurement. Additionally, this method tends to be inaccurate at high frequencies due to a drop in resistance across the PZT at high frequencies due to the capacitive nature of PZTs. The usefulness of the DSP method is hindered by the small memory space of the DSP, which restricts its usable range and frequency resolution [9]. The AD5933, although a low cost solution, faces two distinct disadvantages: it must be calibrated before use [10] and it is limited to a maximum frequency of 100 kHz [9, 10]. The DAQ method however appears advantageous because it allows for a large range of hardware options, including the use of DAQs with exceptionally high sampling rates. This makes it a very appealing choice for high frequency applications, such as microsecond state detection.

The excitation signal applied to the PZT is also a critical factor. The stepped sign measurement approach utilized by impedance analyzers is quite time consuming and thus another method for excitation is required to achieve microsecond state detection. A chirp signal is a logical choice as it can excite a very broad range of frequencies in a very short amount of time. Furthermore, the chirp signal is a common waveform that can be produced by many function generators and as such its use has the advantage of not requiring the creation of any custom voltage signals. Chirp signals have been used to make accurate EMI measurements by other researchers employing various methods, all of which showed that the chirp signal gave comparable results to impedance analyzers [4, 8, 11, 12]. This pervasive use of the chirp signal was also explored further by Baptista et al. who conducted a study comparing uniform white noise, periodic random noise, and a chirp signal for use as an excitation signal and concluded that the chirp signal performed the best measurement [13].

## 29.2 Experimental Setup

The experimental setup and measurement technique used in this work are adaptations from the efforts of other researchers who created "low-cost circuits" for impedance measurements [9, 14]. The low-cost circuit in its simplest form is just an excitation source in series with a known resistance, $R_m$, and an unknown impedance, $Z_{unk}$. If the voltage of the excitation signal, $V_x$ is known and the voltage response of the node between $R_m$ and $Z_{unk}$, $V_y$, is known, then $Z_{unk}$ can be solved for using Eq. (29.1).

$$Z_{unk}(f) = \frac{V_y(f) * R_m}{V_x(f) - V_y(f)} \tag{29.1}$$

However, in order to measure $V_x$ and $V_y$ a data acquisition device needs to be used at both locations. The data acquisition device has its own internal equivalent circuit, represented by $C_{DAQ}$ and $R_{DAQ}$ in parallel, that then gets added to the measurement circuit, which is shown in Fig. 29.2.

The excitation signal used in this study was a linear chirp produced by an Agilent 33220A Function Generator and the data acquisition device used was an NI PXIe-5122 Oscilloscope Card, the impedance for both is given in Table 29.1. The function generator and DAQ were connected to each other at synchronization ports via a BNC cable for triggering purposes. Additionally, they were both connected to the circuit using BNC to grabber cables that were approximately 6 in. long. The wire length was intentionally kept as short as possible to reduce the effects of wire resistance and to avoid introducing any additional environmental noise. The NI PXIe-5122 was connected to an NI PXIe-1082 chassis that also housed an NI PXIe-8133 controller with LabVIEW installed. The voltages $V_x$ and $V_y$ were recorded via a LabVIEW program on the controller and the date was saved as a '.txt' file. This file was then loaded into a MATLAB program that performed all data processing, which includes impedance calculation, averaging, plotting, and error calculation. An overall view of the experimental setup can be seen in Fig. 29.3. More information regarding specific experiments is given in the results section immediately following. Finally, it should be noted that the goal of this work is to extend the measurement frequency range of the EMI method to the MHz range by utilizing the "low-cost" architecture presented in the literature, however, the hardware utilized in this work is not low-cost.

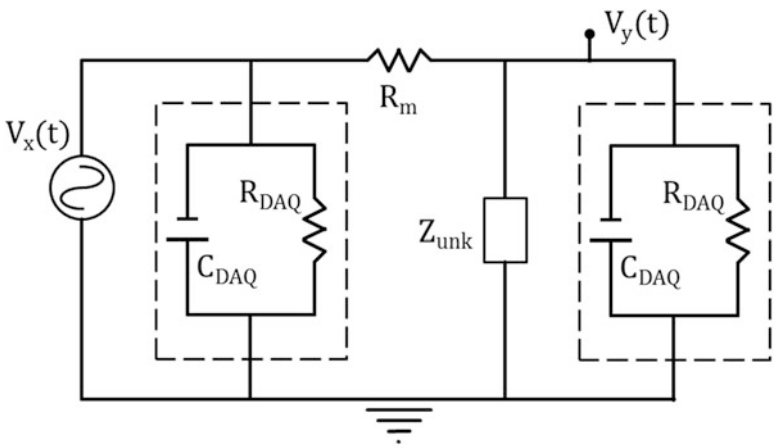


**Fig. 29.2** "Low-cost" impedance measurement circuit

**Table 29.1** Impedance settings applied to the systems utilized for signal generation and acquisition

| System | Impedance |
|---|---|
| Agilent function generator | "High Z load" |
| PXIe-5122 scope card | 1 MΩ |

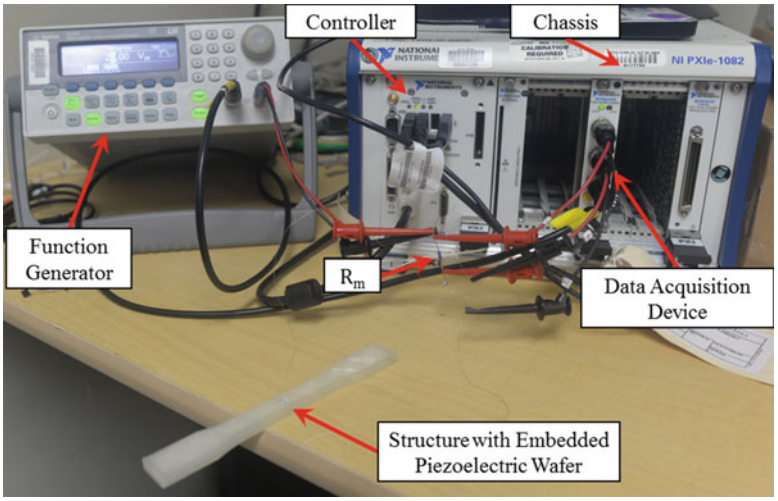


**Fig. 29.3** Experimental setup used for impedance measurement, including a structure to be measured

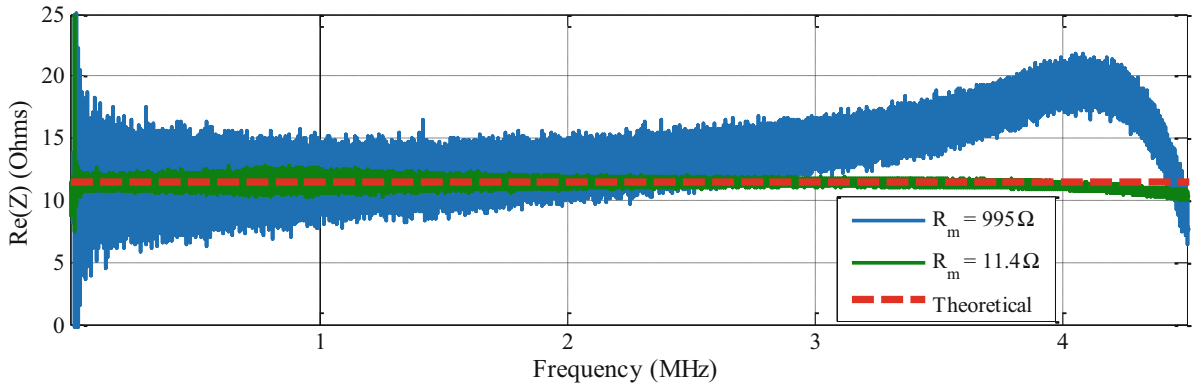


**Fig. 29.4** Impedance measurement of an 11 Ω resistor using different values of $R_m$. 2 million samples were taken at 10 MS/s. The chirp excitation signal had an initial frequency of 100 Hz, a final frequency of 10 MHz, an 18 $V_{pp}$ amplitude, and a sweep time of 0.1 s

## 29.3 Verification of Measurement Methodology

Before measurements to perform state detection were attempted, the accuracy of the measurement method was verified. To do this, simple circuits with well understood impedance responses across wide frequency bands, such as resistors and resistor-inductor-capacitor parallel circuits, were tested. One phenomenon that was observed in early measurements on a simple resistive circuit is that there was a low-pass filtering effect occurring on the signal. At higher frequencies the calculated impedance would suddenly and drastically decrease from the correct value. It was eventually discovered that this was caused by the internal capacitance of the data acquisition device, $C_{DAQ}$, and the known resistance, $R_m$, effectively creating a low pass filter. This effect can be mitigated by choosing appropriately small values of $R_m$, on the order of 10 Ω or less. The effect of the value of $R_m$ on the impedance measurement can be seen in Fig. 29.4, where an 11 Ω resistor was measured with a relatively low $R_m$ of 11.4 Ω and then with a higher $R_m$ of 995 Ω. Since a resistor has negligible values of capacitance and inductance, its theoretical impedance is simply a constant resistance (purely real impedance) across the entire frequency range. Figure 29.4 shows that the higher value of $R_m$ produces inaccurate impedance measurements that vary significantly from the theoretical result. On the contrary, the lower value of $R_m$ was in excellent agreement with the theoretical model below 4 MHz.

A parallel resistor-inductor-capacitor (RLC) circuit was also measured to ensure accurate impedance measurements were being produced when measuring a dynamic circuit. A parallel RLC circuit was chosen because, assuming ideality, it produces a single impedance peak at a known frequency. The frequency of the peak is referred to as the resonance frequency of the circuit. This single resonance peak is a similar, yet simpler, frequency response compared to a PZT, because a PZT typically exhibits multiple peaks in a given frequency band. The resonance frequency of an RLC parallel circuit is given as

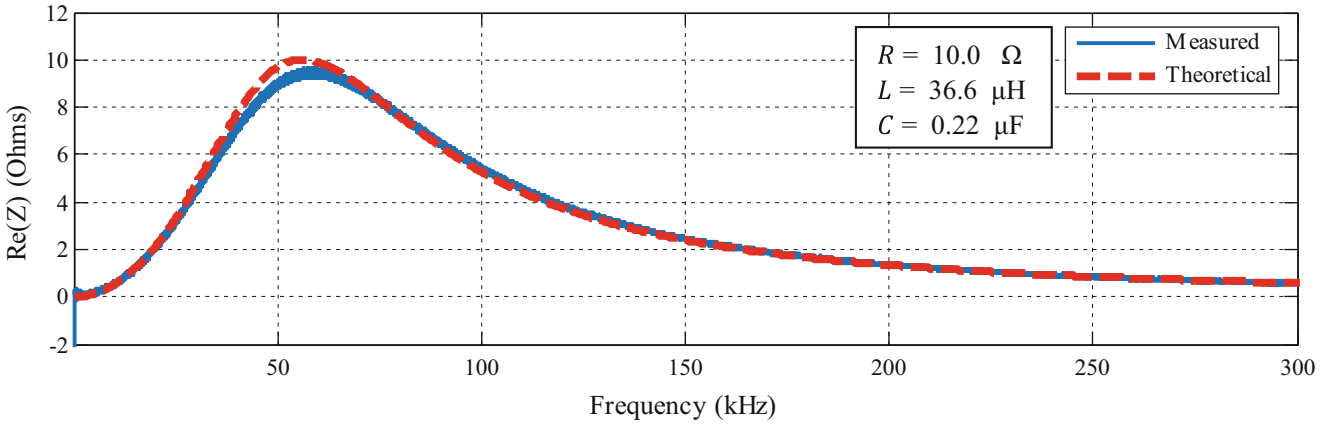


**Fig. 29.5** Impedance measurement of a parallel RLC circuit with an $R_m$ of 10.2 Ω. 2 million samples were taken at 2 MS/s. The chirp excitation signal had an initial frequency of 100 Hz, a final frequency of 1 MHz, a 10 $V_{pp}$ amplitude, and a sweep time of 1 s

$$f_0 = \frac{1}{2\pi\sqrt{LC}}, \tag{29.2}$$

where $f_0$ is the resonance frequency, $L$ is inductance, and $C$ is capacitance. Furthermore, the total impedance response of the circuit is given as

$$Z_T = \left(Z_R^{-1} + Z_C^{-1} + Z_L^{-1}\right)^{-1}, \tag{29.3}$$

where $Z_T$ is the total impedance response, $Z_R$ is the impedance of the resistor, $Z_C$ is the impedance of the capacitor, and $Z_L$ is the impedance of the inductor. The impedance values for the individual components are given as

$$Z_R = R \tag{29.4}$$

$$Z_C = (j2\pi fC)^{-1} \tag{29.5}$$

$$Z_L = j2\pi fL, \tag{29.6}$$

where $R$ is the resistance, $f$ is excitation frequency, and $j$ is the imaginary unit. Figure 29.5 shows the real part of the impedance (resistance) measurement of a parallel RLC circuit with the values of $R = 10.0\ \Omega$, $L = 36.6\ \mu$H, and $C = 0.22\ \mu$F. The real part of the impedance is used exclusively in this work because it has been demonstrated to have the greatest sensitivity to damage [1]. This measurement is compared to the theoretical impedance value calculated using Eq. (29.3), and the measurement shows a good match to the analytical model. Furthermore, for the given values of $R$, $L$, and $C$, Eq. (29.2) gives a calculated resonance frequency $f_0$ ∼56 kHz, and the measurement matches this value reasonably well. The good agreement between the measurement and analytical model of the impedance of the parallel RLC circuit makes a compelling case for the accuracy of the employed measurement method in its ability to measure dynamic impedance response, such as that expected when measuring PZTs.

## 29.4 Damage Detection at High Frequencies

Having proved the accuracy of the impedance measurement methodology using simple circuits, experimentation was then performed on a piezoelectric transducer in the MHz frequency range to investigate the feasibility of microsecond state detection. A small circular PZT wafer with a diameter, $d$, of 6.35 mm and a thickness, $t$, of 0.254 mm made from APC 850 material (PZT-5A) was embedded in a 3D printed structure. The structure was then clamped at one end, effectively forming a cantilever beam simply for the convenience of some initial non-destructive tests. The structure remained in this

cantilever position for consistency with previous tests but this is otherwise unnecessary. Twenty separate measurements were run on the structure, 10 in an undamaged state and 10 in a damaged state. The damage induced was a 0.3″ notch cut into the structure 0.75″ away from the piezoelectric material wafer. Both states of the 3D printed beam can be seen in Fig. 29.6. The 10 measurements in each state were averaged and then plotted for comparison. Initial comparisons made by plotting the impedance spectrums of both the damaged and undamaged states showed very significant divergence in multiple frequency bands at lower frequencies. This is a good example of why structural health monitoring is typically done in the tens to hundreds of kHz. This is however a well-known phenomenon and not important to the goal of microsecond state detection. Results in the MHz range are necessary to prove the feasibility of microsecond state detection, and for this reason will be the sole topic presented and discussed in this work. In this range of frequencies in excess of 1 MHz there was an exceptionally high impedance peak located at roughly 9 MHz; the measurements for both damage states in the region of this peak are shown in Fig. 29.7. Because of the exceptionally high impedance value of this peak in comparison to others in the MHz range, it stands to reason that this peak is caused by the first thickness resonance mode, $f_T$, of the piezoelectric transducer. This can be verified by using the thickness mode frequency constant, $N_T$, to calculate the resonance frequency, given by

$$f_T = \frac{N_T}{t}, \tag{29.7}$$

where $t$ is the thickness of the PZT. With the value of $N_T$ given as 2040 Hz.m from the manufacturer specifications [15], Eq. (29.7) gives $f_T = 8.03$ MHz. The deviation in frequency between this calculation and the measured value can be accounted for by the following reasons. First, the geometry of the PZT wasn't measured before the embedding procedure, and as such the nominal thickness of the ordered part was used in the calculation. The given tolerance of $t$ is $\pm 0.025$ mm and so a simple difference in geometry can account for values of $f_T$ up to 8.9 MHz. Second, since the PZT is embedded in a structure

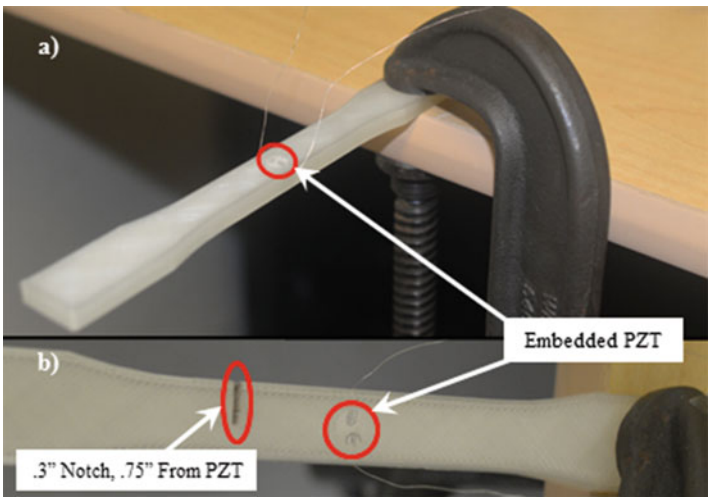


**Fig. 29.6** (**a**) The 3D printed structure with embedded PZT, undamaged. (**b**) The 3D printed structure in a damaged state

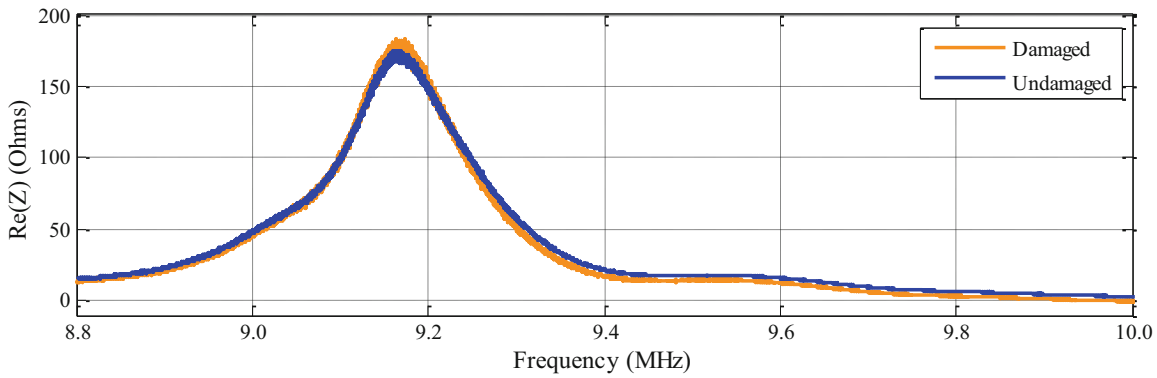


**Fig. 29.7** Comparison between the average of 10 tests of the undamaged state the average of 10 tests of the damaged state with an $R_m$ of 10.7 Ω. 3 million samples were taken at 50 MS/s. The chirp excitation signal had an initial frequency of 200 kHz, a final frequency of 10 MHz, an 18 $V_{pp}$ amplitude, and a sweep time of 0.06 s

**Table 29.2** Root-mean-squared error of damaged and undamaged states compared to 7 measurement averaged baseline

| State | Measurement # | RMSE |
|---|---|---|
| Undamaged | 8 | 0.901 |
| | 9 | 0.896 |
| | 10 | 0.898 |
| Average undamaged | 8, 9, & 10 | 0.898 |
| Damaged | 1 | 3.584 |
| | 2 | 3.535 |
| | 3 | 3.512 |
| | 4 | 3.465 |
| | 5 | 3.487 |
| | 6 | 3.493 |
| | 7 | 3.503 |
| | 8 | 3.487 |
| | 9 | 3.487 |
| | 10 | 3.446 |
| Average damaged | 1–10 | 3.500 |

it has boundary conditions that no longer reflect a free-free condition, but has instead an elastically constrained condition. This stiffer boundary condition would cause the first thickness resonance mode to increase. Third, the value of $f_t$ used in the calculation came from the manufacturer and was not derived from the material properties of the specific sample used and is consequently not exact. It is therefore reasonable to assume that the large peak at 9 MHz is in fact the first thickness resonance mode.

Of particular importance is the fact that the impedance peak illustrates a slight divergence between the damaged and undamaged states. This supports previous work by the authors that predicted thickness modes would be important for damage detection at the high frequencies required for microsecond state detection [16]. While a qualitative evaluation of noticeable difference in signal is important for identifying frequency ranges sensitive to damage, a quantitative evaluation is necessary for any method of automated damage detection. To perform a quantitative comparison between the two states in this frequency range, an averaged baseline signal was constructed using the first 7 measurements of the undamaged state. This baseline was then compared to the remaining 3 undamaged states and the 10 damaged states using the root-mean-squared error (RMSE) given by

$$RMSE = \sqrt{\frac{\sum_{i=1}^{n} (x_{1,i} - x_{2,i})^2}{n}}, \tag{29.8}$$

where $i$ is the index of a given point in a series of data, $n$ is the total number of points in the series, $x_{1,i}$ represents the value of the first series at index $i$, and $x_{2,i}$ represents the value of the second series at index $i$. The results of the RMSE calculations are shown in Table 29.2 and it can be seen that the undamaged cases vary from the baseline by an RMSE of less than 1% and the damaged cases by over 3%. Although the difference between these cases is relatively small, this establishes the fact that there is a measurable, quantitative difference between the signals measured in the damaged and undamaged states, detected at frequencies in the MHz frequency range. The significance of this finding is that it demonstrates the feasibility of detecting structural changes at frequencies in excess of 1 MHz, which is a crucial aspect of microsecond state detection in highly dynamic environments.

## 29.5 Conclusions

The goal of this work is to develop the technologies and methods required to enable microsecond state detection of structures operating in highly dynamic environments using the electrometrical impedance method. A vital step in achieving this goal is successfully detecting structural changes at frequencies greater than 1 MHz. To accomplish this goal, a non-traditional impedance measurement system was utilized instead of a traditional impedance analyzer. To verify the accuracy of the new measurement hardware and methodology, measurements of simple circuits were compared to analytical solutions. First, a high frequency measurement of a resistor was performed, which showed excellent agreement with the analytical solution up to 4 MHz. Second, an impedance peak produced by a parallel resistor-inductor-capacitor circuit was measured that also showed good agreement with the analytical solution. These tests demonstrate that accurate impedance measurements can be

made with non-traditional hardware using the method presented as an alternative to an impedance analyzer. A structure with an embedded PZT was then presented and its impedance measured at high frequencies in a damaged and undamaged state. The two signal were compared and an impedance peak around 9 MHz, caused by the first thickness resonance mode of the transducer, was observed which exhibited a small difference between the two signals. A baseline measurement was then constructed using several measurements from the undamaged state and were compared to individual measurements of both states using the root-mean-squared error. The-root-mean squared error for the tests in the undamaged state were all under 1%, and greater than 3% for the tests taken in the damaged state. It can be concluded from these results that damage can be detected at high frequencies. The accurate measurement of impedance at high frequencies using alternative hardware in place of an impedance analyzer as well as its successful use for damage detection at high frequencies are both important milestones and represent significant steps forward in the pursuit of achieving microsecond state detection in highly dynamic environments.

## 29.6 Future Work

There are three additional routes of future work that remain. First, comparisons between measurements of piezoelectric wafers to theoretical models need to be made. Second is the development of a method to decouple the data acquisition device from the measurement circuit. Currently, the low value of $R_m$ only mitigates the problem caused by the internal data acquisition device's internal impedance. In order to enable accurate impedance measurements at even higher frequencies the development of a method to completely decouple the data acquisition device's internal capacitance is necessary. Lastly, a piezoelectric material which exhibits a higher thickness mode response, which is the phenomenon that creates the amplitude peaks at higher frequencies, should be used to potentially obtain a larger value in the RMSE difference between states.

## References

1. Park, G., Sohn, H., Farrar, C.R., Inman, D.J.: Overview of piezoelectric impedance-based health monitoring and path forward. Shock Vib. Dig. **35**(6), 451–463 (2003)
2. Bhalla, S., Moharana, S.: A refined shear lag model for adhesively bonded piezo-impedance transducers. J. Intell. Mater. Syst. Struct. **24**(1), 33–48 (2013)
3. Kettle, R.A., Dick, A.J., Dodson, J.C., Foley, J.R., Anton, S.R.: Real-time state detection in highly dynamic systems. Presented at the Proceedings of the 34th IMAC, Cham, 2016
4. Peairs, D.M., Park, G., Inman, D.J.: Improving accessibility of the impedance-based structural health monitoring method. J. Intell. Mater. Syst. Struct. **15**(2), 129–139 (2004)
5. Kim, J., Grisso, B.L., Ha, D.S., Inman, D.J.: A system-on-board approach for impedance-based structural health monitoring. Presented at the The 14th International Symposium on: Smart Structures and Materials & Nondestructive Evaluation and Health Monitoring, 2007
6. David, L.M., Michael, D.T., Gyuhae, P., Charles, R.F.: Development of an impedance-based wireless sensor node for structural health monitoring. Smart Mater. Struct. **16**(6), 2137 (2007)
7. Park, S., Lee, J.-J., Yun, C.-B., Inman, D.J.: Electro-mechanical impedance-based wireless structural health monitoring using PCA-data compression and k-means clustering algorithms. J. Intell. Mater. Syst. Struct. **19**(4), 509–520 (2008)
8. Xu, B., Giurgiutiu, V.: A low-cost and field portable electromechanical (E/M) impedance analyzer for active structural health monitoring. Presented at the Proceedings of the 5th International Workshop on Structural Health Monitoring, Stanford University, 2005
9. Baptista, F.G.: A new impedance measurement system for PZT-based structural health monitoring. IEEE Trans. Instrum. Meas. **58**(10), 3602–3608 (2009)
10. Wandowski, T., Malinowski, P., Ostachowicz, W.: Calibration problem of AD5933 device for electromechanical impedance measurements. Presented at the EWSHM-7th European Workshop on Structural Health Monitoring, 2014
11. Baptista, F.G., Vieira Filho, J., Inman, D.J.: Real-time multi-sensors measurement system with temperature effects compensation for impedance-based structural health monitoring. Struct. Health Monit. **11**(2), 173–186 (2012)
12. Saar, T.: Robust piezo impedance magnitude measurement method. Elektronika ir Elektrotechnika. **113**(7), 107–110 (2011)
13. Baptista, F.G., Filho, J.V., Inman, D.J.: Influence of excitation signal on impedance-based structural health monitoring. J. Intell. Mater. Syst. Struct. **21**(14), 1409–1416 (2010)
14. Lewis Jr., G.K., Lewis Sr., G.K., Olbricht, W.: Cost-effective broad-band electrical impedance spectroscopy measurement circuit and signal analysis for piezo-materials and ultrasound transducers. Meas. Sci. Technol. **19**(10), 105102 (2008)
15. (2016, 10/24/16). Physical and Piezoelectric Properties of APC Materials. Available: https://www.americanpiezo.com/apc-materials/piezoelectric-properties.html
16. Kettle, R.A., Anton, S.R.: Rapid evaluation of mechanical boundary conditions using impedance based structural health monitoring. Presented at the SPIE Smart Structures and Materials+ Nondestructive Evaluation and Health Monitoring, 2016

# Chapter 30
# Structural Stiffness Identification of Skewed Slab Bridges with Limited Information for Load Rating Purpose

**Abdollah Bagheri, Mohamad Alipour, Salman Usmani, Osman E. Ozbulut, and Devin K. Harris**

**Abstract** This paper presents a method for identifying structural stiffness of skewed reinforced concrete slab bridges with limited structural information using measured acceleration data. This information might be used for nondestructive evaluation, condition assessment, and load rating of bridges. A large number of slab bridges with different structural dimensions such as skew angle, span, width, and thickness was first analyzed using finite element method to obtain their first modal frequency. This population of data was then used to create an artificial neural network, which can predict a coefficient that plays an important role in identifying the flexural rigidity of slab bridges. This approach was applied to estimate the flexural rigidity of a highly skewed reinforced concrete slab bridge in the state of Virginia for load rating purpose. The bridge was instrumented with wireless accelerometers, and the vibration responses of the bridge under ambient loading and impact hammer test were recorded. An algorithm based on the variational mode decomposition was employed to identify modal properties of the bridge. Then, the flexural rigidity of bridge was computed from the established relationship between the first natural frequency and the flexural rigidity of bridge. Results show that the proposed method is capable of predicting structural stiffness, and can be used for load rating of bridges without structural information.

**Keywords** Structural stiffness identification • Modal frequency • Vibration response • Skewed slab bridge • Variational mode decomposition

## 30.1 Introduction

Load rating is the process of determining the safe load-carrying capacity of a bridge and, thus, serves as a basis for prioritizing maintenance operations and allocation of resources [1–3]. Typically, load ratings are developed in accordance with the rules of structural mechanics using design drawings and details that define the geometry and material properties of the bridge. Therefore, the information needed to carry out this load rating includes the latest safety inspection report, prior load rating files, and design plans or as-built drawings of the structure.

However, there are cases where these design plans are missing or incomplete due to lack of documentation at the time of construction, improper storage or the evolution of data management practices. For these structures, the Manual for Bridge Evaluation (MBE) provides limited guidance on the process for load rating [4]. The language in MBE indicates that an inspection by a qualified inspector and evaluation by a qualified engineer may be sufficient to establish an approximate load rating. This guidance does not explicitly state, but does imply, that engineering judgment may be necessary in which an experienced engineer considers relevant factors, such as the original design live loads, the past performance and current physical condition of the bridge, current loads, and age, to arrive at a judgment-based load rating.

Since the State Departments of Transportation in the United States has responsibility for load rating a large number of bridges and culverts within their inventory [5], structures without existing plans or insufficient details represent a significant bottleneck in the management and decision-making. Bridge engineers might elect to be overly conservative about a given bridge's capacity. As a result, resources may unnecessarily be devoted to the structure instead of others that might truly be in need. Furthermore, overly conservative ratings may restrict the types of vehicles that traverse the bridge, and as a result, hinder commerce within the United States. On the other hand, these judgment-based ratings can be subjective and may pose a risk, as this approach may not accurately describe a bridge's behavior [6]. Therefore, load rating strategies for bridges with limited or missing as-built information are needed, and our aim is to presents methods for load rating these types of structures.

A. Bagheri • M. Alipour • S. Usmani • O.E. Ozbulut (✉) • D.K. Harris
Department of Civil and Environmental Engineering, University of Virginia, Charlottesville, VA 22904, USA
e-mail: ozbulut@virginia.edu



J. Caicedo, S. Pakzad (eds.), *Dynamics of Civil Structures, Volume 2*, Conference Proceedings
of the Society for Experimental Mechanics Series, DOI 10.1007/978-3-319-54777-0_30

Load rating factor is a function of the bridge's capacity and the effect of dead and live loads in bridge, and both of these parameters depend on the stiffness of bridge. This paper describes a method for identifying the bending stiffness of skewed reinforced concrete slab bridges using the measured first modal frequency of the bridge. This information can be used in load rating of bridges with limited or missing as-built information. Vibration testing of an in-service was conducted and the developed method was then employed to estimate the bending stiffness of the bridge.

## 30.2 Stiffness Identification Method

### *30.2.1 Problem Formulation*

For a structural system with a single degree of freedom, the relation between the angular natural frequency $\omega$ of the structure and the structural stiffness $K$ can be written as:

$$\omega^2 = \frac{K}{M} \tag{30.1}$$

where $M$ is the mass of the system. The analogous relationship can be presented for a rectangular plate [7]:

$$\omega^2 = \lambda^2 \frac{D}{\rho} \tag{30.2}$$

where $\rho$ is the mass per unit area of the plate, $\lambda$ is a coefficient which depends to the plate's dimension and boundary condition, and $D$ represents the bending stiffness of the plate and is given as:

$$D = \frac{Et^3}{12\,(1-\upsilon^2)} \tag{30.3}$$

where $t$ is the plate's thickness, and $E$ and $\upsilon$ are the elastic modulus and Poisson's ratio of the plate's material.

Equation (30.2) can be solved to obtain the bending stiffness $D$ of a plate. By measuring the vibration response of the plate and processing the measured signal, one can identify the modal frequency $\omega$ of the plate. Then, by knowing the plate's material, the mass per unit area of the plate can be obtained. The coefficient $\lambda$ can be calculated from a function that depends to the plate's dimension and boundary condition. This function is available in the literature for rectangular plates with different boundary conditions. Finally, the bending stiffness $D$ is obtained by plugging three parameters namely $\omega$, $\lambda$, and $\rho$ in Eq. (30.2) and solving it for the bending stiffness $D$.

A similar method can be employed to identify the bending stiffness of a skewed slab bridge shown in Fig. 30.1. In this figure, $a$ and $b$ represent the bridge's span and width, respectively, and the skew angle is shown by $\theta$. Most slab bridges are built with simple supports at two ends of the span and parapets at two edges along the span, which has a significant contribution in the bridge's stiffness. However, no equation is available in the literature to calculate the coefficient $\lambda$ for such a configuration. Here, a parametric study was conducted to obtain $\lambda$ for simply-supported skewed slab bridges with parapets.

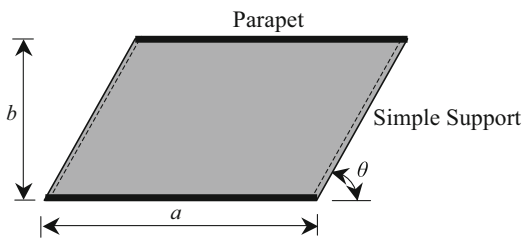


**Fig. 30.1** Top view of a skewed slab bridge with its dimension

### 30.2.2 Parametric Study

In the parametric study, it was assumed that the bridge's parapet has the same rectangular cross-section for the bridges with different span width and length. This is a valid assumption as the parapet's dimensions for most slab bridges are standard. Therefore, $\lambda$ is a function of the bridge's span $a$, width $b$, skew angle $\theta$, and thickness $t$. For given parameters, the first modal frequency of the bridge can be obtained using a modal finite element analysis. Then, $\lambda(a,b,\theta,t)$ is calculated as follows:

$$\lambda\left(a,b,\theta,t\right)=\omega\left(a,b,\theta,t\right)\sqrt{\frac{\rho}{D}} \tag{30.4}$$

The modal finite element analysis was conducted for different values of the bridge's span $a$, width $b$, skew angle $\theta$, and thickness $t$ for obtaining $\lambda(a,b,\theta,t)$. For each parameter, the following ranges were considered:

$$a(m)=[4\ 5\ 6\ 7\ 8\ 9\ 10\ 11\ 12\ 13\ 14\ 15] \tag{30.5}$$

$$b(m)=[4\ 5\ 6\ 7\ 8\ 9\ 10\ 11\ 12\ 13\ 14\ 15] \tag{30.6}$$

$$t(m)=[0.30\ 0.35\ 0.40\ 0.45\ 0.50\ 0.55\ 0.60\ 0.65\ 0.70] \tag{30.7}$$

$$\theta\left(^{\circ}\right)=[0\ 5\ 10\ 15\ 20\ 25\ 30\ 35\ 40\ 45\ 50] \tag{30.8}$$

Based on these ranges for each parameter, the number of finite element models that should be run is $12 \times 12 \times 9 \times 11 = 14{,}256$. To minimize the computational efforts, a finite element code was written in *MATLAB* to model and analyze of slab bridges with all combination of each parameter automatically and continuously.

Figure 30.2a shows the value of $\lambda$ as a function of the bridge's span $a$ and width $b$ for the plate's thickness of 0.3 m and the skew angle of 0°, whereas Fig. 30.2b illustrates the same results for the skew angle of 45°. It can be seen that at short spans and widths the value of $\lambda$ is larger than that for long spans and widths. This is due to the increase in the natural frequency of bridge with the decreasing the bridge's span and width. The skew angle in a bridge causes to increase the stiffness of the

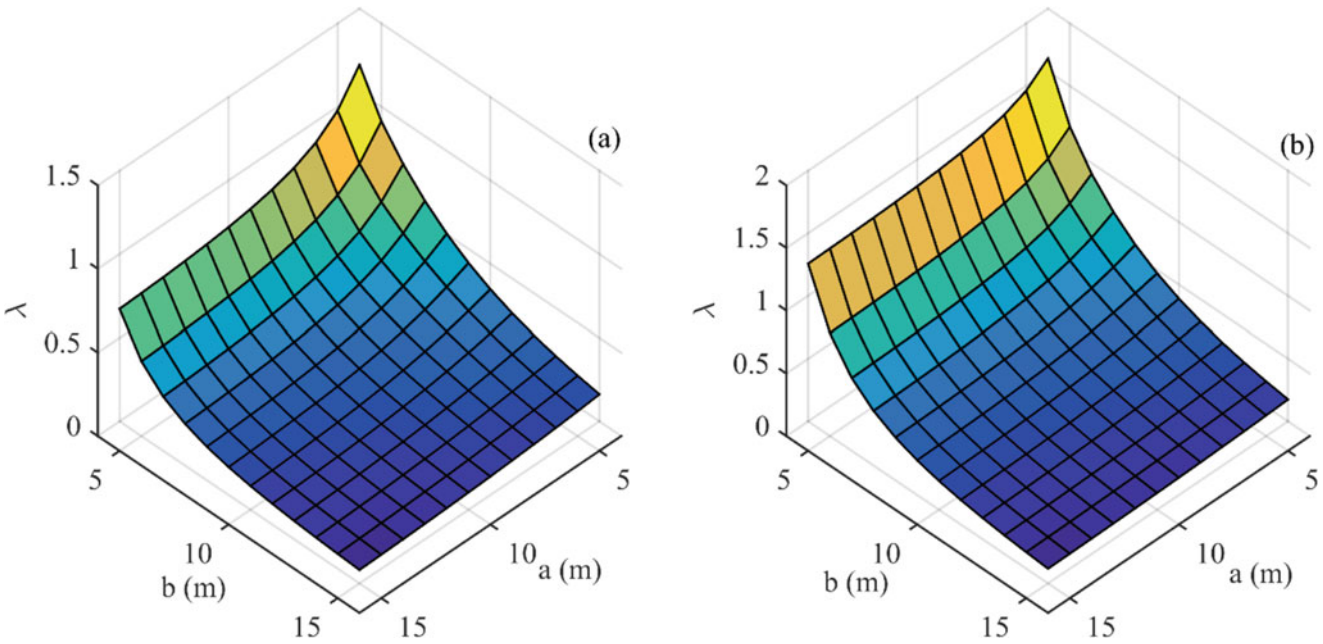


**Fig. 30.2** The value of $\lambda$ as a function of the bridge's span $a$ and width $b$ for the plate's thickness of 0.3 m and: (**a**) the skew angle of 0° and (**b**) the skew angle of 45°

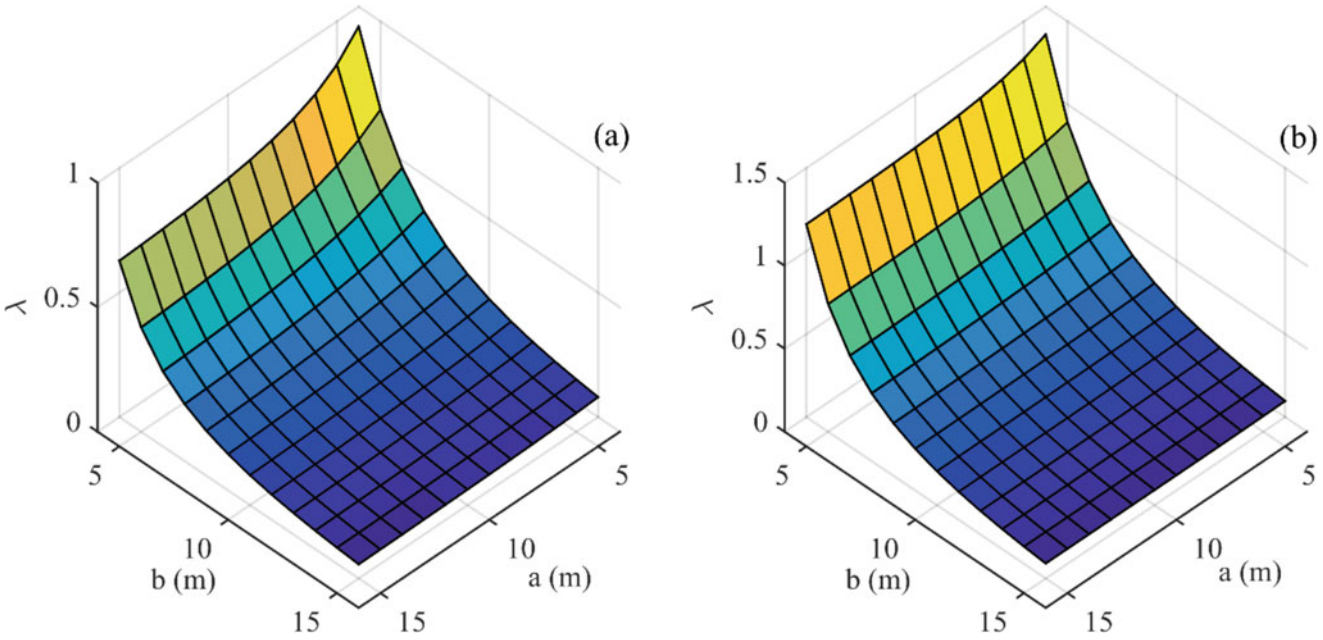


**Fig. 30.3** The value of $\lambda$ as a function of the bridge's span $a$ and width $b$ for the plate's thickness of 0.6 m and: (**a**) the skew angle of 0° and (**b**) the skew angle of 45°

structure which causes to increase the bridge's modal frequency, and this effect increases the value of $\lambda$ which can be seen by comparing Fig. 30.2a, b. In order to see the effect of the plate's thickness on $\lambda$, Fig. 30.3 shows the results of $\lambda$ for the plate's thickness of 0.6 m. By comparing Figs. 30.2 and 30.3, it can be found that the value of $\lambda$ decreases by increasing the plate's thickness at short spans and widths. The changing plate's thickness affects both the mass and stiffness of bridge, and also changes the contribution of the parapet's stiffness on the global stiffness of the structure. Therefore, it can be concluded that there is a complex relation between $\lambda$ and the plate's thickness.

### *30.2.3 Mapping Process*

An artificial neural network (ANN) was employed to predict the relationship between the coefficient of $\lambda$ and the bridge's parameters, namely the bridge's span $a$, width $b$, skew angle $\theta$, and thickness $t$. Neural networks are one of the most effective soft computing algorithms for data fitting and classification. They mimic a human brain by implementing the interconnection of artificial neurons. In this study, a feed-forward back-propagation ANN with three layers was used. The input layer received the data vector containing the four parameters of bridge. The hidden layer processed the data by multiplying the input vectors by weights and adding biases. The results constituted the argument of a transfer function that squashed the output values into a certain range. For the hidden layer, ten neurons were used by means of a trial and error method, and the hyperbolic tangent sigmoid transfer function was employed. For the input and output layers, a liner transfer function was used. The output layer had one node that provided the value of $\lambda$. To train the network, the Levenberg-Marquardt algorithm was used because of its high performance and speed [8].

To study the ability of the network to estimate the value of $\lambda$, we used all 14,256 data for the training. Figure 30.4 shows the ANN estimated $\lambda$ versus the actual $\lambda$, and it can be seen that there is no difference between them, because there is a linear function between the estimated and target values. This trained ANN will be used to estimate $\lambda$ in identifying process of the structural stiffness of a tested slab bridge.

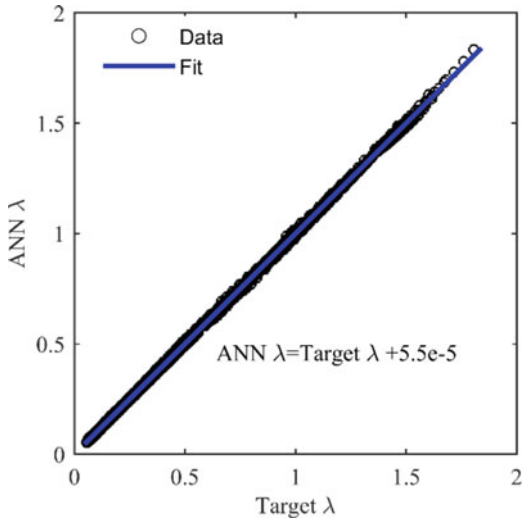


**Fig. 30.4** The ANN estimated $\lambda$ versus the actual $\lambda$

## 30.3 Experimental Study

### *30.3.1 Test Description*

The structure tested in this study was the War Branch Bridge located in the Staunton District in the state of Virginia. The superstructure is comprised of two 9.75-m long, simply-supported reinforced concrete slabs that are 0.53 m thick and have a 45° skew angle (see Fig. 30.5). The deck has 0.3 m diameter voids oriented in the direction of traffic and spaced 0.45 m apart. Built in 1976, the 2014 inspection report described the bridge to be in "fair" condition, with a deck/superstructure condition rating of 7. The bridge was selected from amongst the Virginia Department of Transportation (VDOT) population of reinforced concrete slab bridges with plans, with special consideration given to geometry similarity to the population of this major category of bridges without plans.

For the vibration testing experiments, one of the two spans in the bridge was instrumented with accelerometers. All instrumentation and acquisition comprised of Bridge Diagnostics, Inc. (BDI) equipment, where individual sensors physically connected to four-channel nodes, which in turn interfaced wirelessly with a base station/data acquisition unit. Vibration testing consisted of a series of experiments with excitation provided separately by ambient loading (wind and normal traffic), impact hammer, and electro-magnetic shaker.

### *30.3.2 Modal Data Identification*

In this paper, an algorithm based on the VMD is employed for identifying the modal properties of the bridge. In this method, the measured acceleration signals are decomposed into the modal responses by means of the VMD algorithm, and each obtained modal response has a center frequency which represents the natural frequency of the structure. Then, damping ratios are estimated by doing a fitting process on decaying amplitude of modal response. This method is capable of identifying all natural frequencies and damping ratios using only a single measurement of acceleration response at one suitable location. Mode shapes are then identified from the results of modal responses at all sensing location of the structure.

The VMD is first used to decompose an acceleration signal $S(t)$ into a set of sub-signals (modes), $S_k(t)$, $k = 1, 2, \ldots, K$, which have a compact bandwidth in spectral domain. It can be assumed each sub-signal to be compacted around a center vibration $\omega_k$ which is determined using the decomposition algorithm. Therefore, each sub-signal represents the modal response of structure. In this process, the constrained variational problem is formed by means of Hilbert transform and frequency mixing based on minimizing the bandwidth of sub-signals. In order to render the problem unconstrained, the quadratic penalty and Lagrangian multipliers are employed. More information about the VMD algorithm can be found in [9].

**Fig. 30.5** Photo of the War Branch Bridge

By knowing the modal responses of a structure, it is easy to identify modal damping ratios for all vibration modes. In most engineering structures that have small damping ratio, damping ratio can be estimated from the slop of the decaying amplitude versus time $t$ plot. In this paper, the plot of the decaying amplitude versus time $t$ was fitted to a linear function using the linear last-square fit approach. The slop of the linear function was used to compute the damping ratio.

Acceleration responses of the bridge in the vibration test using impact hammer were used to identify modal frequency and damping ratio of the bridge. The described approach was used to decompose each acceleration signal to sub-signals which represent modal responses of the bridge. The first and second modal frequency of the bridge was 26.07 and 30.59 Hz, respectively. For these modes, the obtained damping ratios were 4.3 and 3.9%, which are close to the common value of the damping ratio 5% mentioned in design codes for concrete structures.

### *30.3.3 Stiffness Identification*

For identifying the bending stiffness of the tested bridge, the trained ANN is first used to obtain the value of $\lambda$ based on the parameters of the bridge. For the War Branch Bridge, the bridge's span $a$, width $b$, skew angle $\theta$, and thickness $t$ are 9.44 m, 9.75 m, 45°, and 0.53 m, respectively. The value of $\lambda$ which is the output of the trained neural network for these bridge's parameters is equal to 0.25. Then, by replacing the obtained value of $\lambda$ and the first modal frequency of 26.07 Hz in Eq. (30.4), the bending stiffness $D$ is obtained as $3.86 \times 10^8$ N m. The elastic modulus of the bridge's material can be computed from Eq. (30.3) based on the identified bending stiffness, which is equal to 31.62 GPa. These results can used for estimating the ultimate compressive strength of the bridge's concrete and the amount of reinforcement area inside the concrete to estimate the bending capacity for computing the load rating factor.

## 30.4 Conclusion

In this paper, a method for identifying the structural stiffness of skewed concrete slab bridges using modal data was presented. A large number of finite element models for slab bridges with different geometric characteristics were analyzed to provide a set of data for mapping bridge's characteristics to a coefficient that is used in identifying the bending stiffness from the modal frequency of a bridge. An ANN was trained to predict this coefficient for a given simply-supported slab bridge. The methodology was used to identify the bending stiffness of an in-service slab bridge. The developed ANN tool and methodology can provide a simple approach to identify the structural stiffness of slab bridges. In a future study, the obtained bending stiffness and elastic modulus of materials will be combined with the measured strain data to calculate the capacity for inventory and operating load rating of the tested bridge.

**Acknowledgments** This material is based upon the work supported by the Virginia Department of Transportation. The authors would like to thank Dr. Bernard L. Kassner of Virginia Transportation Research Council for his helps in conducting the vibration testing of the bridge.

## References

1. Chajes, M., Shenton III, H., O'Shea, D.: Bridge-condition assessment and load rating using nondestructive evaluation methods. Transp. Res. Rec. J. Transp. Res. Board. **1696**, 83–91 (2000)
2. Faber, M.H., Val, D.V., Stewart, M.G.: Proof load testing for bridge assessment and upgrading. Eng. Struct. **22**(12), 1677–1689 (2000)
3. Cai, C.S., Shahawy, M.: Understanding capacity rating of bridges from load tests. Pract. Period. Struct. Des. Constr. **8**(4), 209–216 (2003)
4. AASHTO: Manual for Bridge Evaluation, 2nd edn. with 2016 Interim Revisions. American Association of State Highway and Transportation Officials, Washington (2015)
5. VDOT: State of the Structures and Bridges Report. Virginia Department of Transportation, Richmond (2015)
6. Ma, Y., Wang, L., Zhang, J., Xiang, Y., Liu, Y.: Bridge remaining strength prediction integrated with Bayesian network and In situ load testing. J. Bridg. Eng. **19**(10), 04014037 (2014)
7. Leissa, A.W.: Vibration of plates. National Aeronautics and Space Administration, NASA SP-160 (1969)
8. Bagheri, A., Rizzo, P., Al-Nazer, L.: Determination of the neutral temperature of slender beams by using nonlinear solitary waves. J. Eng. Mech. **141**(6), 04014163 (2014)
9. Dragomiretskiy, K., Zosso, D.: Variational mode decomposition. IEEE Trans. Signal Process. **62**(3), 531–544 (2014)

# Chapter 31
# Online Systems Parameters Identification for Structural Monitoring Using Algebraic Techniques

**L.G. Trujillo-Franco, G. Silva-Navarro, and F. Beltrán-Carbajal**

**Abstract** Nowadays, with the modern techniques and developments on sensors and actuators technologies, disciplines like Operational Modal Analysis (OMA), Structural Health Monitoring (SHM) and Non-Destructive Evaluation (NDE), among others, are now basic parts of the study, modeling and monitoring for modern civil structures and vibrating mechanical systems. The most important system parameters of a given mechanical system, including civil structures, like modal parameters, mass and stiffness matrices are indicatives of the inherent nature and dynamical behavior of it, and, at the same time, a possible way to detect failures by comparing two different sets of such parameters, before and after any failure happens. In this work, a novel fast and online system parameter identification scheme, based on module theory and algebraic techniques for structural monitoring and vibration absorption purposes or model updating for mechanical systems under nominal operation conditions is proposed, that is, in an operational fashion, where only system output information is available. The proposed scheme is evaluated with experimental data.

**Keywords** Algebraic identification • Operational modal analysis • Real time structure monitoring • Structural health monitoring • System identification

## 31.1 Introduction

On the area of mechanical design and modeling (civil structures inclusive), the process called modal parameter identification or modal analysis has become into a basic technological tool, which allows having a correct knowledge and sometimes a prediction of the system response under harmonic excitation. In this information era, modal analysis can specially count on the newest and powerful data analyzers for storing and processing the data under study. In this order of ideas, the task of analyzing engineering structures response and behavior, when the system is working on its nominal operation conditions is a natural consequence [1, 2] (e.g., via the OMA approach). Most of the times, real world systems work under a completely random and hard to measure excitation; furthermore, in some special cases, it is desirable to monitor some interest output in a real-time fashion. Certainly, the actual state of the art for modal analysis has a robust background, consisting of plenty of identification algorithms in time or frequency domain, mainly for off-line estimation of modal parameters. However, it is important to consider that, most of these techniques are essentially asymptotic, recursive, complex and slow for on-line parameter estimation implementations, which could be required for efficient adaptive active noise and vibration control and monitoring applications on dynamic mechanical structures [3–5].

As reported in Refs. [4–7], here we apply a theoretical framework for the algebraic parameter identification on continuous-time linear systems. This identification approach platform consists of powerful mathematical tools as module theory, differential algebra and operational calculus. It is important to remark that, the operational calculus is a quite general approach based on different integral transformations of functions and generalized functions (e.g., Fourier, Laplace, Stieltjes, Hilbert, Bessel) [4–7]. The application of operational calculus in mechanical engineering is quite common for the transformation of functions from time to frequency domain and solving differential equations.

L.G. Trujillo-Franco (✉) • G. Silva-Navarro
Departamento de Ingeniería Eléctrica, Sección de Mecatrónica, Centro de Investigación y de Estudios Avanzados del I.P.N.,
Av. IPN No. 2508, Col. S.P. Zacatenco, C.P. 07360, Mexico, D.F., Mexico
e-mail: ltrujillo@cinvestav.mxgsilva@cinvestav.mx

F. Beltrán-Carbajal
Departamento de Energía, Universidad Autónoma Metropolitana, Unidad Azcapotzalco, Av. San Pablo No. 180,
Col. Reynosa Tamaulipas, C.P. 02200, Mexico, D.F., Mexico
e-mail: fbeltran@correo.azc.uam.mx



J. Caicedo, S. Pakzad (eds.), *Dynamics of Civil Structures, Volume 2*, Conference Proceedings
of the Society for Experimental Mechanics Series, DOI 10.1007/978-3-319-54777-0_31

In this work we propose a novel system parameter monitoring scheme based on algebraic identification. We perform modal testing to the nominal or undamaged structure in order to have a reference for comparisons, and then, we induce changes directly on the structure, simulating failures (e.g., a loose or broken screw or a mass addition), in order to identify in a fast and online fashion the impact of each situation on the system modal parameters.

## 31.2 Illustrative Vibrating Mechanical System

Consider the $n$ Degrees-Of-Freedom (DOF) vibrating mechanical system consisting of a six story building-like structure as shown in Fig. 31.1, where $x_i$, $i = 1, 2, \ldots, n$, are the displacements of 6 masses representing the floors or Degrees-Of-Freedom (DOF) of the structure, respectively. We model the columns as flexural springs with equivalent stiffness $k_i$ and consider the structural damping ratios $c_i$ as Rayleigh damping [8].

The simplified mathematical model of this flexible mechanical system of 6 DOF under harmonic and unknown excitation $f$ is given by:

$$M\ddot{x} + C\dot{x} + Kx = f(t), \quad x, f \in R^6 \tag{31.1}$$

where $x \in R^6$ is the vector of generalized coordinates (displacements) of each floor respect to the main frame reference, and $M$, $C$ and $K$ are symmetric inertia, damping and stiffness $6 \times 6$ matrices, respectively, given by:

$$\mathbf{M}=\begin{bmatrix} m_1 & 0 & 0 & \ldots & 0 & 0 \\ 0 & m_2 & 0 & \ldots & 0 & 0 \\ 0 & 0 & m_3 & \ldots & 0 & 0 \\ . & & & & & \\ . & & & & & \\ . & & & & & \\ 0 & 0 & 0 & \ldots & 0 & m_6 \end{bmatrix}, \mathbf{C}=\begin{bmatrix} c_1+c_2 & -c_2 & 0 & \ldots & 0 & 0 \\ -c_2 & c_2+c_3 & c_3 & \ldots & 0 & 0 \\ 0 & -c_3 & c_3+c_4 & \ldots & 0 & 0 \\ . & & & & & \\ . & & & & & -c_6 \\ . & & & & & \\ 0 & 0 & 0 & \ldots & -c_1 & c_6 \end{bmatrix}, \mathbf{K}=\begin{bmatrix} k_1+k_2 & -k_2 & 0 & \ldots & 0 & 0 \\ -k_2 & k_2+k_3 & -k_3 & \ldots & 0 & 0 \\ 0 & -k_3 & k_3+k_4 & \ldots & 0 & 0 \\ . & & & & & \\ . & & & & & -k_6 \\ . & & & & & \\ 0 & 0 & 0 & \ldots & -k_6 & k_6 \end{bmatrix} \tag{31.2}$$

The modal analysis representation of the mathematical model (31.1) is defined in terms of the modal or principal coordinates $q_i$, where $i = 1, 2, \ldots, 6$ as follows (see, e.g., [1])

$$\ddot{q}_i + 2\zeta_i\omega_i\dot{q}_i + \omega_i^2 q_i = \Psi^T f \tag{31.3}$$

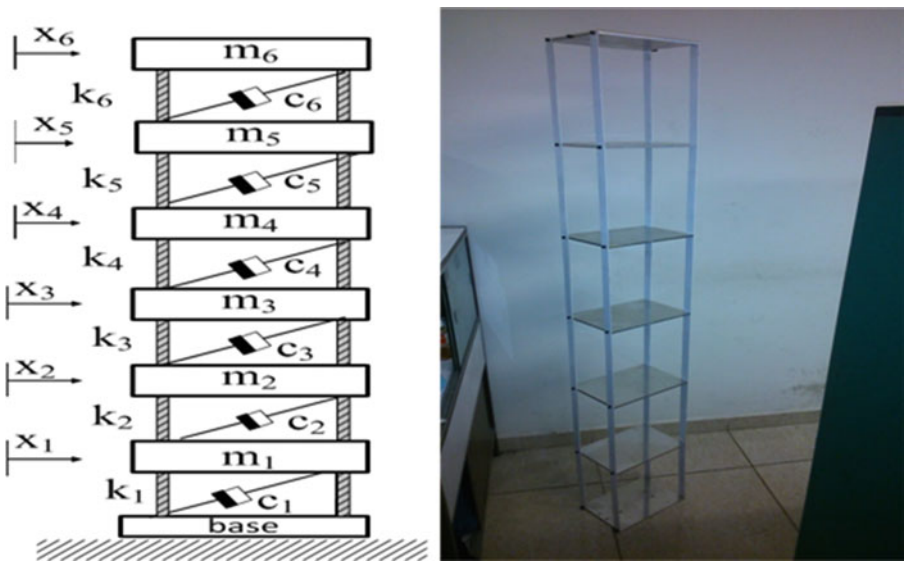


**Fig. 31.1** Six story Building-like structure. (**a**) Schematic diagram. (**b**) Physical plant

with

$$x(t) = \Psi q(t) \tag{31.4}$$

where $\omega_i$ and $\xi_i$ denote the natural frequencies and damping ratios associated to the $i$-th vibration mode, respectively, and $\Psi$ is the so-called $6 \times 6$ modal matrix given by

$$\mathbf{\Psi} = \begin{bmatrix} \psi_{11} & \psi_{12} & \cdots & \psi_{15} & \psi_{16} \\ \psi_{21} & \psi_{22} & \cdots & \psi_{25} & \psi_{26} \\ \vdots & \vdots & \ddots & \vdots & \vdots \\ \psi_{51} & \psi_{52} & \cdots & \psi_{55} & \psi_{56} \\ \psi_{61} & \psi_{62} & \cdots & \psi_{56} & \psi_{66} \end{bmatrix} \tag{31.5}$$

In notation of Mikusiński operational calculus [5, 6], this modal model is then described as

$$\left(s^2 + 2\zeta_i\omega_i s + \omega_i^2\right)\, q_i(s) = p_{0,i} + p_{1,i}s + \psi_{1i}f_1 + \psi_{2i}f_2 + \cdots + \psi_{6i}f_6 \tag{31.6}$$

where $p_{o,i}$ are constants depending on the system initial conditions at the time $t_0 \geq 0$.

From (31.3) and (31.5), one then obtains that

$$x_i(s) = \sum_{j=1}^{n} \frac{\psi_{ij}\left(p_{0,j} + p_{1,j}s\right)}{s^2 + 2\zeta_j\omega_j s + \omega_j^2} \tag{31.7}$$

Therefore, the physical displacements $x_i$ are given by

$$p_c(s)\, x_i(s) = r_{0,i} + r_{1,i}s + \cdots + r_{2n-2,i}s^{2n-2} + r_{2n-1,i}s^{2n-1} \tag{31.8}$$

with

$$p_c(s) = s^{2n} + a_{2n-1}s^{2n-1} + \cdots + a_1 s + a_0 \tag{31.9}$$

where $p_c(s)$ is the characteristic polynomial of the mechanical system and $r_{i,j}$ are constants which can be easily calculated by using the values of the system initial conditions as well as the modal matrix components $\psi_{ij}$. Naturally, the roots of the characteristic polynomial (31.9) provide the damping factors and damped natural frequencies, and hence the most descriptive information about the structure and its status.

## 31.3 Online Structural Monitoring

The proposed online algebraic monitoring scheme shown in Fig. 31.2 works in conjunction with the building like structure shown in Fig. 31.1 for the illustrative cases to be considered in this work.

The ARM (Advanced Risc Machine) takes samples of the acceleration of the sixth floor (in the horizontal axis direction) of the structure at a precisely fixed sample rate of 1Khz, and then, those samples are sent to a standard PC running under *Windows 7*® and *Matlab*®*/Simulink* to finally perform the online identification scheme.

We perform an on-line algebraic identification approach to estimate the modal parameters of the mechanical system through the real-time estimation of the coefficients $a_k$ of the system's characteristic polynomial as reported in [5, 6] using only acceleration measurements of any floor of the structure. The application of the online algebraic identification scheme is performed using cumulative trapezoidal numerical integration with fixed sampling time of 1 ms. The algebraic identification scheme applied here is described on detail in [4] where is shown that by solving the algebraic equation (31.9) also detailed in [4–7] one obtains the parameter vector $\theta$ as:

$$\boldsymbol{\theta} = \mathbf{A}^{-1}\mathbf{B} = \frac{1}{\Delta}\begin{bmatrix} \Delta_1 \\ \Delta_2 \\ \vdots \\ \Delta_{n-1} \\ \Delta_n \end{bmatrix} \tag{31.10}$$

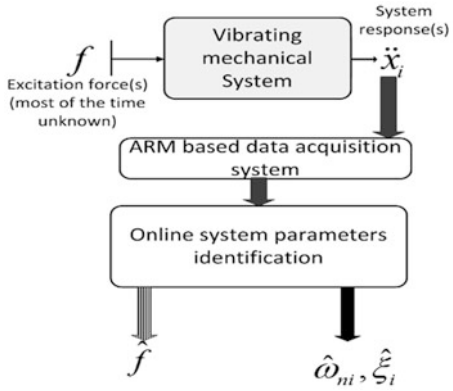


**Fig. 31.2** Block diagram of the proposed identification and monitoring scheme

Then, the algebraic identifiers to estimate the coefficients $a_k$ of the characteristic polynomial without problems of singularities when the determinant $\Delta = \det(\mathbf{A}(t))$ crosses by zero:

$$\widehat{a}_k = \frac{\int |\Delta_{k-1}|}{\int |\Delta|}, \qquad k = 1,\ 2, \cdots, 2n-1 \tag{31.11}$$

Thus, one could implement the algebraic identifiers (31.10) using only any available acceleration measurements $\ddot{x}_i$ of any specific floor or degree of freedom. From the estimated coefficients $\widehat{a}_k$, one can obtain the roots of the characteristic polynomial:

$$\lambda_i = \sigma_i + j\omega_{di}, \qquad \lambda_i^* = \sigma_i - j\omega_{di}, \qquad \mathrm{i} = 1,\ 2, \cdots, \mathrm{n} \tag{31.12}$$

where $\sigma_i$ and $\omega_{di}$ are estimates of the damping factors and damped natural frequencies of the mechanical system, respectively. Hence, the estimates of the natural frequencies and damping ratios are given by

$$\omega_{ni} = \sqrt{\sigma_i^2 + \omega_{di}^2}, \qquad \zeta_i = -\frac{\sigma_i}{\sqrt{\sigma_i^2 + \omega_{di}^2}} \tag{31.13}$$

**Remark:** On the block diagram of Fig. 31.2 the shaded arrow indicates that once we identify the modal parameters or even the complete eigenstructure of the system, we can identify the excitation force and thus counteract it, as we have reported in previous works [5, 7, 9] for vibration absorption schemes or simply characterize this unknown excitation force.

## 31.4 Some Illustrative Cases

In order to evaluate the performance of the proposed monitoring scheme we perform a traditional modal testing on the structure in order to know its natural status or nominal modal parameters. The results of the modal testing (impact hammer based) of the structure is reported in Table 31.1 and in Fig. 31.3.

The algebraic identification of the system modal parameters is shown in Fig. 31.4, notice that the online identification of the modal parameters $\widehat{\zeta}_i$ and $\widehat{\omega}_{ni}$ takes less than 1 taking in to consideration that we compute the natural frequencies and the damping ratios using the estimates of the 12 coefficients $a_k$ corresponding to the characteristic polynomial of the mechanical system.

Once calibrated the algebraic identifier, we consider our first case study: We induce one structural failure in the structure by losing one of the four screws on the third floor; next, we excite the structure with a random impact force and then, identify the new modal parameters of the "damaged" structure with only measurements of the sixth floor acceleration. The structural failure detail and the new system impact response are shown in Fig. 31.5.

**Table 31.1** Modal parameters of the nominal system

| Mode | Frequency (Hz) | Damping ratio (%) |
|---|---|---|
| 1 | 1.148 | 0.15 |
| 2 | 3.39 | 0.39 |
| 3 | 5.44 | 0.18 |
| 4 | 7.16 | 0.19 |
| 5 | 8.53 | 0.18 |
| 6 | 9.34 | 0.17 |

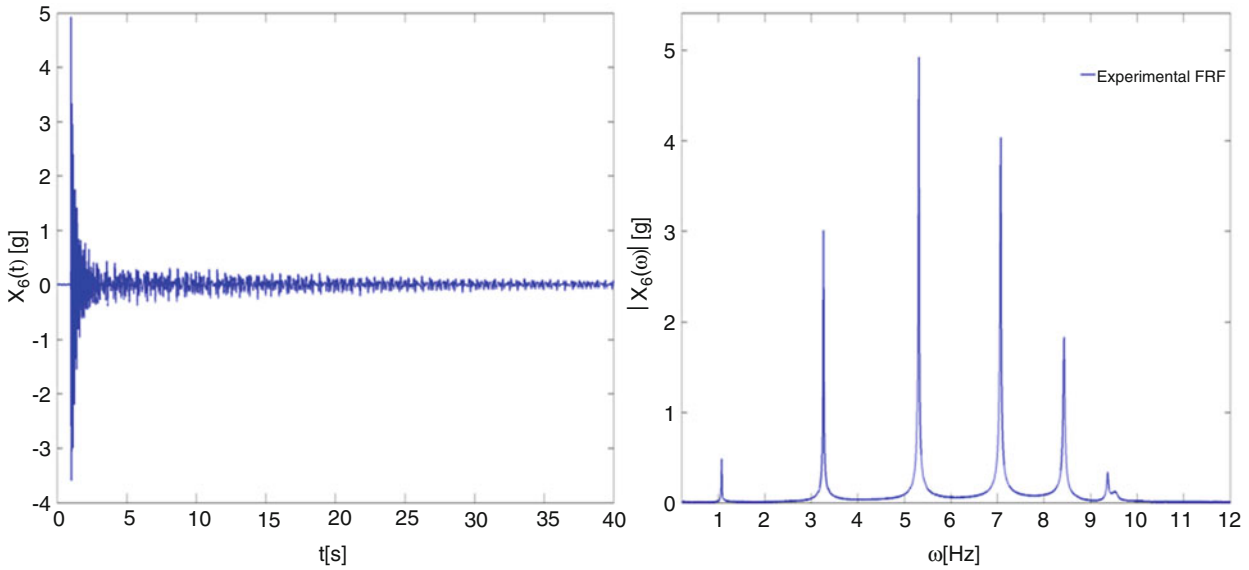


**Fig. 31.3** Impulse response of the six DOF system (sixth floor acceleration measurement) and its FRF (nominal system)

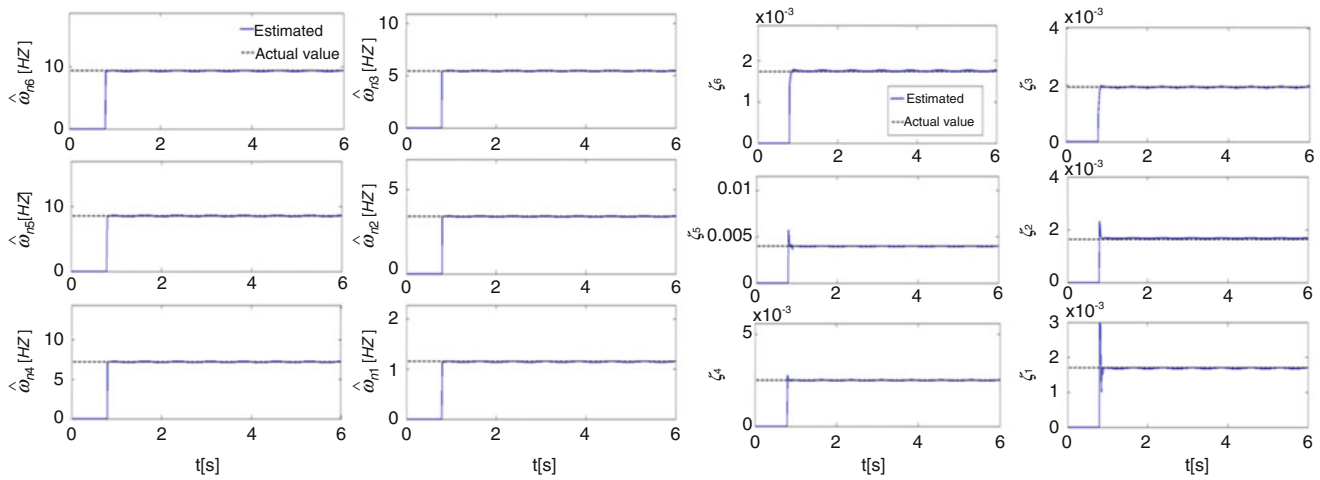


**Fig. 31.4** Online estimation of system modal parameters

The new system modal parameters are shown in Table 31.2, where we can notice the changes on the natural frequencies and damping ratios. Notice that this induced fail does not imply obvious changes on the system dynamic behavior, however, the proposed identifier can detect them in a fast and online fashion, as shown in Fig. 31.6.

The second case study consist on adding a 0.496 kg mass on the third floor only one second after the online estimation of the modal parameters from the nominal structure. This is shown in Fig. 31.7. Where we show the mass added to the third floor and the system time response after suddenly applying the mass and, therefore causing a new impact response of the structure.

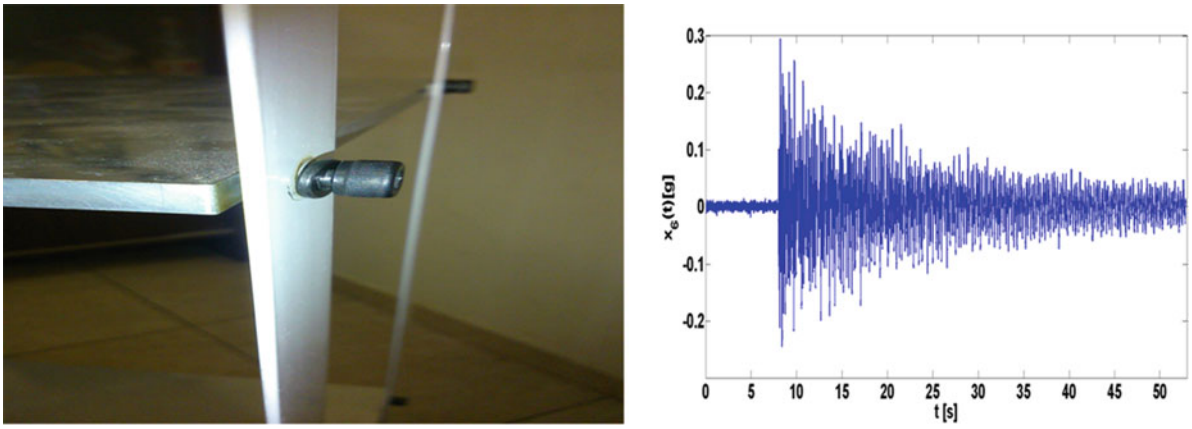


**Fig. 31.5** Loose screw detail and impulse response of damaged structure

**Table 31.2** Change of the system modal parameters with a loose screw

| | Frequency (Hz) | | | Damping ratio (%) | | |
|---|---|---|---|---|---|---|
| Mode | Nominal | Loose screw | %Change | Nominal | Loose screw | %Change |
| 1 | 1.148 | 1.08 | 5.92 | 0.15 | 0.13 | 13.33 |
| 2 | 3.39 | 3.38 | 0.29 | 0.39 | 0.37 | 5.182 |
| 3 | 5.44 | 5.03 | 7.53 | 0.18 | 0.20 | 11.11 |
| 4 | 7.16 | 7.05 | 1.53 | 0.19 | 0.21 | 10.52 |
| 5 | 8.53 | 8.23 | 3.51 | 0.18 | 0.17 | 5.55 |
| 6 | 9.34 | 8.97 | 3.96 | 0.17 | 0.11 | 35.294 |

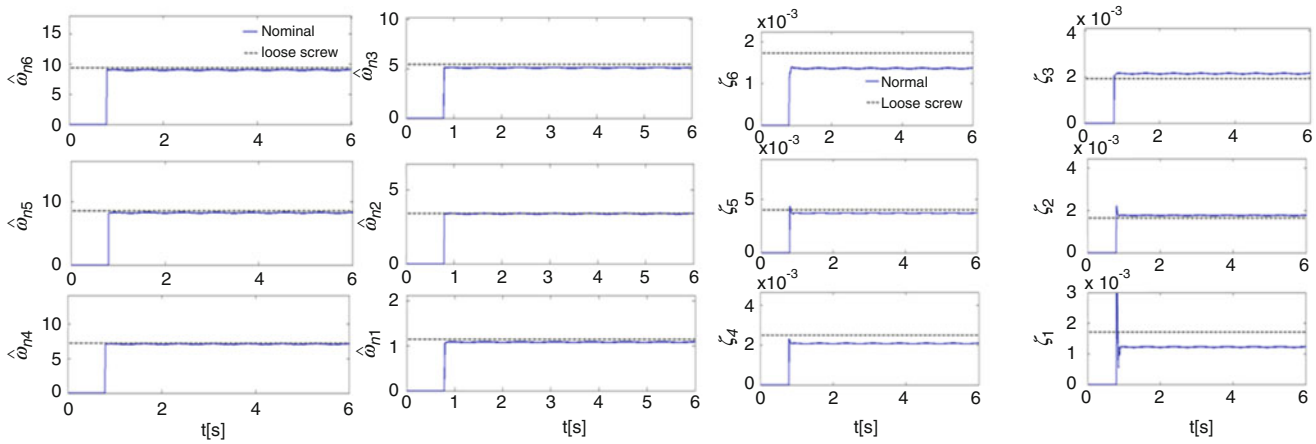


**Fig. 31.6** Online modal parameters identification of structure with a loose screw

The fast and effective online modal parameters estimation is shown in Fig. 31.8 while the comparison of the new structure modal parameters is reported in Table 31.3. We intentionally leave idle the plotting part of the monitoring system for a second in order to plot only coherent parameters, that is, we wait for the algebraic identifier to finish the required estimations.

## 31.5 Conclusions

It is proposed the use of an algebraic identification approach for the on-line monitoring and estimation of modal parameters for multiple degrees-of-freedom mechanical systems. In this application, we have considered that only measurements of one floor acceleration is available for the identification scheme implementation. The algebraic modal parameter identification

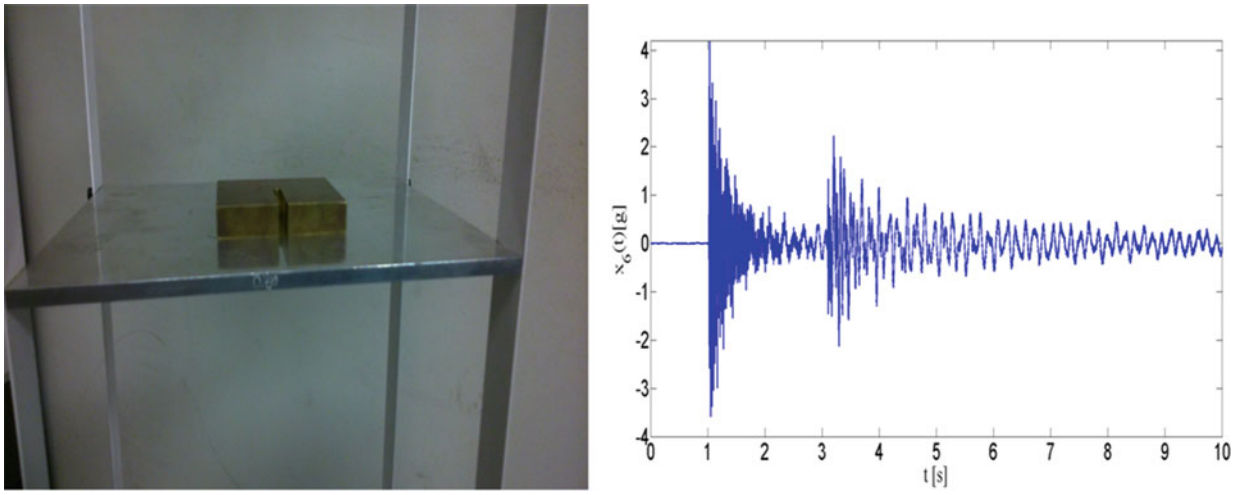


**Fig. 31.7** Mass change induced on the third floor after 3 s

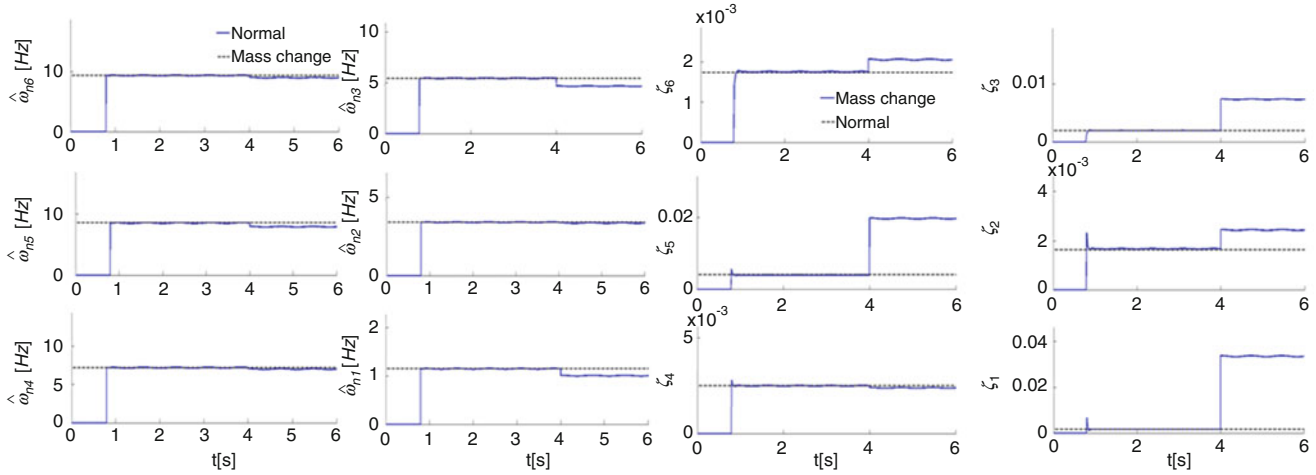


**Fig. 31.8** Online modal parameters identification when the structure has a mass change on the third floor

**Table 31.3** Change of the system modal parameters with a mass added to the third floor

| | Frequency (Hz) | | | Damping ratio (%) | | |
|---|---|---|---|---|---|---|
| Mode | Nominal | With mass added | %Change | Nominal | With mass added | %Change |
| 1 | 1.148 | 0.97 | 15.5 | 0.15 | 0.87 | 480 |
| 2 | 3.39 | 3.35 | 1.17 | 0.39 | 1.5 | 284 |
| 3 | 5.44 | 4.45 | 18.19 | 0.18 | 0.2 | 11.11 |
| 4 | 7.16 | 6.72 | 6.145 | 0.19 | 0.2 | 5.26 |
| 5 | 8.53 | 7.78 | 8.79 | 0.18 | 1.9 | 955 |
| 6 | 9.34 | 8.35 | 10.59 | 0.17 | 0.2 | 17.64 |

scheme was tested for a 6-DOF mechanical system excited by an impact excitation for illustrative purposes. In general, the simulation and experimental results show a satisfactory performance of the proposed identification approach with fast and effective estimations very promising for online applications as future operational modal analysis schemes and adaptive vibration absorption.

## References

1. Yang, Y., Nagarajaiah, S.: Output-only modal identification with limited sensors using sparse component analysis. J. Sound Vib. **332**, 4741–4765 (2013)
2. Brincker, R., Ventura, C.E.: Introduction to Operational Modal Analysis. Wiley, Chichester (2015)
3. Golub, G., Van Loan, C.: An analysis of the total least squares problem. SIAM J. Numer. Anal. **17**, 883–893 (1980)
4. Beltran-Carbajal, F., Silva-Navarro, G., Trujillo-Franco, L.G.: Evaluation of on-line algebraic modal parameter identification methods. In: Proceedings of the 32nd International Modal Analysis Conference (IMAC XXXII), vol. 8, pp. 145–152 (2014)
5. Beltran-Carbajal, F., Silva-Navarro, G., Trujillo-Franco, L.G.: Adaptive-like vibration control in a three-story building-like structure with a PZT stack actuator. In: Proceedings of the 33rd International Modal Analysis Conference (IMAC XXXIII), vol. 10, pp. 123–131 (2015)
6. Beltran-Carbajal, F., Silva-Navarro, G., Chávez-Conde, E.: Design of active vibration absorbers using on line estimation of parameters and signals. In: Beltrán-Carbajal, F. (ed.) Vibration Analysis and Control. New Trends and Developments. InTech, Croatia (2011)
7. Beltran-Carbajal, F., Silva-Navarro, G.: Algebraic parameter identification of multi-degree-of-freedom vibrating mechanical systems. In: Proceedings of the 20th International Congress on Sound and Vibration (ICSV20), Bangkok, Thailand, pp. 1–8 (2013)
8. Soderstrom, T., Stoica, P.: System Identification. Prentice-Hall, New York (1989)
9. Beltran-Carbajal, F., Silva-Navarro, G.: Adaptive-like vibration control in mechanical systems with unknown parameters and signals. Asian J. Control. **15**, 1613–1626 (2013). doi:10.1002/asjc.7272013

# Chapter 32
# Structural Vibration Control Using High Strength and Damping Capacity Shape Memory Alloys

**Soheil Saedi, Farzad S. Dizaji, Osman E. Ozbulut, and Haluk E. Karaca**

**Abstract** Designing structures to withstand dynamic environmental hazards such as earthquakes, strong winds, and hurricanes is of primary concern for civil engineers. In addition, recent advances in architectural forms, structural systems, and high performance materials have enabled the design of very slender and lightweight structures. These flexible structures are susceptible to be exposed to high levels of vibrations under strong winds and earthquakes, which may lead to structural damage and potential failure. Over the past two decades, shape memory alloys (SMAs) have emerged as a smart material that can be used in passive vibration control devices for energy dissipating and re-centering purposes. However, the quantity of equivalent viscous damping provided by superelastic NiTi SMA wires or bars is not sufficient to render the use of SMAs as the sole damping device implemented in a tall structure subjected to severe dynamic loadings. This study explores the performance of recently developed NiTiHfPd alloys that have very high strength, high dissipation/damping capacity, good cyclic stability and large operating temperature for vibration control applications. In particular, superelastic response of single crystal and polycrystalline NiTiHfPd alloys were investigated systematically to reveal the effects of composition alteration and heat treatments. The design of a novel passive vibration control device by utilizing the superelastic effect of NiTiHfPd SMAs under compression was illustrated.

**Keywords** Shape memory alloys • Passive control • Damper • Vibrations • Earthquake

## 32.1 Introduction

To mitigate the adverse effects of dynamic environmental hazards such as earthquakes, strong winds, and hurricanes and achieve a more resilient design under dynamic loads, various passive, active and semi-active control devices have been proposed and developed [1]. The most widely tested and commonly implemented strategies have been passive devices as they are reliable, require no external power, and never destabilize the structure. However, designing buildings with passive systems to provide performance improvement over all ranges of earthquake and wind excitation is a challenging task.

A number of passive energy dissipation systems have been developed to mitigate damaging effects of natural hazards on structures [2]. Passive energy dissipation devices can be grouped into two main categories: hysteretic devices and rate-dependent devices. Examples of hysteretic devices include metallic yielding devices and friction devices. Energy dissipation in hysteretic devices depends primarily on relative displacements within the device. These devices add initial stiffness until yielding or slip occurs and provide hysteretic energy dissipation. However, they do not provide sufficient damping at small vibrations caused by wind excitation or frequent seismic events while increase the forces and accelerations on the structure due to high stiffness. Furthermore, metallic devices usually have a limited number of working cycles and may require replacement after a strong event and friction devices may lead to permanent deformations if no restoring force mechanism is provided. Examples of rate-dependent devices include fluid viscous dampers and viscoelastic dampers. The energy dissipation capacity of these devices depends on the velocity across the device [2]. The viscous damper can provide high force and damping capabilities while the viscoelastic dampers have low force and displacement capacity. In general, rate-dependent devices can dissipate energy at all magnitudes of motion but do not possess the same capacity for energy dissipation as hysteretic devices [3]. Note that these devices also do not have self-centering property to return the structure to its original position.

S. Saedi • H.E. Karaca
Department of Mechanical Engineering, University of Kentucky, Lexington, KY, USA

F.S. Dizaji • O.E. Ozbulut (✉)
Department of Civil and Environmental Engineering, University of Virginia, Charlottesville, VA, USA
e-mail: ozbulut@virginia.edu



J. Caicedo, S. Pakzad (eds.), *Dynamics of Civil Structures, Volume 2*, Conference Proceedings
of the Society for Experimental Mechanics Series, DOI 10.1007/978-3-319-54777-0_32

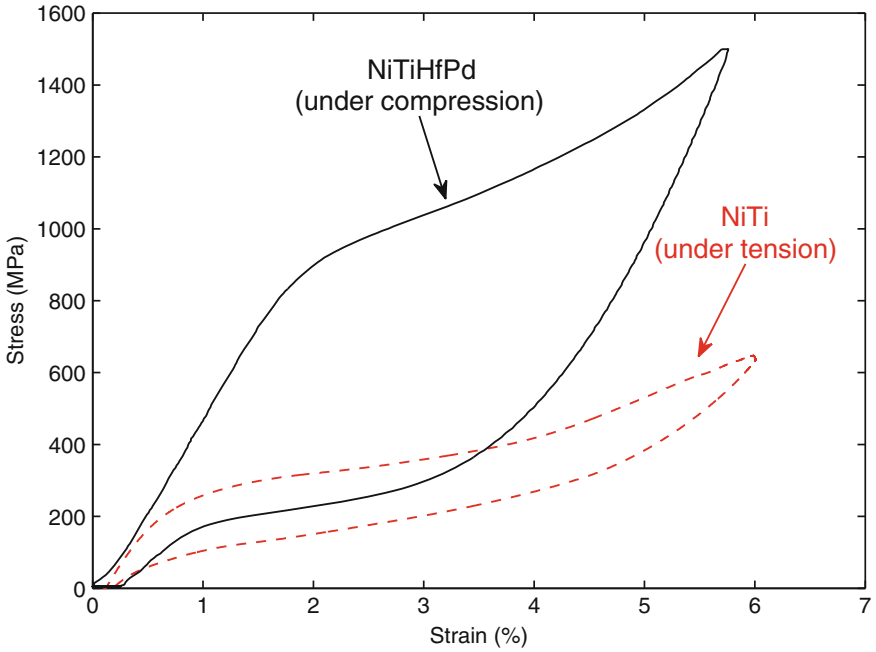


**Fig. 32.1** Strain–stress diagrams for NiTi and NiTiHfPd

Numerous efforts have been carried out to develop new structural systems that can provide stable energy dissipation with full self-centering capabilities [4]. Due to its inherent and excellent re-centering ability, high corrosion and fatigue resistance, several researchers have proposed shape memory alloy (SMA)-based seismic protection systems including, but not limited to, SMA-based bracing systems [5–7]; SMA-based dampers [8–11]; and SMA-based isolation systems [12–16]. Among various SMA compositions, the NiTi alloy has been the most widely studied material for SMA-based dampers. Since NiTi SMAs does not have sufficient energy dissipation capacity to render the use of SMAs as the sole damping device, damping in those devices was supplemented through pre-tensioning SMA elements [17], incorporating a frictional device [18–20], energy-absorbing steel struts [21], viscoelastic device [22, 23], or buckling-restrained braces [24].

A recently developed class of SMAs that consists of NiTiHfPd provides large energy dissipation and high stresses [25] and can overcome the deficiency of currently available SMAs. Figure 32.1 presents typical strain-stress diagrams of NiTi and NiTiHfPd SMAs at room temperature. It can be seen that the area captured within the hysteresis loop, which signifies the dissipated energy, for NiTiHfPd is considerably larger than that of NiTi. The strength of NiTiHfPd is also significantly higher than that of NiTi. Thus, the required cross-sectional area of the SMA elements to develop the design force of a damping device will be considerably smaller for NiTiHfPd. A vibration control device based on NiTiHfPd will avoid employing additional energy dissipation unit and/or requiring large quantities of material due to high energy dissipation capabilities and strength of NiTiHfPd. This study discusses experimental characterization of NiTiHfPd SMAs and conceptual design of a simple but efficient NiTiHfPd SMA-based energy dissipating and re-centering device, which avoids extra fabrication and material costs.

## 32.2 High Damping and High Strength NiTiHfPd SMAs

NiTi SMAs have been studied and employed in a variety of applications due to their superior shape memory properties, corrosion resistance, biocompatibility, ductility, etc. However, they have certain limitations that restrict their functionality for some applications. Alloying is one of the most effective ways to engineer properties and overcome these problems. For instance, an SMA material with good damping capacity needs to have large mechanical hysteresis and transformation strain at high-stress levels to be employed as dampers. While the mechanical hysteresis and damping capacity of binary NiTi alloys has been reported to be 200–400 MPa and 16 J $cm^{-3}$ respectively [26], with the addition of Nb it can be increased to 500–600 MPa and 38 J $cm^{-3}$ [27]. The addition of elements like Zr, Hf, and Pd also has been studied to improve strength, wear resistance and damping capacity of SMAs. Due to its low cost, medium ductility and higher work output, the addition of Hf to NiTi binary found to be the promising [28, 29]. However, one of the main challenges that should be addressed before

NiTiHf alloys can be used in practical applications is their brittleness. Therefore, the addition of a variety of quaternary elements to NiTiHf has been explored in the literature. For example, the addition of Cu to NiTiHf has been found to shrink thermal hysteresis, improve thermal stability, ductility and two-way shape memory effect but no other substantial change has been observed for other shape memory properties of the alloy [30, 31]. The addition of Pd as a quaternary element to NiTiHf alloy has resulted in a significant improvement in the ductility, adjustment of TTs or enhance the shape memory behavior. Toward this goal, Pd can be added in the expense of Ti to increase the transformation temperatures or at the expense of Ni improves superelasticity. Single crystalline NiTiHfPd alloy has been reported to show huge mechanical hysteresis of up to 1270 MPa, superelastic response under extremely high-stress levels (2.5 GPa), and damping capacity of 44 J $cm^{-3}$ [25, 32]. Even polycrystalline NiTiHfPd alloys can generate high work outputs of 32–35 J $cm^{-3}$ (up to 120 °C), which are considerably higher than NiTi and Ni. The ultra high-strength, and the exceptional damping capacity and practical ability to demonstrate superelastic behavior at room temperature makes NiTiHfPd SMAs a great candidate for applications that require high damping. Beside alloying, other most common methods to improve the shape memory and mechanical properties of SMAs are thermomechanical processing (e.g. cold working and post-annealing), precipitate formation, and grain refinement of polycrystalline alloys. However, thermal treatments seem to the most practical and cost-effective method amongst the others. It has been shown that by the formation of precipitates through aging, the strength of the matrix and required critical stress are increased which results in better shape memory response, the fatigue life, and cyclic stability. It should be noted that the strengthening ability of the precipitates depends on the size, volume fraction, antiparticle spacing, and coherency of these particles [33].

## 32.3 Material Characterization

For experiment characterization, Ni-rich single [111] oriented single crystal $Ni_{45.3}Ti_{29.7}Hf_{20}Pd_5$ (at %) and polycrystal $Ni_{45.7}Ti_{29.3}Hf_{20}Pd_5$ (at %) alloys obtained from NASA. Perkin-Elmer Pyris 1 differential scanning calorimetry (DSC), was used to determine the transformation temperatures. Heating–cooling rate was adjusted to 10 °C/min. Aging of the samples was performed using Lindberg/Blue M BF514541 furnace in air atmosphere and then water quenched. The mechanical experiments were performed in an MTS Landmark servo-hydraulic test platform (100 kN) on $8 \times 4 \times 4$ $mm^3$ compression specimens cut by electro-discharge machining. The strain was measured by an MTS high-temperature extensometer with a gage length of 12 mm attached to compression grip faces. A strain rate of $10^{-4}$ $s^{-1}$ was employed during loading of the specimens, while unloading was performed at a rate of 100 N/s. Heating of the specimens was occurred by means of mica band heaters retrofitted to the compression grips, and cooling was achieved through internal liquid nitrogen flow in the compression grips. A heating–cooling rate of 10 °C/min was applied during testing, using an Omega CN8200 series PID temperature controller. K-type thermocouples attached to the test specimens and the compression grips provided real-time temperature feedback.

## 32.4 Results and Discussion

Figure 32.2 demonstrates the superelastic response of [111] oriented single crystal NiTiHfPd. For superelastic experiments, samples were heated up to a temperature well above $A_f$ and loaded up to 2, 4 and 6% strain limit successively and then unloaded. The tests were performed at room temperature since the sample was well-above Af temperature at this temperature. Next sample was loaded until failure to examine the ductility. The critical stress for stress induced martensitic transformation was occurred at about 1300 MPa, and therefore 2% loading did not reach to this point and sample showed a linear behavior. After 4 and 6% deformation, the sample was capable to show full strain recovery at room temperature and mechanical hysteresis was more than 700 MPa at 6% deformation. However, when sample loaded further, it was failed at 1955 MPa and 7.2% deformation without showing the second plateau (for plastic deformation) indicating high brittleness of the sample. As mentioned earlier, it is possible to tailor mechanical properties significantly using thermal treatments. The same alloy has been showed even higher strength as well as higher mechanical hysteresis in homogenized condition (1050 °C–4 h) shown at Fig. 32.3. The homogenized sample shows ultra-high strength with a very wide superelastic window covering from −30 to 50 °C. The critical stress for transformation was more than 1500 MPa at 10 °C. The stress hysteresis was changing from 1270 to 900 MPa and decreasing as a function of critical stress of temperature [25], which is the highest reported hysteresis in NiTi based SMAs literature.

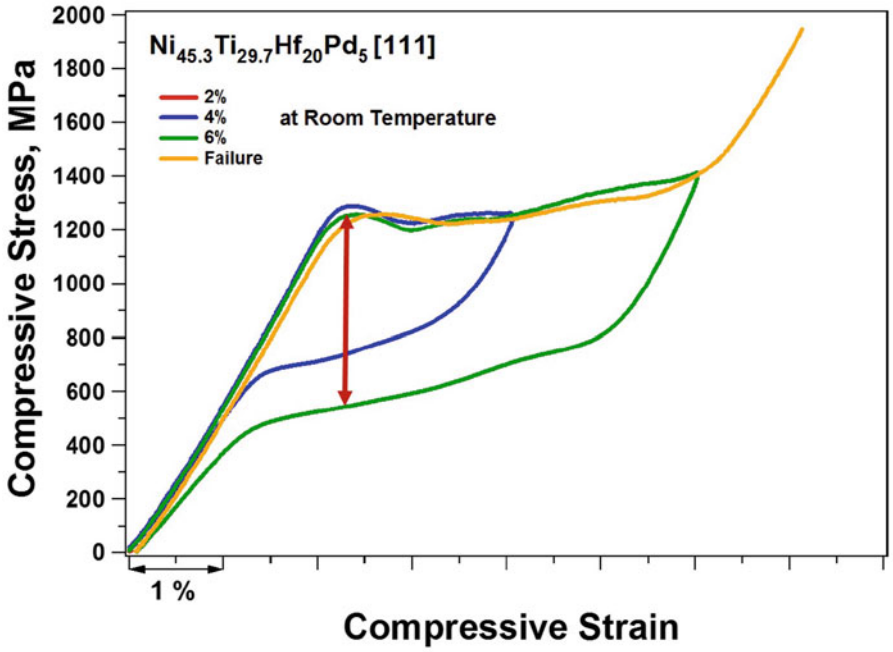


**Fig. 32.2** Superelastic response of [111] oriented single crystal NiTiHfPd—as-received

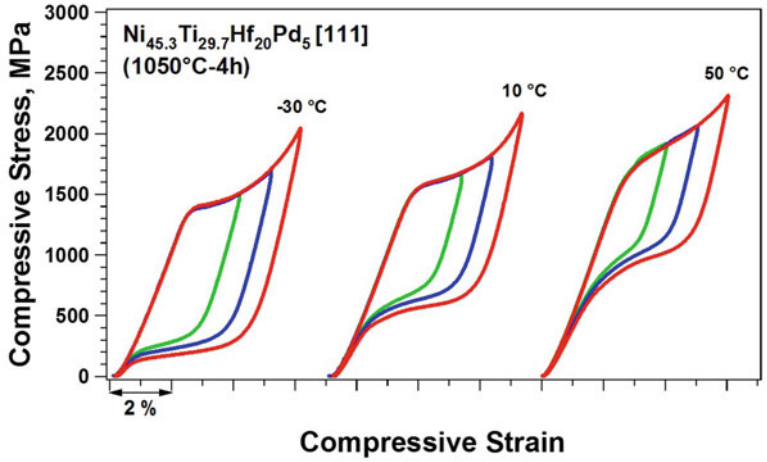


**Fig. 32.3** Superelastic response of [111] oriented single crystal NiTiHfPd in homogenized condition (extracted from [25])

Since single crystal alloys are costlier and difficult to fabricate, polycrystal samples are much more demanding despite their lower strength. However, using precipitation formation through post processing heat treatments, it is possible to improve their characteristics [34]. Figure 32.4 displays the effects of aging time and temperatures on TTs of polycrystal NiTiHfPd samples, aged from 0.5 to 3 h at 350–550 °C. Three heating-cooling cycles have been performed on each sample to find the stabilized TTs. The As-received condition has been included in every figure to ease the comparison. From the Fig. 32.4a, it can be seen that TTs have decreased as a function of time when they aged at 350 °C. A similar trend was observed for samples aged at 450 and 550 °C in Fig. 32.4b, c, however, the decrease is minor. Another important observation is aging at 450 and 550 °C even for 0.5 h causes a huge shift in TTs when compared to the as-received condition. Figure 32.4d compares the samples aged for 3 h at different temperatures. On contrary, TTs were increased as a function of temperature. While Ms and Af temperatures of 350 °C–3 h aged samples were −16 and 27 °C respectively after increasing the aging temperature to 550 °C, they were found to be 189 and 216 °C. The increases in TTs of Ni-rich alloys can be attributed to the formation of large Ni-rich precipitates. These precipitates deplete the matrix from Ni, therefore, TTs are increased [35]. As the aging temperature increases, they grow larger, their volume fraction and inter-particle distance increases, which result in more Ni depletion in the matrix, consequently TTs maintain the increasing trend. Furthermore, internal stress and

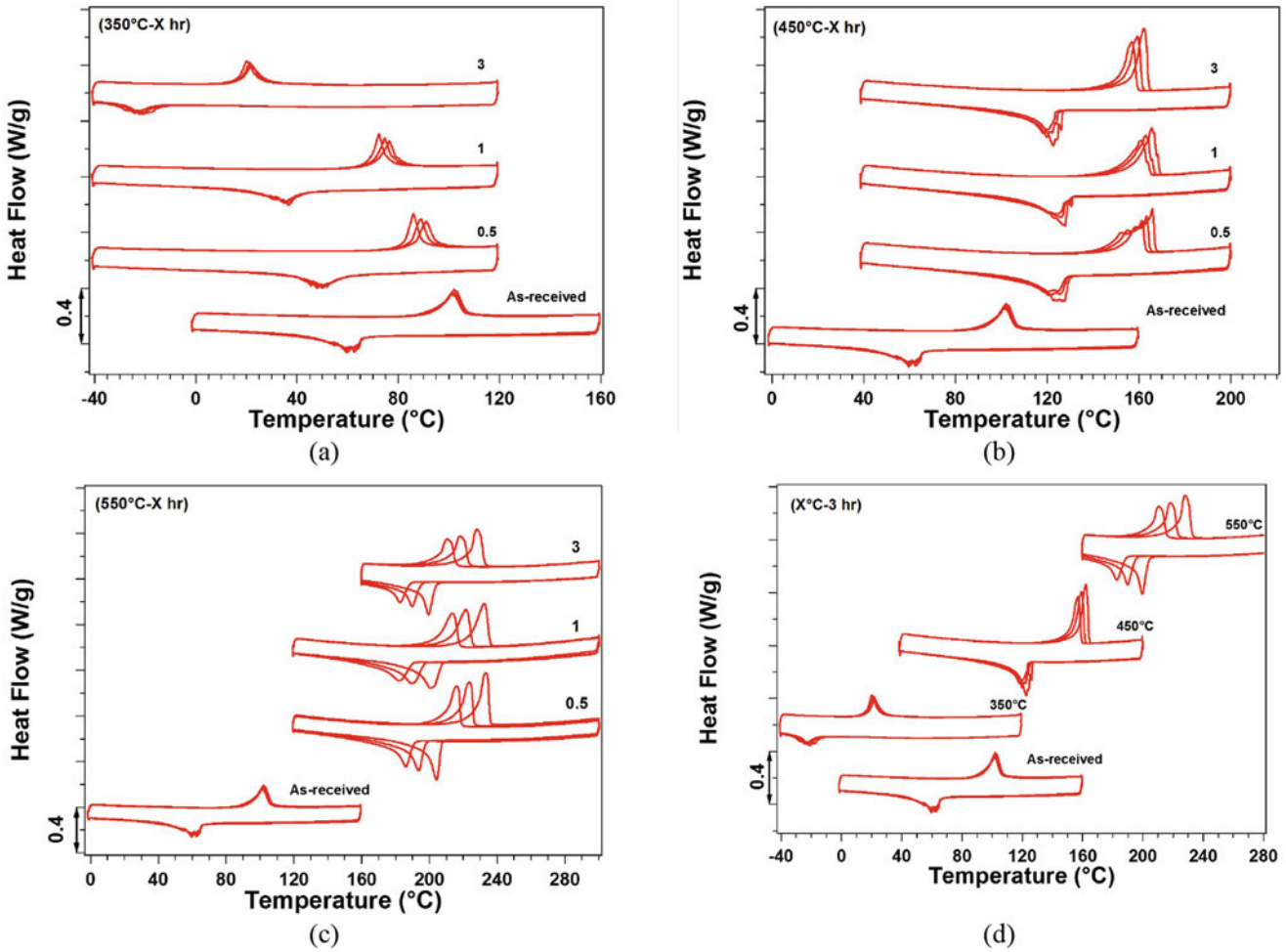


**Fig. 32.4** DSC graphs of poly crustal NiTiHfPd aged at (**a**) 350 °C, (**b**) 450 °C, (**c**) 550 °C and (**d**) 3 h aging comparison

coherency of the formed precipitates are important factors affecting the TTs. The mismatch between matrix and precipitate lattice parameters may cause internal stresses around precipitates that can alter the TTs. Therefore, increasing of the formed precipitates coherency with aging temperatures that causes higher internal stresses can be named as the second reason for increase in TTs. The drop of TTs for 350 °C aging again can be attributed to the formation of precipitates with very small size and short interparticle distance. Thus, the resistance for martensite nucleation was increased and formation of martensite required additional energy change, which in turn required further undercooling in the course of the forward transformation.

Figure 32.5a, b show the superelastic response of NiTiHfPd alloy in as-received and 450 °C–10 h aged conditions, respectively. To avoid further plastic deformation aged sample was loaded up to 5% at last cycle. It can be seen from Fig. 32.4a that in as-received condition sample can display only 2% full recovery and further deformation results in irrecoverable strain. On the other hand, 450 °C–10 h aged sample as shown in Fig. 32.4b showed almost full strain recovery even after 4% deformation. The irrecoverable strain was only 0.65 after 5% deformation. When these condition are compared, it is observed that even though critical stress for stress-induced martensitic transformation occurred at higher stress level for as-received samples than aged samples, strain hardening with a sharp slope was observed after plateau, which causes a plastic deformation of the sample. It is noteworthy that as-received sample also shows a very low energy dissipation, resulting in very narrow stress hysteresis while aged sample showed about 300 MPa stress hysteresis after 2% deformation, which was increased to about 600 MPa when deformed 4%.

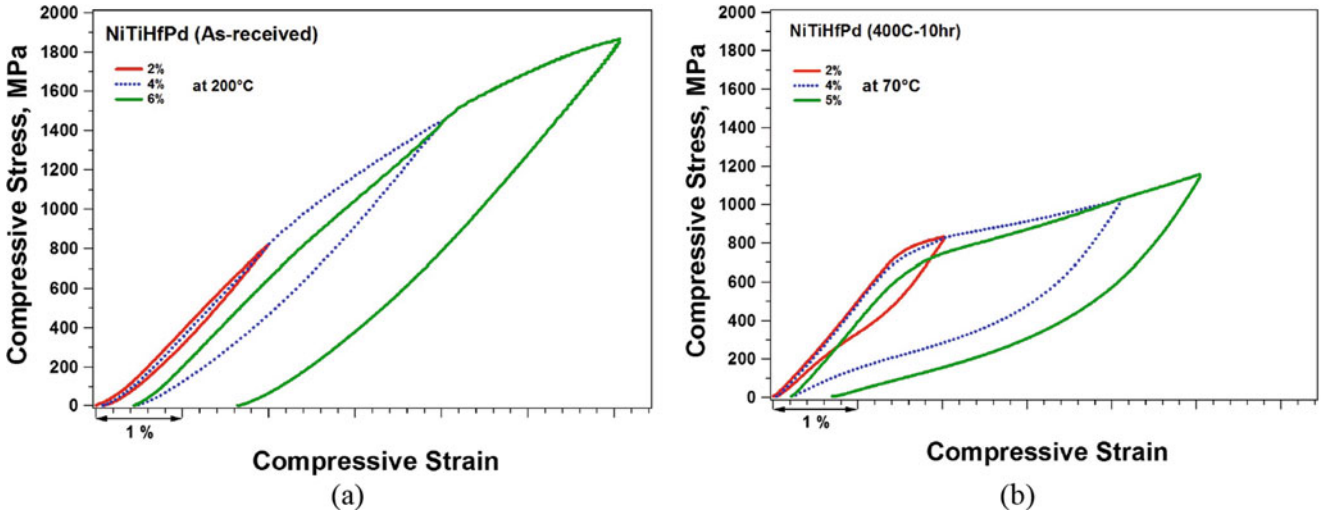


**Fig. 32.5** Superelastic response of NiTiHfPd (**a**) As-received, (**b**) aged 450 °C–10 h

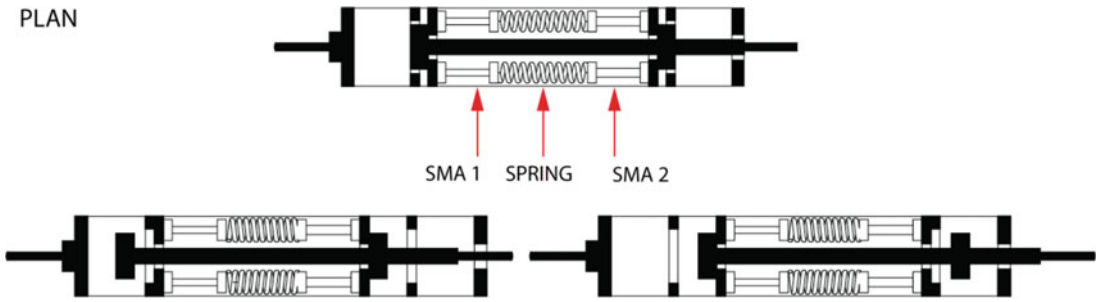


**Fig. 32.6** Plan view of SMARD at its original and displaced positions

## 32.5 Shape Memory Alloy-Based Re-centering Damper

By exploiting the advantageous characteristics of NiTiHfPd SMAs, a new passive vibration device is proposed in this study. The device is named as Shape Memory Alloy-based Re-centering Damper or SMARD. Figure 32.6 shows plan and longitudinal view of the SMARD at its original and displaced positions to describe its operating principle. A three-dimensional rendering of the device is also shown in the Fig. 32.7. The SMARD comprises a SMA-Spring assembly (rendered in yellow), a piston (gray), and an enclosure (black) with rigidly attached baffle plates. The high force steel springs between SMA groups ensure large displacements under load while simultaneously transmitting the force between SMA groups. Voids in the centers of the baffle plates allow the piston to pass through freely while arresting the otherwise free-traveling SMA-Spring assembly. Note that NiTiHfPd SMAs exhibit better superelastic response under compression. Therefore, the device is designed such that whether the piston is drawn out of or forced into the device, the SMA-Spring assembly will undergo compression. Due to the inherent superelastic behavior of NiTiHfPd SMAs, the SMARD can exhibit excellent re-centering ability with enhanced energy dissipation capacity.

In addition, SMA bars with up to four different diameters can be incorporated to the device. That will enable device to produce a damping force that ensures sufficient energy dissipation for various levels of excitation. The SMARD is illustrated with two different diameter bars (SMA1 and SMA2) in Fig. 32.6. As a result of arrangement of SMA bars in the device and inherent re-centering behavior of SMAs, a properly designed SMARD will exhibit a re-centering and energy dissipating behavior during all modes of vibrations under both wind and earthquake excitations. During a weak to moderate event, the SMA bars with lower stiffness will experience relatively larger compressive strains and dissipate the energy while the stiffer SMA bars will undergo small strains. During a moderate to strong event, both SMA groups will engage and dissipate large amounts of energy, and the device will provide a larger damping force. During an extreme event, the SMARD will stiffen due to second stiffening of SMA bars under large strains. This additional stiffening will avoid potentially catastrophic structural displacements even under unforeseen strong ground motions.

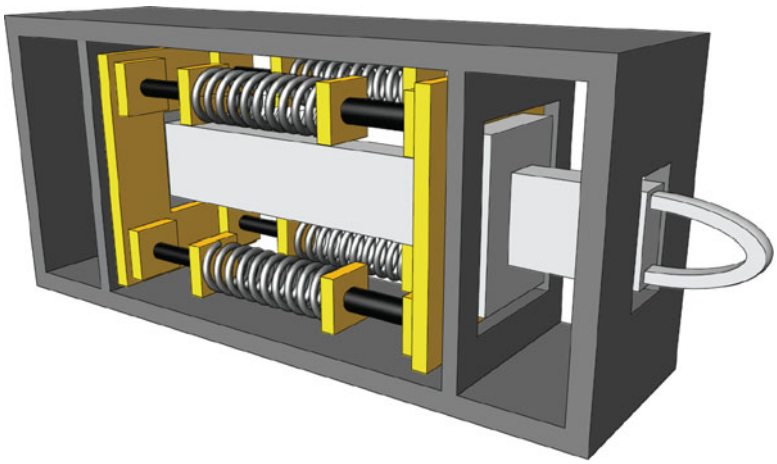

**Fig. 32.7** Three-dimensional rendering of SMARD

## 32.6 Conclusions

This study proposes a new passive vibration control device that incorporates high performance superelastic shape memory alloys. These new superelastic SMAs consist of recently developed NiTiHfPd alloys that have very high strength, high dissipation/damping capacity, good cyclic stability and large operating temperature. Superelastic response of a single crystal NiTiHfPd was briefly discussed. Then, a systematic study was conducted to evaluate the mechanical response of polycrsytal NiTiHfPd SMAs. In particular, differential scanning calorimetry (DSC) was used to determine the effect of aging time and temperature on transformation temperatures. Compressive tests were conducted to reveal the superelastic response of polycrsytal NiTiHfPd alloy in as-received and 450 °C–10 h aged conditions. The results obtained from these initial experimental efforts suggest that polycrystal NiTiHfPd SMAs can also exhibit a superelastic response at very high stress levels and with a large hysteresis loop. However, further investigations will be conducted to determine the effects of heat treatments on transformation temperatures and provide the ability to tailor the microstructure to get superelastic behavior at a temperature range of −20 to 50 °C. Once the material characteristics of polycrystalline NiTiHfPd are optimized, a prototype of the proposed SMARD device will be fabricated and tested.

**Acknowledgements** This material is based upon the work supported by the National Science Foundation under Grant Number CMMI-1538770.

## References

1. Symans, M.D., Charney, F.A., Whittaker, A.S., Constantinou, M.C., Kircher, C.A., Johnson, M.W., McNamara, R.J.: Energy dissipation systems for seismic applications: current practice and recent developments. J. Struct. Eng. **134**(1), 3–21 (2008)
2. Soong, T.T., Dargush, G.F.: Passive Energy Dissipation System Structural Engineering. Wiley, Chichester (1997)
3. Marshall, J.D., Charney, F.A.: Seismic response of steel frame structures with hybrid passive control systems. Earthq. Eng. Struct. Dyn. **41**(4), 715–733 (2012)
4. Chancellor, N.B., Eatherton, M.R., Roke, D.A., Akbaş, T.: Self-centering seismic lateral force resisting systems: high performance structures for the city of tomorrow. Buildings. **4**(3), 520–548 (2014)
5. Ozbulut, O.E., Mir, C., Moroni, M.O., Sarrazin, M., Roschke, P.N.: A fuzzy model of superelastic shape memory alloys for vibration control in civil engineering applications. Smart Mater. Struct. **16**, 818–829 (2007)
6. Qiu, C.X., Zhu, S.: Performance-based seismic design of self-centering steel frames with SMA-based braces. Eng. Struct. **130**, 67–82 (2017)
7. Gao, N., Jeon, J.S., Hodgson, D.E., DesRoches, R.: An innovative seismic bracing system based on a superelastic shape memory alloy ring. Smart Mater. Struct. **25**(5), 055030 (2016)
8. Ozbulut, O.E., Roschke, P.N., Lin, P.Y., Loh, C.H.: GA-based optimum design of a shape memory alloy device for seismic response mitigation. Smart Mater. Struct. **19**, 065004 (2010)
9. Ozbulut, O.E., Hurlebaus, S.: Application of an SMA-based hybrid control device to 20-story nonlinear benchmark building. Earthq. Eng. Struct. Dyn. **41**, 1831–1843 (2012)
10. Mishra, S.K., Gur, S., Chakraborty, S.: An improved tuned mass damper (SMA-TMD) assisted by a shape memory alloy spring. Smart Mater. Struct. **22**(9), 095016 (2013)

11. Parulekar, Y.M., Kiran, A.R., Reddy, G.R., Singh, R.K., Vaze, K.K.: Shake table tests and analytical simulations of a steel structure with shape memory alloy dampers. Smart Mater. Struct. **23**(12), 125002 (2014)
12. Ozbulut, O.E., Hurlebaus, S.: A comparative study on seismic performance of superelastic-friction base isolators against near-field earthquakes. Earthq. Spectra. **28**, 1147–1163 (2012)
13. Ozbulut, O.E., Hurlebaus, S.: Energy-balance assessment of shape memory alloy-based seismic isolation devices. Smart Struct. Syst. **8**, 399–412 (2011)
14. Ozbulut, O.E., Hurlebaus, S.: Seismic assessment of bridge structures isolated by a shape memory alloy/rubber-based isolation system. Smart Mater. Struct. **20**, 015003 (2011)
15. Dezfuli, F.H., Alam, M.S.: Shape memory alloy wire-based smart natural rubber bearing. Smart Mater. Struct. **22**(4), 045013 (2013)
16. Ghodke, S., Jangid, R.S.: Influence of high austenite stiffness of shape memory alloy on the response of base isolated benchmark building. Struct. Control Health Monit. **24**, e1867 (2016). doi:10.1002/stc.1867
17. Dolce, M., Cardone, D., Marnetto, R.: Implementation and testing of passive control devices based on shape memory alloys. Earthq. Eng. Struct. Dyn. **29**, 945–968 (2000)
18. Zhu, S., Zhang, Y.: Seismic behaviour of self-centring braced frame buildings with reusable hysteretic damping brace. Earthq. Eng. Struct. Dyn. **36**, 1329–1346 (2007)
19. Ozbulut, O.E., Hurlebaus, S.: Re-centering variable friction device for vibration control of structures subjected to near-field earthquakes. Mech. Syst. Signal Process. **25**, 2849–2862 (2011)
20. Ozbulut, O.E., Bitaraf, M., Hurlebaus, S.: Adaptive control of base-isolated structures against near-field earthquakes using variable friction dampers. Eng. Struct. **33**, 3143–3154 (2011)
21. Yang, C.W., DesRoches, R., Leon, R.T.: Design and analysis of braced frames with shape memory alloy and energy-absorbing hybrid devices. Eng. Struct. **32**, 498–507 (2010)
22. Silwal, B., Michael, R.J., Ozbulut, O.E.: A superelastic viscous damper for enhanced seismic performance of steel frame structures. Eng. Struct. **105**, 152–164 (2015)
23. Silwal, B., Ozbulut, O.E., Michael, R.J.: Seismic collapse evaluation of steel moment resisting frames with superelastic viscous damper. J. Constr. Steel Res. **126**, 26–36 (2016)
24. Miller, D.J., Fahnestock, L.A., Eatherton, M.R.: Development and experimental validation of a nickel–titanium shape memory alloy self-centering buckling-restrained brace. Eng. Struct. **40**, 288–298 (2012)
25. Karaca, H., et al.: Superelastic response and damping capacity of ultrahigh-strength [111]-oriented NiTiHfPd single crystals. Scripta Mater. **67**(5), 447–450 (2012)
26. Otsuka, K., Ren, X.: Physical metallurgy of Ti–Ni-based shape memory alloys. Prog. Mater. Sci. **50**(5), 511–678 (2005)
27. Tanaka, Y., et al.: Ferrous polycrystalline shape-memory alloy showing huge superelasticity. Science. **327**(5972), 1488–1490 (2010)
28. Karaca, H., et al.: Compressive response of nickel-rich NiTiHf high-temperature shape memory single crystals along the [111] orientation. Scripta Mater. **65**(7), 577–580 (2011)
29. Karaca, H., et al.: NiTiHf-based shape memory alloys. Mater. Sci. Technol. **30**(13), 1530–1544 (2014)
30. Liang, X., et al.: Thermal cycling stability and two-way shape memory effect of Ni–Cu–Ti–Hf alloys. Solid State Commun. **119**(6), 381–385 (2001)
31. Meng, X.L., et al.: Martensite structure in Ti–Ni–Hf–Cu quaternary alloy ribbons containing (Ti,Hf)2Ni precipitates. Acta Mater. **58**(10), 3751–3763 (2010)
32. Karaca, H., et al.: Effects of aging on [111] oriented NiTiHfPd single crystals under compression. Scripta Mater. **67**(7), 728–731 (2012)
33. Saedi, S., et al.: The influence of heat treatment on the thermomechanical response of Ni-rich NiTi alloys manufactured by selective laser melting. J. Alloys Compd. **677**, 204–210 (2016)
34. Turabi, A.S., et al.: Experimental characterization of shape memory alloys. In: Elahinia, M. (ed.) Shape Memory Alloy Actuators: Design, Fabrication and Experimental Evaluation, pp. 239–277. Wiley (2015)
35. Saedi, S., et al.: Thermomechanical characterization of Ni-rich NiTi fabricated by selective laser melting. Smart Mater. Struct. **25**(3), 035005 (2016)

# Chapter 33
# Comparative Study on Modal Identification of a 10 Story RC Structure Using Free, Ambient and Forced Vibration Data

**Seyedsina Yousefianmoghadam, Andreas Stavridis, and Babak Moaveni**

**Abstract** In this study the modal parameters of a ten-story reinforced concrete (RC) building are estimated from recordings of free, ambient, and forced vibrations, using the eigensystem realization algorithm (ERA), the natural excitation technique combined with the eigensystem realization algorithm (NExT-ERA), and peak-picking method, respectively. The structure vibrated freely after it was hit the by a jack hammer used to demolish selected perimeter walls in the second story. The forced vibrations were induced using a portable eccentric mass shaker installed on the second story of the structure. The results obtained from the three methods indicate that the free vibration recordings can provide an accurate estimation of the modal parameters of the structure at lower identification order and with reduced computational cost compared to the NExT-ERA method applied on the ambient vibration recordings.

**Keywords** System identification • Impulse response • Dynamic testing • Comparative study • RC structure

## 33.1 Introduction

Methods to assess the condition of existing structures using vibration-based diagnostic methods are proposed in a number of studies [1–3]. In these studies, the considered vibrations can be caused by ambient excitations such as wind, nearby vehicular or pedestrian traffic [4–11] or by controlled excitations induced by an impact hammer, a shaker, a shake table, a truck, or a jack [12–17]. In terms of the considered structures, these include actual buildings and bridges, as well as large-scale laboratory specimens, with the majority being laboratory specimens since the dynamic testing of actual structures is not common due to the practical implications and risks involved with such tests.

This paper discusses the modal identification of free, ambient, and forced vibration tests on a 10-story reinforced concrete (RC) building at four damage states. The damage states were induced through the demolition of infill walls in the perimeter which was permitted since the structure was to be demolished. The demolition of the walls with an impact hammer induced high amplitude impulses followed by the free vibration of the building. Moreover, harmonic excitations were induced to the structure using a portable shaker. The dynamic properties of the building at each damage state are identified from the free vibration data using the eigensystem realization algorithm (ERA), the ambient vibrations using the natural excitation technique combined with the eigensystem realization algorithm (NExT-ERA), and the forced vibrations using the peak-picking method. The comparison of the dynamic properties obtained from the three types of excitation indicates that all of the methods can provide accurate results, with varying computational costs. Finally, a parametric study using the NExT-ERA method is also performed to investigate the effect of the number and location of selected reference channels on the estimated modal parameters.

S. Yousefianmoghadam (✉)
University at Buffalo, 116 Ketter Hall, Buffalo, NY 14260, USA
e-mail: seyedsin@buffalo.edu

A. Stavridis
University at Buffalo, 224 Ketter Hall, Buffalo, NY 14260, USA

B. Moaveni
Tufts University, Medford, MA, USA



J. Caicedo, S. Pakzad (eds.), *Dynamics of Civil Structures, Volume 2*, Conference Proceedings
of the Society for Experimental Mechanics Series, DOI 10.1007/978-3-319-54777-0_33

**Fig. 33.1** Test structure (view from west side)

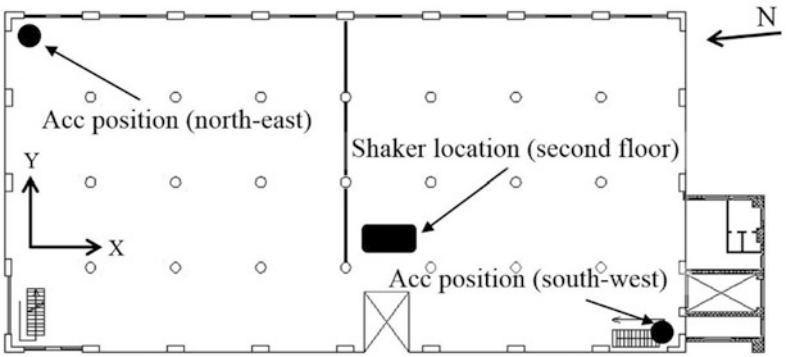


**Fig. 33.2** Second floor plan view showing extension building and acceleration positions

## 33.2 Test Structure

The structure, shown in Fig. 33.1, was a 10-story reinforced concrete (RC) structure with a slab-column structural system and RC infills in the exterior frames. The building was built in 1910s in Utica, NY and characterized by overall length of 48.8 m (160 ft), width of 24.4 m (80 ft), and height of 25.9 m (85 ft).

The plan view of the second floor can be seen in Fig. 33.2. This is similar to the plan view of other floors. On the south side of the building, a five-story clay masonry structure was attached to it to house an elevator shaft and service rooms. More detailed information about the structure can be found in [18].

## 33.3 Dynamic Testing

### *33.3.1 Damage States*

During the testing sequence, six exterior RC walls were removed from the second and third stories of the structure to simulate damage. The walls were removed, two at a time, in three stages, as shown in Fig. 33.3a, introducing four damage states. The first damage state (DS0) was the condition of the structure at the beginning of the tests in which the exterior walls in the first, second, and fifth stories, in the north, west, and south sides were removed for demolition purposes. The second damage state

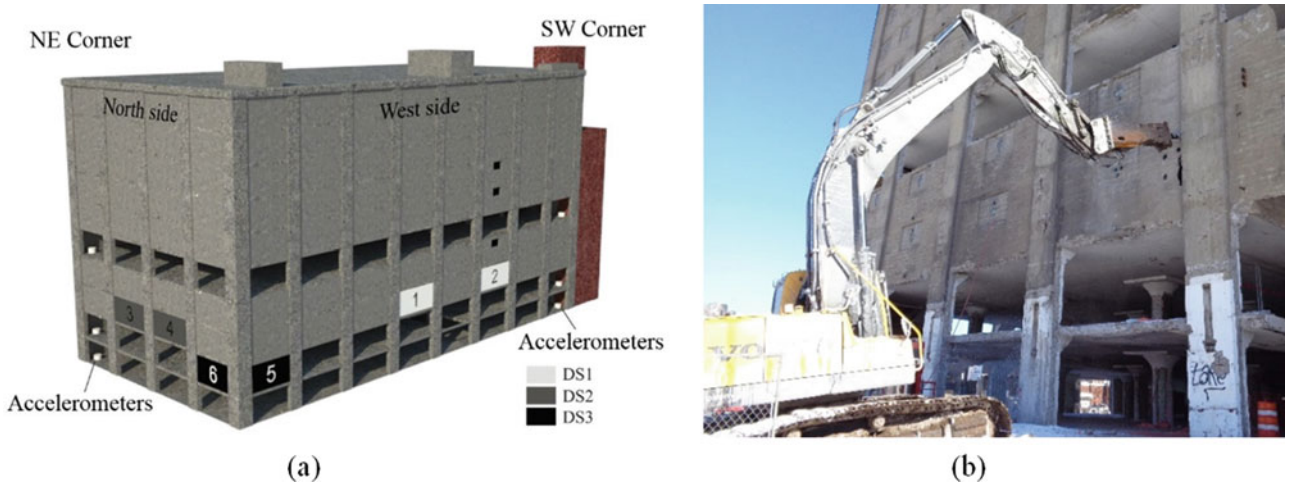


**Fig. 33.3** Wall removal and damage states. (**a**) Structure initial condition and damage states. (**b**) Wall removal using jack hammer

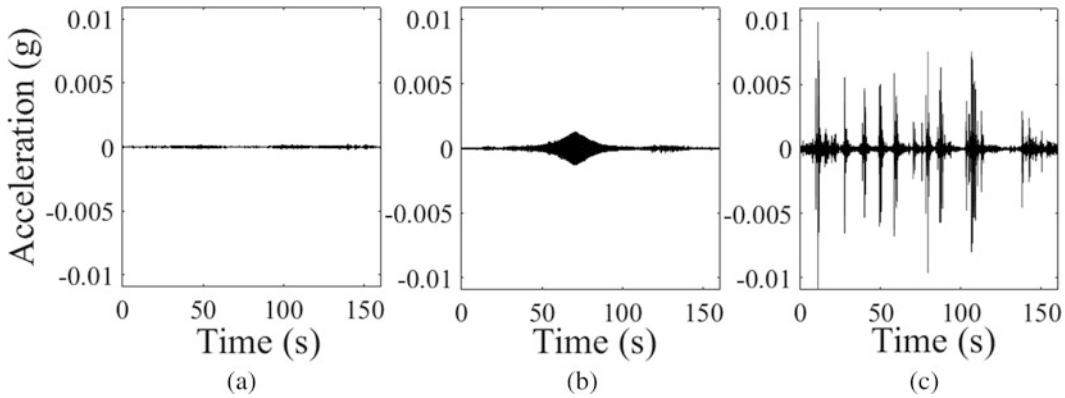


**Fig. 33.4** Example of the time history responses for different excitation types recorded at 10th floor. (**a**) Ambient vibration. (**b**) Forced vibration (sine sweep). (**c**) Wall demolition in 2nd story

(DS1) resulted from the removal of two walls in the western exterior frame on the third story. The third state of damage (DS2) occurred from the removal of two walls in the northern exterior frame on the third story. The fourth and final damage state (DS3) occurred after the demolition of walls in the north-west corner of the second story. The wall removal was achieved using a jack hammer installed on an excavator as shown in Fig. 33.3b.

### *33.3.2 Testing Method and Sequence*

A series of dynamic tests were performed on the building using a mobile shaker bolted to the second floor slab in a location eccentric along the Y axis as shown in Fig. 33.2. The harmonic excitations induced by the shaker were sine sweeps, sine steps, and sine dwells around the identified natural frequencies. More details about the dynamic tests are available in [19]. This study focuses on the sine sweeps and the excitations due to the jack hammer impacts to the exterior RC walls of the structure during the demolition process. Figure 33.4 shows the sample response of the structure recorded at the 10th floor. It can be seen that accelerations induced during the demolition were significantly larger compared to those induced during the forced vibrations using the shaker.

### *33.3.3 Instrumentation*

The accelerations along the vertical and the two horizontal directions at two locations of every slab were recorded with force-balance accelerometers. As indicated in Figs. 33.2 and 33.3, the accelerometers were installed near the NW and SE corners on all stories except for the roof due to safety reasons. This configuration was selected so that the translational, as well as the torsional motion of the structure could be monitored. The data logger used in this study could record accelerations between 0.5 μg and 2 g. The sampling rate was 200 Hz and all accelerometers were synchronized by GPS timing having less than 1 milli-second accuracy [19]. During the testing period, the data acquisition system was continuously recording for 56 h. Hence, the ambient vibrations of the building were recorded, as well as the forced vibrations and the free vibrations.

## 33.4 System Identification

The Eigensystem Realization Algorithm (ERA) and the Natural Excitation Technique combined with the Eigensystem Realization Algorithm (NExT-ERA) are used to estimate the modal properties using the free vibration and ambient measurements respectively. The peak-picking method is used to obtain the modal properties of the building from the transfer function of the force vibrations due to the sine sweep excitations. The modal properties of the test structure are estimated at each damage state using all data sets.

The free vibrations following each impulse were extracted from the recordings. They include, on average, 9 s of the response after the impulse. Since these excitations were induced during the wall demolition, only the free vibrations at the beginning and end of each wall demolition stage are considered here. At the beginning of each wall demolition phase, the vibrations following each hit of the hummer are attributed to the previous damage state while the vibrations towards the end of the demolition are attributed to the following damage state. Figure 33.5 shows an example of free vibration acceleration time history. A total of 60 free vibration sets are obtained.

The obtained records are filtered in the frequency range between 0.2 and 20 Hz using a finite response filter of order 8192 and they are then down-sampled from 200 to 50 Hz. A block Hankel matrix of (40 × 200) × (50 × signal duration) is used for the Eigensystem Realization Algorithm. Table 33.1 summarizes the cases considered here.

In the case of ambient recordings, continuous acceleration recordings of 12 to 15 min are considered. The recordings are filtered and down sampled as those obtained from the free vibrations. The auto- and cross-correlation of signals are estimated as the inverse Fourier transformation of the power and cross spectral densities which are calculated using the Welch method [20]. The spectral densities are averaged over 72-s long windows with 50% overlap to mitigate the effects of noise while a Hanning function [21] is used to eliminate the effects of window leakage. To investigate the effect of the number and location of reference channels, six combinations of reference channels are considered in this study. Once the auto/cross correlations

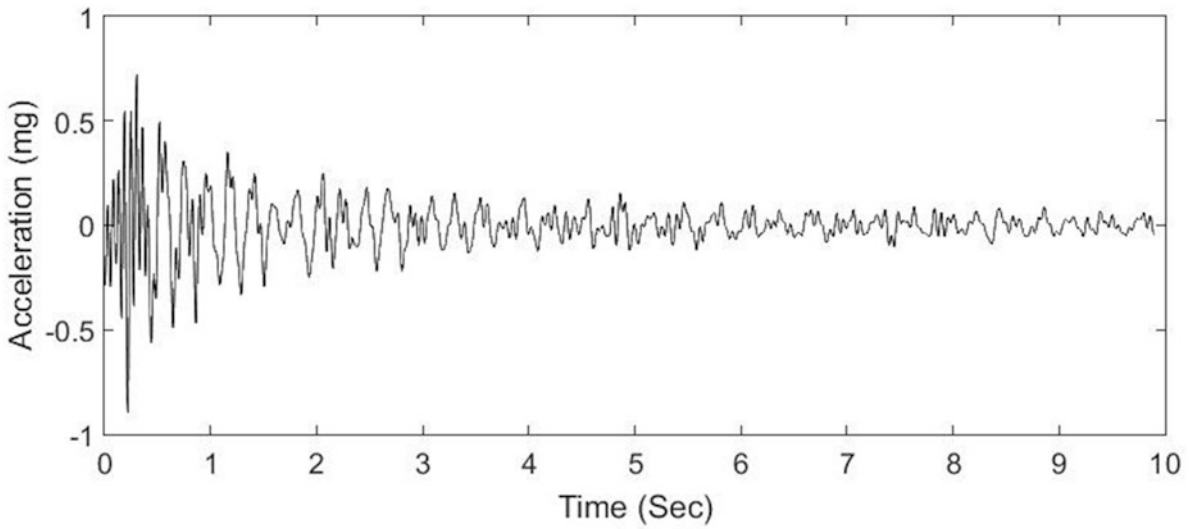


**Fig. 33.5** Acceleration time history of a free vibration measured on the 10th floor at the NE corner

**Table 33.1** Summary of free vibration measurements properties

| Damage state | Number of recordings | Signal duration range (s) | Impulse direction | Max. acceleration range in all 40 channels (mg) |
|---|---|---|---|---|
| DS0 | 12 | 6–25 | Y | 1.5–15 |
| DS1 | 12 | 8–14 | Y | 1.2–14.5 |
| DS2 | 17 | 6–10 | X | 0.4–4.66 |
| DS3 | 19 | 5–12 | X | 0.5–28 |

**Table 33.2** Cases studied for NexT-ERA method

| Case # | # of reference channels | Location of reference channels | Reference channel measurement direction(s) |
|---|---|---|---|
| 1 | 4 | 10th floor: SW and NE corners | X and Y |
| 2 | 2 | 10th floor: SW corner | X and Y |
| 3 | 1 | 10th floor: SW corner | X |
| 4 | 1 | 10th floor: SW corner | Y |
| 5 | 1 | 5th floor: SW corner | Y |
| 6 | 1 | 1st floor: SW corner | X |

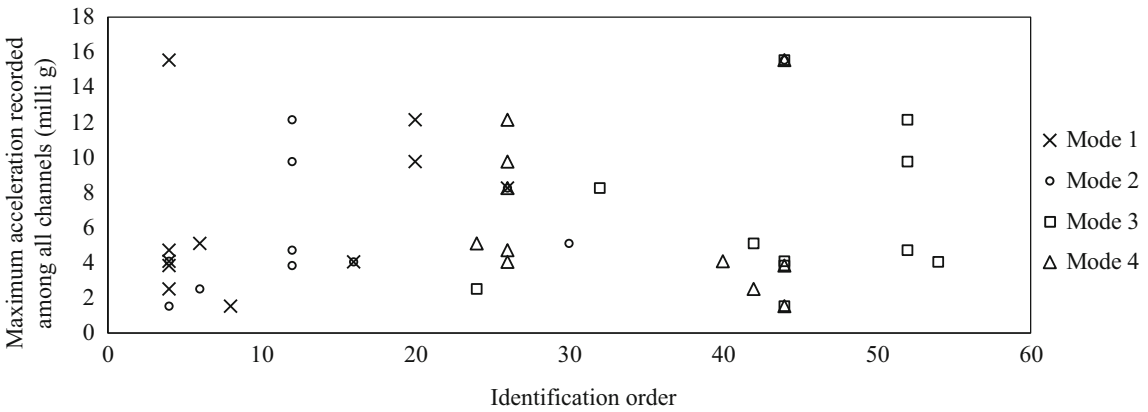


**Fig. 33.6** Identification order dependency on maximum acceleration of the free vibration measurements in Y direction at DS0

are estimated, they are used to form a block Hankel matrix of (40 × 200) × ((50 × 72) × (# of reference channels)). Table 33.2 presents the cases considered in this study.

For the forced vibration recordings the power spectral densities (PSD) of the acceleration measurements are estimated using the Welch method. The signals are averaged over Hamming windows of 8000 points and 50% window overlap. The PSDs are used to obtain the transfer functions. The acceleration measurements in X and Y directions at the SW corner of the 2nd floor are considered as the input excitation due to the proximity to the shaker.

### *33.4.1 Identification Orders and Stabilization Diagrams*

According to a previous study on system identification of the same structure [19], the first mode of the structure is identified at an order of 130 at DS0. Therefore, the system identification process for both ambient vibration and free vibration measurements is performed up to the order of 150. Figure 33.6 illustrates the identification order for the first four modes of the structure plotted against the maximum acceleration recorded among all of the 40 channels during the free vibration response at DS0 using the ERA method. Typically, identification orders as low as 10 are sufficient to identify the first two modes, and orders between 20 and 30 are sufficient for modes 3 and 4. It can be also observed in Fig. 33.6 that in the case of free vibrations no relation can be established between the identification order and the amplitude of the impulse excitations.

The identification orders from the ambient vibration are compared to the average order needed in the analysis of the free vibration recordings at DS0 in Fig. 33.7. It can be observed that the identification orders are much higher using the ambient vibration data for modes 1–3 in all cases of reference channels considered for the first three modes, and in a few cases the modes are not identified at all. The difficulty in identifying the modes in lower system orders may be caused by processing of the signal used to convert the ambient vibration to free vibration as discussed in a previous section. This process is based on the assumption that the signal is broadband excitation which is not accurate. The unavoidable error in this simplifying

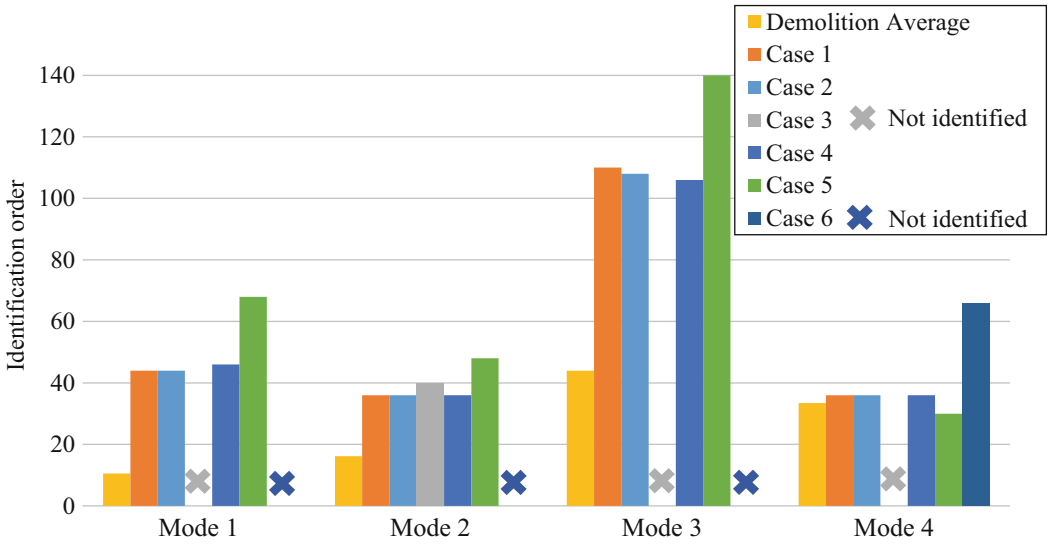


**Fig. 33.7** Comparison of identification orders between the studied cases

assumption along with the computational error added to the system identification because of the conversion process can increase the identification order and required computational resources.

Figure 33.7 also demonstrates the importance of the number and location of the reference channels in the modal identification of ambient vibration recordings using NExT-ERA method. When four, two, or one reference channels at the 10th floor are considered in cases 1, 2, and 4, respectively, the identification order slightly increases as the number of reference channels decreases. However, the computational time needed to run the identification algorithm increases significantly by increasing the number of reference channels as the Henkel matrix size is proportional to the number of channels. Case 5 which considers one reference channel at the fifth floor requires a higher identification order than case 4 which includes one reference channel in the 10th floor. This can be attributed to the fact that the higher floors experience more motion which increases the signal-to-noise ratio.

In case 3, which considers one reference channel at the 10th floor measuring the acceleration in a direction perpendicular to the that of case 4 (X-direction), only mode 2 can be identified at DS0. This can also be observed in Table 33.3 which summarizes the identification order of the considered cases at all damage states. In all damage states, case 3 identifies modes in higher orders than those of case 4. As shown in Fig. 33.8, which illustrates the mode shapes of the structure, the reference channel selected for case 3 (X-direction in the South-West corner at the 10th floor) has a relatively small modal component in all modes except for mode 2. Therefore, if this channel is used as a reference, the relatively low signal-to-noise ratio in the free vibrations is produced from the NExT process. Case 6 which uses reference signal obtained from an accelerometer in the first floor at the direction with small modal components, combines the drawbacks of cases 3 and 5. This results in the highest identification orders among all the considered cases.

### *33.4.2 Modal Frequencies and Mode Shapes*

Table 33.3 also presents the identified natural frequencies of the building for all considered cases. The values match well between cases 1, 2, and 4 with maximum difference within 1%. In cases 3, 5, and 6 the results are more scattered; however, the difference is not considerable. One can note that the natural frequencies identified from the free vibration measurements are lower than those obtained from the recordings of ambient and forced vibrations. This difference can be attributed to the level of motion of the structure as reflected in the acceleration amplitude. As shown in Fig. 33.4, the acceleration of the structure after the jack hammer impulses has a higher amplitude than those resulted from forced and ambient vibrations. The higher amplitude causes opening of minor cracks which reduce the overall stiffness of the structure and therefore the identified natural frequencies. This can be also seen in Fig. 33.9 which presents the identified natural frequency at different damage states for the first two modes of the structure using the different data sets. In all cases, the identified frequencies indicate the same frequency change between the damage states.

Figure 33.8 presents the mode shapes obtained from the average of the free vibration, ambient vibration in cases 1, 2, and 4, and the forced vibration measurements. The modal assurance criterion (MAC) [22] values are also calculated using

**Table 33.3** Summary NExT-ERA system identification on ambient vibration measurements

| Damage state | Mode | Ambient vibration case | | | | | | | | | | | | Free vibration | | Forced vibration |
|---|---|---|---|---|---|---|---|---|---|---|---|---|---|---|---|---|
| | | 1 | | 2 | | 3 | | 4 | | 5 | | 6 | | | | |
| | | Identification order | Frequency (Hz) | Identification order | Frequency (Hz) | Identification order | Frequency (Hz) | Identification order | Frequency (Hz) | Identification order | Frequency (Hz) | Identification order | Frequency (Hz) | Average identification order | Average frequency (Hz) | Average frequency (Hz) |
| DS0 | 1 | 44 | 2.26 | 44 | 2.26 | N/I[a] | N/I[a] | 46 | 2.24 | 68 | 2.26 | N/I[a] | N/I[a] | 11 | 2.23 | 2.23 |
| | 2 | 36 | 3.34 | 36 | 3.34 | 40 | 3.31 | 36 | 3.34 | 48 | 3.35 | N/I[a] | N/I[a] | 16 | 3.31 | 3.32 |
| | 3 | 110 | 4.69 | 108 | 4.69 | N/I[a] | N/I[a] | 106 | 4.68 | 140 | 4.69 | N/I[a] | N/I[a] | 44 | 4.65 | 4.66 |
| | 4 | 36 | 7.37 | 36 | 7.37 | N/I[a] | N/I[a] | 36 | 7.36 | 30 | 7.32 | 66 | 7.35 | 33 | 7.35 | N/A |
| DS1 | 1 | 14 | 2.24 | 14 | 2.24 | 84 | 2.26 | 14 | 2.25 | 24 | 2.24 | 88 | 2.25 | 13 | 2.21 | 2.23 |
| | 2 | 42 | 3.33 | 42 | 3.33 | 78 | 3.30 | 42 | 3.32 | 54 | 3.34 | 144 | 3.33 | 24 | 3.26 | 3.30 |
| | 3 | 42 | 4.71 | 44 | 4.67 | 76 | 4.73 | 42 | 4.72 | 56 | 4.72 | 80 | 4.71 | 35 | 4.70 | 4.71 |
| | 4 | 34 | 7.37 | 38 | 7.37 | 50 | 7.31 | 48 | 7.37 | 94 | 7.36 | N/I[a] | N/I[a] | 35 | 7.32 | N/A |
| DS2 | 1 | 22 | 2.19 | 22 | 2.18 | N/I[a] | N/I[a] | 22 | 2.18 | 24 | 2.18 | 88 | 2.20 | 21 | 2.16 | 2.17 |
| | 2 | 16 | 3.25 | 16 | 3.25 | 18 | 3.25 | 14 | 3.25 | 18 | 3.25 | 54 | 3.25 | 20 | 3.20 | 3.24 |
| | 3 | 8 | 4.71 | 8 | 4.71 | 54 | 4.68 | 6 | 4.71 | 14 | 4.71 | 90 | 4.71 | 30 | 4.67 | 4.68 |
| | 4 | 40 | 7.40 | 46 | 7.37 | 76 | 7.39 | 42 | 7.38 | 28 | 7.34 | 68 | 7.33 | 46 | 7.38 | N/A |
| DS3 | 1 | 48 | 2.11 | 48 | 2.11 | 146 | 2.10 | 40 | 2.12 | 56 | 2.12 | N/I[a] | N/I[a] | 22 | 2.07 | 2.09 |
| | 2 | 24 | 3.10 | 24 | 3.10 | 26 | 3.10 | 26 | 3.10 | 28 | 3.11 | 112 | 3.11 | 27 | 3.05 | 3.08 |
| | 3 | 6 | 4.65 | 6 | 4.65 | 6 | 4.65 | 6 | 4.65 | 6 | 4.65 | 6 | 4.66 | 19 | 4.64 | 4.66 |
| | 4 | 6 | 7.30 | 6 | 7.30 | 90 | 7.25 | 10 | 7.33 | 10 | 7.32 | 8 | 7.33 | 30 | 7.23 | N/A |

[a]The mode was not identified

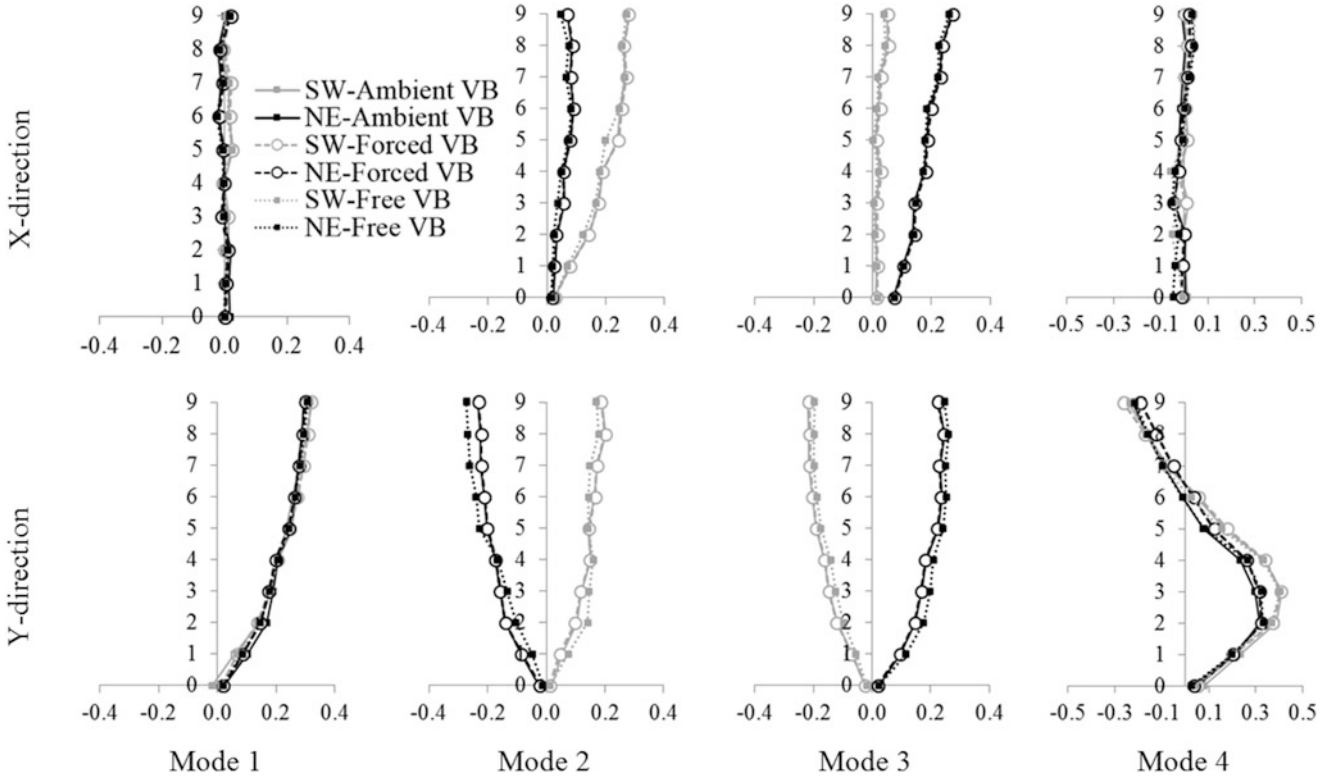


**Fig. 33.8** Mode shapes of the structure at DS0

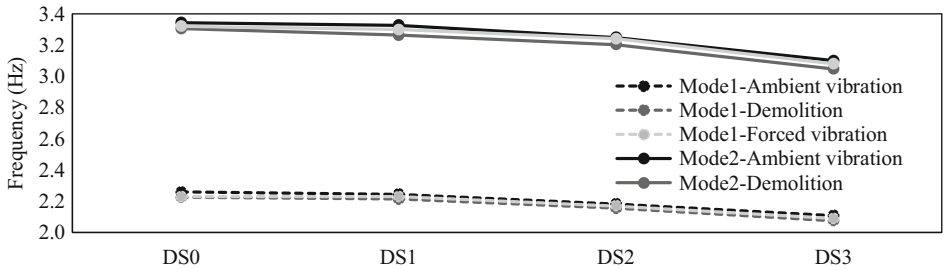


**Fig. 33.9** Identified natural frequencies at different damage states

the 40-component mode shape vectors between the average mode shapes estimated using different sources of excitation described above. It can be seen from the figure that the mode shapes are in excellent agreement with the MAC value of 0.98 or higher.

## 33.5 Conclusions and Remarks

A comparative study between the system identification methods, ERA, NExT-ERA, and peak picking using the free vibration, ambient vibration, and forced vibration data respectively is presented here. The measurements were obtained from dynamic tests of a 10-story RC building which was damaged through the demolition of selected perimeter walls using a jack hammer.

The identification orders used in the ERA method applied on the free vibration measurements are significantly lower than those of NExT-ERA method applied on the ambient vibration recordings. This difference may occur because of the additional processing of the ambient vibration signals to obtain the free vibration signal (NExT) which may add computational errors to the identification process.

The study also investigates the effect of the number and location of the reference channels on the system identification results. Increasing the number of the reference channels results in lower identification orders but no significant difference is observed in the values of the identified natural frequencies. However, the increased number of reference channels requires significantly more computational time. The location of the reference channels affects drastically the results of the modal identification. Hence, when a reference channel measuring the acceleration at a location and direction which has a low participation in mode shapes of the structure is used, the system identification is not accurate as certain modes may not be identified. Moreover, channels with higher signal-to-noise ratio result in more accurate system identification.

The identified frequencies from the three types of measurements indicate the same decreasing trend between the damage states confirming the ability of the all methods to identify the changes in the dynamic properties of the system. It is also observed that higher amplitude of the excitation results in lower identified frequencies as indicated by the comparison of the frequencies obtained from the free vibrations following the impulses induced by the jack hammer and the frequencies identified from the ambient vibration of the building. Finally, using the ERA method accurate results can be obtained at less computational time. Moreover, this method does not suffer from issues related to the choice of reference channels. Based on the observations, at this excitation level, the amplitude of impulse is independent of the modal identification and even low amplitude non-destructive impulses can induce free vibrations to be used for ERA method for healthy and in service structures.

**Acknowledgements** The study presented here is part of a project supported by the National Science Foundation (Award No. 1430180). The collaboration of NEES@UCLA in conducting the experiments is sincerely acknowledged. The authors would also like to thank the New York State Department of transportation (NYSDOT) personnel and director Andrew Roberts for allowing the execution of these tests and for their remarkable cooperation in every part of the experiment. The efforts of the PhD students from Tufts University especially Dr. Iman Behmanesh and Mr. Amin Nozari during and after the testing period is also appreciated. The Authors also want to thank Ms. Andrea Sacco for her helps during the data post processing. However, the opinions expressed in this paper are those of the authors and do not necessarily represent those of the sponsor or the collaborators.

## References

1. Pines, D., Aktan, A.E.: Status of structural health monitoring of long-span bridges in the United States. Prog. Struct. Eng. Mater. **4**(4), 372–380 (2002)
2. Doebling, S.W., Farrar, C.R., Prime, M.B.: A summary review of vibration-based damage identification methods. Shock Vib. Dig. **30**(2), 91–105 (1998)
3. Sohn, H., Farrar, C.R., Hemez, F.M., Shunk, D.D., Stinemates, D.W., Nadler, B.R., Czarnecki, J.J.: A review of structural health monitoring literature: 1996–2001. Report No. LA-13976-MS, Laboratory LaN, Los Alamos, NM, 2004
4. Brincker, R., Zhang, L., Andersen, P.: Modal identification of output-only systems using frequency domain decomposition. Smart Mater. Struct. **10**(3), 441 (2001)
5. Van Overschee, P., De Moor, B.: Subspace Identification for Linear Systems: Theory—Implementation—Applications. Springer Science & Business Media, Berlin (2012)
6. Ventura, C.E., Schuster, N.D.: Structural dynamic properties of a reinforced concrete high-rise building during construction. Can. J. Civ. Eng. **23**(4), 950–972 (1996)
7. Gentile, C., Saisi, A.: Ambient vibration testing and condition assessment of the Paderno iron arch bridge (1889). Constr. Build. Mater. **25**(9), 3709–3720 (2011)
8. Ivanović, S., Trifunac, M., Novikova, E., Gladkov, A., Todorovska, M.: Ambient vibration tests of a seven-story reinforced concrete building in Van Nuys, California, damaged by the 1994 Northridge earthquake. Soil Dyn. Earthq. Eng. **19**(6), 391–411 (2000)
9. Moser, P., Moaveni, B.: Design and deployment of a continuous monitoring system for the Dowling Hall Footbridge. Exp. Tech. **37**(1), 15–26 (2013)
10. Reynders, E., Roeck, G.D., Gundes Bakir, P., Sauvage, C.: Damage identification on the Tilff Bridge by vibration monitoring using optical fiber strain sensors. J. Eng. Mech. **133**(2), 185–193 (2007)
11. Siringoringo, D.M., Fujino, Y.: System identification of suspension bridge from ambient vibration response. Eng. Struct. **30**(2), 462–477 (2008)
12. Astroza, R., Conte, J., Restrepo, J., Ebrahimian, H., Hutchinson, T.: Shake table testing of a full-scale five-story building: system identification of the five-story test structure. In: Proceedings of ASCE Structures Congress, Pittsburgh, PA, 2013
13. Belleri, A., Moaveni, B., Restrepo, J.I.: Damage assessment through structural identification of a three-story large-scale precast concrete structure. Earthq. Eng. Struct. Dyn. **43**(1), 61–76 (2014)
14. Moaveni, B., He, X., Conte, J.P., Restrepo, J.I., Panagiotou, M.: System identification study of a 7-story full-scale building slice tested on the UCSD-NEES shake table. J. Struct. Eng. **137**(6), 705–717 (2010)
15. Moaveni, B., Stavridis, A., Lombaert, G., Conte, J.P., Shing, P.B.: Finite-element model updating for assessment of progressive damage in a 3-story infilled RC frame. J. Struct. Eng. **139**(10), 1665–1674 (2012)
16. Zembaty, Z., Kowalski, M., Pospisil, S.: Dynamic identification of a reinforced concrete frame in progressive states of damage. Eng. Struct. **28**(5), 668–681 (2006)

17. Baghaei Naeini, R.: Vibration-based damage assessment and residual capacity estimation of bridges. Ph.D. thesis, University of California, Irvine, CA (2011)
18. Yousefianmoghadam, S., Behmanesh, I., Stavridis, A., Moaveni, B., Nozari, A.: System identification and modeling of a 100-year-old RC warehouse dynamically tested at several damage states. In: Proceedings of 1st International Conference on Natural Hazards and Infrastructure: Protection, Design, Rehabilitation ICONHIC 2016, Chania, Greece, 2016
19. Yousefianmoghadam, S., Behmanesh, I., Stavridis, A., Moaveni, B., Nozari, A., Sacco, A.: System identification and modeling of a dynamically tested and gradually damaged 10-story RC building. Earthq. Eng. Struct. Dyn. (under review) (2017)
20. Welch, P.D.: The use of fast Fourier transform for the estimation of power spectra: a method based on time averaging over short, modified periodograms. IEEE Trans. Audio Electroacoust. **15**(2), 70–73 (1967)
21. Oppenheim, A.V., Schafer, R.W., Buck, J.R.: Discrete-Time Signal Processing. Prentice Hall, Englewood Cliffs (1989)
22. Allemang, R.J., Brown, D.L.: A correlation coefficient for modal vector analysis. In: Proceedings of the 1st International Modal Analysis Conference, 1982

# Chapter 34
# Kronecker Product Formulation for System Identification of Discrete Convolution Filters

**Lee Mazurek, Michael Harris, and Richard Christenson**

**Abstract** The following paper illustrates a mathematical framework for identifying discrete convolution filters and applies that framework to a time varying dynamic problem. Convolution matrices, formulated using Kronecker products, allow for least means squares solution of arbitrarily structured discrete convolution models. The framework exposes the convolution structure and the filter coefficients independently in order to solve for the time varying weights of a known model, or an unknown time varying filter. Transforms are shown to apply standard discrete spectral processing methods to this architecture. The identification methods were successfully applied to identify the stiffness-like and damping-like operating regimes of a typical viscous damper in a dynamic system subjected to periodic motion. The results show that discrete time varying system identification successfully predicts measured test data and provides intuitive results showing stiffness-like behavior at low force inputs and damping-like behavior for higher force inputs.

**Keywords** Time variant wiener filter • Time frequency analysis • Time variable system identification

## 34.1 Background

The work presented here is an extension of previous system identification methods, which model linear systems using convolution integrals. System theory uses convolution integrals to model the response of a differential equation representing an electrical, mechanical, or other system to an arbitrary input. For continuous linear systems, an output, $y$, can be calculated given an input, $x$, and an impulse response filter, $h$, by

$$y(t) = \int_0^t h(\tau) \cdot x(t-\tau)\, d\tau \tag{34.1}$$

where $t$ is time and $\tau$ is the relative time delay between input and output. The continuous impulse response filter can be solved for given an input and output using spectral factorization methods described by Wiener [1] and Kolmogoroff [2].

The discrete form [3] of the above convolution integral is

$$y[n] = \sum_m h(m) \cdot x(n-m) \quad for \begin{cases} m \geq \max(n-(p-1), 0) \\ m \leq \min(n, (r-1)) \end{cases} \tag{34.2}$$

where lag, $m$, is used to show the sample delay between input and output, $n$ indicates the output sample, $r$ represents the length of the filter, $h$, and $p$ represents the length of the input $x$. The solution for the discrete filter, $h$, is simplified relative to the continuous filter, and was defined in [3].

The work presented here focuses on the time varying discrete convolution problem

$$y[n] = \sum_m H(m, n-m) \cdot x(n-m) \tag{34.3}$$

L. Mazurek • M. Harris • R. Christenson (✉)
Civil & Environmental Engineering, University of Connecticut, 261 Glenbrook Road Unit 3037, Storrs, CT, 06269-3037, USA
e-mail: richard.christenson@uconn.edu



J. Caicedo, S. Pakzad (eds.), *Dynamics of Civil Structures, Volume 2*, Conference Proceedings
of the Society for Experimental Mechanics Series, DOI 10.1007/978-3-319-54777-0_34

where $H$ may be a matrix of time varying impulse response filters, with $n - m$ selecting the impulse response for the corresponding input time. The solution process to find the filter H is the focus of this paper.

The structure of time invariant discrete convolution has been well researched. Linear time invariant discrete convolution is known to possess a repeating structure, whose bases can be derived using Kronecker products. Efficient forward convolution solution methods have been implemented using these bases [4, 5]. The solution for discrete time invariant filter, $h$, can be performed efficiently given knowledge of the repeating structure. Kailath and Sayed [6] discuss this form of matrix structure and provide multiple methods for inversion of these equations. Hansen [7] discusses deconvolution and regularization methodologies for the solution of two dimensional convolution problems related to image processing. These methods are expanded here to address the discrete time variant system identification problem.

Statistical methods are well established for the empirical analysis of discrete time convolution systems. Bendat and Piersol [8] provide methods for assessing the quality of fit of single input single output, and multi input multi output system models. Bendat [9] shows how to transform single input single output nonlinear systems in order to employ standard multi input single output linear statistical processing. One objective of the discrete convolution system identification models documented here is that they may be assessed using these standard statistical methods.

## 34.2 Mathematical Methods

Time varying system identification may be performed using convolution matrix products, which are the basis of this paper and are explained here in detail. The convolution sum, as expressed in Eq. (34.3), is rewritten as a matrix vector product by expanding the terms contributing to each output sample and placing zeros elsewhere. The resulting matrix appears as a series of impulse responses with unit sample delays relative to one another. The discrete output vector $y$ is calculated using

$$y = H_{[CV]} \cdot x = \begin{bmatrix} H_{00} & 0 & \cdots & 0 \\ H_{10} & H_{01} & \vdots & 0 \\ \vdots & H_{11} & \vdots & \vdots \\ H_{r0} & \vdots & \vdots & H_{0p} \\ 0 & H_{r1} & \vdots & H_{1p} \\ \vdots & \vdots & \vdots & \vdots \\ 0 & 0 & \cdots & H_{rp} \end{bmatrix} \cdot \begin{bmatrix} x_0 \\ x_1 \\ \vdots \\ x_p \end{bmatrix} \tag{34.4}$$

where the matrix, $H_{[CV]}$, is equivalent to the time varying convolution operation. Note that for the purpose of this discussion, $H_{[CV]}$ is used to indicate the filter stored in $H$ expanded into a matrix which has convolution structure given by $C_V$ (as defined subsequently in Eq. (34.18)). In the above expressions, $y$ is an $(n \times 1)$ vector, $H_{[CV]}$ is an $(n \times p)$ matrix representing a convolution operation, $x$ is a $(p \times 1)$ vector, and $n = p + r - 1$ where $r$ is the length of each impulse response stored in $H$.

While the above equation is sufficient to solve for output, $y$, it cannot be used directly to solve for the filter, $H$, or its convolution structure, $C_V$, given $x$ and $y$. Generally $H_{[CV]} \neq y \cdot x^{-1}$ because the standard inversion process does not enforce linear dependent structure and x is not directly invertible. The matrices are rearranged using the Kronecker identity as follows

$$y = I_n \cdot H_{[CV]} \cdot x \tag{34.5}$$

$$vec(y) = \left(x^T \otimes I_n\right) \cdot vec\left(H_{[CV]}\right) \tag{34.6}$$

where $\otimes$ indicates the Kronecker product, $vec(\ldots)$ indicates the columns of the enclosed matrix stacked as a vector, and $I_n$ is the identity matrix of size $n$. The Kronecker product identity above is used to expose the expression $vec(H_{[CV]})$, which allows the terms of $H_{[CV]}$ to be grouped and organized into a linear structure as follows

$$vec\left(H_{[CV]}\right) = C_V \cdot vec(H) \tag{34.7}$$

where $C_V$ is the convolution structure and $H$ is a matrix of filter coefficients. The function of the variable $C_V$ is to describe the structure of the convolution. The columns of $C_V$ represent terms in $H$ and the rows represent output time for given

input time. The above equations are combined into one total expression which contains the convolution structure and the filter independently in the equation as

$$y = H_{[CV]} \cdot x = \left(x^T \otimes I_n\right) \cdot vec\left(H_{[CV]}\right) = \left(x^T \otimes I_n\right) \cdot C_V \cdot vec(H) \tag{34.8}$$

where $vec(y) = y$ in this equation because it is assumed that y is already a vector.

The above expression is a form of the discrete convolution product which can be used to solve for H. The left Moore Penrose pseudoinverse [10], indicated by $(\dots)^{-\mathrm{P}}$ is used to solve for $H$ by

$$\left(\left(x^T \otimes I_n\right) \cdot C\right)^{-P} \cdot y = vec(H) \tag{34.9}$$

$$\left(\left(\left(x^T \otimes I_n\right) \cdot C\right)^T \cdot \left(x^T \otimes I_n\right) \cdot C\right)^{-1} \cdot \left(\left(x^T \otimes I_n\right) \cdot C\right)^T \cdot y = vec(H) \tag{34.10}$$

Portions of the above equation are grouped together into equivalent auto and cross-correlation matrices using Kronecker identities as

$$vec(H) = {R_{xx}}^{-1} R_{yx} \tag{34.11}$$

$$R_{yx} = \left(\left(x^T \otimes I_n\right) \cdot C_V\right)^T \cdot y = {C_V}^T \left(x \otimes I_n\right)(1 \otimes y) \tag{34.12}$$

$$R_{yx} = {C_V}^T (x \otimes y) \tag{34.13}$$

$$R_{xx} = \left(\left(x^T \otimes I_n\right) \cdot C_V\right)^T \cdot \left(x^T \otimes I_n\right) \cdot C_V = \left({C_V}^T \left(x \otimes I_n\right)\right) \cdot \left(x^T \otimes I_n\right) \cdot C_V \tag{34.14}$$

$$R_{xx} = {C_V}^T \left(\left(xx^T\right) \otimes I_n\right) C_V \tag{34.15}$$

For the case of linear time invariant convolution (denoted by absence of $V$ subscript on $C$, but otherwise the same), the convolution structure $C$ is composed of a linear mapping of impulse responses and a shift operator by

$$C = \begin{bmatrix} S^0 \cdot I_{nr} \\ S^1 \cdot I_{nr} \\ \vdots \\ S^i \cdot I_{nr} \\ \vdots \\ S^p \cdot I_{nr} \end{bmatrix} = \begin{bmatrix} \begin{bmatrix} I_r \\ 0_{p-1,r} \end{bmatrix} \\ \begin{bmatrix} 0_{1,r} \\ I_r \\ 0_{p-2,r} \end{bmatrix} \\ \vdots \\ \begin{bmatrix} 0_{i,r} \\ I_r \\ 0_{p-1-i,r} \end{bmatrix} \\ \vdots \\ \begin{bmatrix} 0_{p-1,r} \\ I_r \end{bmatrix} \end{bmatrix} \qquad S = \begin{bmatrix} 0 & 0 & 0 & \cdots & 0 \\ 1 & 0 & 0 & \cdots & 0 \\ 0 & 1 & 0 & \cdots & 0 \\ \vdots & \ddots & \ddots & \ddots & \vdots \\ 0 & 0 & 0 & 1 & 0 \end{bmatrix} = \begin{cases} S_{ij} = 1 \ \ for \ \ i - 1 = 1 \\ S_{ij} = 0 \ \ otherwise \end{cases} \tag{34.16}$$

where the shift operator, $S$, is an $(n \times n)$ matrix which $h$ takes a unit input vector and delays it by a single sample. The structure $C$ can be interpreted as $p$ series of $(n \times r)$ matrices mapping impulse $h$ to its appropriately delayed output sample for each input sample. The notation $S^i$ is used to indicate the shift matrix raised to the $i$th power, or multiplied a total of $i$ times, and $S^0$ is an identity matrix. $I_{nr}$ indicates a rectangular identity matrix of dimensions $(n \times r)$, where the lower and right columns of the largest square identity matrix are truncated to yield the rectangular identity matrix.

The expressions for auto and cross correlation can be shown to the standard expressions in Bendat and Piersol [8] when the time invariant $C$ structure is employed. The solution process for time varying $H$ is similar to the one presented previously, but the variable $C_V$ defining the convolution structure now has additional time variance, indicated by the subscript $V$. The number of terms in $H$ that must be solved for grows significantly relative to the time invariant case and therefore, additional

constraints on the structure are needed to aid in the solution process. Often, the time variance in a system can be attributed to an underlying state which has a known or measurable relationship to time. If the state is repeated multiple times during an event, the impulse responses associated with the corresponding time can be made linear dependent to reduce the number of overall variables required to be solved. Another method to assess linear dependence over time is to begin with several candidate models and calculate the sample dependent model weight. These methods are a subset of the general time varying convolution structure and are useful to realize overdetermined solutions.

For the time varying convolution to be used in this paper, each input sample results in an equal length impulse response. $V$ is a weighting matrix with rows equal to number of unique impulse responses, s, and columns equal to number of input time samples, $p$. $V$ can be interpreted as an array of time varying weighting vectors, describing each impulse response's contribution for a given input sample time. In the following notation, a single subscript ($v_i$) indicates the vector associated with one column, or weights for every candidate filter at a single input time, and the row within that vector ($v_{ij}$) represents weighting for each candidate filter individually for the given input time. The $V$ matrix is described by

$$V = \begin{bmatrix} v_{00} \cdots v_{0p} \\ \vdots \ \ldots \ \vdots \\ v_{s0} \cdots v_{sp} \end{bmatrix} = \begin{bmatrix} v_0 & \cdots & v_p \end{bmatrix}. \tag{34.17}$$

The structure $C_V$ uses the terms in $V$ to generate $p$ series of $(n \times pr)$ matrices mapping each impulse stored in $H$ to its appropriately delayed output sample for each input sample. The Kronecker product is used to take the original time invariant structure represented by unit shift operations and copy it with a given weighting for each impulse response model, which can be expressed as

$$C_V = \begin{bmatrix} {v_0}^T \otimes \left({S_n}^0 \cdot I_{nr}\right) \\ {v_1}^T \otimes \left({S_n}^1 \cdot I_{nr}\right) \\ \vdots \\ {v_i}^T \otimes \left({S_n}^i \cdot I_{nr}\right) \\ \vdots \\ {v_p}^T \otimes \left({S_n}^p \cdot I_{nr}\right) \end{bmatrix} = \begin{bmatrix} \begin{bmatrix} v_{00} \cdot {S_n}^0 \cdot I_{nr} \\ v_{01} \cdot {S_n}^1 \cdot I_{nr} \\ \vdots \\ v_{0i} \cdot {S_n}^i \cdot I_{nr} \\ \vdots \\ v_{0p} \cdot {S_n}^p \cdot I_{nr} \end{bmatrix} \cdots \begin{bmatrix} \begin{bmatrix} v_{s0} \cdot {S_n}^0 \cdot I_{nr} \\ v_{s1} \cdot {S_n}^1 \cdot I_{nr} \\ \vdots \\ v_{si} \cdot {S_n}^i \cdot I_{nr} \\ \vdots \\ v_{sp} \cdot {S_n}^p \cdot I_{nr} \end{bmatrix} \end{bmatrix} \end{bmatrix} \tag{34.18}$$

One difficulty associated with the solution for $vec(H)$ is the number of unknown terms relative to the available knowns. To overcome this difficulty, the matrix $V$ should be constructed to introduce linear dependence. Methods of ensuring full rank include measuring multiple independent records of $x$ and $y$, and making assumptions related to the amount of variation the impulse response experiences over time. For example, if $H$ is dependent on a repeating state, $V$ can reflect that the same vector $h_i$ (representing the $i$th column of $H$) appears multiple times. With appropriate structure, and sufficient averaging, it is possible to have more knowns in $x$ and $y$ than unknowns in $vec(H)$.

The only difference in the algebraic solution between time varying and time invariant filter, $H$, is the usage of the known time invariant convolution structure $C$ or the known time variant convolution structure $C_V$. The following discussion describes the solution process for unknown $C_V$ if candidate $H$ is known. In other words, if candidate impulse responses are available, the time varying weights of those impulse responses, which best fit a data set, can be solved for.

### *34.2.1 Solution for Time Varying Weighting Matrix*

The matrix $V$ describing the time varying weighting of a given column in $H$ at each point in time can be solved for directly. The process involves exchanging between different forms of the convolution product, by

$$y = \left(x^T \otimes I_n\right) \cdot C_V \cdot vec(H) = mat_n \left(C_v \cdot vec(H)\right) \cdot x \tag{34.19}$$

where the operator $mat_n(\ldots)$ is the operator which reverses the $vec\,(\ldots)$ operation, and has additional subscript n to ensure the number of rows are unambiguous. The structure $C_V$ is given previously and the Kronecker product notation is exchanged back to triple matrix multiply notation below. The following is an excerpt of $C_V$ structure which demonstrates the exchange.

$$\left(v_i{}^T \otimes \left(S_n{}^i \cdot I_{nr}\right)\right) vec(H) = vec\left(\left(S_n{}^i \cdot I_{nr}\right) \cdot H \cdot v_i\right) \tag{34.20}$$

The output $y$, can now be interpreted as the sum of each element in $x$ multiplied by the appropriately weighted and delayed impulse for its point in time. This representation is shown below in matrix form and as a summation.

$$y = \left[ \left(\left(S_n{}^0 \cdot I_{nr}\right) \cdot H \cdot v_0\right) \left(\left(S_n{}^i \cdot I_{nr}\right) \cdot H \cdot v_i\right) \cdots \left(\left(S_n{}^p \cdot I_{nr}\right) \cdot H \cdot v_p\right) \right] \cdot \begin{bmatrix} x_0 \\ x_i \\ \vdots \\ x_p \end{bmatrix} \tag{34.21}$$

$$y = \sum\nolimits_{i=0}^{p} \left(\left(S_n{}^i \cdot I_{nr}\right) \cdot H \cdot v_i\right) \cdot x_i \tag{34.22}$$

Given that each $v_i$ is a vector indicating the weighted sum of matrices multiplied by scalar values, their location in the equation can be moved while preserving equivalence by

$$y = \left[ \left(\left(S_n{}^0 \cdot I_{nr}\right) \cdot H \cdot x_0\right) \left(\left(S_n{}^i \cdot I_{nr}\right) \cdot H \cdot x_i\right) \cdots \left(\left(S_n{}^p \cdot I_{nr}\right) \cdot H \cdot x_p\right) \right] \cdot \begin{bmatrix} v_0 \\ v_i \\ \vdots \\ v_p \end{bmatrix} \tag{34.23}$$

The least means square solution for $V$ is as follows

$$V = mat_s\left(L \cdot \tilde{v}\right) \tag{34.24}$$

$$\tilde{v} = K^{-P} y = \left(K^T K\right)^{-1} \cdot K^T y \tag{34.25}$$

$$K = \left[ \left(\left(S_n{}^0 \cdot I_{nr}\right) \cdot H \cdot x_0\right) \left(\left(S_n{}^i \cdot I_{nr}\right) \cdot H \cdot x_i\right) \cdots \left(\left(S_n{}^p \cdot I_{nr}\right) \cdot H \cdot x_p\right) \right] \cdot L \tag{34.26}$$

where the vector form of $V$ is

$$vec(V) = \begin{bmatrix} v_0 \\ \vdots \\ v_p \end{bmatrix} \quad \text{or} \quad vec(V) = L \cdot \tilde{v} = \begin{bmatrix} v_0 \\ \vdots \\ v_p \end{bmatrix} \tag{34.27}$$

The variable $L$ has been introduced above to assign linear dependence and improve rank of the pseudo-inverse problem. If $L$ is not set to identity, $\tilde{v}$ will contain the unique terms of the weighting vector, which may be projected to a full weighting vector using $L$. The term $K^T y$ is analogous to the cross correlation of $H$ and $y$ weighted by each term in $x$. The term $K^T K$ is analogous to the auto correlation of $H$ weighted by each term in $x$.

For most problems, the solution for time dependent weight of candidate models involves fewer unknowns than the solution for the fully time dependent filter model. Therefore, if candidate models are available, this method can efficiently use limited test data to better understand the time variance of a system.

### *34.2.2 Equivalence of Time Varying Transfer Function and Time Varying Input*

The previous equations can be equivalently interpreted as a multi-input single-output relationship where time variance is expressed as a transform on the input term rather than the transfer function. A transform between these two forms can enable the use of conventional statistical tools to understand time varying systems, and can be used to show the equivalent time varying transfer function of linearized systems. Bendat [9] employs a similar method to transform time varying systems in order to apply time invariant single output multi input statistical analysis, however this method is more specifically defined for discrete time varying convolution processes.

The matrix $Z$ is a linear $(kp \times p)$ transform which takes an original $x$ vector and produces a multitude of $x$ vectors (stacked together in $vec\ (\ldots)$ format). The following equations show an original time variant convolution structure $C_V$, and the modified multi input time invariant convolution structure $C$.

$$vec(X) = (Z \cdot x) \tag{34.28}$$

$$y = \left(x^T \otimes I_n\right) \cdot C_V \cdot vec\left(H\right)\Big) \tag{34.29}$$

$$y = \left((Z \cdot x)^T \otimes I_n\right) \cdot C \cdot vec(H) = \left(\left(x^T \cdot Z^T\right) \otimes I_n\right) \cdot C \cdot vec(H) \tag{34.30}$$

For the case where a linear time invariant multi-input convolution structure, $C$, and a time dependent transform, $Z$, are both known, the equivalent time variable convolution structure can be defined uniquely.

$$y = \left(\left(x^T \cdot Z^T\right) \otimes I_n\right) \cdot C \cdot vec(H) = \left(x^T \otimes I_n\right) \cdot \left(Z^T \otimes I_n\right) \cdot C \cdot vec(H) \tag{34.31}$$

$$C_V = \left(Z^T \otimes I_n\right) \cdot C \tag{34.32}$$

Given $C_V$ and $C$, it is also possible to solve for the least means squares solution for the transform $Z$.

### *34.2.3 Spectral Processing*

Coherence measures and uncertainty bounds may be developed using the time variant to multi input time invariant transform and will be the subject of future studies. For the empirical demonstration in this paper, simplified coherence measures and spectral processing methods were employed.

The coherence measures shown in this paper are calculated as the ratio between predicted signal power and the sum of predicted and error power as

$$\gamma^2 = \frac{HS_{xx}H^*}{HS_{xx}H^* + S_{\varepsilon\varepsilon}} \tag{34.33}$$

where $HS_{xx}H^*$ is the power spectral density of the response predicted by a given filter, and $S_{\varepsilon\varepsilon}$ is the power spectral density of the error residual after the prediction is subtracted from the total. The predicted response is calculated using Eq. (34.8) and subtracted from the original response to find the error. $HS_{xx}H^*$ and $S_{\varepsilon\varepsilon}$ are calculated in this study using the Matlab cpsd( . . . ) function with predicted response and response error as inputs respectively. This equation reproduces the standard equations for coherence when the error and the prediction are uncorrelated. This assumption is true for time invariant system identification, and potentially overestimates total signal power and underestimates coherence for the system identification methods shown here. The compromise was selected in order to assure the reader that the identified filters are indeed predictive, while leaving the complexity of multi input coherence to later publications.

## 34.3 Experimental Methods

The effect of low frequency vibration on damping performance in a coupled beam damper system was empirically assessed using the time varying system identification. The experiment was performed under laboratory conditions to verify the identification methodology but is generally application (for example to: dampers, braces and general energy dissipation devices in civil applications). Figure 34.1 shows a notional schematic of the components involved in the laboratory test as well as a picture of the experiment in the structures research lab at the University of Connecticut.

The test beam is a 9.1 m long steel pole, with a 0.15 × 0.15 m cross section and 6.3 mm wall thickness. A Taylor devices damper, model number 1x2 D-TC specified for 111 N force at 3 m/s, was placed at approximately 3.7 m from the base of the beam. The damper was intentionally tested at velocities outside (lower than) the typical operating range of the damper in

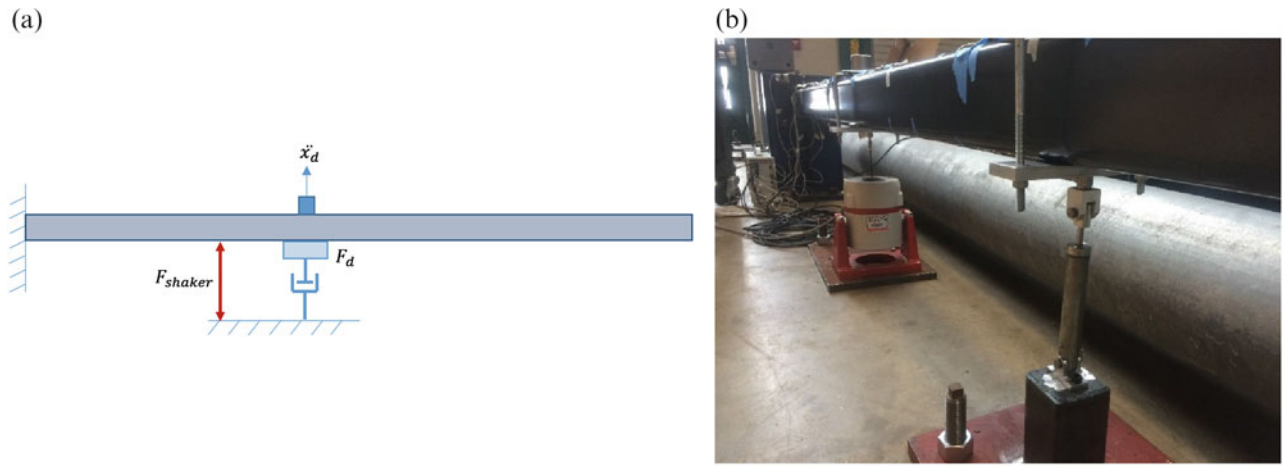


**Fig. 34.1** Experimental beam damper system. (**a**) Notional schematic of test setup. (**b**) Photo of test setup

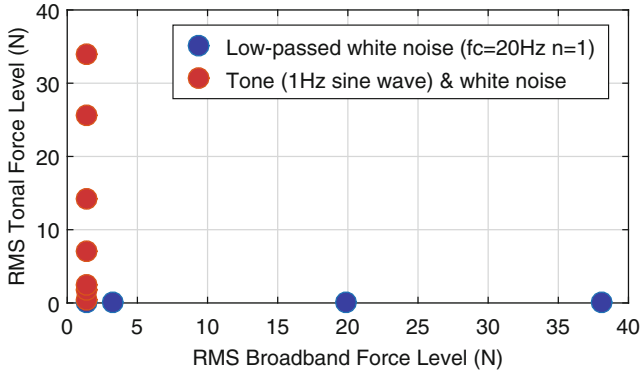


**Fig. 34.2** Broadband and tonal test levels

order to perform identification of stiffening due to time varying seal behavior (the damper is specified at maximum velocity and works as expected at the specified amplitudes).

Vibration test hardware was instrumented to the beam. An LDS V408 electrodynamic shaker was placed between the damper and the foundation of the beam at about 2.4 m from the base. A PCB 208C02 piezoelectric load cell was used to measure the shaker input force and a 208C01 load cell was used to measure the reaction force at the damper. A PCB 393C seismic accelerometer (5% bandwidth 0.025–800 Hz) was placed on the beam at the damper attachment location. Time series were recorded using a DataPhysics acquisition system with SignalCalc software. Input was generated using Matlab Simulink with Quanser I/O boards driving the shaker through a consumer grade voltage amplifier.

The input signals were designed to assess the linear model using conventional system identification and to introduce steady time variance to assess time varying system identification. Figure 34.2 shows the test events along two axes representing the broadband force level and the tonal force level. The broadband input was used to perform conventional system identification, and to provide a small linear perturbation signal for time varying system identification. The tones were superimposed upon broadband input to repeatably vary the damper between physical regimes. Different levels were used in each axes in order to explore the damper behavior at higher force levels near the specified operating point and at very low levels.

The recorded signals of force and acceleration were digitally post processed such that the identified filter would relate force to velocity. This post-processing was performed by digitally filtering the force record with a first order 100 Hz highpass infinite impulse response filter. The result is that in the center of the processing band (<100 Hz) the force derivative was used in calculations. This results in system identification producing a band limited approximation of (s × force/acceleration), where s is the Laplace derivative term, which approximates (force/velocity). The force per velocity transfer function has improved dynamic range for plotting and calculation relative to the force per acceleration transfer function.

The test events were each 512 s in length and the solved for filter length was 1 s, or 256 samples. The filter weighting matrices were set such that each consecutive second was averaged with the previous, and the time varying filter was set so that each consecutive 8 input samples use the same impulse response weight using the L (Eq. (34.24)) and V (Eq. (34.17)) matrices. This was performed so that the time varying system identification (Eq. (34.11)) would result in 16 equivalent block

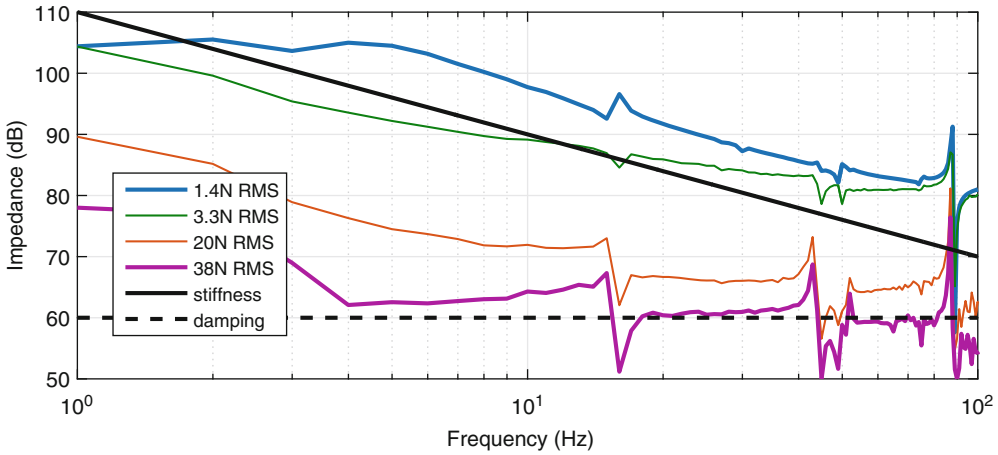


**Fig. 34.3** Linear time invariant models at different broadband input levels

averages (or ratio of knowns to unknowns), and the time varying weight problem (Eq. (34.24)) would result in 256 times as many knowns as unknowns. Note that the time varying system identification problem is more data intensive than the time varying weighting problem due to solving for a full filter length rather than just the weights.

## 34.4 Results

The measured frequency response function between the load cell in series with the damper and the acceleration on the beam at the damper attachment shows the variance of the system with test level. Figure 34.3 shows broadband test events at multiple levels. The results show the force over velocity calculated by taking the Fourier transform of the calculated impulse response for the system (Eq. (34.11) with time invariant structure). Two reference lines are shown on the plot indicating the impedance associated with an ideal stiffness and an ideal damper. The conventional system identification models performed at 1.4N RMS broadband input and 38N RMS (closer to 111N specification) were taken as candidate models for later events.

The time varying weight calculation (Eq. (34.25)) was performed for the tonal and broadband input events. The results are shown in Fig. 34.4. The left column shows the solved coefficients for the weight of the previous 1.4N RMS broadband model over time. The model was judged to be stiffness-like so it was labeled as such in the following figure (despite small amounts of structural interaction). The center column shows the weight for the previous 38N RMS broadband model over time, which is labeled damping-like. The right column shows the effective coherence measured using Eq. (34.33). Each plot was generated using the same low 1.4N RMS level of broadband input and an increasing amount of tonal input.

Figure 34.5 shows the results of time varying system identification (Eq. (34.11)) in presence of underlying disturbance for a 10N tone imposed on 1.4N RMS broadband. This method is different than the previous model weighting method because no model is assumed (other than convolution structure); each impulse response is independently solved for. The pane on the left shows the frequency response over time (Fourier transform of columns of H matrix). The color indicates the total response magnitude, with the vertical axis indicating frequency and the horizontal axis indicating time. The plot on the right shows the effective coherence for the time varying system identification versus linear time invariant system identification for this event.

## 34.5 Discussion

The conventional and time varying system identification methods illustrate different aspects of the time variability of the coupled beam damper system. Figure 34.3 shows the identified linear time invariant model for load cell force to beam velocity at the damper connection varies depending upon broadband drive level. At the lowest excitation level, the model is comparable to a stiffness line, and at the highest level, the model is comparable to a damping line. The curves show some degree of structural interaction due to a mode associated with the beam damper system at 14 Hz. The relative weights of the

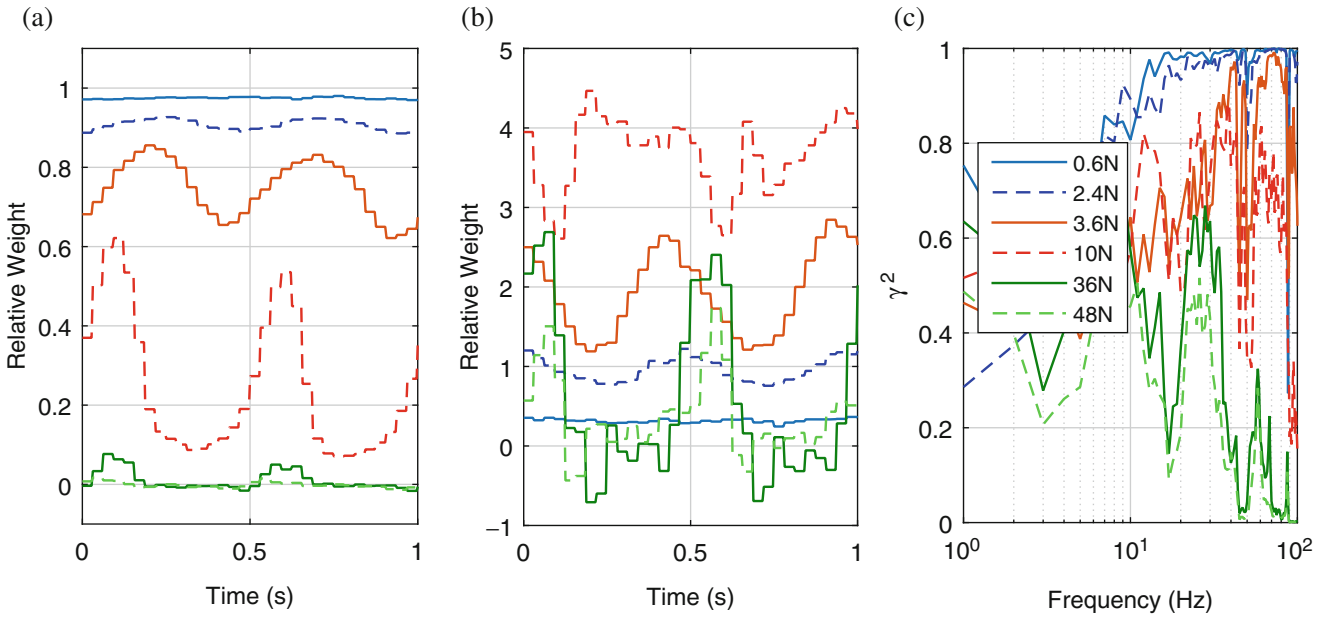


**Fig. 34.4** Time varying stiffness-like and damping-like model weights. (**a**) Stiffness-like model over time. (**b**) Damping-like model over time. (**c**) Coherence

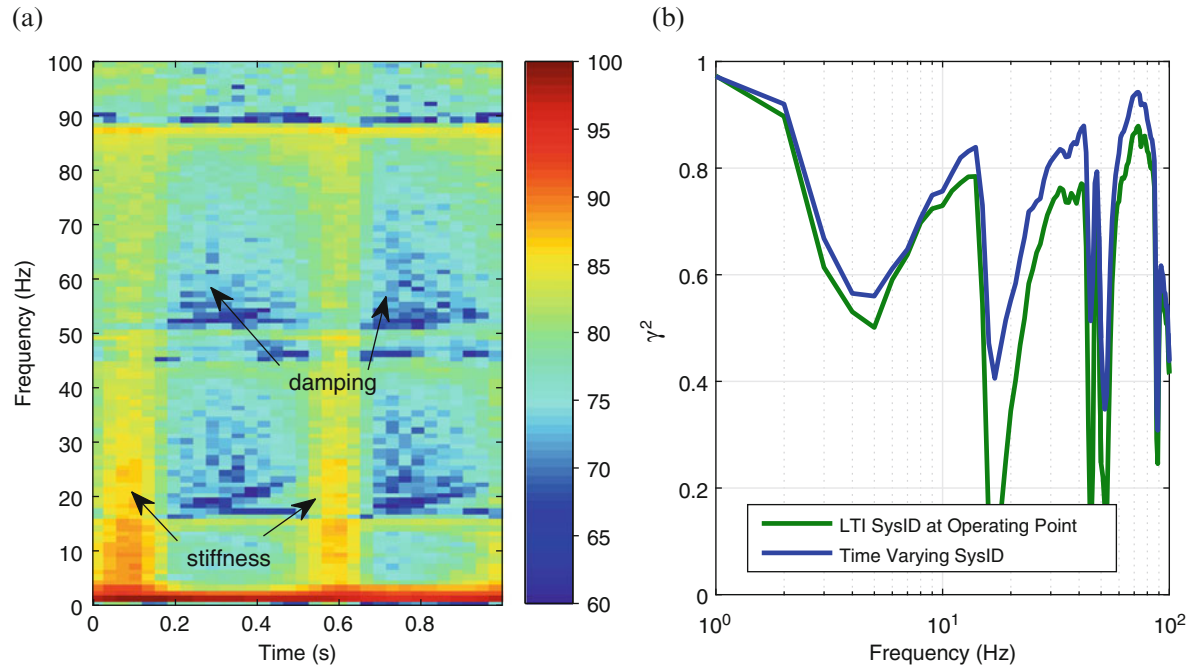


**Fig. 34.5** (**a**) Frequency response versus time (dB). (**b**) Coherence

stiffness-like and damping-like models were found for events with differing levels of tonal force inputs, and the results are shown for a single period in Fig. 34.4. The stiffness-like model weight over time shows that the damper operates in different regimes depending on drive level. At very low levels, the behavior is nearly constantly stiffness-like, at intermediate drive levels the stiffness-like model is dominant at two time instances in the period, and at the highest drive level the stiffness model does not describe the data. The damper exhibits little weighting of the damping-like model at low input levels, very high damping model weight at intermediate drive levels, and approximately 0–2 times the damping-like model at high input levels. Reversal of the seal may account for increased loss at intermediate drive levels. The models best accounted for total signal power at low to intermediate drive levels. In contrast to the previous figure, which shows weights for assumed models,

Fig. 34.5a illustrates the time varying system identification (without assumed model) for a single event (10N tone imposed on 1.4N RMS broadband). The time varying model in Fig. 34.5a provides similar conclusions to Fig. 34.4, showing that the measured force per unit velocity varies over the duration of the event between stiffness and damping trend-lines. Figure 34.5b shows the ratio of predicted signal power to predicted plus error signal power. The time varying system identification more effectively predicts this system's output than the linear time invariant system identification for this event.

## 34.6 Conclusions

The methodology laid out in this writing enables the least means squares solution of arbitrarily structured discrete convolution models. The advantage of this solution methodology is that the form of the model and its inputs and outputs are directly sampled in time and little information is required about physical process being modelled. Two identification methods are discussed in this writing to assess time varying weights for candidate models, and to identify entirely unknown (aside from convolution structure) time dependent discrete convolution models. The discrete sampling and model allows for application of standard statistical tools and spectral processing methods to assess the quality of the fit using the equivalency between time varying single input single output processes and time invariant multi input single output processes, or the single input approximation used in this paper. Future work will discuss statistical properties of these time varying models.

## References

1. Wiener, N.: Extrapolation, Interpolation, and Smoothing of Stationary Time Series: With Engineering Applications. The M.I.T. Press, Massachusetts Institute of Technology, Cambridge (1964)
2. Kolmogoroff, A.N.: Interpolation and extrapolation. Bull. Acad. Sci. U.S.S.R. **5**, 3–14 (1941)
3. Levinson, N.: The Weiner RMS (root mean square) error criterion in filter design and prediction. J. Math. Phys. **XXV**(4), 261–278 (1947)
4. Granata, J., Conner, M., Tolimieri, R.: A tensor product factorization of the linear convolution matrix. IEEE Trans. Circuits Syst. **38**(11), 1364–1366 (1991)
5. Hicks, C.: Discrete Convolution Using Kronecker Products. Thesis, Florida Institude of Technology (1999)
6. Kailath, T., Sayed, A.: Fast Reliable Algorithms for Matrices with Structure. Society for Industrial and Applied Mathematics, Philadelphia (1999)
7. Hansen, P.: Deconvolution and regularization with Toeplitz matrices. Numer. Algorithms. **29**, 323–378 (2002)
8. Bendat, J., Piersol, A.: Random Data: Analysis and Measurement Procedures, 4th edn. Wiley, Hoboken (2010)
9. Bendat, J.: Nonlinear System Techniques and Applications. Wiley, New York (1998)
10. Laub, A.: Matrix Analysis for Scientists and Engineers. Society for Industrial and Applied Mathematics, Philadelphia (2005)

# Chapter 35
# Calibration-Free Footstep Frequency Estimation Using Structural Vibration

**Mostafa Mirshekari, Pei Zhang, and Hae Young Noh**

**Abstract** This paper introduces a calibration-free footstep frequency estimation system using footstep-induced structural vibration. Footstep frequency is an important measure for tracking health status in senior/health care and rehabilitation. Using structural vibrations for this estimation can improve intrusiveness commonly associated with long-term monitoring. Because the large number of structure types and the variety of noise they are subjected to, the main challenges of vibration-based approach are: (1) separating footsteps from other impulsive excitations (such as door shutting, cane striking, object droppings, etc.), (2) providing a system which is compatible to different structures and does not require calibration and training for every structure. To combat these challenges, we introduce an online footstep frequency estimation system which uses human walking pattern heuristics to automatically separate and tune the system to distinguish between footstep-induced vibration and other impulsive excitations in different structures. We validate our approach in two different buildings with human participants. The results show that our approach results in F1 score of 0.87, equal to 8× improvement compared to a baseline approach, which classifies the footsteps using a model trained in a different structure.

**Keywords** Footstep • Online learning • Calibration-free • Structural vibration • SVM classification

## 35.1 Introduction

Detecting gait abnormalities is important for health tracking in many healthcare scenarios. For example, in senior/health care [9, 10]), temporal gait parameters are key indicators of many conditions (e.g. dementia, chronic obstructive pulmonary disease) [6]. Much research has focused on employing mobile devices (e.g., smartphones and wearables) for such step tracking [1, 3]. These approaches are uncomfortable and require direct participant of the patient, which leads to reduced level of cooperation and thus effectiveness.

To combat these limitations, we use footstep-induced floor vibration for counting footsteps and estimating frequency of footsteps. The key intuition behind this sensing system is that footsteps striking on the floor induce vibration waves which propagate through the floor. Such vibration can be measured in a passive manner using vibration sensors mounted on the floor [2, 4, 5]. Main challenges of this approach resides in the fact that (1) impulsive excitation noise whose signal is similar to that of footsteps; and (2) each structure induces unique vibration response to footsteps, which makes the vibration different in different structures. The first challenge results in reduced footstep frequency accuracy by mistakenly considering non-footstep impulsive forces as footsteps, while the second challenge requires training the model for every structure which adds to the deployment difficulty.

In this paper, we introduce an online learning system that learns the footstep induced vibration responses of a specific floor and updates the footstep frequency estimation model on the fly. This system eliminates the need for extensive calibration in different structures. This system consists of three main components: (1) a detection module, (2) a classification module, and (3) an online learning module. The detection module measures the floor vibrations and distinguishes the parts induced by impulsive forces from background noise of harmonic or white nature (such as machinery or measurement noise). Classification module distinguishes footstep-induced vibration signals from other impulsive excitations. Finally, to make

M. Mirshekari (✉) • H.Y. Noh
Department of Civil and Environmental Engineering, Carnegie Mellon University, 5000 Forbes Avenue, 15213 Pittsburgh, PA, USA
e-mail: mmirshekari@cmu.edu

P. Zhang
Department of Electrical and Computer Engineering, Carnegie Mellon University, Building 23, Moffett Field, CA 94035, USA



J. Caicedo, S. Pakzad (eds.), *Dynamics of Civil Structures, Volume 2*, Conference Proceedings
of the Society for Experimental Mechanics Series, DOI 10.1007/978-3-319-54777-0_35

the model compatible with new structures, online learning module leverages trace-level heuristic about walking periodicity to update the classifier model. We validate our system performance using field experiments in different structures with human participants.

## 35.2 Online Footstep Frequency Estimation System

Our system for footstep frequency estimation employs an online learning approach to accurately detect footsteps and estimate footstep frequency without extensive calibration using the following three modules: (1) a Detection Module, (2) a Classification Module, and (3) an Online Learning Module. An overview of our system is presented in Fig. 35.1.

**Detection Module** Detection module measures the floor vibration and detects signal induced by impulsive forces. Ambient floor vibration is measured using sensors mounted on the floor. Using a geophone, ambient vibration consists of parts resulted from impulsive excitations (induced by footsteps, door shutting, walkers, etc.) and parts resulted from harmonic or white background noise (e.g., machinery or measurement noise). We separate the impulsive excitation parts which contains the footstep-induced vibration from the background noise using an energy-based threshold method [7]. This method, assumes a Gaussian distribution for background noise and three standard deviations above the mean ($\mu + 3\sigma$) of the signal energy is set to be the threshold to detect impulses.

**Classification Module** To accurately estimate footstep frequency, we need to accurately distinguish the footsteps from other impulsive excitations. To this end, our system leverages a one-class SVM classifier using features based on frequency-domain representation of the signal. One-class SVM [8], trains the classifier using data related to one cluster (e.g., footsteps) and considers the rest of data points as outliers. This classifier is suitable for our purpose as in real-world application the source of all impulsive non-footstep excitations is not known. Hence, we train the one-class SVM classifier using only the footstep-induced vibrations. However, the waveform of a footstep is different in different structures as shown in Fig. 35.2a. Therefore, trained classifier will be dependent on the structure and is not compatible with different structures. To eliminate extensive calibration for each structure, we introduce an online learning module.

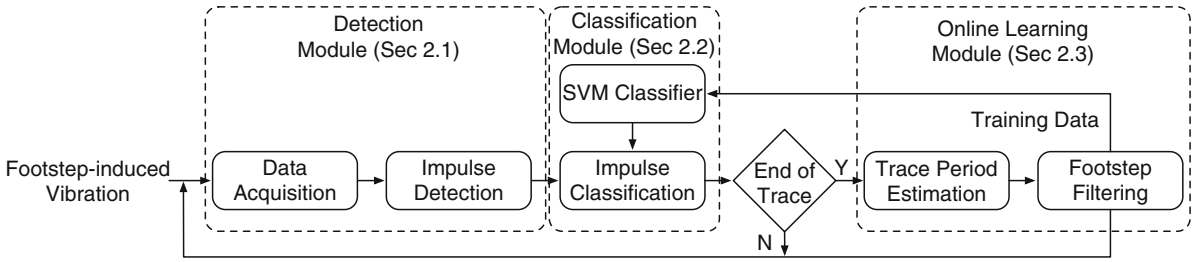


**Fig. 35.1** System overview

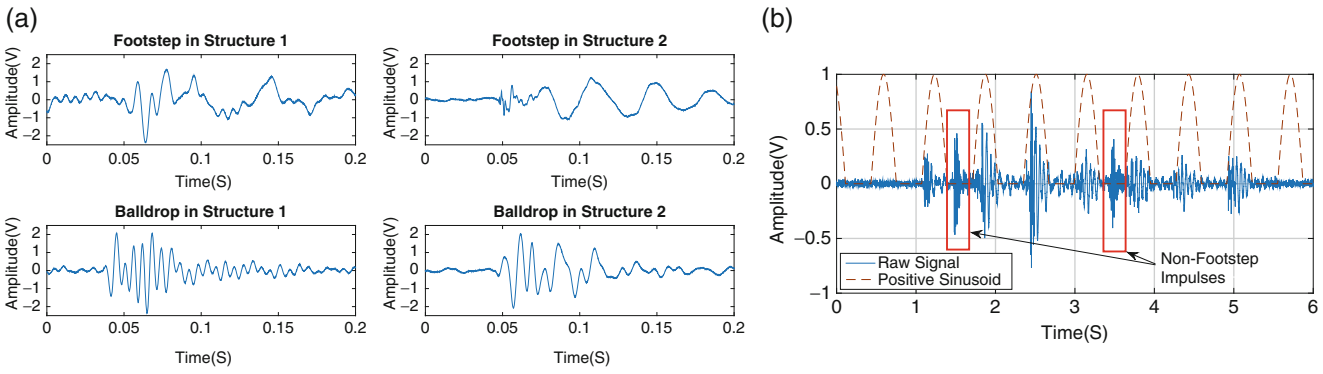


**Fig. 35.2** (**a**) Footstep and ball-drop induced vibrations are different in two structures (*left* and *right*). (**b**) A raw signal is plotted with the positive sinusoid with the period of the estimated footsteps. *Red boxes* mark impulses identified as non-footsteps

**Online Learning Module** Our system employs trace-level heuristics about walking patterns (i.e. periodicity) to detect potential footstep-induced signals on the fly and leverage such footsteps as training data to update the model to accurately represent footstep-induced vibration in each structure. The main intuition is that traces resulted from footsteps are periodic with a specific range of frequencies, whereas other impulses are not generally periodic.

To leverage such periodicity, we find impulse signals that have similar periods as footsteps. The period of potential footsteps is estimated using the dominant frequency component of the auto-correlation function. Next, we separate the parts of the vibration signal which are induced by periodic footsteps in a specific range of frequencies from other non-periodic impulsive excitations. To this end, we find the inner product of the positive sinusoidal signal of the determined frequency with the energy of trace signal. The resulting signal only includes the walking trace and does not contain the impulses of different periodicity. An example of this procedure is presented in Fig. 35.2b.

## 35.3 Evaluation

In order to validate our system, we conducted field experiments with human participants in two structures: a campus building which has a non-carpeted concrete floor with an observed first natural frequency of 23.83 Hz and a nursing home facility which has a carpeted concrete metal deck floor with an observed first natural frequency of 14.84 Hz. The experiments consist of two different people walking in their natural gait and several types of impulses (i.e., object drops, walkers, canes, and door closing). We first train the system in one of the structures. The accuracy of classification in the other structure is then compared for two cases: before and after updating the classifier using our approach. The results show that our approach results in F1 score of 0.87 which is equal to 8× improvement in classification performance.

## 35.4 Conclusions

In this paper, we introduce a non-intrusive system based on footstep-induced floor vibration. We focus on addressing the main challenges of this sensing system: (1) distinguishing footstep-induced vibrations from other impulsive excitations; and (2) providing an algorithm which is compatible to different structures. To address these challenges, we utilize a calibration-free online learning technique that leverages trace-level heuristics to extract footstep-induced vibration in different structures. We validated our approach through field experiments in two structures with human participants. The results show F1 score of 0.87 which is equal to 8× improvement compared to a static learning approach.

## References

1. Foster, R.C., Lanningham-Foster, L.M., Manohar, C., McCrady, S.K., Nysse, L.J., Kaufman, K.R., Padgett, D.J., Levine, J.A.: Precision and accuracy of an ankle-worn accelerometer-based pedometer in step counting and energy expenditure. Prev. Med. **41**(3), 778–783 (2005)
2. Lam, M., Mirshekari, M., Pan, S., Zhang, P., Noh, H.Y.: Robust occupant detection through step-induced floor vibration by incorporating structural characteristics. In: Dynamics of Coupled Structures, vol. 4, pp. 357–367. Springer, Berlin (2016)
3. Melanson, E.L., Knoll, J.R., Bell, M.L., Donahoo, W.T., Hill, J., Nysse, L.J., Lanningham-Foster, L., Peters, J.C., Levine, J.A.: Commercially available pedometers: considerations for accurate step counting. Prev. Med. **39**(2), 361–368 (2004)
4. Mirshekari, M., Pan, S., Bannis, A., Lam, Y.P.M., Zhang, P., Noh, H.Y.: Step-level person localization through sparse sensing of structural vibration. In: Proceedings of the 14th International Conference on Information Processing in Sensor Networks, pp. 376–377. ACM, New York (2015)
5. Mirshekari, M., Pan, S., Zhang, P., Noh, H.Y.: Characterizing wave propagation to improve indoor step-level person localization using floor vibration. In: SPIE Smart Structures and Materials+ Nondestructive Evaluation and Health Monitoring. International Society for Optics and Photonics, pp. 980305–980305 (2016)
6. Öberg, T., Karsznia, A., Öberg, K.: Basic gait parameters: reference data for normal subjects, 10–79 years of age. J. Rehabil. Res. Dev. **30**, 210–210 (1993)
7. Pan, S., Bonde, A., Jing, J., Zhang, L., Zhang, P., Noh, H.Y.: Boes: building occupancy estimation system using sparse ambient vibration monitoring. In: SPIE Smart Structures and Materials+ Nondestructive Evaluation and Health Monitoring. International Society for Optics and Photonics, pp. 90611O–90611O (2014)
8. Schölkopf, B., Platt, J.C., Shawe-Taylor, J., Smola, A.J., Williamson, R.C.: Estimating the support of a high-dimensional distribution. Neural Comput. **13**(7), 1443–1471 (2001)
9. Sudarsky, L.: Gait disorders in the elderly. N. Engl. J. Med. **322**(20), 1441–1446 (1990)
10. Verghese, J., Lipton, R.B., Hall, C.B., Kuslansky, G., Katz, M.J., Buschke, H.: Abnormality of gait as a predictor of non-alzheimer's dementia. N. Engl. J. Med. **347**(22), 1761–1768 (2002)

# Chapter 36
# Optimal Bridge Displacement Controlled by Train Speed on Real-Time

**Piyush Garg, Ali Ozdagli, and Fernando Moreu**

**Abstract** This paper aims to present a controller to optimize the lateral bridge displacement by controlling the speed of the train passing over it. The controller assumed for this purpose is a Linear Quadratic Regulator (LQR) controller. The results will be simulated based on and compared to the actual bridge displacement measured on the bridge during a train passing event.

**Keywords** LQR • Structural control • Displacement • Velocity • Railroad bridge • Structural health monitoring • Real-time

## 36.1 Introduction

Railway system in US is very critical for the freight transportation across the country. It accounts to 40% of freight movement by ton-miles and about 16% by tons [1]. The railways are a $60 billion industry with an operating revenue of over $430 million [1]. More importantly, 91% of all the railway freight are commodities like agriculture and automobile products, construction materials, chemicals, coal, food, metals, and minerals [1]. This makes the optimal and timely performance of the rail network very critical. There is about 140,000 miles of rail track across the country [2]. In addition to this, there are about a 100,000 bridges on the railway network, meaning, on average there is a bridge every 1.4 miles [3]. Thus to ensure a smooth operation of the railways, it is critical to maintain the efficiency of the bridges. The movement of the trains over the bridges cause vibrations on the structure, and if the displacement of the bridge due to the vibration is excessive, it can cause derailment. Some studies have shown that the speed of the train has an almost direct correlation with the bridge displacement [4, 5]. Thus if the train speed can be optimized with the bridge displacements, the excessive bridge movements can be controlled and the train can pass through it at the maximum possible speed. This paper aims to find the optimal speed-displacement value for the bridge using the bridge acceleration measurements.

The importance of the control of movement of structures is very critical and there has been a significant research in this area in the recent times [6]. Types of controls can be classified as Active, Passive, Hybrid or Semi-Active [7]. Active type control is the one which uses external power to control the actuators, while the passive control doesn't use an external source. Hybrid control is a type of control which uses both active and passive type of control, and the Semi-Active control uses devices which consume much less power than the active type devices. To control the movement of the structures, the movement should be accurately measured, so that the appropriate quantity of control signal can be applied. These displacements can be measured using different techniques such as acceleration [8], Global Positioning System (GPS) [9] and digital image processing [9]. This paper uses passive type control and displacement measured from acceleration to implement the control of the bridge displacement.

Magneto-Rheological (MR) Damper is an example of the active device which is most commonly used in the control of the movement of structures. Dyke et al. successfully showed that the acceleration feedback can be used to control the MR dampers [10]. The literature review shows various ways of implementing the control for these active devices. Some of these are PID control [11], Neural Networks [12], Fuzzy Logic [13], and Lyapunov based control [14]. The control techniques

P. Garg (✉)
Department of Electrical and Computer Engineering, MSC01 1100, 1 University of New Mexico, Albuquerque, NM, 87131-001, USA
e-mail: pgarg@unm.edu

A. Ozdagli • F. Moreu
Department of Civil Engineering, MSC01 1070, 1 University of New Mexico, Albuquerque, NM, 87131-001, USA
e-mail: aozdagli@unm.edufmoreu@unm.edu



J. Caicedo, S. Pakzad (eds.), *Dynamics of Civil Structures, Volume 2*, Conference Proceedings
of the Society for Experimental Mechanics Series, DOI 10.1007/978-3-319-54777-0_36

have also been used with the semi-active devices to control the structural movement during the seismic activity [15]. In this paper we will use the LQR technique to control the bridge displacement using the acceleration and train velocity feedback.

In the past, LQR technique is used to control the active [16] and semi-active [17] control of the bridge structures. There have been studies which focus on the control of the bridge displacement resulting from the vibration induced by the motion of the train [18]. The study by Jia Lui et al., also presents the control for the bridge displacement and vibration induced by the train braking and vertical moving loads [19]. However, both these studies control either active or semi-active devices. The disadvantage of this approach is that it takes a lot of additional resources in terms of money, labor, energy, and hardware installation time and efforts for the control of bridge movements. This paper aims to present a control approach which overcomes these disadvantages and is easy to implement.

## 36.2 Dynamic Modelling

The model of the bridge selected for this study is a simple beam structure with rigid supports at each end (Fig. 36.1). The nodes in the bridges are the joints with one degree of freedom (indicated by **w*i*** in Fig. 36.1) along the x axis. The train pass event generates a force on each of these nodes (indicated by **u*i*** in Fig. 36.1). It is assumed that the force acting on the nodes have a linear relationship with the displacement of each node.

The bridge selected for this paper is located over the river Calumet at Chicago, Illinois (Fig. 36.2).

The typical equation of motion for the internal dynamics for the bridge is of the form

$$M\ddot{W} + C\ddot{W} + KW = U \tag{36.1}$$

Here the matrix **M** represents the mass matrix of each node on the bridge. The matrix **C** is the damping matrix and the matrix **K** is the stiffness matrix.

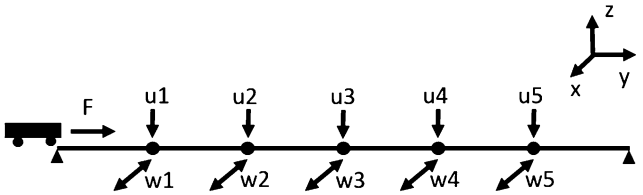


**Fig. 36.1** Structural model of the bridge


**Fig. 36.2** Selected test bridge [20]

The mass matrix for this bridge is given by

$$M = \begin{bmatrix} 3.9\,x\,10^4 & 0 & 0 & 0 & 0 \\ 0 & 3.9\,x\,10^4 & 0 & 0 & 0 \\ 0 & 0 & 3.9\,x\,10^4 & 0 & 0 \\ 0 & 0 & 0 & 3.9\,x\,10^4 & 0 \\ 0 & 0 & 0 & 0 & 3.9\,x\,10^4 \end{bmatrix} \tag{36.2}$$

The stiffness matrix is represented as

$$K = \begin{bmatrix} 3.5\,x\,10^6 & 0 & 0 & 0 & 0 \\ 0 & 5.5\,x\,10^7 & 0 & 0 & 0 \\ 0 & 0 & 2.8\,x\,10^8 & 0 & 0 \\ 0 & 0 & 0 & 8.9\,x\,10^8 & 0 \\ 0 & 0 & 0 & 0 & 2.2\,x\,10^9 \end{bmatrix} \tag{36.3}$$

And the damping matrix is given by.

$$C = \begin{bmatrix} 3.7\,x\,10^3 & 0 & 0 & 0 & 0 \\ 0 & 1.5\,x\,10^3 & 0 & 0 & 0 \\ 0 & 0 & 3.3\,x\,10^4 & 0 & 0 \\ 0 & 0 & 0 & 5.9\,x\,10^4 & 0 \\ 0 & 0 & 0 & 0 & 9.2\,x\,10^4 \end{bmatrix} \tag{36.4}$$

Matrix W represents the displacement states of the nodes, then the matrices $\dot{\mathrm{W}}$ and $\ddot{\mathrm{W}}$ represent the velocities and the accelerations of each of these nodes respectively. These matrices can be shown as

$$W = \begin{bmatrix} w1 \\ w2 \\ w3 \\ w4 \\ w5 \end{bmatrix} \quad \dot{\mathrm{W}} = \begin{bmatrix} \dot{w}1 \\ \dot{w}2 \\ \dot{w}3 \\ \dot{w}4 \\ \dot{w}5 \end{bmatrix} \quad \ddot{\mathrm{W}} = \begin{bmatrix} \ddot{w}1 \\ \ddot{w}2 \\ \ddot{w}3 \\ \ddot{w}4 \\ \ddot{w}5 \end{bmatrix} \tag{36.5}$$

The input to each of the nodes can be represented by the matrix U as

$$U = \begin{bmatrix} u1 \\ u2 \\ u3 \\ u4 \\ u5 \end{bmatrix} \tag{36.6}$$

The State space representation of the internal dynamics of the system is given by the equation

$$\dot{X} = AX + BU \tag{36.7}$$

where X represents the displacement and velocity states of the nodes. This can be represented as

$$X = \begin{bmatrix} X1 \\ X2 \end{bmatrix} = \begin{bmatrix} W \\ \dot{W} \end{bmatrix} \qquad \dot{X} = \begin{bmatrix} \dot{X1} \\ \dot{X2} \end{bmatrix} \tag{36.8}$$

We can calculate the values of the A and B matrices for this system by using the Eqs. (36.1) and (36.7). Thus we can represent these matrices as

$$A = \begin{bmatrix} 0 & I \\ M^{-1}K & M^{-1}C \end{bmatrix} \qquad B = \begin{bmatrix} 0 \\ M^{-1} \end{bmatrix} \tag{36.9}$$

The state space representation for the output of system is given by.

$$Y = CX + DU \tag{36.10}$$

Here Y represents the output states of the system. This is given by

$$Y = [X1] \tag{36.11}$$

The matrices C and D can be found from the Eqs. (36.10) and (36.11), represented as

$$C = \begin{bmatrix} I & 0 \end{bmatrix} \qquad D = [0] \tag{36.12}$$

For this bridge model, the natural frequency of vibration is 1.5 Hz. Using this, we can calculate the expected displacement of the bridge for different speeds [3] using the modal analysis.

Figure 36.3 plots the peak displacements of the mid span (node 3) for different speeds. From this figure, it is clear that the peak displacement for the bridge goes on decreasing as the speed of the train decreases.

In Fig. 36.4, I have plotted the peak displacements of different nodes at different speeds. As we can observe from the graph, the relationship of peak nodal displacement has almost a linear relationship with the speed of the train. For the sake of convenience, we will consider this relationship to be linear in this paper.

It can be seen clearly from the Fig. 36.5, that the peak displacement of node 3 is the greatest at any given speed on the train. Thus if we can optimize the system to control the displacement of node 3 and control the train speed using this node alone.

To prove this theory, we will make the assumption that the train is already over the bridge and peak displacement condition will be the initial condition of the state space model. We will also assume that the force exerted by the train cars (weight of the train) is continuous and equal for the entire duration of the time. Further it is assumed that the train is very long and thus it exerts the force on the structure for the entire duration of the simulation. These assumptions will be addressed in the future work where the train dynamics will also be included along with the bridge dynamics which will cause bridge displacement at real time.

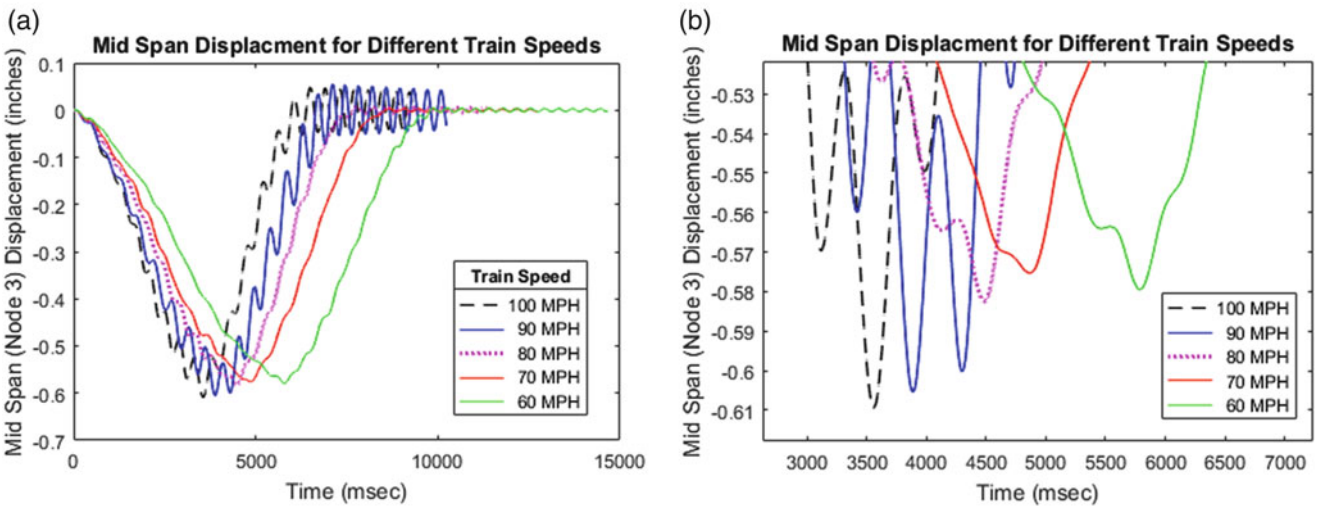


**Fig. 36.3** (**a**) Plot of mid span (node 3) displacements at different train speeds. (**b**) View of peak values for the mid span displacements at different train speeds—magnified

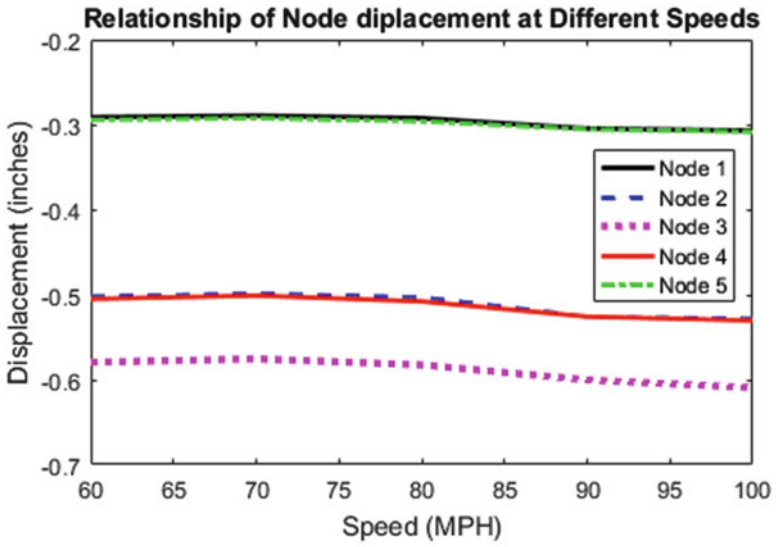


**Fig. 36.4** Plot relating train speed to displacement for different nodes

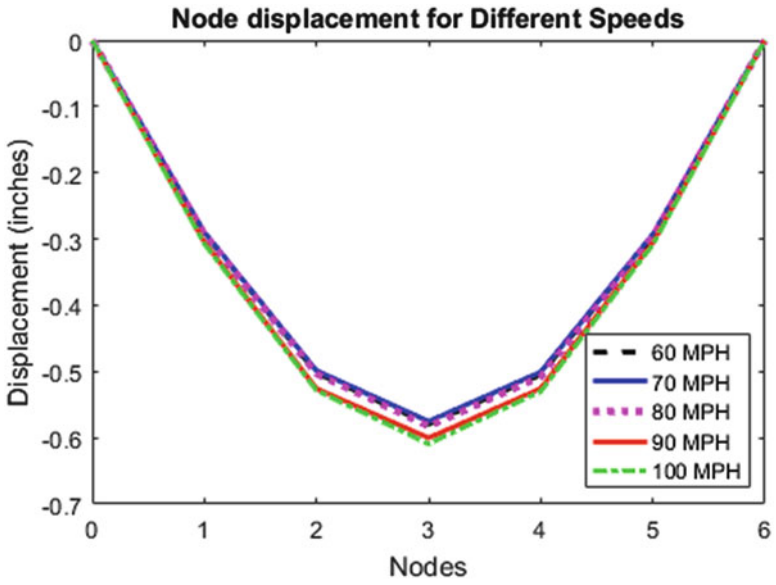


**Fig. 36.5** Plot of mid span (node 3) displacements at different train speeds

## 36.3 Control

Linear Quadratic Regulator (LQR) is an approach to optimize the feedback gains and minimize the cost function. When we apply LQR control to a system, it will optimize for the states to go to zero asymptotically. However, in our problem, if we want to ensure zero displacement for the nodes, the LQR would drive the input to zero, which means we will have the train speed approach zero asymptotically. This does not make any sense for practical implementations. Moreover, the slope of the speed vs displacement curve is such that we will not have a zero displacement for zero velocity. The structure and the train, being dynamic model itself, will have some weight, which will result in some displacement even if the train does not move over the bridge. This also means that at zero displacement, the train speed should be negative, which doesn't make any sense practically. To solve this conundrum, a tracking approach to the LQR problem has been used for this paper.

In tracking using LQR, we force the state to drive to the reference values instead of zero. The above Fig. 36.6 is a typical approach to solve the tracking problem using the LQR approach. In the tracking problem we have a feedback gain $Kx$ and a feed forward gain of $Kr$. Reference input $r$ is the desired value of the state.

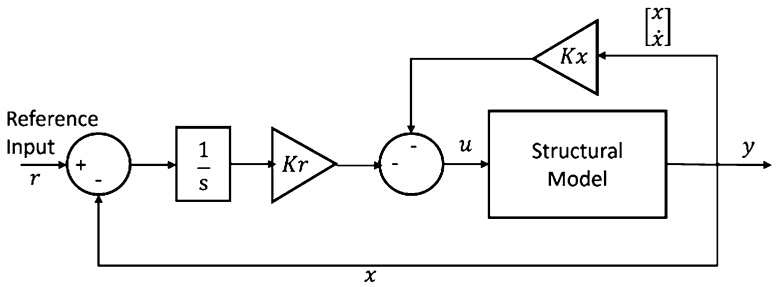


**Fig. 36.6** Typical LQR tracking control block diagram

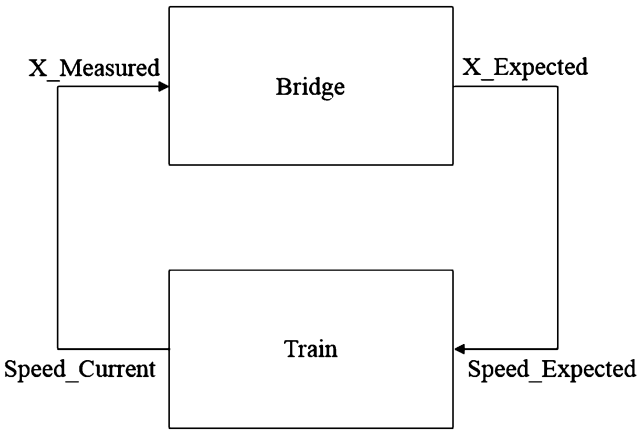


**Fig. 36.7** Closed loop model for bridge and train dynamics

The implementation of LOR for tracking in this paper is applied in the form of two blocks as shown in Fig. 36.7. Here the Bridge block is the state space model of bridge and implements the LQR control. The train model is used to calculate the required speed of the train to provide the desired control input, this block will also estimate the displacement value as per the velocity. We use the plot in Fig. 36.4 to accomplish this. This train block will change in the future work to implement the train dynamic model with displacement feedback from the sensors.

In the tracking problem for the LQR approach, we consider the error in the current state and reference input, along with the state feedback. Thus the control input to the system is calculated using the error and state feedback. This input is given by the equation

$$u = -K_x * x - K_r * r \tag{36.13}$$

In this paper, Linear Quadratic Integral (LQI) technique has been used to achieve the LQR Tracking. In this approach, the gain values for the matrices are calculated using the A and B matrices of the state space equation and the weighting matrices Q and R. Figure 36.8 below, is a typical implementation of the LQI technique. Here the output of the state space model is all the states of the system. This output is multiplied to the gain $K_x$. The displacement states are fed to the train model which gives the train velocity and bridge displacements as discussed earlier. The train model gives the measured displacement as the feedback to this system which is used to calculate the error.

The lqi(A,B,Q,R) function in MATLAB was used for the calculation of for the feedback and the feedforward loops.

## 36.4 Results

The objective of the paper was to limit the movement of the bridge using a reference input. Since the Train system is not dynamic, the initial conditions to the state space models were set at the maximum displacements found from the Figs. 36.3 and 36.4. The optimization was done using the response of the node 3 as according to Fig. 36.5, it has the most displacement at any given speed. Thus at the initial conditions, the system is at maximum displacement and the velocity of the train is

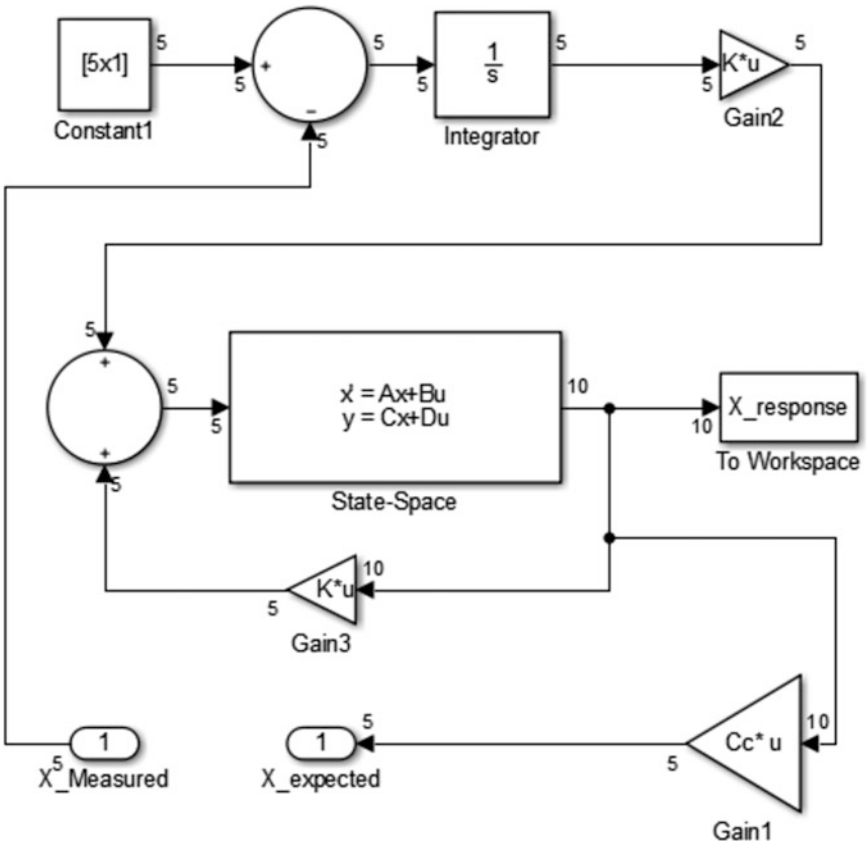


**Fig. 36.8** Linear quadratic integral (LQI) control Simulink model

100 MPH. As we can see from Figs. 36.5 and 36.6, the displacement of the node 3 at 100 MPH is around −0.61 in. We will optimize the system for node 3 to have a fixed displacement of −0.565 in. As the velocity–displacement system is considered to be linear, by observing the slope of the curve for node 3 in Fig. 36.4, we can calculate the speed of the train to be around 40.78 MPH at the displacement of 0.565 in. for node 3.

The control law is considered successful if the displacement of node3 reaches −0.565 in., the train speed mimics the node 3 displacement curve, the velocity of the train settles between 40.5 and 41 MPH, and no nodes have displacement more than node 3. It should be noted that, since the train dynamics are ignored and the relationship between the train speed and displacement is assumed as linear, the train is capable of changing the speed instantaneously. These issues will be addressed in the future work. Also the implementation of the dynamic model of the train will prevent the speed of the train from going to negative when the control is applied.

It is observed in the Fig. 36.9 that the speed of the train after optimization reaches a constant value of 40.73 MPH. It can also be seen from Fig. 36.10, that the node 3 value settles at −0.565 in. Moreover, it can be observed that the displacements of other nodes settle at values closer to 0 and the system will remain stable for this response.

## 36.5 Conclusion

The problem of excessive bridge displacement due to the motion of the train was addressed in this paper. A unique approach of controlling this movement by controlling the train speed was proposed and the theory behind it was proved with results. A simple beam model of the bridge was used to develop the dynamic structural model, and its modes were used to measure the bridge movement in relation to the train speed. The tracking approach was used to optimize the control problem. Tracking was chosen over regulation to maximize the train speed while minimizing the bridge displacement as regulation would result in an impractical system. Linear Quadratic Regulator optimization was applied to tracking problem. Linear Quadratic Integral method of LOR tracking was used and the results were analyzed. This paper will be used as the basis to implement a dynamic train bridge interaction model in the future.

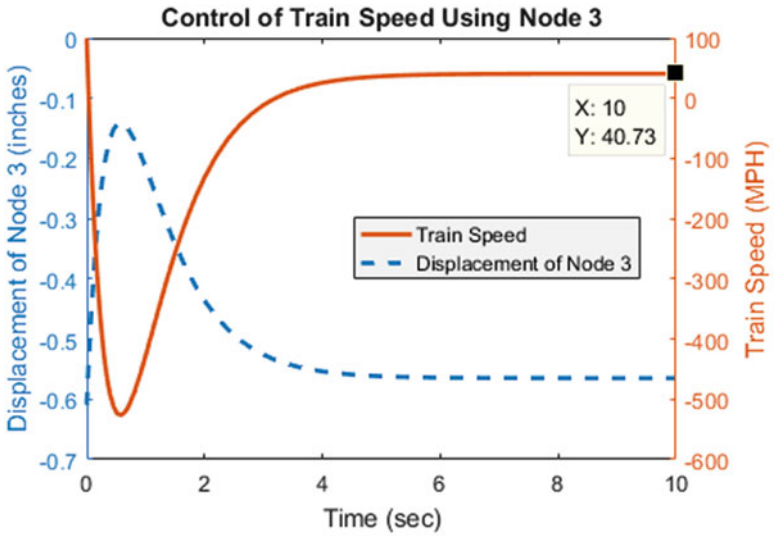


**Fig. 36.9** Train velocity control using node 3 for LQI implementation

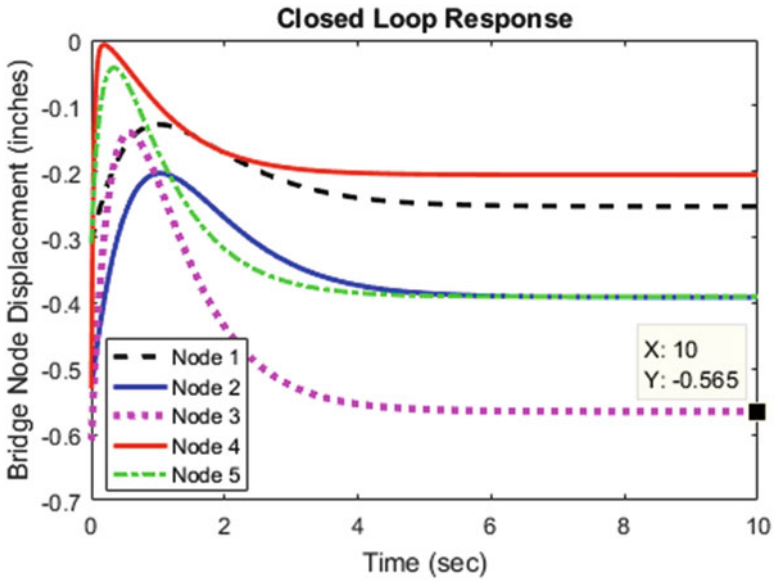


**Fig. 36.10** Plot of node displacements for a closed loop system implemented with LQI optimization

## 36.6 Future Work

As mentioned earlier, in this paper I had assumed a static displacement problem by considering a very long train, already over the bridge and the cars have a constant weight exerting a constant force on the bridge. The next step in this project will be implementation of a time varying system, using a moving load, which will have no initial displacement and as the load passes over the bridge, the displacement will change. As soon as it exceeds the threshold value, the LQR will try to reduce the speed accordingly. This system will then be developed further by cascading with dynamic train model which will interact with the bridge dynamics, simulating a moving mass system. The final model will have LQR optimization to control the train speed and bridge displacement in real time in practical environment.

## References


1. https://www.fra.dot.gov/Page/P0362
2. https://www.aar.org/todays-railroads
3. Kim, R.E., Spencer Jr., B.F.: Modeling and Monitoring of the Dynamic Response of Railroad Bridges Using Wireless Smart Sensors. Newmark Structural Engineering Laboratory. University of Illinois at Urbana-Champaign (2015)
4. Lorieux, L.: Analysis of Train-Induced Vibrations on a Single-Span Composite Bridge. Department of Civil and Architectural Engineering, Division of Structural Design and Bridges, Royal Institute of Technology (KTH), Stockholm, Sweden (2008)
5. Miyashita, T., Ishii, H., Fujino, Y., Shoji, A., Seki, M.: Clarification of the effect of high-speed train induced vibrations on a railway steel box girder bridge using laser Doppler vibrometer. In: Proceedings of the International Conference on Experimental Vibration Analysis for Civil Engineering Structures, pp. 349–357 (2005)
6. Spencer Jr., B.F., Nagarajaiah, S.: State of the art of structural control. J. Struct. Eng. **129**(7), 845–856 (2003)
7. Housner, G.W., Bergman, L., Caughey, T.K., Chassiakos, A.G., Claus, R.O., Masri, S.F., et al.: Structural control: past, present, and future. J. Eng. Mech. **123**(9), 897–971 (1997)
8. Park, K.T., Kim, S.H., Park, H.S., Lee, K.W.: The determination of bridge displacement using measured acceleration. Eng. Struct. **27**(3), 371–378 (2005)
9. Nakamura, S.I.: GPS measurement of wind-induced suspension bridge girder displacements. J. Struct. Eng. **126**(12), 1413–1419 (2000)
10. Dyke, S.J., Spencer Jr., B.F., Sain, M.K., Carlson, J.D.: Modeling and control of magnetorheological dampers for seismic response reduction. Smart Mater. Struct. **5**(5), 565 (1996)
11. Casciati, S., Chen, Z.: An active mass damper system for structural control using real-time wireless sensors. Struct. Control. Health Monit. **19**(8), 758–767 (2012)
12. Kim, J.T., Jung, H.J., Lee, I.W.: Optimal structural control using neural networks. J. Eng. Mech. **126**(2), 201–205 (2000)
13. Symans, M.D., Kelly, S.W.: Fuzzy logic control of bridge structures using intelligent semi-active seismic isolation systems. Earthq. Eng. Struct. Dyn. **28**(1), 37–60 (1999)
14. Wang, X., Gordaninejad, F.: Lyapunov-based control of a bridge using magneto-rheological fluid dampers. J. Intell. Mater. Syst. Struct. **13**(7–8), 415–419 (2002)
15. Ruangrassamee, A., Kawashima, K.: Control of nonlinear bridge response with pounding effect by variable dampers. Eng. Struct. **25**(5), 593–606 (2003)
16. Gluck, N., Reinhorn, A.M., Gluck, J., Levy, R.: Design of supplemental dampers for control of structures. J. Struct. Eng. **122**(12), 1394–1399 (1996)
17. Erkus, B., Abé, M., Fujino, Y.: Investigation of semi-active control for seismic protection of elevated highway bridges. Eng. Struct. **24**(3), 281–293 (2002)
18. Lin, C.C., Wang, J.F., Chen, B.L.: Train-induced vibration control of high-speed railway bridges equipped with multiple tuned mass dampers. J. Bridg. Eng. **10**(4), 398–414 (2005)
19. Liu, J., Qu, W.L., Pi, Y.L.: Active/robust control of longitudinal vibration response of floating-type cable-stayed bridge induced by train braking and vertical moving loads. J. Vib. Control. **16**(6), 801–825 (2010)
20. https://www.google.com/maps/@41.6501474,-87.6210028,652m/data=!3m1!1e3

# Chapter 37
# System Identification and Structural Modelling of Italian School Buildings

**Gerard O'Reilly, Ricardo Monteiro, Daniele Perrone, Igor Lanese, Matthew Fox, Alberto Pavese, and Andre Filiatrault**

**Abstract** Extensive damage to school buildings has been observed during past earthquakes in Italy, with the 2002 Molise event resulting in the complete collapse of a school building leading to numerous casualties. As part of a wider project in Italy to assess the seismic risk in school structures, six school buildings of various construction typologies were surveyed and instrumented to validate detailed numerical models of typical school structures located throughout Italy.

**Keywords** System identification • Structural modelling • School buildings • Reinforced concrete • Masonry

Of the six school buildings considered as part of the aforementioned project, three were reinforced concrete frame building constructed before the introduction of seismic design codes in Italy in the 1970s. The first of these is a three-story frame situated in Ancona, which is along the Adriatic coast of Italy in the province of Marche and is shown in Fig. 37.1a. Similar to this is another three-story frame building located in Carrara, which is along the Mediterranean Sea side of Italy in the province of Tuscany and is illustrated in Fig. 37.1c. Finally, the third reinforced concrete frame school building is shown in Fig. 37.1e and located in Tito, which is in the southern region of Italy in the province of Basilicata, which consists of another three-story frame. In addition to reinforced concrete frame buildings, a number of masonry buildings were also included in the study, such as the two-story masonry building situated in Avola, Sicily and shown in Fig. 37.1f which was constructed in the 1930s. Similarly, Fig. 37.1b shows another school that consists of a two-story masonry school building constructed in 1960's. A third and final typology was also added to include a precast concrete school building constructed in 1987 in Cassino, Italy, as shown in Fig. 37.1d.

Several accelerometers were installed at various locations in each school building to record ambient vibrations. These instruments were used to identify the modal properties of the existing structures. Comparisons were made between the recorded modal properties, such as natural frequencies and mode shapes, and those predicted from eigenvalue analyses using advanced three-dimensional numerical modelling techniques developed to assess the structures under extreme seismic loading. Details of the instrumentation and numerical models will be discussed in the oral presentation. Table 37.1 compares the first three measured ambient vibration natural frequencies for each of the six buildings with those blindly predicted by

G. O'Reilly (✉) • R. Monteiro • D. Perrone
School for Advanced Studies IUSS Pavia, Palazzo del Broletto, Piazza della Vittoria n. 15, 27100, Pavia, Italy
e-mail: gerard.oreilly@iusspavia.it

I. Lanese
European Centre for Training and Research in Earthquake Engineering (EUCENTRE), Via Adolfo Ferrata, 1, 27100, Pavia, Italy

M. Fox
Beca Ltd, 410 Colombo Street, Sydenham, Christchurch 8023, New Zealand

A. Pavese
Department of Civil Engineering and Architecture, University of Pavia 27100, Pavia, Italy

A. Filiatrault
School for Advanced Studies IUSS Pavia, Palazzo del Broletto, Piazza della Vittoria n. 15, 27100, Pavia, Italy

Department of Civil, Structural and Environmental Engineering, State University of New York at Buffalo, Buffalo, NY 14260, USA



J. Caicedo, S. Pakzad (eds.), *Dynamics of Civil Structures, Volume 2*, Conference Proceedings
of the Society for Experimental Mechanics Series, DOI 10.1007/978-3-319-54777-0_37

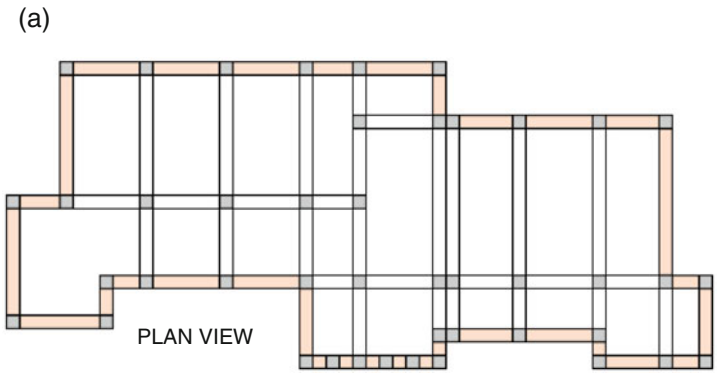


Scuola Elementare Carlo Antognini in Ancona, Italy

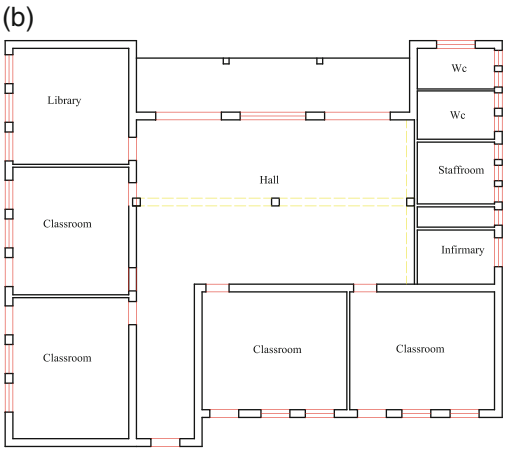


Scuola Elementare "Emiliano Rinaldini" Ghedi, Italy

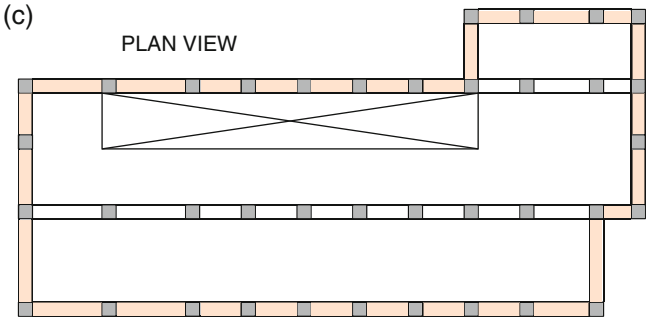


Istruzione Superiore Liceo Classico " E. Repetti" in Carrara, Italy

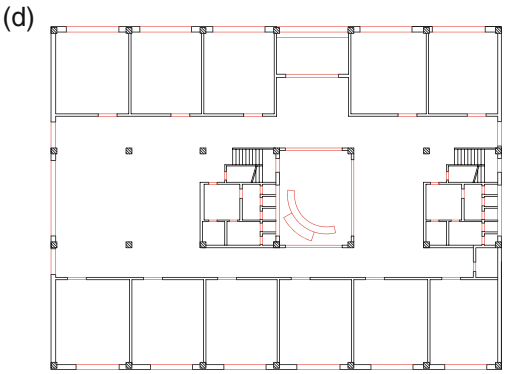


Scuola Elementare Enzo Mattei in Cassino, Italy

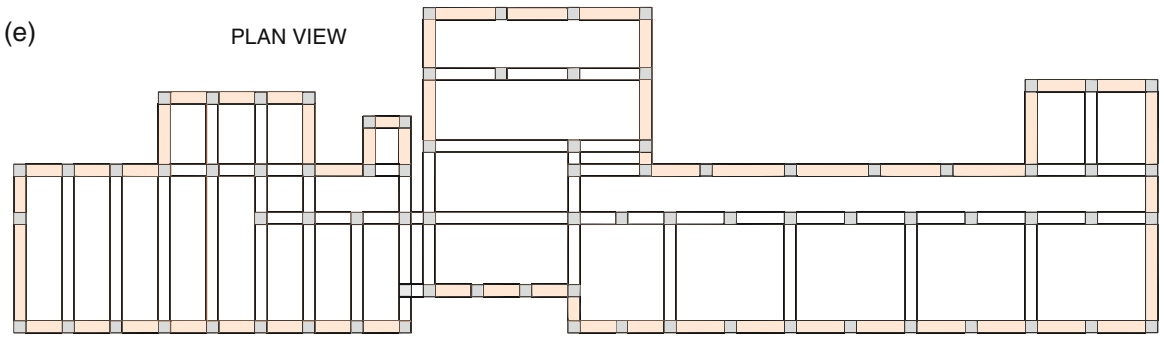


Scuola Media G. Pascoli in Tito, Italy

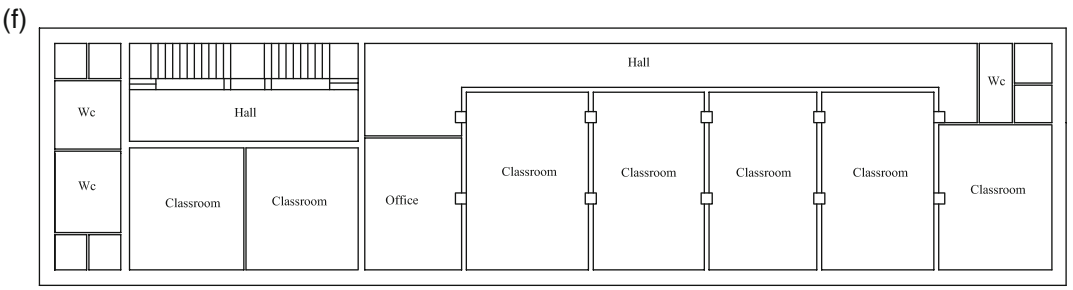


Istituto di Istruzione Superiore "Ettore Majorana" Avola, Italy

**Fig. 37.1** Plan view of the various schools instrumented throughout Italy

**Table 37.1** Measured ambient vibration and numerically predicted natural frequencies

| | | | Natural frequencies (Hz) | | |
|---|---|---|---|---|---|
| School building and location | Mode No. | Mode shape | Ambient vibrations measured | Numerically predicted | Measured/Predicted |
| Scuola elementare Carlo Antognini, Ancona, Italy | 1 | Translation | 5.25 | 1.61 | 3.26 |
| | 2 | Torsion | 6.38 | 2.25 | 2.83 |
| | 3 | Translation | 9.63 | 2.74 | 3.51 |
| Istituto istruzione superiore liceo classico, "E. Repetti" Carrara, Italy | 1 | Translation | 4.50 | 1.49 | 3.02 |
| | 2 | Torsion | 5.13 | 2.36 | 2.17 |
| | 3 | Torsion | 6.38 | 2.51 | 2.54 |
| Scuola elementare Enzo Mattei, Cassino, Italy | 1 | Torsion | 7.50 | 0.99 | 7.58 |
| | 2 | Torsion | 17.8 | 3.97 | 4.48 |
| | 3 | – | Not measured | 0.99 | – |
| Scuola media G. Pascoli, Tito, Italy | 1 | Torsion | 11.6 | 2.43 | 4.77 |
| | 2 | Torsion | 22.0 | 3.17 | 6.94 |
| | 3 | – | Not measured | 3.39 | – |
| Istituto di istruzione superiore "Ettore Majorana" Avola, Italy | 1 | Torsion | 6.63 | 3.13 | 2.12 |
| | 2 | Torsion | 17.5 | 4.35 | 4.02 |
| | 3 | – | Not measured | 4.55 | – |
| Scuola elementare "Emiliano Rinaldini" Ghedi, Italy | 1 | Torsion | 1.38 | 4.35 | 0.32 |
| | 2 | Torsion | 2.88 | 4.72 | 0.61 |
| | 3 | Torsion | 13.75 | 5.00 | 2.75 |

**Table 37.2** Natural frequencies of scuola elementare Carlo Antognini in Ancona, Italy obtained from 2016 Norcia earthquake triggered records and from ambient vibrations measurements

| Mode No. | Earthquake triggered natural frequencies | Ambient vibrations natural frequencies | Earthquake triggered/Ambient vibrations |
|---|---|---|---|
| 1 | 3.88 | 5.25 | 0.74 |
| 2 | 4.50 | 6.38 | 0.71 |
| 3 | 6.63 | 9.63 | 0.69 |

the numerical models. Considerable differences exist between the measured natural frequencies and those predicted by the numerical models. In most cases, the numerical models underpredict the natural frequencies. Reasons for these differences will be discussed during the oral presentation.

The accelerometers installed on the roof of the Scuola Elementare Carlo Antognini in Ancona, Italy were triggered during the recent (August 24, 2016) Norcia earthquake in central Italy [1]. The site of the building is located at approximately 160 km from the epicentre of the earthquake. The response amplitudes of the building under this earthquake event were much larger than that under ambient vibrations. Table 37.2 compares the first three natural frequencies of the building extracted from the earthquake triggered records from those obtained from of ambient vibrations measurements. The natural frequencies extracted from the earthquake triggered records are significantly lower than those obtained from ambient vibrations measurements. Reasons for these reductions in natural frequencies will also be discussed during the oral presentation.

## Reference

1. Celano, F., Cimmino, M., Coppola, O., Magliulo, G., Salzano, P.: Report dei danni registrati a seguito del terremoto del Centro Italia del 24 agosto 2016 (Release 1), p. 26 (2016). Available at: http://www.reluis.it

# Chapter 38
# Investigation of Transmission of Pedestrian-Induced Vibration into a Vibration-Sensitive Experimental Facility

**Donald Nyawako, Paul Reynolds, and Emma J. Hudson**

**Abstract** This paper is based on field measurements that were undertaken in a facility housing ultra-low level vibration sensitive equipment. The aim of these tests was to better understand the vibration transmission from an overhead pedestrian footbridge to a pile supported experimental floor and the supported vibration sensitive equipment.

The results of experimental measurements to estimate the as-built modal properties (natural frequencies, modal damping ratios and mode shapes) of the footbridge structure are presented as well as response measurements at selected locations on the footbridge and experimental floor from controlled walking tests. These series of measurements indicate that vibrations are transmitted from the footbridge to the experimental floor as well as to the supported equipment. This is verified through transmissibility checks which also indicate that vibrations from the experimental floor are transmitted onto the supported equipment over the frequency bandwidth considered. The assessment of vibration levels using vibration criteria curves for response measurements on the experimental floor and the supported equipment for ambient (quiet conditions) and controlled walking excitations on the footbridge structure are also provided.

**Keywords** Vibration • Vibration criteria • Transmissibility

## 38.1 Introduction

Structures housing vibration-sensitive scientific and manufacturing equipment often demand ultra-low level vibration environments, sometimes with tolerances of the order of picometers [1]. Failure to provide such vibration environments can compromise vital experiments or result in severe production losses.

The determination of appropriate vibration levels can be difficult since the equipment specifications for vibration tolerances are often misleading. In [2] and [3], observations are made that when designing vibration-sensitive facilities for advanced technologies or even for research and development applications, it is appropriate to use the generic vibration criterion (VC) curves. These have been developed based on available specifications, tests and experiences and they can apply to a broad range of equipment. Facilities should be made with some flexibility in mind in the sense that they should be designed to meet the requirements of a family of equipment that might be installed there. The generic VC curves can be used with other existing guidelines, for example, [4] and [5] that have been developed for the evaluation of human exposure to vibration in buildings, whole body mechanical vibration and repeated shock.

Additional provisions should be made for the case where the desired vibration limits are not attained in the design phase or in practice [6, 7] for example, through the introduction of vibration mitigation technologies. This might comprise of either controlling the vibrations at source, controlling the transmission of vibrations or controlling vibrations at the receiver using passive, active, semi-active or hybrid technologies.

The three aspects of the vibration source, the vibration transmission path and the vibration receiver are the fundamentals of the work presented here. The vibration source results from pedestrians walking on the footbridge structure, the vibration transmission path results from the footbridge structure onto an experimental floor through the supporting walls and columns and the vibration receiver is the sensitive equipment installed on the experimental floor. Thus, the work presented here investigates the transmission of pedestrian-induced vibration from a footbridge structure onto a vibration sensitive experimental facility. Experimental modal analysis (EMA) tests are carried out to estimate the modal properties of the footbridge structure. Additional EMA tests are carried out to quantify the transmission of vibrations from the footbridge structure onto the experimental facility as well as on the supported equipment. Response measurements at a selected location

D. Nyawako (✉) • P. Reynolds • E.J. Hudson
Vibration Engineering Section, College of Engineering, Mathematics and Physical Sciences, University of Exeter, Exeter EX4 4QF, UK
e-mail: d.s.nyawako@exeter.ac.uk; p.reynolds@exeter.ac.uk; e.j.hudson@exeter.ac.uk



J. Caicedo, S. Pakzad (eds.), *Dynamics of Civil Structures, Volume 2*, Conference Proceedings
of the Society for Experimental Mechanics Series, DOI 10.1007/978-3-319-54777-0_38

on the footbridge structure and at two locations on the experimental floor based on controlled walking tests over the footbridge structure are also presented as well as the transmissibility plots between these responses. Finally, the assessment of vibration levels using vibration criteria curves from response measurements on the experimental floor and supported equipment are shown for both walking and ambient excitation cases.

## 38.2 Estimation of Modal Properties of As-Built Footbridge Structure

The footbridge structure is steel-framed and comprises of two primary beams 610 × 229 × 125 UB running along its edges as shown in Fig. 38.1a. Angular bracing of the beams consist of 165 × 152 × 20 UBT and 90 × 90 × 10 RSEA sections. Two intermediary 100 × 100 × 5 RHS supports with CHS bracings that are introduced at mid-span as props to the primary beams can also be seen in Fig. 38.1a. These were added to provide additional rigidity to the footbridge structure and they in turn alter its dynamic characteristics. Figure 38.1b shows a typical section through the experimental facility around the test location area.

The test grid in Fig. 38.2 was used to determine the modal properties of the footbridge structure. Two excitation shakers, APS Dynamics Model 400 electrodynamic shakers, were placed at TPs 7 and 13 as seen in Fig. 38.3a, b. TPs 5 and 13 are the intermediate support points for the mid-span support seen in Fig. 38.1a. The shakers were driven with statistically uncorrelated random signals so that the frequency response functions (FRFs) corresponding with individual shakers could be evaluated. The shaker forces were measured using Endevco 7754A-1000 accelerometers that were attached to the inertial masses whilst the acceleration of the footbridge was measured using 19 Honeywell QA750 servo accelerometers mounted on levelled perspex base plates and placed at TPs 1–19. Data acquisition was carried out using a Data Physics Mobilyzer II digital spectrum analyser. Figure 38.4 shows the FRFs determined at the collocated actuator and sensor locations.

The results of the modal parameter estimation that were evaluated using ME′scope software are summarised in Table 38.1 and the first four vibration modes are shown in Fig. 38.5.

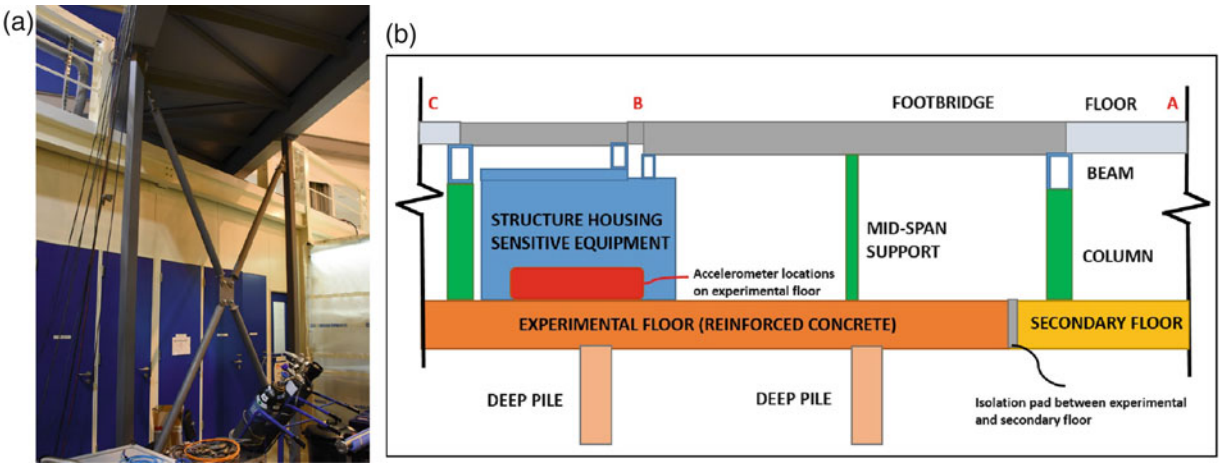


**Fig. 38.1** Photo underneath footbridge structure showing primary beams and bracing elements and 2D section of experimental facility around test location. (**a**) Photo under footbridge. (**b**) Section through experimental facility

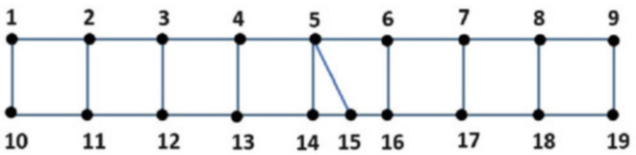


**Fig. 38.2** Test grid for modal testing of footbridge structure (section A to B) in Fig. 38.1b

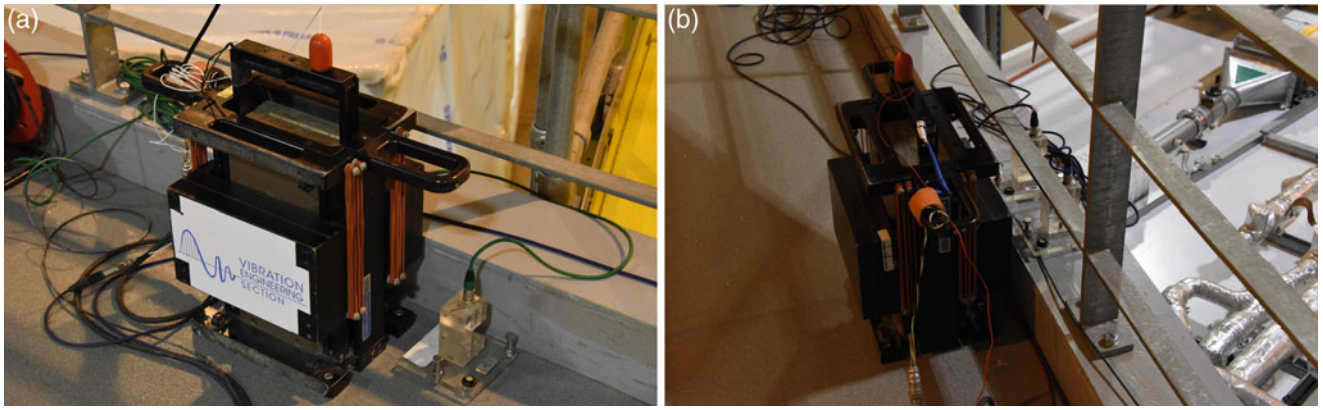


**Fig. 38.3** Excitation shakers and accelerometers at TPs 7 and 13 on the footbridge structure. (**a**) Accelerometer and shaker at TP7. (**b**) Accelerometer and shaker at TP13

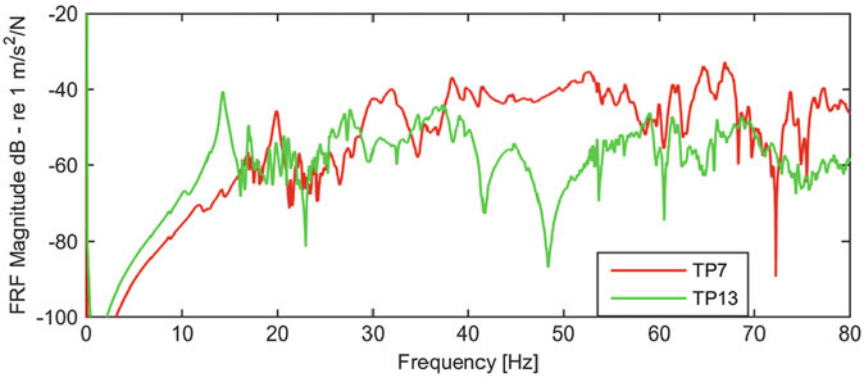


**Fig. 38.4** Point accelerance frequency response functions at TPs 7 and 13 on the footbridge structure

**Table 38.1** Summary of estimated modal properties from EMA tests

| Mode | Natural frequency [Hz] | Damping ratio [%] |
|---|---|---|
| 1 | 5.7 | 0.7 |
| 2 | 8.7 | 0.9 |
| 3 | 10.4 | 3.7 |
| 4 | 12.0 | 2.3 |
| 5 | 12.9 | 0.5 |
| 6 | 14.2 | 1.5 |
| 7 | 15.7 | 0.9 |
| 8 | 16.3 | 0.6 |
| 9 | 17.0 | 0.5 |
| 10 | 17.9 | 0.7 |
| 11 | 19.1 | 0.6 |
| 12 | 19.8 | 1.2 |

## 38.3 Vibration Transmission from Shaker Excitation Tests

The frequency response function (FRF) tests were repeated with the accelerometers at TPs 1–8 being moved to TPs 101–108 that are located within the structure housing sensitive equipment shown in Fig. 38.1b, which is installed on the experimental floor. TPs 101, 103, 105 and 107 are accelerometers on the experimental floor whilst TPs 102, 104, 106 and 108 are accelerometers on equipment resting on the experimental floor. For example, Fig. 38.6 shows the accelerometers at TPs 101 and 102 on the experimental floor and on the equipment it supports at one of the locations. The aim of these tests was to study the transmission of vibrations from the footbridge structure to the experimental floor and the equipment installed on it.

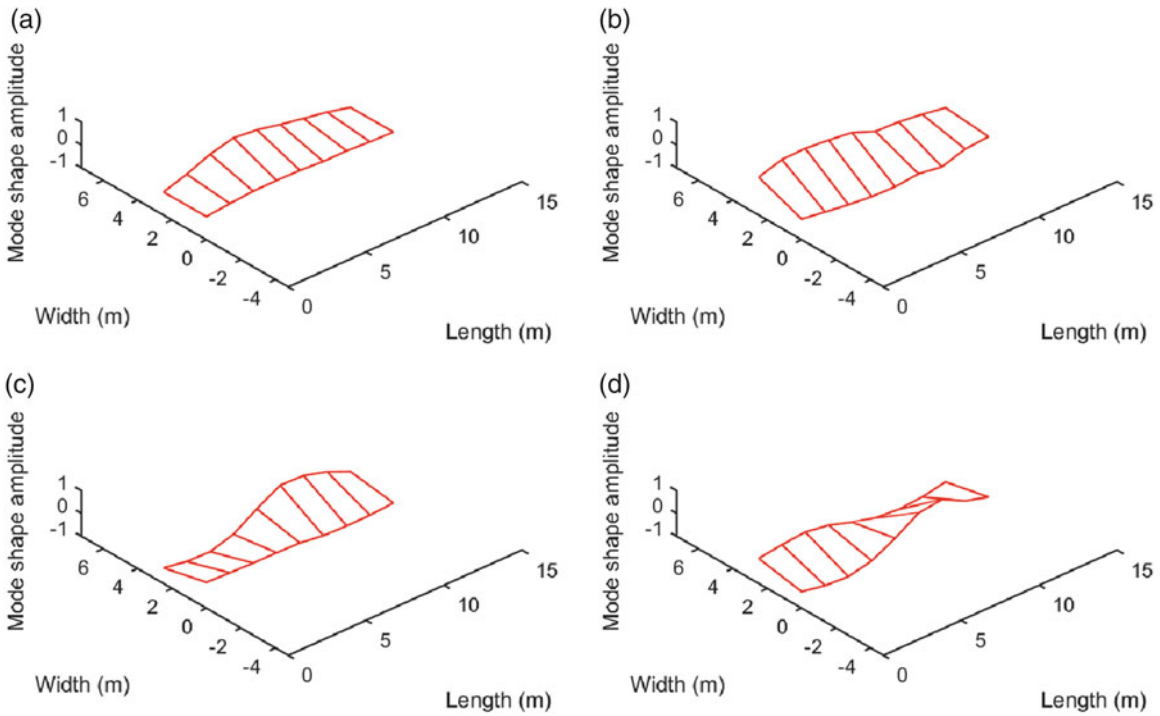


**Fig. 38.5** Estimated mode shapes of the lowest four identified resonant frequencies of the footbridge structure. (**a**) Mode 1. (**b**) Mode 2. (**c**) Mode 3. (**d**) Mode 4

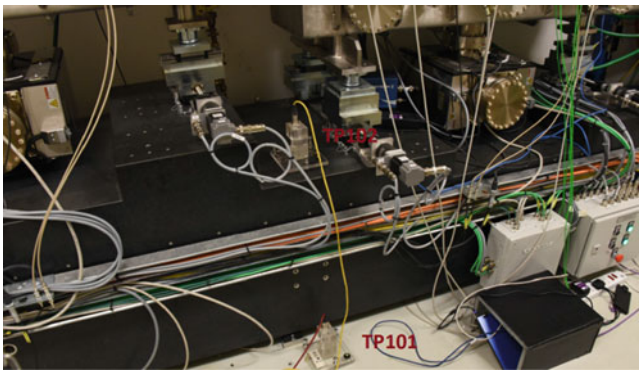


**Fig. 38.6** Accelerometers at TPs 101 and 102 on the experimental floor and on equipment installed on the experimental floor

The most important FRFs at the selected locations of TPs 7, 101 and 102 with reference to the shaker excitation at TP 7 are presented in Fig. 38.7a. Also presented in Fig. 38.7b are FRFs at TPs 13, 101 and 102 with reference to the shaker excitation at TP13. These plots show the potential for transmission of vibrations from the footbridge structure onto the experimental floor as well as on the equipment it supports. A key indicator for these observations are similar resonant peaks being seen on the footbridge structure as well as on the experimental floor and supported equipment. This indicates that the same vibration mode is being engaged at both locations and this would result in vibrations at one point being transmitted onto the other location. This is clearly seen at some particular frequencies, for example, around 20.0 Hz in Fig. 38.7a even though the relative magnitude on the experimental floor and supported equipment is lower by about 50 dB. Figure 38.7a, b also indicate that vibrations from the experimental floor are directly transmitted to the equipment supported on it across the frequency bandwidths considered during the testing.

Figure 38.8 shows the calculated transmissibilities between the response measurements at TPs 13, 101 and 102 for the shaker excitations at TPs 7 and 13. One fundamental feature of this figure is that vibrations from the experimental floor are directly transmitted onto the equipment it supports and even potentially amplified at some frequencies, due to local resonances within the equipment itself.

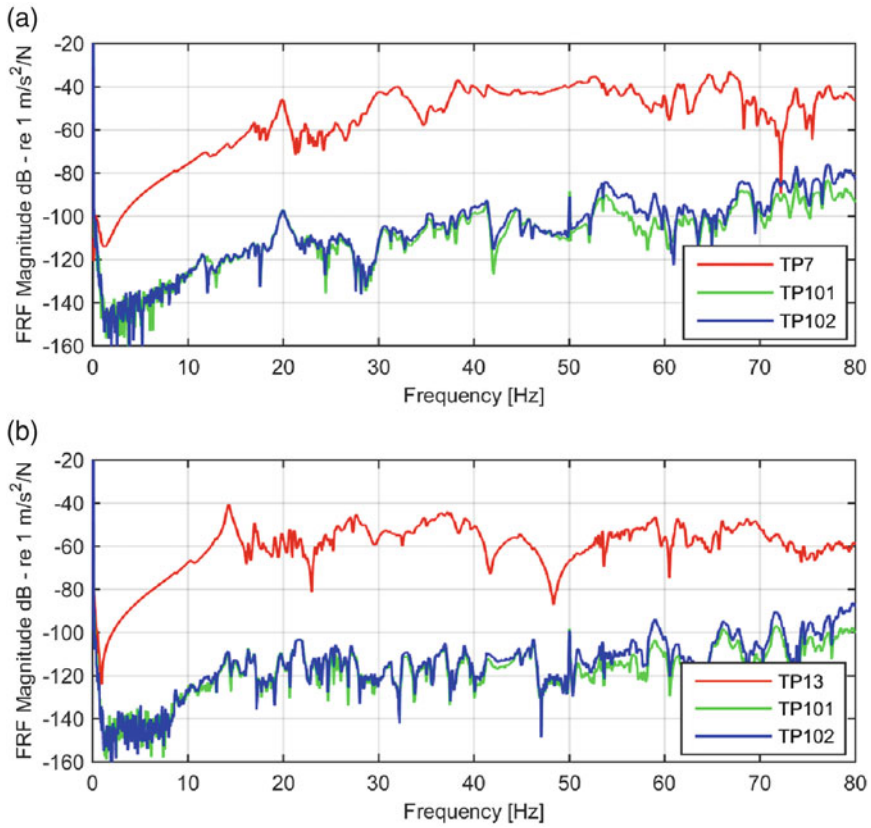


**Fig. 38.7** Frequency response function measurements at TPs 7, 13, 101 and 102. (**a**) FRFs at TPs 7, 101 and 102 corresponding to shaker at TP7. (**b**) FRFs at TPs 7, 101 and 102 corresponding to shaker at TP13

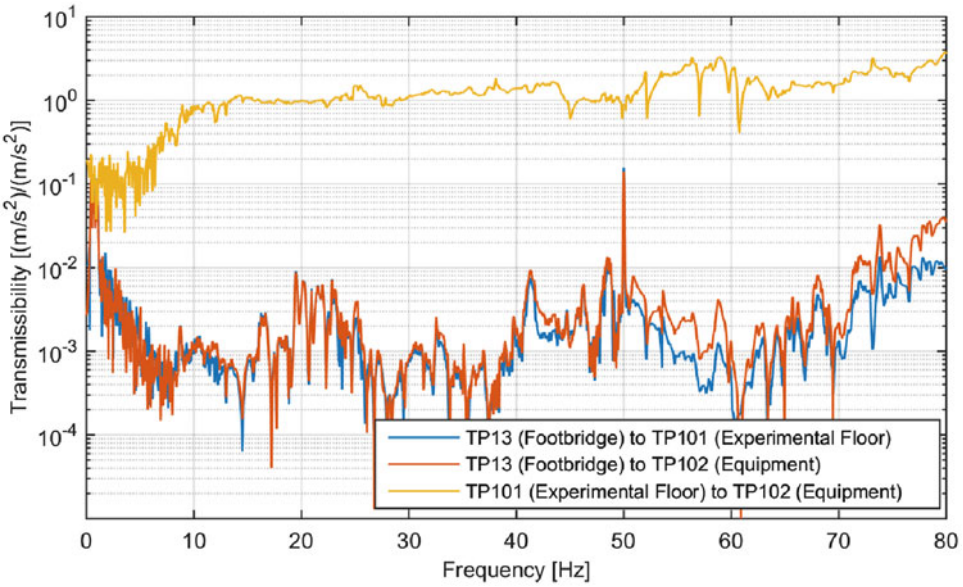


**Fig. 38.8** Transmissibilities between responses measured at TPs 13, 101 and 102 for shaker excitation case

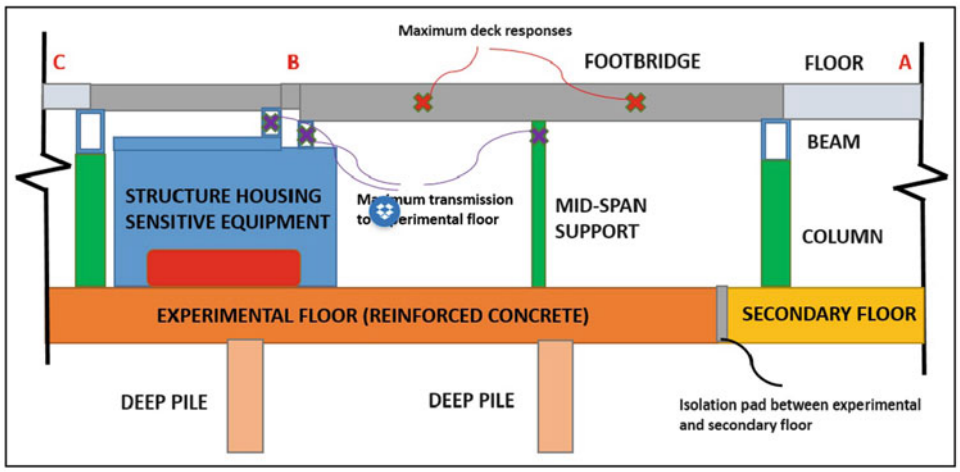


**Fig. 38.9** Section through experimental facility showing points of maximum deck responses and transmission points onto experimental floor

## 38.4 Results from Controlled Walking Tests

Walking tests were performed by a pedestrian walking over the footbridge structure from point A to point C and back to point A, as shown in Fig. 38.9. The pacing frequencies were controlled by a metronome and varied from 1.5 to 2.5 Hz, in steps of 0.1 Hz. The figure also shows the points at which the maximum footbridge responses occur as well as the points of maximum transmission of vibration onto the experimental floor. Only the responses at TPs 13, 101 and 102 are shown in this work in Fig. 38.10a–c, being responses for the entire duration of the walking.

An observation of the responses measured in Fig. 38.10b, c show the potential for transmission of vibrations from the footbridge structure onto the experimental floor and the equipment it supports. In Fig. 38.10, the peak response measurements on the footbridge structure at TP13 are $\pm 1.0\,m/s^2$, whilst those at TPs 101 and 102 are $\pm 0.004\,m/s^2$.

The respective transmissibilities between accelerometer measurements at TPs 13, 101 and 102 for the controlled pedestrian walking tests are shown in Fig. 38.11. An observation from this figure is that all vibrations from the experimental floor are directly transmitted onto the equipment it supports, potentially even amplified at some higher frequencies.

## 38.5 Vibration Criteria Curves for Response Measurements on Experimental Floor and Supported Equipment

Vibration criteria (VC) curves are defined as the root-mean-square (RMS) velocity spectra in 1/3 octave bands. Instead of specifying vibration levels in fixed bands, proportional bands are used as they provide a better measure of how a structure reacts to a broadband excitation at the resonant frequencies. Vibration criteria (VC) curves are often classified in increasing severity from VC-A down to VC-M [3]. More commonly, VC-A to VC-E are seen in most of the literature.

VC curves are used to assess the levels of vibration at key locations on the experimental floor: TPs 101 and 102 in Fig. 38.6. Two different scenarios are considered: walking excitation and ambient conditions. The results of these assessments are seen in VC curves presented in Fig. 38.12. These figures show that the responses measured can, for example, be tolerated by significantly better than a VC-E facility.

## 38.6 Conclusions

This work has provided some clarifications as to the potential for transmission of vibrations from the footbridge structure to the experimental floor and subsequently to the equipment supported on the experimental floor. This is seen from both the experimental modal analysis (EMA) tests as well as from controlled walking tests at different pacing frequencies. It is seen

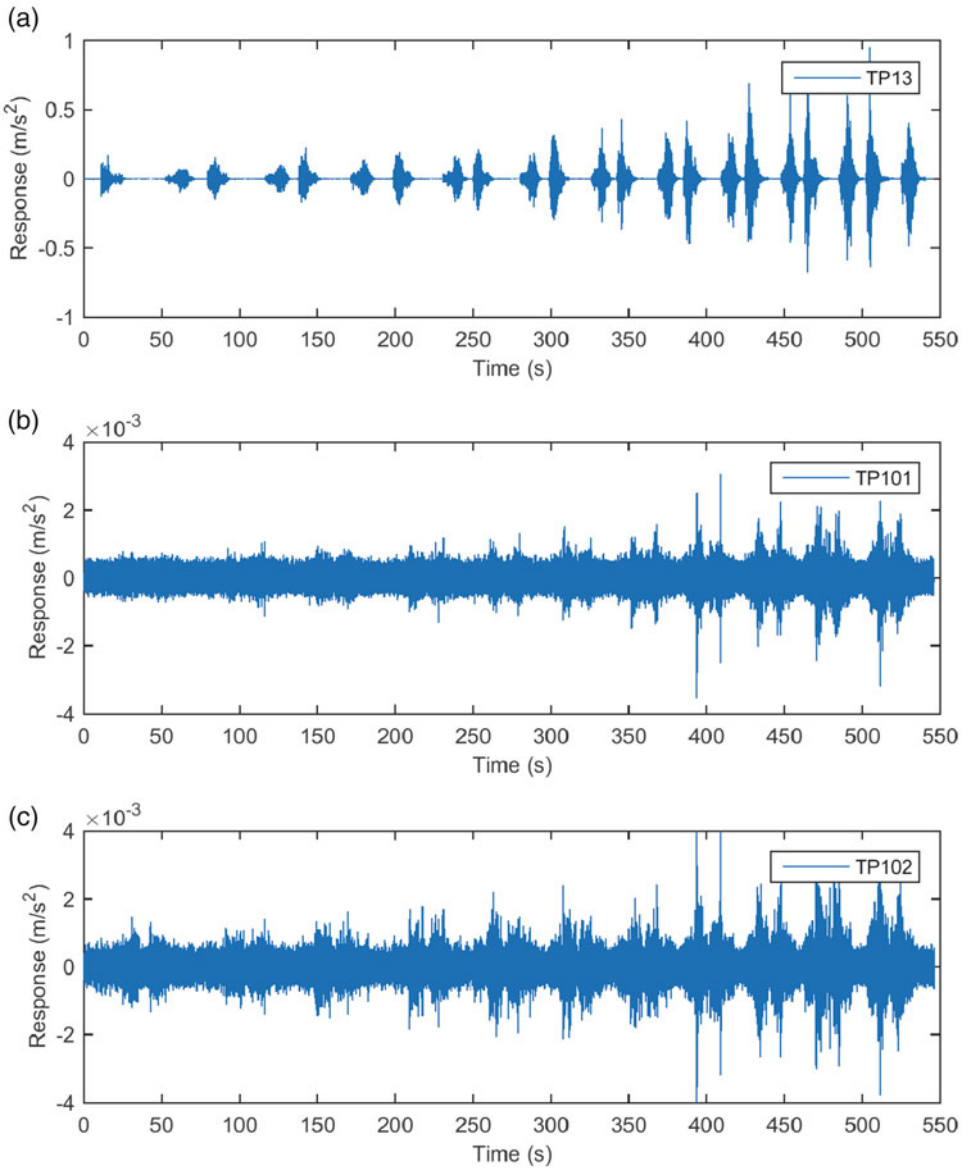


**Fig. 38.10** Responses measured by accelerometers sited at TPs 13, 101 and 102 to pedestrian walking frequencies ranging from 1.5 to 2.5 Hz in steps of 0.1 Hz. (**a**) Response measurement at TP13. (**b**) Response measurement at TP101. (**c**) Response measurement at TP102

that most of the vibrations on the experimental floor are directly transmitted onto the equipment it supports as evidenced by the transmissibility plots. The assessment of vibration using the vibration criteria (VC) curves, for example, show that the responses measured can be tolerated by a VC-E facility.

**Acknowledgements** The authors would like to acknowledge the financial assistance provided by the UK Engineering and Physical Sciences Research Council (EPSRC) through a responsive mode grant (Ref. EP/H009825/1), and a Leadership Fellowship Grant (Ref. EP/J004081/2).

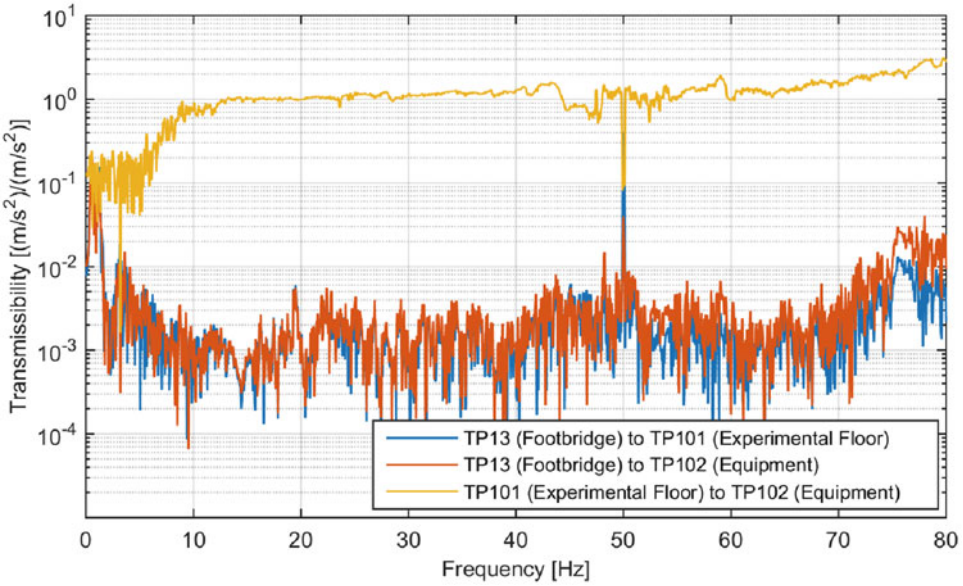


**Fig. 38.11** Transmissibilities between responses measured at TPs 13, 101 and 102 for controlled walking tests

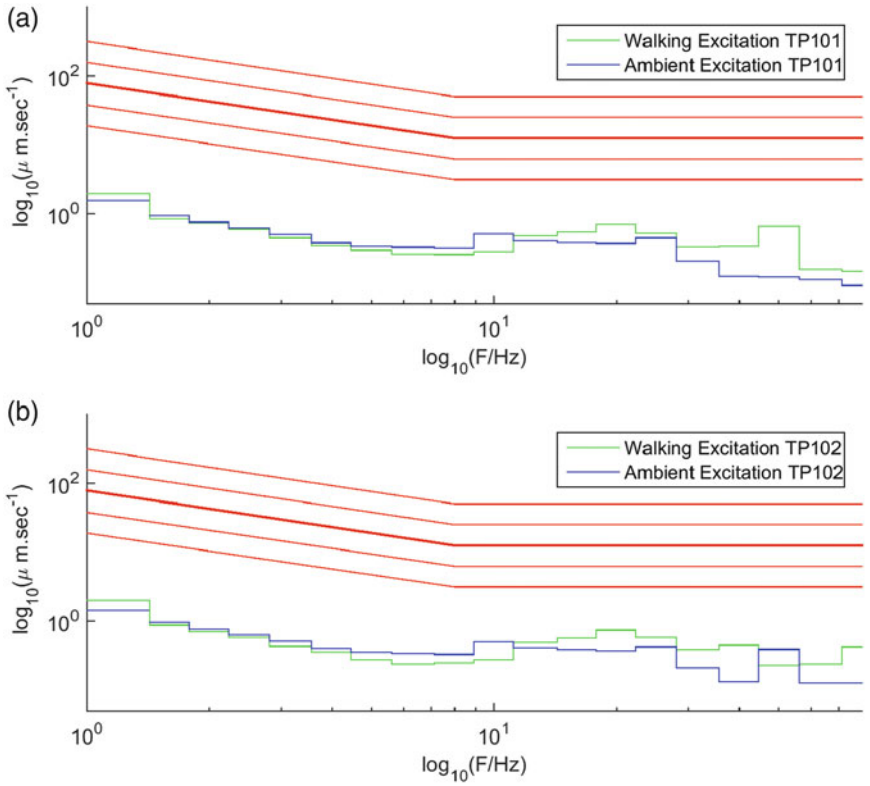


**Fig. 38.12** Vibration criteria (VC) curves for walking and ambient excitations at TPs 101 and 102. (**a**) VC curves for walking and ambient excitations at TP101. (**b**) VC curves for walking and ambient excitations at TP102

## References

1. Brownjohn, J.M.W., Pavic, A.: Vibration control of ultra-sensitive facilities. ICE Proc. Struct. Build. **159**(SB5), 295–306 (2006)
2. Gordon, C.G.: Generic criteria for vibration-sensitive equipment. Proc. Int. Soc. Opt. Eng. (SPIE) **1619**, 22–33 (1999)

3. Amick, C.H., Gendreau, M., Busch, T., Gordon, C.G.: Evolving criteria for research facilities: I - vibration. In: Proceedings of SPIE Conference 5933: Buildings for Nanoscale Research and Beyond, San Diego, vol. 5933, pp. 1–13 (2005)
4. BS6841 guide to measurement and evaluation of human exposure to whole-body mechanical vibration and repeated shock, British Standard (1987)
5. BS6472-1 Guide to evaluation of human exposure to vibration in buildings. Vibration sources other than blasting, British Standard (2008)
6. Amick, C.H., Monteiro, P.J.M.: Vibration control using large pneumatic isolation systems with damped concrete inertia masses. In: International Conference on Motion and Vibration Control, MoViC 04, vol. 118, pp. 1–10 (2004)
7. Abakumov, A.M., Miatov, G.N.: Control algorithms for active vibration isolation systems subject to random disturbances. J. Sound Vib. **289**, 889–907 (2006)

# Chapter 39
# An Ambient Vibration Test of an R/C Wall of an 18-Story Wood Building at the UBC Campus

**Yavuz Kaya, Carlos E. Ventura, and Alireza Taale**

**Abstract** This paper is part of long-term research project, and the main intension of this paper to estimate the stiffness of a concrete core wall of 18-story timber based structure. The 53-meter tall structure has been constructed at the campus of the University of British Columbia in 2016, and it is currently used as a student resident. The building is the tallest timber-based structure in North America. An Ambient Vibration Test (AVT) was conducted on one of the concrete walls to estimate the modal properties of the concrete wall (e.g., modal frequency, modal damping ratio, and mode shape). The construction of the two concrete walls was finished at the time of the AVT, but not the entire structure; therefore, the AVT was conducted only on one of the concrete walls. The modal properties of the Bernoulli Euler and Shear beam are previously used in the literature to estimate the structural response; therefore, they are now used in this study to match the extracted modal response of the concrete wall to estimate the stiffness of the concrete wall. The preliminary results are presented in the paper, but still this work is in progress, and more results will be published in the future.

**Keywords** Modal identification • Shear and bending beam • R/C concrete wall • Modal frequency and mode shape • Stiffness

## 39.1 Introduction

UBC has constructed an 18-story tall wood building at the UBC campus 2016. The 53-meter-high building (the Brock Commons Tall Wood Building) is currently being used as a student residence, housing approximately 400 students and are comprised of approximately 500 CLT panels as well as two concrete cores as seen in Fig. 39.1. The location of the building is at 6088 Walter Gage Road, Gage South Precinct at the UBC campus. UBC is currently installing a permanent structural health monitoring system on the building. Such a system will be used to characterize dynamic behavior of the building and establish a baseline in long term. Any abnormal behavior out of this characterization would trigger an inspection on the building.

In conjunction with this long term goal, an Ambient Vibration Test (AVT) has been conducted on the east R/C concrete wall of the building in order to identify the modal properties (e.g., modal frequencies, damping ratios, and mode shapes) of the R/C wall only. The main purpose of this work is to study the dynamic response and estimate the stiffness of the R/C core-wall using the AVT results.

Preliminary results of the AVT are presented in the paper. The identified mode shapes of the R/C wall is compared with those of theoretical bending- and shear-beam. Results show that the mode shape of the R/C wall is consistent with that of an inverted bending beam; therefore, the stiffness estimation of the R/C wall is done using the inverted bending beam.

Y. Kaya (✉) • A. Taale
University of British Columbia, Vancouver, BC, Canada
e-mail: kayaya@boun.edu.tr

C.E. Ventura
Department of Civil Engineering, The University of British Columbia, 6250 Applied Science Lane, Vancouver, BC, V6T 1Z4, Canada



J. Caicedo, S. Pakzad (eds.), *Dynamics of Civil Structures, Volume 2*, Conference Proceedings
of the Society for Experimental Mechanics Series, DOI 10.1007/978-3-319-54777-0_39

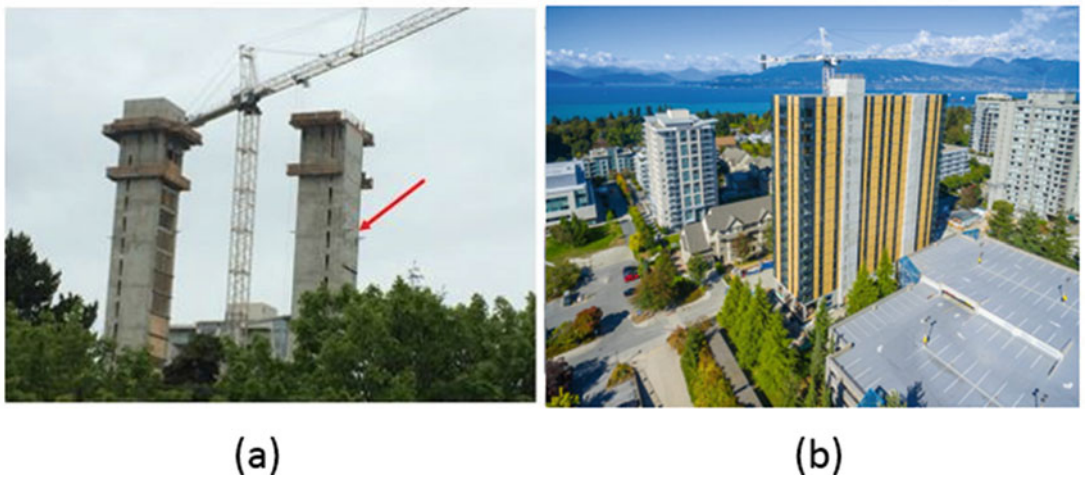


**Fig. 39.1** Construction of Brock Common Tall Wood Building (**a**) Concrete cores on June 3rd, 2016. (**b**) Concrete cores and timber based structure on Aug 23rd, 2016. The *red arrow* indicates the east concrete core

## 39.2 Description of Ambient Vibration Test

The total of eight sensors in three setups are used to test, collect and record the ambient vibration data on the 18-story tall core wall on June 3rd, 2016. The average air temperature was 19 °C, and the test lasted for 3 h and 30 min starting from 9:00 a.m. to 12:30 p.m.

A set of eight Tromino [1] sensors has been used to conduct the AVT test on the east core-wall. One of the sensors was used as a reference sensor located at the 17 ½ floor. The rest of the sensors are places at different floors in three setups to measure the vibration of the structure as shown in Figs. 39.2 and 39.3. The north recording component of the reference sensor is oriented towards to the entrance door (toward the ocean) to the stair hall, and the rest of the sensors are oriented the same. The recording duration for each setup is 20 min with a sampling frequency of 512 Hz.

## 39.3 Data Processing

### *39.3.1 Modal Identification*

The data processing is done in Artemis Modal 5 [2]. Figure 39.4 and Table 39.1 shows the preliminary results for the first two modal frequencies and mode shapes of the east core-wall of the 18-story. The results are presented for both east–west and north–south directions.

### *39.3.2 Comparison of Modal Properties with Theoretical Bending- and Shear-Beam*

The most commonly used beam model, the Euler–Bernoulli beam, also known as bending beam, assumes that the bending effect is the single most important factor in transversely vibrating beams, which includes the strain energy due to the bending and the kinetic energy due to lateral displacements. The shear beam model, on the other hand, adds the effects of shear distortions (i.e. the angle of the rotation of the cross-section due to shear) to the Euler–Bernoulli beam model making it more sensitive to non-slender beams as well [3].

Differential equations of the motion of a bending- and a shear-beam are given in Eqs. (39.1a) and (39.1b), respectively [3, 4]

$$m\frac{\partial^2 u}{\partial t^2} + EI\frac{\partial^4 u}{\partial x^4} = f(x,t) \tag{39.1a}$$


**Fig. 39.2** Sensor locations and orientations along the height of the building for Setup 1 & 2

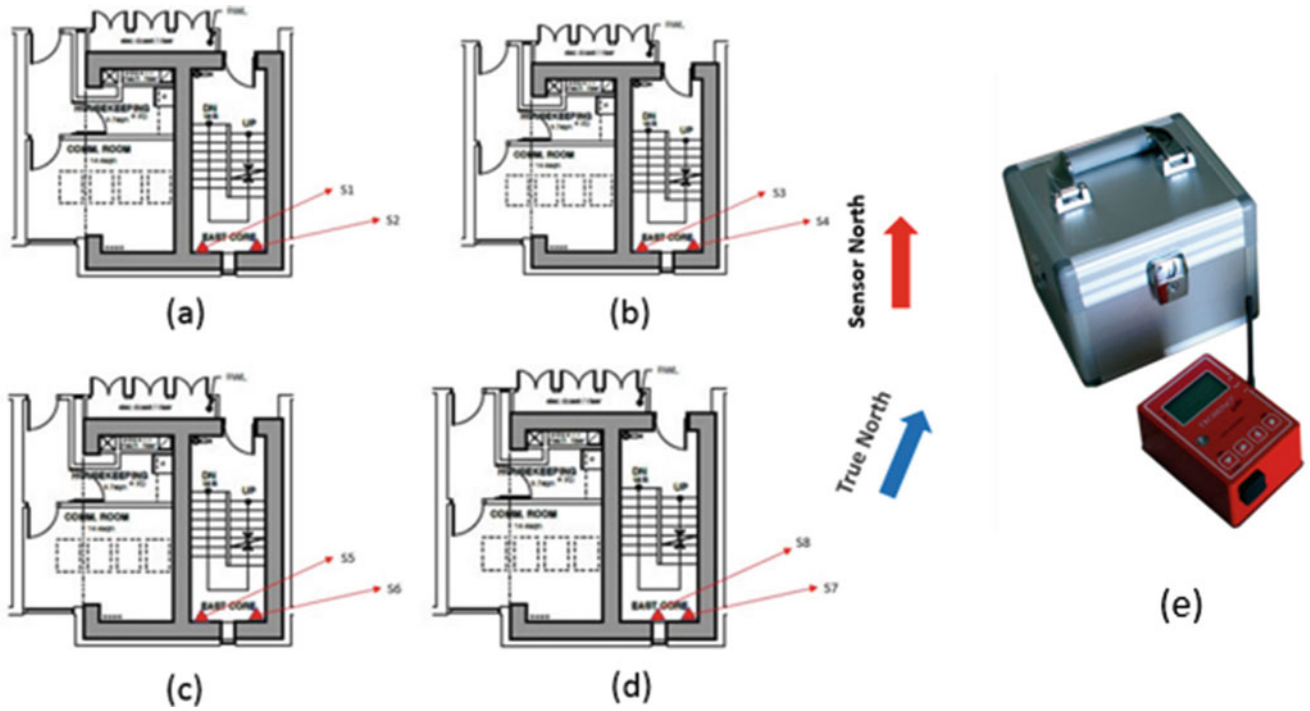


**Fig. 39.3** Sensor locations and orientations along the height of the building for Setup 3: (**a**) at 6 ½ floor; (**b**) at 10 ½ floor; (**c**) at 14 ½ floor; (**d**) at 17 ½ floor, and (**e**) Tromino sensor

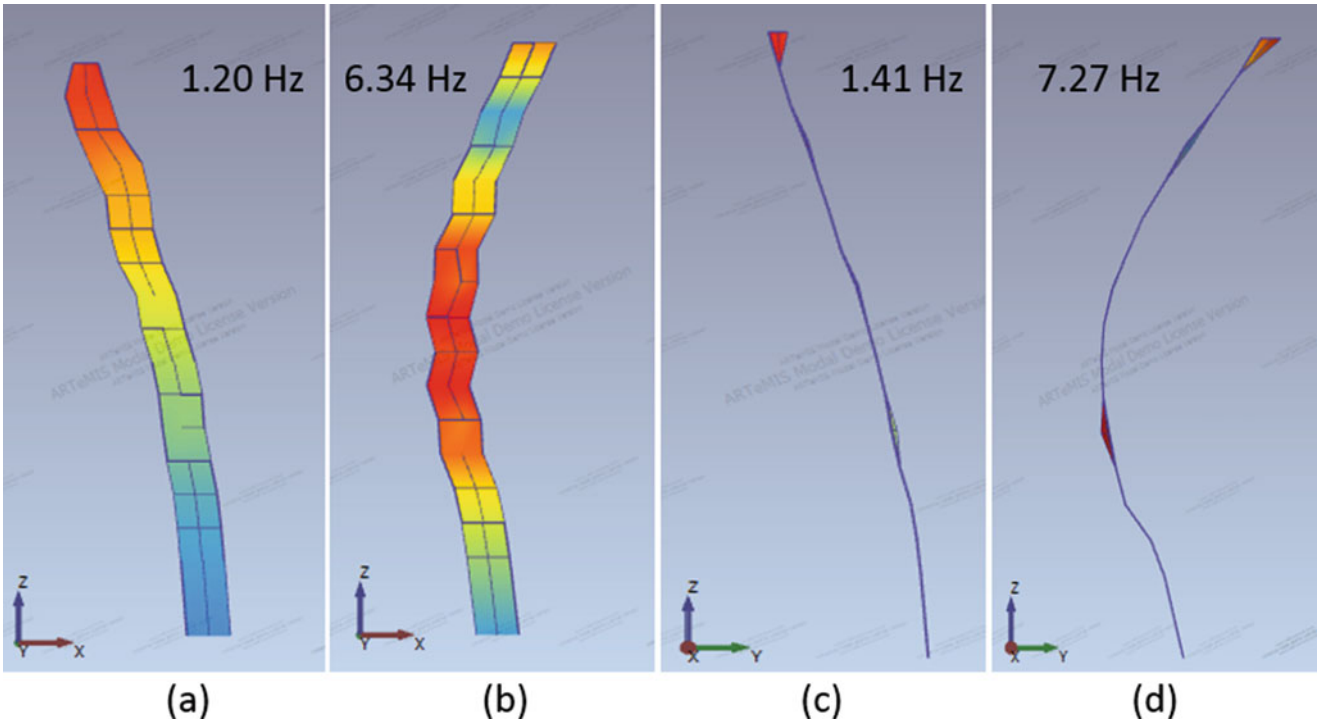


**Fig. 39.4** Estimated modal frequency and mode shapes of the 18-story tall core wall: (**a**) first mode shape (1.20 Hz) in east–west direction; (**b**) second mode shape (6.34 Hz) in east–west direction; (**c**) first mode shape (1.41 Hz) in north–south direction; and (**d**) second mode shape (7.27 Hz) in north–south direction

**Table 39.1** Identified modal frequencies and damping ratios

| | Identified modal frequency (Hz) | Identified modal damping ratio (%) | Description |
|---|---|---|---|
| 1 | 1.205 | 0.922 | 1st bending in EW direction |
| 2 | 1.417 | 0.952 | 1st bending in NS direction |
| 3 | 6.271 | 2.387 | 2nd bending in EW direction |
| 4 | 7.293 | 2.976 | 2nd bending in NS direction |

$$\rho A \frac{\partial^2 u}{\partial t^2} - GA_s \frac{\partial^2 u}{\partial x^2} = f(x,t) \tag{39.1b}$$

where $u$, $m$, $E$, and $I$ are the deflection, mass per unit length, Young modulus of elasticity, and second moment of area of the cross-section of the beam, respectively, $GA_s$ is the elastic stiffness of the shear-beam ($G$ is the modulus of rigidity and $A_s$ is the effective shear area), $\rho A$ is the mass per linear length of the shear-beam where $\rho$ is the mass density, $A$ is the cross sectional area, and $f(x,t)$ is the loading per unit length of the beam. The details of the derivations of a general solution to the mode shapes of a bending-beam and a shear-beam can be found in [2].

In the bending-beam model, the slope and the displacement at the fixed end as well as the moment and the shear force at the free end are zero. In the shear-beam model, the displacement at the fixed end and the slope at the free end are zero. Due to these difference in boundary conditions and the additional effects of shear distortions in the shear-beam model, the two models result in two different mode shapes as shown in Fig. 39.5. It should be noted that both the curvature and the amplitude of the mode shapes are different at all the modes, and the peaks and zero crossings of each mode shape along the length do not occur at the same location.

The first two normalized mode shapes of the inverted cantilever bending and the shear beams along with the identified mode shapes of the R/C core-wall are plotted in Fig. 39.5. The observed natural mode shapes of tall buildings with moment resisting frame are close to those of a shear beam particularly in the 5- to 15-story range; however, tall buildings with concrete shear walls usually exhibit mode shapes of a bending beam [5] as shown in Fig. 39.5.

Using the dispersion relationship of the bending beam, the natural frequency of vibration for an inverted bending beam can be expressed as [2]

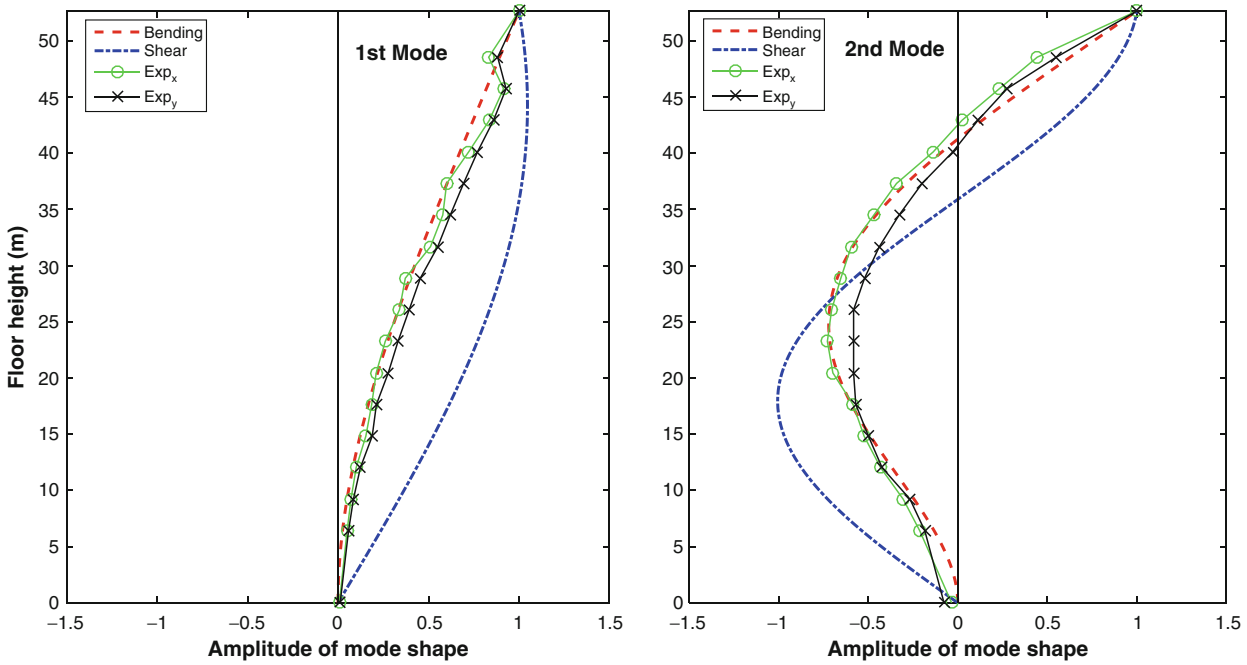


**Fig. 39.5** Comparison of the identified mode shapes of the concrete wall with those of a bending- and shear-beam. The mode shapes of the concrete wall for the first two modes follows that of a bending beam as expected

**Table 39.2** Frequency equation and the first two wave numbers of bending beam model

| | $a$, Wave number $\cos(a)\cosh(a)+1=0$ | Theoretical modal frequency | Identified modal frequencies | | Difference | |
|---|---|---|---|---|---|---|
| | | | x-direction | y-direction | x-direction | y-direction |
| Mode 1 | 1.875104 | 1.229 | 1.205 | 1.417 | 1.95% | 15.30% |
| Mode 2 | 4.694091 | 7.7 | 6.271 | 7.293 | 18.56% | 5.29% |

$$2\pi f = \sqrt{\frac{EI}{\rho A L^4}} \cdot a^2 \tag{39.2}$$

where $a, f$ and $L$ are the wave number, the natural frequency, and the length of the bending beam, respectively. It is very clear from Fig. 39.5 that the modes shapes of the concrete core follows that of bending beam as expected.

From the structural drawings, the material and the cross sectional properties of the high strength concrete have been identified as E = 2.7E10 N/m$^2$, $\rho$ = 2500 kg/m$^3$, A = 11.32 m$^2$, L = 52.66 m. The calculated wave numbers, theoretical and the identified modal frequencies of the bending beam are given in Table 39.2 [2].

Using Eq. (39.2), once can calculate the theoretical modal frequencies of the bending beam by assuming mass moment of inertia of the R/C core-wall as I = 38.85 m$^4$.

The difference in the natural frequencies between the theoretical and the identified modes can be attributed to the boundary conditions of the concrete core wall. The bending beam model assumes that the beam is perfectly fixed at one end, but such condition does not exist in real life: the concrete core is not perfectly fixed to the ground. Due to the soil structure interaction, the boundary condition of the concrete wall at the foundation level can be assumed to be softer than a fixed connection. Therefore, one should expect lower frequency from a system with soft boundary condition, and this is very consistent with modal frequencies obtained from the ambient vibration test for both orthogonal directions (Table 39.2).

### *39.3.3 Future Work*

A permanent structural health monitoring system will be installed on the structure in 2017, and a second AVT will be conducted on the building in 2016 in order to extract the dynamic modal properties of the structure. A detailed Finite

Element (FE) model of the building will be created and calibrated using the AVT test. The permanent monitoring system will assess the health of the structure in real-time using the calibrated FE model of the structure.

## 39.4 Conclusion

The preliminary results that has been shown the following:

1. The mode shapes of the R/C core-wall is consistent with that of an inverted bending beam
2. The first natural frequency of the R/C wall is consistent with that of a bending beam with 1.95% and 18.56% differences in the first and second modes, respectively
3. The difference in the natural frequency between theoretical bending beam and the R/C core wall can be attributed to the differences in the boundary conditions: the theoretical bending beam is assumed to be perfectly fixed at one end, but the R/C wall is not perfectly fixed to the ground.
4. The moment of inertia of the R/C wall is calculated as $I = 38.85\ m^4$ using the dispersion equation.

## References

1. Tromino User's Manual. http://www.tromino.eu
2. Artemis Modal 5. http://www.svibs.com/
3. Han, S.M., Benaroya, B., Wei, T.: Dynamics of transversely vibrating beams using four engineering theories. J. Sound Vib. **225**(5), 935–988 (1999)
4. William, H.K.L., Hiroo, K., Paul, J., Carl, K.: International Handbook of Earthquake & Engineering Seismology, Part 2. Academic Press, London (2003)
5. Kaya, Y., Kocakaplan, S., Safak, E.: System identification and model calibration of multi-story buildings through estimation of vibration time histories at non-instrumented floors. Bull. Earthq. Eng. **13**(11), 3301–3323 (2015)

# Chapter 40
# The Day the Earth Shook: Controlling Construction-Induced Vibrations in Sensitive Occupancies

**Michael J. Wesolowsky, Melissa W.Y. Wong, Todd A. Busch, and John C. Swallow**

**Abstract** Floor motions can disturb occupants, leading to frequent complaints and loss of functionality. In healthcare facilities, this issue can be more critical, as high-resolution imaging equipment with stringent vibration criteria are often employed. As existing healthcare infrastructure ages, extensive renovations and additions to functioning facilities are commonly being planned, designed and constructed. In many cases, these largely invasive projects are occurring while the existing vibration-sensitive facilities remain in operation. The control of construction-related vibrations form an increasingly important component of the planning, design and construction processes for these situations.

This paper provides two case studies of existing hospitals which are undergoing extensive additions. In both cases, the diagnostic imaging (DI) suites, containing Magnetic Resonance Imaging (MRI) and Computed Tomography (CT) equipment, are located directly adjacent the facility additions. For both cases, a series of vibration tests are described that were conducted using a combination of backhoes, excavators, caisson drillers and vibratory compactors to determine the extent of mitigation and monitoring required during the construction process in order to allow the DI equipment to remain in operation. Further commentary is provided regarding the practical realism of vibration criteria for DI equipment, as it was found for one of the cases discussed below that the manufacturer-provided vibration criteria for a CT scanner were apparently inaccurate since construction activity generated vibrations that exceeded the constraints of those criteria without any subjectively apparent loss of performance.

**Keywords** Vibration sensitive equipment • Construction vibration • Vibration measurements • Vibration mitigation • Model validation

## 40.1 Introduction

Over the years, many existing healthcare facilities have required extensive additions and renovations to accommodate new facility demands and technology. Often, these renovations occur while the existing healthcare facilities remain in operation with associated concerns over construction vibration. Healthcare facilities often contain highly vibration-sensitive equipment whose accuracy in operation could be compromised as a result of the construction-induced vibration. As such, the control of construction-related vibrations forms an increasingly important component of the planning, design and construction process for these projects.

Two case studies are presented in this paper that describe the different vibration testing methods as conducted at two hospitals that are, as of the publication of this paper, undergoing extensive facility additions. Both hospitals required that the Diagnostic Imaging (DI) equipment, which has stringent vibration requirements, remain in operation throughout the construction process. The first case study describes vibration testing that included the simulation of construction activity using a variety of construction equipment, in order to determine construction vibration zones of influence for the entire hospital. The second case study describes both simulated construction-vibration testing along with real-time continuous vibration monitoring during the actual construction stage.

M.J. Wesolowsky (✉) • M.W.Y. Wong • J.C. Swallow
Swallow Acoustic Consultants Ltd., Thornton Tomasetti, 23-366 Revus Ave., Mississauga, ON, Canada, L5G 4S5
e-mail: mwesolowsky@swallowacoustic.ca

T.A. Busch
Pinchin Ltd., 2470 Milltower Court, Mississauga, ON, Canada, L5N 7W5



J. Caicedo, S. Pakzad (eds.), *Dynamics of Civil Structures, Volume 2*, Conference Proceedings
of the Society for Experimental Mechanics Series, DOI 10.1007/978-3-319-54777-0_40

## 40.2 Vibration Criteria

A method for defining vibration criteria for human comfort uses the root mean square (RMS) velocity response of each one-third-octave band from 1 to 80 Hz [1]. For sensitive equipment, this criterion may also be expressed in one-third octave bands, or other formats, including power spectral densities, peak-to-peak levels, etc. Over the past 25 years, generic vibration criteria (VC) have been developed which provide frequency-dependent sensitivities for various classes of equipment, and these are applied as performance criteria. These VC curves are internationally accepted as a basis for designing and evaluating the performance of vibration sensitive equipment and the structures that support them. The VC curves currently range from Workshop (least stringent) to VC-G (most stringent). As a point of reference, most laboratories target at least VC-A (50 μm/s) as an uppermost vibration condition.

The VC curves were originally based on the ISO 2631-2 (1989) [2] base curve for human response to whole-body vibration, which is considered the threshold of human perception, but have since evolved. The ISO base curve is often referred to as the ISO—Operating Room criteria of 100 μm/s which is not as stringent as VC-A. The above-noted VC are specified in terms of RMS velocities each one-third octave band. The VC curves are beneficial where manufacturers' specifications are non-existent, incomplete, where specific equipment has not yet been selected, or as an alternative when manufacturer-supplied specifications prove to be inaccurate.

## 40.3 Case Study #1: Construction Zone of Influence

Case Study #1 involves a new patient tower addition for a large existing hospital. As such, parts of the existing hospital will be demolished and re-built, while the rest of the hospital will continue to stay in operation. The hospital has vibration-sensitive areas throughout the facility, although the main area of concern is the DI suite where the Magnetic Resonance Imaging (MRI) and Computed Tomography (CT) scanners are installed. Simulated construction-vibration testing was carried out to determine whether or not construction activities can be expected to cause vibration levels within the hospital that would exceed the equipment's vibration limits. Two types of tests were conducted: (1) vibration propagation into buildings; and (2) vibration propagation with distance. The main purpose of these tests was to develop zone of influence lines to determine just how close to the hospital that construction activities could be conducted while allowing for continued operation of the vibration-sensitive equipment.

To measure the vibration propagation into buildings, three uni-axial accelerometers were set-up to obtain tri-axial acceleration data at various outside and inside locations of the hospital buildings. Accelerometers were placed in the MRI and CT scanner rooms as well as an X-ray room. Measurement rooms were purposely chosen to be in different wings of the hospital, as every wing was built at a different time (with some wings dating back to the year 1929) and had different structural systems. To simulate construction activities, a backhoe/excavator with a bucket was used to strike the pavement repeatedly approximately 100 times, where the time between strikes ranged from 1 to 3 s. The striking location was in the hospital's parking lot in closest proximity to the DI equipment.

The measured VC levels are shown in Table 40.1 and show that at all sensitive areas, the vibration levels exceeded the required VC curves.

As these vibration levels were for one exterior impact location, a second set of tests were conducted to determine the reduction of vibration with distance. This would allow for vibration levels to be estimated anywhere on the future construction site. This testing was conducted in the parking lot (and future site of the new patient tower) and was completed with three different pieces of construction equipment: excavator with a bucket, caisson driller and a vibratory roller (see Fig. 40.1). Tri-axial accelerometers were placed at 5, 10, 15, 20 and 120-m distances from the construction source. The first construction simulation used the excavator with bucket to strike the ground repeatedly. The second simulation consisted of using a caisson driller to drill a hole approximately 1 m in diameter and 3 m deep. Finally, the third simulation consisted of a vibratory roller

**Table 40.1** Measured VC levels during excavator test

| Room type | VC measured | VC limit | Exceeds |
|---|---|---|---|
| X-ray | Office (ISO) | Operating theatre (ISO) | Yes |
| MRI | VC-A | Manufacturer-provided (analogous to VC-B) | Yes |
| CT scanner | VC-A | Manufacturer-provided (analogous to VC-B) | Yes |
| Chemistry lab | Residential night (ISO) | Operating theatre (ISO) | Yes |

**Fig. 40.1** Construction equipment used as vibration generators

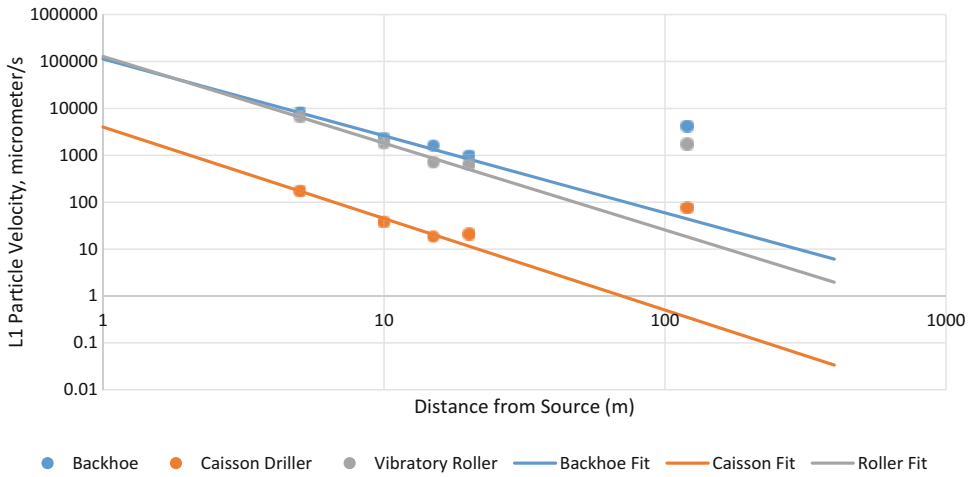


**Fig. 40.2** L1 particle velocity with distance

that was driven back and forth over the newly-refilled, caisson-drilled hole. The three different pieces of equipment were considered to be representative of the types to be used for different phases of future construction.

The L1 vertical particle velocity at each accelerometer location is shown in Fig. 40.2. As can be seen in Fig. 40.2, the 120-m data point has significantly higher vibration amplitudes than the locations closer to the vibration source. This was explained by the fact that the 5, 10, 15 and 20-m measurements were all taken on the parking lot asphalt or sidewalk, while the 120-m measurement was taken on grass. As such, the soil at the 120-m location could be considered "free soil", while all other locations were on compacted soil. The density and wave speed of the "free soil" are less than the compacted soil and thus allows for the amplitudes of vibration to increase in order to conserve the intensity of vibrational power flows. Given that all the equipment in the building would be located on compacted soil below the foundations of buildings, only the 5, 10, 15 and 20-m accelerometer locations were used to calculate propagation curve fits.

In addition to measuring vibration within the rooms where sensitive equipment is installed, accelerometers were placed in the adjacent bays to quantify the vibration reduction within the building over distance. The L1 particle velocity found in one

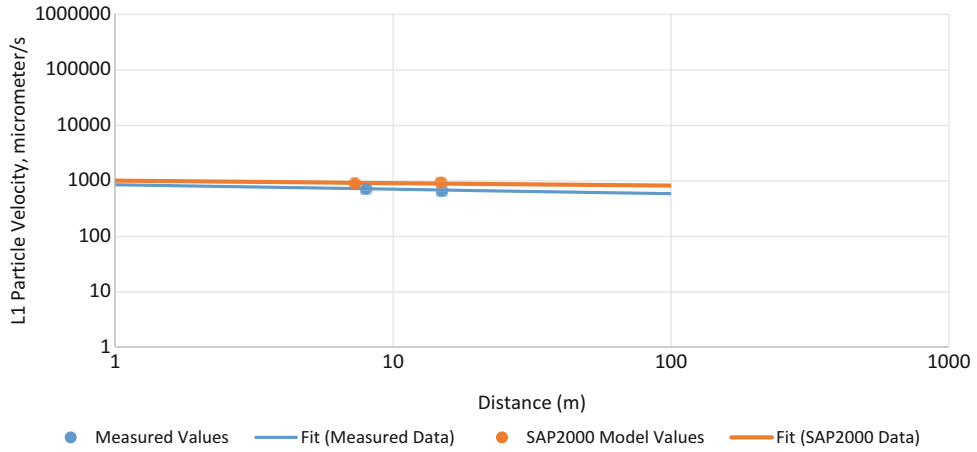


**Fig. 40.3** Vibration attenuation through one wing of the building

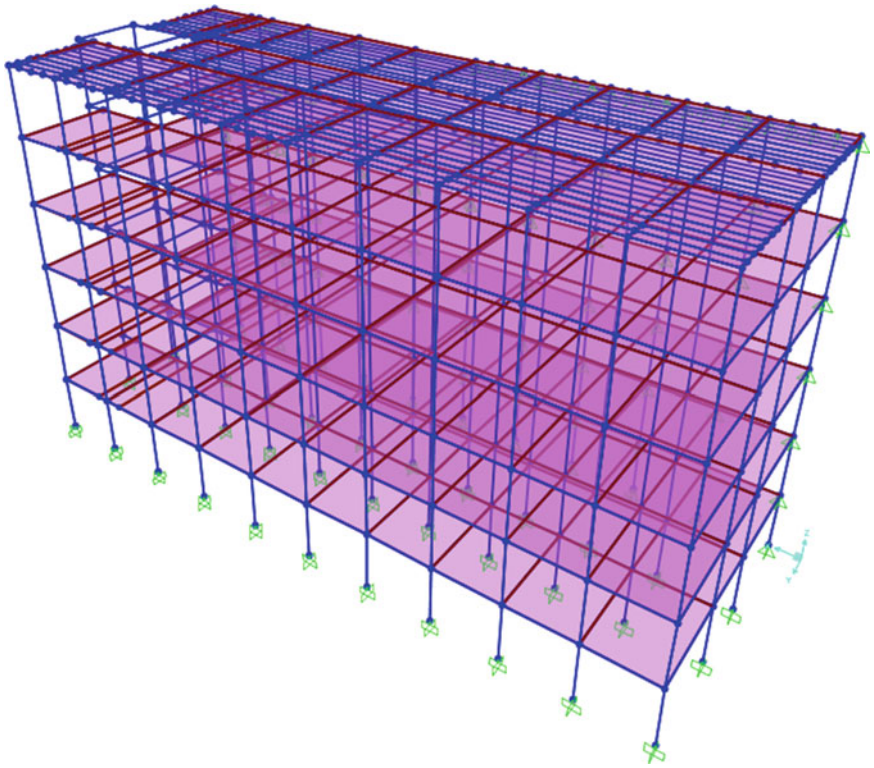

**Fig. 40.4** SAP2000 model of the hospital wing

of the wings is shown in Fig. 40.3. This wing is a steel-framed building built in 1956 with concrete decking and both steel and concrete columns. To confirm the accuracy of the measured values within the building, a SAP2000 finite-element model of the structure was also created and is shown in Fig. 40.4. The measured and expected vibration levels from SAP2000 match quite closely, as is shown in Fig. 40.3. Comparing Figs. 40.2 and 40.3, the velocity vs. distance slope is much shallower within the building as compared to outside the building. This suggests that vibration attenuates more in soil as opposed to through the concrete and steel structure of this particular building.

Along with the change in vibration propagation through the structure of the building, it was observed that a significant loss in vibration amplitudes occurred as the vibrations travelled from the exterior soil into the building foundations. As such, it can be said that the construction-induced vibration goes through three different stages, all with different rates of reduction over distance: (1) reduction through soil, (2) amplitude drop during transmission from soil to the building foundations, and (3) reduction through propagation within the building structure.

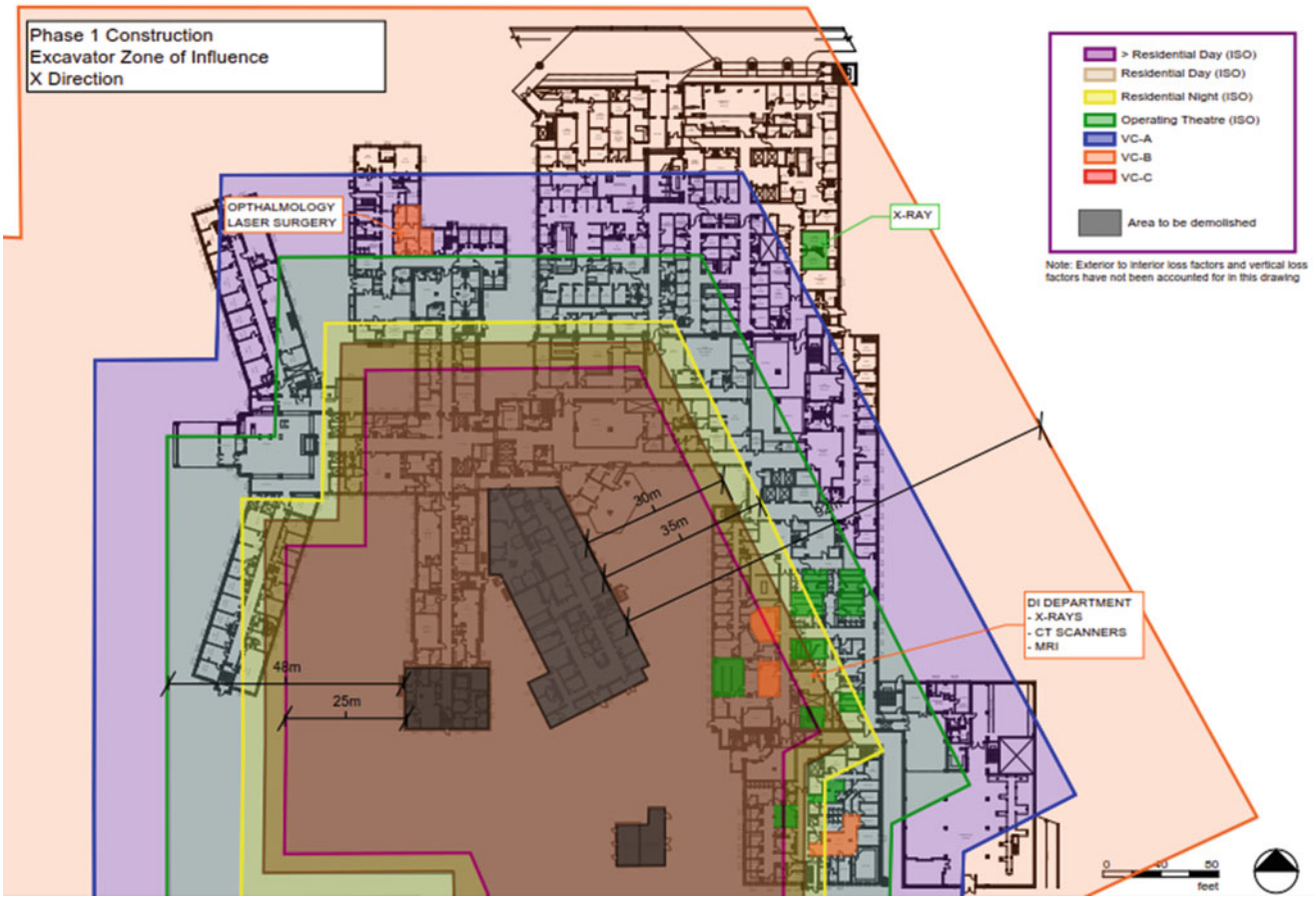


**Fig. 40.5** Construction vibration zone of influence

The zone of influence for each phase of construction was derived from the plots shown in Fig. 40.2. An example of a zone of influence drawing is shown in Fig. 40.5. To create the contour drawing as shown, the demolition area for one phase of construction was highlighted and the estimated distances from the construction site required to reach the different VC levels were outlined relative to that site. All of the vibration-sensitive spaces in the hospital were also highlighted and color-coded with reference to their recommended VC curve, allowing for a convenient means by which to identify whether vibration levels will exceed the VC for a given interior space.

## 40.4 Case Study #2: Hospital Construction Vibration Monitoring

This second case study also involves assessing the effect of construction-induced vibration on hospital equipment. For this hospital, the main equipment of concern were the CT scanners and nuclear medicine cameras in the DI department. Similar to the first case study, future construction activities were simulated through the use of a backhoe with a bucket that struck the ground repeatedly in quick succession. Tri-axial accelerometers were placed within the vibration-sensitive rooms. Additional accelerometers were placed in an area that was deemed a potential site for an additional CT scanner, planned for future installation, should the vibration testing show that the current CT location would not be acceptable during construction.

The manufacturer-provided specifications for the CT scanner stated that the scanner could remain in operation under a VC-A (50 μm/s) vibration environment. This is higher than the manufacturer's requirement for most CT scanners in use today, which typically require a maximum of VC-B (25 μm/s). Measurements from the simulated construction activity indicated that the CT scanner room would expect vibration levels to reach Office (ISO), which is significantly higher than the required VC curve. As a result, the general contractor was required by the hospital to vibration monitor the CT scanner room with an instrumentation system that also transmitted remotely triggered alarms indicating when VC-A was exceeded.

**Table 40.2** Number of exceedances of "Alarm" and "Limit" thresholds

| Exceedances | X-axis | Y-axis | Z-axis |
|---|---|---|---|
| "Alarm" 25 μm/s | 725 | 303 | 1776 |
| Operational limit 50 μm/s | 186 | 61 | 775 |

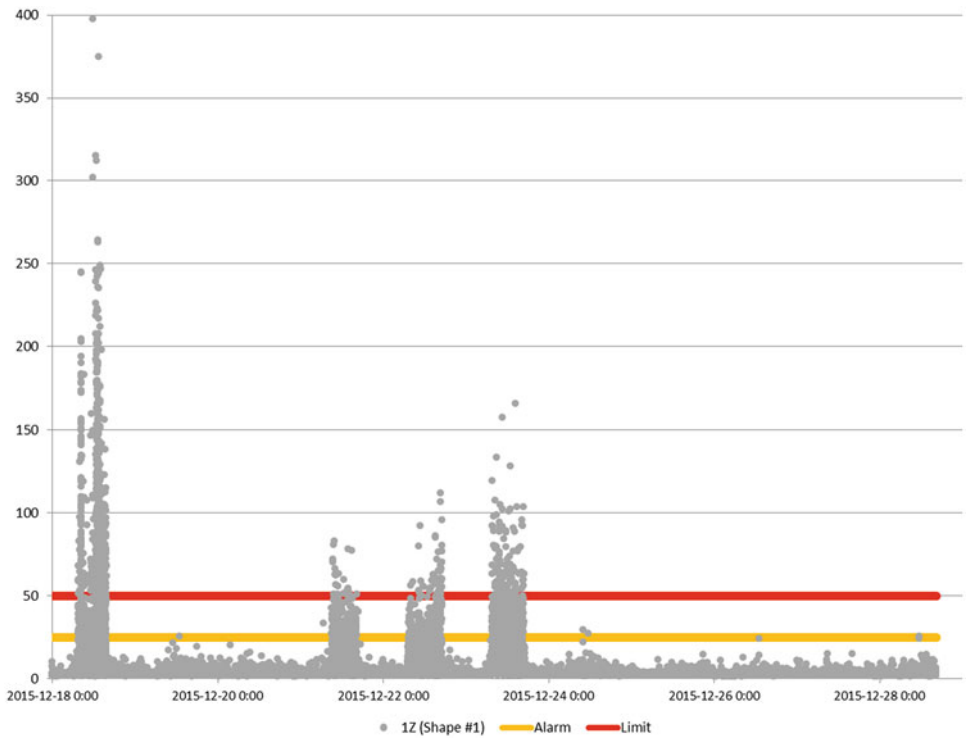


**Fig. 40.6** Measured vibration levels (μm/s)

Tri-axial accelerometers were placed in the CT scanner room and were left unattended for a period of months but that remained remotely accessible through an Internet-based interface. Electronic mail and short message service (SMS) alerts were programmed into the instrumentation system so as to trigger alarm messages should the vibration levels in the CT scanner room exceed the VC. In fact, two VC thresholds were set, where the "alarm" (warning) threshold was 25 μm/s from the 8 to 80 Hz octave bands (VC-B) and the "limit" threshold was 50 μm/s (VC-A). Furthermore, on a weekly basis the measurement results were inspected and documented along with a summary of the number of exceedances that occurred during a week. An "exceedance" was only counted if the duration of an event was over 10 s. Table 40.2 shows an example of the number of exceedances of the "alarm" and "limit" thresholds seen in the course of one typical week of construction.

Further, Fig. 40.6 shows the exceedances over a 10-day period for the vertical accelerometer axis, where it is evident that the VC were exceeded quite significantly; since there were instances where vibration levels were 8-times the "limit" threshold and reaching nearly 400 μm/s (Office (ISO)).

Though vibration levels greatly exceeded the equipment manufacturer's specifications, it was understood from the CT scanner technicians that no malfunctions and imaging artifacts were evident during operation. The technicians further stated that the CT scanner was still operating as intended and as such, did not require further monitoring given that the construction-induced vibration showed no noticeable signs of compromising the equipment. It may be worth noting that such results may not generally occur for a different CT-scanner product or other vibration-sensitive equipment, like an MRI.

## 40.5 Conclusions

Two case studies have been presented in which vibration-sensitive hospital equipment either will be, or has been, subjected to high levels of vibration as a result of expected/actual construction activity for hospital renovations. In both cases, the proper functionality of the DI equipment were of utmost importance to the hospital, and were found to exceed the maximum required VC during simulated and/or actual construction activities. The following conclusions have been made:

1. Vibration reduces at a much greater rate with distance through soil than through the structure of a hospital building.
2. A large drop in vibration amplitudes occurs as the vibrations travel from the exterior of a building into the foundation structure of a building.
3. Manufacturer-provided vibration specifications may potentially be treated with some skepticism as they may not represent the actual VC that is needed for the intended operation of the sensitive equipment.

## References

1. BS 6472:1992: Guide to Evaluation of Human Exposure to Vibration in Buildings (1 Hz to 80 Hz). British Standards Institution (1992)
2. ISO 2631-2: Evaluation of Human Exposure to Whole-Body Vibration—Part 2: Human Exposure to Continuous and Shock-Induced Vibrations in Buildings (1 to 80 Hz). International Standard, ISO 2631 – 2 (1989)

# Chapter 41
# An Exploratory Study on Removing Environmental and Operational Effects Using a Regime-Switching Cointegration Method

**Haichen Shi, Keith Worden, and Elizabeth J. Cross**

**Abstract** Cointegration is a property of some nonstationary time series; it is now widely adopted in various econometric analyses. Recently, cointegration has been successfully adapted to address the issue of environmental and operational variations (EOVs) in structural health monitoring. However, cointegration is a linear algorithm, while many real world structures may exhibit nonlinear behaviour under EOVs. The aim of this paper is to introduce a novel nonlinear cointegration approach, as an extension of the previous work on cointegration. More specifically, the cointegrating relationship is allowed to switch from one regime to another; the augmented Dickey-Fuller (ADF) test statistic is utilised as a tool to determine where to activate the switch. The Johansen procedure is adopted for estimating the cointegration relationship. The proposed approach will be examined with a synthetic example, showing that EOVs can be effectively eliminated.

**Keywords** Nonlinear cointegration • Structural health monitoring • Environmental and operational variation • Regime switching • Nonstationary time series

## 41.1 Introduction

Structural health monitoring (SHM) is increasingly important for the operation and maintenance of mechanical and civil systems, given the reality that many of them are approaching or exceeding their original design life. SHM normally includes collecting sensor data periodically from structures, extracting damage-sensitive features, and analysing those features using statistical or machine learning tools [1]. However, as most engineering structures are operating in an ambient environment which is constantly changing, sensor readings are therefore inevitably corrupted by environmental and operational variations (EOVs). The effects of EOVs have become a major headache for SHM practitioners, the changes caused by ambient temperature can be so large that potential system failures will be falsely masked, which is obviously an unwanted situation. A good survey on this issue can be found in [2].

*Cointegration* is an important concept of nonstationary time series, which was first proposed by Engle and Granger (EG hereafter) in 1987 [3]. It is now widely used in the economic world when dealing with nonstationary time series, and essentially expresses the idea that the difference between two nonstationary time series is more predictable than a single time series. In honour of their achievements, EG were awarded the 2003 Nobel prize in Economics "for methods of analysing economic time series with common trends (cointegration)". Opposite to deterministic trends, stochastic trends exist widely in the real world; EOVs can be regarded as a kind of stochastic trend. Seeing the possible links between cointegration and EOVs, some pioneering work of bringing cointegration to the world of SHM has been done; readers are suggested to refer to [4] as a tutorial, where cointegration elegantly projected out the influence of EOVs in the SHM system, a stationary damage-sensitive residual series was obtained. Since then, several efforts have been attempted to further explore the power of the cointegration method: Cross et al. [5] compared the cointegration method with two other methods: outlier analysis and principal component analysis. Dao and Staszewski applied the Johansen procedure and stationarity test in the context of Lamb-wave-based SHM [6]. Worden et al. attempted to improve the cointegration method by extracting the nonstationary components from time series using the discrete wavelet transform. Cross and Worden carried out exploratory studies on nonlinear cointegration; however, the method produced a heteroskedastic residual [7]; Zolna et al. tried to remedy this issue via a scaling transformation which produced a residual stationary in the variance [8]. The current authors also investigated a nonlinear cointegration approach in the EG framework, with Gaussian process regression performing as a cointegrating regression function [9].

H. Shi (✉) • K. Worden • E.J. Cross
Department of Mechanical Engineering, Dynamics Research Group, University of Sheffield, Mappin Street, S1 3JD Sheffield, UK
e-mail: haichen.shi@sheffield.ac.uk



J. Caicedo, S. Pakzad (eds.), *Dynamics of Civil Structures, Volume 2*, Conference Proceedings
of the Society for Experimental Mechanics Series, DOI 10.1007/978-3-319-54777-0_41

Although cointegration has increasingly been employed in the context of SHM, the fact that cointegration is a linear approach may not always satisfy the nonlinear context in a more general sense. Many real world engineering systems might at times respond nonlinearly to any changes in ambient environment, and conventional linear cointegration might therefore not suffice to model this situation correctly. This paper is concerned with a further exploration of the previous work, and a novel nonlinear cointegration method named *regime-switching cointegration* will be presented, which will allow cointegration relationships to switch according to certain criteria. In the rest of this paper, the basic theory of cointegration and unit roots will be briefly covered, and then the idea of regime switching will be illustrated with a synthetic example; finally, discussion and conclusions are presented.

## 41.2 Unit Roots and Cointegration

In terms of nonstationarity, econometricians have developed various tools for testing for it. The unit root process is one of the most popular and well established modelling methods for nonstationary time series. Consider the first order autoregressive model of a time series $x_t$:

$$x_t = \alpha x_{t-1} + \xi_t, (t = 1, 2, \ldots N) \tag{41.1}$$

where $\xi_t$ is a stationary process with zero mean and variance $\sigma^2$, $\alpha$ is a real number that determines the stationarity of $x_t$: if $|\alpha| < 1$, $x_t$ is stationary; if $|\alpha| > 1$, then $x_t$ is nonstationary, and its variance grows explosively with time; if $|\alpha| = 1$, then the variance of $x_t$ will be $t\sigma^2$, which will grow with time, thus the process is nonstationary. Such a data generating process is termed a *unit root process*. A unit root process can achieve stationarity by simply differencing it once, so it is also known as a difference stationary process.

The test for the presence of unit root processes used in this paper is perhaps the most commonly used statistical test, the augmented Dickey-Fuller (ADF) test, and the steps for implementing the test will only be briefly outlined here, but readers can refer to [10] and [11] for further details. The ADF test is to fit the time series $x_t$ to the following form:

$$\Delta x_t = \pi x_{t-1} + \sum_{j=1}^{m} \gamma_j \Delta x_{t-j} + \varepsilon_t \tag{41.2}$$

where $\Delta$ is a differencing operator such that $\Delta x_t = x_t - x_{t-1}$, the $\gamma_j$ are the coefficients of the autoregressive terms, $m$ is the lag number. In this regression, a sufficient number of lags should be included to achieve a white noise residual term $\varepsilon_t$; an information criteria is a common choice for determining the lag number. In this form, the value of $\pi$ will determine the stationarity of the series; if $\pi = 0$ then $x_t$ possesses a unit root and is nonstationary. Therefore, a statistical test is employed with a hypothesis $H_0 : \pi = 0$ and an alternative hypothesis $H_1 : \pi < 0$. The test for the null is simply a $t$ test:

$$\hat{\tau} = \frac{\hat{\pi}}{se(\hat{\pi})} \tag{41.3}$$

where $\hat{\pi}$ is the least-squares estimate of $\pi$, and $se(\hat{\pi})$ is the standard error of $\hat{\pi}$. The critical values of the $t$-statistics are given in [11]. The null hypothesis is rejected if $\hat{\tau}$ is smaller that the corresponding critical value, and accepted otherwise. The model form of Eq. (41.2) can also be further adapted to include shift terms and/or trend terms [12].

Having reviewed the fundamentals of unit root processes and their statistical tests, one can now ascertain the nonstationarity of a series through these procedures. It is not difficult to find that the test statistic is the key ingredient in the unit root test, therefore in this paper, the power of the test statistic will be explored, and attempts to measure the degree of stationarity with it, and determine the best possible model form, will be carried out.

As previously stated, cointegration is a powerful tool to understand nonstationary data, two or more nonstationary series are cointegrated if a linear combination of them can be found to be stationary. Let $\mathbf{x_t} = (x_{1t}, x_{2t}, \ldots x_{mt})$ denote an $m$-variate time series, and suppose there exists a vector $\boldsymbol{\beta}$ that makes

$$u_t = \boldsymbol{\beta} \cdot \mathbf{x}_t \tag{41.4}$$

a univariate stationary time series. Here, the vector $\boldsymbol{\beta} = (\beta_1, \beta_2, \ldots \beta_m)'$ is referred to as a *cointegrating vector*. Usually there are more than one possible cointegrating relationships for a multivariate series $\mathbf{x}_t$, and many methods to estimate

the cointegrating vectors are available in the literature, readers can refer to [13, 14] and [15] for comprehensive reviews. The Johansen procedure, an efficient maximum likelihood (ML) estimator, will be adopted in this paper to estimate the cointegrating relationship in engineering data, successful applications can be found in [4, 6] and [16].

To perform the Johansen procedure, one should have a Vector Error Correction model (VECM) of the $m$-variate time series $\mathbf{x_t}$, which takes the form:

$$\Delta X_t = AB^T X_{t-1} + \sum_{j=1}^{p-1} \Psi_j \Delta X_{t-j} + \mathbf{u}_t \tag{41.5}$$

where $\mathbf{u_t}$ is a $m$-dimensional vector Gaussian noise series, $\mathbf{u}_t \sim N(\mathbf{0}, \Omega)$; $A$ and $B$ are two $m \times r$ matrices, where $r$ is the rank of the matrix $B$. Matrix $B$ is the cointegration vector matrix to be found, consisting of $r$ cointegrating vectors. Matrix $A$ is the adjustment matrix. Expression (41.5) is also referred to as the *Granger expression theorem*, which explicitly depicts the dynamics between the long run equilibrium (cointegration) and short term adjustments. To find the cointegrating matrix $B$, one needs to employ steps involving decomposition, forming the likelihood function, optimisation and solving a characteristic equation. Finally the estimate of $B$ can be obtained:

$$\hat{B} = (\boldsymbol{\beta}_1, \boldsymbol{\beta}_2, \ldots, \boldsymbol{\beta}_r) \tag{41.6}$$

where $\boldsymbol{\beta}_1, \boldsymbol{\beta}_2, \ldots, \boldsymbol{\beta}_r$ are the corresponding cointegrating vectors. As the first cointegrating vector $\boldsymbol{\beta}_1$ corresponds to the largest eigenvalue, so it is natural to select $\boldsymbol{\beta}_1$ as the "most stationary" cointegrating vector, so as to make the stationary residual series.

The Johansen procedure offers an efficient framework that not only estimates multiple cointegrating vectors at the same time, but also produces a test statistic for determining the number of cointegrating vectors. In the SHM context, it is more of interest to estimate the cointegrating vectors than to perform tests on the number of cointegrating vectors, because it is the most stationary combination that one looks for to eliminate the EOV-induced "nonstationary components" in the data. Due to the limited space available here, the details of implementing the Johansen procedure and the full theory behind it will not be covered; again readers interested can refer to [15].

## 41.3 A Regime-Switching Cointegration Method

The motivation behind developing a nonlinear cointegration approach is actually straightforward: operating structures may have significantly different behaviours under different operating conditions. For example, a bridge operating in summer time and the same bridge with icing conditions in winter time will probably have very distinct dynamic responses, linear cointegration may not suffice in this case. Similar phenomena can also be observed in economics. For instance in a case of statistical arbitrage, cointegration is a common technique for choosing a profitable portfolio from the stock market; but once some important monetary policy is announced, the economical impact might have a significant influence on the original cointegrated variables. A new cointegration relationship needs to be evaluated so as to make a new portfolio, the change position here is normally termed a *breakpoint*.

Reviewing the econometric literature on nonlinear cointegration, a mainstay of this is the extension to threshold cointegration, first proposed by Balke and Fomby in 1997 [17]. In their framework, the adjustment term in the cointegrating regression is allowed to shift once some indication variable exceeds a threshold. Furthermore, there are several other variants built on the vector error correction (VEC) model, as expressed above in Eq. (41.5). In [18] and [19] for example, they allow a threshold effect on the lag terms and the intercept term respectively. Gregory and Hansen [20], however, take the opposite direction to let the cointegrating relationship change, or in their terms, shift regime. More specifically, the cointegrating vector can change its value after a certain breakpoint, after which the system will stabilise itself at another long term equilibrium. The position of the breakpoint is unlikely to be determined in advance, thus they calculate the unit root statistic for each possible regime shift, and evaluate the smallest values across all possible breakpoints.

As cointegration has proved to be a powerful tool for modelling EOVs, the goal here becomes to further improve it by creating a piecewise linear cointegration model, which can shift its cointegration form with respect to the condition of EOVs. Inspired by Gregory and Hansen's work, a regime-switching cointegration method will be adopted to address the issue above. Different from their method however, instead of using the Engle-Granger framework, the more efficient Johansen procedure is implemented to estimate cointegrating vectors. The procedure of the method is summarised as follows:

1. Choose suitable monitored variables, rearrange the monitored series in the order of environmental or operational variable.
2. Insert a breakpoint at a position ranging from ([0.15 $N$,[0.85 $N$]), where $N$ is the sample size.
3. At each possible breakpoint, the series is split into two halves; use the Johansen procedure to estimate the cointegrating vectors for each half.
4. With the estimated cointegrating vectors, calculate the residual series of both halves and then merge them into one series, and determine the ADF $t$-statistic of the merged residual series.
5. Repeat procedures from step 2 to 4 at each point from [0.15 $N$] to [0.85 $N$], and construct a plot of all ADF statistics with respect to the breakpoint positions. Pick the minimum value of the curve, the corresponding position represents the optimal breakpoint.
6. With the optimal results from step 5, using the environmental or operational variable as an index variable, construct a switching cointegration relationship and a stationary residual series, which should be purged of EOVs and still have the power to predict damage.

By utilising the procedure above, one can build a regime-switching cointegration model that is capable of capturing the nonlinear effects of EOVs. In this exploratory study, only the case of two regimes are investigated, systems that accommodate more regimes can be possibly addressed by inserting more breakpoints in the proposed model. Next, the proposed method will be examined with a synthetic example.

## 41.4 A Case Study

To illustrate the proposed method, a simple linear system is simulated, the results from using the conventional cointegration method will be compared.

Figure 41.1 shows a four degree-of-freedom (DOF) spring-mass system, where four lumped masses are in a chain with both ends connected to ground. As is known, the stiffness of the metal material changes with temperature, which is a major source of EOVs in SHM data; besides, freezing conditions of structures may always have a great influence on the masses, stiffness and boundary conditions. To simulate the circumstances above, a bilinear relationship between spring stiffness and temperature is created as shown in Eq. (41.7). Real temperature data recorded from the Tamar Bridge is used here as a simulated thermal field [21]. The data length is 10000, and the temperature ranges approximately from −10 °C to 20 °C, as plotted in the lower panel of Fig. 41.2. One can also produce nonlinearity by simply letting the third spring behave distinctly from the other springs, as expressed in (41.8). The stiffness-temperature relationship has the following forms:

$$k_1 = k_2 = k_4 = k_5 = \begin{cases} -0.15 \times T + 4, & \text{if } T < 0 \\ -0.05 \times T + 4, & \text{if } T \geq 0 \end{cases} \tag{41.7}$$

$$k_3 = \begin{cases} -0.15 \times T + 5, & \text{if } T < 0 \\ -0.25 \times T + 5, & \text{if } T \geq 0 \end{cases} \tag{41.8}$$

Because of the different behaviour of $k_3$, the nonlinear effect can therefore be introduced into the vibration modes in which the third spring is participating—the second and the fourth modes to be specific. To perform damage detection, a fault in the stiffness of the spring is simulated: after 5000 data points, the stiffness of the second spring $k_2$ becomes $0.8k_2$ immediately. A small amount of Gaussian noise is added to account for measurement errors.

All natural frequencies of the system are identified at every time instant. They are all arranged with respect to time, as shown in the upper panel of Fig. 41.2. Because of the nonlinearity in Eqs. (41.7) and (41.8), one can see that natural frequency series tend to have larger variances in the cold temperature zone (for example, data points around 4000). It is also clear to see that the effect of temperature is significant. The red dashed vertical line in Fig. 41.2 indicates where damage occurs; however, due to the high variance of the series, any information of damage is overwhelmingly masked.

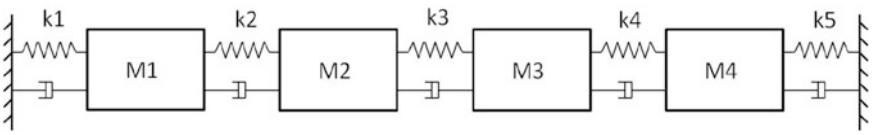


**Fig. 41.1** A four-DOF spring mass system

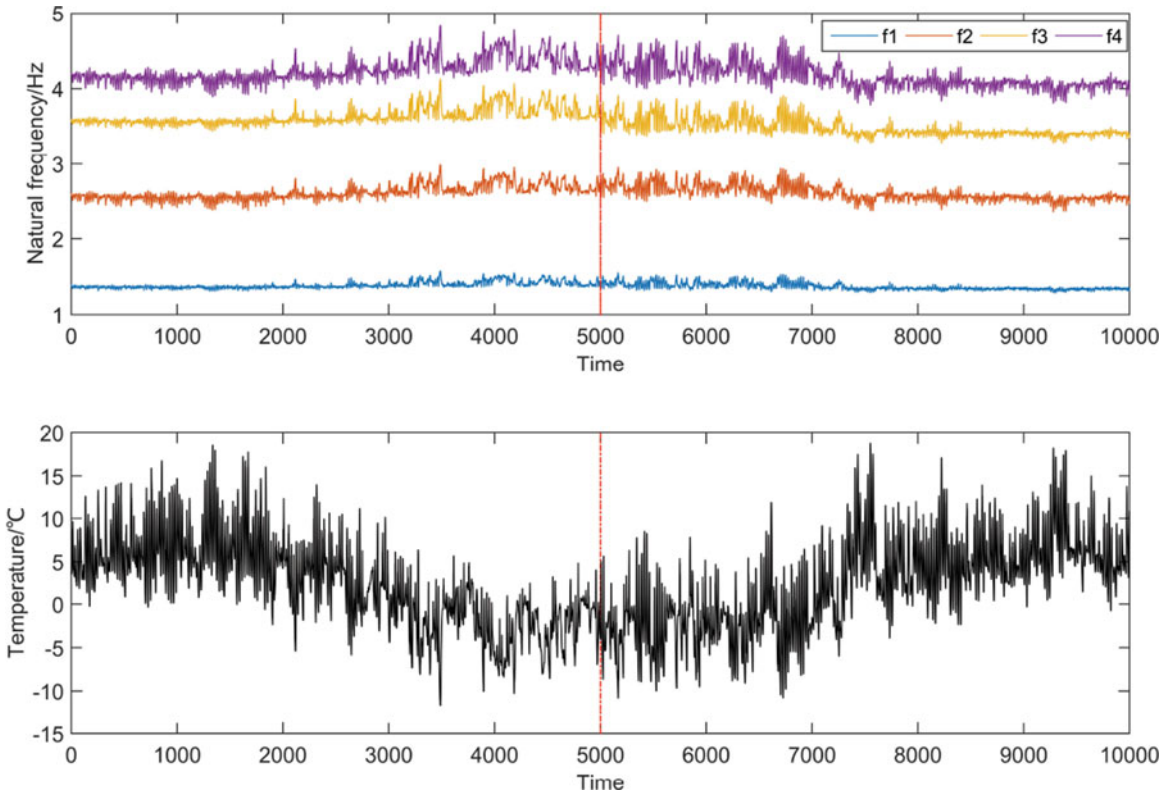


**Fig. 41.2** *Upper panel*: the time series of the four natural frequency series of the system in Fig. 41.1 plotted as a function of time; *Lower panel*: temperature series plotted against time. *Red dashed line* imposes damage introduction

Following the conventional cointegration procedures proposed in [4], one can obtain a residual series as shown in Fig. 41.3. Because the underlying cointegration has not been accurately modelled, only the first part of the residual series stays largely stationary, the high variance from the cold zone has been consequently left in the residual, damage indication has therefore failed. By further investigating the mutual relationship of the four natural frequency series in Fig. 41.1, one can see a clear bilinear relationship as plotted in Fig. 41.4. The knee points in the figure correspond to the breakpoint where the cointegrating relationship changes. Thus, a two-regime cointegration model should be appropriate to model this four-DOF system.

Following the procedure in Section 3 to validate the performance of the regime-switching cointegration method:

1. Not all data points are needed for estimating the model, only the alternative points from point 5000 to 8000 are chosen as a training set. In order to find the relationship between the frequency series and temperature, the training set is rearranged according to the magnitude of the temperature series, as displayed in Fig. 41.5 along with the temperature series. Denote the shuffled series as $\mathbf{f}_t = (f_{1t}, f_{2t}, f_{3t}, f_{4t}), t = 1, 2, \ldots N$, where $N$ is the sample size. Even though the stiffness is set to have a bilinear relationship with temperature, Fig. 41.5 does not show any clear sign of a breakpoint.
2. Next, the ADF test statistic is utilised as a tool to ascertain the position of the breakpoint. As the breakpoint can be anywhere in the series from the beginning to the end, the following step is to evaluate the ADF statistic at every possible breakpoint. However, in practice, it needs a minimum amount of data to calculate the ADF statistic, so only the data in the middle are used to evaluate it, that is the data set in the interval $([0.15N], [0.85N])$. Assume a breakpoint is inserted at position $\tau$, then the original $\mathbf{f}_t(1 : N)$ is split into two sets: $\mathbf{f}_{1\tau}(1 : \tau)$, $\mathbf{f}_{2\tau}(\tau + 1 : N)$. One then uses the Johansen procedure presented earlier to estimate the cointegrating vector of each set, say $\boldsymbol{\beta}_{1\tau}$ and $\boldsymbol{\beta}_{2\tau}$, and to construct the residual series at this breakpoint, $e_\tau = (\boldsymbol{\beta}_{1\tau}\mathbf{f}_{1\tau}; \boldsymbol{\beta}_{2\tau}\mathbf{f}_{2\tau})$, where ";" is used to concatenate these two vector series; the subscript $\tau$ denotes the fact the residual series depends on the position of the breakpoint.
3. Repeat the procedure above to evaluate all the points in $([0.15N], [0.85N])$ as breakpoints, and calculate the respective ADF statistics, which are plotted in Fig. 41.6; the horizontal axis represents the number index of the training set. The blank space at the beginning and the end of the figure indicates the fact that ADF statistics are only evaluated in the interval $([0.15N], [0.85N])$. The smallest value of the curve is at data point 976, corresponding to the temperature 0.4767 °C, which is quite close to the simulation assumption.

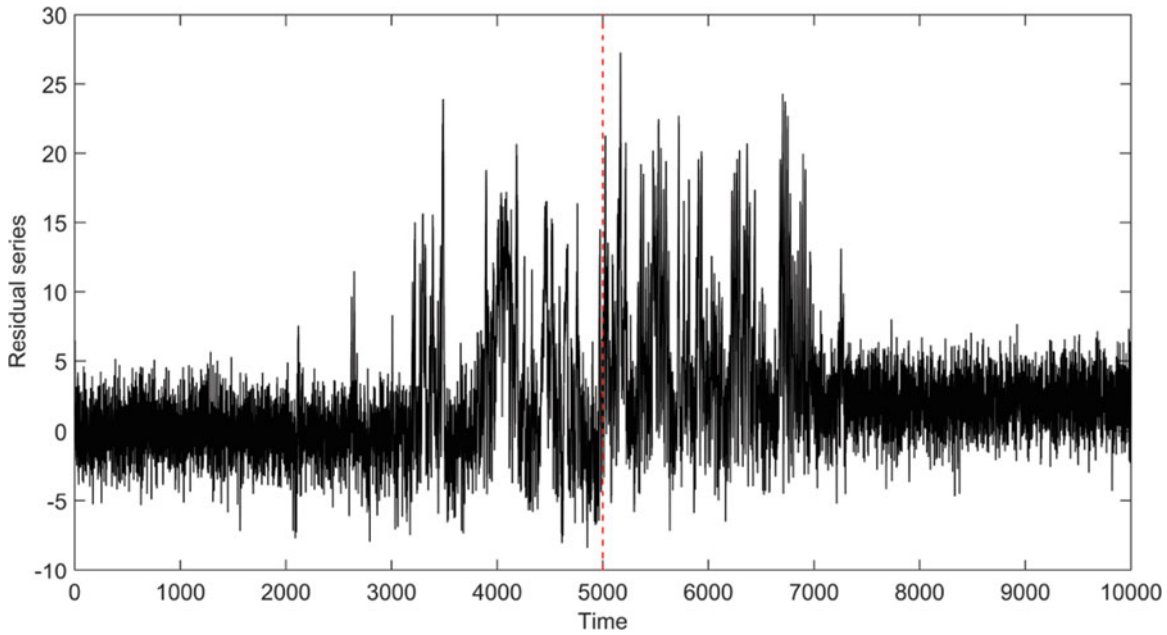


**Fig. 41.3** Residual series obtained using the conventional cointegration method, the *red dashed line* indicates where damage occurs

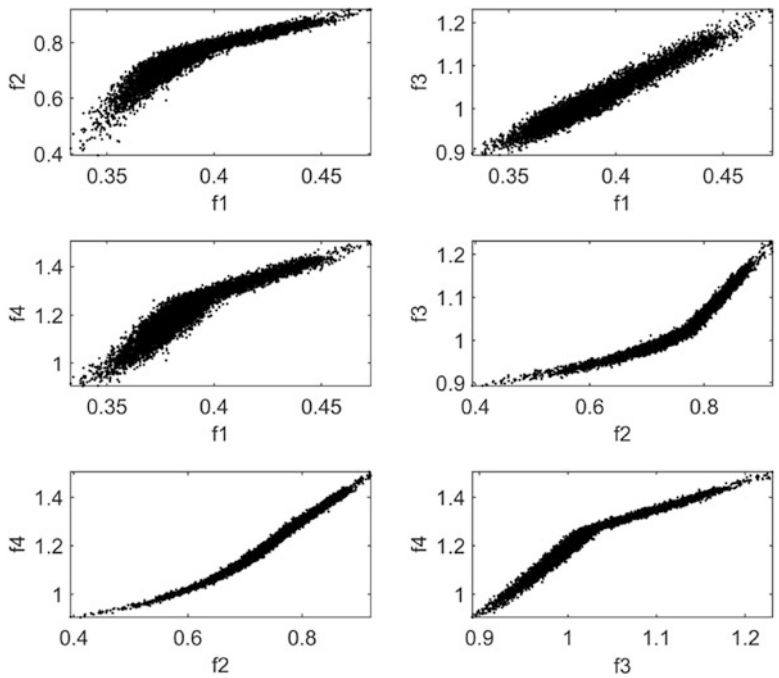


**Fig. 41.4** Mutual relationship between natural frequency series

4. With the estimated best breakpoint and cointegrating vectors correspondingly, one can have the following regime-switching cointegration relationship which is indexed by the value of temperature:

$$\varepsilon_t = \begin{cases} 147.90 \times y_{1t} - 107.29 \times y_{2t} - 122.96 \times y_{3t} + 10.69 \times y_{4t} - 3.54, & \text{if } T \leq 0.4767 \\ -4.51 \times y_{1t} - 84.87 \times y_{2t} - 127.87 \times y_{3t} - 165.07 \times y_{4t} - 24.19, & \text{if } T > 0.4767 \end{cases} \tag{41.9}$$

Figure 41.7 shows the residual series from (41.9), the red horizontal lines are the three times standard error bars which show the confidence interval of the health state.

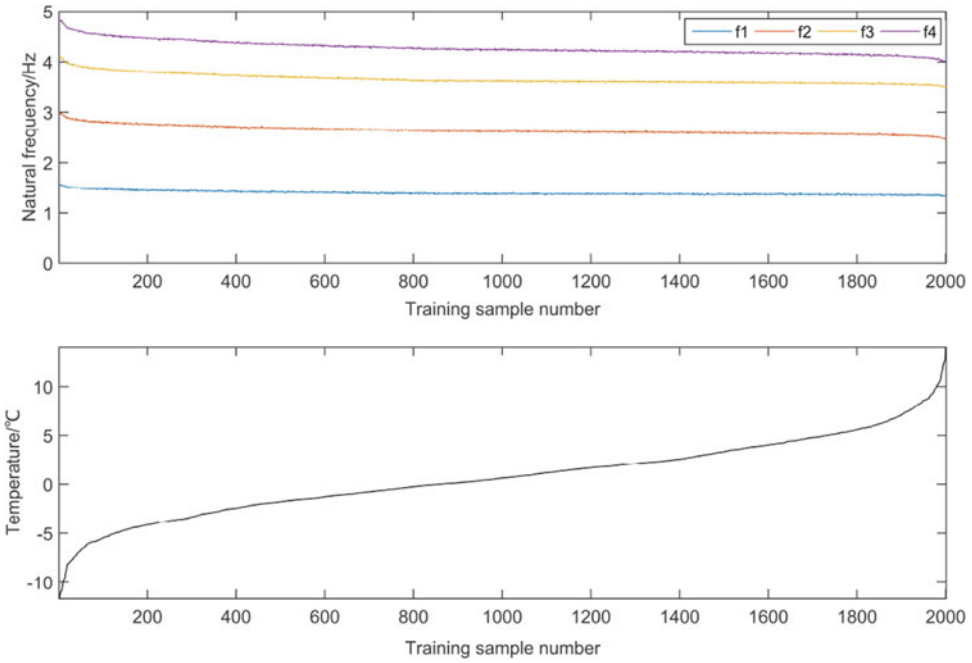


**Fig. 41.5** *Upper panel*: natural frequency series rearranged in the order of temperature; *Lower panel*: temperature series rearranged in the order of magnitude

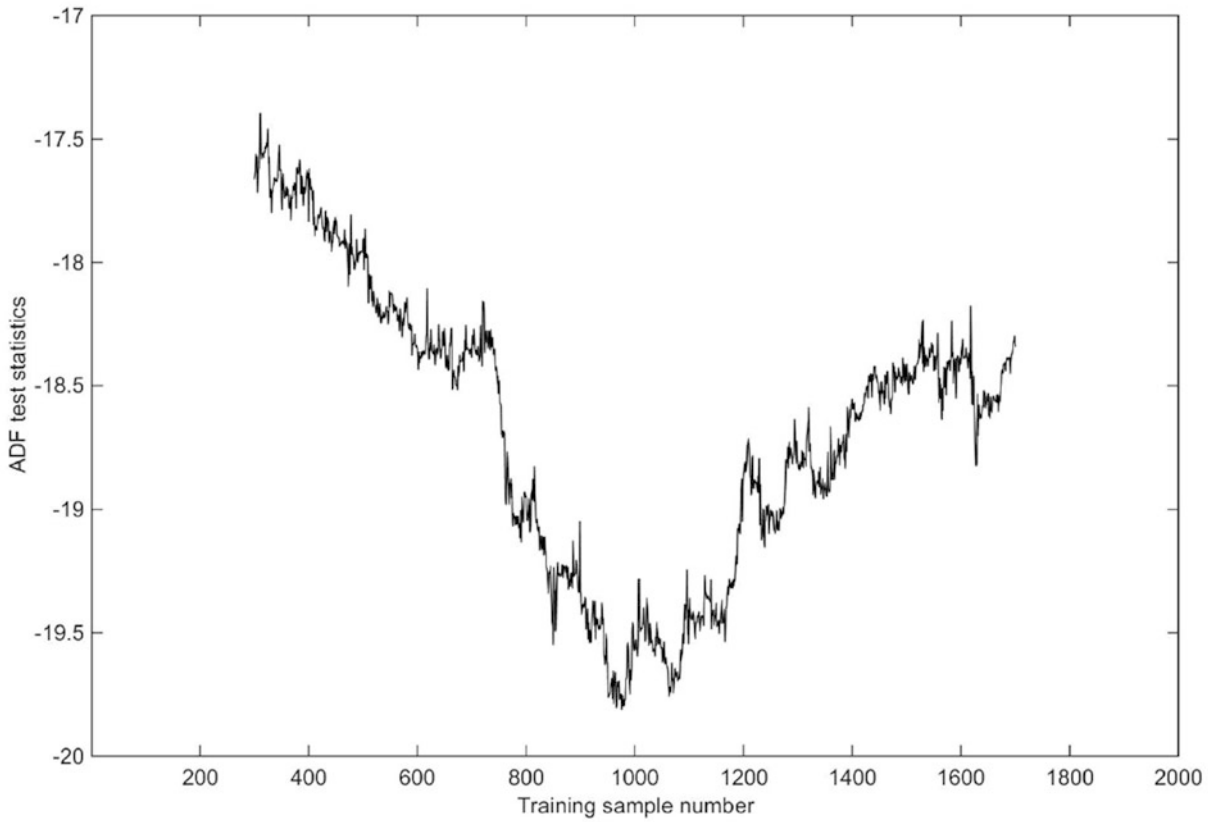


**Fig. 41.6** ADF statistics plot of the training sample points, the lowest point position determines the breakpoint position for the regime switch

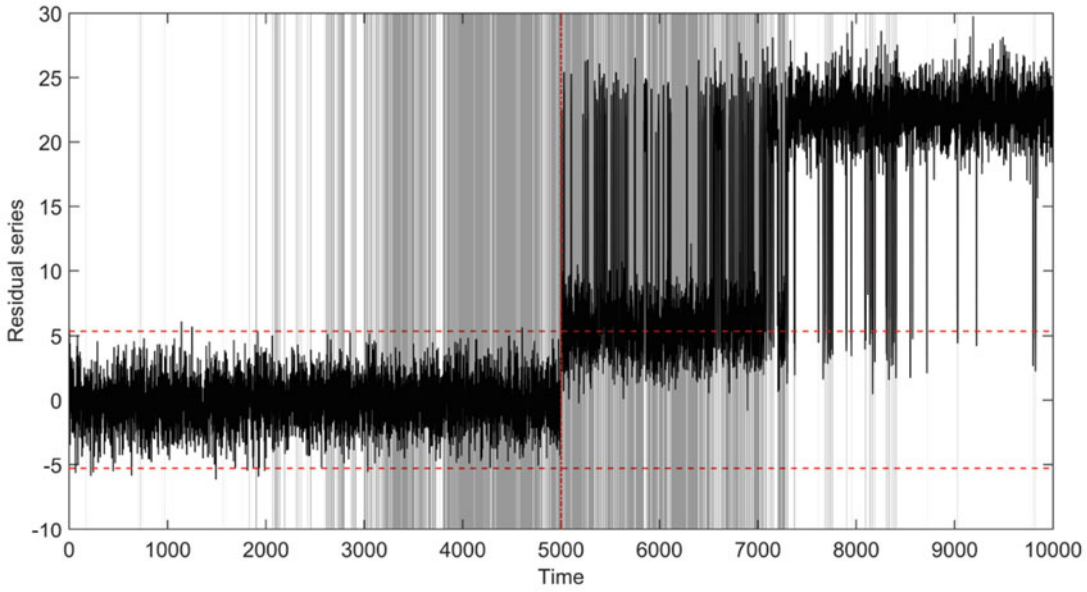


**Fig. 41.7** Residual series of the cointegration model, the *vertical red dashed line* indicates damage introduction, the *two horizontal red lines* represent the three standard error bars; the *grey shaded areas* show where cointegration switches regimes

It is clear that the residual series is stationary before damage introduction, any effect from temperature is effectively eliminated, and the nonlinear behaviour of the frequency response is precisely captured. After 5000 data points, the magnitude of the residual series exceeds the confidence interval immediately, which indicates strongly the occurrence of damage, the overlaid grey areas show where cointegration switches from one regime to the other. The result can be interpreted by the fact that the regime-switching cointegration is estimated with training data under normal condition, and the health state of the system has been accurately modelled. Whenever damage occurs, the long term relationship of the variables no longer holds, thus the residual series turns nonstationary immediately.

## 41.5 Discussions and Conclusions

Despite the fact that the method suggests very good results, one may still argue that shuffling the original series may break the underlying cointegrating relationship, therefore the estimation procedure might be ill-conditioned. This argument is partly true, that rearranging the order of series will surely break the underlying error correction mechanism [as expressed in Eq. (41.5)], but the long term relationship stays the same, or in other words, the rearranged series have the same cointegrating vectors as the original series, because the cointegrating relationships are stacked pointwise in time. One should bear in mind that the final goal here is fundamentally different from the aim of the econometricians, the concern is more about the long term relationship between variables, the short term adjustments are less of interest for the moment. Therefore, it is legitimate to use temperature as a reference series to rearrange the original series, and estimate the cointegrating vectors of the yielded series.

This paper is concerned with exploring a new nonlinear cointegration method aiming to address the issue of nonlinear effects of EOVs in SHM data. The proposed method is based on a breakpoint model from econometrics to build a piecewise linear cointegration model. The proposed method is validated with a synthetic case, the results suggest that environmental effects on systems can be successfully removed; it needs the authors to further investigate this approach to solve real engineering problems.

## References


1. Farrar, C.R., Worden, K.: Structural Health Monitoring: A Machine Learning Perspective. Wiley, New York (2012)
2. Sohn, H.: Effects of environmental and operational variability on structural health monitoring. Philos. Trans. R. Soc. Lond. A Math. Phys. Eng. Sci. **365**(1851), 539–560 (2007)
3. Engle, R.F., Granger, C.W.: Co-integration and error correction: representation, estimation, and testing. Econometrica **55**, 251–276 (1987)
4. Cross, E.J., Worden, K., Chen, Q.: Cointegration: a novel approach for the removal of environmental trends in structural health monitoring data. In: Proceedings of the Royal Society of London A: Mathematical, Physical and Engineering Sciences, The Royal Society (2011). doi:p. rspa20110023
5. Cross, E., Manson, G., Worden, K., Pierce, S.: Features for damage detection with insensitivity to environmental and operational variations. In: Proceedings of the Royal Society of London A: Mathematical, Physical and Engineering Sciences, The Royal Society (2012). doi:p. rspa20120031
6. Dao, P.B., Staszewski, W.J.: Cointegration approach for temperature effect compensation in Lamb-wave-based damage detection. Smart Mater. Struct. **22**(9), 095002 (2013)
7. Cross, E.J. Worden, K.: Approaches to nonlinear cointegration with a view towards applications in SHM. J. Phys. Conf. Ser. **305**, 012069 (2011). IOP Publishing, Bristol
8. Zolna, K., Dao, P.B., Staszewski, W.J., Barszcz, T.: Towards homoscedastic nonlinear cointegration for structural health monitoring. Mech. Syst. Signal Process. **75**, 94–108 (2016)
9. Shi, H., Worden, K., Cross, E.J.: A nonlinear cointegration approach with applications to structural health monitoring. J. Phys. Conf. Ser. **744**, 012025 (2016). IOP Publishing, Bristol
10. Cross, E.J.: On structural health monitoring in changing environmental and operational conditions. Ph.D. thesis, University of Sheffield (2012)
11. Dickey, D.A., Fuller, W.A.: Distribution of the estimators for autoregressive time series with a unit root. J. Am. Stat. Assoc. **74**(366a), 427–431 (1979)
12. Hamilton, J.D.: Time Series Analysis, vol. 2. Princeton University Press, Princeton (1994)
13. Perman, R.: Cointegration: an introduction to the literature. J. Econ. Stud. **18**(3), 3–30 (1991)
14. Enders, W.: Applied Econometric Time Series. Wiley, New York (2008)
15. Johansen, S.: Likelihood-Based Inference in Cointegrated Vector Autoregressive Models. Oxford University Press, Oxford (1995)
16. Worden, K., Cross, E., Antoniadou, I., Kyprianou, A.: A multiresolution approach to cointegration for enhanced SHM of structures under varying conditions - an exploratory study. Mech. Syst. Signal Process. **47**(1), 243–262 (2014)
17. Balke, N.S., Fomby, T.B.: Threshold cointegration. Int. Econ. Rev. **38**, 627–645 (1997)
18. Hansen, B.E., Seo, B.: Testing for two-regime threshold cointegration in vector error-correction models. J. Econ. **110**(2), 293–318 (2002)
19. Lo, M.C., Zivot, E.: Threshold cointegration and nonlinear adjustment to the law of one price. Macroecon. Dyn. **5**(4), 533–576 (2001)
20. Gregory, A.W., Hansen, B.E.: Residual-based tests for cointegration in models with regime shifts. J. Econ. **70**(1), 99–126 (1996)
21. Cross, E.J., Koo, K., Brownjohn, J., Worden, K.: Long-term monitoring and data analysis of the Tamar Bridge. Mech. Syst. Signal Process. **35**(1), 16–34 (2013)

# Chapter 42
# Evaluation of Contemporary Guidelines for Floor Vibration Serviceability Assessment

**Zandy O. Muhammad, Paul Reynolds, and Emma J. Hudson**

**Abstract** Technological advances in the construction sector and innovative lightweight and large span structural layouts in modern building floors increasingly mean that vibration serviceability is the governing design criterion. As this trend continues, excessive vibrations induced by human activities are becoming a significant concern. Prediction of floor vibrations at the design stage is often done using currently available design guidelines, such as AISC Design Guide 11, Concrete Society Technical Report 43 Appendix G, SCI P354, Concrete Centre CCIP-016 and HiVoSS.

In this paper, the aforementioned design guidelines are used to predict the vibration responses of a typical office floor, which are then compared with the actual measured responses. It is clear that different guidelines provide different tolerance limits which make the satisfactory/unsatisfactory decision imprecise. The results show that the case-study floor is unsatisfactory according to CSTR43 App G and CCIP-016, whereas it satisfies the requirements of AISC-DG11, SCI P354 and HiVoSS. Nevertheless, the experimental vibration response indicates that there is a perceptible level of vibrations but with no adverse comments. These discrepancies highlight the need for a better prediction techniques and more reliable assessment criteria.

**Keywords** Vibration serviceability • Floors • Design guidelines • R factor • Pedestrian loading

## 42.1 Introduction

Vibration serviceability of building floors is an area of particular interest in light of advancements in construction technologies and efficient use of materials. Driven by architectural demands for innovative and aesthetically pleasing designs, modern office floors have ever more open-plan layouts and longer spans with fewer internal partitions. In these floors, significant reductions in mass and damping are reported [1, 2] due to the modern paperless offices (computerised layouts) rather than conventional heavy offices (compartmentalised layouts). As a consequence, floors are becoming ever more prone to exhibit excessive vibrations in the range of frequencies generated by human activities, such as walking.

A number of design guidelines, available at the design stage, have been developed to predict the vibration performance of floors and their ability to satisfy prescribed serviceability thresholds. These include:

- American Institute of Steel Construction Design Guide 11 2016 (AISC DG11) [3]
- Concrete Society Technical Report 43 Appendix G 2005 (CSTR43 App G) [4]
- Concrete Centre Industry Publication 016 2006 (CCIP-016) [5]
- European guideline, Human Induced Vibration of Steel Structures 2007 (HiVoSS) [6]
- Steel Construction Institute publication 354 2009 (SCI P354) [7]

These design codes have provided methodologies to predict the vibration responses of floor systems using multi-mode SDOF approach under single person loading scenario. However, their reliabilities and limitations have not yet been fully investigated, in particular where the floors are on the borderline of being acceptable or unacceptable in terms of vibration response. Amongst the aforementioned guidelines there are different vibration design procedures which vary in both the serviceability assessment and the tolerance limits.

Z.O. Muhammad (✉) • P. Reynolds • E.J. Hudson
Vibration Engineering Section, College of Engineering, Mathematics and Physical Sciences, University of Exeter, North Park Road, Exeter EX4 4QF, UK
e-mail: zm247@exeter.ac.uk; p.reynolds@exeter.ac.uk; e.j.hudson@exeter.ac.uk



J. Caicedo, S. Pakzad (eds.), *Dynamics of Civil Structures, Volume 2*, Conference Proceedings of the Society for Experimental Mechanics Series, DOI 10.1007/978-3-319-54777-0_42

This paper examines the application of the above design guidelines for predicting the vibration response of a typical office floor using the design procedures provided by each guideline and evaluates them against actual vibration responses measured under a single person walking. The paper starts with a description of the case study floor, followed by a description of the measurement campaign and FE analysis. Then, the design guidelines with their procedures are employed to predict the vibration response and comparisons are made. The outcome of the analysis is discussed, both in terms of the reliability of the methods to predict accurate response levels and also with respect to the appropriateness of the various tolerance limits.

## 42.2 Experimental and Analytical Investigation of Case Study Floor

### *42.2.1 Floor Configuration*

The floor is a composite steel-concrete construction in a steel framed office building. This floor is irregular by design with the primary beams varying from 7.193 to 10.013 m in length and spanning between column lines, as shown in Fig. 42.1. The secondary beams also range from 9.53 to 13.0 m in length. The floor features composite steel beams supporting slabs cast of light weight concrete poured over steel profiled decking. A total height of 130 mm of concrete slab is used acting compositely with the secondary beams. The majority of the floor area is open plan office space furnished and there are few partition walls. Columns are located along the two sides of the building as well as along the centrelines.

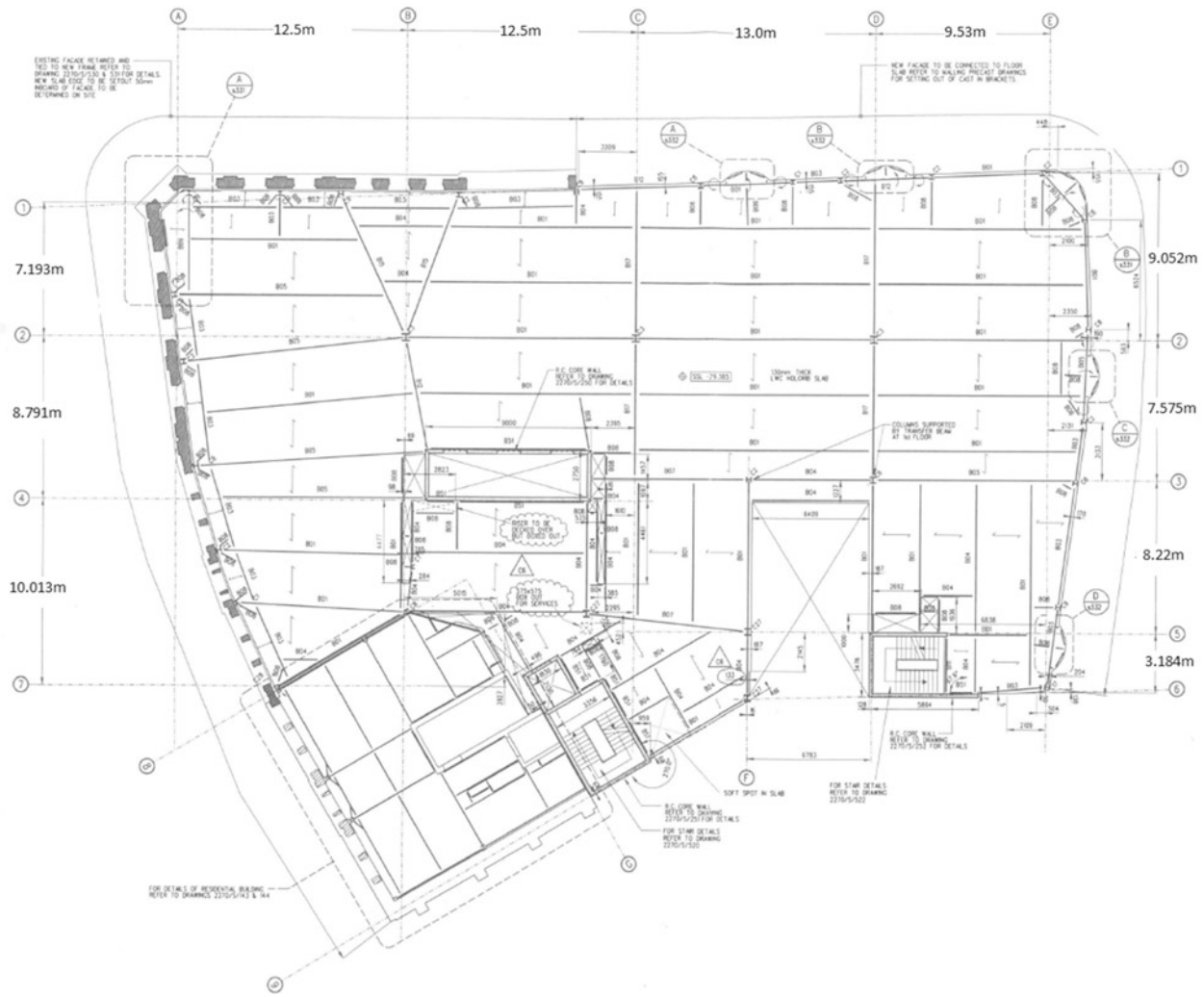


**Fig. 42.1** Plan of floor configuration

### *42.2.2 Data Acquisition*

Experimental Modal Analysis (EMA) was performed to find modal properties (i.e natural frequencies, modal damping and mode shapes) of the floor, which are shown in Fig. 42.2. Full details of the modal testing and vibration monitoring are discussed elsewhere [8] and some key points are repeated here. Four electrodynamic shakers were used to excite the floor and responses were measured using high quality accelerometers (Honeywell QA750). A test gird of 65 test points were utilised for acquisition of frequency response functions (FRF). For walking responses, the accelerometers were located at a point of high response and data were acquired at different pacing rates ranging from 104 steps per minute to 132 steps

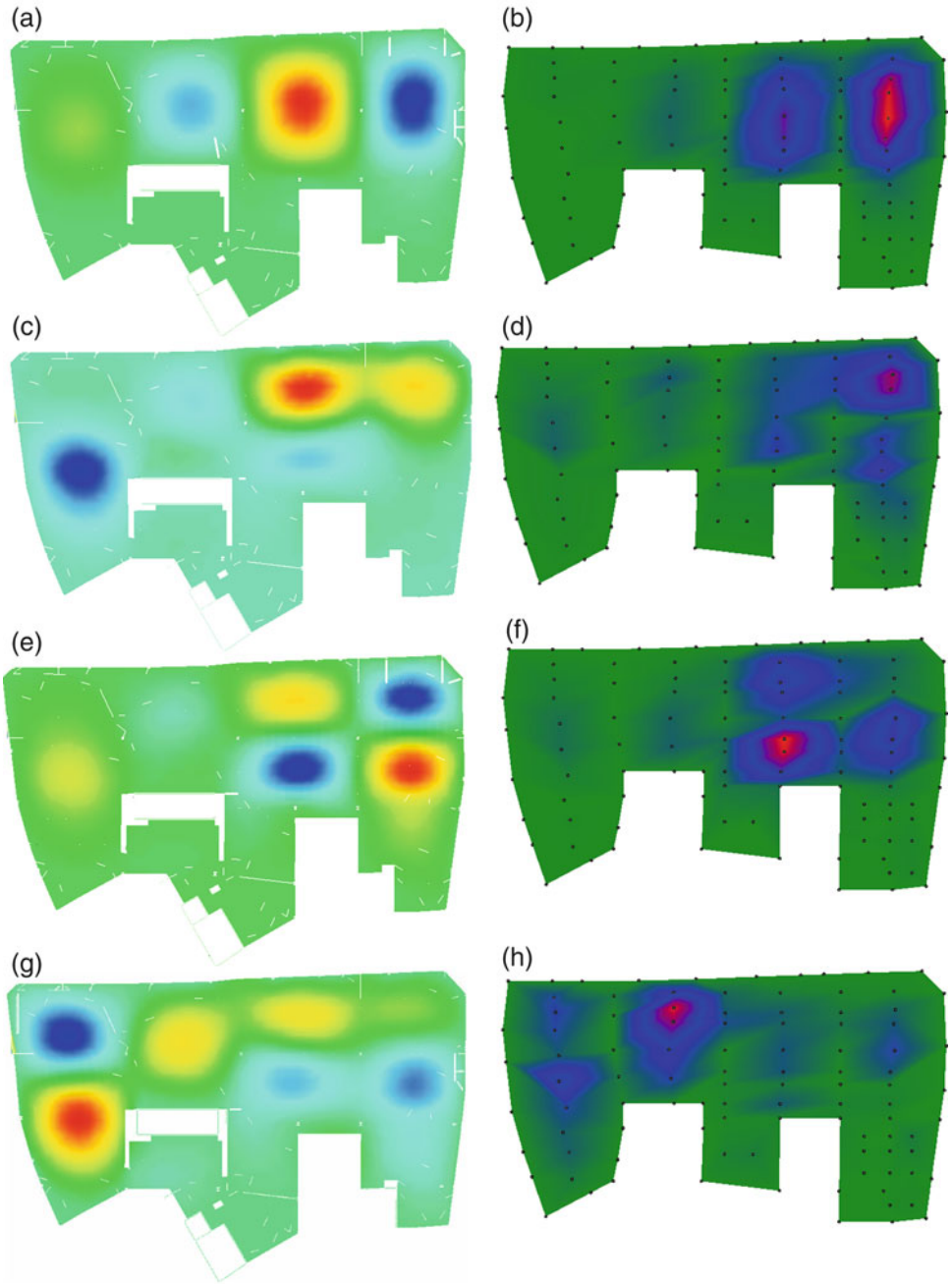


**Fig. 42.2** First four modes from FE analysis and experimental modal analysis. (**a**) FE analysis, $f_1$ = 5.23 Hz, m = 36.02 tonnes. (**b**) EMA $f_1$ = 5.24 Hz, $\zeta$ = 3.16%. (**c**) FE analysis, $f_2$ = 6.52 Hz, m = 28.54 tonnes. (**d**) EMA $f_2$ = 6.06 Hz, $\zeta$ = 2.24%. (**e**) FE analysis, $f_3$ = 6.33 Hz, m = 35.95 tonnes. (**f**) EMA $f_3$ = 6.58 Hz, $\zeta$ = 1.87%. (**g**) FE analysis, $f_4$ = 6.87 Hz, m = 39.95 tonnes. (**h**) EMA $f_4$ = 7.31 Hz, $\zeta$ = 2.60%

per minute. The walking path was between grid line D-1 and E-6 (Fig. 42.1), since it was noticed that the lowest mode shapes were concentrated in this region and it was within the reach of walking frequency ranges. The response data were sampled at 204 Hz and subsequent to the measurements the following steps were performed to obtain the measured vibration responses:

- BS6841 $W_b$ frequency weighting was applied to the acceleration time history, which takes into account the variation of human perception of vibration at different frequencies.
- Running root-mean-square (RMS) trends were calculated for the 1 s integration time for the weighted acceleration.
- The RMS values for all the weighted accelerations were found.
- The peak of running RMS trends was found, which is termed as maximum transient vibration value (MTVV).
- Response factor (R-factor) was calculated by dividing the MTVV value by the base curve value of 0.005 m/s$^2$.

### *42.2.3 FE Analysis*

A 3D FE model of the floor structure was developed in ANSYS from the structural drawings. SHELL63 elements were utilised to model the orthotropic composite floor and BEAM188 was assumed to model all the beams and columns. Manual model updating was performed to match the measured frequencies. A modal analysis was conducted to obtain natural frequencies and mode shapes of the floor. There are a significant number of vibration modes less than 12 Hz and due to space limits only the first four mode shapes are shown in Fig. 42.2.

## 42.3 Vibration Responses Using Current Guidelines

This section presents the design procedures available in the vibration guidelines, i.e [3–7] to estimate the vibration responses to a single person walking. The design methodologies of each guideline are briefly discussed, then the results are presented with the corresponding tolerance limits.

### *42.3.1 Source of Excitation: Walking Loads*

The walking load model described by each guideline is different and takes various forms. It is widely accepted by the available guidelines that vibration responses of floors are in two types: a resonance build-up for low-frequency floors and a transient response for high-frequency floors. The threshold frequency between these two categories is around 10 Hz. For the considered office floor, the fundamental frequency is less than 10 Hz; hence, the walking load model only relevant to the low-frequency floors is discussed.

The walking load model used in AISC DG11, CSTR43 App G, CCIP-016, and SCI P354 is a Fourier series representation considering only the first four harmonics [3–5, 7], the general from is shown in Eq. (42.1).

$$F(t) = G\left[1 + \sum_{n=1}^{N} \alpha_n \sin(n2\pi f_p t + \Phi_n)\right] \tag{42.1}$$

where, $F(t)$ = walking load time history (N); $G$ = static weight of a person ( (168 lb) 750 N in AISC DG11; 700 N in both CSTR43 App G, CCIP-016 and 746 N in SCI P354); $\alpha$ = Dynamic Load Factors (DLFs); n = order of harmonic of the walking rate (n = 1, …); $f_p$ = pacing frequency (Hz); t = time (sec); $\Phi$ = harmonic phase angle; N = total number of harmonics.

The values of DLFs provided by CSTR43 App G and CCIP-016 are statistically defined to have 25% chance of being exceeded, while in AISC DG11 deterministic values are used and in SCI P354 the values depend on pacing frequencies. Also, the pacing frequency ranges between 1.0–2.8 Hz in CSTR43 App G and CCIP-016, whereas the design range covered by SCI P354 and AISC DG 11 is narrowed down to 1.8–2.2 Hz and 1.6–2.2 Hz, respectively.

HiVoSS [6, 9], however, assumes a completely different approach by modelling walking as a step-by-step polynomial function with eight terms. The pacing frequency and pedestrian weight is defined probabilistically and it is a cumulative distribution for each combination of the pacing frequency and pedestrian weight.

### *42.3.2 Dynamic Properties of the Floor by the Guidelines*

The current guidelines characterise the dynamic properties of the floors by modal parameters, such as natural frequency of the floor, modal mass and damping ratio. Among the design guidelines, CSTR43 App G allows to use the measured modal parameters and it is applicable to all materials of construction. HiVoSS presents slightly a different approach to include transfer function procedure to estimate the modal properties; however, graphs are provided by HiVoSS as a result of beforehand calculation of the transfer function to find the vibration responses. Hence, the graphs can be used directly by reading off the vibration responses. This guideline is only applicable to steel structures, which implies a significant limitation of the use of this guideline.

CCIP-016 [5], similar to CSTR43 App G, is applicable to any construction materials, with the extension of being applicable to floors as well as footbridges. Both AISC DG11 and SCI P354 are only applicable to steel structures.

### *42.3.3 Vibration Response Estimation and Evaluation*

For low-frequency floors, the resonant response occurs when one of the harmonics of walking matches a frequency of the floor. Mode superposition is an effective tool in all the guidelines to obtain the final response. The guidelines calculate acceleration responses of each mode, then by using the mode superposition the final outcome is obtained. AISC DG11 [3], in particular, suggests using analytical FRFs to determine which mode provides the highest response and thus the peak magnitude of the FRF will be used to estimate the acceleration response. For the considered floor, the peak FRF value obtained from harmonic (steady state) analysis (see Fig. 42.3) is $0.80 \times 10^{-3}$ m/s$^2$/N, which occurred between grid line B-1 and C-2 (Fig. 42.1).

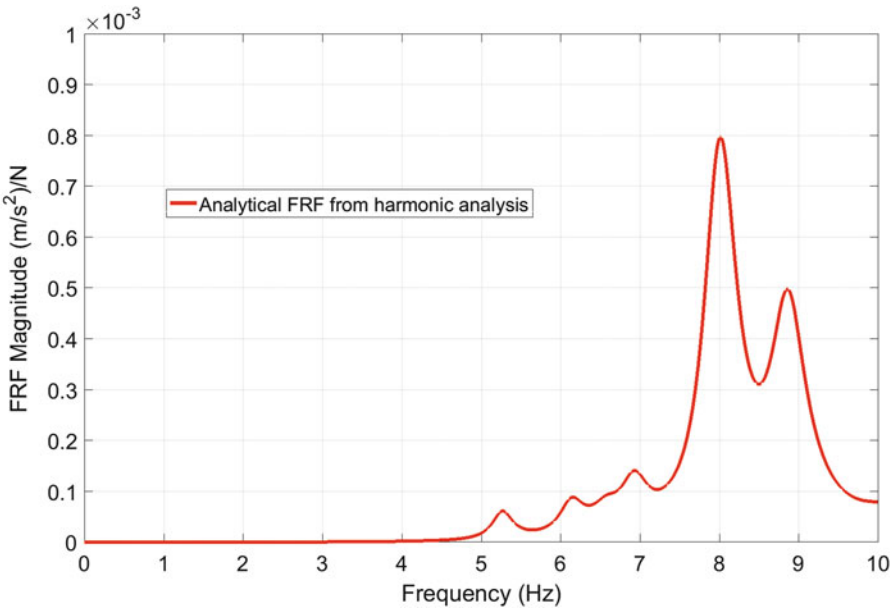


**Fig. 42.3** Peak FRF magnitude from FE harmonic analysis between grid line B-1 & C-2

Different vibration criteria are provided to evaluate the vibration responses predicted by each guideline. CSTR43 App G and CCIP-016 calculate the response factor (R factor), which is then compared to recommended tolerance limits based on the floor usage. For office floors, similar to the case study floor, the recommend vibration limit is an R factor of 4. However, SCI P354 only provides a higher recommended limit, which is R factor of 8.

On the other hand, AISC DG 11 only sets the peak acceleration as the vibration limit, which is 0.5%g for office floors, this value corresponds to an equivalent R factor of 7. HiVoSS considers a different criterion, which is one step root-mean-square (OS-RMS). This value has a dimension of mm/s. It is based on the peak root mean square velocity calculated from the inverse of Fourier transformation of the weighted velocity response [10]. This value provides different "recommended class" as acceptable criteria, which ranges from class A (highly recommend) to class F (not recommended). The OS-RMS for each class is calculated from a combination of walking frequency and pedestrian weights, the 90% percentile of those values are considered to be the highest response under the walking load. In calculating the $\text{OS-RMS}_{90}$ value, the walking path is not taken into account, this implies that the excitation point is kept fixed. Hence, this method is believed to be "semi-probabilistic" [11]. The $\text{OS-RMS}_{90}$ multiplied by a value of 10 gives the equivalent R factor [10]. The recommended values for office floors according to HiVoSS is between a lower limit (5% probability of complaints) of $\text{OS-RMS}_{90} = 0.8$ mm/s and upper limit (95% probability of complaints) of $\text{OS-RMS}_{90} = 3.2$ mm/s, which corresponds to an R factor of 32.

## 42.4 Results and Discussion

The vibration serviceability assessment is performed based on the tuned FE model for all the modes less than 12 Hz for CSTR 43 App G, and SCI P354, while 15 Hz for the CCIP-016. The FRF for AISC DG 11 was performed up to frequency of 10 Hz under a unit amplitude load at location of the highest mode amplitude and the response was measured at the same point (Fig. 42.3). The modal damping ratio of 3% was assumed for all modes of vibration. The response was calculated for a range of the floor frequencies to obtain the peak vibration response (i.e R factor).

The results of the maximum predicted R factor are shown in Fig. 42.4. It can be seen that all the guidelines predict different values of R factor. CSTR43 App G and CCIP-016 predict an R factor of greater than 4, which results in an unsatisfactory floor evaluation. SCI P354 gives an R factor of 7.86 from the calculations, which results in a positive assessment of the floor. Both AISC DG 11 and HiVoSS predict the equivalent R factor of 4.19 (0.30%g) and 12.75 ($\text{OS-RMS}_{90} = 1.275$ mm/s), respectively. Hence, the floor is acceptable by AISC and it is within the recommended region by HiVoSS. Also, the distribution of R factor under various pacing frequencies is presented in Fig. 42.5. It is clear that there are R factor values predicted by a wide range of pacing frequencies from CSTR43 App G and CCIP-016, whereas SCI P354 range of pacing frequencies seems to be inadequate.

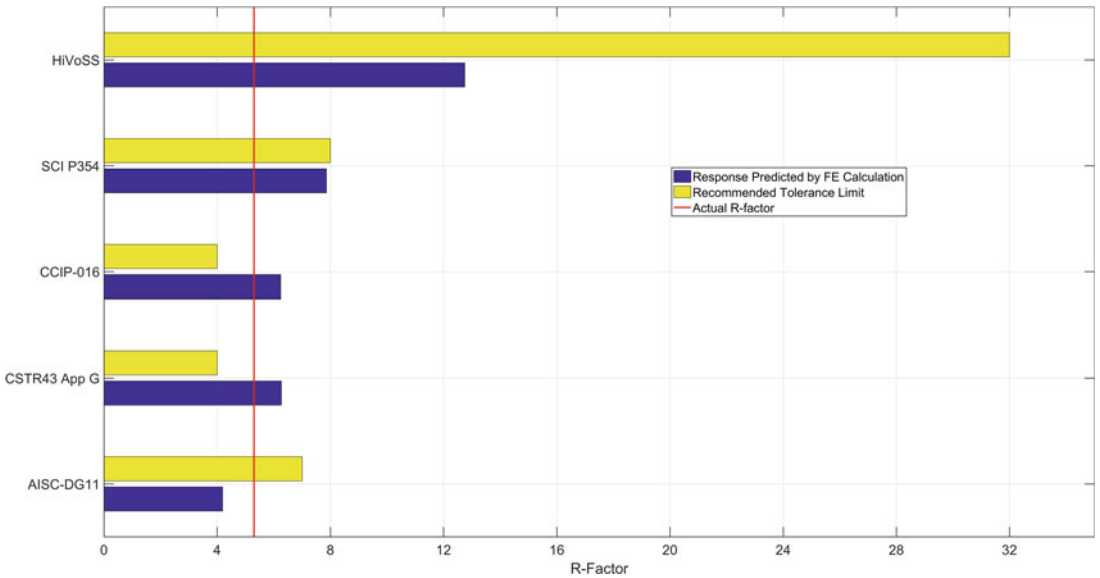


**Fig. 42.4** Predicted R factor by different guidelines with recommended tolerance limits

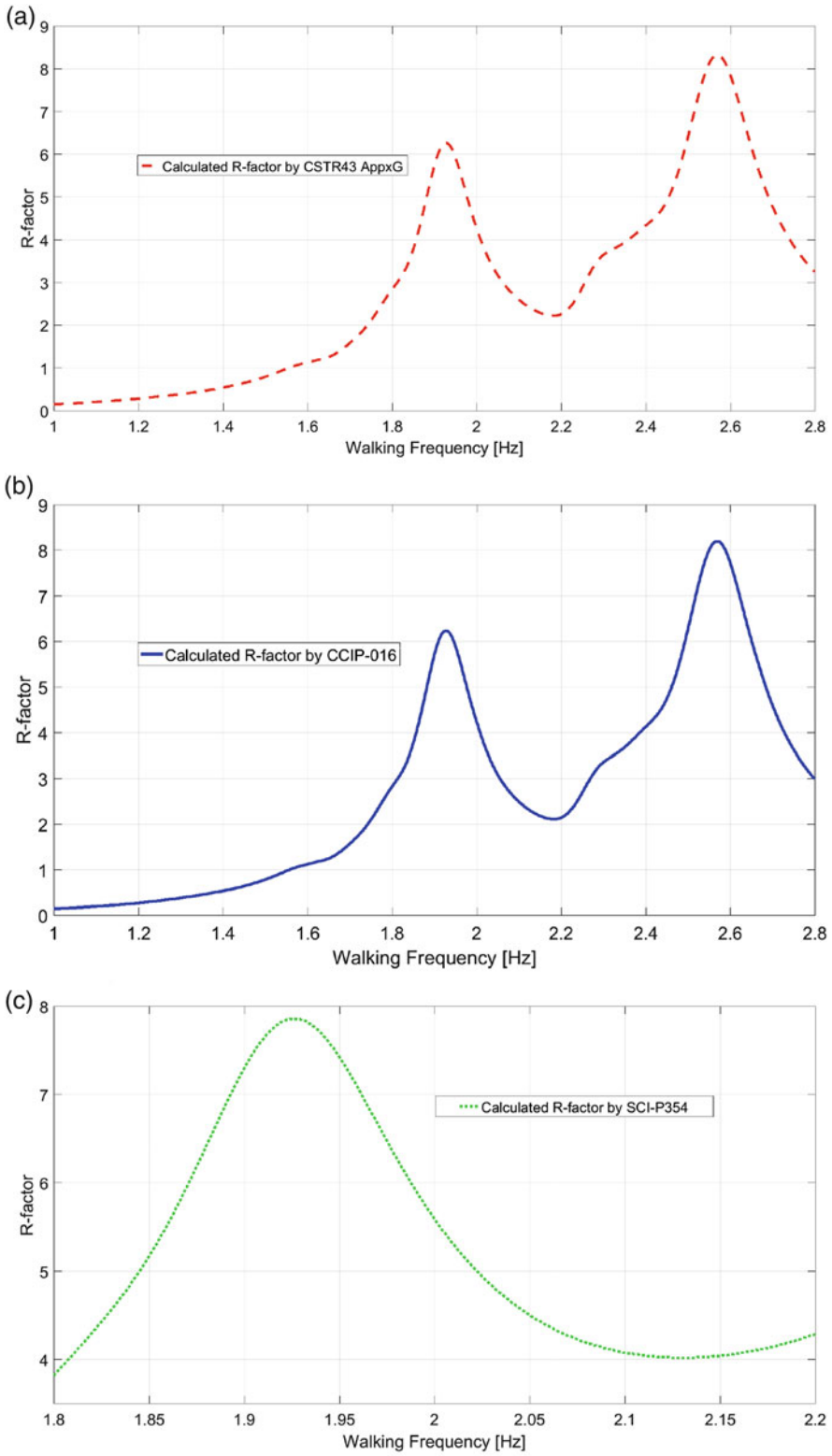


**Fig. 42.5** Distribution of different pacing frequency against R-factor in guidelines. (**a**) Distribution of pacing frequency against R-factor in CSTR43 App G. (**b**) Distribution of pacing frequency against R-factor in CCIP-016. (**c**) Distribution of pacing frequency against R-factor in SCI P354

From the actual response standpoint, the measured R factor is 5.3 (MTVV $= 0.026\,\mathrm{m/s^2}$). This value corresponds "subjectively" to a perceptible level of the vibration by floor occupants, but it resulted in no adverse comments. It is worth noting that the peak values predicted by the guidelines are scattered in comparison to the actual response. The predicted values provide only a single value for prediction with different descriptors (peak acceleration, peak R factor and OS-$RMS_{90}$), which do not give reliable information on the event occurrence. These peak values may not occur as frequently as predicted (i.e the probability of occurrence and exceedance is not known), despite being assessed as unacceptable/acceptable according to the provided recommended limits.

These discrepancies highlight that the current design guidelines can potentially result in unreliable assessment of floor vibrations, which may lead to imprecise assessment as satisfactory/unsatisfactory. Therefore, better calculation techniques and more reliable criteria are required to predict more reliably the vibration responses of floors [12].

## 42.5 Conclusion

This paper has highlighted vibration response prediction by contemporary guidelines relative to the measured response obtained from experimental walking measurements. The response prediction is based on a single peak value of acceleration or R factor, which is not a representative value and may not occur as often as expected by the guidances. Also, the response criteria provided by HiVoSS is obviously much higher than its counterparts, despite being on the basis of a probabilistic approach. Whilst different guidelines provide various assessment criteria, the satisfactory and unsatisfactory decision seem to be imprecise. As a result, the serviceability assessment procedure and recommended vibration tolerance limits of different guidelines seem to be unreliable and misleading, since the prediction is based on a single person loading and the single peak value. Hence, various probability of exceedance needs to be defined in order to reflect the actual behaviour of the floor at different excitations. It is clear that there is a need for further research and investigations to carry out extensive work in in-servicing office environments and develop or improve a more reliable assessment tools.

**Acknowledgements** The authors gratefully acknowledge the financial support of the Qatar National Research Fund (QNRF) through grant NPRP8-836-2-353 entitled "A Unified Approach to Vibration Serviceability Assessment of Floors".

## References

1. Hewitt, C.M., Murray, T.M.: Office fit-out and floor vibrations. Mod. Steel Constr. **44**, 35–38 (2004)
2. Middleton, C., Brownjohn, J.: Simplified methods for estimating the response of floors to a footfall. In: Structures Congress 2011, Las Vegas, Nevada, vol. 41171, pp. 383–403. ASCE, New York (2011)
3. Murray, T.M., Allen, D.E., Ungar, E.E., Davis, D.B.: Vibrations of steel-framed structural systems due to human activity: AISC DG11, 2nd edn (2016)
4. Pavic, A., Willford, M.: Vibration serviceability of post- tensioned concrete floors. Appendix G, Technical Report 43, 2nd edn. Concrete Society, Slough (2005)
5. Willford, M., Young, P.: A design guide for footfall induced vibration of structures - CCIP-016. The Concrete Centre, Surrey (2006)
6. HiVoSS: Human induced vibrations of steel structures-vibration design of floors (HiVoSS): guideline. European Commission (2007)
7. Smith, A., Hicks, S., Devine, P.: Design of floors for vibration: a new approach(SCI P354). Steel Construction Institute (SCI), Berkshire (2009)
8. Hudson, E.J., Reynolds, P.: Implications of structural design on the effectiveness of active vibration control of floor structures. Struct. Control. Health Monit. **21**(5), 685–704 (2014)
9. HiVoSS: Human induced vibrations of steel structures-vibration design of floors (HiVoSS): background document. European Commission (2007)
10. Van Nimmen, K., Gezels, B., De Roeck, G., Van Den Broeck, P.: The effect of modelling uncertainties on the vibration serviceability assessment of floors. In: Proceedings of the 9th International Conference on Structural Dynamics, EURODYN 2014, Porto, pp. 959–966 (2014)
11. Hassan, O.A.B., Girhammar, U.A.: Assessment of footfall-induced vibrations in timber and lightweight composite floors. Int. J. Struct. Stab. Dyn. **13**(2), 26 (2013)
12. Reynolds, P., Pavic, A.: Reliability of assessment criteria for office floor vibrations. In: 50th United Kingdom Conference on Human Responses to Vibration, Southampton (2015)

# Chapter 43
# Excitation Energy Distribution of Measured Walking Forces

**Atheer F. Hameed and Aleksandar Pavic**

**Abstract** For vibration serviceability of floors, current design guidelines propose different force models to represent human walking on structures. Those models have been derived based on many assumptions to simplify the real force induced by human walking. One of those assumptions states that the force is assumed periodic. Other simplification is that the spectrum of the force is assumed to have very low energy beyond a certain frequency limit, hence it can be neglected in that higher frequency region. Those assumptions have been verified and validated over time for conventional floor structures. However, modern floors are slender, made of lightweight materials, and have strong orthotropic properties and low point stiffness. Hence they feature localized higher modes that could be excited even with small amount of energy. In this paper, real walking forces are used to demonstrate the excitation energy distribution over frequency range of 0–60 Hz. A unique database of 852 vertical continuous ground reaction forces (GRF) measured on an instrumented treadmill due to walking is used for that purpose. Excitation energy is calculated by summing the power of the measured force in the frequency domain. It is found that there are considerable amounts of excitation energy well beyond the frequency limits proposed by the current floor design procedures. Boxplots are presented showing the realistic energy distribution which could excite the higher modes of lightweight and slender floors.

**Keywords** Vibration serviceability • Human walking • Signal energy • Parseval's theorem • Fourier spectrum

## 43.1 Introduction

While the ultimate limit states used to govern the design of conventional floor structures in the past, serviceability limit states, specifically vibration serviceability, has become the governing design criterion for modern lightweight and slender floor structures. This is because modern floors feature lightweight materials that are strong enough but not stiff enough. Although these floors are designed in accordance with the procedures proposed by the state-of-the-art design guidelines, floors designed "to code" are increasingly failing to meet the required occupants comfort level. This is considered as a serious issue, and suggests that the current design procedure might not be suitable anymore for the design of modern floor structures. To rationalize this problem, it is crucial to identify the following, as proposed by ISO 10137:2007 [1]:

1. Vibration source,
2. Transmission path, and
3. Vibration receiver.

This paper investigates the vibration source, which could be any human activity that can excite a structure such as walking, jogging, or running. For floor structures, walking is the most common human activity that could excite the structure. Current design guidelines propose different forcing models that can be used to represent excitation due to human walking on a

A.F. Hameed (✉)
Vibration Engineering Section, College of Engineering, Mathematics, and Physical Sciences, University of Exeter, Kay Building, North Park Road, Exeter, EX4 4QF, UK

Civil Engineering Department, University of Anbar, Ramadi, Anbar, 31001, Iraq
e-mail: afhh201@exeter.ac.uk

A. Pavic
Vibration Engineering Section, College of Engineering, Mathematics, and Physical Sciences, University of Exeter, Kay Building, North Park Road, Exeter, EX4 4QF, UK

Full Scale Dynamics Ltd., 40 Leavygreave Road, Sheffield, South Yorkshire, S3 7RD, UK
e-mail: a.pavic@exeter.ac.uk



J. Caicedo, S. Pakzad (eds.), *Dynamics of Civil Structures, Volume 2*, Conference Proceedings of the Society for Experimental Mechanics Series, DOI 10.1007/978-3-319-54777-0_43

structure. Although those forcing models are easy to implement, they are based on many assumptions, hence are not able to reflect real walking scenarios. All these models are assuming periodicity of human walking as opposed to real walking which are considered narrow-band random forces. Moreover, it is assumed that human walking forces have negligible ability to excite higher modes of vibration with natural frequencies above certain value. For example, when considering resonant vibration analysis, the proposed forcing model has only four harmonics, which extend up to 11.2 Hz [2, 3]. In this paper, measured walking forces are used to demonstrate how the walking excitation energy is actually spread over a much wider range of frequencies that goes well beyond the suggested level by the current design guidelines.

## 43.2 Methodology

The measured walking forces were collected from 85 participants using an instrumented treadmill where 852 continuous vertical walking force time histories were recorded [4]. The walking forces were recorded with a sampling frequency of 200 Hz and the speed of each test subject was controlled, hence each measured force has a unique pacing frequency. The test sequence can be cited in details by Brownjohn et al. [4]. A typical normalized (by the weight of the test subject) walking force time history is shown in Fig. 43.1 along with its discrete Fourier amplitudes for a data block of 20.48 s.

To determine the pacing frequency of each measured walking force, the Fourier spectrum was analyzed and all forces were categorized into groups according to their pacing frequencies. The distribution of all measured forces according to their pacing frequency is shown in the histogram in Fig. 43.2.

The total energy, E, of a continuous signal x(t) is defined as [5]:

$$E = \int_{-\infty}^{\infty} x^2(t)dt \tag{43.1}$$

In the case of a discrete-time signal, the total energy is defined by [5]:

$$E = \sum_{n=-\infty}^{\infty} x^2[n] \tag{43.2}$$

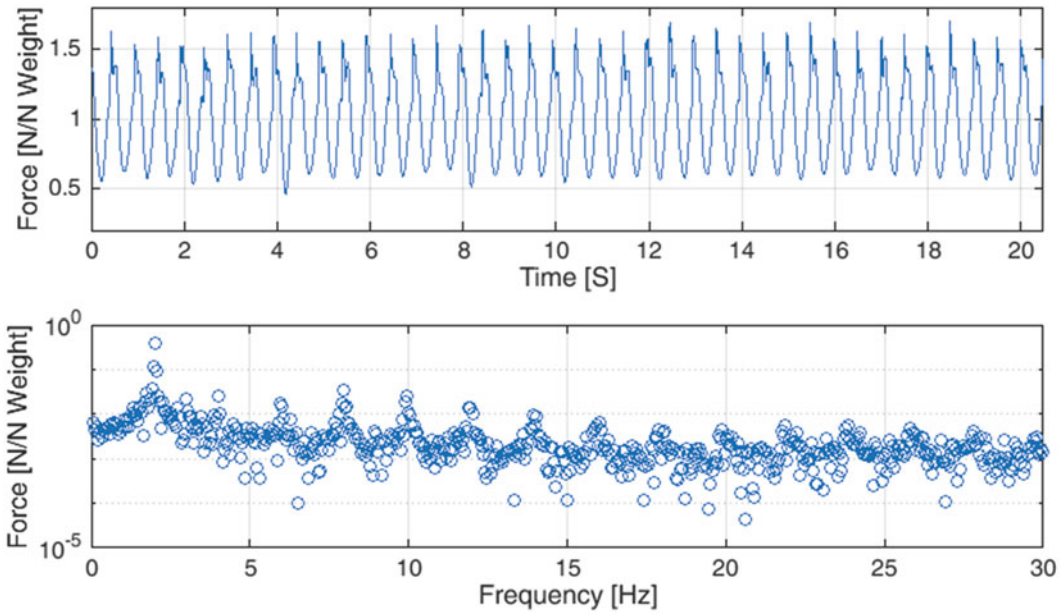


**Fig. 43.1** Typical walking force time history and Fourier amplitudes (Pacing frequency is 2 Hz)

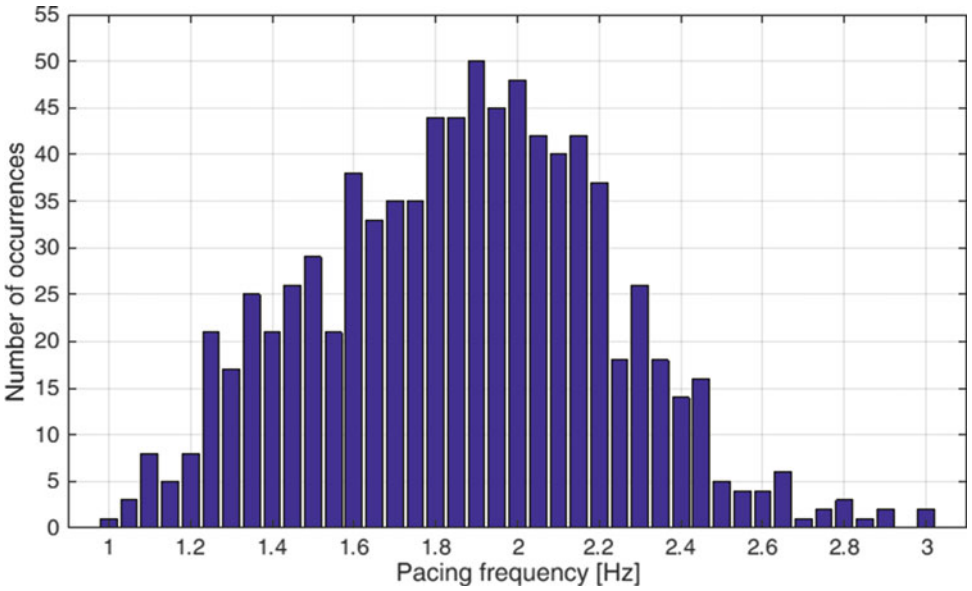


**Fig. 43.2** Histogram of pacing frequencies

Where x[n] is the discrete-time signal, and n is the sample number. The result of Eq. (43.2) is the energy of the whole signal. However, when the energy of a desired frequency band is required then the calculation is best performed in the frequency domain using Parseval's theorem. Parseval's theorem is given as [6]:

$$E = \sum_{n=-\infty}^{\infty} x^2[n] = \frac{1}{N} \sum_{k=-\infty}^{\infty} |X(k)|^2 \tag{43.3}$$

Where X(k) is the Discrete Fourier Transform of the discrete-time signal x[n] and k is the sample number in the frequency domain. Parseval's theorem could be interpreted as follows: while the energy of the total signal could be calculated by summing the squared value of each sample in the time domain, it is also possible to get the same results by summing the squared spectral lines in the frequency domain. In this paper, Eq. (43.3) is used to evaluate the energy of each walking force time history over predefined frequency range. It is important to emphasize that the energy calculated using any of the Eqs. (43.1)–(43.3) is a signal metric and not the energy defined in physics as "the ability to do work". The physical energy has units of Joules, while the 'signal energy' has units that depend on the units of the signal itself: (unit$^2$/s) or (unit$^2$/Hz).

## 43.3 Results

As explained in Sect. 43.2 Methodology, the forces were divided into groups according to their corresponding pacing frequencies. This allowed forces of similar frequency characteristics to be processed independently. The process was based on the analysis of the Fourier amplitudes of each force. The Fourier amplitudes of all forces with pacing frequency of 2 Hz, for example, is shown in Fig. 43.3.

Using Eq. (43.3), the signal energy of each force was calculated in frequency bands of 1 Hz for frequency range between 0 and 60 Hz. The 1 Hz frequency band is centered around an integer frequency. For instance, the signal energy at 2 Hz is calculated for a frequency band between 1.5 and 2.5 Hz. The excitation energy is presented statistically by means of box plots. Figure 43.4 shows the calculated energies for the group with pacing frequency of 2 Hz shown previously in Fig. 43.3. It can be seen that the excitation energy is noticeable beyond the limit of 11.2 Hz. The red crosses of the box plot shown in Fig. 43.4 are the outliers [7].

For better representation, Fig. 43.5 shows the total of signal energy over specified frequency bands defined as:

1. 0.5–2.8 Hz: this is where the first harmonic of walking occurs.
2. 2.9–11.8 Hz: this is where the second, third, and fourth harmonics appear.

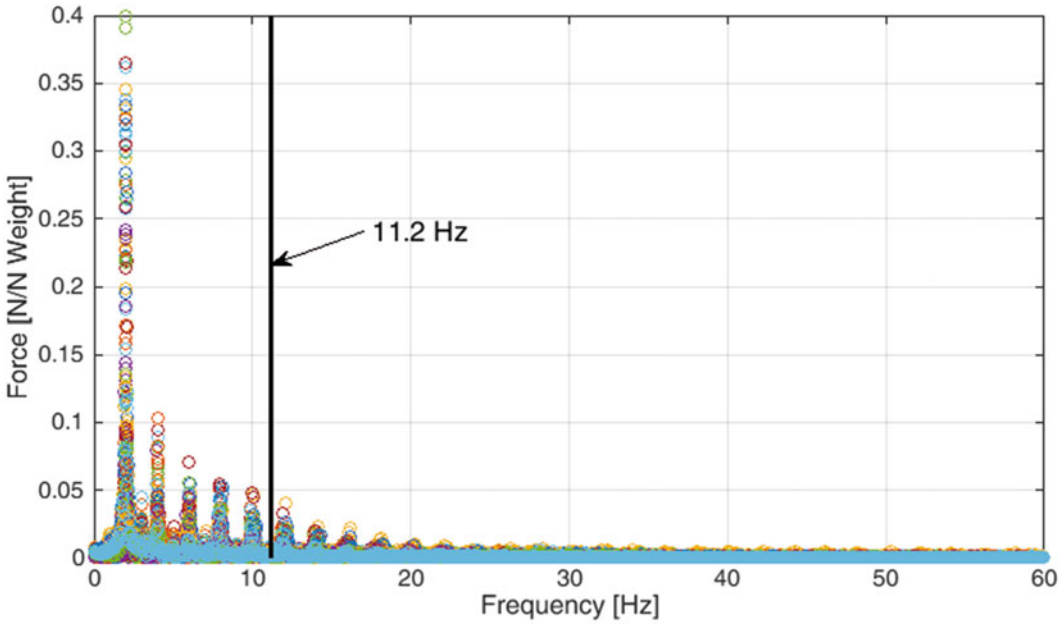


**Fig. 43.3** Fourier amplitudes of 48 walking forces with pacing frequency of 2.00 Hz

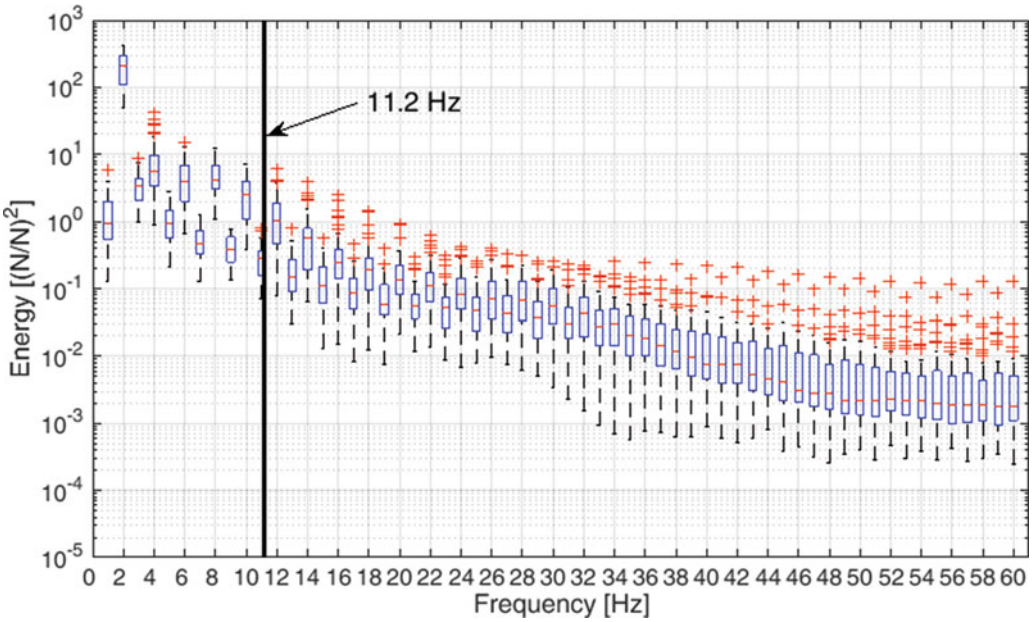


**Fig. 43.4** Energy distribution of 48 walking forces with pacing frequency of 2.00 Hz

3. 11.9–30 Hz: this is where other harmonics are visually recognized (from Fig. 43.4).
4. 30.1–60 Hz: this is the rest of the frequency range of interest.

The first two bands, i.e. up to 11.2 Hz, are the only part of the walking force that is been considered by the current design procedures. It can be noticed from Fig. 43.5 that the other parts of walking forces, i.e. beyond 11.2 Hz, cannot be neglected if the excited structure has modes of vibration in that range of frequencies. Especially when those modes are localized and generate frequency response function (FRF) amplitudes higher an order of magnitude than the FRFs corresponding to the lower modes of vibration.

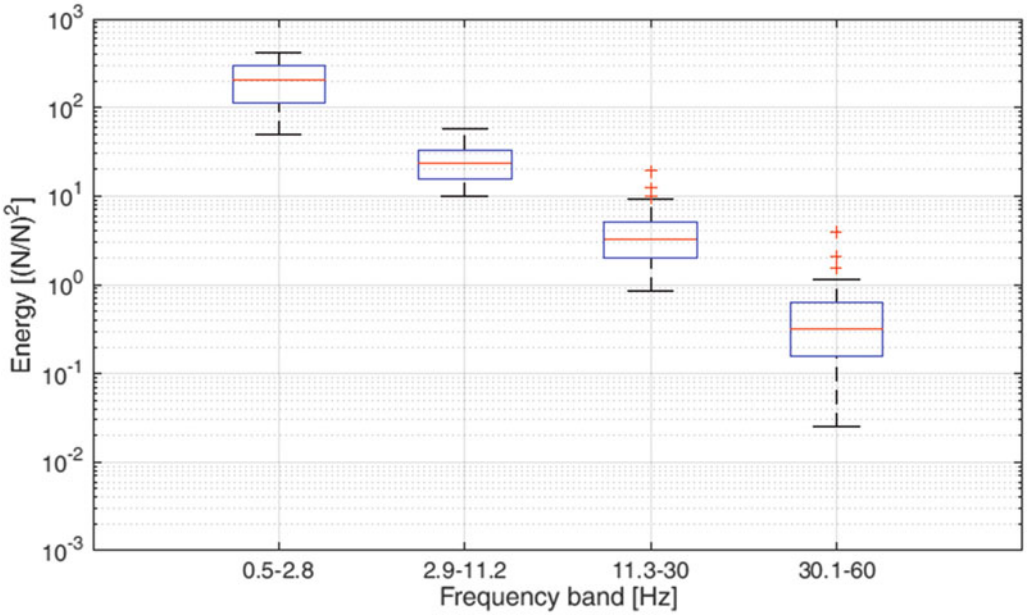


**Fig. 43.5** Accumulative energy over certain frequency bands of 48 walking forces with pacing frequency of 2.00 Hz

## 43.4 Conclusions

Analysis of the excitation energy was conducted using 850 measured walking forces from 85 participants. The analysis showed that the energy is distributed well beyond the limits of the proposed walking models of the current design guidelines. Boxplots were used to statistically represent the results where a pacing frequency of 2 Hz was considered. It is suggested that these higher frequency ranges should not be neglected especially when calculating the vibration response of structures with significant contribution from higher modes of vibration.

**Acknowledgements** The database of walking forces was created courtesy of funding by the UK Engineering and Physical Sciences Research Council, Grant EP/E018734/1 (Human walking and running forces: novel experimental characterization and application in civil engineering dynamics). The paper was prepared with the support of the Engineering and Physical Sciences Research Council (EPSRC) grant reference EP/G061130/1 (Dynamic Performance of Large Civil Engineering Structures: An Integrated Approach to Management, Design and Assessment) for which the writers are grateful. The financial support of The Higher Committee for Education Development in Iraq (HCED IRAQ scholarship reference GD-13-5) is highly appreciated as well.

## References

1. ISO 10137:2007: Bases for Design of Structures – Serviceability of Buildings and Walkways Against Vibrations – Reviewed in 2012, 2nd edn. Internation Standards Organisation, Geneva (2012)
2. Willford, M.R., Young, P.: A Design Guide for Footfall Induced Vibration of Structures – CCIP-016. The Concrete Centre, Slough (2006)
3. Pavic, A., Willford, M.R.: Vibration Serviceability of Post-tensioned Concrete Floors – CSTR43 App G, Append. G Post-Tensioned Concr. Floors Des. Handb. – Tech. Rep. 43, pp. 99–107 (2005)
4. Brownjohn, J.M.W., Racic, V., Chen, J.: Universal response spectrum procedure for predicting walking-induced floor vibration. Mech. Syst. Signal Process. 1–15 (2015). doi:10.1016/j.ymssp.2015.09.010
5. Haykin, S., Van Veen, B.: Signals and Systems, 1st edn. Wiley, Hoboken (1998)
6. Smith, J.O.: Mathematics of the Discrete Fourier Transform (DFT) with Audio Applications, 2nd edn. W3K Publishing (2008)
7. Montgomery, D.C., Runger, G.C.: Applied Statistics and Probability for Engineers, 3rd edn. Wiley, Hoboken (2002)

# Chapter 44
# Identification of Human-Induced Loading Using a Joint Input-State Estimation Algorithm

**Katrien Van Nimmen, Kristof Maes, Peter Van den Broeck, and Geert Lombaert**

**Abstract** This paper uses a state-of-the-art joint input-state estimation algorithm to identify the modal load induced by a single pedestrian on a laboratory structure. The experimental setup involves a simply-supported concrete slab with a length of 7 m. A dynamic model of the lab structure is constructed from a finite element model that is calibrated using a set of experimentally identified modal characteristics. The estimated modal load as is compared with the numerically predicted modal load which uses the average single-step walking load as determined from direct force measurements, the location of the individual steps as identified from video processing and a numerical model of the structure. For the time interval where the pedestrian is crossing the slab, the estimated modal load is found to be in good agreement with the numerically predicted values. Following the last footstep of the pedestrian, the slab passes into a decaying free vibration whereby an exponentially decaying estimated input compensates for small errors in the modal properties.

**Keywords** Human-induced vibrations • Force identification • Footbridge • Human-structure interaction • Vibration serviceability

## 44.1 Introduction

Although the dynamic performance of footbridges under high crowd densities is often imperative for design, the available load models are rudimentary and have virtually never been verified [1]. Concerns about these load models are further strengthened by the fact that human-structure interaction (HSI) phenomena are not well-understood [2]. In-field observations are the only way to obtain detailed and accurate information on representative operational loading data [1, 3]. As direct force measurements are in this case practically infeasible, inverse force identification where the input forces are reconstructed from the resulting vibrational response and a dynamic model of the structure, constitutes a promising alternative.

This contribution uses a joint input-state estimation technique as described in Maes et al. [4] to identify the modal load induced by a single pedestrian on a laboratory structure. The results are compared to the numerically predicted modal load which is based on the average single-step walking load as determined from direct force measurements, the location of the individual steps as identified from video processing and a numerical model of the structure.

## 44.2 Experimental Setup

The laboratory structure consists of a simply-supported hollow-core pre-stressed concrete slab with a span of 7 m (Fig. 44.1). The structure only has a single mode, the vertical bending mode, with a natural frequency within the dominant spectrum of pedestrian excitation ($< 10$ Hz). The corresponding modal parameters ($\tilde{f}_j = 6.05$ Hz, $\tilde{\xi}_j = 0.39$ Hz) are experimentally identified [5].

K. Van Nimmen (✉) • P. Van den Broeck
Department of Civil Engineering, Structural Mechanics, KU Leuven, B-3001 Leuven, Belgium

Department of Civil Engineering, Technology Cluster Construction, Structural Mechanics and Building Materials Section, KU Leuven, Technology Campus Ghent, Ghent, Belgium
e-mail: katrien.vannimmen@kuleuven.be

K. Maes • G. Lombaert
Department of Civil Engineering, Structural Mechanics, KU Leuven, B-3001 Leuven, Belgium



J. Caicedo, S. Pakzad (eds.), *Dynamics of Civil Structures, Volume 2*, Conference Proceedings of the Society for Experimental Mechanics Series, DOI 10.1007/978-3-319-54777-0_44

**Fig. 44.1** The hollow-core pre-stressed concrete slab excited by a single pedestrian

The experimental study considered a single pedestrian walking along the slab (see Fig. 44.1). The vertical acceleration response of the slab was recorded at 13 locations, uniformly distributed along its length. The pedestrian is instrumented with sensors allowing a 3D tracking of the motion. The registered pedestrian motion allows to identify the average step frequency and the onset of each step [6]. The location of the individual footsteps are identified from video processing (Fig. 44.1). The results show that the average step frequency of the pedestrian equals $\tilde{f}_s = 1.98$ Hz.

## 44.3 Results

The forces are estimated using a data set consisting of one displacement ($n_{\mathrm{d,d}} = 1$) and 13 acceleration measurements ($n_{\mathrm{d,a}} = 13$. The noise covariance matrices $\mathbf{Q}$ and $\mathbf{S}$ used in the force identification are assumed to be zero as the force $\mathbf{p}_{[k]}$ accounts for all excitation present. The matrix $\mathbf{R}$ in this case accounts for sensor noise and is constructed from the (known) standard deviation of the measurement noise [4]. The initial state estimate vector $\mathbf{x}_{[0|-1]}$ and its error covariance matrix $\mathbf{P}_{[0|-1]}$ are both assumed zero.

To verify the results of the joint input-state estimation algorithm, the estimated forces are ideally compared to the directly measured input force. Although direct measurements of the pedestrian load are not available in this case, a reasonable approximation of the real walking load is obtained using a generalized single-step load model characterized by the weight of the person and the identified pacing rate [6]. The average step frequency ($\tilde{f}_s = 1.98$ Hz) and the onset of each step are identified from the tracked pedestrian motion [6]. The single-step walking load follows from previous research involving the same participant, whereby the ground reaction forces (GRFs) were measured directly by an instrumented split-belt treadmill [6]. The averaged vertical single-step walking load for a step frequency of 2.00 Hz was determined from more than 200 consecutive steps. The variations in amplitude of the single-step walking load resulting from small variations of the pacing rate (e.g. $1.98 < f_s < 2.00$ Hz) are found to be negligible [7]. Moreover, the resulting forces and structural response are found to be much more sensitive to the timing of successive footfalls than to small variations in force amplitude or contact time of the single-step walking load [8]. Together, the averaged vertical single-step walking load ($\mathrm{p}_s$) and the identified onset of each step in time ($t_q$), allow to reconstruct the force $\mathrm{p}_q$ due to step $q$ in time:

$$\mathrm{p}_q(t) = \kappa\left(t - t_q\right)\mathrm{p}_s\left(t - t_q\right), \qquad \text{with} \quad \kappa\left(t\right) = \begin{cases} 1 & 0 \le t \le t_c \\ 0 & \text{otherwise} \end{cases} \tag{44.1}$$

with $t$ [s] the general time of the experiment and $t_c$ the duration of contact between the foot and the supporting structure. Taking into account the identified location of each step and the mass-normalized mode shape, the modal load induced by the pedestrian is calculated.

Figure 44.2 compares the numerically predicted modal load and individual foot traces with the results of the joint input-state estimation algorithm. Both the comparison in time (Fig. 44.2a) and frequency domain (Fig. 44.2b) show a fairly good agreement between the numerical predictions and the vibration-based estimated input. The harmonics of the walking load can be clearly observed in the corresponding amplitude spectrum (see Fig. 44.2b).

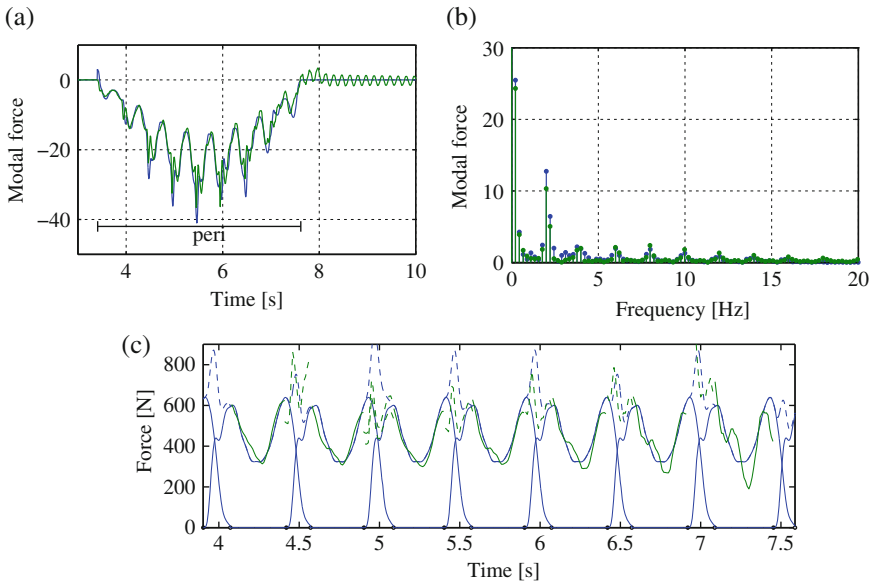


**Fig. 44.2** Comparison between the identified (*green*) and simulated (*blue*) modal load corresponding to fundamental bending mode of the slab: (**a**) time series and (**b**) amplitude spectrum of the peri phase (when the pedestrian is on the slab) and (**c**) the reconstructed foot traces

## 44.4 Conclusions

This contribution uses a state-of-the-art inverse force identification technique to reconstruct the pedestrian-induced load from the resulting vibrational response and a dynamic model of the structure. The experimental study involves a simply-supported concrete slab with a length of 7 m excited by a single pedestrian. The results of the joint input-state estimation algorithm are verified by comparison with the numerically predicted modal load. A good agreement is found between the estimated modal load and the corresponding numerical predictions.

**Acknowledgements** The first author is a post-doctoral fellow of the Research Foundation Flanders (FWO). The financial support is gratefully acknowledged.

## References

1. Georgakis, C., Ingólfsson, E.: Recent advances in our understanding of vertical and lateral footbridge vibrations. In: Proceedings of the 5th International Footbridge Conference, London, July (2014)
2. Bruno, L., Venuti, F.: Crowd-structure interaction in footbridges: modelling, application to real case-study and sensitivity analysis. J. Sound Vib. **323**, 475–493 (2009)
3. Živanović, S.: Benchmark footbridge for vibration serviceability assessment under vertical component of pedestrian load. J. Struct. Eng. **138**, 1193–1202 (2012)
4. Maes, K., Van Nimmen, K., Lourens, E., Rezayat, A., Guillaume, P., De Roeck, G., Lombaert, G.: Verification of joint input-state estimation for force identification by means of in situ measurements on a footbridge. Mech. Syst. Signal Process. **75**, 245–260 (2016)
5. Van Nimmen, K., Maes, K., Van den Broeck, P., De Roeck, G., Lombaert, G.: Inverse identification of pedestrian-induced loads. In: Sas, P., Moens, D., Denayer, H. (eds.) Proceedings of ISMA 2016 International Conference on Noise and Vibration Engineering, Leuven, Sept (2016)
6. Van Nimmen, K., Lombaert, G., Jonkers, I., De Roeck, G., Van den Broeck, P.: Characterisation of walking loads by 3D inertial motion tracking. J. Sound Vib. **333**, 5212–5226 (2014)
7. Racić, V., Pavić, A., Reynolds, P.: Experimental identification and analytical modelling of walking forces: a literature review. J. Sound Vib. **326**, 1–49 (2009)
8. Middleton, C.: Dynamic performance of high frequency floors. PhD thesis, University of Sheffield (2009)